EVALUATING MECHANISM OF METASTASIS OF PROSTATE CANCER TO BONE USING 3D BONE MIMETIC TISSUE ENGINEERED SCAFFOLDS

A Dissertation
Submitted to the Graduate Faculty
of the
North Dakota State University
of Agriculture and Applied Science

By

MD Shahjahan Molla

In Partial Fulfillment of the Requirements
for the Degree of
DOCTOR OF PHILOSOPHY

Major Program:
Materials and Nanotechnology

December 2018

Fargo, North Dakota

North Dakota State University
Graduate School

Title

EVALUATING MECHANISM OF METASTASIS OF PROSTATE CANCER TO BONE USING 3D BONE MIMETIC TISSUE ENGINEERED SCAFFOLDS

By

MD Shahjahan Molla

The Supervisory Committee certifies that this ***disquisition*** complies with North Dakota State University's regulations and meets the accepted standards for the degree of

DOCTOR OF PHILOSOPHY

SUPERVISORY COMMITTEE:

Kalpana. S. Katti
Chair

Dinesh R. Katti

Achintya Bezbaruah

Sanku Mallik

Approved:

02/19/2019
Date

Erik Hobbie
Department Chair

ABSTRACT

The complex nature of cancer metastasis necessitates the development of a cancer model based on specific metastatic stages. In this dissertation, we report a polymer-nanoclay based in vitro tumor model which recapitulates early stage of prostate cancer skeletal metastasis. A unique cell culture system termed as 'sequential culture' has been applied to create a bone-mimetic niche for colonization of prostate cancer cells. Sequentially cultured MDA PCa 2b cells with MSCs formed self-organized multicellular tumoroids with distinct tight cellular junctions and hypoxic core regions. Further, the sequentially cultured PC-3 cell formed multicellular tumoroid like clusters. We performed immunocytochemical confocal microscopy, qRT-PCR, ELISA assays, nanomechanical evaluation and SEM imaging to characterize our tumor model. We observed that in the in vitro model that MSCs differentiated to matured osteoblasts, EMT (epithelial to mesenchymal transition) was inhibited, MET was enhanced, and hypoxia increased angiogenesis when prostate cancer cells were sequentially cultured with MSCs. We also studied the effect of prostate cancer metastasis on bone microenvironment using different prostate cancer cell lines. We found that the less metastatic MDA PCa 2b cells inhibited mineralized collagen formation whereas, highly metastatic PC-3 cells enhanced mineralized collagen formation. All the experimental results indicated osteoblastic bone formation by PC-3 cells and osteolytic bone resorption by MDA PCa 2b cells.

Cancer metastasis is a complex process requiring dramatic remodeling of the cell cytoskeleton. Bone metastasis is characterized by complex biochemical, morphological, pathophysiological, and genetic changes to cancer cells as they colonize at remote bone sites. These changes can be captured in sum by changes to nanomechanical properties of cancer cells during metastasis. Using a specially designed nanoindentation apparatus, we observed significant

softening of prostate cancer cells during MET and then further softening during the disease progression at the metastatic site. We observed a substantial reduction in elastic modulus of prostate cancer cells during MET arising from actin reorganization and depolymerization. This is the first study that reveals changes to nanomechanical characteristics of prostate cancer cells with correlation to cytoskeletal changes during MET and progression of the disease at the metastatic bone site.

ACKNOWLEDGMENTS

First and foremost, I would like to express my deepest gratitude to my advisor and co-advisor, Dr. Kalpana Katti and Dinesh Katti, for their continuous guidance, encouragement, and motivation. I appreciate their contributions of time, ideas, and funding to make my Ph.D. experience dynamic and worthwhile. The joy and enthusiasm they have for their research was contagious and motivational for me. I am also thankful for the excellent example they have provided as outstanding researchers and teachers. I would also like to thank my thesis committee members, Prof. Achintya Bezbaruah, and Prof. Sanku Mallik, for sharing their precious advice and insights.

I would like to acknowledge NDSU grand challenges grant for "Center for Engineered Cancer Test-Beds" for supporting my research work. The SEM experiments performed in this dissertation work are made possible through instrumentation obtained using MRI grant from the National Science Foundation. The electron microscopy experiments discussed in this dissertation would not have been possible without the sincere help of Scott Payne and Jayma Moore. I thank them for helping this project with scanning electron microscopy and transmission electron microscopy. I would like to thank Dr. Tao Wang, manager of core biology facility at NDSU, for helping to perform qRT PCR and western blotting experiments. I would acknowledge Dr. Pawel Borowicz, Director of NDSU Advanced Imaging and Microscopy (AIM) Core Lab, and Jordan Flaten, for helping to perform immunostaining and confocal microscopy. Support from ND EPSCoR for tissue engineering laboratory is also acknowledged. ND EPSCoR and the National Science Foundation (NSF) is also acknowledged for awarding me the "Doctoral Dissertation Fellowship."

Also, I thank Jan Lofberg and Milka Singha for being helpful and supportive to me in many aspects during my graduate studies. I acknowledge Department of Civil and Environmental for hiring me as a teaching assistant/ research assistant and giving me financial support.

The members of the Dr. Katti's Research Group have contributed immensely to my personal and professional time at NDSU. The group members have been a source of friendships as well as professional advice and collaboration. The past and present group members that I have had the pleasure to work with or alongside of are Avinash Ambre, Anurag Sharma, Chunju Gu, Him Upadhyay, Mohammad Reza Parsa, Keshab Thapa, Sumanta Kar, Krishna Kundu, Nasrullah Faisal, and Haneesh Jasuja.

Finally, and most importantly, I would like to thank my family for all their love and encouragement, especially my mother (Momena Begum) who raised me with a love of education and supported me in all my pursuits. I would like to express gratitude to my wife Dr. Nujhat Fatima for unconditional love and support.

DEDICATION

This dissertation is lovingly dedicated to my mother, Momena Begum. Her encouragement, support, and constant love have sustained me throughout my life.

TABLE OF CONTENTS

LIST OF TABLES

LIST OF FIGURES

LIST OF ABBREVIATIONS

NCI.....National cancer institute.

MSCs.....Mesenchymal Stem Cells.

SC.....Sequential Culture.

hFOB.....Human Osteoblast cells.

PCa.....Prostate cancer.

ADT .....Androgen Deprivation Therapy.

CAR-T.....Chimeric Antigen Receptor-T Cell.

EMT .....Epithelial to Mesenchymal Transition.

MET .....Mesenchymal to Epithelial Transition.

ECM.....Extracellular Matrix.

VEGF .....Vascular Endothelial Growth Factor.

HIF1 .....Hypoxia Inducible Factor-1.

IL-8 .....Interleukin 8.

Snail1 .....Zinc Finger Protein.

Twist1 .....Twist-related protein 1.

HAP.....Hydroxyapatite.

PCL .....Polycaprolactone.

2D.....Two Dimensional.

3D.....Three Dimensional.

PCN.....Polymer Clay Nanocomposites.

Na-MMT .....Sodium Montmorillonite.

MMT.....Montmorillonite.

FTIR.....Fourier Transform Infrared.

AFM.....Atomic Force Microscopy.

SEM .....Scanning Electron Microscopy.

FESEM.....Field-Emission Scanning Electron Microscopy.

TEM .....Transmission Electron Microscopy.

ChiPgA.....Chitosan-Polygalacturonic Acid.

hMSCs.....Human Mesenchymal Stem Cells.

BM-ECM .....Bone Marrow-Derived Extracellular Matrix.

PSA .....Prostate-Specific Antigen.

TFM .....Traction Force Microscopy.

PCR.....Polymerase chain reaction.

qRT .....Quantitative Reverse Transcription.

HPCC .....Human Prostate Cancer Cells.

PEG.....Polyethylene Glycol.

PLA .....Polylactic Acid.

PBS .....Phosphate Buffer Saline.

ALP .....Alkaline Phosphatase.

ELISA .....Enzyme-Linked Immunosorbent Assay.

RUNX2 .....Runt-Related Transcription Factor 2.

PSMA.....Prostate-Specific Membrane Antigen.

RANKL.....Receptor Activator Nuclear Factor KappaB Ligand.

GAPDH.....Glyceraldehyde 3-Phosphate Dehydrogenase.

DHT .....Dihydrotestosterone.

FGFR2.....Fibroblast Growth Factor Receptor 2.

OPG.....Osteoprotegerin.

ET-1 .....Endothelin-1.

CC .....Coculture.

TGF .....Transforming Growth Factor.

FGF .....Fibroblast Growth Factor.

PTHrP .....Parathyroid Hormone-Related Protein.

DAPI .....4′,6-Diamidino-2-Phenylindole.

PCA SC.....Sequential Culture of MDA PCa 2b with MSCs.

PC-3 SC .....Sequential Culture of PC-3 with MSCs.

OCN .....Osteocalcin.

OPN.....Osteopontin.

MMP .....Matrix Metallopeptidase.

DKK-1.....Dickkopf-Related Protein 1.

COL1a1.....Collagen, type I, alpha 1.

WASp.....Wiskott–Aldrich Syndrome protei.

Arp 2/3 .....Actin-Related Protein 2/3.

CDC42 .....Cell Division Control Protein 42.

L-D.....Load-Displacement.

LIST OF APPENDIX FIGURES

CHAPTER 1. INTRODUCTION

1.1. Prostate cancer background

According to the National Cancer Institute (NCI), cancer is a complex disease in which cells in the body begin to divide and grow uncontrollably and are able to invade to surrounding tissues. Cells in nearly any part of the body can become cancerous and are capable of spreading to the other parts of the body. The basic unit of body, cells, grow by dividing in a controlled way, and apoptosis or cell death occurs when cells are old and damaged. Sometimes the regular cell cycle may be affected by the genetic mutation, and after a certain period of time, instead of dying, cells form new cells. In this way, an extra mass of tissues, called tumor is formed. Cancer cells are capable of invading, migrating through and colonizing on a distant organ [1]. The cancer cells which spread away from their place of origin are known as metastatic cancer and the process through which cancer cells invade a distant organ is known as metastasis. Further, 90% of the cancer-associated deaths are attributed to metastasis, yet in cancer pathogenesis, the mechanism of cancer metastasis remains obscure [1, 2].

Prostate cancer (PCa) starts when cells in the prostate gland begin to grow without control. The prostate is a gland which is found only in males. It makes the fluid which is part of semen. The seminal vesicles, a gland just behind the prostate, make the most of the fluid for semen. The urethra, carrier of urine and semen out of the body through the penis, goes through the center of the prostate. The gland prostate is in front of the rectum and below the bladder. With age, the size of the prostate gland changes. A newborn has a prostate size of ~1.4 mL and the average size of the prostate of an 80-92 years old male is ~37 mL [3].

Prostate cancers are primarily adenocarcinomas. Almost all prostate cancers are adenocarcinomas, a type of tumors that formed from glandular structures in epithelial tissue. But it also could be sarcoma (originates from connective tissue), small cell carcinoma, neuroendocrine tumors or transitional cell carcinoma. It is very rare to have these other types of prostate cancer. Prostate cancer grows slowly, but in some instances can grow and spread quickly as well. [4]. Carcinogenesis in the prostate is thought to progress over the course of years from an initial deleterious event in the DNA of prostate epithelial cells. Various factors can contribute to prostate cancer evolution have been identified including age, race, diet, inflammation, and genetics [5]. It has been reported that various genetic changes can introduce prostate cancer development in various in vivo models [6, 7]. Although many human gene homologs manipulated in animal models are found to be disturbed in human cancers, there is often an unclear relationship between the role of genetic changes in animal models and the connection to human prostate carcinogenesis.

According to the National Cancer Institute (NCI), in 2018 the estimated new cases of prostate cancer is 164,690, and the estimated number of deaths is 29,430 [8]. Based on 2011-2015 cases and deaths, the number of new cases and deaths of prostate cancer was 112.6, and 19.5 per 100,000 men per year respectively [8]. Based on 2013-2015 data, approximately 11.2% of men will be diagnosed with prostate cancer at some point during their lifetime [8]. In the United States alone, an estimated 3,120,176 men were living with prostate cancer in 2015 [8]. According to the NCI, the percentage of prostate cancer deaths is highest among men aged between 75-84 and black men have the highest incidence of prostate cancer. Considerable diaparity exists in the incidence and cure of prostate cancer among various populations [8]. The 5-year survival for localized and regional prostate cancer is 100.0%, but for the distant stage, it is

only 30.0% [8]. According to a report by Negoita et al., the incidence of distant-stage disease increased from 2010 to 2014 [9]. However, they have also reported that overall prostate cancer incidence rates declined approximately 6.5% per year from 2007 [9].

1.2. Current state in therapeutic-treatment for prostate cancer

The general course of treatment for the patients, who are diagnosed with the initial stage prostate cancer, is radiation treatment, surgical resection or cryotherapy. These treatments are often effective in inhibiting the cancer progression and are usually used one at a time. However, in some cases they could be combined to treat prostate cancer patients. Typically, men older than 75 years do not undergo surgery or radiation and men younger than 65 years are most likely to be treated with radical prostatectomy with or without radiotherapy [10]. The most common type of surgery for prostate cancer is a radical prostatectomy. In a radical prostatectomy, the entire prostate gland plus some of the tissue around it, including the seminal vesicles are removed from the patients' body [11]. High energy wavess or particles are used to kill cancer cells in radiation therapy. In cryotherapy which is also known as cryosurgery or cryoablation, freezing temperatures are used to destroy prostate cancer cells. Active supervision rather than immediate treatment is commonly recommended for older men or men who have less aggressive tumors. If the prostate cancer metastasizes or progresses beyond the initial stage, chemotherapy, hormone therapy, bone-directed therapy (such as zoledronic acid or denosumab), radiation, vaccine treatment, CAR-T cell therapy or a combination of these treatments are used [12-14]. At the distant stage prostate cancer is a very aggressive disease and effective therapeutic treatments are only palliative. Hormone therapy which is also known as androgen deprivation therapy (ADT) or androgen suppression therapy, is used to reduce the level androgens in the body or to stop them

from affecting prostate cancer cells [15]. However, it is useful for only androgen-dependent prostate cancer cells. Anti-cancer drugs are injected into a vein or given by mouth in chemotherapy. Chemotherapy is used for advanced stages of prostate cancer when androgen deprivation therapy (ADT) does not work. Recent studies have also shown that chemo is helpful if given along with androgen deprivation therapy [16]. Some of the chemo drugs that are used to treat prostate cancer patients include Docetaxel, Cabazitaxel, Mitoxantrone, and Estramustine. Some vaccines are used to treat prostate cancer patients. These vaccines boost the immune system to attack the prostate cancer cells unlike traditional vaccines, which mainly play a preventive role [17]. However, there is no evidence to date that this techniques to treat advanced-stage prostate cancer contributes to reduced mortality [18]. The lack of effective therapeutic techniques for the treatment of prostate cancer patients is a severe issue in the current clinical regimen, and therefore, there is a critical need for better understanding of prostate cancer metastasis and more appropriate therapeutic strategies.

1.3. Cancer metastasis

Cancer cells are capable of invading, migrating through and colonizing on a distant organ [2]. The cancer cells which spread away from its place of origin are known as metastatic cancer, and the process through which cancer cells invade a distant organ is known as metastasis. 90% of the cancer-associated deaths are attributed to metastasis, yet in cancer pathogenesis, the mechanism of it remains obscure [1, 19, 20].

A complex metastatic cascade is involved in the dissemination of cancer cells to the distant organ. It includes the sequence of phases: local invasion, intravasation, circulation, arrest and extravasation, proliferation and angiogenesis [21, 22].

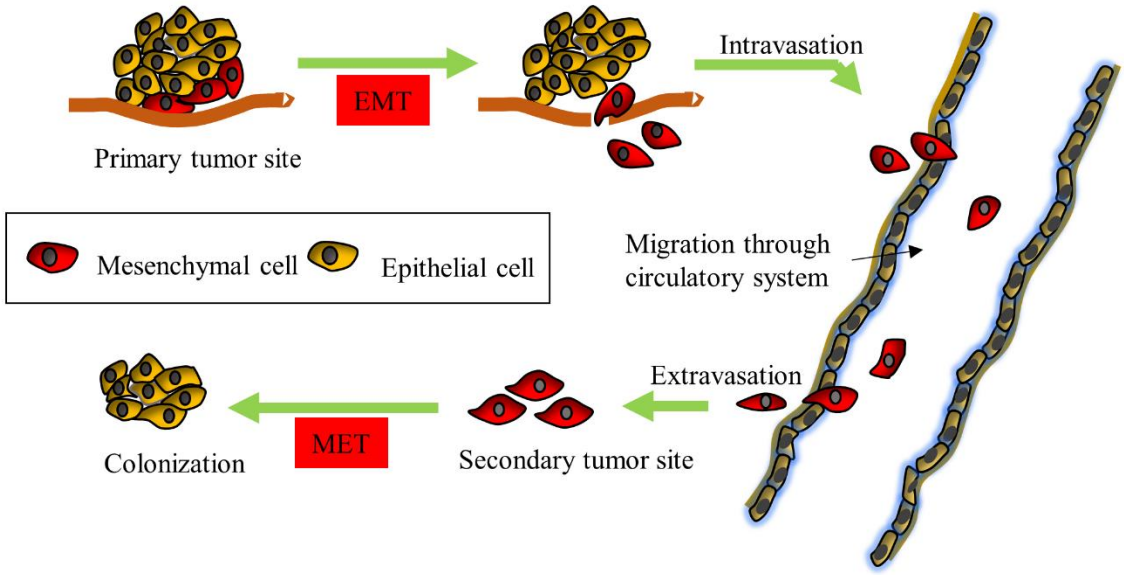

Figure 1.1. Multistep process of prostate cancer metastasis. It includes the sequence of phases: local invasion, intravasation, circulation, extravasation, and colonization. Initially, single cells or clumps of cancer cells leave the primary tumor to invade the local stroma and ECM (extracellular matrix). At this time cancer cells undergo a unique phenotypic change called epithelial to mesenchymal transition (EMT). On the second step of metastatic cascade, cancer cells intravasate either into blood vessels or lymphatic system. They translocate through the bloodstream to the microvessels of a distant site, extravasate from the bloodstream, and the survived cells are arrested at a remote tissue and acclimate to the foreign microenvironment resulting in metastatic colonization.

A schematic description of the multistep process of prostate cancer metastasis is given in figure 1.1. Initially single or clumps of cancer cells leave the primary tumor to invade the local stroma and ECM (extracellular matrix). On the second step of metastatic cascade, cancer cells intravasate either into blood vessels or lymphatic system. They translocate in a raucous environment through the bloodstream to the microvessels of a distant site, extravasate from the bloodstream and survived cells become arrested at a distant tissue [23]. On the new site cancer cells must acclimate to the foreign microenvironment to prevail. In metastatic colonization step cancer cells proliferate to form micrometastases which hereafter disrupt the vessel wall [24]. Through the angiogenesis process, a network of blood vessel penetrates into this cancerous growth to supply nutrients and oxygen and to remove waste products [22]. The efficient

completion of all these stages would result in metastasis and the formation of a lesion at a distant site which is known as a secondary tumor. Metastasis is paradoxically considered to be an inefficient process since it has been estimated that less than 0.01% intravaseted cancer cells can efficiently form secondary tumor at a distant site [25].

1.4. Epithelial to mesenchymal transition (EMT) and mesenchymal to epithelial transition (MET)

Two very significant events take place during the complex cascade of metastasis including epithelial to mesenchymal transition (EMT) and mesenchymal to epithelial transition (MET) where cell phenotype changes between epithelial to mesenchymal state and vice-versa [21]. The epithelium exist in a vertebrate from the very beginning by itself, whereas mesenchyme as the second tissue type that evolved and developed from preexisting epithelia through a phenotypic conversion known as epithelial-mesenchymal transition (EMT). EMT was first depicted as a distinct morphological process in 1982 by Greenburg et al. [26]. EMT is a process when epithelial cells lose many of their epithelial features and simultaneously acquire the typical traits of mesenchymal cells in response to a specific set of extracellular stimuli. During EMT several molecular and structural alteration occurs in epithelial cells including change in cell-cell contacts, loss of apical-basal polarity, loss of cell-cell tight junctions, cytoskeletal reorganization, dissolution of the basement membrane, elongated cell shape with filopodia on basal sites, and invasion through the basement membrane. Contrarily, mesenchymal cells are also capable of converting to epithelial cells under certain prospects through a process known as mesenchymal to epithelial transition (MET), which is a reverse process of EMT. Contrarily, mesenchymal cells are also capable of converting to epithelial cells under certain

prospects through a process known as mesenchymal to epithelial transition (MET), which is a reverse process of EMT. During MET, mesenchymal cells lose their mesenchymal features followed by gaining of epithelial traits [27]. Mesenchymal cells undergo a series of events during MET, including gaining of apical-basal polarity, an aggregation of previously disbanded mesenchymal cells, reorganization of cytoskeletal features, deposition of basement membrane [28]. EMT at the primary tumor location and MET at the site of a secondary tumor during the initial stage of colonization have generated a lot of interest as both have the potential of an effective drug target [29]. Considering the critical roles they play in metastasis, understanding the molecular mechanism of EMT and MET offers new hope for inhibiting tumor formation and developing anti-cancer therapeutics. EMT is viewed as an essential early step in tumor metastasis [30]. Transcription factors like Snail1, Twist1, vimentin is greatly associated with EMT process which prompted to use them as EMT biomarkers [31-33]. E-Cadherin has a crucial role both in EMT and MET. Silencing or switching of E-Cadherin to N-cadherin during EMT and significant expression of E-Cadherin during MET are two significant features that have been revealed about EMT and MET respectively [34]. Expression of transcriptional factors like Snail, Twist, and Vimentin are other major hallmarks for EMT [35]. Another area of intense focus is angiogenesis or new blood vessel formation during colonization of disseminated cancer cells on the site of metastases [36]. Proangiogenic factors like VEGF, IL-8, and HIF-1 encourage the growth and colonization of prostate cancer cells on bone microenvironment to aid skeletal dissemination.

1.5. Bone metastasis of prostate cancer

Cancer metastasis is a complex multistage process which consists of a series of sequential, interrelated steps. The intrinsic properties of cancer cells and the response of the host

both influence the fate of the metastasized cancer cells [37]. It has been long accepted that each type of malignant cancer cells exhibit a characteristic preference for an organ-specific pattern of metastasis. For example, prostate cancer cells preferentially metastasize to bone, and colon cancer cells metastasize to liver and lung but rarely to the bone. This specific development of secondary tumors at distant organ requires the effective completion of a number of steps by metastasizing tumor cells. Now the question is why and how some tumor cells exhibit an organ-specific predilection for metastasis. A number of hypotheses have been proposed for the organ selectivity of cancer metastases, including secretion of organ derived chemoattractant [38], tumor cell surface characteristics [39], response to specific host tissue growth factors [40], and adhesion between tumor cells and the distant organ components [41]. The current concept that tumor cells metastasize to those organs of which microenvironment is advantageous for their growth is not new. In 1889, Stephen Paget, the English surgeon, answered the question, "What is it that decides what organs shall suffer in a case of disseminated cancer?" in his report titled "Distribution of secondary growths in cancer of the breast" [42]. He examined the autopsy reports of 735 breast cancer patients and was surprised by the inconsistency between the relative blood supply and the recurrence of metastasis in some organs. Proposing the everlasting "seed and soil" principle Paget commented that "remote organs cannot be altogether passive or indifferent regarding embolism," and "When a plant goes to seed, its seeds are carried in all directions; but they can only live and grow if they fall on congenial soil." Paget's so-called seed and soil theory suggest that the organ-specific metastasis of tumor cells does not happen accidentally, but it depends on the attraction of cancer cells (the seeds) for the target organ (the soil). This means that the metastasis is developed due to a specific cancer cell tropism towards a distant organ, and the fate of which depends on the molecular characteristics of cancer cells. The

study of the “soil” could be paramount to understand the mechanisms of the “seed” inducing cancer metastasis of a specific remote site.

Later, Paget’s seed and soil theory were challenged by Ewing (1928), proposing that organ-specific metastasis occurs due to the vascular system’s anatomy [43]. Ewing hypothesized that the preferential sites of metastasis are those organs that are sprayed and contains interconnected blood vessels to the primary site. In addition, the anatomic adjacency to a primary tumor site is also another factor influencing cancer metastasis. The two theories proposed by Paget and Ewing are not in contradictory but entirely correlative to each other.

The preferred site for prostate cancer metastasis is bone, with an incidence up to 90 % [34]. Other cancers, such as colon cancer and breast cancer also have been known to metastasis to bone. Bone metastasis leads to high morbidity caused by pain, pathologic fractures, hypercalcemia, and spinal cord compression as well as nerve root compression. Metastasized prostate cancer cells primarily target cancellous bones. Highly vascular structure of cancellous bone provides easy access to oxygen and nutrients for metastasized prostate cancer cells which creates a welcoming environment for colonization. Bone-forming osteoblasts and bone-resorbing osteoclast reside in the bone microenvironment that is responsible for creating a dynamic nature of bone. In normal bone, constant remodeling of old bone by osteoclast follows mineralized new bone formation by osteoblast. But when prostate cancer cells metastasize to bone, they cause either excessive bone degradation in the osteoclastic lesion or excessive bone regeneration in the osteoblastic lesion.

The leading cause of mortality and morbidity in prostate cancer is the skeletal dissemination of tumor cells. Nevertheless, the bone-metastatic mechanism in prostate cancer is not entirely understood. To prevent bone metastasis, it is crucial to target not only bone

metastatic features in the tumor cells but also tumor nurturing bone. In order to advance current therapies, the effect of metastasized cancer cells on bone microenvironment have to be better understood which needs reliable models able to mimic the biophysical processes occurring in patients.

1.6. Why we need 3D in vitro model

2D cultures are widely used for the maintenance of cells and the biological experiments. Monolayer cultures are convenient and easy to use with high cell viability. However, petri dish culture lacks the realistic complexity of 3D microenvironment of intrinsic tissue and hence impose highly unnatural mechanical and geometric constraints on cells [44]. Bone microenvironmental condition is naturally three-dimensional which controls cancer formation [45, 46]. 2D petri dish culture lacks anatomical architecture and thus encounter severe transport limitations. In 2D substrates, cells exhibit tight junctions, rapid growth, monolayer structure, poor differentiation capability, non-optimal physiological responses and intense physical contact with a substrate which results in altered tumor cell behavior. When cells are cultured on solid 2D substrates such as coverslips or tissue culture treated polymer plastics, nutrition incorporated by the cells are mostly from the basolateral surface comparable to the surface near blood supply; therefore, cells with tight cellular junctions do not obtain proper nutrition when cultured on Petri dishes causing the cells to exhibit partially dedifferentiated and depolarized phenotype [47]. It has also been reported that cells grown in monolayer exhibit unusual organization and cell shape, malignant cell-like inappropriate growth-rates, and the failure to express tissue-specific genetic and molecular features [48].

In vivo models have been widely used in biological studies for growth and progression as well as for therapeutic purposes. Human xenograft models [49], chemically induced mouse model [50], transgenic mouse model [51], are few in vivo models that have been used extensively. Genetically modified rodent models earned popularity over other models because of their ability to manipulate molecular features and provide apparently perfect models for investigating cancer and effects of anti-cancer drugs [52]. However, it has been reported that in vivo model can appropriately mimic the initial stages of cancer development and metastasis [52]. In most of the in vivo models used in the biotechnological industries, human xenografts are placed subcutaneously into the rodents which lack the necessary host-tumor interactions. Orthotopic transplantations have been used to overcome the limitations of subcutaneous transplantations, where human tumors are injected in the physiologically relevant area of the animals [53]. For instance, in the case of prostate cancer, the xenograft would be placed in the prostate of the rodent model to recapitulate the prostate tumor development in humans. Some other limitations that are associated with in vivo models are lack of control over the malignant cell microenvironment, and Other challenges encountered while using in vivo models are the lack of control over the tumor microenvironment and adversity in real-time micrography [54].

In vitro 3D models overcome many of the difficulties and limitations associated with animal experimentations and monolayer cultures. It bridges the gap between animal models and petri dish culture. It defeats the disadvantages related to in vivo models by avoiding host immune complexity. 3D in vitro models are reproducible, cost-effective and reliable for statistical analysis. Moreover, there is an ethical issue associated with animal models. The disease development and pathology of human may not be accurately represented in animal models due to species differences [55]. In addition, in vitro 3D models have uncovered new data associated

with cellular phenotypic changes, cell-cell signaling, angiogenesis, chemoresistance, cell-matrix interaction, tumor-microenvironment interaction [56-60].

1.7. Bone

Bone is a hard connective tissue that constitutes the major component of almost all vertebral skeleton. Cytoskeleton appears to be nonliving. In fact, the root of the word skeleton is derived from the Greek word κύτοςσκελετός which means ‘dried up’. Bone is a living structure which is composed of living cells and tissues, blood vessels, organic and inorganic materials. Vertebrate skeleton protects and supports the internal soft organs of the body. For instance, the rib bones safeguard hearts and lung; the skull protects the brain. Bone produces specific white blood cells, platelets, and red blood cells. It provides a structural framework for mobility. Bone stores minerals like calcium which is necessary for the activity of muscle and nerve cells. It provides a surface for muscles attachment. Bone is a dense connective tissue which has a honeycomb-like internal matrix. The rigidity of a bone comes from this dense tissue of mineralized matrix. The major organic component of the bone matrix is mineralized extracellular matrix collagen whereas, the various salts (mostly calcium phosphate in the chemical arrangement termed hydroxyapatite) make up the inorganic portion of the bone matrix.

Collagen, mineral, and water are the three primary components of bone as shown by chemical analysis. The weight of human cortical bone typically consists of 60% hydroxyapatite, 20% type I collagen, 9% water and 11% salts and noncollagenous protein [61]. At maturity, the human body is made up of 206 bones, which account for 14 percent of the body’s total weight [61]. The strongest and largest bone in the body is the thigh-bone or femur which is about 20

inches long and 1 inch wide in an adult human. The smallest is the stapes, one of the three tiny bones in the middle ear which is only .07 inch long.

1.8. Structure of bone

Components of are assembled in a unique hierarchical structure at many length scales which work in a specific pattern to perform various chemical, mechanical, and biological functions; such as protection and storage, healing cells, structural support, storage of minerals and ion homeostasis. Hierarchical materials are consist of structural components which themselves have recognizable structure. The scale has vital importance in discussing bone architecture as the structure is complicated and hierarchical. Different techniques of assessing structural properties of bone have its own resolution, and therefore a combination of these methods is required to reveal the structural features of bone at the many different length scales. Bone has been described in terms of up to 6 hierarchical levels of organization from nanoscale collagen to macroscale femur bone. The hierarchical structure of bone is described at following levels:

- Level 1: Collagen fibrils and minerals (nanometer scales)
- Level 2: Mineralized fibril (sub-micron scale)
- Level 3: Fibrillar arrays (micro-scale)
- Level 4: Fibrillar array patterns (micro-scale)
- Level 5: Osteon (micro-scale)
- Level 6: Whole bone (mesoscale)

The hierarchical structure of bone is depicted in figure 1.2. Bone is separated into the compact (cortical) and trabecular (cancellous) types at the macro-structure level. Compact bone

is solid, with the only porosity for osteocyte lacunae, canaliculi, erosion cavities, and blood vessels. Trabecular bone has a porosity which is easily visible to the naked eye. Typically, the bone matrix that has a porosity less than 25% is considered to be compact, and if or more is trabecular [62]. Microstructurally, there is no difference between normal compact and trabecular bones.

The primary structural unit of cortical bone is osteon which as also known as Harversian system (figure 1.2b). The parallel layers of lamellae surround the Haversian canal in the osteons. The Haversian canal which is parallel to the long axis of the bone, contains the blood vessels bone's nerves. Between adjacent Harversian system, there are angular intervals that are occupied by interstitial lamellae.

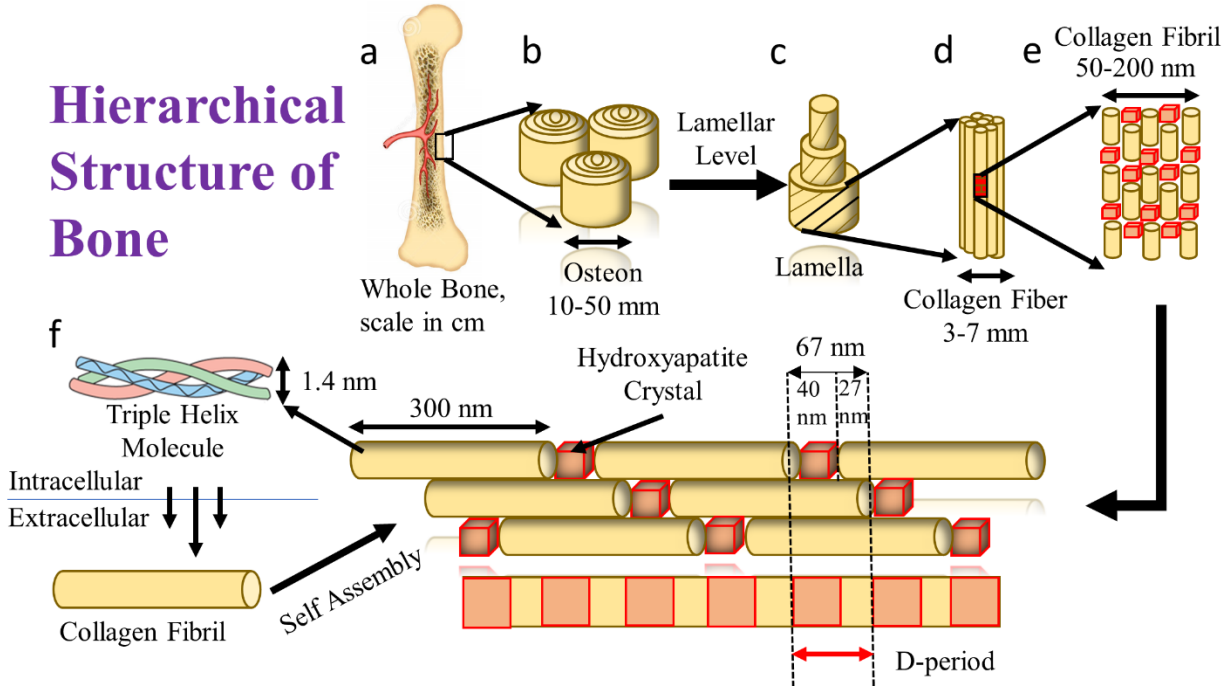

Figure 1.2. Hierarchical organization of a human bone from macro- to the nanoscale. (a) Macrostructure-human bone. (b) submacro structure-osteon. (c) Micro structure-lamellae (d) Meso structure-fiber bundle. (e) Nanostructure-mineralized fibril. (f) Molecular structure-collagen molecule and mineral particle.

The thickness of bone lamellae is 3–7 μm (figure 1.2c) [63]. Collagen fibers are arranged parallelly in each lamella with a different orientation pattern of fibrils. Four of the most common

patterns of fibril orientation in a lamella includes parallel fibrils array, woven fibrils array, plywood-like structure array, and radial fibril arrays [64].

The mineralized fibrils are self-assembled into fiber bundles along their length and the bundles may fuse with neighboring bundles. The way mineralized fibrils are aligned in a fiber bundle has gained a lot of attention since it leads to a significant variation in the mechanical properties of bone. Two different orientations of fibrils have been proposed. In both of the orientations, mineralized fibrils are aligned with respect to fibril axes. In one of the orientations, fibrils are also aligned with respect crystal layers [64].

The single collagen fibrils are 50-200 nm [65]. Collagen molecules are self-arranged into the fibril in a staggered arrangement (figure 1.2e). At extracellular space type I collagen molecules pack together side-by-side, forming fibrils with a diameter of roughly 50-200 nm. The saturated calcium and phosphate ions secreted by osteoblasts precipitate into hydroxyapatite crystals which are cemented to this collagen fibril. . The saturated calcium and phosphate ions secreted by osteoblasts precipitate into hydroxyapatite crystals which are cemented to this collagen fibril. In collagen fibrils, adjacent collagen molecules are displaced from one another by 67 nm, about one-quarter of their length produces a characteristic pattern of bands of length 67 nm. D-period of collagen fibrils is divided into two sections, overlap and gap, where the overlap is around 27nm, and the gap is 40nm.

Almost 90% of total organic components of bone are made of type I collagen molecules also known as triple helices (figure 1.2f). Triple helices consist of three polypeptide chains having supercoiled assemblies of two identical α1- chains and one α2-chain, each with over 1000 amino acid residues. The cylindrical shaped triple helical molecules have an average diameter of ~1.5nm, and lengths of 300nm.

1.9. Tissue engineering

Tissue engineering, a continuously expanding interdisciplinary field, involves materials science, cell biology, bio-physiology, mechanobiology, bioengineering, biomedical engineering, and clinical research, with the aim of creating new tissues and organs. The term tissue engineering is closely related to the applications that repair or replace part of or the whole tissues (i.e., skin, cartilage, bone, blood vessels, bladder, muscle, etc.). Tissue engineering gained significant popularity in the early 1990s when Robert Langer et al. distinctly described it as a surrogate approach having advantages over traditional techniques to treat tissue defects and associating combined use of cells, 3D scaffolds and growth factors for regeneration of tissue and organ [66, 67]. Cell culture based tissue engineering usually related to the use of a multi-component engineered biomaterials in the form of 3D porous scaffolds, living cells, and growth factors [68, 69]. A schematic diagram depicting the concept of bone tissue engineering developed by Katti et al. is shown in figure 1.3 [70]. In a traditional approach, cells are harvest (progenitor cells, stem cells, mesenchymal stem cells) from a patient, which would be expanded in 2D tissue culture treated Petri dishes, cultured on a 3D biomaterial scaffold, and differentiated through specific culture conditions into the targeted tissue, then implanted into the patient. Studies in the field of tissue engineering and regenerative medicine have shown rapid progress, expansion, and development due to the recognition of its vast potential over the years for other therapeutic applications and as a platform for studying various diseases. Traditional treatment techniques to regenerate tissue defects such as allografts, autografts, xenografts, and metallic implants are thought to have drawbacks. As an alternative for grafts and transplants, tissue engineering intends to culture living tissue in vitro for implantation.

The critical components of tissue engineering are 3D scaffolds, cells and growth factors. Each of these components has been the origin of several vital research interest in the interdisciplinary field of tissue engineering. Biomaterial 3D scaffolds and mesenchymal stem cells have been the primary focus of a considerable number of studies over the course of progression of tissue engineering since the early 1990s, and these interdisciplinary studies have laid the basis for the evaluation of tissue engineering concepts beyond tissue regeneration. The studies reported in this dissertation deal with the use of polymer composite scaffolds for bone tissue engineering. Studies in this dissertation are related to interactions of human prostate cancer cells (MDA PCa 2b and PC-3) with bone tissue-engineered 3D porous scaffolds that have been developed using nanoclay, hydroxyapatite, polymer, and human osteoblasts, human mesenchymal stem cells (MSCs).

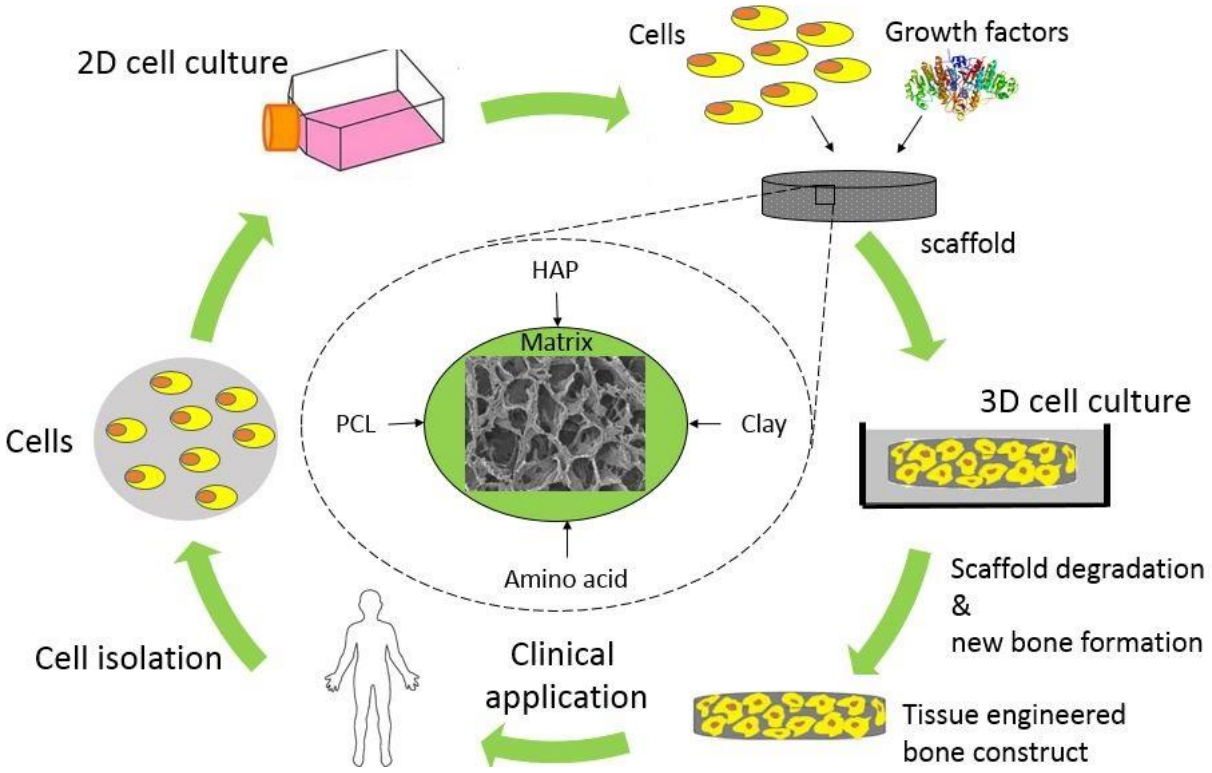

Figure 1.3. Schematic depicting the concept of bone tissue engineering.

1.10. Background of bone tissue engineered PCL/nanoclay scaffold system

Studies in this dissertation involve the use of 3D porous PCL/nanoclay scaffold system for the tissue engineered prostate cancer model. Use of nanoclay in polymer composites for the enhancement of mechanical properties is not new. In 1990, Okada et al. of Toyota research group, reported the improvement of mechanical properties by adding clay on nylon-6 polymer composite [71]. Ever since numerous studies have reported the effect of the addition of nanoclay on biodegradability [72], flammability [73, 74], and permeability [75, 76], of polymer nanoclay composites (PCNs) besides the dramatic improvement in mechanical properties [77]. In 2008, our research group proposed the groundbreaking 'altered phase model' of PCN composite which describes the mechanism associated with the enhancement of mechanical properties in polymer clay nanocomposites (PCNs) [78]. Some experimental [79, 80] and simulation [81-83] studies led this 'altered phase model' of PCNs according to which the volume of the polymer is significantly influenced by molecular level interactions between the components of PCNs that leads to an alteration in the crystallinity of the polymer in the altered zone around the intercalated clay particles [78].

The ability of Na-MMT clay of reinforcing PCNs led to the use of Na-MMT clay as a component of polymer-based scaffolds in tissue engineering. Previous studies by our research group have shown that intercalated Na-MMT clay influence the polymer crystallinity and nanomechanical characteristics [84, 85]. Our research group has also demonstrated that the ability of Na-MMT clay to affect the nanomechanical properties can be useful to influence cellular nature and the cells are reactive to the mechanical cues from their surrounding microenvironment [85-87]. Other factors that influenced the use of Na-MMT clays in the design and development of 3D porous scaffold system for bone tissue engineering by our research group

includes its ability to degrade polymeric structure under physiological condition, use of it in drug delivery and drug release applications [88, 89], medicinal use of it in health conditions (like diarrhea, ulcers, and hyperthyroidism) [90], and its ability to be excreted from the body [91].

Previous studies in the group used unnatural amino acids to modify the Na-MMT clay, and this modified MMT clay was further characterized using experimental techniques including Fourier Transform Infrared (FTIR) spectroscopy and X-ray diffraction [92]. Results of this study suggested that 5-aminovaleric acid is most effective to intercalate the Na-MMT clay and use of modified Na-MMT clay for biomaterial application. Our research group used Na-MMT clay modified with 5-aminovaleric acid in the chitosan-polygalacturonic acid (ChiPgA) bipolymer composite scaffolds. The suitability of nanoclay-ChiPgA scaffolds for bone tissue engineering applications was investigated [93]. Chitosan and polygalacturonic acid both have been reported as excellent biocompatible materials for tissue engineering [94, 95]. To enhance the osteoconductivity and osteoinductivity of polymer clay composite (PCN) scaffolds, hydroxyapatite (major extracellular components of bone) was biomineralized in 5-aminovaleric acid clay using a processing route the to obtain a novel three-component nanoclay-hydroxyapatite hybrid (in situ HAPclay) [86, 96-98]. Comprehensive biological assays and imaging experiments performed by our research group suggested that human mesenchymal stem cells undergo osteoblastic differentiation in the scaffolds containing HAPclay without the use of osteogenic supplements [86]. When MSCs cultured in this scaffolds, vesicles containing crystalline calcium minerals were found to be emerged from MSCs and deposited in the extra cellular space [165]. Ca/P ratio in this vesicles lower than the stoichiometric Ca/P ratio of HAP indicates new bone formation and remodeling of bone. Further, in our research group polycaprolactone (PCL), a synthetic polymer was used instead of chitosan and polygalacturonic

acid to design the HAPclay 3D porous scaffold [99]. PCL provides immense prospects for tissue engineering applications as it exhibits lesser complexities as compared to biopolymers like chitosan.

1.11. Tissue-engineered 3D metastatic cancer models

Considerable efforts have been made to recapitulate prostate cancer microenvironment as preclinical models by including the elements from primary tumors into ex vivo culture environment which causes the disease progression in a manner that better mimics cancer development. Tissue-engineered 3D models are an excellent preclinical platform to investigate the crosstalk between and cancer cells bone microenvironment [56, 60, 100]. Heroon et al. reported a 3D culture approach to study the interaction between bone and metastatic prostate cancer cells where they used a transwell based system [101]. The transwell system was composed of adipocytes in 3D collagen I gel and reconstituted basement membrane-overlayed prostate cancer cells spheroids. Curtin et al. developed and utilized a 3D bone-cancer metastasis model where they used the free-floating live mouse calvarial bones in the presence of prostate cancer cells in a roller tube system [102]. Fitzgerald et al. studied the cancer bone interaction using three different collagen-based 3D scaffolds (scaffolds containing either glycosaminoglycan or nanohydroxyapatite in two different concentration) [103]. In that study, they used the 3D in vitro model for the delivery of gene therapeutics to the prostate cancer cells. In a separate study, Fitzgerald et al. co-cultured human osteoblasts with prostate cancer cells in collagen-nanohydroxyapatite scaffolds in order to enhance the efficacy of the bone mimicking in vitro model [104]. Fang et al. reported a 3D co-culture model, using double layered alginate hydrogel microspheres to incorporate prostate cancer cell and stromal cells [105]. In a study, Florczyk et

al. reported chitosan-alginate (CA) based 3D porous scaffolds for culturing human prostate cancer (PCa) cells and studying tumor cell interaction with human peripheral blood lymphocytes ex vivo [106]. Wang et al. also reported the use of 3D chitosan-alginate based scaffolds with prostate cancer cells and confirmed the efficacy of these for long-term culture and 3D spheroid formation that mimicked in vivo morphologies [107]. Kwon et al. utilized 3D silk to investigate the metastasis of prostate cancer to bone [108]. They cultured PC-3 cells in 3D silk scaffolds which enabled the prostate cancer cells to behave like in vivo undergoing cell invasion and migration into the engineered bone (silk scaffold) as like to bone metastasis. Kwon et al. hypothesized that in 3D silk scaffolds PC-3 cells underwent osteomimicry which enabled them to behave like osteoblast to enhance bone formation in the tissue-engineered bone microenvironment [108]. Salamanna et al. explored an in vitro 3D cancer-bone metastasis model bu culturing human prostate cancer cells with human bone tissue isolated from male patients [59]. The bone tissue collected from total hip replacement surgery was grown in a rolling apparatus system in a hypoxic and normoxic condition. By performing gene-expression, protein level, histological, and immunocytochemical analysis, they exhibited that prostate cancer cells have a distinct specificity for bone colonization and ingrowth [59]. To enhance the understanding the of the mechanism underlying prostate cancer bone metastasis, Lescarbeau et al. developed a tissue-engineered in vitro model incorporating human mesenchymal stem cells (hMSCs), and bone marrow-derived extracellular matrix (BM-ECM) to investigate the biological significance of hMSCs and BM-ECM in the process of the disease progression [109]. In that study, Lescarbeau et al. used LNCaP and MDA PCa 2b cell line to mimic many features observed in prostate cancer patients which could provide a platform for mechanistic in vitro experiments.

One of the significant limitations of these prior studies was the use of cell line for bone tissue engineering and culture techniques. Currently, there are no in vitro bone metastasis models that used human MSCs to generate bone tissue initially then seeded prostate cancer cells sequentially. Studies in this dissertation cultured human prostate cancer cells sequentially with human mesenchymal stem cells in an osteoconductive and osteoinductive 3D porous scaffold system where MSCs underwent osteoblastic differentiation without osteogenic supplements.

One of the most crucial components of an in vitro cancer model is the cell lines being utilized. Dozens of prostate cancer cell lines across a variety of malignancies have been developed for preclinical studies [110]. These cell lines vary in many of their properties including their origin, phenotype, invasiveness, malignancy, proliferative rate, genetic background, etc. Studies in this dissertation utilized PC-3 and MDA PCa 2b cell lines to explore the differences in cell lines on various outcomes. MDA PCa 2b cells are androgen sensitive, express prostate-specific antigen (PSA) and noninvasive in nature [111]. PC-3 cells are invasive, castration-resistant and do not express androgen receptors and prostate-specific antigen (PSA) [112]. Both of the cell lines are derived from bone metastasis.

1.12. Bio-nanomechanics of cells

Living cells in human body, as physical entities, possess structural and physical properties and constantly subjected to mechanical stimulations throughout life. It has been shown that cellular functions such as growth, differentiation, migration, apoptosis, motility, gene expression, signal transduction, wound healing, etc. are influenced by cellular biophysics and biomechanics [113-118]. Any changes of these biophysical or biomechanical properties of human cells may interrupt regular physiological functions of cells and may lead to diseases. For

example, when red blood cells are affected by malaria-causing bacteria, Plasmodium falciparum, the molecular and structural properties of red blood cells are significantly compromised [118-121]. Biomechanical properties of individual cells can influence the physio-structural properties of whole tissue by interacting with extracellular matrix as well as mechanical stress on the whole tissue can be transmitted to the cellular level compromising their physiological functions significantly [122]. Other than disease causing virus and bacteria, many chemicals are also known to have an effect on mechanical properties of human cells. For instance, latrunculin B cytochalasin D have an adverse effect on the cytoskeletal structure of the cells [123-125]. Chemotactic agent fMLP significantly increases the stiffness of neutrophils [126, 127]. The primary structural element of cytoskeleton actin filament and microtubules are affected by colchicine [128-130].

The past few decades has seen a substantial growth of the research in the field of biomechanical properties of cells. Various methods have been applied to determine the biophysical properties of cells [131-133]. But it is still a challenge to study the nanomechanics of single cell considering dynamic nature of cells during progression of different diseases [134-136].

With the advent of nanotechnology, it has now become feasible to probe cellular mechanics at single cell level. For instance, biophysical techniques such as micropipette aspiration [125, 137-140], optical tweezers [141-143], cell stretchers [144-147], flow rheometry [138, 147-149], magnetic bead cytometry [150, 151], traction force microscopy (TFM) [152, 153], atomic force microscopy (AFM) [154-157], micropillar arrays [158] and nanoindentation [87, 159-164], have been used extensively in the past decade to probe mechanical properties of various cell types. Of these above-mentioned techniques, a majority have been employed to

apply controlled force to the cells (micropipette aspiration, optical tweezers, cell stretchers, flow rheometry, magnetic bead cytometry, AFM, and nanoindentation, while the rest are used to monitor the cells' ability to deform itself by intracellular forces (TFM, and micropillar arrays) to obtain their mechanical properties.

AFM Force curves has been widely used for evaluating nanomechanical properties of cells. Using AFM-based nanomechanical analysis cross et al. demonstrated that cancer cell stiffness is 70–80% less than that of normal cells [171]. Lekke et al. performed AFM nanoindentation on normal and cancerous human bladder cells showing that normal cells are stiffer than their cancerous counterparts [166]. In another study they found a strong correlation between the reduction of glycolytic activity and the increase stiffness using the bladder cancer cells treated with chitosan [167]. Using AFM nanoindentation, Li et al. compared the elastic modulus of a normal breast cancer cell line (MCF10A) with a cancerous breast cancer cell line (MCF7) and found that cancerous MCF-7 is significantly softer as compared to MCF10A [168]. Faria et al. investigated nanomechanical properties of 3 prostate cancer cell line using AFM analysis [169]. They found that normal prostate cancer cell line (BPH) possess higher elastic modulus as opposed to cancerous prostate cancer cell lines (LNCaP and PC-3). In another AFM based study, Bastatas et al. evaluated nanomechanical characteristics of highly metastatic prostate cancer cells (CL-1/ CL-2) and non-metastatic cells (LNCaP) [170]. And they found highly metastatic cells are stiffer as compared to non-metastatic cells. The authors concluded that stiffer response from highly metastatic prostate cancer cells are regulated by actin dynamics. Hayashi et al. also used AFM indentation method to investigate the mechanical properties of cancer cells [172]. They compared normal human cervical cells (End1/E6E7) with cancerous human cervical cells (HeLa) and concluded that HeLa cells are significantly softer than the E6E7

cells. Zhou et al. also demonstrated similar results using human cervical squamous carcinoma cells (CaSki) and normal cervical epithelial cells (CRL2614) [173]. Using AFM force curve, Li et al. investigated the mechanical properties of blood cells and aggressive cancer cells and also concluded that aggressive cancer cells are softer than normal cells [174].

1.13. Research objectives

The specific objectives of the current research are as follows:

1. To create a physiologically relevant prostate cancer model that mimics the bone microenvironment for metastasized prostate cancer and ultimately which could be useful for therapeutic studies.
2. To study the interaction between prostate cancer cells and bone microenvironment using the nanoclay/polymer-based 3D scaffolds that have been developed in our research group.
3. To evaluate the effect of the sequential culture (SC) culture, a novel cell culture technique, on prostate cancer cells utilizing gene expression analysis, immunocytochemistry, electron microscopies and cellular assays.
4. To study the effect of using mesenchymal stem cells instead of human osteoblast in the sequential culture with prostate cancer cells.
5. To investigate the effect of metastasized prostate cancer cells on bone mineralization and extracellular matrix formation.
6. To evaluate the alteration in nanomechanical properties of prostate cancer cells during mesenchymal to epithelial transiotion (MET) and during the disease progression using nanoondentation experiments on live cells.

7. To investigate the chenges in prostate cancer cell cytoskeletal during the disease progression using immunocytochemical analysis and qRT-PCR experiments.
8. To establish a correlation between cytoskeletal changes and alteration in nanomechanical characteristics of prostate cancer cells during the disease progression.

1.14. Organization of this dissertation

This dissertation is organized into different chapters as follows:

1. Chapter 1. It initially provides a brief background of prostate cancer and and a brief overview of current state in therapeutic-treatment for prostate cancer. Then it shortly describes the mechanism of cancer metastasis, detailed EMT and MET process and bone metastasis of prostate cancer. Then it describes the previous works done in our research group to design and develop the HAPclay/PCL 3D scaffolds for bone tissue engineering. Then a brief literature survey is presented on concurrent in vitro 3D bone metastasis models of prostate cancer. It also gives brief overview on nanomechanics of cells.
2. Chapter 2. It describes the formation of 3D tumoroids in the sequential culture based in vitro model.
3. Chapter 3. This chapter describes the mimicking of mesenchymal to epithelial transition (MET) of prostate cancer cells in an in vitro 3D model using the cell line MDA PCa 2B.
4. Chapter 4. This chapter describes the mimicking of mesenchymal to epithelial transition (MET) of prostate cancer cells in an in vitro 3D model using the cell line PC-3.
5. Chapter 5. This chapter describes the effects of metastasized prostate cancer cells on bone mineralization and extra cellular matrix formation.

6. Chapter 6. This chapter describes biomechanics of cells as potential biomarkers for cancer and principle of nanoindentation.
7. Chapter 7. This chapter describes the nanomechanical and cytoskeletal alterations in prostate cancer cells during the progression of the disease.

1.15. References

[1] C.L. Chaffer, R.A. Weinberg, A Perspective on Cancer Cell Metastasis, Science 331(6024) (2011) 1559-1564.

[2] S. Pranav, J.A. Kelber, J.W. Lee, T.N. Wright, K.S. Vecchio, R.L. Klemke, S.C. Chen, Cancer cell migration within 3D layer-by-layer microfabricated photocrosslinked PEG scaffolds with tunable stiffness, Biomaterials 33(29) (2012) 7064-7070.

[3] S.-J. Xia, X.-X. Xu, J.-B. Teng, C.-X. Xu, X.-D. Tang, Characteristic pattern of human prostatic growth with age, Asian journal of andrology 4(4) (2002) 269-272.

[4] B.F. Hankey, E.J. Feuer, L.X. Clegg, R.B. Hayes, J.M. Legler, P.C. Prorok, L.A. Ries, R.M. Merrill, R.S. Kaplan, Cancer surveillance series: interpreting trends in prostate cancer—part I: evidence of the effects of screening in recent prostate cancer incidence, mortality, and survival rates, Journal of the National Cancer Institute 91(12) (1999) 1017-1024.

[5] E. Giovannucci, Y. Liu, E.A. Platz, M.J. Stampfer, W.C. Willett, Risk factors for prostate cancer incidence and progression in the health professionals follow-up study, International journal of cancer 121(7) (2007) 1571-1578.

[6] J. Kim, M. Roh, I. Doubinskaia, G.N. Algarroba, I.A. Eltoum, S.A. Abdulkadir, A mouse model of heterogeneous, c-MYC-initiated prostate cancer with loss of Pten and p53, Oncogene 31(3) (2012) 322.

[7] Q. Lei, J. Jiao, L. Xin, C.-J. Chang, S. Wang, J. Gao, M.E. Gleave, O.N. Witte, X. Liu, H. Wu, NKX3. 1 stabilizes p53, inhibits AKT activation, and blocks prostate cancer initiation caused by PTEN loss, Cancer cell 9(5) (2006) 367-378.

[8] N. Howlader, A.M. Noone, M. Krapcho, D. Miller, K. Bishop, C.L. Kosary, M. Yu, J. Ruhl, Z. Tatalovich, A. Mariotto, SEER cancer statistics review, 1975–2014. Bethesda, MD: National Cancer Institute; 2017, 2017.

[9] S. Negoita, E.J. Feuer, A. Mariotto, K.A. Cronin, V.I. Petkov, S.K. Hussey, V. Benard, S.J. Henley, R.N. Anderson, S. Fedewa, Annual report to the nation on the status of cancer, part II: recent changes in prostate cancer trends and disease characteristics, Cancer (2018).

[10] K.D. Miller, R.L. Siegel, C.C. Lin, A.B. Mariotto, J.L. Kramer, J.H. Rowland, K.D. Stein, R. Alteri, A. Jemal, Cancer treatment and survivorship statistics, 2016, CA: a cancer journal for clinicians 66(4) (2016) 271-289.

[11] H.J. Jewett, The present status of radical prostatectomy for stages A and B prostatic cancer, The Urologic clinics of North America 2(1) (1975) 105-124.

[12] H.I. Scher, K. Fizazi, F. Saad, M.-E. Taplin, C.N. Sternberg, K. Miller, R. de Wit, P. Mulders, K.N. Chi, N.D. Shore, Increased survival with enzalutamide in prostate cancer after chemotherapy, New England Journal of Medicine 367(13) (2012) 1187-1197.

[13] T.M. Beer, A.J. Armstrong, D.E. Rathkopf, Y. Loriot, C.N. Sternberg, C.S. Higano, P. Iversen, S. Bhattacharya, J. Carles, S. Chowdhury, Enzalutamide in metastatic prostate cancer before chemotherapy, New England Journal of Medicine 371(5) (2014) 424-433.

[14] M.D. Molina, Abiraterone and Increased Survival in Metastatic Prostate Cancer, (2011).

[15] M. Bolla, L. Collette, L. Blank, P. Warde, J.B. Dubois, R.-O. Mirimanoff, G. Storme, J. Bernier, A. Kuten, C. Sternberg, Long-term results with immediate androgen suppression and

external irradiation in patients with locally advanced prostate cancer (an EORTC study): a phase III randomised trial, The Lancet 360(9327) (2002) 103-108.

[16] T. Gilligan, P.W. Kantoff, Chemotherapy for prostate cancer, Urology 60(3) (2002) 94-100.

[17] H.L. Kaufman, W. Wang, J. Manola, R.S. DiPaola, Y.-J. Ko, C. Sweeney, T.L. Whiteside, J. Schlom, G. Wilding, L.M. Weiner, Phase II randomized study of vaccine treatment of advanced prostate cancer (E7897): a trial of the Eastern Cooperative Oncology Group, Journal of Clinical Oncology 22(11) (2004) 2122-2132.

[18] D.E. Drachenberg, Treatment of prostate cancer: watchful waiting, radical prostatectomy, and cryoablation, Wiley Online Library, pp. 37-44.

[19] C.L. Chaffer, J.P. Brennan, J.L. Slavin, T. Blick, E.W. Thompson, E.D. Williams, Mesenchymal-to-epithelial transition facilitates bladder cancer metastasis: role of fibroblast growth factor receptor-2, Cancer Res 66(23) (2006) 11271-8.

[20] C.L. Chaffer, E.W. Thompson, E.D. Williams, Mesenchymal to epithelial transition in development and disease, Cells Tissues Organs 185(1-3) (2007) 7-19.

[21] I.J. Fidler, The pathogenesis of cancer metastasis: the 'seed and soil' hypothesis revisited, Nature reviews. Cancer 3(6) (2003) 453.

[22] P.S. Steeg, Tumor metastasis: mechanistic insights and clinical challenges, Nature medicine 12(8) (2006) 895.

[23] S. Valastyan, R.A. Weinberg, Tumor metastasis: molecular insights and evolving paradigms, Cell 147(2) (2011) 275.

[24] A.B. Al-mehdi, K. Tozawa, A.B. Fisher, L. Shientag, A. Lee, R.J. Muschel, A.B. Al-Mehdi, Intravascular origin of metastasis from the proliferation of endothelium-attached tumor cells: a new model for metastasis, Nature medicine 6(1) (2000) 100.

[25] I.J. Fidler, Metastasis: quantitative analysis of distribution and fate of tumor emboli labeled with 125I-5-iodo-2′-deoxyuridine, Journal of the National Cancer Institute 45(4) (1970) 773-782.

[26] G. Greenburg, E.D. Hay, Epithelia suspended in collagen gels can lose polarity and express characteristics of migrating mesenchymal cells, The Journal of cell biology 95(1) (1982) 333-339.

[27] A. Moustakas, C.H. Heldin, Signaling networks guiding epithelial–mesenchymal transitions during embryogenesis and cancer progression, Cancer science 98(10) (2007) 1512-1520.

[28] E.D. Hay, An overview of epithelio-mesenchymal transformation, Cells Tissues Organs 154(1) (1995) 8-20.

[29] A. Singh, J. Settleman, EMT, cancer stem cells and drug resistance: an emerging axis of evil in the war on cancer, Oncogene 29(34) (2010) 4741-4751.

[30] S.A. Mani, W. Guo, M.-J. Liao, E.N. Eaton, A. Ayyanan, A.Y. Zhou, M. Brooks, F. Reinhard, C.C. Zhang, M. Shipitsin, The epithelial-mesenchymal transition generates cells with properties of stem cells, Cell 133(4) (2008) 704-715.

[31] A. Barrallo-Gimeno, M.A. Nieto, The Snail genes as inducers of cell movement and survival: implications in development and cancer, Development 132(14) (2005) 3151-3161.

[32] M.G. Mendez, S.-I. Kojima, R.D. Goldman, Vimentin induces changes in cell shape, motility, and adhesion during the epithelial to mesenchymal transition, The FASEB Journal 24(6) (2010) 1838-1851.

[33] J. Yang, S.A. Mani, J.L. Donaher, S. Ramaswamy, R.A. Itzykson, C. Come, P. Savagner, I. Gitelman, A. Richardson, R.A. Weinberg, Twist, a master regulator of morphogenesis, plays an essential role in tumor metastasis, cell 117(7) (2004) 927-939.

[34] L. Bubendorf, A. Schöpfer, U. Wagner, G. Sauter, H. Moch, N. Willi, T.C. Gasser, M.J. Mihatsch, Metastatic patterns of prostate cancer: an autopsy study of 1,589 patients, Human pathology 31(5) (2000) 578-583.

[35] S. Casimiro, T.A. Guise, J. Chirgwin, The critical role of the bone microenvironment in cancer metastases, Molecular and Cellular Endocrinology 310(1–2) (2009) 71-81.

[36] S.-m. Käkönen, G.R. Mundy, S.-M. Käkönen, Mechanisms of osteolytic bone metastases in breast carcinoma, Cancer 97(3 Suppl) (2003) 834.

[37] G. Poste, I.J. Fidler, The pathogenesis of cancer metastasis, Nature 283(5743) (1980) 139.

[38] E.S. Hujanen, V.P. Terranova, Migration of tumor cells to organ-derived chemoattractants, Cancer research 45(8) (1985) 3517-3521.

[39] A. Raz, R. Lotan, Endogenous galactoside-binding lectins: a new class of functional tumor cell surface molecules related to metastasis, Cancer and Metastasis Reviews 6(3) (1987) 433-452.

[40] G.L. Nicolson, K.M. Dulski, Organ specificity of metastatic tumor colonization is related to organ-selective growth properties of malignant cells, International journal of cancer 38(2) (1986) 289-294.

[41] G.L. Nicolson, Cancer metastasis: tumor cell and host organ properties important in metastasis to specific secondary sites, Biochimica et Biophysica Acta (BBA)-Reviews on Cancer 948(2) (1988) 175-224.

[42] S. Paget, Distributionof secondarygrowthsin cancerof the breast, Lancet, I 571 (1989).

[43] J. Ewing, A treatise on tumors, Neoplastic disease (1928).

[44] A. Birgersdotter, R. Sandberg, I. Ernberg, Gene expression perturbation in vitro—a growing case for three-dimensional (3D) culture systems, Elsevier, pp. 405-412.

[45] M.J. Bissell, D. Radisky, Putting tumours in context, Nature Reviews Cancer 1(1) (2001) 46-54.

[46] M.J. Bissell, P.A. Kenny, D.C. Radisky, Microenvironmental regulators of tissue structure and function also regulate tumor induction and progression: the role of extracellular matrix and its degrading enzymes, Cold Spring Harbor symposia on quantitative biology 70 (2005) 343.

[47] M.M.P. Zegers, L.E. O'Brien, W. Yu, A. Datta, K.E. Mostov, Epithelial polarity and tubulogenesis in vitro, Trends in cell biology 13(4) (2003) 169-176.

[48] M.J. Bissell, Glandular Structure and Gene Expression: Lessons from the Mammary Glanda, Annals of the New York Academy of Sciences 842(1) (1998) 1-6.

[49] T. Voskoglou-Nomikos, J.L. Pater, L. Seymour, Clinical predictive value of the in vitro cell line, human xenograft, and mouse allograft preclinical cancer models, Clinical Cancer Research 9(11) (2003) 4227-4239.

[50] S. Wirtz, C. Neufert, B. Weigmann, M.F. Neurath, Chemically induced mouse models of intestinal inflammation, Nature protocols 2(3) (2007) 541.

[51] A.A. Hurwitz, B.A. Foster, E.D. Kwon, T. Truong, E.M. Choi, N.M. Greenberg, M.B. Burg, J.P. Allison, Combination immunotherapy of primary prostate cancer in a transgenic mouse model using CTLA-4 blockade, Cancer Research 60(9) (2000) 2444-2448.

[52] T. Van Dyke, T. Jacks, Cancer modeling in the modern era: progress and challenges, Cell 108(2) (2002) 135-144.

[53] M.C. Bibby, Orthotopic models of cancer for preclinical drug evaluation: advantages and disadvantages, European journal of cancer 40(6) (2004) 852-857.

[54] K.M. Yamada, E. Cukierman, Modeling Tissue Morphogenesis and Cancer in 3D, Cell 130(4) (2007) 601-610.

[55] Á. González, C. García de Durango, V. Alonso, B. Bravo, A. Rodríguez de Gortázar, A. Wells, J. Forteza, F. Vidal-Vanaclocha, Distinct Osteomimetic Response of Androgen-Dependent and Independent Human Prostate Cancer Cells to Mechanical Action of Fluid Flow: Prometastatic Implications, The Prostate 77(3) (2017) 321-333.

[56] S. Talukdar, S.C. Kundu, Engineered 3D Silk-Based Metastasis Models: Interactions Between Human Breast Adenocarcinoma, Mesenchymal Stem Cells and Osteoblast-Like Cells, Advanced Functional Materials 23(42) (2013) 5249-5260.

[57] S.D. Kundu, K.A. Roehl, X. Yu, J.A.V. Antenor, B.K. Suarez, W.J. Catalona, Prostate Specific Antigen Density Correlates With Features of Prostate Cancer Aggressiveness, The Journal of Urology 177(2) (2007) 505-509.

[58] P. Hesami, B.M. Holzapfel, A. Taubenberger, M. Roudier, L. Fazli, S. Sieh, L. Thibaudeau, L.S. Gregory, D.W. Hutmacher, J.A. Clements, A humanized tissue-engineered in vivo model to dissect interactions between human prostate cancer cells and human bone, Clinical & experimental metastasis 31(4) (2014) 435-446.

[59] F. Salamanna, V. Borsari, S. Brogini, G. Giavaresi, A. Parrilli, S. Cepollaro, M. Cadossi, L. Martini, A. Mazzotti, M. Fini, An in vitro 3D bone metastasis model by using a human bone tissue culture and human sex-related cancer cells, Oncotarget 7(47) (2016) 76966.

[60] S.P. Pathi, D.D.W. Lin, J.R. Dorvee, L.A. Estroff, C. Fischbach, Hydroxyapatite nanoparticle-containing scaffolds for the study of breast cancer bone metastasis, Biomaterials 32(22) (2011) 5112-5122.

[61] D. Shier, J. Butler, R. Lewis, Human anatomy and physiology, McGraw-Hill Boston, MA, USA2001.

[62] H. Ou-Yang, E.P. Paschalis, A.L. Boskey, R. Mendelsohn, Chemical structure-based three-dimensional reconstruction of human cortical bone from two-dimensional infrared images, Applied spectroscopy 56(4) (2002) 419-422.

[63] G. Marotti, A new theory of bone lamellation, Calcified Tissue International 53(1) (1993) S47-S56.

[64] S. Weiner, H.D. Wagner, The material bone: structure-mechanical function relations, Annual Review of Materials Science 28(1) (1998) 271-298.

[65] M.P.E. Wenger, L. Bozec, M.A. Horton, P. Mesquida, Mechanical properties of collagen fibrils, Biophysical journal 93(4) (2007) 1255-1263.

[66] R. Langer, J.P. Vacanti, C.A. Vacanti, A. Atala, L.E. Freed, G. Vunjak-Novakovic, Tissue engineering: biomedical applications, Tissue engineering 1(2) (1995) 151-161.

[67] R.S. Langer, J.P. Vacanti, Tissue engineering: the challenges ahead, Scientific American 280(4) (1999) 86-89.

[68] P. Zorlutuna, N. Annabi, G. Camci-Unal, M. Nikkhah, J.M. Cha, J.W. Nichol, A. Manbachi, H. Bae, S. Chen, A. Khademhosseini, Microfabricated Biomaterials for Engineering 3D Tissues, Advanced Materials 24(14) (2012) 1782-1804.

[69] R.B. Berish, A.N. Ali, P.G. Telmer, J.A. Ronald, H.S. Leong, Translational models of prostate cancer bone metastasis, Nature Reviews Urology (2018) 1.

[70] D.R. Katti, A. Sharma, A.H. Ambre, K.S. Katti, Molecular interactions in biomineralized hydroxyapatite amino acid modified nanoclay: In silico design of bone biomaterials, Mater Sci Eng C Mater Biol Appl 46 (2015) 207-17.

[71] A. Okada, M. Kawasumi, A. Usuki, Y. Kojima, T. Kurauchi, O. Kamigaito, Synthesis and properties of nylon-6/clay hybrids, Polymer based molecular composites 171 (1990) 45-50.

[72] S. Sinha Ray, K. Yamada, M. Okamoto, K. Ueda, Polylactide-layered silicate nanocomposite: a novel biodegradable material, Nano Letters 2(10) (2002) 1093-1096.

[73] J.W. Gilman, Flammability and thermal stability studies of polymer layered-silicate (clay) nanocomposites1, Applied clay science 15(1-2) (1999) 31-49.

[74] J.W. Gilman, C.L. Jackson, A.B. Morgan, R. Harris, E. Manias, E.P. Giannelis, M. Wuthenow, D. Hilton, S.H. Phillips, Flammability properties of polymer− layered-silicate nanocomposites. Polypropylene and polystyrene nanocomposites, Chemistry of materials 12(7) (2000) 1866-1873.

[75] K. Yano, A. Usuki, A. Okada, T. Kurauchi, O. Kamigaito, Synthesis and properties of polyimide–clay hybrid, Journal of Polymer Science Part A: Polymer Chemistry 31(10) (1993) 2493-2498.

[76] K. Yano, A. Usuki, A. Okada, Synthesis and properties of polyimide-clay hybrid films, Journal of Polymer Science Part A: Polymer Chemistry 35(11) (1997) 2289-2294.

[77] C. Viseras, C. Aguzzi, P. Cerezo, A. Lopez-Galindo, Uses of clay minerals in semisolid health care and therapeutic products, Applied Clay Science 36(1-3) (2007) 37-50.

[78] D. Sikdar, S.M. Pradhan, D.R. Katti, K.S. Katti, B. Mohanty, Altered phase model for polymer clay nanocomposites, Langmuir 24(10) (2008) 5599-5607.

[79] D. Sikdar, D. Katti, K. Katti, B. Mohanty, Effect of organic modifiers on dynamic and static nanomechanical properties and crystallinity of intercalated clay–polycaprolactam nanocomposites, Journal of applied polymer science 105(2) (2007) 790-802.

[80] D. Sikdar, D.R. Katti, K.S. Katti, B. Mohanty, Influence of backbone chain length and functional groups of organic modifiers on crystallinity and nanomechanical properties of

intercalated clay-polycaprolactam nanocomposites, International Journal of Nanotechnology 6(5-6) (2009) 468-492.

[81] K.S. Katti, D. Sikdar, D.R. Katti, P. Ghosh, D. Verma, Molecular interactions in intercalated organically modified clay and clay–polycaprolactam nanocomposites: experiments and modeling, Polymer 47(1) (2006) 403-414.

[82] D. Sikdar, K.S. Katti, D.R. Katti, Molecular interactions alter clay and polymer structure in polymer clay nanocomposites, Journal of nanoscience and nanotechnology 8(4) (2008) 1638-1657.

[83] D. Sikdar, D.R. Katti, K.S. Katti, The role of interfacial interactions on the crystallinity and nanomechanical properties of clay–polymer nanocomposites: a molecular dynamics study, Journal of applied polymer science 107(5) (2008) 3137-3148.

[84] A.H. Ambre, K.S. Katti, D.R. Katti, Nanoclay based composite scaffolds for bone tissue engineering applications, Journal of Nanotechnology in Engineering and Medicine 1(3) (2010) 031013.

[85] A. Ambre, K.S. Katti, D.R. Katti, In situ mineralized hydroxyapatite on amino acid modified nanoclays as novel bone biomaterials, Materials Science and Engineering: C 31(5) (2011) 1017-1029.

[86] A.H. Ambre, D.R. Katti, K.S. Katti, Nanoclays mediate stem cell differentiation and mineralized ECM formation on biopolymer scaffolds, Journal of Biomedical Materials Research Part A 101A(9) (2013) 2644-2660.

[87] R. Khanna, K.S. Katti, D.R. Katti, Experiments in nanomechanical properties of live osteoblast cells and cell–biomaterial interface, Journal of Nanotechnology in Engineering and Medicine 2(4) (2011) 041005.

[88] T. Takahashi, Y. Yamada, K. Kataoka, Y. Nagasaki, Preparation of a novel PEG–clay hybrid as a DDS material: Dispersion stability and sustained release profiles, Journal of controlled Release 107(3) (2005) 408-416.

[89] A. des Rieux, V. Fievez, M. Garinot, Y.-J. Schneider, V. Préat, Nanoparticles as potential oral delivery systems of proteins and vaccines: a mechanistic approach, Journal of controlled release 116(1) (2006) 1-27.

[90] L.-H. Long, Y.-T. Zhang, X.-F. Wang, Y.-X. Cao, Montmorillonite adsorbs urea and accelerates urea excretion from the intestine, Applied Clay Science 46(1) (2009) 57-62.

[91] M.I. Carretero, Clay minerals and their beneficial effects upon human health. A review, Applied Clay Science 21(3-4) (2002) 155-163.

[92] K.S. Katti, A.H. Ambre, N. Peterka, D.R. Katti, Use of unnatural amino acids for design of novel organomodified clays as components of nanocomposite biomaterials, Philosophical Transactions of the Royal Society A: Mathematical, Physical and Engineering Sciences 368(1917) (2010) 1963-1980.

[93] A.H. Ambre, K.S. Katti, D.R. Katti, Nanoclay Based Composite Scaffolds for Bone Tissue Engineering Applications, Journal of Nanotechnology in Engineering and Medicine 1(3) (2010) 031013-031013.

[94] J.K.F. Suh, H.W.T. Matthew, Application of chitosan-based polysaccharide biomaterials in cartilage tissue engineering: a review, Biomaterials 21(24) (2000) 2589-2598.

[95] D. Verma, K.S. Katti, D.R. Katti, B. Mohanty, Mechanical response and multilevel structure of biomimetic hydroxyapatite/polygalacturonic/chitosan nanocomposites, Materials Science and Engineering: C 28(3) (2008) 399-405.

[96] D. Verma, K.S. Katti, D.R. Katti, Osteoblast adhesion, proliferation and growth on polyelectrolyte complex-hydroxyapatite nanocomposites, Philosophical Transactions of the Royal Society a-Mathematical Physical and Engineering Sciences 368(1917) (2010) 2083-2097.
[97] A. Ambre, K.S. Katti, D.R. Katti, In situ mineralized hydroxyapatite on amino acid modified nanoclays as novel bone biomaterials, Materials Science & Engineering C-Materials for Biological Applications 31(5) (2011) 1017-1029.
[98] A.H. Ambre, D.R. Katti, K.S. Katti, Biomineralized hydroxyapatite nanoclay composite scaffolds with polycaprolactone for stem cell-based bone tissue engineering, Journal of Biomedical Materials Research Part A (2014) n/a-n/a.
[99] A.H. Ambre, D.R. Katti, K.S. Katti, Biomineralized hydroxyapatite nanoclay composite scaffolds with polycaprolactone for stem cell-based bone tissue engineering, Journal of Biomedical Materials Research Part A 103(6) (2015) 2077-2101.
[100] B. Subia, T. Dey, S. Sharma, S.C. Kundu, Target Specific Delivery of Anticancer Drug in Silk Fibroin Based 3D Distribution Model of Bone–Breast Cancer Cells, ACS applied materials & interfaces 7(4) (2015) 2269-2279.
[101] M.K. Herroon, J.D. Diedrich, I. Podgorski, New 3D-culture approaches to study interactions of bone marrow adipocytes with metastatic prostate cancer cells, Frontiers in endocrinology 7 (2016) 84.
[102] P. Curtin, H. Youm, E. Salih, Three-dimensional cancer-bone metastasis model using ex-vivo co-cultures of live calvarial bones and cancer cells, Biomaterials 33(4) (2012) 1065-1078.
[103] K.A. Fitzgerald, J. Guo, E.G. Tierney, C.M. Curtin, M. Malhotra, R. Darcy, F.J. O'Brien, C.M. O'Driscoll, The use of collagen-based scaffolds to simulate prostate cancer bone metastases

with potential for evaluating delivery of nanoparticulate gene therapeutics, Biomaterials 66 (2015) 53-66.

[104] K.A. Fitzgerald, J. Guo, R.M. Raftery, I.M. Castaño, C.M. Curtin, M. Gooding, R. Darcy, F.J. O'Brien, C.M. O'Driscoll, Nanoparticle-mediated siRNA delivery assessed in a 3D co-culture model simulating prostate cancer bone metastasis, International journal of pharmaceutics 511(2) (2016) 1058-1069.

[105] X. Fang, S. Sivanandane, K. Gyabaah, K.C. Balaji, Novel 3D co-cultural model for epithelial-stromal cells interaction in prostate cancer, AACR, 2013.

[106] S.J. Florczyk, G. Liu, F.M. Kievit, A.M. Lewis, J.D. Wu, M. Zhang, 3D porous chitosan–alginate scaffolds: a new matrix for studying prostate cancer cell–lymphocyte interactions in vitro, Advanced healthcare materials 1(5) (2012) 590-599.

[107] K. Wang, F.M. Kievit, S.J. Florczyk, Z.R. Stephen, M. Zhang, 3D Porous Chitosan–Alginate Scaffolds as an In vitro Model for Evaluating Nanoparticle-Mediated Tumor Targeting and Gene Delivery to Prostate Cancer, Biomacromolecules (2015).

[108] H. Kwon, H.J. Kim, W.L. Rice, B. Subramanian, S.H. Park, I. Georgakoudi, D.L. Kaplan, Development of an in vitro model to study the impact of BMP-2 on metastasis to bone, Journal of Tissue Engineering and Regenerative Medicine 4(8) (2010) 590-599.

[109] R.M. Lescarbeau, F.P. Seib, M. Prewitz, C. Werner, D.L. Kaplan, In vitro model of metastasis to bone marrow mediates prostate cancer castration resistant growth through paracrine and extracellular matrix factors, PloS one 7(8) (2012) e40372.

[110] A. van Bokhoven, M. Varella-Garcia, C. Korch, W.U. Johannes, E.E. Smith, H.L. Miller, S.K. Nordeen, G.J. Miller, M.S. Lucia, Molecular characterization of human prostate carcinoma cell lines, The Prostate 57(3) (2003) 205-225.

[111] N.M. Navone, M. Olive, M. Ozen, R. Davis, P. Troncoso, S.-M. Tu, D. Johnston, A. Pollack, S. Pathak, A.C. Von Eschenbach, Establishment of two human prostate cancer cell lines derived from a single bone metastasis, Clinical Cancer Research 3(12) (1997) 2493-2500.

[112] M.E. Kaighn, K.S. Narayan, Y. Ohnuki, J.F. Lechner, L.W. Jones, Establishment and characterization of a human prostatic carcinoma cell line (PC-3), Investigative urology 17(1) (1979) 16-23.

[113] C.S. Chen, M. Mrksich, S. Huang, G.M. Whitesides, D.E. Ingber, Geometric Control of Cell Life and Death, Science 276(5317) (1997) 1425.

[114] N. Boudreau, M.J. Bissell, Extracellular matrix signaling: integration of form and function in normal and malignant cells, Curr Opin Cell Biol 10(5) (1998) 640-6.

[115] S. Huang, D.E. Ingber, The structural and mechanical complexity of cell-growth control, Nat Cell Biol 1(5) (1999) E131-E138.

[116] M.A. Schwartz, M.H. Ginsberg, Networks and crosstalk: integrin signalling spreads, Nat Cell Biol 4(4) (2002) E65-E68.

[117] S. Suresh, Biomechanics and biophysics of cancer cells, Acta Materialia 55(12) (2007) 3989-4014.

[118] S. Suresh, J. Spatz, J.P. Mills, A. Micoulet, M. Dao, C.T. Lim, M. Beil, T. Seufferlein, Reprint of: connections between single-cell biomechanics and human disease states: gastrointestinal cancer and malaria, Acta biomaterialia 23 (2015) S3-S15.

[119] D.A. Fedosov, H. Lei, B. Caswell, S. Suresh, G.E. Karniadakis, Multiscale modeling of red blood cell mechanics and blood flow in malaria, PLoS Comput Biol 7(12) (2011) e1002270.

[120] B.M. Cooke, N. Mohandas, R.L. Coppel, The malaria-infected red blood cell: Structural and functional changes, Advances in Parasitology, Academic Press2001, pp. 1-86.

[121] L. Bannister, G. Mitchell, The ins, outs and roundabouts of malaria, Trends in Parasitology 19(5) (2003) 209-213.

[122] F. Guilak, V.C. Mow, The mechanical environment of the chondrocyte: a biphasic finite element model of cell-matrix interactions in articular cartilage, J Biomech 33(12) (2000) 1663-73.

[123] K. Nagayama, Y. Nagano, M. Sato, T. Matsumoto, Effect of actin filament distribution on tensile properties of smooth muscle cells obtained from rat thoracic aortas, Journal of Biomechanics 39(2) (2006) 293-301.

[124] T. Wakatsuki, B. Schwab, N.C. Thompson, E.L. Elson, Effects of cytochalasin D and latrunculin B on mechanical properties of cells, J Cell Sci 114(Pt 5) (2001) 1025-36.

[125] M. Sato, N. Ohshima, R.M. Nerem, Viscoelastic properties of cultured porcine aortic endothelial cells exposed to shear stress, Journal of Biomechanics 29(4) (1996) 461-467.

[126] G.I. Zahalak, W.B. McConnaughey, E.L. Elson, Determination of cellular mechanical properties by cell poking, with an application to leukocytes, J Biomech Eng 112(3) (1990) 283-94.

[127] G.S. Worthen, B. Schwab, 3rd, E.L. Elson, G.P. Downey, Mechanics of stimulated neutrophils: cell stiffening induces retention in capillaries, Science 245(4914) (1989) 183-6.

[128] M.A. Tsai, R.E. Waugh, P.C. Keng, Passive mechanical behavior of human neutrophils: effects of colchicine and paclitaxel, Biophys J 74(6) (1998) 3282-91.

[129] G.G. Borisy, E.W. Taylor, The mechanism of action of colchicine, The Journal of cell biology 34(2) (1967) 525-533.

[130] M. Imazio, A. Brucato, P. Ferrazzi, A. Pullara, Y. Adler, A. Barosi, A.L. Caforio, R. Cemin, F. Chirillo, C. Comoglio, Colchicine for prevention of postpericardiotomy syndrome and

postoperative atrial fibrillation: the COPPS-2 randomized clinical trial, Jama 312(10) (2014) 1016-1023.

[131] D. Stamenovic, J.J. Fredberg, N. Wang, J.P. Butler, D.E. Ingber, A microstructural approach to cytoskeletal mechanics based on tensegrity, J Theor Biol 181(2) (1996) 125-36.

[132] C.T. Lim, M. Dao, S. Suresh, C.H. Sow, K.T. Chew, Large deformation of living cells using laser traps, Acta Materialia 52(7) (2004) 1837-1845.

[133] D. Stamenovic, D.E. Ingber, Models of cytoskeletal mechanics of adherent cells, Biomech Model Mechanobiol 1(1) (2002) 95-108.

[134] G. Bao, S. Suresh, Cell and molecular mechanics of biological materials, Nat Mater 2(11) (2003) 715-725.

[135] C. Zhu, G. Bao, N. Wang, Cell mechanics: mechanical response, cell adhesion, and molecular deformation, Annu Rev Biomed Eng 2 (2000) 189-226.

[136] Y.C. Fung, S.Q. Liu, Elementary mechanics of the endothelium of blood vessels, J Biomech Eng 115(1) (1993) 1-12.

[137] E. Evans, A. Yeung, Apparent viscosity and cortical tension of blood granulocytes determined by micropipet aspiration, Biophysical Journal 56(1) (1989) 151-160.

[138] Q. Guo, S. Park, H.S. Ma, Microfluidic micropipette aspiration for measuring the deformability of single cells, Lab on a Chip 12(15) (2012) 2687-2695.

[139] M. Sato, M.J. Levesque, R.M. Nerem, Micropipette aspiration of cultured bovine aortic endothelial cells exposed to shear stress, Arteriosclerosis 7(3) (1987) 276-86.

[140] O. Thoumine, O. Cardoso, J.J. Meister, Changes in the mechanical properties of fibroblasts during spreading: a micromanipulation study, European Biophysics Journal with Biophysics Letters 28(3) (1999) 222-234.

[141] M. Balland, N. Desprat, D. Icard, S. Fereol, A. Asnacios, J. Browaeys, S. Henon, F. Gallet, Power laws in microrheology experiments on living cells: Comparative analysis and modeling, Physical Review E 74(2) (2006).

[142] G. Coceano, M.S. Yousafzai, W. Ma, F. Ndoye, L. Venturelli, I. Hussain, S. Bonin, J. Niemela, G. Scoles, D. Cojoc, E. Ferrari, Investigation into local cell mechanics by atomic force microscopy mapping and optical tweezer vertical indentation, Nanotechnology 27(6) (2016).

[143] S. Henon, G. Lenormand, A. Richert, F. Gallet, A new determination of the shear modulus of the human erythrocyte membrane using optical tweezers, Biophysical Journal 76(2) (1999) 1145-1151.

[144] A.R. Harris, J. Bellis, N. Khalilgharibi, T. Wyatt, B. Baum, A.J. Kabla, G.T. Charras, Generating suspended cell monolayers for mechanobiological studies, Nature Protocols 8(12) (2013) 2516-2530.

[145] A. Katsumi, J. Milanini, W.B. Kiosses, M.A. Del Pozo, R. Kaunas, S. Chien, K.M. Hahn, M.A. Schwartz, Effects of cell tension on the small GTPase Rac, The Journal of cell biology 158(1) (2002) 153-164.

[146] R. Krishnan, C.Y. Park, Y.C. Lin, J. Mead, R.T. Jaspers, X. Trepat, G. Lenormand, D. Tambe, A.V. Smolensky, A.H. Knoll, J.P. Butler, J.J. Fredberg, Reinforcement versus Fluidization in Cytoskeletal Mechanoresponsiveness, Plos One 4(5) (2009).

[147] R.L. Steward, C.M. Cheng, J.D. Ye, R.M. Bellin, P.R. LeDuc, Mechanical stretch and shear flow induced reorganization and recruitment of fibronectin in fibroblasts, Scientific Reports 1 (2011).

[148] D.R. Gossett, H.T.K. Tse, S.A. Lee, Y. Ying, A.G. Lindgren, O.O. Yang, J.Y. Rao, A.T. Clark, D. Di Carlo, Hydrodynamic stretching of single cells for large population mechanical

phenotyping, Proceedings of the National Academy of Sciences of the United States of America 109(20) (2012) 7630-7635.

[149] H. Lu, L.Y. Koo, W.C.M. Wang, D.A. Lauffenburger, L.G. Griffith, K.F. Jensen, Microfluidic shear devices for quantitative analysis of cell adhesion, Analytical Chemistry 76(18) (2004) 5257-5264.

[150] L.H. Deng, X. Trepat, J.P. Butler, E. Millet, K.G. Morgan, D.A. Weitz, J.J. Fredberg, Fast and slow dynamics of the cytoskeleton, Nature Materials 5(8) (2006) 636-640.

[151] B. Fabry, G.N. Maksym, J.P. Butler, M. Glogauer, D. Navajas, J.J. Fredberg, Scaling the microrheology of living cells, Physical Review Letters 87(14) (2001).

[152] S. Munevar, Y.-l. Wang, M. Dembo, Traction force microscopy of migrating normal and H-ras transformed 3T3 fibroblasts, Biophysical journal 80(4) (2001) 1744-1757.

[153] W.R. Legant, J.S. Miller, B.L. Blakely, D.M. Cohen, G.M. Genin, C.S. Chen, Measurement of mechanical tractions exerted by cells in three-dimensional matrices, Nature methods 7(12) (2010) 969-971.

[154] A.N. Ketene, E.M. Schmelz, P.C. Roberts, M. Agah, The effects of cancer progression on the viscoelasticity of ovarian cell cytoskeleton structures, Nanomedicine-Nanotechnology Biology and Medicine 8(1) (2012) 93-102.

[155] T.G. Kuznetsova, M.N. Starodubtseva, N.I. Yegorenkov, S.A. Chizhik, R.I. Zhdanov, Atomic force microscopy probing of cell elasticity, Micron 38(8) (2007) 824-833.

[156] M. Lekka, Discrimination Between Normal and Cancerous Cells Using AFM, Bionanoscience 6(1) (2016) 65-80.

[157] Y. Nematbakhsh, C.T. Lim, Cell biomechanics and its applications in human disease diagnosis, Acta Mechanica Sinica 31(2) (2015) 268-273.

[158] J. Fu, Y.-K. Wang, M.T. Yang, R.A. Desai, X. Yu, Z. Liu, C.S. Chen, Mechanical regulation of cell function with geometrically modulated elastomeric substrates, Nature methods 7(9) (2010) 733-736.

[159] J. Chen, M.A. Birch, S.J. Bull, Nanomechanical characterization of tissue engineered bone grown on titanium alloy in vitro, Journal of Materials Science: Materials in Medicine 21(1) (2010) 277-282.

[160] P.F. Duan, J.J. Chen, Nanomechanical and microstructure analysis of extracellular matrix layer of immortalized cell line Y201 from human mesenchymal stem cells, Surface & Coatings Technology 284 (2015) 417-421.

[161] R. Khanna, D.R. Katti, K.S. Katti, AFM and nanoindentation studies of bone nodules on chitosan-polygalacturonic acid-hydroxyapatite nanocomposites, Cmes-Computer Modeling in Engineering & Sciences 87(6) (2012) 530-555.

[162] D.P. McDaniel, G.A. Shaw, J.T. Elliott, K. Bhadriraju, C. Meuse, K.H. Chung, A.L. Plant, The stiffness of collagen fibrils influences vascular smooth muscle cell phenotype, Biophysical Journal 92(5) (2007) 1759-1769.

[163] Y.-T. Yang, C.-C.K. Lin, J.-D. Liao, C.-W. Chang, M.-S. Ju, Continuous depth-sensing nano-mechanical characterization of living, fixed and dehydrated cells attached on a glass substrate, Nanotechnology 21(28) (2010) 285704.

[164] S. Miyamoto, Y. Miyamoto, Y. Shibata, K. Yoshimura, E. Izumida, H. Suzuki, T. Miyazaki, K. Maki, R. Kamijo, In situ quasi-static and dynamic nanoindentation tests on calcified nodules formed by osteoblasts: Implication of glucocorticoids responsible for osteoblast calcification, Acta Biomaterialia 12 (2015) 216-226.

[165] K.S. Katti, A.H. Ambre, S. Payne, D.R. Katti, Vesicular delivery of crystalline calcium minerals to ECM in biomineralized nanoclay composites, Materials Research Express 2(4) (2015) 045401.

[166] M. Lekka, P. Laidler, D. Gil, J. Lekki, Z. Stachura, A.Z. Hrynkiewicz, Elasticity of normal and cancerous human bladder cells studied by scanning force microscopy, European Biophysics Journal 28(4) (1999) 312-316.

[167] M. Lekka, P. Laidler, J. Ignacak, M. Labedz, J. Lekki, H. Struszczyk, Z. Stachura, A.Z. Hrynkiewicz, The effect of chitosan on stiffness and glycolytic activity of human bladder cells, Biochimica Et Biophysica Acta-Molecular Cell Research 1540(2) (2001) 127-136.

[168] Q.S. Li, G.Y.H. Lee, C.N. Ong, C.T. Lim, AFM indentation study of breast cancer cells, Biochemical and biophysical research communications 374(4) (2008) 609-613.

[169] E.C. Faria, N. Ma, E. Gazi, P. Gardner, M. Brown, N.W. Clarke, R.D. Snooka, Measurement of elastic properties of prostate cancer cells using AFM, Analyst 133(11) (2008) 1498-1500.

[170] L. Bastatas, D. Martinez-Marin, J. Matthews, J. Hashem, Y.J. Lee, S. Sennoune, S. Filleur, R. Martinez-Zaguilan, S. Park, AFM nano-mechanics and calcium dynamics of prostate cancer cells with distinct metastatic potential, Biochimica Et Biophysica Acta-General Subjects 1820(7) (2012) 1111-1120.

[171] S.E. Cross, Y.S. Jin, J. Tondre, R. Wong, J. Rao, J.K. Gimzewski, AFM-based analysis of human metastatic cancer cells, Nanotechnology 19(38) (2008).

[172] K. Hayashi, M. Iwata, Stiffness of cancer cells measured with an AFM indentation method, Journal of the Mechanical Behavior of Biomedical Materials 49 (2015) 105-111.

[173] X.Q. Zhao, Y.X. Zhong, T. Ye, D.J. Wang, B.W. Mao, Discrimination Between Cervical Cancer Cells and Normal Cervical Cells Based on Longitudinal Elasticity Using Atomic Force Microscopy, Nanoscale Research Letters 10 (2015) 1-8.

[174] M. Li, L.Q. Liu, N. Xi, Y.C. Wang, Z.L. Dong, X.B. Xiao, W.J. Zhang, Atomic force microscopy imaging and mechanical properties measurement of red blood cells and aggressive cancer cells, Science China-Life Sciences 55(11) (2012) 968-973.

CHAPTER 2. SEQUENTIAL CULTURE ON BIOMIMETIC NANOCLAY SCAFFOLDS FORMS THREE-DIMENSIONAL TUMOROIDS[1]

This chapter describes the formation of 3D tumoroids in the sequential culture based in vitro model. Most of the contents of this chapter has been published in K.S. Katti, MD.S. Molla, F. Karandish, M.K. Haldar, S. Mallik, D.R. Katti, Sequential culture on biomimetic nanoclay scaffolds forms three-dimensional tumoroids, Journal of Biomedical Materials Research Part A 104(7) (2016) 1591-1602.

2.1. Introduction

In the United States around 40% of the overall population encounters at least one form of cancer in their lifetime and in the long run 1 in 4 of cancer patients dies making it the second leading cause of death [1, 2] . According to the National Cancer Institute (NCI), the term 'cancer' designates for complex diseases in which aberrant cells divide without control and can invade other tissues. All cancer grows in cells. The basic unit of body, cells grow by dividing in a controlled way and apoptosis occurs when cells are old and damaged. Sometimes the regular cell cycle may be affected by the genetic mutation, and after a certain period instead of dying, cells form new cells. In this way an extra mass of tissues, the tumor is formed. Cancer cells are capable of invading, migrating through and colonizing on a distant organ [3]. The cancer cells which spread away from its place of origin are known as metastatic cancer, and the process through which cancer cells invade a distant organ is known as metastasis. 90% of the

[1]This chapter was co-authored by K.S. Katti, MD.S. Molla, F. Karandish, M.K. Haldar, S. Mallik, and D.R. Katti. MD. S. Molla had primary responsibility for preparing samples, conducting all tests, and drafting this chapter. Kalpana Katti and Dinesh Katti directed the research orientation and revised this chapter. F. Karandish, M.K. Haldar, and S. Mallik prepared the anticancer drug nanocarrier polymersomes.

cancer-associated deaths are attributed to metastasis, yet in cancer pathogenesis, the mechanism of it remains obscure [4].

A complex metastatic cascade is involved in the dissemination of cancer cells to the distant organ. It includes the sequence of phases: local invasion, intravasation, circulation, arrest and extravasation, proliferation and angiogenesis [5, 6]. Initially single or clumps of cancer cells leave the primary tumor to invade the local stroma and ECM (extracellular matrix). On the second step of metastatic cascade, cancer cells intravasate either into blood vessels or lymphatic system. They translocate in a raucous environment through the bloodstream to the microvessels of a distant site, extravasate from the bloodstream and survived cells become arrested at a distant tissue [7]. On the new site cancer cells must acclimate to the foreign microenvironment to prevail. In metastatic colonization step cancer cells proliferate to form micrometastases which hereafter disrupt the vessel wall [8]. Through the angiogenesis process, a network of blood vessel penetrates into this cancerous growth to supply nutrients and oxygen and to remove waste products [6].

Cancer cells have a characteristic preference for the metastasis to a distant organ. For instance, prostate cancer always has a strong propensity to metastasize to bone [9]. Crosstalk between the metastatic cancer cells and bone microenvironment make the bone an alluring niche for the colonization of disseminated tumor cells.

Bone cells like osteoblast, osteoclast, immobilized bone matrix and cell-secreted proteins are the main constituents of bone microenvironment [10]. Growth factors released by degradation of osteoclasts stimulate osteoblasts to form new bones. Tumor growth in bone occurs due to an imbalance between the bone formation by osteoblasts and bone resorption by osteoclasts. Bone metastasis can be either osteoblastic, when bone formation run over the bone

resorption; or osteolytic, when bone density is decreased by excessive bone resorption [11]. Cancer cells in contact of bone microenvironment produce cytokines like parathyroid hormone-related protein (PTHrP), interleukin-11 (IL-11), interleukin (IL-8), vascular endothelial growth factor (VEGF) which promote osteoclast formation due to which excessive boney tissue resorption results. This degradation of bone derives growth factors like TGF-β which causes tumor expansion. Again tumor cells in contact of osteoblasts produce RANKL (receptor activator of nuclear factor kappa-B ligand) which stimulates osteoclast formation [12]. Bradykinin promotes VEGF expression and increases angiogenesis in human prostate cancer cells [13]. Other factors like MMP-1, ADAMTS1, osteopontin (OPN) also stimulate osteoclast activity and promote cancer cell colonization on bone microenvironment [14, 15]. Cancer cells secrets Matrix metalloproteinase (MMP) enzymes which involve in the breakdown of extracellular matrix and promote cancer growth [16, 17].

These interactions between the bone microenvironment and cancer cells initiate a vicious cycle to impair the homeostatic balance between bone formation and bone resorption which is responsible for tumor growth and bone remodeling [18].

For investigating cancer cell biology to determine anticancer drug efficacy, in vivo models and 2D substrates has been used for so long. But bone microenvironment is poorly reflected by these conventional two-dimensional cell culture systems. In 2D substrates, cells exhibit tight junctions, rapid growth, monolayer structure, poor differentiation capability, non-optimal physiological responses and strong physical contact with a substrate which results in altered tumor cell behavior. Bone microenvironmental condition is naturally three dimensional which controls cancer formation [19]. The recent introduction of 3D in vitro tumor model has brought a drastic change in cancer research to overcome the limitations of 2D culture [20-22].

3D in vitro model allows cheap, relatively less time-consuming study of cancer cell without the complexity of in vivo models. It has been observed that 3D and 2D cultured cells differ from each other in terms of cell morphology [23], cell density [24], drug resistance [25, 26], ECM synthesis [27], and cell metabolic activity [28], gene expression [29], [30], expression of angiogenic factors [31], cell migration [32], invasiveness [25] [26]. Another advantage of 3D scaffold system is, it allows coculture of multiple cells [33, 34]. It has also been reported that in vitro cancer cells develop morphology and phenotype similar to in vivo observed [35, 36]. Thus, in vitro 3D models bridge the gap between 2D substrates and subcutaneous animal experiments.

Variety of in vitro 3D models are being developed to mimic human pathophysiological microenvironment more closely [37]. In 2007, Fischbach et al. Developed a 3D cancer model that recreated microenvironmental characteristics of tumors in vivo [35]. Kwon et al. developed an in vitro model to study the impact of BMP-2 on metastasis to bone, and they found that BMP-2 stimulates the PC-3 cancer cells to migrate to bone [38]. In 2010, Hartman et al. developed a 3D pharmacokinetic cancer model based on PCL with perlecan domain IV peptide [39]. Pathi et al. developed a HAP-based scaffold to study breast cancer, and they showed cancer cell behavior changes with the particle size and crystallinity of HAP [40]. In a study in 2012, Soman et al. developed a precise log pile microstructure scaffold to study cancer which allows accurate control of the internal structure of the scaffold [3]. Szot et al. showed that tumor aggressiveness might be enhanced due to signaling between the cells in spatially distinct outside and inside cells of a tumor [41]. Talukdar et al. cocultured bone cells with cancer cells and cells were found to interact through secreted product[33]. In 2014. Sieh et al. reported a paracrine interaction between the cancer cells and their 3D in vitro culture reflected molecular changes during bone metastasis [42]. In 2014 Bersini et al. developed a microfluidic 3D in vitro model and

demonstrated that CXCR2 and CXCL5 play a significant role in the extravasation process of breast cancer cells [43].

Tumorigenesis is a complex dynamic process where cancer cells differentiate, migrate, proliferate interacting among themselves and its 3D microenvironment. This complex biological mechanism is complicated to recreate artificially. The existing bioengineered 3D tumor models need to be improved to reveal biology underlying cancer initiation and progression. In this study, we used PCL/ in situ HAPclay scaffold to create a bone mimic 3D prostate cancer model. In our previous study we presented the characteristics of PCL/ in situ HAPclay scaffold [44]. PCL has been extensively used for mimicking tissue structure and creating tumor models [39, 45-47]. In this study, we used PCL/ in situ HAPclay scaffold to generate a bone mimicking 3D prostate cancer model. Incorporation of in situ HAPclay has introduced osteoconductivity and osteoinductivity. These scaffolds have around 86% porosity and the pore size range between 100 µm to 300 µm which is large enough for cellular infiltration. We have reported that PCL/ in situ HAPclay scaffolds are very stable as the overall structure of these scaffolds remained intact and were retrievable over 18 days period of degradation study. The elastic modulus of PCL/ in situ HAPclay scaffolds were found 495 MPa which is significantly different from PCL polymer. These scaffolds were also found to support mesenchymal stem cells (MSCs) to attach and infiltrate into scaffolds (infiltration depth 3.5 mm and 6 mm from the scaffold surface) and to undergo osteogenic differentiation without osteogenic supplement in the culture media. HAP played a pivotal role to improve the osteoconductive nature of this PCL/ in situ HAPclay scaffold [48]. In our previous studies, similar observation was made on the behavior of osteoblast which formed bone nodules on biopolymer/HAP composite without osteogenic supplements in the culture media [49, 50].

Mesenchymal stem cells (MSCs) play a key role in bone microenvironment which influences cancer progression. It has been found that in the presence of MSCs enhance the growth of cancer cells in vitro and in vivo [51]. But in another study, it has been shown tumorigenesis is suppressed by mesenchymal stem cells (MSCs) [52]. Bone marrow mesenchymal stem cells are capable of differentiating along multiple lineages like cartilage, bone, fat, muscle, etc. [53-56]. It has been demonstrated that under appropriate tissue culture conditions, entire MSCs population can undergo osteogenic differentiation [57]. In the presence of dexamethasone, ascorbic acid and beta glycerol phosphates MSCs assume a cuboidal morphology, up-regulate alkaline phosphatase enzyme activity, express osteoblastic cell surface antigens, and form mineralized extracellular matrix [58].

In this study, we introduced a unique sequential cell culture system in 3D in vitro bone model to provide cancer cells an extraordinary bone mimicking microenvironment. Human mesenchymal stem cells (MSCs) were seeded onto PCL/ in situ HAPclay scaffolds, allowed to differentiate for enough time and then cancer cells were seeded on top of it. We have investigated cellular differentiation on the PCL/ in situ HAPclay scaffolds and found that MSCs can differentiate without osteogenic supplements. We studied the cellular morphology and observed that cancer cells form in vivo like tumoroids with tight cellular junctions only in sequential culture with MSCs.

Doxorubicin and gemcitabine are two extensively used anticancer drugs [59-61]. In one of our previous studies, a multifunctional polymersome has been developed for cytosolic delivery of these drugs [62]. Here we studied the cytotoxic efficacy of these polymersomes encapsulated with anticancer drugs gemcitabine and doxorubicin on our 3D cancer model.

Doxorubicin and gemcitabine are two extensively used anticancer drugs [59-61]. In one of our previous studies, a multifunctional polymersome has been developed for cytosolic delivery of these drugs [62]. Here we studied the cytotoxic efficacy of these polymersomes encapsulated with anticancer drugs gemcitabine and doxorubicin on our 3D cancer model.

2.2. Materials and methods

2.2.1. PCL/ in situ HAPclay 3D scaffolds preparation

The preparation procedure of PCL/ in situ HAPclay 3D scaffolds is described in detail in our previous works [44, 63]. In short, Na-MMT was modified with 5-aminovaleric acid, the procedure of which are described in our earlier works [48, 64-67]. In situ HAPclay was also prepared following the procedure described in our previous studies [48, 68]. 3D PCL scaffolds were prepared with 10 wt % in situ HAP clay. For this, PCL solution was prepared by dissolving 3.6 grams of the polymer in 40 ml of 1, 4 dioxane. Sonicated suspension of in situ HAPclay was prepared by adding 4 grams of in situ HAPclay into 16 ml dioxane which was then added to the polymer solution and then stirred for two hours. Freeze extraction method was used to obtain 3D scaffolds from this solution. Na-MMT clay was obtained from Clay Minerals Respiratory at the University of Missouri, Columbia. PCL, 5-aminovaleric acid, 1, 4 dioxane were purchased from Sigma Aldrich. Na_2HPO_4 and $CaCl_2$ which was used for the preparation of in situ HAPclay were obtained from J.T. Baker.

2.2.2. Cell line and culture medium

Human bone marrow Mesenchymal stem cells (MSCs) were obtained from Lonza, Walkersville (PT-2501) and maintained in MSCGM™ Bulletkit™ medium (Lonza, Walkersville, PT-3001). The Bulletkit™ medium was prepared by adding MSCGM™ SingleQuots™ (Lonza, Walkersville, PT-4105) to MSCBM™ (Lonza, Walkersville, PT-3238).

Human prostate cancer cell (HPCC) line MDAPCa2b were purchased from American Type Culture Collection (ATCC) which was maintained in a medium consist of 80% BRFF-HPC1 (AthenaES, 0403) and 20% fetal bovine serum (ATCC, 30-2020). Human osteoblast cell line (hFOB 1.19) were purchased from ATCC and maintained in a media consist of 90% HyQ Dulbecco's Modified Eagle medium DMEM-12(1:1) from Hyclone, 10% FBS from ATCC and 0.6% G418 solution (antibiotic) from JR scientific. All the cells were maintained at 37 °C and 5% CO_2 in completely humidified incubator. Cell culture waste media were changed in every other day to add fresh supplements.

2.2.3. Cell seeding and tissue culture

PCL/ in situ HAPclay scaffolds with a diameter 12 mm and thickness 3 mm, were generated in 24- well plates for cell seeded. Before seeding the cells, scaffolds were sterilized in UV lights for 45 minutes, kept under 70% ethanol overnight, washed with PBS, and then immediately kept in humidified incubator immerged in culture medium for 24 hours. 3.36 x 10^4 MSCs were seeded per scaffold and cultured in 800 µl of Bulletkit™ medium. After 23 days 3.0 x 10^4 human prostate cancer cells (HPCCs) were seeded per scaffold on the top of the MSCs and then culture was continued for different periods of time. For this sequential culture (SC), 1:1 ratio of MSCs and HPCCs media were used. For making comparison after 23 days MSCs culture was continued without seeding HPCCs for the same time periods. Only Human prostate cancer cells were also seeded on the scaffolds (3.0 x 10^4 per well) and cultured on HPCCs medium for the same periods of time. All of the media were changed in every 3 days, and for all the experiments 800 µl of the media were used per scaffolds. Human osteoblast cells were cultured on the PCL/ in situ HAPclay scaffolds for 18 days, and then prostate cancer cells were seeded on top of it. In this case, culture media were changed in every other day.

2.2.4. WST-1 assay

WST-1 (Roche, Indianapolis) assay was used to perform cell proliferation analysis following the manufacturer's protocol. In brief, cells were culture on scaffolds for 28, 33, 38 days (sequential culture was continued for 23+5, 23+10, 23+15 days) and then cell-seeded scaffolds were removed from the culture medium, washed with PBS and then placed in a new 24- well plate with a solution consist of 700 µl BRFF-HPC1 and 70 µl WST-1 reagent per well and then incubated for 4 hours in standard humidified condition. The slightly red color solution turned into yellow as metabolically active cells cleaved the tetrazolium salts of WST-1 reagent to formazan. Then scaffolds were removed from the 24-well plates and the intensity of yellow color, which directly represents the number of live cells, was read at 450 nm using a microplate spectrophotometer (Bio-Rad, Benchmark Plus). The number of cells was determined as the WST-1 reagent does not go into the cell through the membrane, the same samples were used for the ALP assay.

2.2.5. Alkaline phosphate assay

Samples obtained from proliferation assay were washed with PBS and placed in fresh 24-well plates with 850 µl Triton X-100 (Sigma-Aldrich, X-100) per well. This System was treated with two cycles of freezing-thawing (-70 °C to 37 °C) to obtain cell lysates. 250 µl of cell lysates were added to 250 µl of p-nitrophenyl phosphate (Sigma-Aldrich, N7653) in a new 24 well plate per well and then incubated for 1 hour at room temperature. Subsequently, 70 µl of 3N NaOH was added to each scaffold containing well, and the well plate was shaken for 60 seconds. Scaffolds were removed from the well plate, and the absorbance was measured at 405 nm using a microplate spectrophotometer (Bio-Rad, Benchmark Plus).

2.2.6. Scanning electron microscopy

SEM imaging was done to determine the cell adhesion to scaffolds and study the morphology of cell-scaffold surface using a JEOL JSM-6490LV scanning electron microscope. Samples were removed from the culture medium, washed with PBS and then fixed with 2.5% glutaraldehyde. Subsequently treated with ethanol series (10 % v/v, 30% v/v, 50 % v/v, 70 % v/v and 100 % v/v) to dehydrate and then dried using hexamethyldisilazane.

2.2.7. Preparation of polymersomes

The detailed preparation method of polymersomes is described in our previous work [62]. Initially, amphiphilic-block copolymer of PEG and PLA were synthesized with hydrophilic fraction 25%. The molecular weight used for PLA and PEG were 5800 and 1900 respectively. PEG was reacted with succinic anhydride, followed by conjugation of cystamine to incorporate the disulfide bonds. P5 polymersomes were prepared using solvent exchange method [69]. Then pH gradient method was followed to encapsulate doxorubicin (Bridge Bioservices) and gemcitabine (Matrix Scientific) into polymersomes [70]. For targeting of these polymersomes to prostate cancer cells, 1 mole % folate-conjugated lipid (DSPE-PEG-Folate, commercially available from NANOCS, NY) with PEG was added to the polymers during polymersome preparation. Mechanism of drug interaction with cancer cell has been illustrated in figure 2.1.

2.2.8. Drug treatment

The ability of anticancer drug encapsulated polymersomes to kill HPCCs was assessed using WST-1 cell viability assay. Sequential cultures were obtained as described earlier. In brief, same no of MSCs (3.36 x 10^4) were seeded on 3D scaffolds and cultured for 23 days. Then same no of HPCCs (3.0 x 10^4) was seeded on top of it, and the culture was continued for 15 more days. For HPCCs monoculture, HPCCs were cultured for 23+15 days.

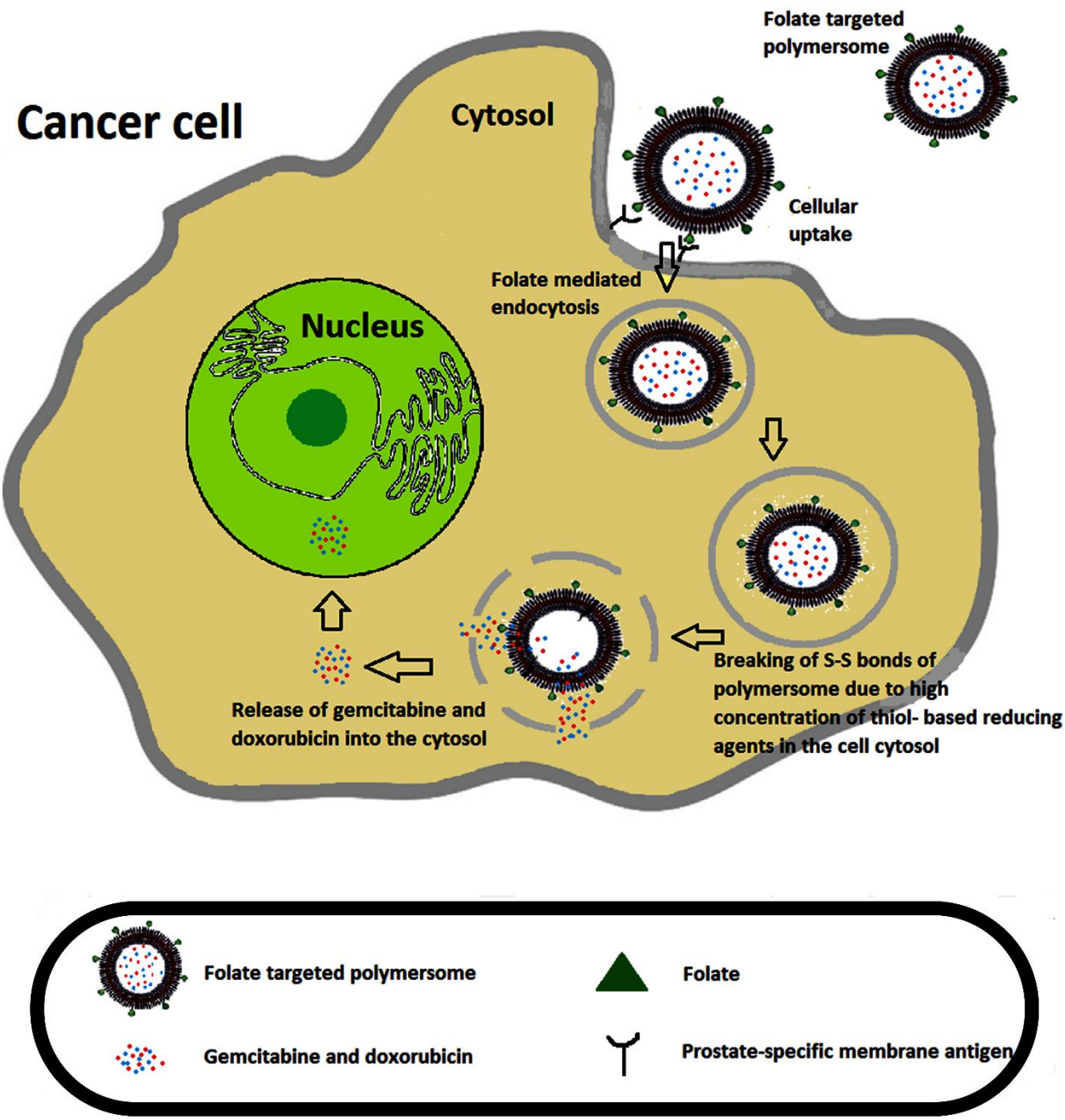

Figure 2.1. Illustration of cytosolic drug delivery.

Then samples were removed from the culture medium and incubated with drug-containing media for 48 hours in standard humidified condition at 37 °C and 5% CO_2. Triplicate samples were treated with the following 3 types of drug-containing the solution. A. 800 µl of culture medium, 8 µl of gemcitabine free drug and 5 µl of doxorubicin free drug; B. 800 µl of

culture medium and 800 µl of drug solution which consist of gemcitabine + doxorubicin encapsulated in folate-targeted polymersomes; C. 800 µl of culture medium and 800 µl of drug solution which consist of gemcitabine + doxorubicin encapsulated in non-targeted polymersomes. It has been made sure that 800 µl of drug solution contains the same amount of gemcitabine and doxorubicin (8 µl of gemcitabine and 5 µl of doxorubicin). Cell viability of the drug-treated samples was analyzed using the WST-1 assay following the procedure as described earlier. 23+15+2 days of drug untreated samples were served as a control for the assay. It has been made sure that 800 µl of drug solution contains the same amount of gemcitabine and doxorubicin (8 µl of gemcitabine and 5 µl of doxorubicin). Cell viability of the drug-treated samples was analyzed using the WST-1 assay following the procedure as described earlier. 23+15+2 days of drug untreated samples were served as a control for the assay. The percentage cell viability was calculated by dividing the drug-treated viable cell number by untreated viable cell number.

2.2.9. Statistical analysis

One-way ANOVA followed by Tukey's post hoc multiple comparison tests were used for the statistical analysis. Quantitative data were expressed as a mean ± standard deviation. Data were considered significantly different when probability values were less than 0.05 ($P < 0.05$). All experiments were performed triplicate.

2.3. Results and discussion

2.3.1. SEM imaging of the osteoblast seeded sequential culture

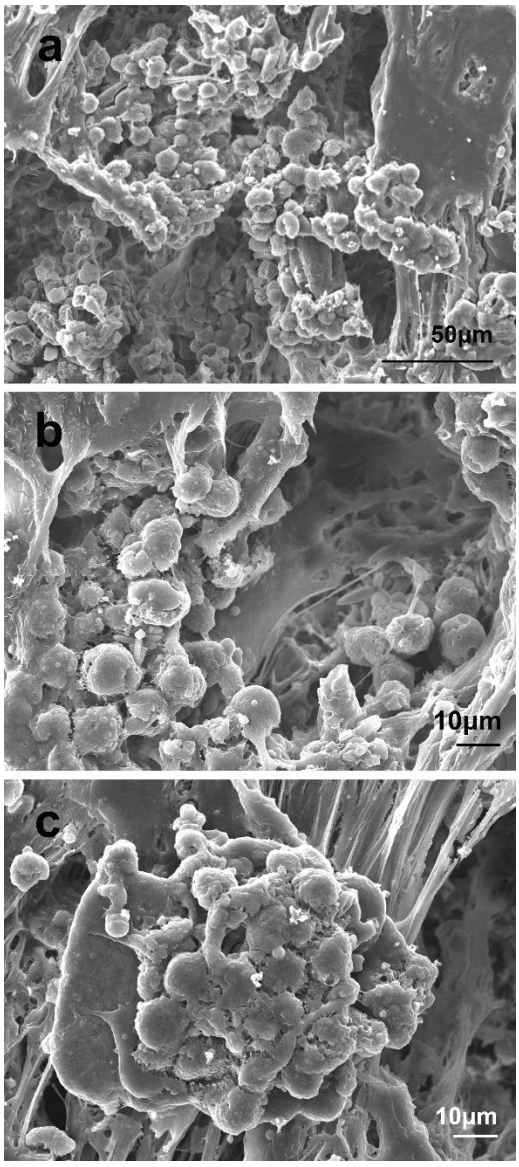

Figure 2.2. SEM micrographs of PCa+hFOB. SEM micrographs of sequential culture of human osteblast hOB and human prostate cancer cells after 18+10 days (A-C). (X+Y days: hOBs were cultured on PCL/ *in situ* HAPclay scaffolds for X days, then cancer cells were seeded on top of it and culture was continued for Y more days).

Initially, we started a sequential culture of prostate cancer with human osteoblast cells. The culture method is described in detail in the 'materials and method' section. Figure 2.2 (a-c) shows the SEM micrographs of the sequential culture of osteoblast with human prostate cancer

cells. These micrographs clearly indicate that both human osteoblast cells and prostate cancer cells are thriving on nanoclay the scaffolds. We can see the formation of flat morphology by osteoblast cells (Figure 2.2, a) like we observed in our previous study. Cells were able to grow and infiltrated into the scaffolds. We can also observe in the SEM images, the formation of the extracellular matrix by the cells. In the micrographs, round shaped cells are human prostate cancer cells. Both the cell types adhered to the surface of the scaffold. Human prostate cancer cells showed spherical morphology, but there was lack of intercellular adhesion. So, we did not observe the formation of multicellular spheroids with the hypoxic core as we observe tumoroids grow in vivo. But we observed formation of cell cluster (Figure 2.5, c) that merged into multiple layers which possibly could be formed by osteoblast cells because similar morphology we observed for osteoblast cells in our previous study.

2.3.2. Cell proliferation analysis

The WST-1 assay was performed after 28, 33 and 38 days for monocultures and for sequential culture after 5, 10 and 15 days of HPCCs seeding (HPCCs was seeded after 23 days on MSCs seeded scaffolds) to maintain the same time period. WST-1 assay indicated cell proliferation of MSCs and HPCCs on PCL/ in situ HAPclay scaffolds (figure 2.3). No significant difference has been observed in no of viable cells between MSCs and sequential culture after 28 days. But no of viable cells has greatly increased in day 33 and 38 for SC compared to MSCs. Cell proliferation for HPCCs was much higher than the MSCs and SC but like MSCs cell viability was decreased for HPCCs after day 28. We observed that (figure 2.3) for only sequential culture no of viable cells has increased after day 28. It has been reported that MSCs promoted human prostate cancer cell, PC-3 growth in vivo and in vitro [71].

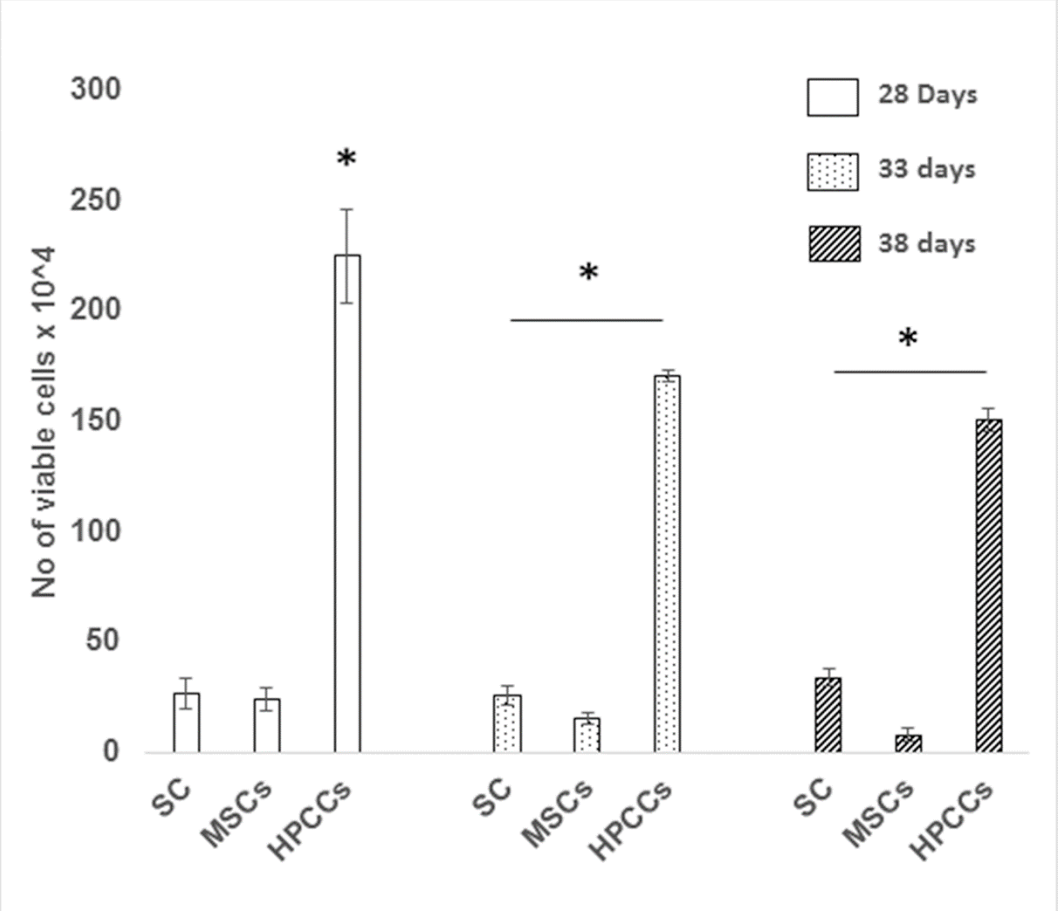

Figure 2.3. Viability assay. Comparative results from WST-1 cell proliferation assay for Sequential culture (SC), mesenchymal stem cells (MSCs) and human prostate cancer cells (HPCCs). Results are shown as mean ± standard deviation. Statistical Significance is shown by a single asterisk ($p<0.05$, $n=3$).

It also has been reported that the proliferation of BM-MSCs in coculture with HPCCs cell was accelerated [72]. Again, MDA PCa2b is osteoblastic in nature [73]. That means the osteoblast population should increase in sequential culture. So increased proliferation rate of either MSCs or HPCCs or both could be the possible reason of increased no of viable cells in sequential culture. Mesenchymal stem cells usually go through complex series cellular events which include terminal and nonterminal differentiation, growth arrest, etc. [74, 75]. It has been demonstrated that self-renewing MSCs have a have higher proliferation rate compared to

differentiating MSCs [76]. Again observation by Bruder et al. contradicts that result [57]. Figure 2.3 & 2.4 shows that both proliferation and differentiation has decreased for MSCs. The relationship between proliferation and differentiation for MSCs is yet to make clear. Considering these facts, it is hard to make any inference from the data obtained for the WST-1 assay. The relationship between proliferation and differentiation for MSCs is yet to make clear to understand the mechanism.

2.3.3. Osteogenic differentiation

ALP is a key marker for osteoblastic activity [77]. ALP assay was performed on each same MSCs and SC samples after WST-1 cell proliferation assay. The experimental results are given in figure 2.4. ALP activity clearly indicated the osteogenic differentiation of mesenchymal stem cells. From figure 2.4, it can be seen that ALP activity was higher for sequential culture compared to MSCs on day 28. From which we can make an inference that the presence of HPCCs enhances the differentiation of MSCs. Though the difference is not statistically significant, it can be seen that ALP activity has a little bit increased on day 33. Again, on day, 38 ALP activities were decreased significantly for both Sequential culture and MSCs. It has been reported before that ALP activity decreases after a certain period of time due to late stage of differentiation [78, 79]. Thibault et al. reported a decrease in ALP activity of MSC cell after 8 days culturing on PCL scaffolds [78]. In this study, we performed first ALP assay after 28 days of MSCs seeding. Only the differentiating MSCs are expected to produce ALP and after 28 days, MSCs could be at the last stage of differentiation which could be a possible reason for lower ALP activity observed from the data for ALP assay. ALP is an osteoblast marker and ALP assay is used to study the differentiation of MSCs to the osteoblastic lineage.

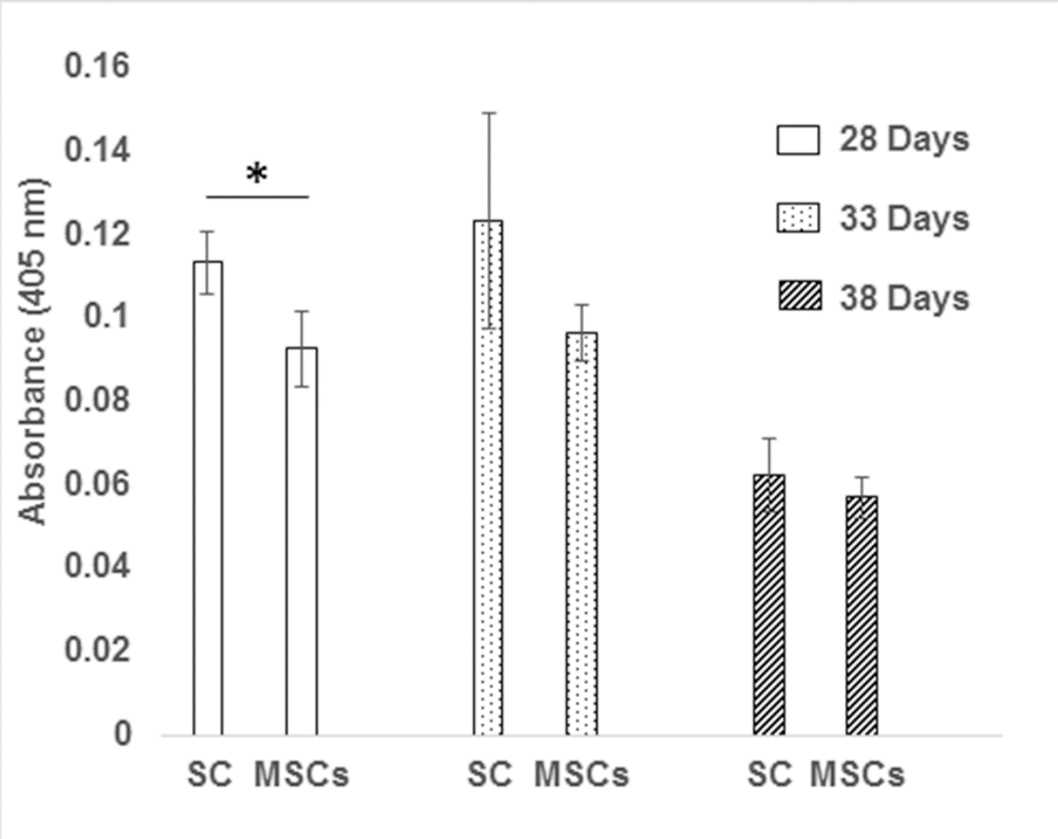

Figure 2.4. ALP assay. Comparative results from ALP assay for sequential culture (SC) and mesenchymal stem cells (MSCs). Results are shown as mean ± standard deviation. Statistical Significance is shown by a single asterisk ($p<0.05$, $n=3$).

2.3.4. Sequential cell-seeded scaffold morphology and tumoroid formation

SEM images (figure 2.5) has been taken for sequential culture on days 28, 33 and 38. These micrographs indicate cell spreading, adhesion, infiltration and extracellular matrix formation on the PCL/ in situ HAPclay scaffolds. Our previous work showed that MSCs exhibit both flat and spheroid morphology on PCL/ in situ HAPclay scaffolds [44]. But spheroids formed by MSCs were kind of rugged and had a rough surface. Microtissues with organized, tight cellular junctions, indistinguishable cellular boundaries, and even surfaces has been observed on the sequential culture in this current study (figure 2.5). Unlike our previous study with only MSCs, cells formed a cluster that merged into multilayered mass. Similar morphology

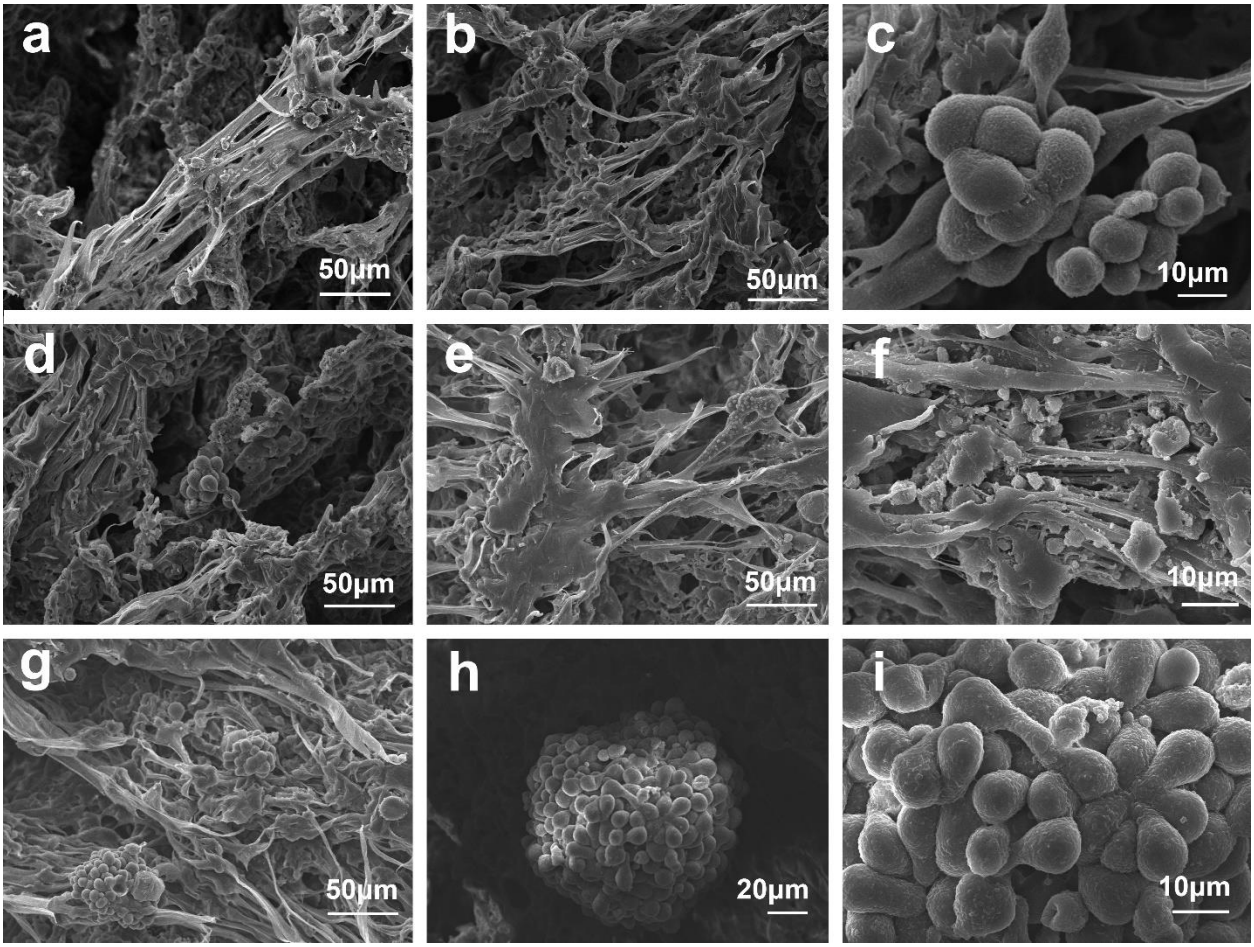

Figure 2.5. SEM micrographs. SEM micrographs of sequential culture of human mesenchumal stem cells (hMSCs) with human prostate cancer cells (HPCCs)after 23+5 days (a-c), 23+10 days (d-f), 23+15 days (g-i). (X+Y days: MSCs were cultured on PCL/ in situ HAPclay scaffolds for X days, then cancer cells were seeded on top of it and culture was continued for Y more days.) of osteoblastic LNCaP prostate cancer cells in coculture with osteoblast on PCL bone.

scaffold was reported earlier [80]. These tight 3D structures have been designated as 'tumoroids' [81].

So, these compact spheroids with smooth surface observed on the sequential cultures can be assigned for HPCCs. Moreover, Lua et al. reported prostate cancer cells grew as spheres when cocultured with BM-MSCs [72]. In that case, MSCs or differentiated MSCs can be distinguished from the HPCCs with their flattened structure which is mainly arranged on the surface of the scaffolds. Unlike our previous study cell growth on the scaffolds were dispersed and scattered and did not cover the whole surface of the scaffolds. One of the major limitations of 3D cell

culture on static condition is the insufficient oxygen and nutrient transport to and removal of waste products from the inner sides of scaffolds, which leads to inhomogeneous cell distribution on the surface of the scaffold [82-84]. No significant morphological changes have been observed among the samples on these day periods but tumoroids possibly formed by HPCCs were larger on day 38 compared to day 33 (Figure 2.5, g-i).

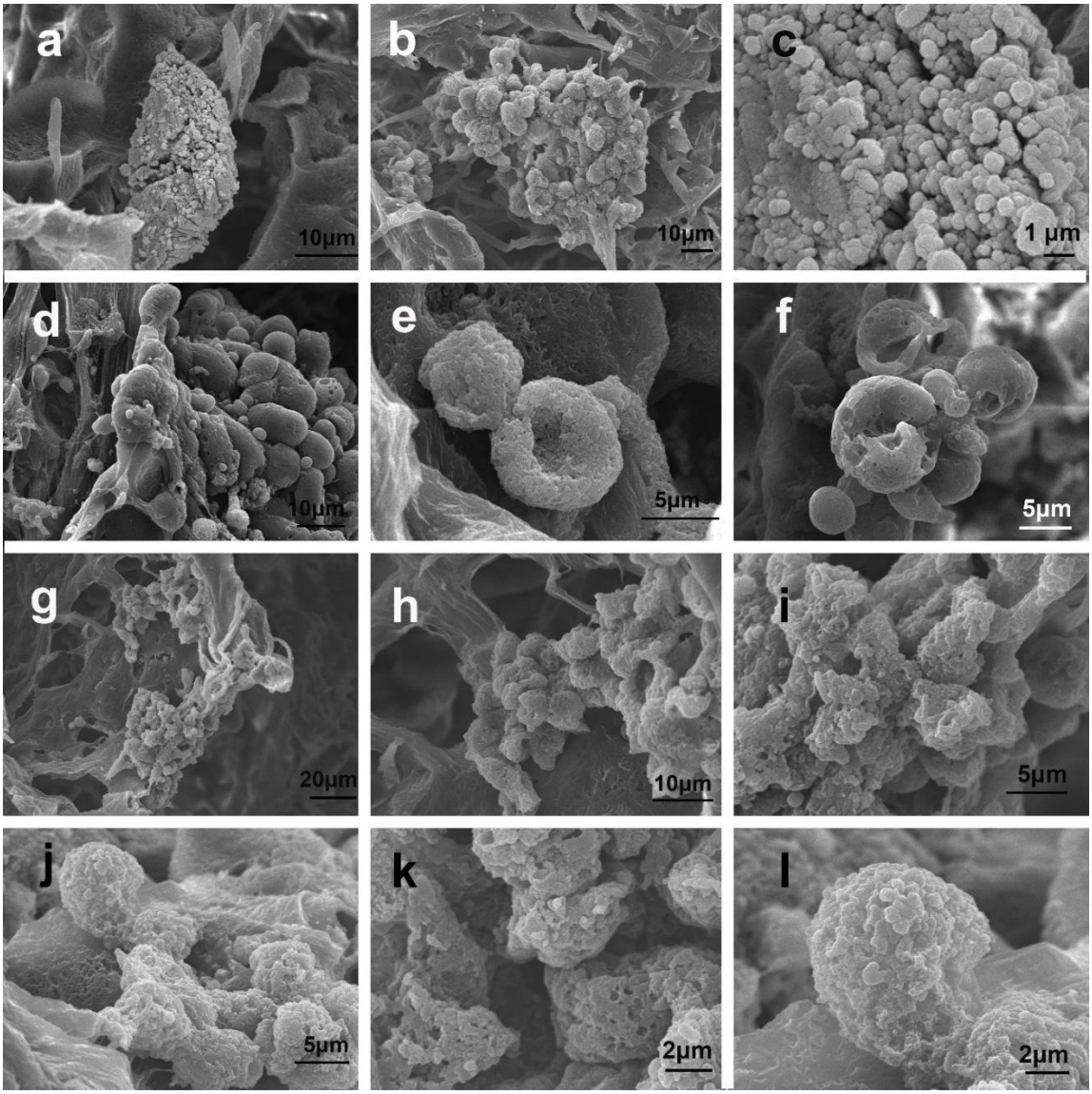

Figure 2.6. Drug treated SEM micrographs. SEM micrographs of only HPCCs seeded scaffolds after 40 days (A-C), HPCCs treated with free drugs (d-f), folate-targeted polymersomes (g-i), non-targeted polymersomes (j-l).

2.3.5. SEM imaging of HPCCs seeded scaffolds with and without drug treatment

Despite having greater cell proliferation, HPCCs seeded on PCL/ in situ HAPclay scaffolds did not appear to spread across the surface of the scaffolds. Figure 2.6 (a-c) shows disorganized aggregates of HPCCs on the scaffolds with less adhesion which clearly lacked the defined shape. Microtissue formed on only HPCCs seeded scaffolds, showed loose architecture and rough surface. Which means HPCCs did not form tumroids in the absence of differentiated mesenchymal stem cells. The mechanisms underlying the development of tumoroids are presently unknown. Our data clearly indicated that cell-cell/ cell-matrix interaction played the most vital role in the development of tumoroids. Scaffold materials also could be critical in tumoroid formation which has been reported earlier [81]. No flattened cell structure was observed in this HPCCs monoculture. Micrographs (Figure 2.6, d-l) for the drug-treated samples appear to have curved spheroids. Unlike nontreated samples, lots of holes can be observed on the surface of the spheroids. Appears like drug destroyed the architecture of the cells.

2.3.6. Drug response

WST-1 cell viability assay has been performed to determine the cytotoxic effect of anticancer drugs encapsulated polymersomes on the HPCCs. Mechanism of drug interaction with cancer cell has been illustrated in figure 2.1. Prostate-specific membrane antigen (PSMA) is a unique folate hydrolase which is significantly upregulated in prostate cancer cells[85]. Yao et al. demonstrated that expression PSMA increases cell folate uptake which inspired us for the folate-targeted drug delivery to the prostate cancer cells [86]. When polymersomes enter into the cancer cells, a high concentration of thiol-based reducing agents intrigues disintegration of polymersomes by breaking of S-S bonds between the copolymer blocks which results in rapid release of encapsulated drugs [87, 88]. From figure 2.7 we can see that for both sequential

culture and only HPCCs gemcitabine + doxorubicin free drug showed higher killing unlike our previous observation [62]. For only HPCCs, targeted polymersomes showed significantly higher killing than non-targeted polymersomes. For sequential culture though, mean killing is higher for non-targeted polymersomes, but it is not significantly different than targeted polymersomes. Percentage killing is more elevated in only HPCCs compare to sequential culture which could be explained by the fact that gemcitabine and doxorubicin kills most of the cancer cells and also randomly kill few osteogenic cells.

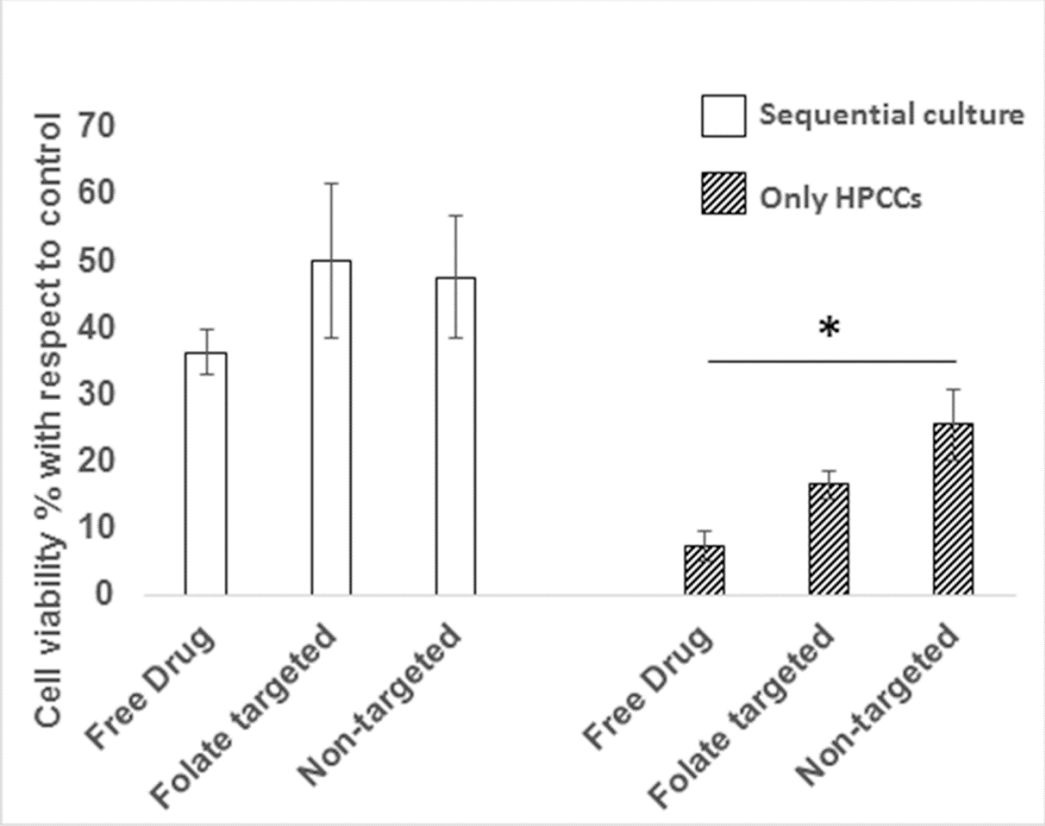

Figure 2.7. Percentage cell viability of the sequential culture and only human prostate cancer cells after drug treatment determined by WST-1 assay. 23+15+2 days of drug untreated samples were served as control for the assay.

2.4. Conclusion

Here we present a new 3D in vitro tumor model based on PCL/Nanoclay scaffold seeded with a sequential culture of hMSCs followed by HPCCs which has opened a new window to

study the bone metastasis of osteotropic cancers by providing cellular viability and proliferation, osteogenic differentiation without using osteogenic media and formation of 3D tight junction tumoroids with hypoxic core region. Formation of these tightly packed multicellular spheroids is very important for the in vitro tumor models because it replicates intratumoral microenvironment more closely. We present a novel sequential cell culture system in 3D in vitro bone model which can provide a unique environment, mimicking the physiological cell-cell and cell-matrix interactions and leading more relevant osteotropic cancer cell behavior. The hMSC seeded scaffolds are seeded with cancer cells after the hMSCs have differentiated into osteoblasts. The number of viable cells on SC was significant and increased from 33 to 38 days of culture.

Interestingly only on SC experiments, the number of viable cells increased after day 28; no of viable cells decreased for HPCCs and MSCs monocultures. The differentiated hMSCs appear to promote the growth of cancer cells. So increased viability of either MSCs or HPCCs or both could be the possible reason of increased number of viable cells in sequential culture. Overall, the experiments do indicate that the scaffold system with SC is a good model for evaluation of cancer cell growth in bone environment.

SEM images from SC indicate cell spreading, adhesion, infiltration and extracellular matrix formation on the PCL/ in situ HAPclay scaffolds. The hMSCs or differentiated hMSCs are quite distinguishable from the HPCCs due to their flattened morphology and arrangement on the surface of the scaffolds. The sequential culture of HPCCs with MSCs on the scaffolds has shown organized multicellular spheroids with tight cellular junctions. These tight 3D structures have been designated as ‘tumoroids’. Interestingly these tumoroids did not form on HPCCs monoculture or when HPCCs sequentially cultured with human osteoblasts on the same

scaffolds. The role of the newly differentiating hMSCs appears to be vital for tumoroid formation.

Further, the ability of anticancer drug encapsulated polymersomes to kill HPCCs was assessed using WST-1 cell viability assay. Generally, the anticancer drugs delivered through the polymersomes is shown to be effective on the SC seeded scaffolds. Thus, in conclusion, PCL/Nanoclay scaffold system seeded with SC of hMSCs and HPCCs presents a good model system for evaluation of drugs, drug carriers, combinations, and their effectiveness. Besides, this 3D in vitro model has opened a new window to study the interaction between osteotropic cancer and bone microenvironment.

2.5. Acknowledgments

Experiments (AFM, FTIR, Electron microscopy) conducted in this work are made possible through instrumentation obtained using grants from National Science Foundation (IMR and MRI). Support from ND EPSCoR for tissue engineering laboratory is also acknowledged.

2.6. References

[1] B.J. Gill, J.L. West, Modeling the tumor extracellular matrix: Tissue engineering tools repurposed towards frontiers in cancer biology, Journal of Biomechanics 47(9) (2014) 1969-78

[2] S.S. Verbridge, E.M. Chandler, C. Fischbach, Tissue-engineered three-dimensional tumor models to study tumor angiogenesis, Tissue engineering. Part A 16(7) (2010) 2147.

[3] S. Pranav, J.A. Kelber, J.W. Lee, T.N. Wright, K.S. Vecchio, R.L. Klemke, S.C. Chen, Cancer cell migration within 3D layer-by-layer microfabricated photocrosslinked PEG scaffolds with tunable stiffness, Biomaterials 33(29) (2012) 7064-7070.

[4] C.L. Chaffer, R.A. Weinberg, A Perspective on Cancer Cell Metastasis, Science 331(6024) (2011) 1559-1564.

[5] I.J. Fidler, The pathogenesis of cancer metastasis: the 'seed and soil' hypothesis revisited, Nature reviews. Cancer 3(6) (2003) 453.

[6] P.S. Steeg, Tumor metastasis: mechanistic insights and clinical challenges, Nature medicine 12(8) (2006) 895.

[7] S. Valastyan, R.A. Weinberg, Tumor metastasis: molecular insights and evolving paradigms, Cell 147(2) (2011) 275.

[8] A.B. Al-mehdi, K. Tozawa, A.B. Fisher, L. Shientag, A. Lee, R.J. Muschel, A.B. Al-Mehdi, Intravascular origin of metastasis from the proliferation of endothelium-attached tumor cells: a new model for metastasis, Nature medicine 6(1) (2000) 100.

[9] L. Bubendorf, A. Schopfer, U. Wagner, G. Sauter, H. Moch, N. Willi, T.C. Gasser, M.J. Mihatsch, Metastatic patterns of prostate cancer: an autopsy study of 1,589 patients, Hum Pathol 31(5) (2000) 578-83.

[10] S. Casimiro, T.A. Guise, J. Chirgwin, The critical role of the bone microenvironment in cancer metastases, Molecular and Cellular Endocrinology 310(1–2) (2009) 71-81.

[11] S.-m. Käkönen, G.R. Mundy, S.-M. Käkönen, Mechanisms of osteolytic bone metastases in breast carcinoma, Cancer 97(3 Suppl) (2003) 834.

[12] J.A. Sterling, J.R. Edwards, T.J. Martin, G.R. Mundy, Advances in the biology of bone metastasis: How the skeleton affects tumor behavior, Bone 48(1) (2011) 6-15.

[13] H.-S. Yu, S.-W. Wang, A.-C. Chang, H.-C. Tai, H.-I. Yeh, Y.-M. Lin, C.-H. Tang, Bradykinin promotes vascular endothelial growth factor expression and increases angiogenesis in human prostate cancer cells, Biochemical Pharmacology 87(2) (2014) 243-253.

[14] Y. Kang, P.M. Siegel, W. Shu, M. Drobnjak, S.M. Kakonen, C. Cordón-cardo, T.A. Guise, J. Massagué, C. Cordón-Cardo, A multigenic program mediating breast cancer metastasis to bone, Cancer cell 3(6) (2003) 537.

[15] X. Lu, Q. Wang, G. Hu, C. Van Poznak, M. Fleisher, M. Reiss, J. Massagué, Y. Kang, ADAMTS1 and MMP1 proteolytically engage EGF-like ligands in an osteolytic signaling cascade for bone metastasis, Genes & development 23(16) (2009) 1882.

[16] R. Nicholson, G. Murphy, R. Breathnach, Human and rat malignant-tumor-associated messenger-rnas encode stromelysin-like metalloproteinases, Biochemistry 28(12) (1989) 5195-5203.

[17] P. Gassmann, J. Haier, G.L. Nicolson, Cell adhesion and invasion during secondary tumor formation: interactions between tumor cells and host organs, Cancer Growth and Progression-Dordrecht 11 (2008) 21-32.

[18] T. Yoneda, T. Hiraga, Crosstalk between cancer cells and bone microenvironment in bone metastasis, Biochemical and Biophysical Research Communications 328(3) (2005) 679-687.

[19] M.J. Bissell, D. Radisky, Putting tumours in context, Nature Reviews Cancer 1(1) (2001) 46-54.

[20] Y. Yoshii, A. Waki, K. Yoshida, A. Kakezuka, M. Kobayashi, H. Namiki, Y. Kuroda, Y. Kiyono, H. Yoshii, T. Furukawa, T. Asai, H. Okazawa, J.G. Gelovani, Y. Fujibayashi, The use of nanoimprinted scaffolds as 3D culture models to facilitate spontaneous tumor cell migration and well-regulated spheroid formation, Biomaterials 32(26) (2011) 6052-6058.

[21] R.Z. Lin, H.Y. Chang, Recent advances in three-dimensional multicellular spheroid culture for biomedical research, Biotechnol J 3(9-10) (2008) 1172-84.

[22] N.T. Elliott, F. Yuan, A review of three-dimensional in vitro tissue models for drug discovery and transport studies, J Pharm Sci 100(1) (2011) 59-74.

[23] M.J. Bissell, P.A. Kenny, D.C. Radisky, Microenvironmental regulators of tissue structure and function also regulate tumor induction and progression: the role of extracellular matrix and its degrading enzymes, Cold Spring Harbor symposia on quantitative biology 70 (2005) 343.

[24] K.W. Ng, D.T.W. Leong, D.W. Hutmacher, The challenge to measure cell proliferation in two and three dimensions, Tissue Engineering 11(1-2) (2005) 182-191.

[25] M.A.D. Faute, L. Laurent, D. Ploton, M.F. Poupon, J.C. Jardillier, H. Bobichon, Distinctive alterations of invasiveness, drug resistance and cell-cell organization in 3D-cultures of MCF-7, a human breast cancer cell line, and its multidrug resistant variant, Clinical & Experimental Metastasis 19(2) (2002) 161-168.

[26] M. Leung, F.M. Kievit, S.J. Florczyk, O. Veiseh, J. Wu, J.O. Park, M.Q. Zhang, Chitosan-Alginate Scaffold Culture System for Hepatocellular Carcinoma Increases Malignancy and Drug Resistance, Pharmaceutical Research 27(9) (2010) 1939-1948.

[27] K.A. Beningo, M. Dembo, Y.I. Wang, Responses of fibroblasts to anchorage of dorsal extracellular matrix receptors, Proceedings of the National Academy of Sciences of the United States of America 101(52) (2004) 18024-18029.

[28] N.P. Rhodes, J.K. Srivastava, R.F. Smith, C. Longinotti, Metabolic and histological analysis of mesenchymal stem cells grown in 3-D hyaluronan-based scaffolds, Journal of Materials Science-Materials in Medicine 15(4) (2004) 391-395.

[29] S. Ghosh, G.C. Spagnoli, I. Martin, S. Ploegert, P. Demougin, M. Heberer, A. Reschner, Three-dimensional culture of melanoma cells profoundly affects gene expression profile: a high density oligonucleotide array study, Journal of cellular physiology 204(2) (2005) 522.

[30] P.A. Kenny, G.Y. Lee, C.A. Myers, R.M. Neve, J.R. Semeiks, P.T. Spellman, K. Lorenz, E.H. Lee, M.H. Barcellos-Hoff, O.W. Petersen, J.W. Gray, M.J. Bissell, The morphologies of breast cancer cell lines in three-dimensional assays correlate with their profiles of gene expression, Molecular Oncology 1(1) (2007) 84-96.

[31] R. Jarrahy, W. Huang, G.H. Rudkin, J.M. Lee, K. Ishida, M.D. Berry, M. Sukkarieh, B.M. Wu, D.T. Yamaguchi, T.A. Miller, Osteogenic differentiation is inhibited and angiogenic expression is enhanced in MC3T3-E1 cells cultured on three-dimensional scaffolds, American journal of physiology. Cell physiology 289(2) (2005) C408.

[32] K. Wolf, P. Friedl, Mapping proteolytic cancer cell-extracellular matrix interfaces, Official Journal of the Metastasis Research Society 26(4) (2009) 289-298.

[33] S. Talukdar, S.C. Kundu, Engineered 3D Silk-Based Metastasis Models: Interactions Between Human Breast Adenocarcinoma, Mesenchymal Stem Cells and Osteoblast-Like Cells, Advanced Functional Materials 23(42) (2013) 5249-5260.

[34] R. Marlow, G. Honeth, S. Lombardi, M. Cariati, S. Hessey, A. Pipili, V. Mariotti, B. Buchupalli, K. Foster, D. Bonnet, A. Grigoriadis, P. Rameshwar, A. Purushotham, A. Tutt, G. Dontu, A novel model of dormancy for bone metastatic breast cancer cells, Cancer research 73(23) (2013) 6886.

[35] C. Fischbach, R. Chen, T. Matsumoto, T. Schmelzle, J.S. Brugge, P.J. Polverini, D.J. Mooney, Engineering tumors with 3D scaffolds, Nature methods 4(10) (2007) 855.

[36] X. Wang, L. Sun, M.V. Maffini, A. Soto, C. Sonnenschein, D.L. Kaplan, A complex 3D human tissue culture system based on mammary stromal cells and silk scaffolds for modeling breast morphogenesis and function, Biomaterials 31(14) (2010) 3920-3929.

[37] E.T. Roussos, J.S. Condeelis, A. Patsialou, Chemotaxis in cancer, Nat Rev Cancer 11(8) (2011) 573-587.

[38] H. Kwon, H.J. Kim, W.L. Rice, B. Subramanian, S.H. Park, I. Georgakoudi, D.L. Kaplan, Development of an in vitro model to study the impact of BMP-2 on metastasis to bone, Journal of Tissue Engineering and Regenerative Medicine 4(8) (2010) 590-599.

[39] O. Hartman, C. Zhang, E.L. Adams, M.C. Farach-Carson, N.J. Petrelli, B.D. Chase, J.F. Rabolt, Biofunctionalization of electrospun PCL-based scaffolds with perlecan domain IV peptide to create a 3-D pharmacokinetic cancer model, Biomaterials 31(21) (2010) 5700-5718.

[40] S.P. Pathi, D.D.W. Lin, J.R. Dorvee, L.A. Estroff, C. Fischbach, Hydroxyapatite nanoparticle-containing scaffolds for the study of breast cancer bone metastasis, Biomaterials 32(22) (2011) 5112-5122.

[41] C.S. Szot, C.F. Buchanan, J.W. Freeman, M.N. Rylander, 3D in vitro bioengineered tumors based on collagen I hydrogels, Biomaterials 32(31) (2011) 7905-7912.

[42] S. Sieh, A.V. Taubenberger, M.L. Lehman, J.A. Clements, C.C. Nelson, D.W. Hutmacher, Paracrine interactions between LNCaP prostate cancer cells and bioengineered bone in 3D in vitro culture reflect molecular changes during bone metastasis, Bone (0).

[43] S. Bersini, J.S. Jeon, G. Dubini, C. Arrigoni, S. Chung, J.L. Charest, M. Moretti, R.D. Kamm, A microfluidic 3D in vitro model for specificity of breast cancer metastasis to bone, Biomaterials 35(8) (2014) 2454-2461.

[44] A.H. Ambre, D.R. Katti, K.S. Katti, Biomineralized hydroxyapatite nanoclay composite scaffolds with polycaprolactone for stem cell-based bone tissue engineering, Journal of Biomedical Materials Research Part A (2014) n/a-n/a.

[45] P. Zorlutuna, N. Annabi, G. Camci-Unal, M. Nikkhah, J.M. Cha, J.W. Nichol, A. Manbachi, H. Bae, S. Chen, A. Khademhosseini, Microfabricated Biomaterials for Engineering 3D Tissues, Advanced Materials 24(14) (2012) 1782-1804.

[46] E.L.S. Fong, S.-E. Lamhamedi-Cherradi, E. Burdett, V. Ramamoorthy, A.J. Lazar, F.K. Kasper, M.C. Farach-Carson, D. Vishwamitra, E.G. Demicco, B.A. Menegaz, H.M. Amin, A.G. Mikos, J.A. Ludwig, Modeling Ewing sarcoma tumors in vitro with 3D scaffolds, Proceedings of the National Academy of Sciences 110(16) (2013) 6500-6505.

[47] E.L. Fong, M. Santoro, M.C. Farach-Carson, F.K. Kasper, A.G. Mikos, Tissue engineering perfusable cancer models, Current Opinion in Chemical Engineering 3(0) (2014) 112-117.

[48] A. Ambre, K.S. Katti, D.R. Katti, In situ mineralized hydroxyapatite on amino acid modified nanoclays as novel bone biomaterials, Materials Science & Engineering C-Materials for Biological Applications 31(5) (2011) 1017-1029.

[49] D. Verma, K.S. Katti, D.R. Katti, Osteoblast adhesion, proliferation and growth on polyelectrolyte complex-hydroxyapatite nanocomposites, Philosophical Transactions of the Royal Society a-Mathematical Physical and Engineering Sciences 368(1917) (2010) 2083-2097.

[50] R. Khanna, K.S. Katti, D.R. Katti, Bone nodules on chitosan-polygalacturonic acid-hydroxyapatite nanocomposite films mimic hierarchy of natural bone, Acta Biomater 7(3) (2011) 1173-83.

[51] K. Suzuki, R. Sun, M. Origuchi, M. Kanehira, T. Takahata, J. Itoh, A. Umezawa, H. Kijima, S. Fukuda, Y. Saijo, Mesenchymal stromal cells promote tumor growth through the enhancement of neovascularization, Mol Med 17(7-8) (2011) 579-87.

[52] L. Qiao, Z. Xu, T. Zhao, Z. Zhao, M. Shi, R.C. Zhao, L. Ye, X. Zhang, Suppression of tumorigenesis by human mesenchymal stem cells in a hepatoma model, Cell Res 18(4) (2008) 500-7.

[53] S. Wakitani, T. Goto, S.J. Pineda, R.G. Young, J.M. Mansour, A.I. Caplan, V.M. Goldberg, Mesenchymal cell-based repair of large, full-thickness defects of articular cartilage, J Bone Joint Surg Am 76(4) (1994) 579-92.

[54] J.N. Beresford, Osteogenic stem cells and the stromal system of bone and marrow, Clin Orthop Relat Res (240) (1989) 270-80.

[55] J.N. Beresford, J.H. Bennett, C. Devlin, P.S. Leboy, M.E. Owen, Evidence for an inverse relationship between the differentiation of adipocytic and osteogenic cells in rat marrow stromal cell cultures, J Cell Sci 102 (Pt 2) (1992) 341-51.

[56] T. Saito, J.E. Dennis, D.P. Lennon, R.G. Young, A.I. Caplan, Myogenic Expression of Mesenchymal Stem Cells within Myotubes of mdx Mice in Vitro and in Vivo, Tissue Eng 1(4) (1995) 327-43.

[57] S.P. Bruder, N. Jaiswal, S.E. Haynesworth, Growth kinetics, self-renewal, and the osteogenic potential of purified human mesenchymal stem cells during extensive subcultivation and following cryopreservation, Journal of Cellular Biochemistry 64(2) (1997) 278-294.

[58] N. Jaiswal, S.E. Haynesworth, A.I. Caplan, S.P. Bruder, Osteogenic differentiation of purified, culture-expanded human mesenchymal stem cells in vitro, J Cell Biochem 64(2) (1997) 295-312.

[59] L. Toschi, G. Finocchiaro, S. Bartolini, V. Gioia, F. Cappuzzo, Role of gemcitabine in cancer therapy, Future Oncol 1(1) (2005) 7-17.

[60] S. Mussi, R. Sawant, F. Perche, M. Oliveira, R. Azevedo, L.M. Ferreira, V. Torchilin, Novel Nanostructured Lipid Carrier Co-Loaded with Doxorubicin and Docosahexaenoic Acid Demonstrates Enhanced in Vitro Activity and Overcomes Drug Resistance in MCF-7/Adr Cells, Pharmaceutical Research 31(8) (2014) 1882-1892.

[61] Y. Liu, J. Fang, Y.-J. Kim, M.K. Wong, P. Wang, Codelivery of Doxorubicin and Paclitaxel by Cross-Linked Multilamellar Liposome Enables Synergistic Antitumor Activity, Molecular Pharmaceutics 11(5) (2014) 1651-1661.

[62] R. Nahire, M.K. Haldar, S. Paul, A.H. Ambre, V. Meghnani, B. Layek, K.S. Katti, K.N. Gange, J. Singh, K. Sarkar, S. Mallik, Multifunctional polymersomes for cytosolic delivery of gemcitabine and doxorubicin to cancer cells, Biomaterials 35(24) (2014) 6482-97.

[63] D.R. Katti, A. Sharma, A.H. Ambre, K.S. Katti, Molecular interactions in biomineralized hydroxyapatite amino acid modified nanoclay: In silico design of bone biomaterials, Mater Sci Eng C Mater Biol Appl 46 (2015) 207-17.

[64] A.H. Ambre, D.R. Katti, K.S. Katti, Nanoclays mediate stem cell differentiation and mineralized ECM formation on biopolymer scaffolds, J Biomed Mater Res A 101(9) (2013) 2644-60.

[65] K.S. Katti, A.H. Ambre, N. Peterka, D.R. Katti, Use of unnatural amino acids for design of novel organomodified clays as components of nanocomposite biomaterials, Philosophical Transactions of the Royal Society a-Mathematical Physical and Engineering Sciences 368(1917) (2010) 1963-1980.

[66] A.H. Ambre, K.S. Katti, D.R. Katti, Nanoclay Based Composite Scaffolds for Bone Tissue Engineering Applications, Journal of Nanotechnology in Engineering and Medicine 1(3) (2010) 031013-031013.

[67] D.R. Katti, P. Ghosh, S. Schmidt, K.S. Katti, Mechanical Properties of the Sodium Montmorillonite Interlayer Intercalated with Amino Acids, Biomacromolecules 6(6) (2005) 3276-3282.

[68] A.H. Ambre, D.R. Katti, K.S. Katti, Nanoclays mediate stem cell differentiation and mineralized ECM formation on biopolymer scaffolds, Journal of Biomedical Materials Research Part A 101(9) (2013) 2644-2660.

[69] J.S. Lee, J. Feijen, Polymersomes for drug delivery: Design, formation and characterization, Journal of Controlled Release 161(2) (2012) 473-483.

[70] L.D. Mayer, L.C.L. Tai, M.B. Bally, G.N. Mitilenes, R.S. Ginsberg, P.R. Cullis, Characterization of liposomal systems containing doxorubicin entrapped in response to pH gradients, Biochimica et Biophysica Acta (BBA) - Biomembranes 1025(2) (1990) 143-151.

[71] H. Ye, J. Cheng, Y. Tang, Z. Liu, C. Xu, Y. Liu, Y. Sun, Human bone marrow-derived mesenchymal stem cells produced TGFbeta contributes to progression and metastasis of prostate cancer, Cancer Invest 30(7) (2012) 513-8.

[72] J. Luo, S.O. Lee, L. Liang, C.K. Huang, L. Li, S. Wen, C. Chang, Infiltrating bone marrow mesenchymal stem cells increase prostate cancer stem cell population and metastatic ability via secreting cytokines to suppress androgen receptor signaling, Oncogene 33(21) (2014) 2768-2778.

[73] K. Fizazi, J. Yang, S. Peleg, C.R. Sikes, E.L. Kreimann, D. Daliani, M. Olive, K.A. Raymond, T.J. Janus, C.J. Logothetis, G. Karsenty, N.M. Navone, Prostate cancer cells-osteoblast interaction shifts expression of growth/survival-related genes in prostate cancer and reduces expression of osteoprotegerin in osteoblasts, Clin Cancer Res 9(7) (2003) 2587-97.

[74] M. Plaisant, S. Giorgetti-Peraldi, M. Gabrielson, A. Loubat, C. Dani, P. Peraldi, Inhibition of hedgehog signaling decreases proliferation and clonogenicity of human mesenchymal stem cells, PLoS One 6(2) (2011) e16798.

[75] M. Filipak, D.N. Estervig, C.Y. Tzen, P. Minoo, B.J. Hoerl, P.B. Maercklein, M.A. Zschunke, M. Edens, R.E. Scott, Integrated control of proliferation and differentiation of mesenchymal stem cells, Environ Health Perspect 80 (1989) 117-25.

[76] T. Mets, G. Verdonk, In vitro aging of human bone marrow derived stromal cells, Mech Ageing Dev 16(1) (1981) 81-9.

[77] Y. Gotoh, K. Hiraiwa, M. Nagayama, In vitro mineralization of osteoblastic cells derived from human bone, Bone and Mineral 8(3) (1990) 239-250.

[78] R.A. Thibault, L. Scott Baggett, A.G. Mikos, F.K. Kasper, Osteogenic differentiation of mesenchymal stem cells on pregenerated extracellular matrix scaffolds in the absence of osteogenic cell culture supplements, Tissue Eng Part A 16(2) (2010) 431-40.

[79] J.B. Lian, G.S. Stein, Concepts of osteoblast growth and differentiation: basis for modulation of bone cell development and tissue formation, Crit Rev Oral Biol Med 3(3) (1992) 269-305.

[80] S. Sieh, A.A. Lubik, J.A. Clements, C.C. Nelson, D.W. Hutmacher, Interactions between human osteoblasts and prostate cancer cells in a novel 3D in vitro model, Organogenesis 6(3) (2010) 181-188.

[81] Y.K. Girard, C. Wang, S. Ravi, M.C. Howell, J. Mallela, M. Alibrahim, R. Green, G. Hellermann, S.S. Mohapatra, S. Mohapatra, A 3D Fibrous Scaffold Inducing Tumoroids: A Platform for Anticancer Drug Development, PLoS ONE 8(10) (2013) e75345.

[82] M. Stiehler, C. Bunger, A. Baatrup, M. Lind, M. Kassem, T. Mygind, Effect of dynamic 3-D culture on proliferation, distribution, and osteogenic differentiation of human mesenchymal stem cells, J Biomed Mater Res A 89(1) (2009) 96-107.

[83] S.L. Ishaug, G.M. Crane, M.J. Miller, A.W. Yasko, M.J. Yaszemski, A.G. Mikos, Bone formation by three-dimensional stromal osteoblast culture in biodegradable polymer scaffolds, Journal of Biomedical Materials Research 36(1) (1997) 17-28.

[84] X. Zou, H. Li, A. Baatrup, M. Lind, C. Bunger, Engineering of bone tissue with porcine bone marrow stem cells in three-dimensional trabecular metal: in vitro and in vivo studies, APMIS Suppl (109) (2003) 127-32.

[85] A. Ghosh, W.D.W. Heston, Tumor target prostate specific membrane antigen (PSMA) and its regulation in prostate cancer, Journal of Cellular Biochemistry 91(3) (2004) 528-539.

[86] V. Yao, C.E. Berkman, J.K. Choi, D.S. O'Keefe, D.J. Bacich, Expression of prostate-specific membrane antigen (PSMA), increases cell folate uptake and proliferation and suggests a novel role for PSMA in the uptake of the non-polyglutamated folate, folic acid, The Prostate 70(3) (2010) 305-316.

[87] G. Saito, J.A. Swanson, K.D. Lee, Drug delivery strategy utilizing conjugation via reversible disulfide linkages: role and site of cellular reducing activities, Adv Drug Deliv Rev 55(2) (2003) 199-215.

[88] K.R. West, S. Otto, Reversible covalent chemistry in drug delivery, Curr Drug Discov Technol 2(3) (2005) 123-60.

CHAPTER 3. IN VITRO DESIGN OF MESENCHYMAL TO EPITHELIAL TRANSITION OF PROSTATE CANCER METASTASIS USING 3D NANOCLAY BONE-MIMICKING SCAFFOLDS[2]

This chapter describes the mimicking of mesenchymal to epithelial transition (MET) of prostate cancer cells in an in vitro 3D model using the cell line line MDA PCa 2B. Most of the contents of this chapter has been published in MD. S. Molla, Dinesh R. Katti, Kalpana S. Katti, In vitro design of mesenchymal to epithelial transition of prostate cancer metastasis using 3D nanoclay bone-mimetic scaffolds, Journal of Tissue Engineering and Regenerative Medicine 12(3) (2017) 727-737.

3.1. Introduction

Prostate cancer is one of the most commonly diagnosed types of cancer in the United States. Currently, only in the United States, approximately 2.8 million men are living with prostate cancer, and 14.0% of men will be diagnosed with this disease at some point in their life [1].

Like most other solid malignancies, the majority of prostate cancer-associated deaths occur due to metastasis [2]. Bone is a preferred site of metastasis for prostate cancer as it has been found in a study that approximately 80% death suffered by prostate cancer patients, possessed skeletal metastases [3]. Thus, a more comprehensive study is needed to understand the crosstalk between prostate cancer cells and skeletal milieu in osteotropic metastasis. Metastasis involves a complex cascade of sequential events, making it the most enigmatic aspect of the

[2]This chapter was co-authored by MD.S. Molla, K.S. Katti and D.R. Katti. MD. S. Molla had primary responsibility for preparing samples, conducting all tests, and drafting this chapter. Kalpana Katti and Dinesh Katti directed the research orientation and revised this chapter.

disease [4]. To prevent cancer metastasis, it is important to understand the cellular and molecular basis of metastasis which is most likely controlled by distinct genes and signaling pathways. Some extraordinary events take place during the complex cascade of metastasis including epithelial to mesenchymal transition (EMT) and mesenchymal to epithelial transition (MET), where cell phenotype changes between epithelial to mesenchymal state and vice-versa [5]. EMT at the primary tumor location and MET at the site of a secondary tumor during the initial stage of colonization have generated a lot of interest as both have the potential of an effective drug target [6, 7]. Considering the critical roles, they play in metastasis, understanding the molecular mechanism of EMT and MET offers new hope for inhibiting tumor formation and developing anti-cancer drugs. E-Cadherin has a crucial role both in EMT and MET. Silencing or switching of E-Cadherin to N-cadherin during EMT and significant expression of E-Cadherin during MET are two major features that have been revealed about EMT and MET respectively [8, 9]. Expression of transcriptional factors like Snail, Twist, and Vimentin are other major hallmarks for EMT [10]. Another area of intense focus is angiogenesis or new blood vessel formation during colonization of disseminated cancer cells on the site of metastases [11]. Proangiogenic factors like VEGF, IL-8, and HIF-1 encourage the growth and colonization of prostate cancer cells on bone microenvironment to aid skeletal dissemination.

Bone metastasis of prostate cancer could be either osteoblastic or osteoclastic in nature. Osteoblastic factors like Endothelin-1 secreted by prostate cancer causes the osteoblastic lesion, whereas, in osteolytic lesion RANKL secreted by osteoblast activates osteoclast which leads to excessive bone lysis. Factors secreted by prostate cancer cells affects the natural functional balance between osteoblast and osteoclast in the bone native environment [12]. Growth factors secreted by osteoblast also play a seminal role in the progression of prostate cancer [13].

Similarly, growth factors secreted by prostate cancer cells also affects the proliferation and differentiation of osteoblast. In bone microenvironment, bone-derived mesenchymal stem cells (MSCs) differentiate into osteoblast in favorable condition [14]. A transcriptional factor essential for osteoblastic differentiation of MSCs is RUNX2[15]. MSCs are multipotent cells which have the ability to differentiate not only into osteoblastic precursors but also into adipocytes, chondrocytes, fibroblasts, and some other types of cells [16, 17]. Unlike osteoblast, the role of MSCs in prostate cancer development is not clear yet. Recent studies have shown that mesenchymal stem cells contribute to facilitating tumor growth, metastasis, and angiogenesis [18, 19]. It has also been reported that MSCs inhibit tumor development by suppressing proliferation of certain types of cancer [20].

Cancer microenvironments are inherently three dimensional. The recent introduction of 3D in vitro tumor models has brought a tectonic shift in cancer research to overcome the limitations of 2D models as well as understanding tumor biology. 3D models mimic native tissue microenvironment more closely which plays a significant role in cancer progression and cellular responses to the anticancer drugs. Although several osteotropic 3D cancer models have been reported so far [21-23], this area still needs to be explored in to create more bone-mimetic microenvironment as an alternative to animal models to study cell-cell communication.

In order to recapitulate prostate cancer bone metastasis, we have engineered an in vitro 3D tumor model based on PCL/HAPClay scaffolds which have been reported in our earlier studies. It contains natural bone component hydroxyapatite (HAP), modified clay, cell secreted ECM and native bone cells. It has been reported that HAP nanoparticle containing scaffolds are an excellent tool to study 3D tumor biology [24], osteogenic differentiating [25], osteoconductivity and osteoinductivity [26]; whereas the promising role of MMT clay in tissue

engineering is well known. In our previous study, we have shown that not only scaffolds materials play significant roles in recreating tumor microenvironment but also cell types and method of cell seeding. We introduced a novel cell culture method which we termed as 'sequential culture'. We demonstrated that multicellular tumoroids with tightly packed cellular junctions are formed when prostate cancer cells are sequentially cultured with human mesenchymal stem cells (MSCs) but not with human osteoblasts [27].

In this study, we intended to investigate the differences in cellular crosstalk among different cultural conditions during osteotropic prostate cancer metastasis in 3D bone mimicking microenvironment. Monoculture, coculture and sequential culture of human prostate cancer cells (PCa), human osteoblasts (hFOB) and human mesenchymal stem cells (MSCs) in PCL/HAPClay scaffolds were analyzed with qRT-PCR technique to evaluate the expression of essential genes which play crucial roles in bone metastasis of prostate cancer cells.

3.2. Materials and method

3.2.1. Preparation of the PCL/HAPClay 3D scaffolds and 2D films

Na-MMT clay was purchased from Clay Minerals Respiratory at the University of Missouri, Columbia. Initially, Na-MMT is modified with 5-aminovaleric acid (Sigma-Aldrich) following the procedure described in prior studies which increased the d-spacing of Na-MMT clay [28-31]. To achieve scaffolds with excellent osteoconductivity, we bio-mineralized hydroxyapatite on modified clay as described in our earlier studies which we termed as in situ HAPClay [32, 33]. Simple wet chemistry was used to prepare in situ HAPClay from Na_2HPO_4 and $CaCl_2$ which were obtained from J.T. Baker. Finally, 3D PCL/HAPClay scaffolds were prepared by adding 10 wt% PCL polymers into the in situ HAPClay using freeze drying method

[27, 34, 35]. PCL polymer (average M_n 80,000; Sigma-Aldrich) was dissolved in 1, 4 dioxane (Sigma-Aldrich) and then HAPClay was added into it to prepare the solution for the scaffolds. The same solution was subjected to room temperature evaporation for making PCL/HAPClay 2D films.

3.2.2. Cell line and culture media

Human osteoblast cell line (hFOB 1.19) was obtained from ATCC and maintained in a medium consist of 90% HyQ Dulbecco's Modified Eagle medium DMEM-12(1:1) from Hyclone, 10% FBS from ATCC and 0.6% G418 solution (antibiotic) from JR scientific. Human prostate cancer cell (PCa) line MDA PCa 2b was obtained from American Type Culture Collection (ATCC) and maintained in a medium consist of 80% BRFF-HPC1 (AthenaES, 0403) and 20% fetal bovine serum (ATCC, 30-2020). Human bone marrow Mesenchymal stem cells (MSCs) were purchased from Lonza, Walkersville (PT-2501) and maintained in MSCGM™ Bulletkit™ medium (Lonza, Walkersville, PT-3001). The Bulletkit™ medium was prepared by adding MSCGM™ SingleQuots™ (Lonza, Walkersville, PT-4105) to MSCBM™ (Lonza, Walkersville, PT-3238). All the cells were maintained at 37 °C and 5% CO_2 in a completely humidified incubator.

3.2.3. Cell seeding: monoculture, coculture, and sequential culture

PCL/HAPClay scaffolds with a diameter 12 mm and thickness 3 mm and PCL/HAPClay films with diameter 12 mm and thickness 0.5 mm, were sterilized and generated in 24- well plates for cell seeding. For 2D monocultures, hFOB cells and PCa cells were seeded per film in a density 5×10^4 and cultured in the respective medium as described earlier. For 3D monocultures, hFOB cells, MSCs, and PCa cells were seeded per scaffold in a density 5×10^4 for each and cultured in the respective medium as described above. For coculture studies 5×10^4 hFOB cells

and PCa cells were seeded simultaneously onto 3D scaffolds in a density 1:1. Similar coculture studies were performed for MSCs and PCa cells. For Sequential culture, initially, 5 x 10^4 hFOB were seeded onto PCL/HAPClay scaffolds. From our previous studies we know that when bone cells are seeded on these scaffolds, they took at least 18 days for ECM and mineralized bone nodule formation [27, 32, 34]. So, we kept hFOB cells culturing for 23 days, and then we seeded the PCa cells on top of the hFOB cells seeded scaffolds in a density 5 x 10^4. For MSCs+PCa cells sequential culture, initially, 5 x 10^4 MSCs were seeded onto PCL/HAPClay scaffolds and cultured to allow osteogenic differentiation and mineralized bone formation. After 23 days we seeded the PCa cells on top of the MSCs seeded scaffolds in a density 5 x 10^4.

3.2.4. Alkaline phosphatase assay

ALP, a plasma membrane enzyme, is marker for osteogenic differentiation of human mesenchymal stem cells. This assay is used to study the differentiation of MSCs to bone cells. Alkaline phosphatase assay was performed only for monoculture of MSCs seeded in scaffolds at day 3, 5, 7, 10, 23 and 33. Samples were washed with PBS and then each sample was placed in a 24-well plate under 850 µl Triton X-100 (Sigma-Aldrich, X-100) per well. The system was then treated with two cycles of freezing-thawing (-70 °C to 37 °C) To obtain cell lysates. The Cell lysate was added to equal volume of (250 µl) p-nitrophenyl phosphate (Sigma-Aldrich, N7653) in a different 24 well-plate and then incubated for an hour at room temperature. In order to deprotonate the p-nitrophenol, 70 µl of 3N NaOH was added to each scaffold and the system was shaken for 60 seconds. Absorbance was measured at 405 nm using a microplate spectrophotometer (Bio-Rad, Benchmark Plus). ALP, a plasma membrane enzyme, is marker for osteogenic differentiation of human mesenchymal stem cells which were used to determine if the MSCs have differentiated to osteoblasts.

3.2.5. Scanning electron microscopy imaging

To study the cell morphology, cell adhesion, infiltration, and mineralized extracellular matrix (ECM) formation we performed SEM imaging using JEOL JSM-6490LV scanning electron microscope. After a given period of tissue culture, samples were removed from the culture condition, washed with PBS. Then fixed with 2.5% glutaraldehyde followed by ethanol series treatment (10 % v/v, 30% v/v, 50 % v/v, 70 % v/v and 100 % v/v) for dehydration. After alcohol treatment, the samples were dried using hexamethyldisilazane. Then gold-coated samples were mounted on SEM stub to observe under scanning electron microscope.

3.2.6. Quantitative reverse transcription-polymerase chain reaction (qRT-PCR) analysis

Total RNA was extracted from cells cultured on PCL/HAPClay 2D films and 3D scaffolds using TRI reagent (Sigma) and purified using Direct-zol^{TM} RNA MiniPrep (Zymo Research). M-MLV reverse transcriptase from Promega. SYBR Green Master MIX (ThermoFisher Scientific) was used for template amplification with a primer for each of the transcripts by following manufacturer's protocol in a 7500 Fast Real-Time PCR system (Applied Biosystems, USA). The samples were incubated for 2 minutes at 50 °C, and PCR was performed at 95 °C for 10 minutes followed by 40 cycles of 15 seconds denaturation at 95 °C, 30 seconds annealing at primer specific temperature and elongation at 60 °C for 1 minute. Gene expression of GAPDH, PSA, E-Cadherin, N-Cadherin, VEGF, RUNX-2, RANKL, FAK PTK2, HIF-1, Snail, and Endothelin-1 was studied using 2D and 3D monoculture, 3D coculture and 3D sequential culture of MSCs, human osteoblast and human prostate cancer (PCa) cells samples, each in triplicate**.** GAPDH served as the house-keeping gene and 2D human osteoblast culture served as control. Target gene expressions were calculated as $2^{-\Delta\Delta Ct}$. Primer sequences were

obtained either from the literature or the primer bank website The primer sequence used in this experiment are listed in Table 3.1.

Table 3.1. The primer sequence used for the qRT-PCR experiment.

Gene	Forward Primer	Reverse Primer
GAPDH [36]	5'-CATCTTCTTTTGCGTCGCCA-3'	5'-TTAAAAGCAGCCCTGGTGACC-3'
PSA	5'-GACCAAGTTCATGCTGTGTGC-3'	5'-CCACTCACCTTTCCCCTCAAG-3'
E-Cadherin [37]	5'-AAG TGA CCG ATGATGAT-3'	5'-R-(5'- CTC TGT CCA TCT CAG CG-3'
N-Cadherin	5'-AGG GTG GAC GTCATTGTA GC-3'	5'-CTG TTG GGG TCT GTC AGG AT-3'
VEGF [38]	5'-GAC AAG AAA ATC CCT GTGGGC-3'	5'-AAC GCG AGT CTG TGT TTT TGC-3'
RUNX-2	5'-CCGCCTCAGTGATTTAGGGC-3'	5'-GGGTCTGTAATCTGACTCTGTCC-3'
RANKL	5'-CAACATATCGTTGGATCACAGC A-3'	5'-GACAGACTCACTTTATGGGAAC C-3'
HIF-1 [39]	5'-CATAAAGTCTGCAACATGGAA GGT-3'	5'-ATTTGATGGGTGAGGAATGGGT T-3'
Snail [37]	5'-TCC AAA CCC ACT CGG ATG TGA-3'	5'-GTG CTT GTG GAG CAA GGA CAT-3'
Endothelin-1	5'-AGAGTGTGTCTACTTCTGCCA-3'	5'-CTTCCAAGTCCATACGGAACAA-3'

For all of the monocultures and cocultures, RNA was collected at day 10 of initial cell seeding. For sequential culture of PCa with osteoblasts, RNA was collected at day 18+10 (10

days after PCa cell seeding). For the sequential culture of PCa with MSCs, RNA was collected at day 28+10 (10 days after PCa cell seeding).

3.2.7. Immunocytochemistry and confocal microscopy

Immunocytochemical analysis was performed for vimentin, cytokeratin and VEGF in PCa 2D and MSCs+PCa SC (Sequential culture of MSCs with prostate cancer cells). Sequential culture and control samples were fixed with 4% paraformaldehyde (PFA) for 30 minutes and then wash three times with fresh 1X PBS (Each wash for five minutes). Samples were treated with 0.5% Triton X-100 in PBS for 5 minutes to permeabilize cells followed by 45 minutes blocking with 1% fish skin gelatin (FSG). Samples were incubated overnight with primary antibodies at 4 °C 1(:150 dilution of anti-vimentin, anti-cytokeratin 7 and anti-VEGF). Then samples were washed with fresh PBS three times and then incubated with corresponding secondary antibodies for an hour at room temperature (Goat Anti-Rabbit IgG H&L Alexa Fluor® 488, Goat Anti-Mouse IgG H&L Alexa Fluor® 488, and Goat Anti-Rabbit IgG H&L Alexa Fluor® 647). Before taking images, samples were stained with 4',6-diamidino-2-phenylindole (DAPI) for 5 minutes. Zeiss Axio Observer Z1 was used for inverted confocal microscopy and Imaris software was used for image analysis.

3.2.8. Statistical analysis

For the statistical analysis one-way ANOVA followed by Tukey's post hoc multiple comparison test was used. Data was considered significantly different when probability values were less than 0.05 ($P < 0.05$). Quantitative data were expressed as a mean ± standard deviation. Triplicate samples were used for performing all the experiments.

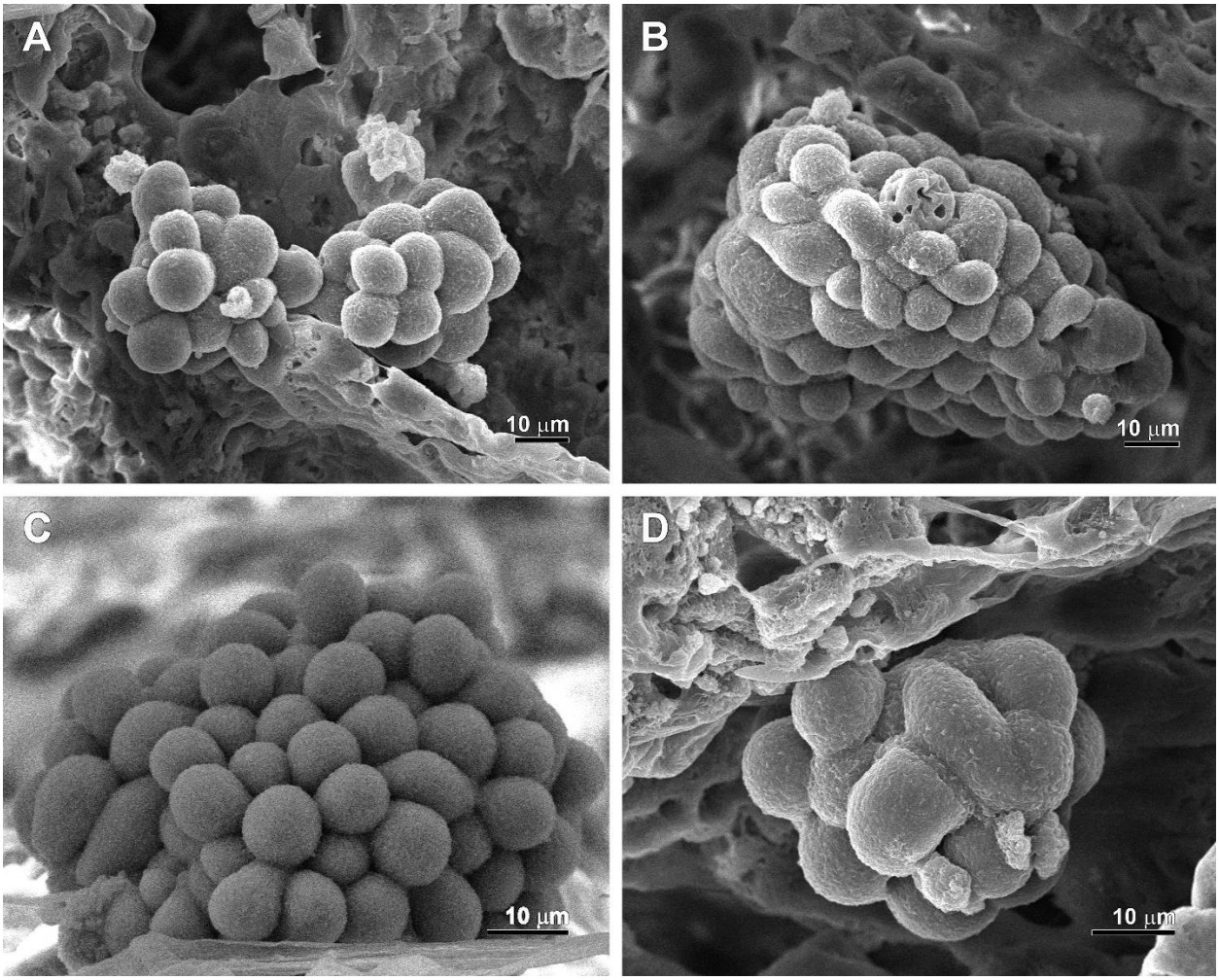

Figure 3.1. SEM micrographs of tumoroids. SEM micrographs showing tumoroids formed in PCL/HAPClay scaffolds by the sequential culture of prostate cancer cells with mesenchymal stem cells (MSCs+PCa SC). PCa cells were seeded on the MSCs seeded scaffolds at day 23, and the culture was continued for 10 more days (Total culture time was 23+10 days).

3.3. Results

3.3.1. Morphological analysis

To analyze cell-constructs on the surface of the scaffolds, we investigated the cellular morphology by performing scanning electron microscopy (SEM). SEM was performed on the sequential culture of PCa cells with MSCs (MSCs+PCa SC) at day 33 (23+10), and the result is shown in the figure 3.1. 3D structures of multicellular tumoroids with tight junctions, hypoxic

core regions, and indistinguishable cellular boundaries were observed for MSCs+PCa SC (figure 3.1 A-D). But like our previous study [27], these tumoroids were not observed on the sequential culture of PCa cells with osteoblasts (hFOB+PCa SC) at day 23+10. There was an evident lack of cell-cell adhesion among the spherical cancer cells as single cells were randomly attached to the scaffold surface instead of aggregating at a place. Similar morphology was observed for the osteoblast, prostate cancer cells, and MSCs monocultures as described in our previous studies [27, 34]. Cell spreading, adhesion, infiltration and extracellular matrix formation was observed on the PCL/HAPClay scaffolds. In MSCs and osteoblast seeded scaffolds, Flattened and elongated cells were observed. Few MSCs and osteoblasts also exhibited rugged and rough surfaced spherical morphology. For prostate cancer (PCa) monoculture, scaffolds did appear to have disorganized aggregates of cells with spherical morphology having loose architecture and rough surface. Unlike MSCs/ osteoblasts, PCa cells did not seem to spread across the surface of the scaffolds.

3.3.2. Osteogenic differentiation and effect of differentiation on formation of tumoroids

To assess if the mesenchymal stem cells (MSCs) have differentiated into the osteoblastic lineage and also to evaluate the effect of differentiation on tumoroid formation, we analyzed the expression of RUNX2 by qRT-PCR. RUNX2 is most familiar as the master regulator of differentiation to osteoblastic lineage [15]. How the RUNX2 expression is changed during the differentiation MSCs to osteoblastic lineage is described in the schematic diagram (figure 3.2C). RUNX2 was analyzed for coculture and sequential of prostate cancer cells with osteoblasts/MSCs (hFOB/MSCs+PCa CC/SC), monocultures of prostate cancer cells (PCa 2D/

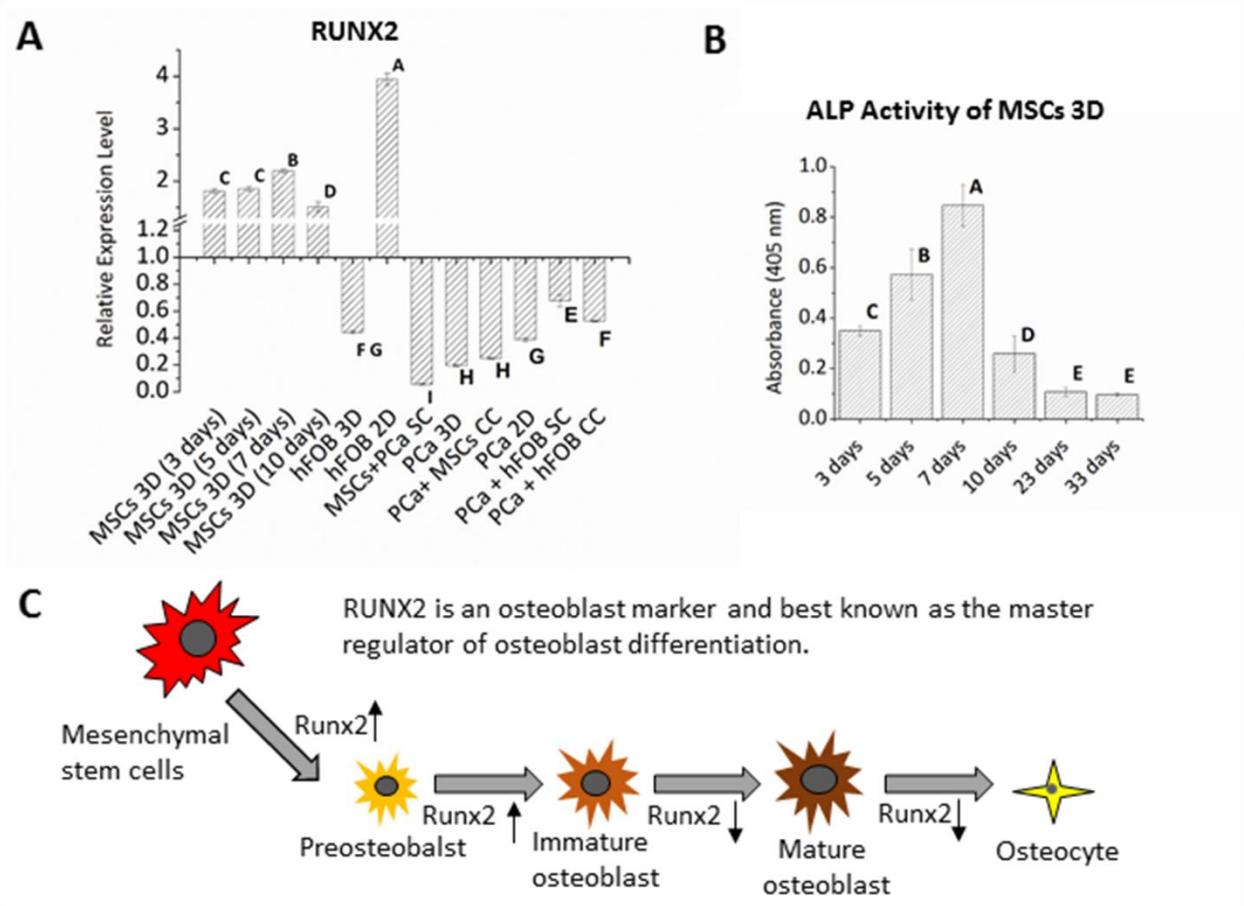

Figure 3.2. Osteogenic differentiation. A) Relative gene expression level of RUNX2, which is normalized to GAPDH and where undifferentiated cultured on 2D TCPS films at day 2 served as control. B) Comparative results from ALP assay for MSCs grown in PCL/HAPClay scaffolds. MSCs: Mesenchymal stem cells; hFOB: osteoblasts; PCa: prostate cancer cells; 3D: Cultured in scaffolds; 2D: Cultured on films; SC: sequential culture; CC: Coculture. All the SCs and CCs were grown on 3D scaffolds. Results are shown as a mean ± standard deviation. Means that do not share a letter are significantly different ($p<0.05$, $n=3$). C) Illustration of RUNX2 activity during osteoblastic differentiation process of MSCs. At the initial stage of the process, RUNX2 expression is upregulated (↑) which positively influences bone matrix related genes. At the later stage of osteoblast maturation, RUNX2 expression is inhibited. It is further inhibited (↓) when mature osteoblast turns into osteocytes.

3D), and monocultures of osteoblasts (hFOB 2D/ 3D). RUNX2 was also analyzed at 48 hours for the MSCs seeded on TCPS and at 3, 5, 7, and, 10 days for MSCs seeded on PCL/HAPClay scaffolds (MSCs 3D). Undifferent iated MSCs seeded on TCPS at day 2 (48 hours) served as

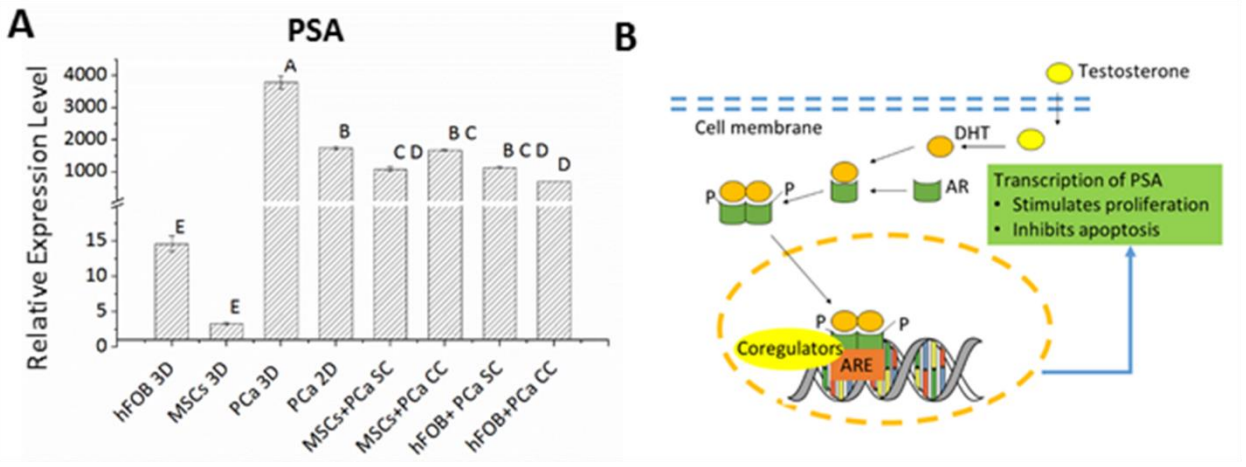

Figure 3.3. PSA expression. A) Relative gene expression level of PSA, which is normalized to GAPDH and where osteoblasts cultured on 2D PCL/HAPClay films at day 10 served as control. MSCs: Mesenchymal stem cells; hFOB: osteoblasts; PCa: prostate cancer cells; 3D: Cultured in scaffolds; 2D: Cultured on films; SC: sequential culture; CC: Coculture. All the SCs and CCs were grown on 3D scaffolds. Results are shown as a mean ± standard deviation. Means that do not share a letter are significantly different ($p<0.05$, $n=3$). B) Illustration of androgen activity to upregulate PSA in the prostate cancer patient. Testosterone gets activated when it transforms into dihydrotestosterone (DHT). DHT gets binds to androgen receptors (ARs). This complex gets phosphorylated, dimerized, and finally, translocates to the nucleus. In the nucleus, it binds to androgen response elements (AREs) and recruits coregulators. This process ultimately upregulates PSA expression leading to increased cell proliferation.

control. The result is shown in the figure 3.2A. We can see from the figure 3.2A that osteoblasts cultured on 2D films (hFOB 2D), has ~4-fold higher expression of RUNX2 than the control (undifferentiated MSCs). RUNX2 expression is elevated when MSCs are seeded on PCL/HAPClay scaffolds at day 3 and its ~2.2 fold increased at day 7. At day 10, RUNX2 expression downregulates compared to day 7. Compared to the control (undifferentiated MSCs), RUNX2 expression downregulates in all the samples including monoculture, coculture and sequential culture of PCa cells with both MSCs and osteoblasts. RUNX2 expression most significantly downregulates in the sequential culture of PCa with MSCs (MSCs+PCa SC). We also performed alkaline phosphatase (ALP) assay to evaluate the differentiation of MSCs to osteogenic lineage and the result is shown in the figure 3.2B. ALP is a cellular membrane bound enzyme which is a key marker for osteoblastic differentiation [40]. ALP activity of MSCs

monoculture in PCL/HAPClay scaffolds (MSCs 3D) was measured at day 3, 5, 7, 10, 23, and, 33 after cell seeding. ALP activity is gradually increased from day 3 to day 7. The peak in ALP activity is observed at day 7. ALP activity at day 10 is significantly lower than day 7. ALP activity is further lowered at day 23 and day 33. There is no statistically significant difference in ALP activity between day 23 and 33.

3.3.3. Analysis of prostate-specific antigen (PSA) expression

To investigate how prostate-specific antigen (PSA) level changes during the different stages of metastasis, we performed a comparative study of PSA expression level in our samples using qRT-PCR experiment. PSA is an androgen-regulated gene, and rising levels of PSA are associated with prostate cancer and other prostatic disorders [41]. The schematic of PSA activity is shown in the figure 3.3B. The comparative expression level of PSA in our 2D and 3D samples of monocultures, cocultures, and sequential cultures is shown in the figure 3.3A where osteoblast cultured on PCL/HAPClay films served as control. In the case of the PCa monocultures, PSA level is very significantly upregulated in the monoculture of PCa in scaffolds (PCa 3D) compared to the monoculture of PCa in 2D films (PCa 2D) at day 10. There is no statistically significant difference in PSA expression levels among the sequential cultures and cocultures of PCa and MSCs/osteoblasts. The PSA expression in the sequential culture of PCa with MSCs (MSCs+PCa SC) is significantly downregulated compared to the monoculture of PCa in 3D scaffolds (PCa 3D). The same observation was made for coculture and sequential culture of PCa cells with osteoblasts (hFOB+PCa CC, hFOB+PCa SC). This data evidently indicates that the tumoroid model that we have developed with the sequential culture of MDA PCa 2b with hMSCs express high level of PSA like in vivo prostate cancer.

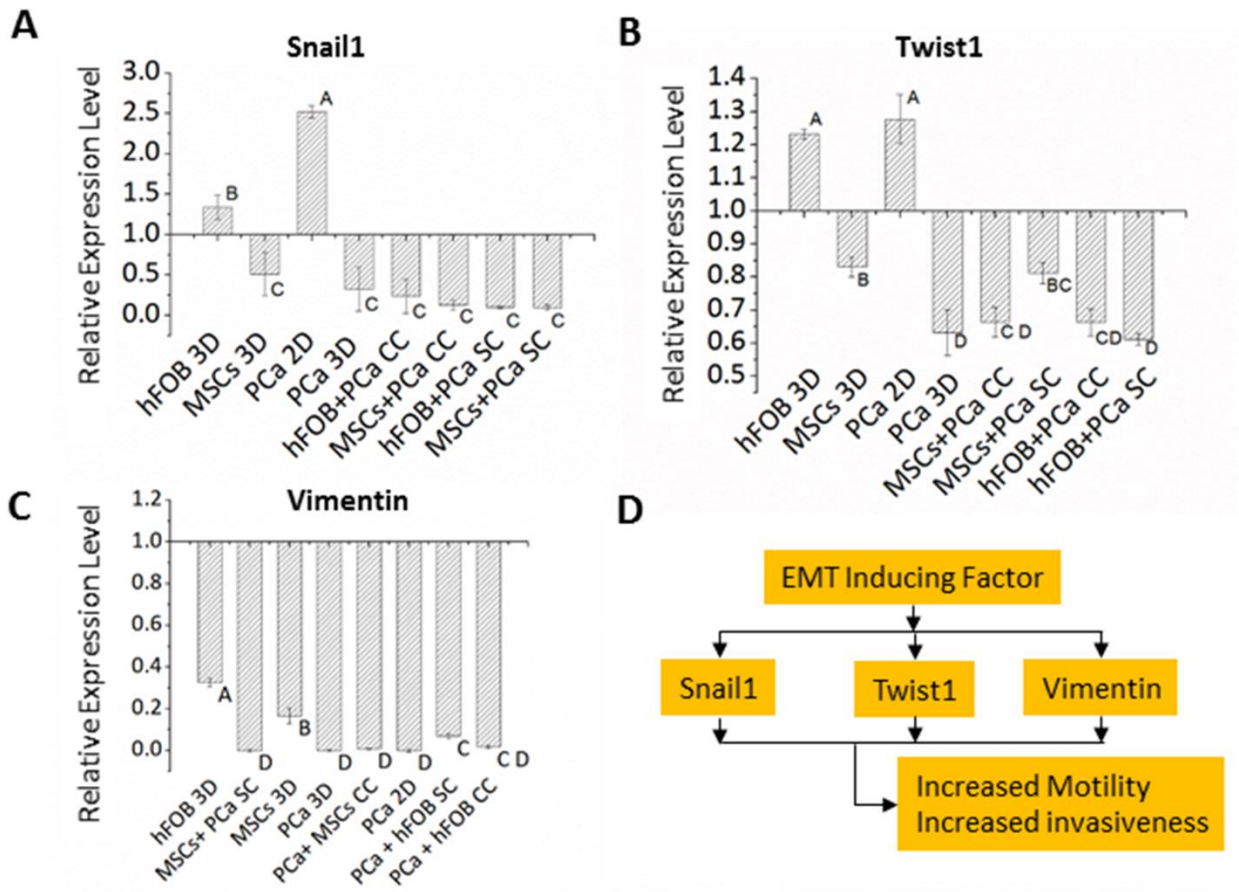

Figure 3.4. Inhibited EMT. Relative gene expression level of A) Snail1; B) Twist1; C) Vimentin; which is normalized to GAPDH and where osteoblasts cultured on 2D PCL/HAPClay films at day 10 served as control. MSCs: Mesenchymal stem cells; hFOB: osteoblasts; PCa: prostate cancer cells; 3D: Cultured in scaffolds; 2D: Cultured on films; SC: sequential culture; CC: Coculture. All the SCs and CCs were grown on 3D scaffolds. Results are shown as a mean ± standard deviation. Means that do not share a letter are significantly different ($p<0.05$, $n=3$). D) EMT marker transcription factors.

3.3.4. Analysis of genes related to epithelial to mesenchymal transition (EMT)

To assess if the sequential culture of PCa cells with MSCs in PCL/HAPClay scaffolds has enhanced the metastatic properties, we analyzed the expressions level of EMT marker genes: N-Cadherin [8], Snail1 [42], Twist1 [43], and, Vimentin [44] on our samples by qRT-PCR experiment. The results are shown in figure 3.4. The expression of N-cadherin was not detected on any of the samples except 2D monocultures of hFOB and PCa. So, the result is not included

in the figure. The expression of Snail1 has downregulated in all the samples compared to the control 2D osteoblast monoculture except in 3D monoculture of osteoblasts (hFOB 3D) and 2D monoculture of prostate cancer cells (PCa 2D). The Snail1 expression is 2.5-fold higher only in the PCa 2D (figure 3.4A). Similar to the Snail1, the Twist1 expression is insignificantly higher only in hFOB 3D and PCa 2D compared to the control hFOB 2D (figure 3.2B). In all of the cocultures, sequential cultures, and 3D PCa monoculture, Twist1 expression is downregulated compared to the control. Vimentin, which is a cytoskeletal filament, is a marker for mesenchymal phenotype [44]. Vimentin was highly expressed in all the samples except monocultures of PCa. Vimentin is most highly expressed in the control (2D osteoblast). Compared to the control, the expression of vimentin in cocultures and sequential cultures of prostate cancer (PCa) cells is almost zero (figure 3.4C).

3.3.5. Analysis of genes related to mesenchymal to epithelial transition (MET)

As if the EMT marker gene expressions are significantly diminished in the sequential culture of prostate cancer (PCa) cells, we further probed the ability of PCa cells to undergo MET. We analyzed the expression of MET marker genes (E-Cadherin and FGFR2) to assess if colonization property of PCa cells has enhanced in our PCL/HAPClay scaffolds during sequential culture with MSCs. While E-Cadherin is known as the hallmark of MET [9], it is also reported that overexpression of FGFR2 is associated with epithelial phenotype during cancer cell colonization at the secondary metastatic site [45-47]. The result is shown in figure 3.5. In figure 3.5A, we can see that E-Cadherin is highly overexpressed in 3D monoculture and sequential culture of PCa cells with MSCs (PCa 3D and MSCs+PCa SC). Compared to the sequential culture of PCa cells with osteoblasts (hFOB+PCa) cells with MSCs and hFOB cells (MSCs/ hFOB+PCa CC), E-cadherin expression is highly upregulated in MSCs+PCa SC. Though E-

cadherin expression is also upregulated in MSCs 3D, hFOB 3D, and PCa 2D compared to the control, however, it is not statistically significant.

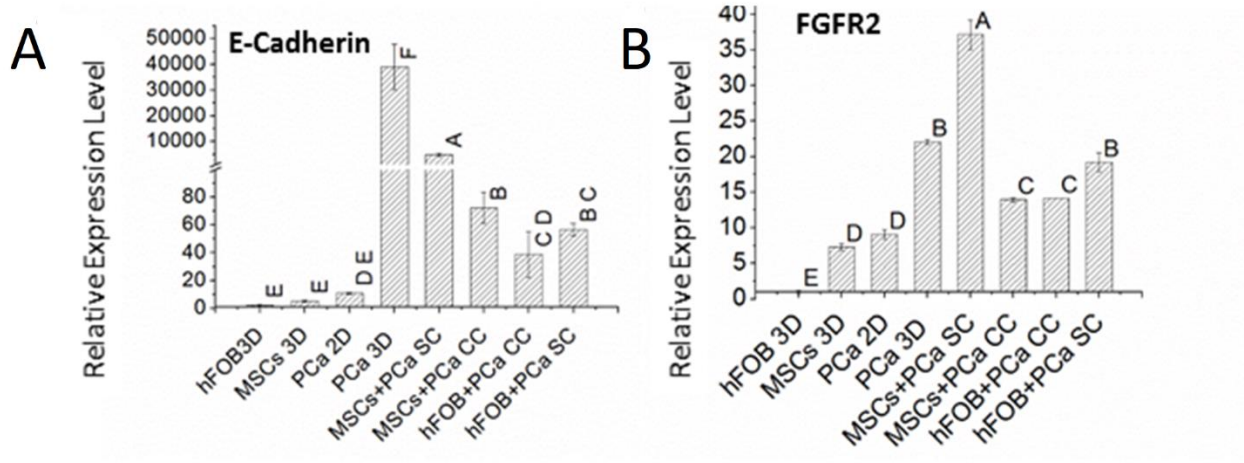

Figure 3.5. Enhanced MET. Relative gene expression level of A) E-Cadherin; B) FGFR2; which is normalized to GAPDH and where osteoblasts cultured on 2D PCL/HAPClay films at day 10 served as control. MSCs: Mesenchymal stem cells; hFOB: osteoblasts; PCa: prostate cancer cells; 3D: Cultured in scaffolds; 2D: Cultured on films; SC: sequential culture; CC: Coculture. All the SCs and CCs were grown on 3D scaffolds. Results are shown as a mean ± standard deviation. Means that do not share a letter are significantly different ($p<0.05$, $n=3$).

FGFR2 expression level is also significantly increased only in the sequential culture of PCa cells with MSCs (MSCs+PCa SC) (figure 3.5B). But like the E-Cadherin, the upregulation level of FGFR2 expression is not that high. On the contrary to E-Cadherin, FGFR2 expression is significantly greater in the sequential culture of PCa cells with MSCs compared to the 3D monoculture of PCa cells in our PCL/HAPClay scaffolds.

Further, immunocytochemical analysis of cytokeratin 7 and vimentin in PCa 2D and MSCs+PCa SC was performed. Results are shown in figure 3.6. Cytokeratin is predominantly expressed in epithelial cells while vimentin is expressed in mesenchymal cells. As seen in figure 3.6 cytokeratin is present in both PCa 2D and tumoroids of MSCs+PCa SC and stained PCa cells in MSCs+PCa SC more intensely than the 2D PCa cells. On the contrary, there were no

expression of vimentin on the tumoroids in MSCs+PCa SC while little expression vimentin was observed in 2D PCa cells. Another conclusion from these observations is that the tumoroids in MSCs+PCa SC are entirely formed by PCa cells as no vimentin expression was observed in the tumoroids.

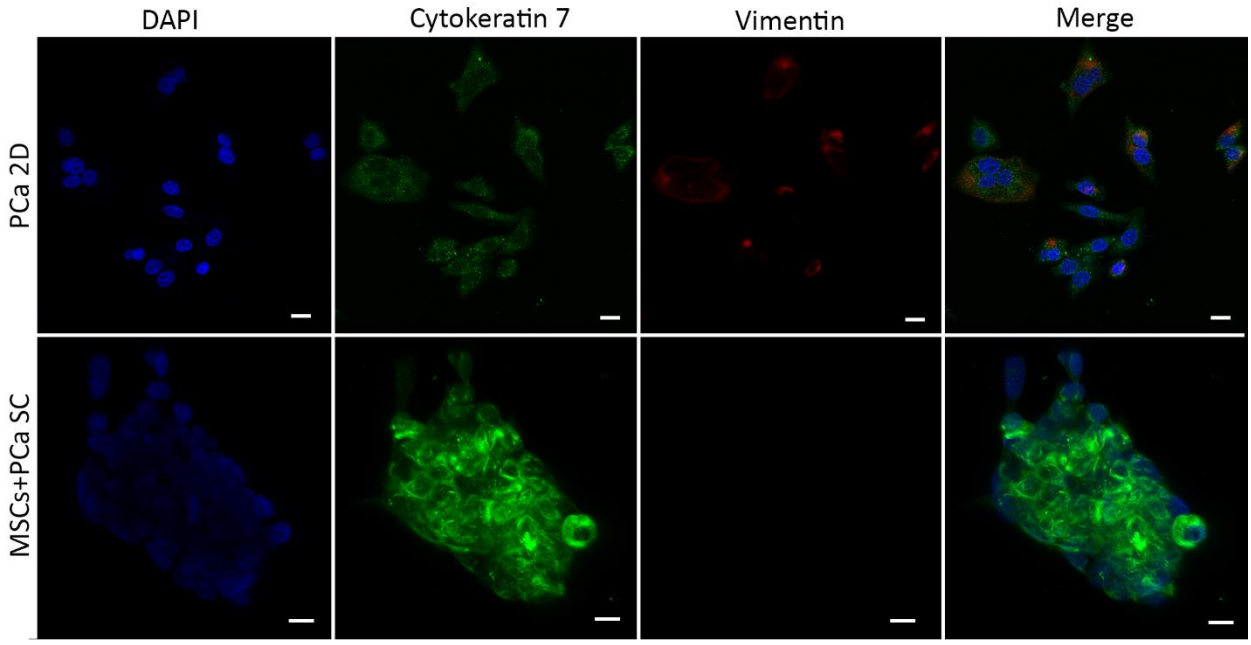

Figure 3.6. Immunocytochemical analysis of EMT and MET markers. Immunofluorescence localization of nuclei (blue, DAPI), cytokeratin 7 (green, Alexa Fluor® 488) and vimentin (red, Alexa Fluor® 647) in 2D prostate cancer cells (PCa 2D) and sequential culture of PCa cells with MSCs (MSCs+PCa SC). PCa cells expressed vimentin in 2D culture, but when they formed multicellular tumoroids in MSCs+PCa SC, no vimentin was observed in the PCa cells.

3.3.6. Analysis of the gene markers related to angiogenesis and hypoxia

Most transcriptional responses to hypoxia are mediated by hypoxia-inducible factors (HIFs) [48]. Hypoxia is the principal regulator of pro-angiogenic factor VEGF, as it is a direct transcriptional target of HIF1 [49]. The role of VEGF and HIF-1 in angiogenesis is explained in the schematic diagram (figure 3.7C). Expression of vascular endothelial growth factor (VEGF) and hypoxia-inducible factor 1 (HIF1) was evaluated using the qRT-PCR technique. The result is

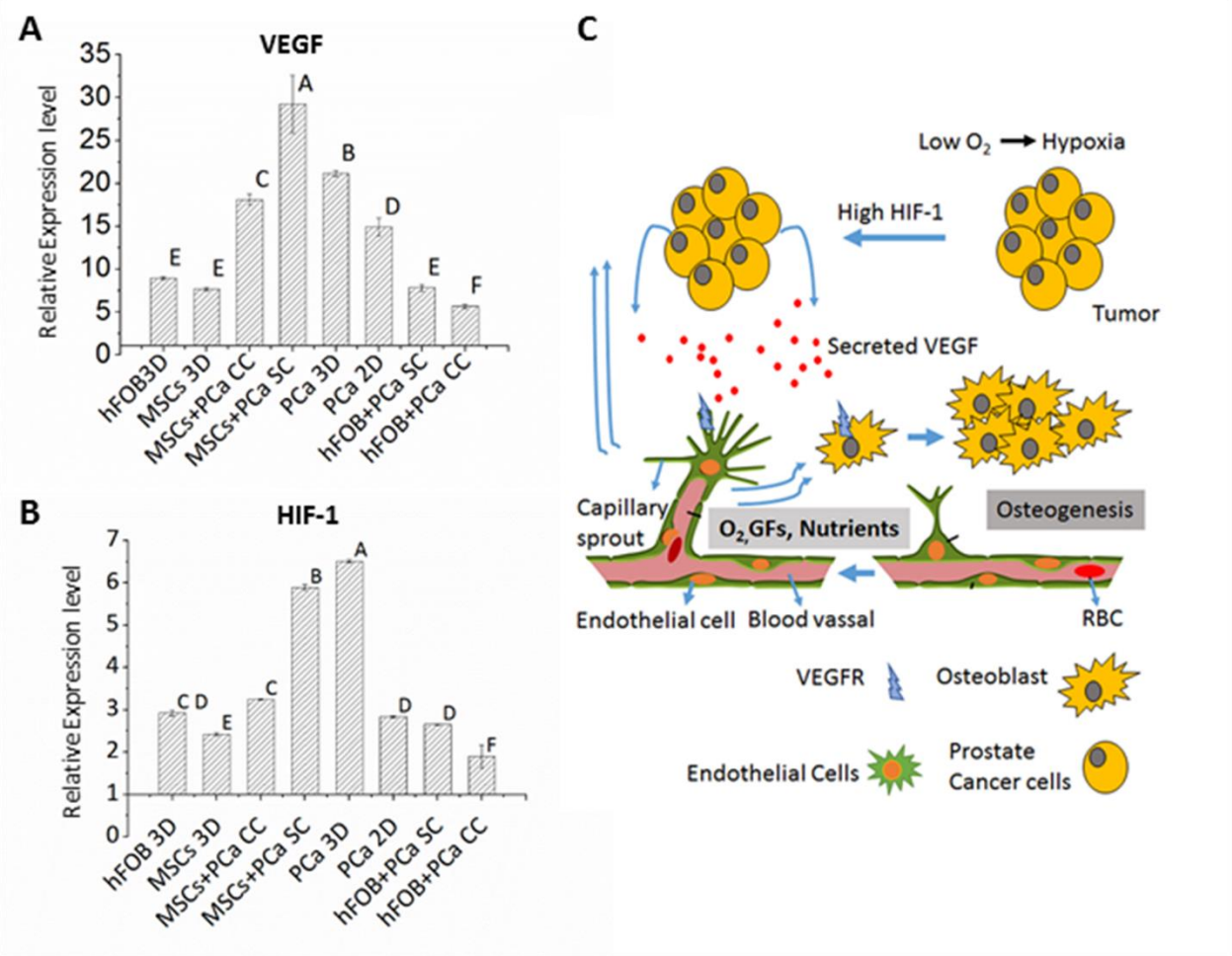

Figure 3.7. Enhanced angiogenesis. Relative gene expression level of A) VEGF; B) HIF-1; which is normalized to GAPDH and where osteoblasts cultured on 2D PCL/HAPClay films at day 10 served as control. MSCs: Mesenchymal stem cells; hFOB: osteoblasts; PCa: prostate cancer cells; 3D: Cultured in scaffolds; 2D: Cultured on films; SC: sequential culture; CC: Coculture. All the SCs and CCs were grown on 3D scaffolds. Results are shown as a mean ± standard deviation. Means that do not share a letter are significantly different ($p<0.05$, $n=3$). C) Regulation of VEGF and HIF-1 during angiogenesis. Hypoxia created in a solid tumor enhances the HIF-1 expression which ultimately positively influences VEGF expression. VEGFR at the surface of capillary sprouts, which are generated by endothelial cells of blood vessel wall, gets attracted by VEGF secreted by hypoxic regions. Capillary tubes hollow out to form new blood vessels. VEGF secreted by tumors also attracted by VEGFR at the surface of osteoblasts which ultimately attracts capillary sprouts of endothelial cells leading to enhanced osteogenesis.

shown in figure 3.7 (A & B). VEGF is significantly overexpressed in the sequential culture of PCa with MSCs (MSCs+PCa SC) compared to all other types of samples (figure 3.7A). It is almost 30-fold upregulated in MSCs+PCa SC compared to the control (2D osteoblast). VEGF is

downregulated in the coculture and sequential culture of PCa cells with osteoblasts (hFOB+PCa CC, hFOB+PCa SC) compared to prostate cancer (PCa) cells monoculture (for both 2D and 3D).

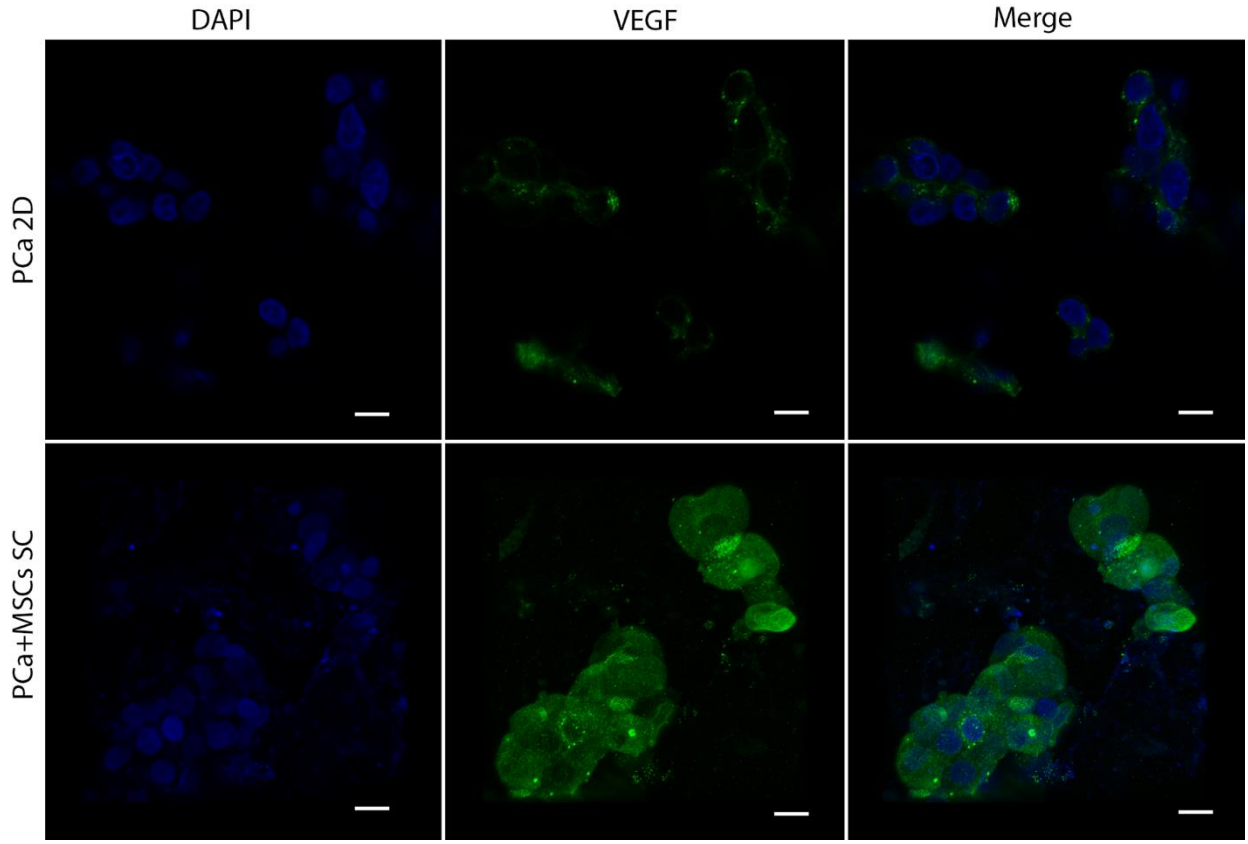

Figure 3.8. Immunocytochemical analysis of VEGF. Immunofluorescence staining of nuclei (blue, DAPI), VEGF (green, Alexa Fluor® 488) in 2D prostate cancer cells (PCa 2D) and sequential culture of PCa cells with MSCs (MSCs+PCa SC). Fluorescent staining for VEGF is brighter in tumoroids formed by PCa cells in MSCs+PCa SC compare to PCa 2D.

HIF1 expression is increased almost 6-fold in the 3D monoculture of prostate cancer (PCa) cells and sequential culture of PCa cells with MSCs (MSCs+PCa SC) compared to the control (2D osteoblasts) (figure 3.7B). The expression level of HIF1 in PCa cells was inhibited when cocultured or sequential cultured with osteoblast (hFOB+PCa CC, hFOB+PCa SC) compared to 3D PCa monoculture. The HIF-1 expression level in 3D osteoblast, 3D MSCs, and 2D PCa cells are not significantly different.

The immunocytochemical analysis was performed to analyze the VEGF expression in MSCs+PCa SC further, and the result is shown in figure 3.8. The result indicates that VEGF is stained both in 2D PCa and MSCs+PCa SC samples but staining is more intense on tumoroids in MSCs+PCa SC than the 2D PCa Cells which is in agreement with our gene expression data for VEGF.

3.3.7. Evaluation of PCa cells activity to create osteoblastic lesion

To evaluate how PCa cells activity to create osteoblastic lesion was affected in the sequential culture during tumoroids formation, we performed a comparative study of Endothelial-1 (ET-1) and RANKL expression level on our samples using qRT-PCR experiment. ET-1 is secreted by prostate cancer cell which plays a key role in the osteoblastic response of bone to metastatic prostate cancer [50]. On the contrary, RANKL is found on the surface of osteoblasts and directly activates osteoclast [51]. During osteoblastic prostate cancer lesion, osteoclast activation by RANKL is inhibited by osteoprotegerin (OPG) which binds to RANKL [12]. The schematic diagram to describe the role of RANKL in osteoblastic-osteoclastic lesion cascade is illustrated in the figure 3.9C. In the figure 3.9B, we can observe that ET-1 expression is significantly higher in the coculture or sequential culture of PCa with osteoblasts cells (hFOB PCa CC, hFOB+PCa SC) compared to the control (2D osteoblasts). The ET-1 expression is also significantly upregulated in the sequential culture of PCa with MSCs (MSCs+PCa SC). In contrast, ET-1 expression in coculture of PCa with MSCs (MSCs+PCa CC) is significantly downregulated compared to the control. Again MSCs+PCa SC has significantly higher expression of ET-1 compared to (hFOB+PCa SC). In all the monocultures (PCa 2D, PCa 3D, hFOB 3D, MSCs 3D), ET-1 expressions are lower compared to cocultures and sequential cultures. The expression level of RANKL is shown in figure 3.9B. RANKL expression is

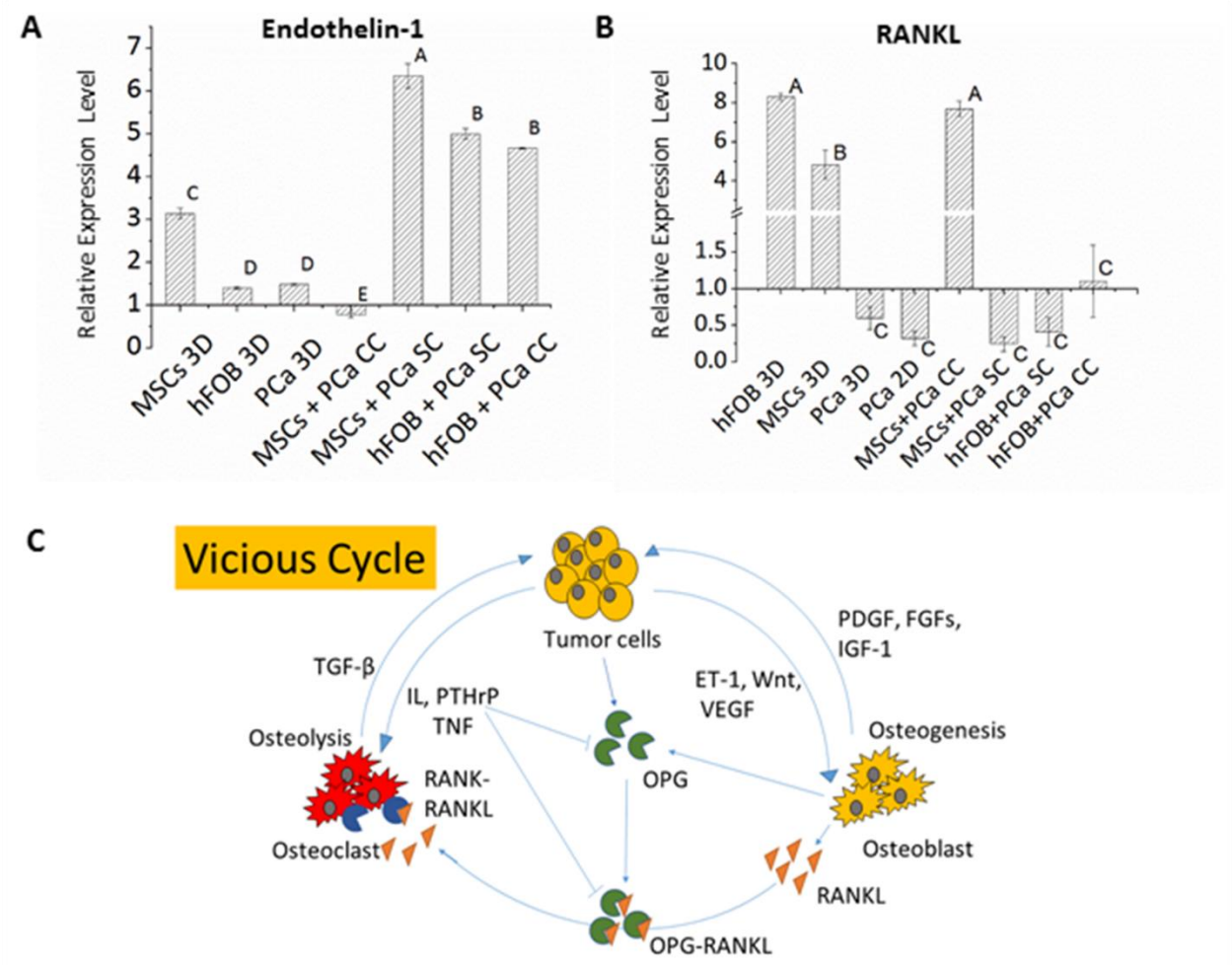

Figure 3.9. Osteoblastic lesion. Relative gene expression level of A) Endothelin-1; B) RANKL; which is normalized to GAPDH and where osteoblasts cultured on 2D PCL/HAPClay films at day 10 served as control. MSCs: Mesenchymal stem cells; hFOB: osteoblasts; PCa: prostate cancer cells; 3D: Cultured in scaffolds; 2D: Cultured on films; SC: sequential culture; CC: Coculture. All the SCs and CCs were grown on 3D scaffolds. Results are shown as a mean ± standard deviation. Means that do not share a letter are significantly different ($p<0.05$, $n=3$). C) Inhibition of RANKL during osteoblastic prostate cancer lesion. In the osteoclastic lesion, RANKL secreted by osteoblasts binds to RANK at the surface of osteoclast leading to osteolysis. But in the osteoblastic lesion, the translocation of RANKL to osteoclast is blocked by OPG which binds to RANKL leading to form RANKL-OPG complex.

significantly downregulated in both cocultures and sequential culture of PCa with hFOB (hFOB PCa CC, hFOB+PCa SC). On the other hand, for coculture (MSCs+PCa CC) and sequential culture (MSCs+PCa SC) of MSCs with PCa, we can see totally contrasted result. RANKL expression is significantly upregulated for MSCs+PCa CC and significantly downregulated in

MSCs+PCa SC. RANK expression also significantly upregulated both in 3D monocultures of MSCs and hFOB and downregulated in both of the monocultures of PCa cells (PCa 2D, PCa a limitations of 2D petri dish cell culture systems have instigated the design and development of tissue engineered in vitro 3D cell culture models.

3.4. Discussion

The use of 3D tumor models in cancer research has brought a drastic change in the study of understanding tumor biology and drug discovery as these models closely mimic biochemical and physiological microenvironment of solid tumor regarding cell organization, differentiation, homeostasis, migration, and metastasis. Recently, various bone replicating 3D tumor models have been reported to recapitulate skeletal metastasis of cancer cells although it is challenging to imitate the entire metastatic cascade [24, 52, 53]. Attempts have been made to study the crosstalks between metastasized cancer cells and bone microenvironment using direct/ indirect coculture of cancer cells with bone cells like osteoblasts, MSCs, osteoclasts, and osteocytes [10, 22, 54]. One of the major limitations of this coculture system is both of the cells are seeded simultaneously on the scaffold system whereas in in vivo condition cancer cells find these bone cells already growing, differentiating and releasing molecular factors which cause a high affinity of prostate cancer cells for the skeletal milieu. Herein, we implemented a specialized culture system which we termed as ‘sequential culture’ to simulate a unique tumor niche for skeletal metastasis. It allows prostate cancer cells to colonize in a 3D environment where multiple cell layers of osteoblastic tissue are already formed. In the sequential culture of prostate cancer cells, initially, we seeded human mesenchymal stem cells (MSCs) on our PCL/HAPClay scaffolds and cultured them for 23 days to allow the differentiation to osteoblastic lineage and bone formation.

After 23 days, we seeded human prostate cancer (PCa) cells on MSCs seeded scaffolds to facilitate tumor initiation and progression. Our earlier studies indicated cell attachment, cell infiltration, cell spreading and mineralized extracellular matrix (ECM) formation without using osteogenic supplements when MSCs are seeded on PCL/HAPClay scaffolds [34]. The presence of hierarchically organized reminiscent of natural bone was also observed in this MSCs seeded scaffolds. We also sequentially cultured PCa cells with human osteoblast (hFOB) cells. As SEM images indicate, when human PCa cells are sequentially cultured with human MSCs, multicellular tumoroids with the cellular tight junction and a 3D architecture are formed. Similar tumoroids were not observed in PCa cells monoculture, in coculture with MSCs/hFOB, or even in the sequential culture of PCa cells with human osteoblasts [27]. The roles of MSCs in prostate cancer development has not been elucidated yet. In our sequential cell culture system, PCa cells and differentiated/ undifferentiated MSCs were directly in contact with each other, and the culture medium contained the soluble factors released by both MSCs and PCa cells. Sequential cell culture system of PCa cells with MSCs allowed the tumor growth in the presence of undifferentiated MSCs, premature/ mature osteoblasts and soluble factors released by those cells which created a more bone-mimetic microenvironment for PCa cells. The PCL/HAPClay scaffolds could have played a key role in tumoroid formation. Formation of tumoroids have been reported on ultra-low attachment culture plates/ hydrophobic surfaces [10, 55] which are not the case here as well-attachment and spreading of MSCs/ osteoblasts, even attachment of single prostate cancer cells in PCL/HAPClay scaffolds have been reported in our earlier studies. It has been reported that mechanical (elastic modulus, stiffness) and structural (porosity, pore size and, topography) properties of a substrate crucially influence the fate of cells in 3D scaffolds [56-58].

To investigate the key markers gene expressions for MSCs differentiation to osteogenic lineage, prostate specific antigen (PSA) expression, EMT/ MET properties, colonization, angiogenesis, and activity of PCa cells to create osteoblastic lesion using qRT-PCR experiment. Differentiation of MSCs to bone precursor is very crucial for creating a humanoid bone-replicating tissue model. The entire population of MSCs can undergo osteogenic differentiation under appropriate culture condition [59]. In our earlier studies, we demonstrated using ALP assay that MSCs undergo osteogenic differentiation in PCL/HAPClay scaffolds without osteogenic supplements [27, 34]. Herein, we observed the RUNX2 activity along with ALP to investigate the osteogenic differentiation of the MSCs in PCL/HAPClay scaffolds. RUNX2 plays a crucial role in early stage of osteogenic differentiation of MSCs. It positively influences the initial stage of differentiation but in the later phase, the RUNX2 expression is inhibited [60]. How RUNX2 regulates osteoblastic differentiation is described in figure 3.2C. RUNX2 expression data evidently indicates osteogenic differentiation of MSCs in PCL/ HAPClay scaffolds (MSCs 3D) at the early stage of cell seeding as RUNX2 expression is upregulated at day 3, 5 and 7 (figure 3.2A). Downregulation of RUNX2 after day 7 indicates initiation of the osteoblast maturation. RUNX2 expression is substantially downregulated in the sequential culture of PCa cells with MSCs (MSCs+PCa SC) which suggests that PCa cells possibly enhances osteoblast maturation at the later stage of MSCs differentiation. It has also been reported that RUNX2 enhances prostate cancer invasiveness and inhibit proliferation [61]. We observed a decrease in invasiveness in MSCs+PCa SC at day 33 which also could be a possible reason for downregulation of RUNX2. Similar to RUNX2, ALP activity was higher in the early stage of MSCs seeding. Drop in ALP activity of MSCs during osteogenic differentiation after day 8 is reported in the literature [62]. Little ALP activity was also observed in our earlier studies

at the later stage of cell seeding. Loss of ALP activity has been correlated with the mineralized extracellular matrix deposition by the osteoblasts.

PSA is uniquely secreted by prostate epithelial cells and therefore remains the gold standard marker for the early prostate cancer diagnosis [63]. In the figure 3B, it has been described how elevated level of PSA is associated with androgen-dependent prostate cancer [64]. In figure 3.3A, we observed significantly higher expression of PSA in PCa 3D compared to PCa 2D which indicates enhancement of aggressiveness of prostate cancer cells when cultured in the PCL/ HAPClay scaffolds [65]. Compared to PCa 3D monoculture, PSA expression is downregulated in all of the cocultures/ sequential cultures of PCa cells with the osteoblasts/ MSCs. These results could be explained by the fact that when PCa cells reach bone microenvironment, initially PSA expression downregulates in response to the soluble factors released by bone cells [66].

Epithelial to mesenchymal transition (EMT) is a biological process that involves the functional transformation of cancerous epithelial cells at the site of a primary tumor to undergo multiple biochemical changes that allow it to assume a mobile mesenchymal cell phenotype [67]. EMT is viewed as an essential early step in tumor metastasis [68]. Transcription factors like Snail1, Twist1, vimentin is greatly associated with EMT process which prompted to use them as EMT biomarkers [69-71]. High expression of these EMT marker genes is considered to be associated with migration and invasive capability of metastatic cancer cells. Both of Snail1 and TWIST1 is downregulated in PCa 3D (seeded in scaffolds) either in monoculture or coculture/sequential culture compared to PCa 2D cells (figure 3.4A, 3.4B). This result indicates that EMT property (migration/ invasiveness) of PCa cells is inhibited in contact of PCL/ HAPClay scaffolds. Vimentin is a cytoskeletal protein that is highly expressed in all

mesenchymal cell phenotype [72]. Therefore, high level of vimentin activity was observed in all of the samples containing MSCs/ hFOB cells (figure 3.4C). Vimentin expression is significantly downregulated in sequential cultures/ cocultures of PCa with MSCs/hFOB compare to control hFOB 2D indicating a migratory property of PCa cells was restrained in MSCs/hFOB+PCa SC/CC cultures. Downregulation of EMT inducers like Twist1, Snail1 are also associated with the reversal of EMT or mesenchymal to epithelial transition (MET), indicating enhancement of MET properties in the sequential culture of PCa cells with MSCs/ osteoblasts [73]. MET at the site of the disseminated tumor metastases is another essential step in the complex metastatic cascade. There is evidence from a number of solid tumors that MET plays a key role during the initial phase of metastatic cancer cell colonization [7, 74]. It is considered that MET is essential for growth of prostate cancer cells when they reach at the bone microenvironment [75]. It has been reported that E-cadherin expression downregulates at the primary metastatic site and highly upregulates at secondary metastases [76]. Therefore, the expression of E-cadherin is considered as the gold hallmark for MET [9]. The peak in E-cadherin expression was observed in the 3D monoculture of PCa cells (PCa 3D). E-cadherin expression also is substantially upregulated (~5000 fold) in MSCs+PCa SC compare to other co/sequential cultures, indicating colonization properties is highly increased (figure 3.5A). E-cadherin also plays a critical role as a cell-cell adhesion molecule [77]. High upregulation of E-cadherin in PCa 3D and MSC+PCa SC is in agreement with our SEM observation as we have seen tight junction tumoroid formation only in the MSCs+PCa SC and disorganized aggregates of cells with strong cell-cell adhesions in the PCa 3D cells. Enhancement of MET and initiation of macrometastases in the MSCs+PCa SC is further confirmed by the expression of another MET related gene FGFR2, as the peak of FGFR2 expression is found in the MSCs+PCa SC (figure 3.5B). One of the major challenges to fight

prostate cancer is the early stage detection of cancer cell colonization at bone microenvironment, because of the refractory nature of bone and lack of applicable in vitro models [78]. Expressions of EMT and MET markers along with SEM micrographs evidently indicates that early stage of PCa cell colonization at the bone microenvironment is replicated by MSCs+PCa SC which enhances MET and inhibits EMT in PCL/ HAPClay scaffolds.

Angiogenesis refers to the growth and development of new blood vessels from pre-existing vasculature [79]. Vascular endothelial growth factor (VEGF) is a well-known angiogenic stimulator which is highly upregulated in solid tumor including prostate cancer [80]. A hypoxic core region is developed when a solid tumor is formed as tumors outgrow their blood vessel which supplies oxygen to the core cells of a tumor [81]. Hypoxia induces transcription of hypoxia-inducible factor 1 (HIF1) which stimulates pro-angiogenic factors like VEGF [11]. As hypoxic tumoroids were observed only in the sequential culture of PCa cells with MSCs, HIF1 and VEGF both of the genes are highly expressed in MSCs+PCa SC indication enhancement in angiogenic activity. The HIF1 expression is higher in PCa 3D which could be because as we observed from SEM images, in PCa 3D, cells formed larger aggregates of cells which created hypoxia at the center of the aggregates. It is paramount to develop hypoxia in in vitro tumor models to replicate the in vivo tumors as hypoxia is one of the hallmarks of a solid tumor. In recent years hypoxic region of a tumor has become a target for anticancer drugs or genetic treatments as it makes treatment ineffective by inhibiting drug delivery at the core of a tumor [82].

Endothelin-1 (ET-1) is an osteoblastic factor which promotes osteoblastic proliferation and inhibits osteoclastic bone resorption in osteoblastic lesion by prostate cancer cells [83]. When PCa cells reach bone milieu, PSA secreted by PCa cells upregulates ET-1 expression

which enhances PCa cell proliferation to form macrometastases [84]. ET-1 expression was upregulated in the coculture or sequential of PCa cells with Osteoblasts compared to control 2D osteoblasts. The peak of ET-1 is observed in MSCs+PCa SC, indicating ET-1 secretion by PCa cells are increased in contact of osteoblasts as RUNX2 expression and ALP assay (figure 3.2A) revealed that MSCs are fully differentiated into matured osteoblast in MSCs+PCa SC. Although, the ET-1 expression is downregulated in MSCs+PCa CC compared to the control. In MSCs+PCa CC, MSCs are not fully differentiated (MSCs and PCa cells were cocultured for only 10 days) indicating ET-1 secretion by PCa cells is inhibited in the presence of MSCs or immature osteoblasts. RANKL is a cytokine secreted by osteoblasts, and it activates osteoclasts by binding with RANK [75]. How RANKL expression is inhibited in the osteoblastic bone lesion is explained in the figure 3.9C. Figure 3.9B indicates upregulation of RANKL in osteoblasts (hFOB 3D) and immature osteoblasts (MSCs 3D). RANKL expression is inhibited in osteoblasts in the presence of PCa cells (hFOB+PCa CC/SC, MSCs+PCa SC) confirming initiation of the osteoblastic lesion by PCa cells. Interestingly, RANKL expression was upregulated in the MSCs+PCa CC indicating RANKL secretion by MSCs/ immature osteoblasts is not affected by the presence of PCa cells.

3.5. Conclusion

In this study, we intended to investigate the effects of sequential culture (SC) of PCa cells with MSCs in the PCL/ HAPClay scaffolds on the regulation of key genes involve in bone metastasis of prostate cancers. Thus, we analyzed key genes expression related to skeletal metastasis of PCa cells by qRT-PCR experiment in MSCs+PCa SC along with some other culture method. Herein, all the results indicate that MSCs+PCa SC in PCL/ HAPClay scaffolds

closely mimics early stage of osteoblastic prostate cancer colonization by developing tight junction tumoroids and inducing mesenchymal to epithelial transition (MET). We demonstrated that tight junction tumoroids were formed, MSCs differentiated to matured osteoblasts, EMT was inhibited, MET was enhanced, hypoxia increased angiogenesis, and finally PCa cells initiated osteoblastic lesion when PCa cells were sequentially cultured with MSCs (MSCs+PCa SC) in PCL/ HAPClay scaffolds. Our MSCs+PCa SC in PCL/ HAPClay platform, which strikes a balance between experimental efficiency and retention of biological complexity, could be used for studying PCa cancer cell biology in the early stage cell colonization and in vitro testing of anticancer drugs.

3.6. Acknowledgement

The SEM experiments conducted in this work are made possible through instrumentation obtained using MRI grant from National Science Foundation. Dr. Tao Wang, manager of core biology facility at NDSU, is acknowledged for help in use of the qRT PCR experiments. Scott Payne and Jayma Moor is acknowledged for helping with scanning electron microscopy. Support from ND EPSCoR for tissue engineering laboratory is also acknowledged. Partial support from NDSU grand challenges grant for "Center for Engineered Cancer Test-Beds" is also acknowledged.

3.7. References

[1] N. Howlader, A.M. Noone, M. Krapcho, J. Garshell, N. Neyman, S.F. Altekruse, C.L. Kosary, M. Yu, J. Ruhl, Z. Tatalovich, SEER cancer statistics review, 1975–2010. 2013, Bethesda, MD: National Cancer Institute (2013).

[2] A. Jemal, R. Siegel, J. Xu, E. Ward, Cancer statistics, 2010, CA: a cancer journal for clinicians 60(5) (2010) 277-300.

[3] L. Bubendorf, A. Schopfer, U. Wagner, G. Sauter, H. Moch, N. Willi, T.C. Gasser, M.J. Mihatsch, Metastatic patterns of prostate cancer: an autopsy study of 1,589 patients, Hum Pathol 31(5) (2000) 578-83.

[4] C.L. Chaffer, R.A. Weinberg, A Perspective on Cancer Cell Metastasis, Science 331(6024) (2011) 1559-1564.

[5] J.P. Thiery, Epithelial–mesenchymal transitions in tumour progression, Nature Reviews Cancer 2(6) (2002) 442-454.

[6] A. Singh, J. Settleman, EMT, cancer stem cells and drug resistance: an emerging axis of evil in the war on cancer, Oncogene 29(34) (2010) 4741-4751.

[7] C.L. Chaffer, E.W. Thompson, E.D. Williams, Mesenchymal to epithelial transition in development and disease, Cells Tissues Organs 185(1-3) (2007) 7-19.

[8] K. Gravdal, O.J. Halvorsen, S.A. Haukaas, L.A. Akslen, A switch from E-cadherin to N-cadherin expression indicates epithelial to mesenchymal transition and is of strong and independent importance for the progress of prostate cancer, Clinical Cancer Research 13(23) (2007) 7003-7011.

[9] A. Wells, C. Yates, C.R. Shepard, E-cadherin as an indicator of mesenchymal to epithelial reverting transitions during the metastatic seeding of disseminated carcinomas, Clinical & experimental metastasis 25(6) (2008) 621-628.

[10] H.-W. Han, S.-h. Hsu, Chitosan-hyaluronan based 3D co-culture platform for studying the crosstalk of lung cancer cells and mesenchymal stem cells, Acta Biomaterialia (2016).

[11] N. Ferrara, H.-P. Gerber, J. LeCouter, The biology of VEGF and its receptors, Nature medicine 9(6) (2003) 669-676.

[12] C.J. Logothetis, S.-H. Lin, Osteoblasts in prostate cancer metastasis to bone, Nat Rev Cancer 5(1) (2005) 21-28.

[13] M.B. Choueiri, S.-M. Tu, L.-Y. Yu-Lee, S.-H. Lin, The central role of osteoblasts in the metastasis of prostate cancer, Cancer and Metastasis Reviews 25(4) (2006) 601-609.

[14] E. Birmingham, G.L. Niebur, P.E. McHugh, Osteogenic differentiation of mesenchymal stem cells is regulated by osteocyte and osteoblast cells in a simplified bone niche, (2012).

[15] M. Bruderer, R.G. Richards, M. Alini, M.J. Stoddart, Role and regulation of RUNX2 in osteogenesis, Eur Cell Mater 28 (2014) 269-86.

[16] J.N. Beresford, Osteogenic stem cells and the stromal system of bone and marrow, Clin Orthop Relat Res (240) (1989) 270-80.

[17] J.N. Beresford, J.H. Bennett, C. Devlin, P.S. Leboy, M.E. Owen, Evidence for an inverse relationship between the differentiation of adipocytic and osteogenic cells in rat marrow stromal cell cultures, J Cell Sci 102 (Pt 2) (1992) 341-51.

[18] V. Paunescu, F.M. Bojin, C.A. Tatu, O.I. Gavriliuc, A. Rosca, A.T. Gruia, G. Tanasie, C. Bunu, D. Crisnic, M. Gherghiceanu, F.R. Tatu, C.S. Tatu, S. Vermesan, Tumour-associated fibroblasts and mesenchymal stem cells: more similarities than differences, J Cell Mol Med 15(3) (2011) 635-46.

[19] A. Kabashima-Niibe, H. Higuchi, H. Takaishi, Y. Masugi, Y. Matsuzaki, Y. Mabuchi, S. Funakoshi, M. Adachi, Y. Hamamoto, S. Kawachi, K. Aiura, Y. Kitagawa, M. Sakamoto, T. Hibi, Mesenchymal stem cells regulate epithelial-mesenchymal transition and tumor progression of pancreatic cancer cells, Cancer Sci 104(2) (2013) 157-64.

[20] I.A. Ho, H.C. Toh, W.H. Ng, Y.L. Teo, C.M. Guo, K.M. Hui, P.Y. Lam, Human bone marrow-derived mesenchymal stem cells suppress human glioma growth through inhibition of angiogenesis, Stem Cells 31(1) (2013) 146-55.

[21] S.S. Verbridge, E.M. Chandler, C. Fischbach, Tissue-engineered three-dimensional tumor models to study tumor angiogenesis, Tissue engineering. Part A 16(7) (2010) 2147.

[22] S. Talukdar, S.C. Kundu, Engineered 3D Silk-Based Metastasis Models: Interactions Between Human Breast Adenocarcinoma, Mesenchymal Stem Cells and Osteoblast-Like Cells, Advanced Functional Materials 23(42) (2013) 5249-5260.

[23] W. Zhu, M. Wang, Y. Fu, N.J. Castro, S.W. Fu, L.G. Zhang, Engineering a biomimetic three-dimensional nanostructured bone model for breast cancer bone metastasis study, Acta biomaterialia 14 (2015) 164-174.

[24] S.P. Pathi, D.D.W. Lin, J.R. Dorvee, L.A. Estroff, C. Fischbach, Hydroxyapatite nanoparticle-containing scaffolds for the study of breast cancer bone metastasis, Biomaterials 32(22) (2011) 5112-5122.

[25] Y. Liu, G. Wang, Y. Cai, H. Ji, G. Zhou, X. Zhao, R. Tang, M. Zhang, In vitro effects of nanophase hydroxyapatite particles on proliferation and osteogenic differentiation of bone marrow-derived mesenchymal stem cells, Journal of biomedical materials research Part A 90(4) (2009) 1083-1091.

[26] A. Ambre, K.S. Katti, D.R. Katti, In situ mineralized hydroxyapatite on amino acid modified nanoclays as novel bone biomaterials, Materials Science and Engineering: C 31(5) (2011) 1017-1029.

[27] K.S. Katti, M.D.S. Molla, F. Karandish, M.K. Haldar, S. Mallik, D.R. Katti, Sequential culture on biomimetic nanoclay scaffolds forms three-dimensional tumoroids, Journal of Biomedical Materials Research Part A 104(7) (2016) 1591-1602.

[28] K.S. Katti, A.H. Ambre, N. Peterka, D.R. Katti, Use of unnatural amino acids for design of novel organomodified clays as components of nanocomposite biomaterials, Philosophical Transactions of the Royal Society a-Mathematical Physical and Engineering Sciences 368(1917) (2010) 1963-1980.

[29] A.H. Ambre, D.R. Katti, K.S. Katti, Nanoclays mediate stem cell differentiation and mineralized ECM formation on biopolymer scaffolds, Journal of Biomedical Materials Research Part A 101(9) (2013) 2644-2660.

[30] A.H. Ambre, K.S. Katti, D.R. Katti, Nanoclay based composite scaffolds for bone tissue engineering applications, Journal of Nanotechnology in Engineering and Medicine 1(3) (2010) 031013.

[31] D.R. Katti, P. Ghosh, S. Schmidt, K.S. Katti, Mechanical Properties of the Sodium Montmorillonite Interlayer Intercalated with Amino Acids, Biomacromolecules 6(6) (2005) 3276-3282.

[32] A.H. Ambre, D.R. Katti, K.S. Katti, Nanoclays mediate stem cell differentiation and mineralized ECM formation on biopolymer scaffolds, J Biomed Mater Res A 101(9) (2013) 2644-60.

[33] A. Ambre, K.S. Katti, D.R. Katti, In situ mineralized hydroxyapatite on amino acid modified nanoclays as novel bone biomaterials, Materials Science & Engineering C-Materials for Biological Applications 31(5) (2011) 1017-1029.

[34] A.H. Ambre, D.R. Katti, K.S. Katti, Biomineralized hydroxyapatite nanoclay composite scaffolds with polycaprolactone for stem cell-based bone tissue engineering, Journal of Biomedical Materials Research Part A 103(6) (2015) 2077-2101.

[35] D.R. Katti, A. Sharma, A.H. Ambre, K.S. Katti, Molecular interactions in biomineralized hydroxyapatite amino acid modified nanoclay: In silico design of bone biomaterials, Mater Sci Eng C Mater Biol Appl 46 (2015) 207-17.

[36] X. Gong, C. Lin, J. Cheng, J. Su, H. Zhao, T. Liu, X. Wen, P. Zhao, Generation of multicellular tumor spheroids with microwell-based agarose scaffolds for drug testing, PloS one 10(6) (2015) e0130348.

[37] K. Wang, F.M. Kievit, S.J. Florczyk, Z.R. Stephen, M. Zhang, 3D Porous Chitosan–Alginate Scaffolds as an In vitro Model for Evaluating Nanoparticle-Mediated Tumor Targeting and Gene Delivery to Prostate Cancer, Biomacromolecules (2015).

[38] X. Xu, L.A. Gurski, C. Zhang, D.A. Harrington, M.C. Farach-Carson, X. Jia, Recreating the tumor microenvironment in a bilayer, hyaluronic acid hydrogel construct for the growth of prostate cancer spheroids, Biomaterials 33(35) (2012) 9049-9060.

[39] P. van Uden, Niall S. Kenneth, S. Rocha, Regulation of hypoxia-inducible factor-1α by NF-κB, Biochemical Journal 412(Pt 3) (2008) 477-484.

[40] E. Lieb, T. Vogel, S. Milz, M. Dauner, M.B. Schulz, Effects of transforming growth factor β1 on bonelike tissue formation in three-dimensional cell culture. II: osteoblastic differentiation, Tissue engineering 10(9-10) (2004) 1414-1425.

[41] A. Christensson, H. Lilja, Complex-formation between protein-c inhibitor and prostate-specific antigen in-vitro and in human semen, European Journal of Biochemistry 220(1) (1994) 45-53.

[42] S.E. Moody, D. Perez, T.-c. Pan, C.J. Sarkisian, C.P. Portocarrero, C.J. Sterner, K.L. Notorfrancesco, R.D. Cardiff, L.A. Chodosh, The transcriptional repressor Snail promotes mammary tumor recurrence, Cancer cell 8(3) (2005) 197-209.

[43] K. Fizazi, J. Yang, S. Peleg, C.R. Sikes, E.L. Kreimann, D. Daliani, M. Olive, K.A. Raymond, T.J. Janus, C.J. Logothetis, G. Karsenty, N.M. Navone, Prostate cancer cells-osteoblast interaction shifts expression of growth/survival-related genes in prostate cancer and reduces expression of osteoprotegerin in osteoblasts, Clin Cancer Res 9(7) (2003) 2587-97.

[44] A. Satelli, S. Li, Vimentin in cancer and its potential as a molecular target for cancer therapy, Cellular and Molecular Life Sciences 68(18) (2011) 3033-3046.

[45] C.L. Chaffer, J.P. Brennan, J.L. Slavin, T. Blick, E.W. Thompson, E.D. Williams, Mesenchymal-to-epithelial transition facilitates bladder cancer metastasis: role of fibroblast growth factor receptor-2, Cancer Res 66(23) (2006) 11271-8.

[46] S. Oltean, B.S. Sorg, T. Albrecht, V.I. Bonano, R.M. Brazas, M.W. Dewhirst, M.A. Garcia-Blanco, Alternative inclusion of fibroblast growth factor receptor 2 exon IIIc in Dunning prostate tumors reveals unexpected epithelial mesenchymal plasticity, Proceedings of the National Academy of Sciences 103(38) (2006) 14116-14121.

[47] S. Oltean, P.G. Febbo, M.A. Garcia-Blanco, Dunning rat prostate adenocarcinomas and alternative splicing reporters: powerful tools to study epithelial plasticity in prostate tumors in vivo, Clinical & experimental metastasis 25(6) (2008) 611-619.

[48] G.L. Semenza, Hypoxia-inducible factors in physiology and medicine, Cell 148(3) (2012) 399-408.

[49] S. Rey, G.L. Semenza, Hypoxia-inducible factor-1-dependent mechanisms of vascularization and vascular remodeling, Cardiovascular research (2010) cvq045.

[50] J.B. Nelson, S.P. Hedican, D.J. George, A.H. Reddi, S. Piantadosi, M.A. Eisenberger, J.W. Simons, Identification of endothelin-1 in the pathophysiology of metastatic adenocarcinoma of the prostate, Nat Med 1(9) (1995) 944-949.

[51] L. Huang, Y.Y. Cheng, L.T.C. Chow, M.H. Zheng, S.M. Kumta, Tumour cells produce receptor activator of NF-κB ligand (RANKL) in skeletal metastases, Journal of clinical pathology 55(11) (2002) 877-878.

[52] S.K. Sahoo, A.K. Panda, V. Labhasetwar, Characterization of porous PLGA/PLA microparticles as a scaffold for three dimensional growth of breast cancer cells, Biomacromolecules 6(2) (2005) 1132-1139.

[53] D.W. Hutmacher, Biomaterials offer cancer research the third dimension, Nature materials 9(2) (2010) 90-93.

[54] R. Marlow, G. Honeth, S. Lombardi, M. Cariati, S. Hessey, A. Pipili, V. Mariotti, B. Buchupalli, K. Foster, D. Bonnet, A. Grigoriadis, P. Rameshwar, A. Purushotham, A. Tutt, G. Dontu, A novel model of dormancy for bone metastatic breast cancer cells, Cancer research 73(23) (2013) 6886.

[55] P. Ingram, M. Im, S. McDermott, M. Wicha, E. Yoon, Spheroid cell culture on PDMS hydrophobic surfaces and integration into microfludic devices, pp. 1539-1541.

[56] W.L. Murphy, T.C. McDevitt, A.J. Engler, Materials as stem cell regulators, Nature materials 13(6) (2014) 547-557.

[57] A. Ranga, S. Gobaa, Y. Okawa, K. Mosiewicz, A. Negro, M.P. Lutolf, 3D niche microarrays for systems-level analyses of cell fate, Nature communications 5 (2014).

[58] X. Yang, S.K. Sarvestani, S. Moeinzadeh, X. He, E. Jabbari, Three-dimensional-engineered matrix to study cancer stem cells and tumorsphere formation: effect of matrix modulus, Tissue Engineering Part A 19(5-6) (2012) 669-684.

[59] S.P. Bruder, N. Jaiswal, S.E. Haynesworth, Growth kinetics, self-renewal, and the osteogenic potential of purified human mesenchymal stem cells during extensive subcultivation and following cryopreservation, Journal of Cellular Biochemistry 64(2) (1997) 278-294.

[60] T. Komori, Runx2, a multifunctional transcription factor in skeletal development, Journal of cellular biochemistry 87(1) (2002) 1-8.

[61] S.K. Baniwal, O. Khalid, Y. Gabet, R.R. Shah, D.J. Purcell, D. Mav, A.E. Kohn-Gabet, Y. Shi, G.A. Coetzee, B. Frenkel, Runx2 transcriptome of prostate cancer cells: insights into invasiveness and bone metastasis, Molecular cancer 9(1) (2010) 1.

[62] R.A. Thibault, L. Scott Baggett, A.G. Mikos, F.K. Kasper, Osteogenic differentiation of mesenchymal stem cells on pregenerated extracellular matrix scaffolds in the absence of osteogenic cell culture supplements, Tissue Eng Part A 16(2) (2010) 431-40.

[63] T. Sun, R. McKay, G.-S.M. Lee, P. Kantoff, The role of miRNAs in prostate cancer, European urology 68(4) (2015) 589-590.

[64] J. Kim, G.A. Coetzee, Prostate specific antigen gene regulation by androgen receptor, Journal of cellular biochemistry 93(2) (2004) 233-241.

[65] S.D. Kundu, K.A. Roehl, X. Yu, J.A.V. Antenor, B.K. Suarez, W.J. Catalona, Prostate Specific Antigen Density Correlates With Features of Prostate Cancer Aggressiveness, The Journal of Urology 177(2) (2007) 505-509.

[66] Y. Li, R.A. Sikes, B.S. Malaeb, F. Yeung, A. Law, S.E. Graham, M. Pei, C. Kao, J. Nelson, K.S. Koeneman, L.W. Chung, Osteoblasts can stimulate prostate cancer growth and

transcriptionally down-regulate PSA expression in cell line models, Urol Oncol 29(6) (2011) 802-8.

[67] R. Kalluri, R.A. Weinberg, The basics of epithelial-mesenchymal transition, The Journal of clinical investigation 119(6) (2009) 1420-1428.

[68] S.A. Mani, W. Guo, M.-J. Liao, E.N. Eaton, A. Ayyanan, A.Y. Zhou, M. Brooks, F. Reinhard, C.C. Zhang, M. Shipitsin, The epithelial-mesenchymal transition generates cells with properties of stem cells, Cell 133(4) (2008) 704-715.

[69] M.G. Mendez, S.-I. Kojima, R.D. Goldman, Vimentin induces changes in cell shape, motility, and adhesion during the epithelial to mesenchymal transition, The FASEB Journal 24(6) (2010) 1838-1851.

[70] A. Barrallo-Gimeno, M.A. Nieto, The Snail genes as inducers of cell movement and survival: implications in development and cancer, Development 132(14) (2005) 3151-3161.

[71] J. Yang, S.A. Mani, J.L. Donaher, S. Ramaswamy, R.A. Itzykson, C. Come, P. Savagner, I. Gitelman, A. Richardson, R.A. Weinberg, Twist, a master regulator of morphogenesis, plays an essential role in tumor metastasis, cell 117(7) (2004) 927-939.

[72] J.E. Eriksson, T. Dechat, B. Grin, B. Helfand, M. Mendez, H.-M. Pallari, R.D. Goldman, Introducing intermediate filaments: from discovery to disease, The Journal of clinical investigation 119(7) (2009) 1763-1771.

[73] T. Brabletz, EMT and MET in Metastasis: Where Are the Cancer Stem Cells?, Cancer Cell 22(6) (2012) 699-701.

[74] T. Brabletz, A. Jung, S. Reu, M. Porzner, F. Hlubek, L.A. Kunz-Schughart, R. Knuechel, T. Kirchner, Variable β-catenin expression in colorectal cancers indicates tumor progression driven

by the tumor environment, Proceedings of the National Academy of Sciences 98(18) (2001) 10356-10361.

[75] J.K. Jin, F. Dayyani, G.E. Gallick, Steps in prostate cancer progression that lead to bone metastasis, International journal of cancer 128(11) (2011) 2545-2561.

[76] B. Saha, A. Arase, S.S. Imam, D. Tsao-Wei, W.Y. Naritoku, S. Groshen, L.W. Jones, S.A. Imam, Overexpression of E-cadherin and β-Catenin proteins in metastatic prostate cancer cells in bone, The Prostate 68(1) (2008) 78-84.

[77] G. Christofori, H. Semb, The role of the cell-adhesion molecule E-cadherin as a tumour-suppressor gene, Trends in Biochemical Sciences 24(2) (1999) 73-76.

[78] R. Dhurjati, V. Krishnan, L.A. Shuman, A.M. Mastro, E.A. Vogler, Metastatic breast cancer cells colonize and degrade three-dimensional osteoblastic tissue in vitro, Clinical & experimental metastasis 25(7) (2008) 741-752.

[79] M.H. Sokoloff, L.W.K. Chung, Targeting angiogenic pathways involving tumor–stromal interaction to treat advanced human prostate cancer, Cancer and Metastasis Reviews 17(4) (1998) 307-315.

[80] E. Roberts, D.A.F. Cossigny, G.M.Y. Quan, The role of vascular endothelial growth factor in metastatic prostate cancer to the skeleton, Prostate cancer 2013 (2013).

[81] T.G. Graeber, C. Osmanian, T. Jacks, D.E. Housman, C.J. Koch, S.W. Lowe, A.J. Giaccia, Hypoxia-mediated selection of cells with diminished apoptotic potential in solid tumours, nature 379(6560) (1996) 88-91.

[82] P. Kulkarni, M.K. Haldar, S. You, Y. Choi, S. Mallik, Hypoxia-Responsive Polymersomes for Drug Delivery to Hypoxic Pancreatic Cancer Cells, Biomacromolecules (2016).

[83] T.A. Guise, J.J. Yin, K.S. Mohammad, Role of endothelin-1 in osteoblastic bone metastases, Cancer 97(S3) (2003) 779-784.

[84] J.W. Chiao, B.S. Moonga, Y.M. Yang, R. Kancherla, A. Mittelman, J.R. Wu-Wong, T. Ahmed, Endothelin-1 from prostate cancer cells is enhanced by bone contact which blocks osteoclastic bone resorption, British journal of cancer 83(3) (2000) 360.

CHAPTER 4. AN IN VITRO MODEL OF PROSTATE CANCER BONE METASTASIS FOR BOTH HIGHLY METASTATIC AND NON-METASTATIC PROSTATE CANCER USING NANOCLAY BONE-MIMETIC SCAFFOLDS[3]

This chapter describes the mimicking of mesenchymal to epithelial transition (MET) of prostate cancer cells in an in vitro 3D model using the cell line line PC-3. Most of the contents of this chapter is published in M.D.S. Molla, D.R. Katti, K.S. Katti, An in vitro model of prostate cancer bone metastasis for highly metastatic and non-metastatic prostate cancer using nanoclay bone-mimetic scaffolds, MRS Advances 1-7. The article is coauthored by MD. S. Molla; D. R. Katti; and K.S. Katti.

4.1. Introduction

Prostate cancer has a strong preference for metastasizing to bone which is the primary cause of prostate cancer-related morbidity and mortality. The complex nature of cancer metastasis leads to develop the translational models that recapitulate a specific metastatic stage. Herein, we report the mimicking of mesenchymal to epithelial transition (MET) of prostate cancer cells using a highly metastatic and a non-metastatic prostate cancer cell lines. A unique cell culture technique that we termed as 'sequential culture' was used to create a biomimetic bone microenvironment for metastasized prostate cancer cells by depositing bioactive factors from osteogenic induction of human mesenchymal stem cells (MSCs) within the porous 3D scaffolds. The in vitro 3D tumor model could be used as a testbed to study the interaction between prostate cancer and bone microenvironment as well as for novel therapeutic studies.

[3]This chapter wass co-authored by MD. S. Molla, Kalpana Katti, and Dinesh Katti. MD. S. Molla had primary responsibility for preparing samples, conducting all tests, and drafting this chapter. Kalpana Katti and Dinesh Katti directed the research orientation and revised this chapter.

Cancer-associated deaths are mostly attributed to metastasis, a process in which cancer spreads from its place of origin to other parts of the body, yet the mechanism of cancer metastasis remains obscure. A complex metastatic cascade is involved in the dissemination of cancer cells to the distant organ. It includes the sequence of phases: local invasion, intravasation, circulation, arrest and extravasation, proliferation and angiogenesis. Two very significant events take place during this complex cascade including epithelial to mesenchymal transition (EMT) and mesenchymal to epithelial transition (MET) where cell phenotype changes between epithelial to mesenchymal state and vice-versa. Mesenchymal cells undergo a series of events during MET, including gaining of apical-basal polarity, an aggregation of previously disbanded mesenchymal cells, and reorganization of cytoskeletal features. Considering the critical role MET plays in metastasis, understanding the molecular mechanism of MET offers new hope for inhibiting tumor formation and developing anti-cancer therapeutics.

The 5-year survival for localized and regional prostate cancer is 100.0%, but for the distant stage, it is only 30.0% [1]. The strong predilection of prostate cancer for metastasizing to bone is the principal cause of prostate cancer-related morbidity and mortality. Currently, there is no cure for the bone metastasized prostate cancer due to lack of understanding of the mechanism that underlies bone metastasis. Hence, translational models that recapitulate bone metastasis of prostate cancer are paramount for investigation of the late stage of the disease.

In our previous studies, we have reported the occurrence of mesenchymal to epithelial transition (MET) in an in vitro 3D tumor model of prostate cancer using androgen-dependent, less metastatic MDAPCa2b (PCa) cell line [2-4]. In this study, we have investigated the ability of highly metastatic PC-3 cells to undergo mesenchymal to epithelial transition in a tissue-

engineered bone-mimetic 3D in vitro model and presented a comparative study between the two cell lines.

4.2. Materials and method

The detailed preparation procedure for PCL/HAPclay has been described in our previous work [2, 5]. In an attempt to enhance the mechanical properties of polymer-based three-dimensional scaffolds, a polymer- clay composite (PCN) were designed by adding HAPclay to polycaprolactone (PCL). HAPclay was obtained by in situ biomineralization of hydroxyapatite (HAP) into intercalated nanoclay [6, 7]. Na-MMT clay was modified using 5-aminovaleric acid using simple wet-chemistry following the protocol described in our previous study [8].

Human mesenchymal stem cell (MSCs) line was purchased from Lonza and maintained in MSCGM™ Bulletkit™ medium (Lonza, PT-3001). Human prostate cancer cell lines PC-3 and MDA PCa 2b (PCa) were purchased from ATCC. PC-3 cells were maintained in a medium consisting of 89% DMEM-12 (1:1) from Hyclone, 10% FBS from ATCC, and 1% Pen-Strep solution (Gibco). PCa cells were maintained in 80% BRFF-HPC-1 (AthenaES) and 20% FBS. For 2D cultures, cells were seeded on tissue culture treated Petri dishes. For the sequential culture, human mesenchymal stem cells MSCs were seeded on scaffolds at a density of 5 x 104 number cells per scaffolds. MSCs were cultured for 23 days to allow bone tissue formation. In our previous studies, we have shown that bone tissue starts to form by the MSCs after 18 days of initial seeding [5, 9]. Prostate cancer cells PC-3/ PCa were seeded on newly formed bone tissue in the 3D scaffolds at a density of 5 x 104 per scaffolds. For the sequential culture, 1:1 ratio of MSCs and PC-3/ PCa was used. For migration study, PC-3/PCa prostate cancer cells were seeded on transwell inserts of 8.0 μm pore size at a density of 5 x 104 number of cells per

inserts. The cells were allowed to migrate toward the serum-containing lower chamber (control) or bone tissue engineered construct (MSCs cultured in PCL/in situ HAPclay scaffolds for 23 days) in the lower chamber. Percentage of prostate cancer cells migrated from the upper chamber into the lower chamber was calculated using DAP staining of the porous membrane and counting the total number of non-migrated cells.

Standard protocols were followed as described in our previous studies to perform FESEM, immunostaining, confocal microscopy, RNA extraction, and qRT-PCR analysis [2, 3]. Student's t-test analytical method was used for the statistical analysis to compare two conditions. Differences were considered significant at *P<0.05, **P<0.005, and ***P<.001. Triplicate biological samples were used for performing all the experiments. Mean ± standard deviations were used to express quantitative data.

4.3. Result and discussion

4.3.1. Migration of PC-3 cells towards bone-mimicking scaffolds

Migration of PC-3/PCa cells towards bone-tissue was performed using the transwell assay, and the result is shown in figure 4.1. Prostate cancer cells were allowed to migrate through a porous membrane with or without bone like construct at the lower chamber. Without bone like construct at the lower chamber served as control. Percentage of prostate cancer cells migrated from the upper chamber into the lower chamber was calculated for each cell line. PC-3 cells showed a higher percentage of migration with or without bone construct as opposed to MDA PCa 2b cells. In the presence of a bone construct, almost 75% of the cells migrated into the lower chamber indicating cytokines and chemokines secreted from the bone cells in the bone like

construct were able to attract cancer cells towards them. For MDA PCa 2b cells, there are no significant differences in percentage migration with or without presence of a bone-like construct.

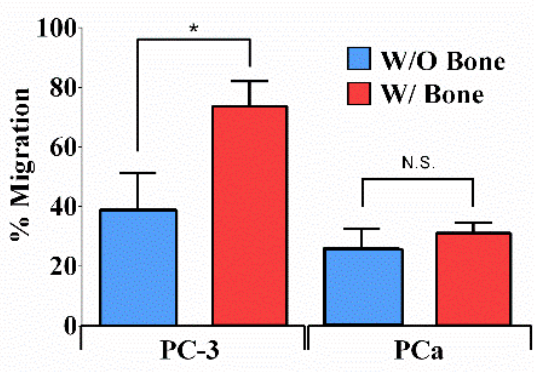

Figure 4.1. Percentage migration of PC-3/PCa cells with or without bone mimicking scaffolds.

4.3.2. PCa cells formed tumoroids and PC-3 cells formed gap-junction aggregates

To investigate the cell morphology, infiltration, cell adhesion, and mineralized extracellular matrix (ECM) formation we performed immunocytochemical analysis of the sequential culture of PC-3 and PCa (PC-3 SC and PCa SC) stained with DAPI, F-actin, and □-tubulin at day 23+10. The immunostained confocal micrographs are shown in figure 4.2A. We observed good adhesion of cells to the scaffolds. MDA PCa 2b cells formed tight junction multicellular tumoroids with hypoxic core region. Unlike PCa SC, PC-3 SC formed microtissues with tight junctions, and hypoxic core region as well as microtissues of cell aggregates with

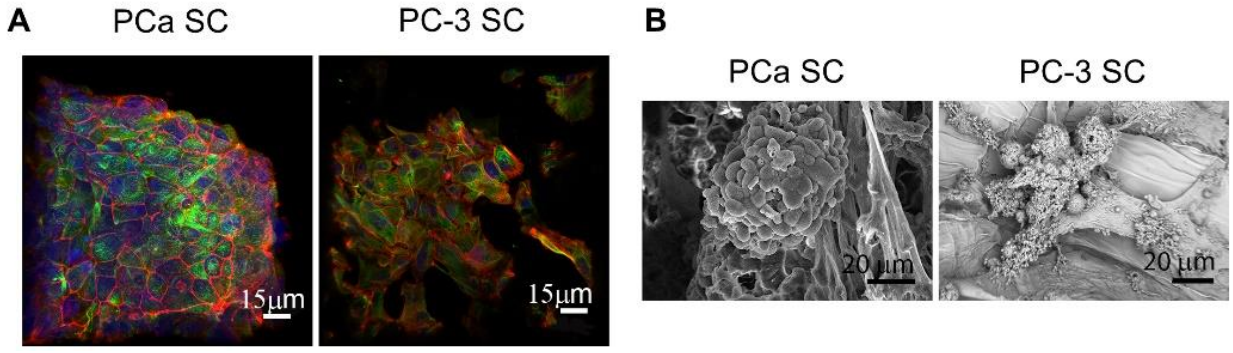

Figure 4.2. Morphology of PCa SC and PC-3 SC. A. PCa and PC-3 Cells stained with α-tubulin, F-actin (red) and DAPI (blue) using immunocytochemistry. (B) SEM micrographs of the tumoroid and cell cluster in the PCa SC and PC-3 SC respectively.

loose cell-cell adhesion, and non-hypoxic core region. MSCs and osteoblastic differentiated MSCs possess mesenchymal phenotype. We have observed in our previous studies that MSCs form mostly flat morphology of cells when cultured in PCL/nanoclay 3D porous scaffolds [2, 5, 9]. Therefore, these compact spheroids with tight junctions and cellular aggregates observed on the sequential cultures of PC-3 and PCa with MSCs can be assigned for PC-3/ PCa cells. Unlike PCa SC [2, 3], clusters formed in PC-3 SC exhibit rugged surface and indistinguishable cellular boundaries. Similar observations were made from SEM/FESM images of PCa SC and PC-3 SC (figure 4.2B). Tumoroids formed in PCa SC exhibit strong cell-cell adhesion, whereas, in PC-3 SC cells come together and establish a cell-cell adhesion, but their cell attachments are loose with gap-junctions.

4.3.3. EMT was inhibited, and MET was enhanced in the sequential culture

Epithelial to mesenchymal transition (EMT) and mesenchymal to epithelial transition (MET) are two very significant events that take place during the metastatic cascade of prostate cancer cells' skeletal metastasis1. E-cadherin is considered as the hallmark of MET, which profoundly upregulates when cancer cells undergo mesenchymal to epithelial transition and start to colonize at a distant organ. We have analyzed the expression of E-cadherin to assess if PC-3/PCa cells have experienced MET in the PCL/HAPClay scaffolds during sequential culture with MSCs. The gene expression analysis of E-cadherin in the PC-3 SC, PC-3 2D, PCa SC, and PCa 2D is shown in the figure 4.3A, where differentiated MSCs served as control. E-cadherin expression is ~12 fold enhanced in the PC-3 SC as opposed to 2D PC-3 cells. But in PCa SC, E-cadherin is ~8000 fold higher than PCa 2D or PCa SC. This observation of E-cadherin is in agreement with our morphological observation. Tight cellular junctions are made of E-cadherins. High expression of E-cadherins cause the formation of tumoroids in the PCa SC. A cytoskeletal

component, cytokeratin is also predominantly expressed in the epithelial phenotypes. We also analyzed the expression of cytokeratin 18 in the 2D and sequential cultures of PCa and PC-3 using immunocytochemical analysis (figure 4.3C). Cytokeratin is intensely stained in the PC-3 SC/ PCa SC as compared to 2D PC-3/ 2D PCa cells. Cytokeratin is highly expressed in PC-3 SC/ PCa SC and poorly expressed in 2D PC-3/ 2D PCa cells suggesting mesenchymal to epithelial transition (MET) of PC-3/PCa cells when sequentially cultured with MSCs in the bone tissue-engineered 3D scaffolds.

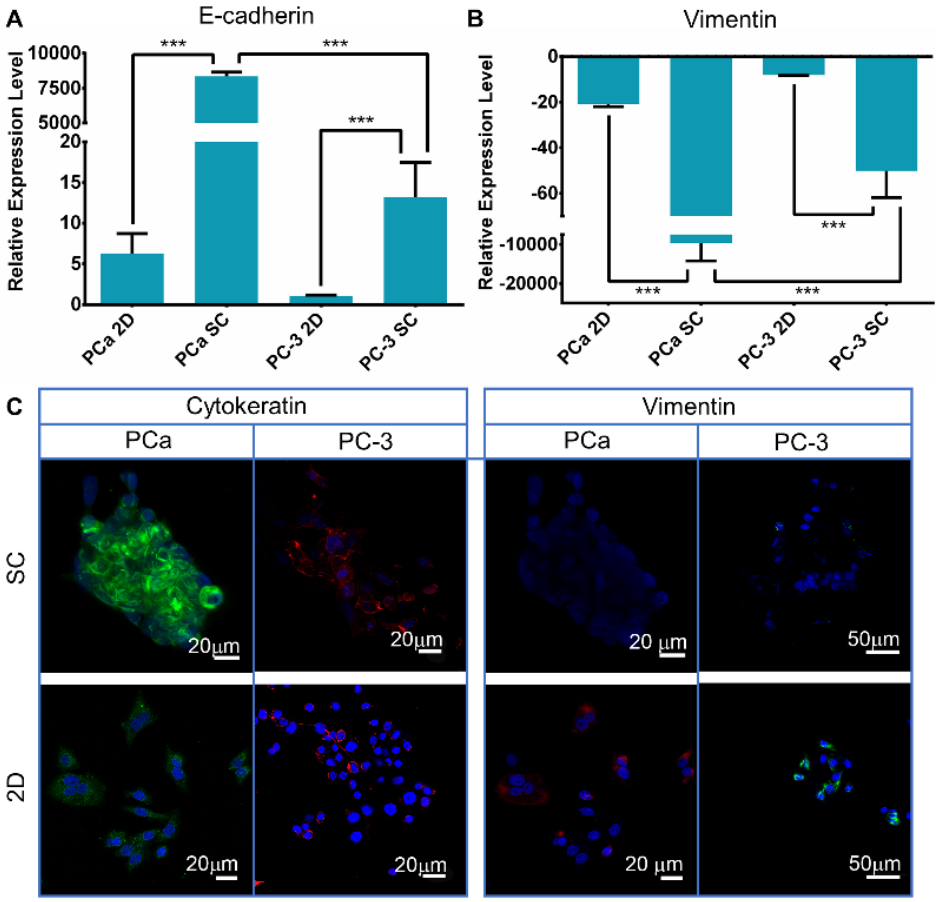

Figure 4.3. A. Relative E-cadherin expression level in the PCa SC, PCa 2D, PC-3 SC, and PC-3 2D cells. B. Relative vimentin expression level in the PCa SC, PCa 2D, PC-3 SC, and PCa 2D cells. C. Immunostained cytokeratin (green in PCa and red in PC-3), vimentin (red in PCa and green in PC-3), and nuclei (blue) in the PCa SC, PCa 2D, PC-3 SC, and PC-3 2D.

Since the E-cadherin/ Cytokeratin expression was significantly downregulated in the PC-3 SC and PCa SC, we further evaluated the expression of an EMT marker in the PC-3/PCa SC

and PC-3/PCa 2D cells to further confirm MET. The cytoskeletal filament vimentin is a marker for the mesenchymal phenotype. To evaluate the expression of vimentin, an EMT marker, in the sequential culture of PC-3/PCa cells with MSCs cultured in PCL/HAPClay scaffolds (PC-3 SC/ PCa SC), we performed qRT-PCR experiment and immunocytochemical analysis. The gene expression analysis of vimentin in the PC-3/PCa cells is shown in the figure 4.3B, where differentiated MSCs served as control. In the PC-3 SC, vimentin expression is ~40 fold downregulated as compared to the PC-3 2D. In the PCa SC, vimentin expression is ~10000 fold downregulated as compared to the PCa 2D. Downregulation of vimentin expression is significantly higher in PCa SC as compared to PC-3 SC. We also evaluated the protein expression of vimentin using immunocytochemical analysis, and the result is shown in figure 4.3C. It can be observed from the figure that vimentin is stained in 2D PC-3/PCa cells but in PC-33 SC/ PCa SC vimentin expression was not observed. Immunocytochemical analysis and gene expression analysis clearly indicate inhibition of EMT in the PCa SC and PC-3 SC. All the experimental results indicate MET is much higher in the PCa SC as compared to PC-3 SC.

4.3.4. Angiogenesis was promoted in the sequential culture

During the mesenchymal to epithelial transition (MET) at the metastatic tumor site, cancer cells colonize to form tumors. The hypoxic core region of the tumors suffers from oxygen/blood supply which induces the secretion of HIF-1. HIF-1 is known to upregulate proangiogenic factors like VEGF. To further confirm the mesenchymal to epithelial transition (MET) of the prostate cancer cell in the sequential culture, we evaluated the expression of qRT-PCR experiment. The result is shown in Figure 4.4 (A & B). Fig 4A shows the VEGF vascular endothelial growth factor (VEGF), and hypoxia-inducible factor 1 (HIF-1) using the expression in the PC-3 SC, PC-3 2D, PCa SC, and PCa 2D where differentiated MSCs served as control.

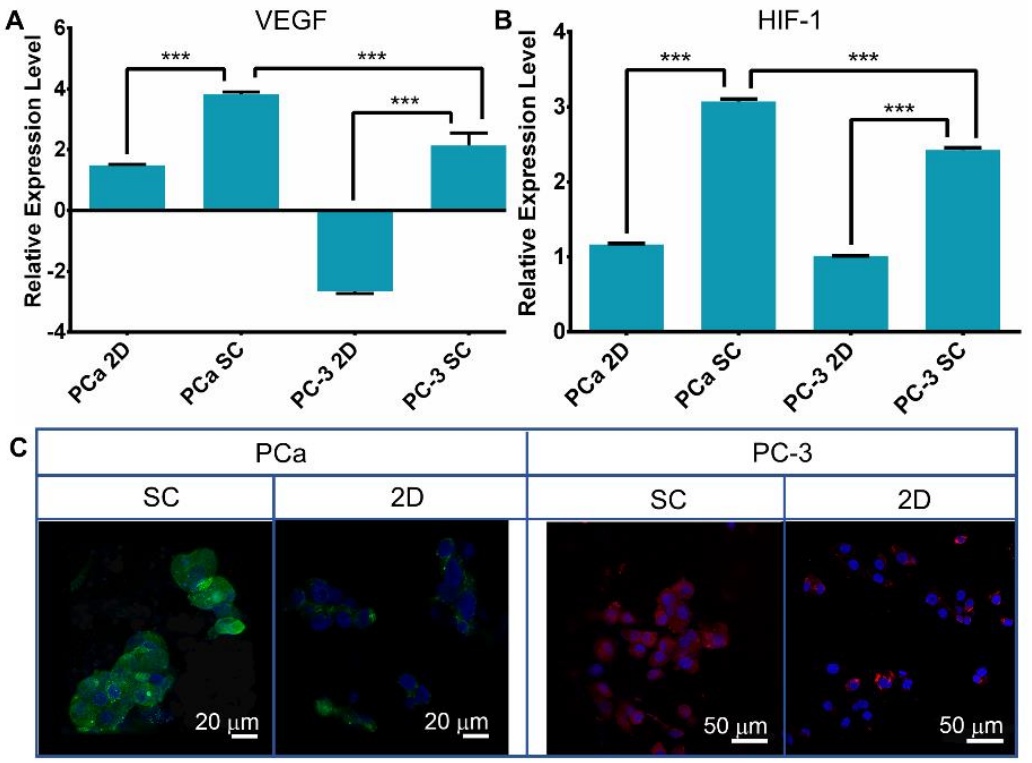

Figure 4.4. A. Relative VEGF expression level in the PCa SC, PCa 2D, PC-3 SC, and PC-3 2D cells. B. Relative HIF-1 expression level in the PCa SC, PCa 2D, PC-3 SC, and PC-3 2D cells. C. Immunostained VEGF (green in PCa and red in PC-3), and nuclei (blue) in the PCa SC, PCa 2D, PC-3 SC, and PC-3 2D cells.

VEGF expression is ~4 fold upregulated in the PC-3 SC as compared to 2D PC-3 cells. VEGF expression is ~2 fold upregulated in the PCa SC as compared to 2D PCa cells. VEGF expression is significantly higher in PCa SC as compared PC-3 SC. The HIF1 expression in the PC-3 SC, PC-3 2D, PCa SC, and PCa 2D is shown in figure 4.4B, where differentiated MSCs served as control. In the PC-3 SC, the HIF-1 expression is ~2 fold upregulated as opposed to 2D PC-3 cells. The HIF-1 expression is ~2 fold upregulated in the PCa SC as compared to 2D PCa cells. The HIF-1 expression is significantly higher in PCa SC as compared PC-3 SC.

To further confirm the enhancement of angiogenesis in the PC-3 SC, we probed the protein expression of VEGF using immunocytochemical analysis. 2D PC-3/PCa cells and PC-3/PCa SC were stained with VEGF, and the representative micrographs are shown in the figure 4.4C. VEGF was stained both in 2D PC-3/PCa and PC-3/PCa SC. But staining is significantly

intense in the PC-3/PCa SC. The immunocytochemical analysis clearly indicates that angiogenesis is upregulated in the sequential culture.

4.4. Conclusion

In this study we have developed a biologically relevant 3D tissue-engineered prostate cancer model that display a critical feature of cancer metastases in bone. A highly metastatic prostate cancer cell line PC-3 and a non-metastatic prostate cancer cell line MDAPCa2b experience epithelial to mesenchymal transition in a humanoid bone microenvironment. This study further confirms the ability the model to retain and recapitulate osteotropic metastatic ability of various prostate cancer cells. The 3D model presented here represents a platform for investigating the molecular [10] and nanomechanical [11] mechanism that underlies the disease progression.

4.5. References

[1] N. Howlader, A.M. Noone, M. Krapcho, D. Miller, K. Bishop, C.L. Kosary, M. Yu, J. Ruhl, Z. Tatalovich, A. Mariotto, SEER cancer statistics review, 1975–2014. Bethesda, MD: National Cancer Institute; (2017).

[2] K.S. Katti, M.D.S. Molla, F. Karandish, M.K. Haldar, S. Mallik, D.R. Katti, Sequential culture on biomimetic nanoclay scaffolds forms three-dimensional tumoroids, Journal of Biomedical Materials Research Part A 104(7) (2016) 1591-1602.

[3] M.D.S. Molla, R. Katti Dinesh, S. Katti Kalpana, In vitro design of mesenchymal to epithelial transition of prostate cancer metastasis using 3D nanoclay bone-mimetic scaffolds, Journal of Tissue Engineering and Regenerative Medicine 12(3) (2017) 727-737.

[4] K.S. Katti, D.R. Katti, M.S. Molla, S. Kar, Evaluation of Cancer Tumors in 3D Porous Bone Mimetic Scaffolds, Poromechanics VI, pp. 881-888.

[5] A.H. Ambre, D.R. Katti, K.S. Katti, Biomineralized hydroxyapatite nanoclay composite scaffolds with polycaprolactone for stem cell-based bone tissue engineering, Journal of Biomedical Materials Research Part A 103(6) (2015) 2077-2101.

[6] A.H. Ambre, K.S. Katti, D.R. Katti, Nanoclay Based Composite Scaffolds for Bone Tissue Engineering Applications, Journal of Nanotechnology in Engineering and Medicine 1(3) (2010) 031013-031013.

[7] A. Ambre, K.S. Katti, D.R. Katti, In situ mineralized hydroxyapatite on amino acid modified nanoclays as novel bone biomaterials, Materials Science and Engineering: C 31(5) (2011) 1017-1029.

[8] K.S. Katti, A.H. Ambre, N. Peterka, D.R. Katti, Use of unnatural amino acids for design of novel organomodified clays as components of nanocomposite biomaterials, Philosophical Transactions of the Royal Society A: Mathematical, Physical and Engineering Sciences 368(1917) (2010) 1963-1980.

[9] A.H. Ambre, D.R. Katti, K.S. Katti, Nanoclays mediate stem cell differentiation and mineralized ECM formation on biopolymer scaffolds, Journal of Biomedical Materials Research Part A 101A(9) (2013) 2644-2660.

[10] C.L. Chaffer, R.A. Weinberg, A Perspective on Cancer Cell Metastasis, Science 331(6024) (2011) 1559-1564.

[11] D.R. Katti, K.S. Katti, S. Molla, S. Kar, Biomechanics of Cells as Potential Biomarkers for Diseases: A New Tool in Mechanobiology, in: R. Narayan (Ed.), Encyclopedia of Biomedical Engineering, Elsevier, Oxford, 2019, pp. 1-21.

CHAPTER 5. EFFECT OF METASTASIZED PROSTATE CANCER CELLS ON TISSUE-ENGINEERED HUMONOID BONE[4]

This chapter describes the effects of metastasized prostate cancer cells on bone mineralization and extra cellular matrix formation. in an in vitro 3D model using the cell lines PC-3 and MDA PCa 2b. The content of this chapter is going to be submitted for publication. The to be submitted article is coauthored by MD. S. Molla; D. R. Katti; and K.S. Katti.

5.1. Introduction

The Most frequent destination of prostate cancer metastasis is bone with up to 90% of advanced stage patients having skeletal metastases [1]. It is no longer curable once prostate cancer cells metastasize to bone. Multiple bone-related complications including bone pain, weak bones, hypercalcemia, spinal cord compression, pathological fracture, stiffness or pain in the hip, thighs, or back are caused by skeletal metastasis of prostate cancer. Currently, all available treatments for patients having metastasized prostate cancer are the only palliative with an aim to improve the quality of patient's life. The 5-year survival rate of the patients having metastasized prostate cancer is only 29% [2].

The specific mechanism that influences prostate cancer cells for bone metastasis is not properly elucidated yet. After undergoing epithelial to mesenchymal transition (EMT) when cancer cells escape the primary tumor site and enter blood circulation, they favor to arrest to the first organ they reach where they undergo mesenchymal to epithelial transition (MET) for colonization. The blood vein that rises from prostate drains into the iliac vein which connects to

[4]This chapter was co-authored by MD. S. Molla, Kalpana Katti, and Dinesh Katti. MD. S. Molla had primary responsibility for preparing samples, conducting all tests, and drafting this chapter. Kalpana Katti and Dinesh Katti directed the research orientation and revised this chapter.

the vertebral vein. Vertebral vein goes throughout the entire spinal column that could be the reason behind extravasation of prostate cancer cells into bone microenvironment [3].

Metastasized prostate cancer cells primarily target cancellous bones. Highly vascular structure of cancellous bone provides easy access to oxygen and nutrients for metastasized prostate cancer cells which creates a welcoming environment for colonization. Bone-forming osteoblasts and bone-resorbing osteoclast reside in the bone microenvironment that is responsible for creating a dynamic nature of bone. In normal bone, constant remodeling of old bone by osteoclast follows mineralized new bone formation by osteoblast. But when prostate cancer cells metastasize to bone, they cause either excessive bone degradation in the osteoclastic lesion or excessive bone regeneration in the osteoblastic lesion.

Bone metastasis is the primary cause of morbidity and mortality in prostate cancer. Nevertheless, the bone metastatic mechanism in prostate cancer is not entirely understood. To prevent bone metastasis, it is crucial to target not only bone metastatic features in the tumor cells but also tumor nurturing bone. In order to advance current therapies, the effect of metastasized cancer cells on bone microenvironment have to be better understood which needs reliable models able to mimic the biophysical processes occurring in patients.

The inability of 2D models to recapitulate the complex nature of bone-cancer microenvironment and failing of animal models to reproduce some vital programs specific to human leads to developing several *in vitro* 3D models for systematic studies of interactions between prostate cancer cells and the bone microenvironment. Several 3D in vitro models have been reported that investigated the interaction between bone microenvironment and metastasized prostate cancer cells [4-6]. Sieh et al. studied the interactions between human osteoblasts and prostate cancer cells in 3D tissue engineered bone [7, 8]. Fitzgerald et al. reported a collagen-

based scaffolds to simulate prostate cancer bone metastases [9]. Windus et al. evaluated the role of alpha 6 and beta 1 integrin subunits in mediating tumor-bone stromal interactions in matrigels [10]. Holzapfel et al. investigated species-specific homing mechanisms of human prostate cancer metastasis in tissue engineered bone [11]. Wang et al. used a 3D co-culture models to study prostate cancer growth, progression, and metastasis to bone [12]. Kwon et al. reported a 3D *in vitro* model to study the impact of BMP-2 on metastasis to bone [13]. 3D *in vitro* models can be tailored to mimic different stages of cancer progression. We reported a 3D *in vitro* model that simulates mesenchymal to epithelial transition (MET) of prostate cancer cells during bone metastasis [14].

Variety of biomaterial-based 3D structures has been used to recapitulate bone matrix for prostate cancer metastasis including chitosan-alginate scaffold [15], alginate hydrogel [5], hyaluronan-based hydrogels [16], collagen-based hydrogel [17], PEG-based hydrogels [8], Silk fibroin scaffolds [13]. In this study we have used mesenchymal stem cells (MSCs) seeded PCL/nanoclay-hydroxyapatite based 3D scaffolds to recapitulate bone microenvironment for prostate cancer metastasis. In our previous studies, we have shown that when MSCs are seeded in these scaffolds, they differentiate into bone cells without osteogenic supplements [18]. We also reported that when prostate cancer cells sequentially cultured with MSCs in these scaffolds, they undergo mesenchymal to epithelial transition (MET) to form multicellular tumoroids that mimic the early colonization stage of prostate cancer bone metastasis [14, 19, 20]. In this study, we investigated the effect of metastasized prostate cancer cells on bone regeneration, degradation, mineralization, and collagen synthesis using two different prostate cancer cell lines, PC-3 and MDA PCa 2b. PC-3 is highly metastatic cell line while MDA PCa 2b is less metastatic in nature [21]. Experiments such as ELISA, qRT-PCR immunocytochemical analysis, SEM

imaging, FESEM imaging, and cell-based assays were performed to investigate the effect of metastasized prostate cancer cells on bone microenvironment. The 3D tumor that we have developed in our previous studies were used to study the effect of metastasized prostate cancer cells on bone microenvironment. Effect of two different prostate cancer cell lines were compared and we found that both osteoblastic and osteolytic bone lesion could be recapitulated in the tumor model that we have developed.

5.2. Materials and methods

5.2.1. Preparation of bone mimicking 3D porous scaffolds

In our previous studies, we described the detailed procedure of the scaffold preparation method [18, 22-24]. In brief, hydroxyapatite was initially biomineralized on modified Na-MMT nanoclay using Na_2HPO_4 and $CaCl_2$ by precipitation method. 5-aminovaleric acid was used to modify Na-MMT clay. Freeze drying method was used to prepare porous scaffolds from α-polycaprolactone (PCL) and HAPClay.

5.2.2. Cell lines and culture media

Human mesenchymal stem cell line (PT-2501) were purchased from Lonza, Walkersville and maintained in MSCGM™ Bulletkit™ medium (Lonza, Walkersville, PT-3001). Human prostate cancer cell line MDA PCa 2b (ATCC® CRL-2422™) was purchased from ATCC and maintained in a medium consisting of 80% BRFF-HPC1 (AthenaES, 0403) and 20% fetal bovine serum (ATCC, 30–2020). Human prostate cancer cell line PC-3 (ATCC® CRL-1435™) was purchased from ATCC and maintained in a medium consisting of 90% HyQ Dulbecco's Modified Eagle medium DMEM-12 (1:1) from Hyclone, 10% FBS from ATCC. All the cells were maintained at 37 °C and 5% CO_2 in a completely humidified incubator

5.2.3. Cell seeding, 3D tissue culture, and tumoroid formation by sequential culture

Cylindrical disks of porous scaffolds (Thickness 3mm, diameter 12 mm) were sterilized and maintained in culture medium overnight. Human mesenchymal stem cells (MSCs) were seeded on scaffolds and cultured for 23 days (5.0 X 10^5 cells/ scaffold). Human prostate cancer cell lines MDA PCa 2b and PC-3 cells were seeded on MSCs seeded scaffolds after 23 days (5.0 X 10^5 cells/ scaffold) and maintained in 1:1 MSCs and prostate cancer cells (CaP) media. CaP cells were cultured for 5, 10 and 15 days after seeding on MSCs seeded scaffolds. The detailed method of sequential culture for tumoroid formation has been described in our previous studies [14, 19]. In this study, the sequential culture of PC-3 with MSCs is addressed as PC-3 SC, and sequential culture of MDA PCa 2b cells with MSCs is addressed as PCa SC. MSCs Monoculture is addressed as Bone cells.

5.2.4. WST-1 assay

Tetrazolium salts-based reagent WST-1 was purchased from Roche (IN, USA). WST-1 cell viability assay was performed for the bone cells, PC-3 SC and PCa SC samples on day 23+5, 23+10 and 23+15. The colorimetric assay was performed following manufacturer's protocol. Briefly, Cell seeded samples harvested from the growth medium, washed with PBS and placed in the reagent solution (10% in DMEM-12) followed by incubation at 37 °C for 4 hours in a humidified incubator. Absorbance was measured at 450 nm using a microplate spectrophotometer (Bio-Rad). The total number of cells were counted from the ODs using predetermined standard curves.

5.2.5. Migration assay

A predetermined number of PC-3 and MDA PCa 2b prostate cancer cells were seeded on transwell inserts (Corning, USA) of 8.0 µm pore size in serum-containing media. The cells were

allowed to migrate toward the serum-containing in the lower chamber (control) or bone tissue engineered construct (MSCs cultured in PCL/in situ HAPclay scaffolds for 23 days) in the lower chamber as shown in Figure 5.2B. The total number of cells on the upper surface of the porous membrane were counted before and after migration to calculate percentage migration.

5.2.6. Immunostaining and confocal microscopy

Immunocytochemical analysis was performed without harvesting the cells from scaffolds. MSCs monocultures, sequential cultures of MDA PCa 2b and PC-3 samples were immunostained for α-collagen. MSCs were also immunostained for Runx2 expression To observe the tumoroid formation by MDA PCa 2b and PC-3 cells, sequential culture samples were also stained for F-actin. Samples were fixed with 4% paraformaldehyde (PFA) for 30 minutes and then washed three times with ice-cold 1X PBS (Each wash for five minutes). For permeabilization, samples were treated with 0.5% Triton X-100 in PBS for 5 minutes. 1% fish skin gelatin (FSG) was used for blocking followed by incubation with primary antibodies (abcam, ab34710 and ab76956) at 4 °C (1:150 dilution with PBS). Then, samples were washed with fresh PBS three times (Each wash for five minutes) and then incubated with corresponding secondary antibodies for an hour at room temperature (Goat Anti-Rabbit IgG H&L Alexa Fluor® 488, and Goat Anti-Rabbit IgG H&L Alexa Fluor® 647). Primary and secondary antibodies were purchased from Abcam (Cambridge, MA) For F-actin staining, cell-seeded scaffold samples were incubated with Rhodamine Phalloidin (ThermoFisher Scientific, R415) for 30 minutes at 37 °C. For nucleus staining, samples were incubated with 4',6-diamidino-2-phenylindole (DAPI) for five minutes. Z-stacks of the scaffold samples were obtained using Zeiss AxioObserver Z1 microscope equipped with LSM700 laser-scanning module (Zeiss,

Thornwood, NY). Rendered 3D images were analyzed using Imaris software (Bitplane, South Windsor, CT).

5.2.7. Scanning electron microscopy (SEM) and field emission scanning electron microscopy (FESEM)

Scanning electron microscopy was performed to observe cellular morphology, mineralized ECM, and collagen formation using microscopes JEOL JSM- 6490LV for SEM and JEOL JSM-7600F for FE SEM (JEOL USA, Peabody, MA, USA). Initially, the samples were fixed with 2.5% glutaraldehyde followed by ethanol series treatment (10%, 30%, 50%, 70%, and 100% v/v) for dehydration. Hexamethyldisilazane was also used as a drying agent. Samples were mounted on cylindrical aluminum mounts with colloidal silver paste (Structure Probe Inc., West Chester PA, USA) and then coated with gold (for SEM) and carbon (for FESEM). An accelerating voltage of 15 kV was used for SEM and 2.0 kV for FESEM.

5.2.8. RNA extraction and qRT-PCR analysis

Total RNAs were extracted from scaffold samples using TRI reagent (Sigma) and purified using Direct-zol ™ RNA MiniPrep (Zymo Research, Irvine, CA). Total RNA was quantified using Nanodrop ND 2000 (Nanodrop products, Wilmington DE, USA) spectrophotometer. cDNA was reverse transcribed from RNA using random primers and M-MLV reverse transcriptase (Promega, Madison, WI). SYBR Green Master MIX (ThermoFisher Scientific, USA) was used for template amplification with a primer for each of the transcripts by following manufacturer's protocol in a 7500 Fast Real-Time PCR system (Applied Biosystems, USA). The list of primer sequence used in this experiment has been listed in Table 1. GAPDH served as a house-keeping gene, and target gene expressions were calculated as $2^{-\Delta\Delta Ct}$. GAPDH served as a house-keeping gene, and target gene expressions were calculated as $2^{-\Delta\Delta Ct}$.

5.2.9. Alizarin red S assay

Samples were fixed with 2.5% glutaraldehyde overnight followed by three times PBS wash (5 minutes each wash). Further, samples were stained with Alizarin Red S dye (2 g/100 mL deionized water, pH = 4.10–4.15). Then, samples were washed with cell culture grade water to remove excess dye. Z-stacks of the samples were obtained using Zeiss AxioObserver Z1 microscope equipped with LSM700 laser-scanning module (Zeiss, Thornwood, NY). Rendered 3D images were analyzed using Imaris software (Bitplane, South Windsor, CT).

5.2.10. ELISA

The amounts of secreted MMP-9 and osteocalcin protein were calculated using enzyme-linked immune assay (ELISA). After centrifugation at 2000 rpm, the supernatants from conditioned media were collected at day 23+5 and day 23+10 from the cell-seeded scaffolds and used for ELISA. The level of MMP-9 protein in the supernatants was calculated using Human MMP-9 PicoKine™ ELISA Kit (EK0465, Boster Bio; Pleasanton, CA) following manufacturer's protocol. The level of osteocalcin (OCN) protein in the supernatants was measured using Osteocalcin Human ELISA Kit (KAQ1381, ThermoFisher Scientific, USA) following manufacturer's protocol.

5.2.11. Alkaline phosphatase assay

Alkaline phosphatase (ALP) assay was performed for monoculture of MSCs seeded in the scaffolds. At day 3, 5, 7, 10, and 33 cell lysates were collected. Initially, samples were washed with PBS and then each sample was placed in a 24-well plate under Triton X-100 which was purchased from Sigma-Aldrich (X-100). The samples were then treated with two cycles of freezing-thawing (-70 °C to 37 °C) to obtain cell lysates. Further, equal volume of (250 µl) p-nitrophenyl phosphate (Sigma-Aldrich, N7653) was added to the cell lysate in a different 24

well-plate and then incubated for an hour at room temperature. 70 µl of 3N NaOH was added to each scaffold, to deprotonate the p-nitrophenol, and then the samples were shaken for 60 seconds. Microplate spectrophotometer (Bio-Rad, Benchmark Plus) was used to obtain the absorbance at the wavelength 405 nm.

5.2.12. Statistical analysis

Statistical analysis was performed using Student's t-test to compare two conditions. Differences were considered significant at *P<0.05, **P<0.005, and ***P<.001. Triplicate samples were used for performing all the experiments. Mean ± standard deviations were used to express quantitative data.

5.3. Results

5.3.1. Mesenchymal stem cells differentiated into bone cells

To evaluate if the MSCs have differentiated into the osteoblastic lineage, we performed ALP osteogenic differentiation assay. We also have analyzed the expression of Runx2 using qRT-PCR experiment and immunocytochemical analysis. MSCs were seeded in PCL/HAPnanoclay scaffolds, and cell lysates were extracted at day 3, 5, 7, 10, 23 and 33 for ALP assay. A cellular membrane-bound enzyme, ALP is a key marker for osteoblast. ALP assay is used to evaluate the differentiation of MSCs into the osteoblastic lineage. Figure 5.1A shows a gradual increase of osteoblastic activity at the initial days of cell seeding (from day 3 to day 7). Decrease of ALP activity has been observed from day 10. It has been reported that the mineralization of ECM is associated with decreased level of ALP activity [25]. Decrease in ALP activity of MSCs during osteogenic differentiation after Day 8 is also reported in the literature [26].

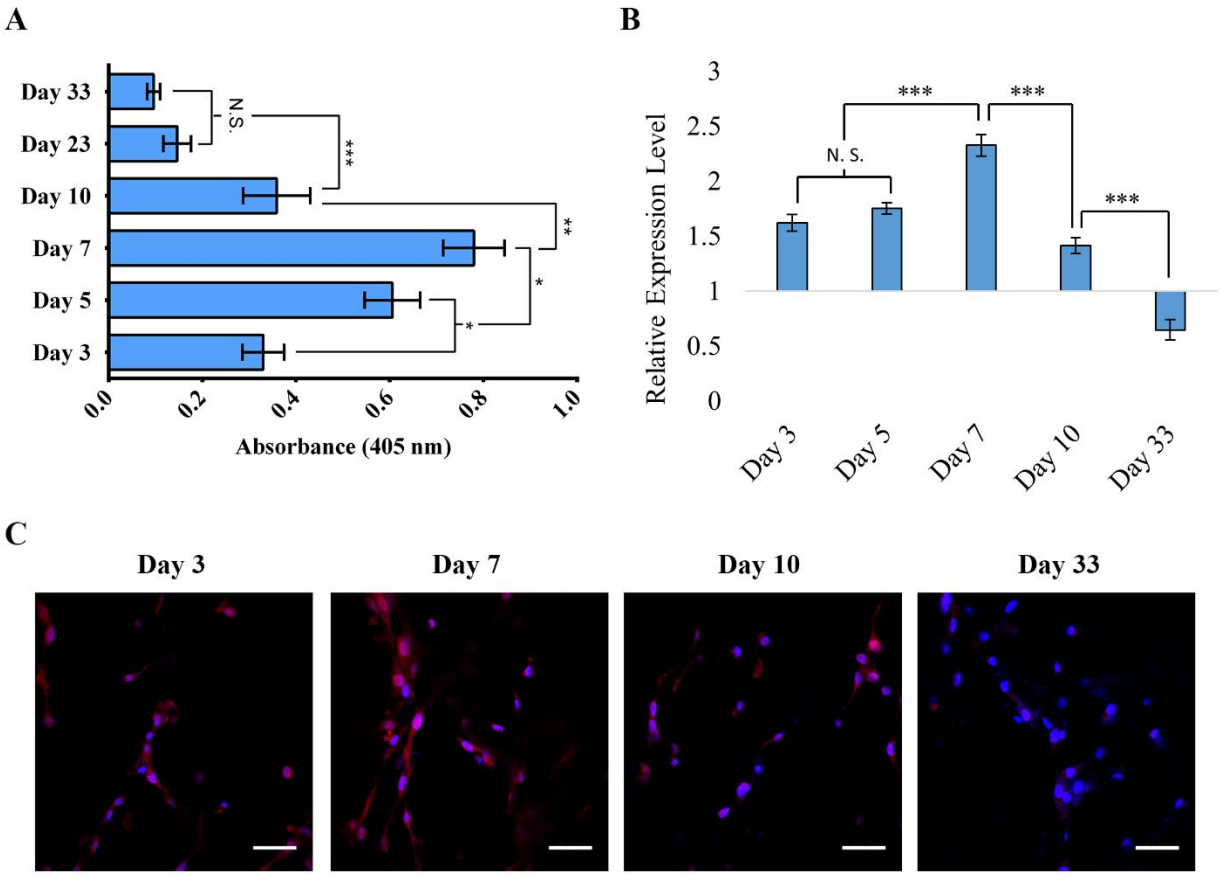

Figure 5.1. Osteogenic differentiation of MSCs. A. Comparative results from ALP assay for sequential culture (SC) and mesenchymal stem cells (MSCs). Results are shown as mean ± standard deviation. Statistical Significance is shown by a single asterisk ($p<0.05$, $n=3$.). B. Relative gene expression level of RUNX2, which is normalized to GAPDH and where undifferentiated cultured on 2D MSCs at day 2 served as control. C. Immunocytochemical analysis of Runx2 (red) and nuclei (blue) stained in MSCs cultured in 3D scaffolds.

Runx2 expression in MSCs cultured in 3D scaffolds was evaluated compared to MSCs cultured on 2D Petri dish and the result is presented in figure 5.1B. To evaluate the expression of Runx2, total RNAs were extracted from MSCs seeded scaffolds at day 3, 5, 7, 10 and 33 to perform the qRT-PCR experiment. Similar to ALP activities, Runx2 expression was gradually increased from day 3 and reached the peak at day 7 (Figure 5.1B). At day 33, the Runx2 expression was significantly downregulated compared to control. We also evaluated the expression of Runx2 in the MSCs seeded scaffolds with immunocytochemical analysis at day 3,

day 7, day 10, and day 33 of the initial seeding of MSCs. The result is shown in figure 5.1C. In figure 5.1C, blue represents nuclei and red represents Runx2 of MSCs. We can observe that Runx2 staining is increased from day 3 to day 7 and then again decrease from day 7 to day 10. At day 33, Runx2 staining is very insignificant. At day 7, the Runx2 staining reached the peak in MSCs cultured on PCL/Hapclay scaffolds which is suggestive of osteoblastic differentiation. The immunocytochemical analysis is in agreement with our observation from gene expression analysis of Runx2. Runx2 is an osteoblastic marker and best known as the master regulator of osteoblastic differentiation. It has been reported that at the initial stage of osteogenic differentiation of MSCs, the Runx2 expression is upregulated [27]. At the later stage of osteoblast maturation, the Runx2 expression is inhibited. Initial upregulation of Runx2 in MSCs cultured in 3D scaffolds evidently indicate osteogenic differentiation of MSCs at the early stage of 3D cell culture. Downregulation of Runx2 at the later days indicates maturation of osteoblast differentiated from MSCs and further downregulation at day 33 (Figure 5.1B) means mature osteoblast turn into osteocytes [28].

All the results from ALP assay, gene expression, and immunocytochemical analysis of Runx2 indicate the differentiation of MSCs into osteoblastic lineage without osteoblastic supplements in PCL/HAPnanoclay scaffolds. Osteoblastic differentiation of MSCs without osteogenic supplements. The results also suggest that PCL/nanoclay scaffolds are osteoconductive and osteoinductive in nature.

5.3.2. Growth and *in vitro* migration of prostate cancer cells towards engineered bone tissue construct

The growth of prostate cancer cells as a function of time in the sequential culture with bone cells was evaluated using WST-1 cell viability assay, and the results are shown in figure

5.2A. Cell viability assay was performed on day 23+5, day 23+10 and day 23+15. Cell population in the sequential cultures (SCs) for both of the cell lines has been increased over the time from day 23+5 to day 23+15. Cell population in PC-3 SC is significantly higher as opposed to PCa SC. This is probably because the doubling time for MDA PCa 2b cells (42–73 hours) is higher than the doubling time of PC-3 cells (~33 hours) [29]. There is no significant difference between the total population of bone cells and PCa SC on day 23+5 which indicates that PCa cells probably initially has an adverse effect on the growth of bone cells leading to a decreased population of bone cells in the PCa SC. The initial effect of PC-3 on the growth of bone cells cannot be determined from this data as the overall population of PC-3 SC as is more than two times higher compared to bone cells. It is possible that PC-3 has a positive effect on the growth of bone cells. The overall population of in the sequential cultures (SCs) is significantly higher for both cell lines on both day 23+10 and 23+15 as compared to bone cells. This indicates that sequential culture of prostate cancer cells with bone cells possibly could be advantageous for the growth of both cancer and bone cells or only for cancer cells. It is also possible that one of the prostate cancer cells line has a positive effect and another has a negative effect on the growth of bone cells. The population of bone cells differentiated from MSCs has been decreased over the time from day 23+5 to day 23+15. Studies have found that MSCs can go through complex cellular events such as growth arrest during initial and terminal differentiation [30]. Heterogeneity regarding proliferating capabilities has been observed in MSCs [31]. It has been reported that a small portion of differentiated MSCs is responsible for cell proliferation and a large portion of the overall population do not undergo self-replication. The intricacy associated with differentiating MSCs and the lack of clear understanding the interconnection between

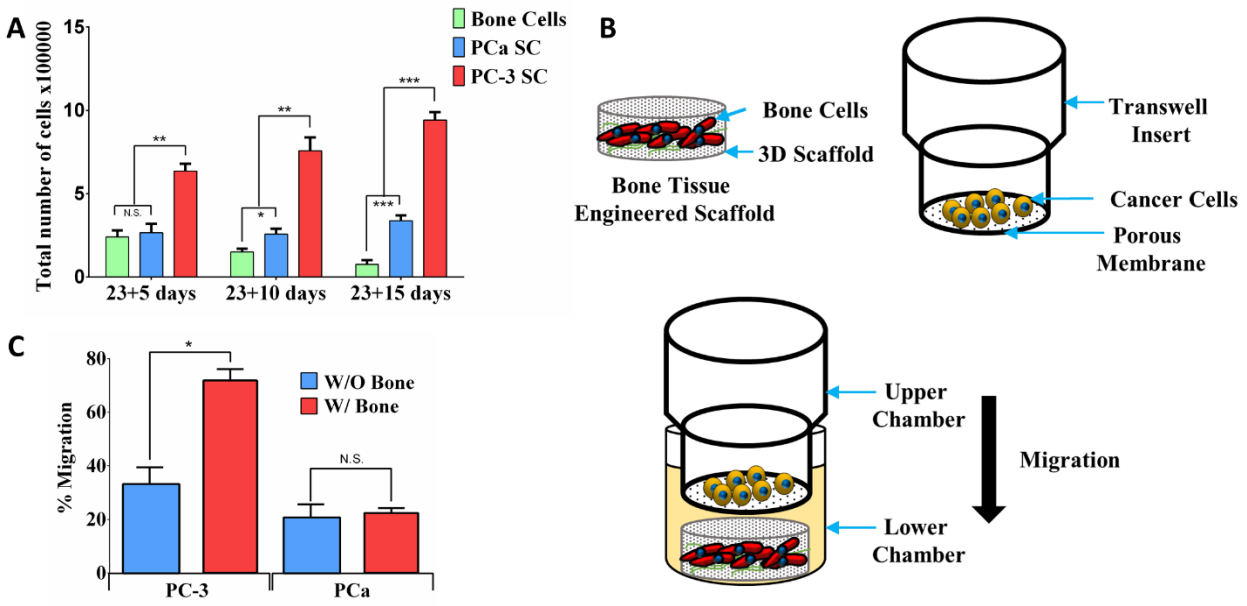

Figure 5.2. Growth and migration of prostate cancer cells. A. Comparative results from WST-1 cell viability assay for bone cells (differentiated from MSCs), PCa SC (sequential culture of MDA PCa 2b cells with MSCs), and PC-3 SC (sequential culture of PC-3 cells with MSCs). Results are shown as mean ± standard deviation. Statistical significance is shown by ***$p < 0.001$, **$p < 0.005$, *$p < 0.05$, n=3.). B. Schematic representation of migration assay set-up. The cells were allowed to migrate toward the lower chamber (control) or bone tissue-engineered construct (MSCs cultured in PCL/in situ HAPclay scaffolds for 23 days) in the lower chamber. C. Percentage migration of PC-3 cells with or without bone mimicking scaffolds. Results are shown as mean ± standard deviation. Statistical Significance is shown by *$p < 0.05$, n=3.).

differentiation and proliferation of MSCs makes it difficult to interpret possible reasons for the decrease in overall population of bone cells from day 23+5 to day 23+15.

Migration of prostate cancer cells into bone-like construct was performed as described in the schematic diagram (figure 5.2B). Prostate cancer cells were allowed to migrate through a porous membrane with or without bone like construct at the lower chamber. Without bone like construct at the lower chamber served as control. Percentage of prostate cancer cells migrated from the upper chamber into the lower chamber was calculated for each cell line, and the result is shown in figure 5.2C. PC-3 cells showed a higher percentage of migration with or without bone

construct as opposed to MDA PCa 2b cells. In the presence of a bone construct, almost 75% of the cells migrated into the lower chamber indicating cytokines and chemokines secreted from the bone cells in the bone like construct were able to attract cancer cells towards them. For MDA PCa 2b cells, there are no significant differences in percentage migration with or without the presence of a bone-like construct.

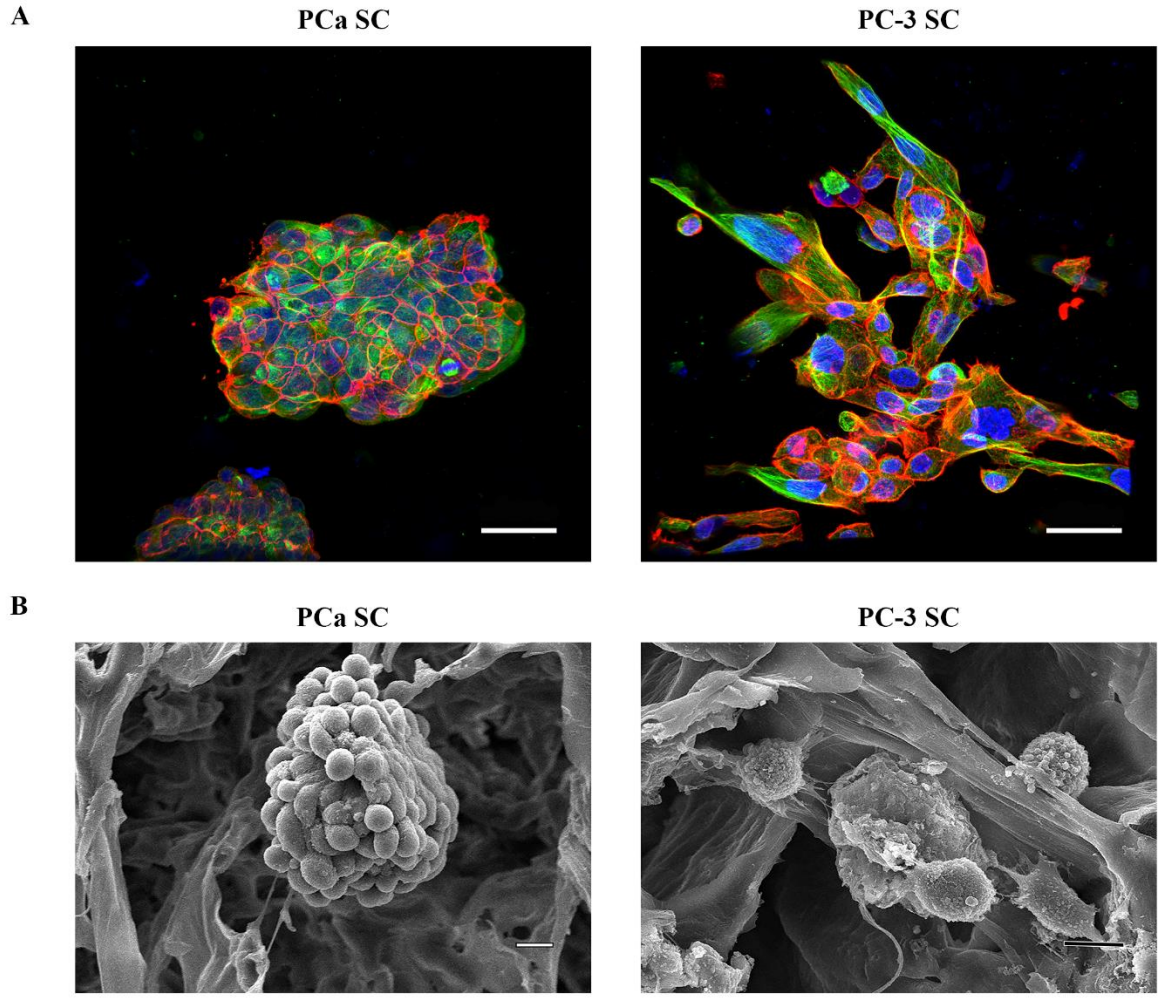

Figure 5.3. Morphological analysis of PCa SC and PC-3 SC. A. Immunostained α-tubulin (green), F-actin (red) and nuclei (blue) in PCa SC and PC-3 SC. Bar = 50 µm. B. SEM micrographs of PCa SC and PC-3 SC showing tumoroid and cluster of cells respectively formed in the PCL/in situ HAPclay scaffolds. Bar = 10 µm.

5.3.3. MDA PCa 2b forms tumoroids and PC-3 assembled into disorganized clusters in sequential culture

To investigate the morphology of cancer cells in the tissue-engineered bone microenvironment, we performed SEM imaging, FESEM imaging and confocal microscopy of actin stained cells in the scaffolds. We have introduced a unique and novel cell culture technique that we termed as 'sequential culture' [19]. When MDA PCa 2b prostate cancer cells are sequentially cultured with human mesenchymal stem cells (MSCs), they form multicellular organized microtissues (Figure 5.3A/B). These microtissues with hypoxic core regions are termed as 'tumoroids.' These tumoroids have tight cellular junctions and distinguishable cellular boundaries (Figure 5.3A/B). In the sequential culture of PC-3 cells with MSCs results aggregation of PC-3 cells. These aggregates of cells are disorganized and exhibit rough surface. There are strong cell-cell adhesion in the tumoroids formed by MDA PCa 2b cells. When PC-3 cells are sequentially cultured with human MSCs, they come together and establish a cell-cell adhesion, but their cell junctions are loose. Immunostained confocal microscopy images of MDA PCa 2b and PC-3 cells in the sequential culture also demonstrated the similar behavior of cancer cells. MDA PCa 2b forms tumoroid with tight cellular junctions but PC-3 cells form cell aggregates with loose cellular junctions.

5.3.4. Mineralized bone nodule formation is enhanced in the PC-3 metastatic site

When MSCs are differentiated to osteoblasts, it can be induced to produce extracellular calcium deposition *in vitro*. The process is known as mineralization. Osteoblast secret calcium and phosphate ions into the ground substance until it becomes saturated at which point the minerals begin to precipitate into hydroxyapatite crystals. Calcium deposits are an indication of *in vitro* bone formation and can be stained bright orange-red using Alizarin Red S. Alizarin red S

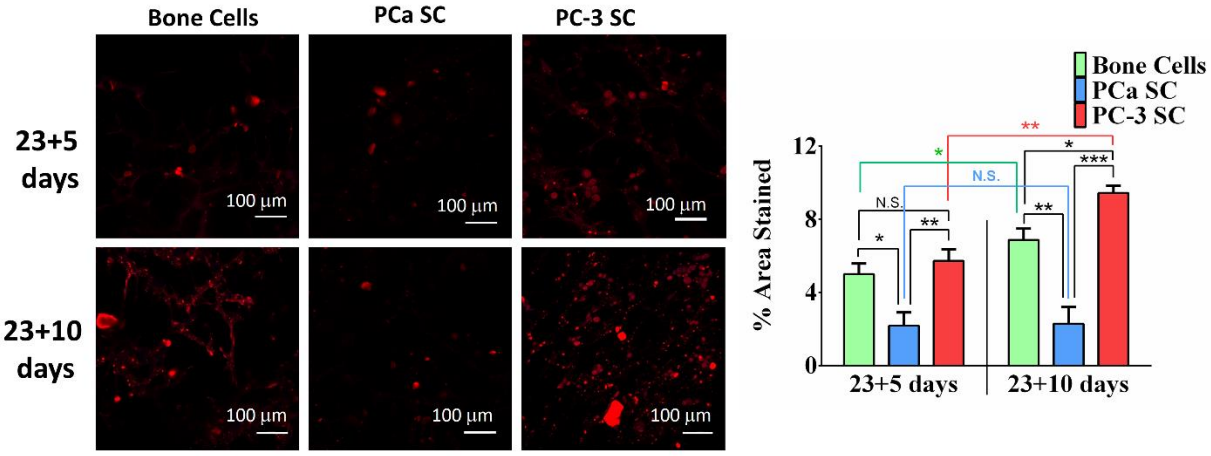

Figure 5.4. Effect on mineralization. A. Alizarin red S stained bone cells (differentiated from MSCs), PCa SC (sequential culture of MDA PCa 2b cells with MSCs), and PC-3 SC (sequential culture of PC-3 cells with MSCs) samples. Bar = 100 µm. B. Calculated percentage of area stained in alizarin red S assay. Results are shown as mean ± standard deviation. Statistical significance is shown by ***p < 0.001, **p < 0.005, *p < 0.05, n=3.).

reacts with calcium cation to form a chelate. To assess the effect of metastasized prostate cancer cells on mineralization, we performed Alizarin Red S assay. Bone cells, the PC-3 SC and the PCa SC samples were stained, and the results are demonstrated in figure 5.4A. Positive alizarin red staining was observed for all the samples indicating mineralized nodule formation. The percentage area covered by the nodules on each sample (n=3) were calculated using ImageJ, and the result is presented in figure 5.4B. On day 23+5, no significant difference was observed between bone cells and the PC-3 SC. But mineralization in PC-3 SC is rapidly increased on day 23+10 compared to bone cells and PCa SC. On day 23+10, A branched pattern of mineralization was observed in the bone cells which is not observed in case of PC-3 SC or PCa SC. On both days, PCa SC showed a significantly lower level of mineralization as opposed to bone cells and PC-3 SC but there is no significant difference in mineralized nodule formation at the interval of five days. In case of bone cells, mineralization is slightly increased from day 23+5 to day 23+10.

The Alizarin Red S assay data evidently indicates that metastasized PC-3 cells enhance the mineralized bone nodule formation. This data also suggests that calcium deposition by osteoblast cells is either decreased or stopped in the presence of MDA PCa 2b cells at the metastatic site.

5.3.5. Excessive collagen synthesis in the PC-3 metastatic site

Collagen type I is the most abundant protein in the bone extracellular matrix (ECM), accounting for up to 95% of the organic matrix. To assess the effect of metastasized prostate cancer cells on type I collagen synthesis, we performed FESEM imaging, qRT-PCR, and immunocytochemical analysis. Figure 5.5A shows the bone cells, the PC-3 SC, and the PCa SC samples were stained with Anti-Collagen I (red) and nuclei (blue). Positive staining for Anti-Collagen I was observed on bone cells. On day 23+5, secreted collagen by bone cells are mostly in the monomeric form, but the initiation of collagen monomer assembly was observed as indicated by arrows (figure 5.5A). In the PC-3 SC at the same period, anti-collagen I antibody staining is significantly higher (figure 5.5A), and the collagens are mostly structural indicating faster collagen fibril synthesis in PC-3 SC. At day 23+5, the PCa SC also showed positive collagen type I staining which is noticeably less intense as opposed to the bone cells and the PC-3 SC (figure 5.5A). Collagen synthesis is increased, and monomers assembled to form a fibrillar structure in the bone cells at the interval of 5 days on day 23+10 (figure 5.5A). These collagen fibrils were much more abundant in the PC-3 SC samples on day 23+10 (figure 5.5A). On day 23+10, the PCa SC samples showed negative type I collagen staining (figure 5.5A).

Collagen gene expression was further evaluated using qRT-PCR experiment. Total mRNA was extracted from the bone cells, the PC-3 SC and the PCa SC on day 23+10. Resulting relative mRNA level is plotted in figure 5.5B where the bone cells samples served as control. Collagen expression is significantly upregulated in the PC-3 SC but downregulated in PCa SC

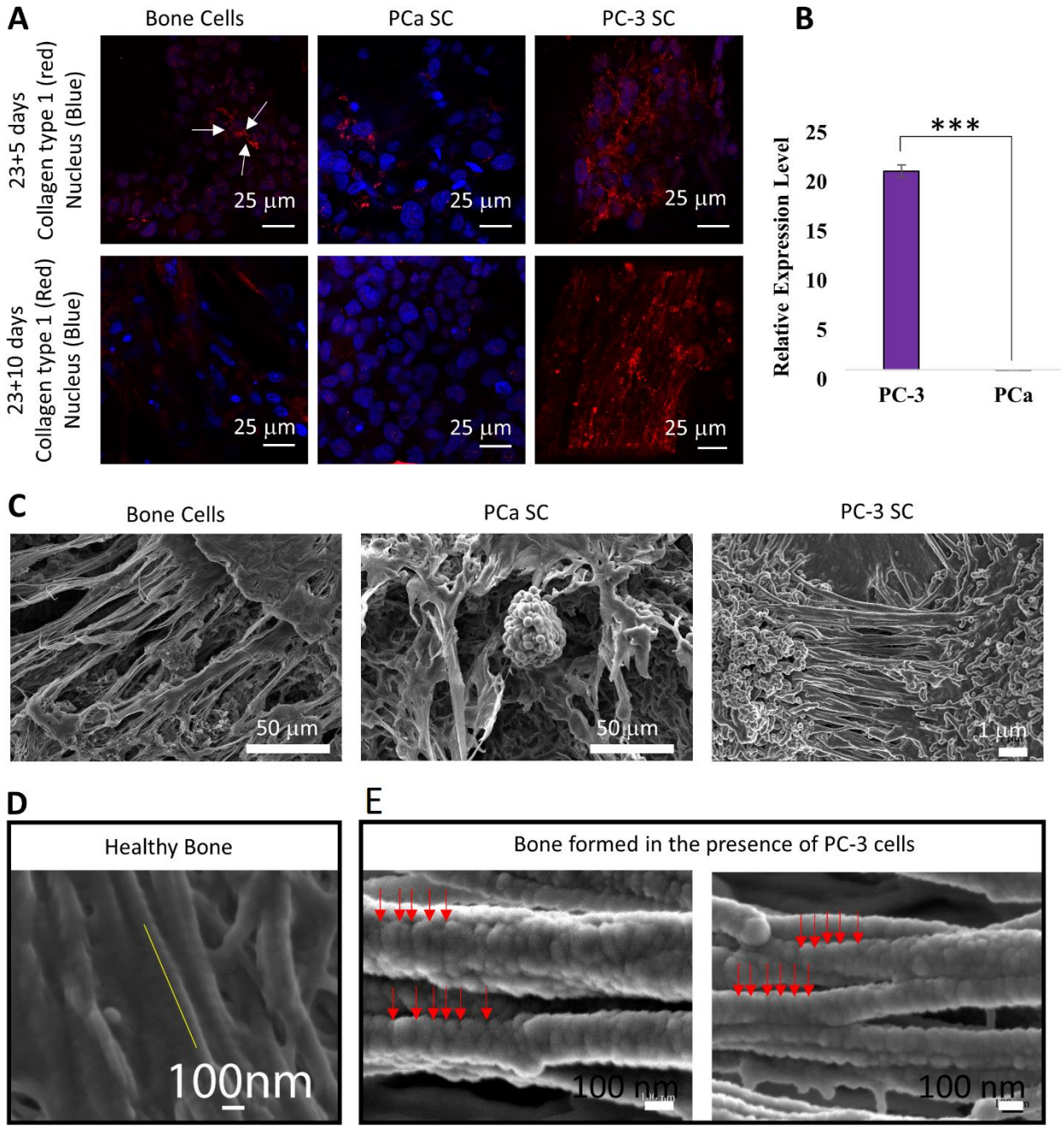

Figure 5.5. Effect on mineralized collagen formation. A. Immunostained type I collagen (red), and nuclei (blue) in the bone cells (differentiated from MSCs), PCa SC (sequential culture of MDA PCa 2b cells with MSCs), and PC-3 SC (sequential culture of PC-3 cells with MSCs) samples. B. Relative type I collagen gene expression level at day 23+10 in the PC-3 SC and PCa SC, where bone cells (differentiated from MSCs) served as control (relative expression=1). Results are shown as mean ± standard deviation. Statistical significance is shown by ***$p < 0.001$, n=3.). C. SEM images of extracellular spaces of Bone cells, PCa SC and PC-3 SC. D. 67 nm banding patterns in the collagen fibril structure observed in the healthy bone (adopted from Gu et al. with permission [39]). E. FESM micrographs of mineralized type I collagen fibrils formed in the PC-3 SC.

compared to the control. This qRT-PCR result coincides with our immunocytochemical observation. From the SEM images (figure 5.5C) we can observe that the extracellular space of bone cells, PC-3 SC and PCa SC samples are very different from each other.

Collagen fibrils synthesized in the PC-3 SC was further analyzed using field emission scanning electron microscopy (FESEM), and the micrographs are shown in figure 5.5E. Collagen Fibrils are a couple of microns long (figure 5.5D) and ~100 nm in diameter. The 67 nm banding patterns, which is a unique property of collagen fibrils, was also observed. Figures shows collagen fibrils are in the process of making collagen fibers by parallel self-assembly. FESEM micrographs also coincide with our immunocytochemical observations.

5.3.6. Osteocalcin is upregulated in PC-3 metastatic site

Osteocalcin (OCN) is the most abundant non-collagenous bone matrix protein and is regarded as a marker of bone formation, but it seems to be involved in the process of mineralization rather than matrix production. It is primarily deposited in the extracellular matrix of bone. To investigate the effect of metastasized prostate cancer cells on the bone matrix, we analyzed osteocalcin in protein and RNA level using ELISA and qRT-PCR experiment. Total osteocalcin protein expression was evaluated for the bone cells at day 28, for the PC-3 SC and the PCa SC at day 23+5 and 23+10; the result is shown in figure 5.6A. OCN protein expression observed in bone cells sample was ~29 ng/ml at day 28. At the same day, OCN protein expression was noticeably higher by ~5 ng/ml in the PC-3 SC samples. The peak of the OCN protein expression was observed in PC-3 SC samples at day 23+10 (~45 ng/ml). At the interval of 5 days, OCN protein expression was increased by ~10 ng/ml in the PC-3 SC. OCN protein expression in the PCa SC was significantly lower as opposed to the bone cells and the PC-3 SC. There was no significant difference was observed in OCN protein expression of the PCa SC

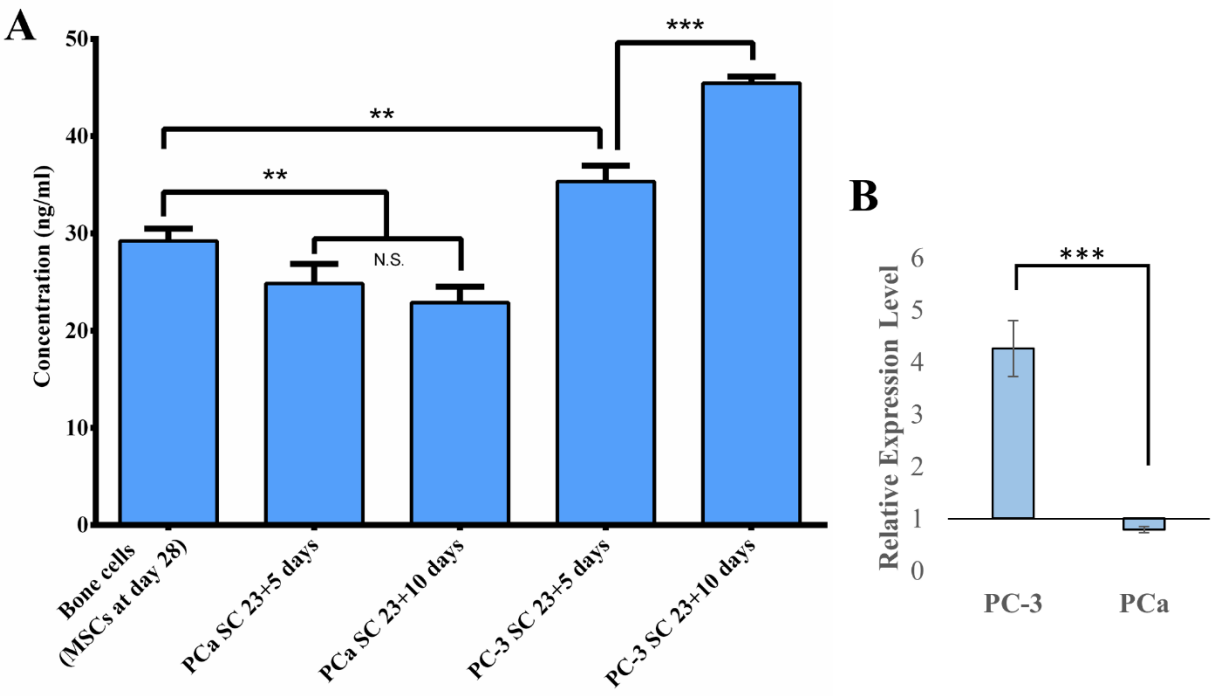

Figure 5.6. Osteocalcin (OCN) expression. A. OCN protein secretion in bone cells, PC-3 SC, and PCa SC measured by ELISA. Results are shown as mean ± standard deviation. Statistical significance is shown by ***p < 0.001, **p < 0.005, *p < 0.05, n=3.). B. Relative OCN gene expression level at day 23+10 in the PC-3 SC and PCa SC, where bone cells (differentiated from MSCs) served as control (relative expression=1). Results are shown as mean ± standard deviation. Statistical significance is shown by ***p < 0.001, n=3.).

samples at day 23+5 and 23+10. Gene expression of osteocalcin (OCN) in the PC-3 SC and the PCa SC was evaluated at day 23+10, and the result is demonstrated in figure 5.6B where the bone cells sample served as control. OCN gene expression is significantly upregulated in the PC-3 SC as compared to control. OCN gene expression was downregulated in the PCa SC as opposed to the control. This significantly increased gene expression of osteocalcin in the PC-3 SC coincided with the protein expression of osteocalcin. The increased osteocalcin expression was probably due to the increased expression of collagen type 1 at both the gene and extracellular matrix levels. It has been reported that increased collagen type 1 expression leads to upregulate downstream osteocalcin expression [32]. It is evidently obvious that osteocalcin

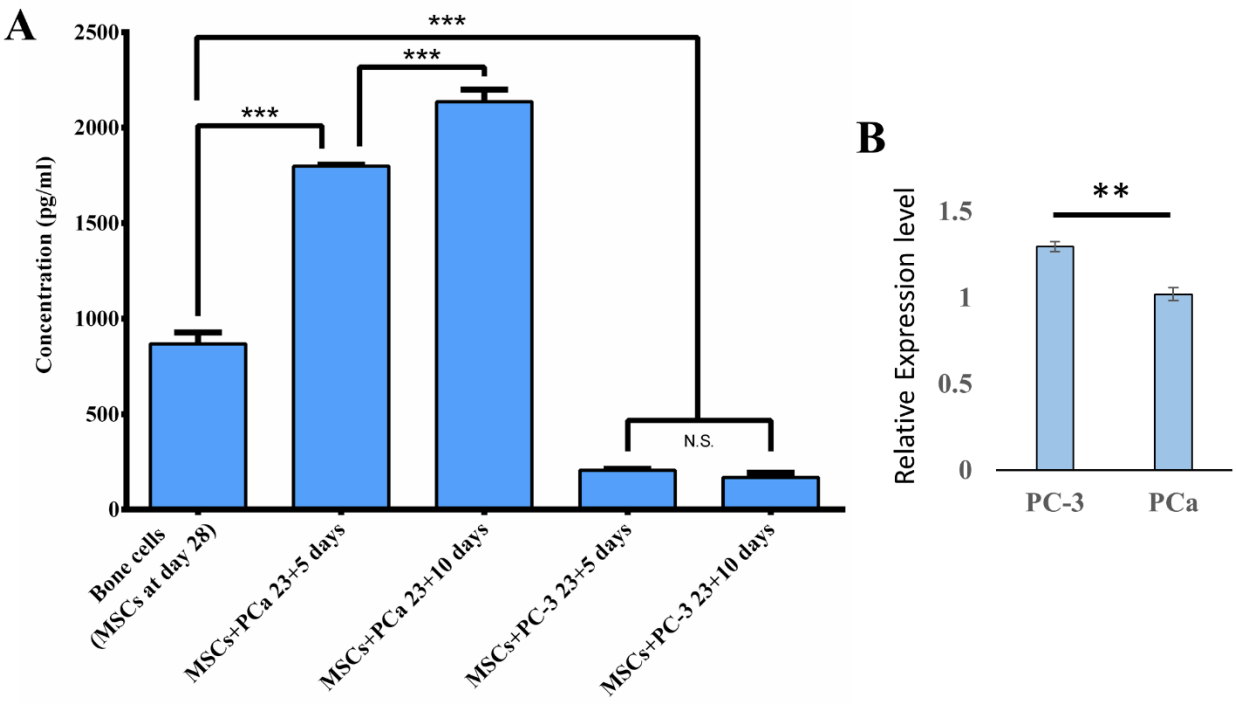

Figure 5.7. MMP-9 expression. A. MMP-9 protein secretion in bone cells, PC-3 SC, and PCa SC measured by ELISA. Results are shown as mean ± standard deviation. Statistical significance is shown by ***p < 0.001, **p < 0.005, *p < 0.05, n=3.). B. Relative MMP-9 gene expression level at day 23+10 in the PC-3 SC and PCa SC, where bone cells (differentiated from MSCs) served as control (relative expression=1). Results are shown as mean ± standard deviation. Statistical significance is shown by **p < 0.005, n=3.).

mediated extracellular mineralization of bone matrix is increased in the presence of PC-3 cells. On the other hand, the presence of MDA PCa 2b cells has a negative effect on osteocalcin mediated extracellular mineralization of bone matrix.

5.3.7. An elevated level of ECM degradation at the PCa metastatic site

One of the dominant group of enzymes responsible for collagen and other extracellular matrix protein degradation is matrix metalloproteinases (MMPs). MMP-9, which is one of the most widely investigated MMPs, is directly associated with ECM protein degradation. MMP-9 proteolytically processes several extracellular matrix proteins such as collagen, fibronectin, and

laminin. To investigate how metastasized prostate cancer cells, play a role in extracellular matrix degradation, we evaluated the expression of MMP-9 using ELISA and qRT-PCR experiment, and the result is plotted in figure 5.7. The total amount of MMP-9 excreted by the bone cells at day 28 is 868 pg/ml. Metastasized PC-3 cells significantly inhibit the secretion of the MMP-9 protein. MMP-9 secretion in PC-3 SC is significantly lower as opposed to the bone cells and the PCa SC. On day 23+5, MMP-9 secreted in PC-3 SC was ~206 pg/ml (figure 5.7A). MMP-9 secretion in PC-3 SC has further decreased at the interval of 5 days at day 23+10, and the difference is statistically significant. MMP-9 secretion is significantly enhanced at the PCa metastatic site as we can see the peak of MMP-9 secretion is observed in the PCa SC. On day 23+5, MMP-9 secreted in PCa SC was ~1800 pg/ml as shown in figure 5.7A. MMP-9 secretion in PCa SC was further increased at the interval of 5 days at say 23+10 which is almost 2.5-fold higher than the secretion by the bone cells.

The MMP-9 gene expression analysis for PC-3 SC and PCa SC is shown in the figure 5.7B. Although the expression in PC-3 SC and PCa SC are statistically significant, there is no fold-change as opposed to the control.

5.4. Discussion

The interaction between prostate cancer and bone microenvironment has been the focus of interest for years due to the characteristic preference of prostate cancer cells to metastasize to bone. One of the significant injunctions of investigating the osteotropic nature of prostate cancer cells has been the lack of an appropriate *in vitro* model that mimics closely the *in vivo* live bone microenvironment in response to bone-cancer interaction under specific conditions. In recent years, with the rising acceptance of 3D *in vitro* models as tools for investigating the molecular

mechanism of cancer metastasis, a significant number of novel and innovative 3D models have been reported in an attempt to recapitulate the native tumor microenvironment [33]. Many of these models have been key to manifest the gravity of 3D tumor architecture in the mechanistic understanding of bone-prostate cancer interaction [34, 35]. However, to the best of our knowledge, none of these models used the 3D sequential culture of MSCs to generate human bone tissue initially to seed prostate cancer cells. Our 3D sequential culture model consists of prostate cancer cells cultured within an engineered bone tissue formed by differentiated MSCs. By using human MSCs instead of osteoblast and sequential culture instead of coculture, we have improved the biomimetic nature of the 3D *in vitro* model with respect to the native human bone microenvironment.

Two different cell lines have been used to evaluate the effect of metastasized prostate cancer cells on the bone microenvironment. From the 3D sequential culture model, apparent cell-cella and cell-matrix interactions were observed for both of the cell lines. Figure 5.2 shows the proliferation of prostate cancer cells in the sequential culture and migration towards the tissue-engineered bone suggesting affinity of the prostate cancer cells for bone matrix and integration within this microenvironment. Our migration study also is in agreement with the literature since PC-3 has been reported as highly metastatic in nature while MDA PCa 2b has been identified as less metastatic [36].

Bone cells can be induced to produce vast extracellular calcium deposits *in vitro*. This process is known as bone mineralization. Calcium deposits are an indication of successful *in vitro* bone formation. In this study, calcium deposition by bone cells is stained with bright orange-red using Alizarin Red S (figure 5.4). This data suggest that mineralization is enhanced in the presence of PC-3 cells whereas, MDA PCa 2b cells inhibited bone mineralization in the 3D

tissue-engineered bone model. More importantly, mineralization or osteogenic differentiation of MSCs occurred in the absence of common osteogenic agents dexamethasone and β-glycerophosphate, demonstrating the remarkable osteoinductive ability of the hydroxyapatite-polymer-nanoclay based 3D scaffolds that we have developed in our previous studies [18, 37]. Osteogenic differentiation of MSCs on 3D scaffolds in the absence of osteogenic supplements has been reported in prior studies [37, 38]. This is highly important with regard to developing materials for *in vitro* bone-tumor model. However, increased mineralization is indicative of osteoblastic osteotropism and inhibited mineralization points to osteolytic osteotropism of prostate cancer cells.

Type I collagen accounts for about 95 % of the organic matrix proteins in bone. A hallmark of osteoblast differentiation is the formation of type I collagen. At day 23+5 collagen molecules are mostly inside intracellular space (procollagen) in bone cells and PCa SC as shown by type I collagen staining (Figure 5.5A). At day 23+5 in PC-3 SC some extracellular type I collagen has been observed. At extracellular space type I collagen molecules pack together side-by-side, forming fibrils with a diameter of roughly 100 nm. The saturated calcium and phosphate ions secreted by osteoblasts precipitate into hydroxyapatite crystals which are cemented to this collagen fibril. In collagen fibrils, adjacent collagen molecules are displaced from one another by 67 nm, about one-quarter of their length, produces a characteristic pattern of bands of length 67 nm. This characteristic 67 nm banding patterns of the mineralized collagen fibrils was observed in healthy bone in our previous study (figure 5.5D) [39]. Similar collagen fibrils with a diameter of roughly 100 nm was observed in the PC-3 SC (figure 5.5E). These fibril are several micrometers long and are packed side-by-side in parallel bundles. However, the banding patterns of the collagen fibrils that formed in the presence of PC-3 cells were not exactly 67 nm as shown

by the red arrows (figure 5.5E). This indicates the possibility of changed collagen structure that forms in the presence of metastasized prostate cancer cells. Extracellular space of the bone cells, the PCa SC and the PC-3 SC was quite different from each other (figure 5.5C). Collagen fibers can be observed in PC-3 SC and bone cells at day 23+10 but not in PCa SC (figure 5.5A). Our micrographs observation of type I collagen also coincides with the qRT-PCR expression of type I collagen which shows significant upregulation in the PC-3 SC as compared to PCa SC and where bone cells served as control (figure 5.5B).

Osteocalcin (OCN) is an essential non-collagenous protein which binds extracellular calcium to bone matrix. It is considered as a late marker for osteoblast differentiation. OCN protein expression was found in all types of samples. Figure 5.6A suggests that the presence of PC-3 cells enhances OCN expression whereas the presence of PCa cells inhibited OCN expression. It has been reported that the increased collagen expression leads to increased downstream expression of OCN [40]. This significantly increased protein expression of OCN in PC-3 SC as compared to PCa SC coincided with the gene expression of OCN within 10 days in sequential culture (figure 5.6B).

Matrix metalloproteinases (MMPs) are key enzymes in matrix degradation. They can digest all the matrix macromolecules synergistically. MMP-9 is one of the most extensively investigated MMPs and directly associated with ECM protein degradation. It has been reported that MMP-9 is able to cleave collagens I in their native form and in a manner that is characteristic of the unique collagenolytic activity of MMP collagenases [41]. In the current study, MMP-9 protein expression (Figure 5.7A) coincides with the type I collagen expression that is shown in figure 5.5. We can conclude that higher expression of MMP-9 inhibited type I collagen synthesis in PCa SC or enhanced type I collagen synthesis is facilitated by inhibited

MMP-9 expression in PC-3 SC. However, MMP-9 gene expression does not coincide with the protein expression level (figure 5.7A and B). A poor correlation between mRNA and its associated protein level has been reported before [42]. Interpreting protein expression levels based on gene expression level could be misleading. Changes in gene expression levels and protein levels may not correlate well mainly because of the regulation control at different levels, i. e. RNA processing, RNA stability, transcription, translation, protein stability, protein modification, proteolytic cleavage.

All the experimental results in this study indicate osteoblastic bone formation by PC-3 cells and osteolytic bone resorption by MDA PCa 2b whereas, PC-3 is predominantly identified as osteolytic and MDA PCa 2b as osteoblastic in nature [36, 43-45]. However, Curtin et al. demonstrated the osteoblastic characteristic of PC-3 cells in a 3D cancer-bone model using ex vivo coculture of live calvarial bones and cancer cells [4]. Salamanna et al. demonstrated a mixed (osteoblastic and osteolytic) characteristic of PC-3 cells in an *in vitro* 3D bone model by using human bone tissue culture [46]. Hall et al. reported the induction of osteoblastic activity by the PC-3 cell by inhibiting DKK-1 [47]. Knerr et al. demonstrated an increase of bone-related genes, type I collagen, osteonectin, osteopontin, and ALP in the coculture of PC-3 with human osteoblast. Hesami et al. reported osteolytic nature of PC-3 cells in a humanized tissue engineered *in vivo* model where PC-3 cell undergo epithelial to mesenchymal transition (EMT) in the bone microenvironment [43]. Whereas, in real bone microenvironment prostate cancer cells undergo MET which is a reverse process of EMT. In a different study we have shown that PC-3 cells undergo MET in our tissue-engineered bone model indicating the more biomimetic nature of our 3D *in vitro* model with respect to the native human bone microenvironment [48]. The protein expression, gene expression and immunocytochemistry results of this study

evidently indicate osteolytic bone resorption by MDA PCa 2b cells. To the best of our knowledge, this is the first-time osteolytic bone resorption phenomenon has been observed with the MDA PCa 2b cancer cell line either *in vivo* and *in vitro* studies. However, Fizazi et al. reported a mixed osteoblastic and osteolytic activity of MDA PCa 2b cells [36]. They found that when MDA PCa 2b cocultured with osteoblasts, OPG expression was inhibited and RANKL expression was enhanced. In light of our observation in this study, we conclude that whether or not one observes osteolytic or osteoblastic bone metastasis depends not only on the cancer type/ tissue origin but also influenced significantly by the bone microenvironment the cells are grown in.

5.5. Conclusion

In this study, we have investigated the effect of metastasized prostate cancer cells on bone mineralization and extracellular matrix (ECM) formation using an *in vitro* 3D tumor model. Two different prostate cancer cell lines, highly metastatic PC-3 and a non-metastatic MDAPCa2b (PCa) were used to explore various outcomes. Our experimental results indicate that PCa is less prolific, less metastatic, and forms multicellular tumoroids in the bone microenvironment. Whereas, PC-3 is more prolific, highly metastatic, and do not form multicellular tumoroids in the bone microenvironment. The metastasized prostate cancer cells exhibit significant effect on bone mineralization and ECM formation. From the Alizarin Red S staining and collagen type I expression analysis, we observed excessive bone formation in the presence of PC-3 and significant osteolysis in the presence of PCa. This observation is further confirmed by the osteocalcin and MMP-9 expression analysis using ELISA and qRT-PCR. FESEM images revealed that the structure of collagen that formed in the presence of PC-3 is

different than the healthy bone. All the experimental results indicate that both osteolytic and osteoblastic bone lesion can be recapitulated in our tumor model. Our *in vitro* tumor model does not entirely recapitulate the bone tumor microenvironment found in a patient with metastatic disease, but with the inclusion of human MSCs and sequential culture technique, it certainly provides an improved reproducible and controllable system which is a useful tool to elucidate the osteotropism of prostate cancer cells. The model may be extended by including more human components, such as human hematopoietic stem cells, to provide osteoclast and immune cells in the bone microenvironment. This model provides an intriguing opportunity to dissect the role of genes, proteins, and other factors in the bone microenvironment subsequent to the arrival of prostate cancer cells with a significant contribution to the understanding of the molecular, cellular and mechanical mechanism [49]. The model can be used to investigate the various aspect of prostate cancer-bone interaction at a cellular, molecular and genetic level as well as to test various cancer therapeutics[50, 51].

5.6. Acknowledgments

This work was supported by NDSU grand challenges grant for “Center for Engineered Cancer Test-Beds.” The SEM experiments conducted in this work are made possible through instrumentation obtained using MRI grant from the National Science Foundation. Dr. Tao Wang, manager of core biology facility at NDSU, is acknowledged for help in use of the qRT PCR experiments. Dr. Pawel Borowicz, Director of NDSU Advanced Imaging and Microscopy (AIM) Core Lab, is acknowledged for help in use of the confocal microscope. Support from ND EPSCoR for tissue engineering laboratory is also acknowledged. ND EPSCoR is also acknowledged for “Doctoral Dissertation Award.”

Table 5.1. The primer sequence used for the qRT-PCR experiment.

Gene	Forward Primer	Reverse Primer
GAPDH	5′-CATCTTCTTTTGCGTCGCCA-3′	5′-TTAAAAGCAGCCCTGGTG ACC-3′
COL1A1	5′-CATCGGTGGTACTAAC–3′	5′-CTGGATCATATTGCACA–3′
OCN	5′-GAGCTGCCCTGCACTGGGTG-3′	5′-TGGCCCCAGACCTCTTCCCG–3′
MMP-9	5′-GGGACGCAGACATCGTCATC–3′	5′-TCGTCATCGTCGAAATGGGC–3′
RUNX-2	5-CCGCCTCAGTGATTTAGGGC-3′	5′-GGGTCTGTAATCTGACTCTG TCC-3′

5.7. References

[1] L. Bubendorf, A. Schopfer, U. Wagner, G. Sauter, H. Moch, N. Willi, T.C. Gasser, M.J. Mihatsch, Metastatic patterns of prostate cancer: an autopsy study of 1,589 patients, Hum Pathol 31(5) (2000) 578-83.

[2] N. Howlader, A.M. Noone, M. Krapcho, D. Miller, K. Bishop, C.L. Kosary, M. Yu, J. Ruhl, Z. Tatalovich, A. Mariotto, SEER cancer statistics review, 1975–2014. Bethesda, MD: National Cancer Institute; 2017, 2017.

[3] O.V. Batson, The function of the vertebral veins and their role in the spread of metastases, Annals of surgery 112(1) (1940) 138.

[4] P. Curtin, H. Youm, E. Salih, Three-dimensional cancer-bone metastasis model using ex-vivo co-cultures of live calvarial bones and cancer cells, Biomaterials 33(4) (2012) 1065-1078.

[5] X. Fang, S. Sittadjody, K. Gyabaah, E.C. Opara, K.C. Balaji, Novel 3D co-culture model for epithelial-stromal cells interaction in prostate cancer, PloS one 8(9) (2013) e75187.

[6] H. Qiao, T. Tang, Engineering 3D approaches to model the dynamic microenvironments of cancer bone metastasis, Bone research 6(1) (2018) 3.

[7] S. Sieh, A.A. Lubik, J.A. Clements, C.C. Nelson, D.W. Hutmacher, Interactions between human osteoblasts and prostate cancer cells in a novel 3D in vitro model, Organogenesis 6(3) (2010) 181-188.

[8] S. Sieh, A.V. Taubenberger, M.L. Lehman, J.A. Clements, C.C. Nelson, D.W. Hutmacher, Paracrine interactions between LNCaP prostate cancer cells and bioengineered bone in 3D in vitro culture reflect molecular changes during bone metastasis, Bone 63 (2014) 121-131.

[9] K.A. Fitzgerald, J. Guo, E.G. Tierney, C.M. Curtin, M. Malhotra, R. Darcy, F.J. O'Brien, C.M. O'Driscoll, The use of collagen-based scaffolds to simulate prostate cancer bone metastases with potential for evaluating delivery of nanoparticulate gene therapeutics, Biomaterials 66 (2015) 53-66.

[10] L.C.E. Windus, T.T. Glover, V.M. Avery, Bone-stromal cells up-regulate tumourigenic markers in a tumour-stromal 3D model of prostate cancer, Molecular cancer 12(1) (2013) 112.

[11] B.M. Holzapfel, F. Wagner, D. Loessner, N.P. Holzapfel, L. Thibaudeau, R. Crawford, M.-T. Ling, J.A. Clements, P.J. Russell, D.W. Hutmacher, Species-specific homing mechanisms of human prostate cancer metastasis in tissue engineered bone, Biomaterials 35(13) (2014) 4108-4115.

[12] R. Wang, J. Xu, L. Juliette, A. Castilleja, J. Love, S.-Y. Sung, H.E. Zhau, T.J. Goodwin, L.W.K. Chung, Three-dimensional co-culture models to study prostate cancer growth, progression, and metastasis to bone, Elsevier, pp. 353-364.

[13] H. Kwon, H.J. Kim, W.L. Rice, B. Subramanian, S.H. Park, I. Georgakoudi, D.L. Kaplan, Development of an in vitro model to study the impact of BMP-2 on metastasis to bone, J Tissue Eng Regen Med 4(8) (2010) 590-9.

[14] M.D.S. Molla, R. Katti Dinesh, S. Katti Kalpana, In vitro design of mesenchymal to epithelial transition of prostate cancer metastasis using 3D nanoclay bone-mimetic scaffolds, Journal of Tissue Engineering and Regenerative Medicine 12(3) (2017) 727-737.

[15] S.J. Florczyk, G. Liu, F.M. Kievit, A.M. Lewis, J.D. Wu, M. Zhang, 3D porous chitosan–alginate scaffolds: a new matrix for studying prostate cancer cell–lymphocyte interactions in vitro, Advanced healthcare materials 1(5) (2012) 590-599.

[16] L. David, V. Dulong, D. Le Cerf, C. Chauzy, V. Norris, B. Delpech, M. Lamacz, J.-P. Vannier, Reticulated hyaluronan hydrogels: a model for examining cancer cell invasion in 3D, Matrix biology 23(3) (2004) 183-193.

[17] D. Harjanto, J.S. Maffei, M.H. Zaman, Quantitative analysis of the effect of cancer invasiveness and collagen concentration on 3D matrix remodeling, PloS one 6(9) (2011) e24891.

[18] A.H. Ambre, D.R. Katti, K.S. Katti, Biomineralized hydroxyapatite nanoclay composite scaffolds with polycaprolactone for stem cell-based bone tissue engineering, Journal of Biomedical Materials Research Part A 103(6) (2015) 2077-2101.

[19] K.S. Katti, M.D.S. Molla, F. Karandish, M.K. Haldar, S. Mallik, D.R. Katti, Sequential culture on biomimetic nanoclay scaffolds forms three-dimensional tumoroids, Journal of Biomedical Materials Research Part A 104(7) (2016) 1591-1602.

[20] K.S. Katti, D.R. Katti, M.S. Molla, S. Kar, Evaluation of Cancer Tumors in 3D Porous Bone Mimetic Scaffolds, Poromechanics VI, pp. 881-888.

[21] R.E. Sobel, M.D. Sadar, Cell lines used in prostate cancer research: a compendium of old and new lines—part 1, The Journal of Urology 173(2) 342-359.

[22] A.H. Ambre, K.S. Katti, D.R. Katti, Nanoclay based composite scaffolds for bone tissue engineering applications, Journal of Nanotechnology in Engineering and Medicine 1(3) (2010) 031013.

[23] A. Ambre, K.S. Katti, D.R. Katti, In situ mineralized hydroxyapatite on amino acid modified nanoclays as novel bone biomaterials, Materials Science and Engineering: C 31(5) (2011) 1017-1029.

[24] A. Sharma, M.D.S. Molla, K.S. Katti, D.R. Katti, Multiscale Models of Degradation and Healing of Bone Tissue Engineering Nanocomposite Scaffolds, Journal of Nanomechanics and Micromechanics 7(4) (2017) 04017015.

[25] J. Taylor-Papadimitriou, M. Stampfer, J. Bartek, A. Lewis, M. Boshell, E.B. Lane, I.M. Leigh, Keratin expression in human mammary epithelial cells cultured from normal and malignant tissue: relation to in vivo phenotypes and influence of medium, Journal of cell science 94(3) (1989) 403-413.

[26] S. Rey, G.L. Semenza, Hypoxia-inducible factor-1-dependent mechanisms of vascularization and vascular remodeling, Cardiovascular research (2010) cvq045.

[27] S. Oltean, B.S. Sorg, T. Albrecht, V.I. Bonano, R.M. Brazas, M.W. Dewhirst, M.A. Garcia-Blanco, Alternative inclusion of fibroblast growth factor receptor 2 exon IIIc in Dunning prostate tumors reveals unexpected epithelial mesenchymal plasticity, Proceedings of the National Academy of Sciences 103(38) (2006) 14116-14121.

[28] P. Nikolaev, M.J. Bronikowski, R.K. Bradley, F. Rohmund, D.T. Colbert, K.A. Smith, R.E. Smalley, Gas-phase catalytic growth of single-walled carbon nanotubes from carbon monoxide, Chemical Physics Letters 313(1) (1999) 91-97.

[29] D. Cunningham, Z. You, In vitro and in vivo model systems used in prostate cancer research, Journal of biological methods 2(1) (2015).

[30] M. Filipak, D.N. Estervig, C.Y. Tzen, P. Minoo, B.J. Hoerl, P.B. Maercklein, M.A. Zschunke, M. Edens, R.E. Scott, Integrated control of proliferation and differentiation of mesenchymal stem cells, Environ Health Perspect 80 (1989) 117-25.

[31] M.J. Whitfield, W.C.J. Lee, K.J. Van Vliet, Onset of heterogeneity in culture-expanded bone marrow stromal cells, Stem cell research 11(3) (2013) 1365-1377.

[32] D. Couchourel, I. Aubry, A. Delalandre, M. Lavigne, J. Martel-Pelletier, J.P. Pelletier, D. Lajeunesse, Altered mineralization of human osteoarthritic osteoblasts is attributable to abnormal type I collagen production, Arthritis & Rheumatology 60(5) (2009) 1438-1450.

[33] A.M. Sitarski, H. Fairfield, C. Falank, M.R. Reagan, 3D tissue engineered in vitro models of cancer in bone, ACS biomaterials science & engineering 4(2) (2017) 324-336.

[34] R.M. Lescarbeau, F.P. Seib, M. Prewitz, C. Werner, D.L. Kaplan, In vitro model of metastasis to bone marrow mediates prostate cancer castration resistant growth through paracrine and extracellular matrix factors, PloS one 7(8) (2012) e40372.

[35] X. Bi, J.A. Sterling, A.R. Merkel, D.S. Perrien, J.S. Nyman, A. Mahadevan-Jansen, Prostate cancer metastases alter bone mineral and matrix composition independent of effects on bone architecture in mice—a quantitative study using microCT and Raman spectroscopy, Bone 56(2) (2013) 454-460.

[36] K. Fizazi, J. Yang, S. Peleg, C.R. Sikes, E.L. Kreimann, D. Daliani, M. Olive, K.A. Raymond, T.J. Janus, C.J. Logothetis, G. Karsenty, N.M. Navone, Prostate cancer cells-osteoblast interaction shifts expression of growth/survival-related genes in prostate cancer and reduces expression of osteoprotegerin in osteoblasts, Clin Cancer Res 9(7) (2003) 2587-97.

[37] A.H. Ambre, D.R. Katti, K.S. Katti, Nanoclays mediate stem cell differentiation and mineralized ECM formation on biopolymer scaffolds, Journal of Biomedical Materials Research Part A 101A(9) (2013) 2644-2660.

[38] R.A. Thibault, L. Scott Baggett, A.G. Mikos, F.K. Kasper, Osteogenic differentiation of mesenchymal stem cells on pregenerated extracellular matrix scaffolds in the absence of osteogenic cell culture supplements, Tissue Eng Part A 16(2) (2010) 431-40.

[39] C. Gu, D.R. Katti, K.S. Katti, Photoacoustic FTIR spectroscopic study of undisturbed human cortical bone, Spectrochimica Acta Part A: Molecular and Biomolecular Spectroscopy 103 (2013) 25-37.

[40] B.K. Hall, Chapter 15 - Cells to Make and Cells to Break, Bones and Cartilage (Second Edition), Academic Press, San Diego, 2015, pp. 239-258.

[41] H.F. Bigg, A.D. Rowan, M.D. Barker, T.E. Cawston, Activity of matrix metalloproteinase-9 against native collagen types I and III, The FEBS journal 274(5) (2007) 1246-1255.

[42] C. Vogel, E.M. Marcotte, Insights into the regulation of protein abundance from proteomic and transcriptomic analyses, Nature Reviews Genetics 13(4) (2012) 227.

[43] P. Hesami, B.M. Holzapfel, A. Taubenberger, M. Roudier, L. Fazli, S. Sieh, L. Thibaudeau, L.S. Gregory, D.W. Hutmacher, J.A. Clements, A humanized tissue-engineered in vivo model to dissect interactions between human prostate cancer cells and human bone, Clinical & experimental metastasis 31(4) (2014) 435-446.

[44] Á. González, C. García de Durango, V. Alonso, B. Bravo, A. Rodríguez de Gortázar, A. Wells, J. Forteza, F. Vidal-Vanaclocha, Distinct Osteomimetic Response of Androgen-Dependent and Independent Human Prostate Cancer Cells to Mechanical Action of Fluid Flow: Prometastatic Implications, The Prostate 77(3) (2017) 321-333.

[45] X.-H. Liu, A. Kirschenbaum, S. Yao, G. Liu, S.A. Aaronson, A.C. Levine, Androgen-induced Wnt signaling in preosteoblasts promotes the growth of MDA-PCa-2b human prostate cancer cells, Cancer research 67(12) (2007) 5747-5753.

[46] F. Salamanna, V. Borsari, S. Brogini, G. Giavaresi, A. Parrilli, S. Cepollaro, M. Cadossi, L. Martini, A. Mazzotti, M. Fini, An in vitro 3D bone metastasis model by using a human bone tissue culture and human sex-related cancer cells, Oncotarget 7(47) (2016) 76966.

[47] C.L. Hall, A. Bafico, J. Dai, S.A. Aaronson, E.T. Keller, Prostate cancer cells promote osteoblastic bone metastases through Wnts, Cancer research 65(17) (2005) 7554-7560.

[48] M.D.S. Molla, D.R. Katti, K.S. Katti, An in vitro model of prostate cancer bone metastasis for highly metastatic and non-metastatic prostate cancer using nanoclay bone-mimetic scaffolds, MRS Advances 1-7.

[49] D.R. Katti, K.S. Katti, S. Molla, S. Kar, Biomechanics of Cells as Potential Biomarkers for Diseases: A New Tool in Mechanobiology, (2014).

[50] T. Anajafi, J. Yu, A. Sedigh, M.K. Haldar, W.W. Muhonen, S. Oberlander, H. Wasness, J. Froberg, M.D.S. Molla, K.S. Katti, Nuclear localizing peptide-conjugated, redox-sensitive polymersomes for delivering curcumin and doxorubicin to pancreatic cancer microtumors, Molecular pharmaceutics 14(6) (2017) 1916-1928.

[51] R. Nahire, M.K. Haldar, S. Paul, A.H. Ambre, V. Meghnani, B. Layek, K.S. Katti, K.N. Gange, J. Singh, K. Sarkar, S. Mallik, Multifunctional polymersomes for cytosolic delivery of gemcitabine and doxorubicin to cancer cells, Biomaterials 35(24) (2014) 6482-97.

CHAPTER 6. BIOMECHANICS OF CELLS AS POTENTIAL BIOMARKERS FOR DISEASE: A NEW TOOL IN MECHANOBIOLOGY[5]

This chapter describes biomechanics of cells as potential biomarkers for disease progression and principle of nanoindentation. The content of this chapter has been published in D.R. Katti, K.S. Katti, S. Molla, S. Kar, Biomechanics of Cells as Potential Biomarkers for Diseases: A New Tool in Mechanobiology, in: R. Narayan (Ed.), Encyclopedia of Biomedical Engineering, Elsevier, Oxford, 2019, pp. 1-21.

6.1. Introduction

The connection between human disease and biophysics of cells has become a subject of intense scientific research interest for few decades. Cellular nanomechanics is strongly connected to the molecular and physiological changes introduced by the progression of certain disease and invasion by various external organisms such as a virus, bacteria or other parasites [1-4]. Cellular pathology and pathophysiology are heavily influenced by these changes in elastic and viscoelastic properties of cells [3-5]. In the past two decades, advancement in the field of tissue engineering and bioengineering has enabled us to investigate the real-time biomechanical changes during the progression of certain diseases. The nanomechanical properties of living cells such as elastic modulus or stiffness can either increase or decrease in a pathogenic progression depending on the biomolecular and biochemical restructure [6].

Several studies showed that the stiffness of the substrate in the in vitro studies hugely affects the growth and differentiation of cells. For instance, Lu et al. showed that when cortical

[5]This chapter was co-authored by D.R. Katti, K.S. Katti, MD. S. Molla, S. Kar. MD. S. Molla and S. Kar had primary responsibility for drafting this chapter. Kalpana Katti and Dinesh Katti directed the orientation and revised this chapter.

brain cells are cultured in a softer substrate (0.15–0.30 kPa), neurons grow selectively. On the other hand, when same cells were cultured in a stiffer substrate (2 kPa), the neurons attach to glial cells, and astrocytes proliferate [13, 14]. The elastic modulus of some of the tissues such as liver, lung, breast, kidney has been reported in the range of 0.2 to 4.0 kPa [15]. The variance in elastic modulus of cells within same tissue has been reported to be within a 10-15% range, and under normal physiological conditions, this controlled mechanical property of cells helps them to maintain homeostatic cell-cycle progression [10]. Changes in elastic properties greater than 12 kPa leads to abnormal cell cycle progression which may cause irregular cell growth and differentiation [16-19]. It has been reported that live breast, liver and pancreatic cancer cells obtained from a body fluid of patients possess very different nanomechanical properties than their normal counterparts although cancerous and normal cells exhibit similar morphologies [20]. Baker et al. (2009) demonstrated that cancerous breast cancer cells are stiffer (4 kPa) than the normal breast tissue (0.2 kPa) [15, 21]. It has been reported that dense and stiffer breast tissue is more likely to develop cancer. In vitro studies suggested that stiffer substrate increases the invasive nature of cancer cells by increasing ERK and Rho activity of breast cancer cells [22]. Further, normal cells (Hu609 and HCV29) have higher Young's modulus than their cancerous counterpart (Hu456, T24, BC3726) [23]. Nanomechanical properties of cells also play a significant role in various cardiac diseases [9, 24]. It has been reported that in some cardiac-related diseases, heart ventricle is stiffer than the normal which causes heart failure. It was demonstrated that the muscle tissues of these hearts are stiffer than the regular heart muscle cells [9]. Arterial stiffness is another risk factor for cardiac diseases such as stroke and heart failure [25, 26]. Arterial Stiffness is usually developed by numerous factors such as aging, genetic factors, blood pressure, etc. [27, 28]. High aortic stiffness leads to irregular mechanical

properties of the arterial system, impaired cardiac performance, and difficulty in supplying blood to the heart and cardiac hypertrophy. Cell mechanics is also associated with liver diseases [11]. The elastic modulus of healthy liver cells (0.4-0.6 kPa) could increase to as much 15 kPa following an injury [10]. Different liver cells (stellate cells, hepatocytes, portal fibroblasts) develop changes in differentiation and proliferative characteristics when subjected to the stiffer matrix [29]. It has been reported that renal diseases also associated with reduced stiffness renal glomerular podocyte cells. The glomerular podocytes from a mouse model of HIV-associated nephropathy are significantly softer than normal podocytes [30].

It has been demonstrated that the mechanics of cells paly critical role in cellular growth and disease progression such as cancer, cardiovascular diseases, liver diseases, renal glomerular diseases etc. [7-12].

In this chapter, we will overview two advanced techniques, namely AFM and nanoindentation, as relevant methodologies for evaluation of mechanical properties of cells that will possibly play an important role in medical diagnostics as well as contribute towards understanding mechanisms of disease progression.

6.2. Theory of nanoindentation

Nanoindentation is a sophisticated technique which involves the application of a controlled load to penetrate an indenter into the surface of a specimen and uses recorded load-displacement curve to measure the hardness, elastic modulus, and, some other mechanical properties of the specimen. It is considered as a nondestructive technique as it imprints the sample at very shallow depths. Besides the elastic modulus, other mechanical properties such as fracture toughness, yield strength, hardening index, and residual stress, etc. can be measured

using nanoindentation technique. It is essential to understand the basic principle of nanoindentation for an accurate interpretation of the experimental data. There are several review papers and book chapters on the basic principle of nanoindentation [31-35].

At the later part of the 19th century, Hertz developed elastic equations of contact for contacting spherical surfaces [36]. To relate contact radius a, to the combined radius R, where R>>a, Hertz equation is:

$$a^3 = \frac{3}{4}\frac{PR}{E^*} \tag{1}$$

Where, P is the applied force and E* is the elastic modulus. Love in 1939 [37] formulated an equation to relate the force P, implemented by the indenter and the resulting penetration depth or displacement h, as follows:

$$P_m = \frac{P}{\pi a^2}\cosh^{-1}\left(\frac{a}{r}\right) \text{ and } P = \frac{2E^*\tan\alpha}{\pi}h^2 \tag{2}$$

Where, α denotes the semi-angle of the conical indenter and the combined elastic modulus E*, defined regarding Young Modulus E, and the Poisson ratio ν as follows:

$$E^* = \frac{E}{1-\nu^2} \tag{3}$$

Sneddon who employed the integral transformation method to derive the same formula as (2) concluded the slope of a load-displacement curve for a linearly isotropic half space indented by an axisymmetric of arbitrary profile as follows [38]:

$$\frac{dP}{dh} = \frac{4E^*\tan\alpha}{\pi}h \tag{4}$$

Where penetration depth h is related to contact depth h_c as follows:

$$h = \frac{\pi}{2}h_c \tag{5}$$

The relationship between h and h_c, the height of the part of the indenter which is in contact with elastic half-space is illustrated in figure 6.1.

Now for a conical indenter of half-apical angle α, the contact area is given by

$$A = \pi a^2 = \pi h_c^2 \tan^2\alpha = \frac{4}{\pi} h^2 \tan^2\alpha \tag{6}$$

Now if we introduce equation (6) into equation (2) and (4),

$$\frac{P}{A} = \frac{E^* \cot\alpha}{2} \tag{7}$$

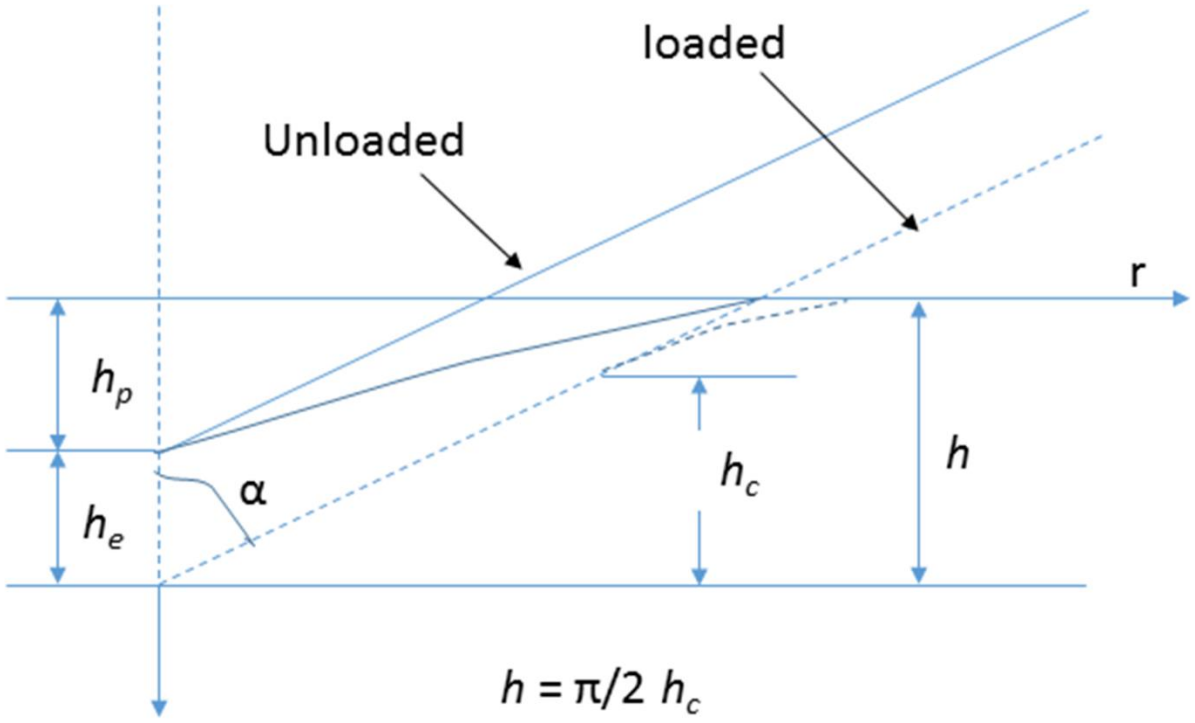

Figure 6.1. Schematic of the nanoindentation of an elastoplastic solid by a conical cone at full load and unload.

$$\frac{dP}{dh} = 2E^*\sqrt{A/\pi} \tag{8}$$

Although the tangent stiffness regarding projected contact area in equation (8) is derived for a conical indenter, it is also applicable for all asymmetric indenters such as cylindrical punches and spherical indenters [39, 40].

But in the case of the circular flat punch of radius a [41], the relation between applied load P, and depth of penetration h, is as follows:

$$P_m = \frac{P}{2\pi a^2}\left(1 - \frac{r^2}{a^2}\right)^{-0.5} \text{ and } P = 2aE^*h \tag{9}$$

Where, $A = \pi a^2$. Now if we consider a rigid spherical indenter of radius R that is pressed into a linearly elastic specimen, then Hertz formula can be expressed [35]:

$$P_m = \frac{3P}{2\pi a^2}\left(1 - \frac{r^2}{a^2}\right)^{0.5} \text{ and } P = \frac{4}{3}E^*\sqrt{R}h^3 \tag{10}$$

Now if a is expressed as the radius circular contact surface then $a^2 = Rh$ and equation (10) certainly satisfies equation (8).

Using equation (2) and (4), reduced modulus of a linearly isotropic solid could be easily determined theoretically. But in practice, it is very complex to determine elastic modulus using this simple equation from a load-displacement curve.

The indenter with the three-sided geometry, known as Berkovich indenter, is the most popular to perform nanoindentation experiments. For a Berkovich indenter the contact area is calculated as follows:

$$A = 3\sqrt{3}h_c^2 \tan^2\theta \tag{11}$$

Where, h_c is the contact depth, and semi-angle for a Berkovich indenter is 65.27. So, from equation (4), we can obtain the relationship between contact area A and contact depth h_c for a Berkovich indenter as follows:

$$A = 24.5h_c^2 \tag{12}$$

In most nanoindentation experiments, the indenter is in contact with a semi-infinite half space which makes R as the radius of the indenter alone but E* as the elastic modulus of the combined contacting bodies. Usually, the indenter is made of diamonds which is strongly resistant to the deformation, and so for most materials, E* is dominated by the elastic properties of the specimen. This relationship is described as followes:

$$\frac{1}{E'} = \frac{(1-\mu_{tip}^2)}{E_{tip}} + \frac{(1-\mu_{sample}^2)}{E_{sample}} \tag{13}$$

Now the experimental P-h curve is quite different than the parabolic P-h curve that is predicted equation (10). Figure 6.2 shows the schematic diagram of a P-h curve for an elastoplastic specimen indented by a conical indenter. Here, maximum penetration (h_{max}) by the indenter is the combination of elastic penetration (h_e) and plastic penetration (h_p) or $h_{max} = h_e + h_p$.

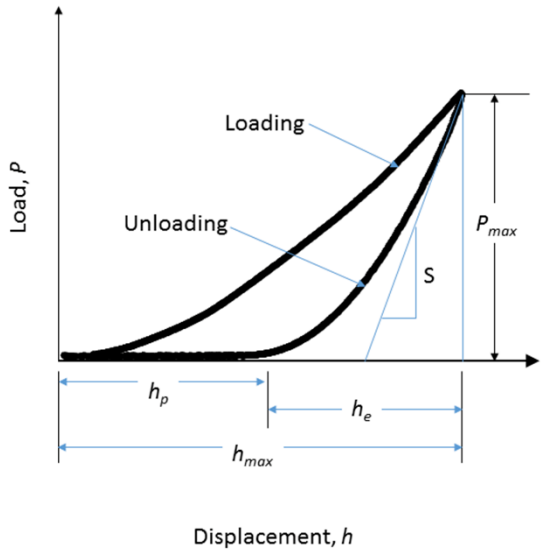

Figure 6.2. Schematic of a load–displacement curve corresponding to the nanoindentation.

Now, above equations have some limitations to analyze a P-h curve obtained by a nanoindentation experiments as these equations do not consider several factors such as the tip has a finite radius, and indenter leaves a residual imprint on the specimen due to plastic deformations. So, Equation (16) could be modified as follows:

$$\frac{dP}{dh}|h_{max} = 2\beta E^{*}\sqrt{\frac{A}{\pi}} \quad (14)$$

Where β is a dimensionless constant which accounts for the factors in a nanoindentation experiments which are ignored in the above equations and the value of which, is a debatable issue. Considering the factors of a nanoindentation experiments, Oliver and Pharr (1992) proposed an equation which is widely used in nanoindentation experiments [42]:

$$h_c = h_{max} - \beta\xi P_{max}/\frac{dP}{dh}|h_{max} \quad (15)$$

Where the aforementioned correction factor, $\xi \approx 0.72$ for a conical indenter. Though the Oliver-Pharr method is quite popular in nanoindentation experiments, it has its own limitations.

6.3. Modes of nanoindentation

6.3.1. Dynamic nanoindentation

Dynamic Nanoindentation is a mode of nanoindentation to determine the viscoelastic properties [43, 44]. It involves applying an oscillatory force to the indenter during static indentation. It involves applying an oscillatory force to the indenter during static indentation. Dynamic properties can be determined by monitoring phase lag between applied displacement and measured force. The dynamic nanoindentation technique was reported by Loubet et al. for the very first time, who used this technique to determine the storage and loss modulus of the rubber polyisoprene [44].

6.3.2. Modulus mapping

Modulus mapping is another technique to investigate the loss modulus and storage modulus characteristics of materials by using the aspect of nanoDMA and in situ SPM. In this technique, the indenter tip oscillates with a small force to monitor the phase lag due to material response as a result of displacement. The advantage of this technique is in-situ SPM imaging enables the indenter tip to scan across the specimen to obtain a topographic image of the sample surface. This way modulus mapping allows performing dynamic indentation at each point of the surface. In this technique, a large number of indentation can be carried out within a very short period to obtain overall material characteristics like loss and storage modulus, loss and storage stiffness, tan delta maps, etc.

6.3.3. Load control

In this mode of operation, one can specify the force applied to the indenter as a function of time, the displacement is achieved with that applied force and the resultant load-displacement curve is used to determine the stiffness, elastic modulus, hardness and other mechanical properties. In a load control test, the load is increased at a particular rate. In load-controlled operation, force can be conveniently applied and removed. Load controlled nanoindentation operation is preferred for conducting experiments at a very low rate as for a given period, applied force can be kept constant. The force field condition can be represented more closely in this mode of operation.

6.3.4. Displacement control

In this mode of operation, displacement is applied in a particular uniform rate. At any moment of operation, displacement is known for a sample, so at that displacement magnitude of the required force is needed to draw the load-displacement curve. The load-displacement curve

can be easily analyzed that is obtained in this mode of operation as the curve beyond the maximum load can be observed only in a displacement-controlled indentation. This mode of operation is preferred when a given displacement needs to be achieved.

6.4. Examples of nanomechanical testing of cells

In this section, we are going to discuss some examples of measuring cellular nanomechanics using nanoindentation technique. For the very first time, mechanical properties of soft tissue using nanoindentation technique was measured by Ebenstein et al. in 2004 [45]. The purpose of the study was to develop a system to keep the sample hydrated, select an appropriate indenter for soft tissue like material indentation, determine an appropriate control material for the development of future indentation protocols and identify a substrate to be used for blunt tip alignment. They developed a hydration system to keep the sample hydrated for more than 8 hours without completely submerging the sample. To identify appropriate indenter for the hydrated, soft tissue, they performed indentation with different types of the indenter. Three sided sharp Berkovich indenter with an average radius of curvature of 100–200 nm and conosperical diamond indenters with radius of 10, 50, 100 and 800 microns radius of curvature. They found that conosperical tip with a 100-micron radius of curvature is most suitable for the indentation of the vascular tissue sample and agarose gel is most effective for the tip alignment. The used Oliver and Pharr method to calculate reduced elastic modulus and found that artery tissue has an elastic modulus of ≈0.73 MPa. In orthopedic research, cartilage repair is one of the main challenges. To address this challenge Ebenstein et al. studied the mechanical properties of cartilage repair tissue using nanoindentation experiments [46]. They reported that the mechanical properties of cartilage inferior tissue are lesser than the control cartilage tissue. In another study,

Ebenstein et al. used nanoindentation technique to study the mechanical properties of fibrous tissue, blood clots, partially calcified fibrous tissue, and bulk calcifications from human atherosclerotic plaque tissue [47]. The ultimate goal of that study was to investigate the mechanical changes in plaques tissues during atherosclerotic disease progression as clinical events such as stroke, and heart attack can be caused by the rupture of atherosclerotic plaques in blood vessel walls. They demonstrated that the stiffness of the plaque tissue increases with the increase of mineral content in the tissue.

In bone tissue engineering, the interaction between bone cells and engineered biomaterial is an important area to explore. We studied the nanomechanical properties of bone cells and bone cell-substrate construct using nanoindentation technique under physiological condition. Cells were seeded on tissue culture treated polystyrene (TCPS) [48]. Once cells are attached, cell seeded TCPS were placed in a fluid cell submerged under cell culture media and then nanoindentation experiment carried out placing the sample on the temperature-controlled stage of nanoindentation. In displacement control mode operation, cells demonstrated completely elastic load-deformation response and cell elastic modulus was found 1.3 to 12.4 MPa using Oliver and Pharr method. In another study, Khanna et al reported a novel in situ nanoindentation technique developed to evaluate the composite mechanical behavior of cell-biomaterial construct under physiological conditions over the time scale of bone nodule generation [49]. The schematic illustration of cell-substrate indentations on a single cell attached to Chi-PgA-HAP film deposited onto TCPS substrate is shown in figure 6.3. Nanomechanical properties of cells over the time of adhesion, proliferation, development and bone nodule formation were evaluated. The study implied that unique interactions between cells and nanocomposite films provided a favorable mechanical environment for the formation of bone nodules.

Table 6.1. Summary of the nanoindentation based nanomechanical experiments carried out to evaluate elastic modulus for different cells and tissues.

Cell/ Tissue	Indenter	Method	Elastic modulus	Reference
Mineralized matrix formed on glass coverslips by immortalized cell line Y201 from human mesenchymal stem cells	Berkovich	Oliver and Pharr	10-45 GPa	[53]
Calcospherulite crystals produced by rat osteoblasts	Berkovich	Oliver and Pharr	0.41 ± 0.15 GPa	[54]
Cartilage repair tissue	100 µm conosperical	Oliver and Pharr	Not reported	[46]
Porcine aorta tissue	100 µm conosperical	Oliver and Pharr	0.7– 0.8 MPa	[45]
Human carotid bifurcation plaque tissue	100 µm conosperical	Compliance method	.05-43.4 MPa	[47]
Osteoblast	Berkovich	Oliver and Pharr	1.1-12.0 MPa	[49]
Osteoblast	Berkovich	Oliver and Pharr	1.3-12.4 MPa	[48]
Nodule formed by mouse osteoblastic MC3T3-E1 cells	Berkovich	Oliver and Pharr	10 GPa	[50]
Embedded cross section of aorta and vena Cava tissue	10 µm conosperical	Oliver and Pharr	8-35 MPa	[51]
3T3 mouse embryonic fibroblast cells	Berkovich	Reported as continuous harmonic contact stiffness (HCS)		[52]

Miyamoto et al. performed in situ quasi-static and dynamic nanoindentation tests on calcified nodules formed by mouse osteoblasts to investigate the effects of glucocorticoid hormones such as dexamethasone and hydrocortisone on the nanomechanical properties [50]. The proliferation or calcium deposition of the cells were not affected by dexamethasone, but nodules formed in the presence of dexamethasone were significantly stiffer than the nodules

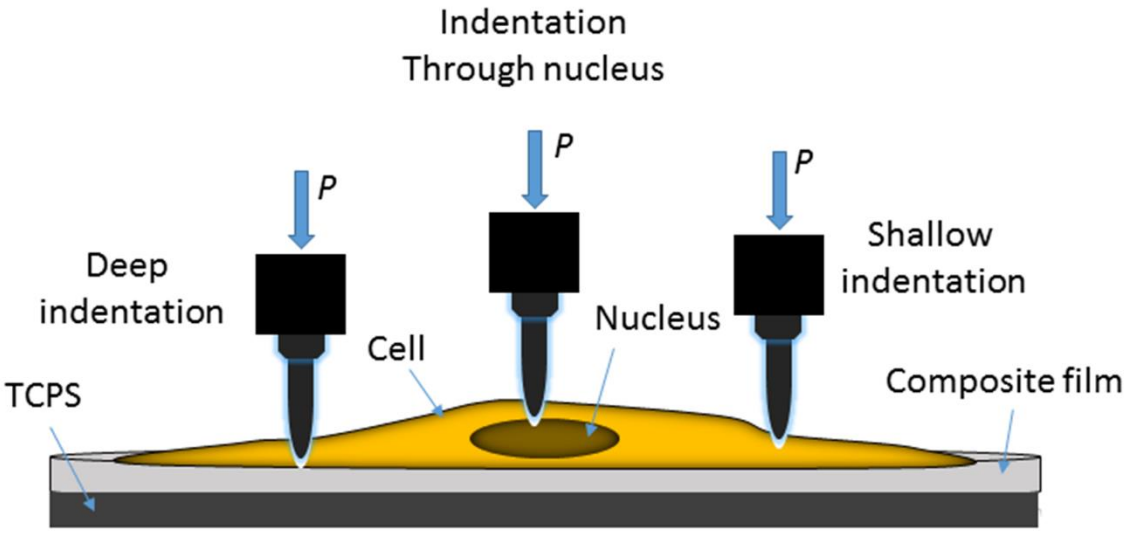

Figure 6.3. Schematic showing cell-substrate indentations on a single cell attached to Chi-PgA-HAP film deposited onto TCPS substrate and sectional view of an indenter.

formed in the absence of dexamethasone. Their result suggested that hormones like dexamethasone are essential for in vitro formation of mature calcified nodules by bone cells.

In an attempt to map the elastic properties of soft tissues, Akhtar et al. performed nanoindentation experiments to investigate the micromechanical properties of 5-mm-thick sections of ferret aorta and vena cava and to relate these mechanical properties to the histological distribution of fluorescent elastic fibers [51]. They reported the elastic modulus of the blood vessel tissues varies from 8 MPa to 35 MPa depending on a different layer of the tissue using extended Oliver and Pharr method and 10 μm conosperical indenter. They demonstrated that it is possible to distinguish the differences in the micromechanical properties of blood vessels, which are related to the tissue microstructure. Yang et al. performed continuous depth-sensing nanomechanical characterization of living, fixed and dehydrated cells attached on a glass substrate using a dynamic contact module [52]. The nanomechanical characteristics of the cells were reported as the continuous harmonic contact stiffness (HSC). In this study, they tried to

understand how the underlying substrate influences the interpretation of the nanomechanical property of thin soft matter on a hard substrate.

6.5. Current challenges in nanoindentation of live cells

Challenges of nanoindentation experiments on biological soft samples include problem associated with instrumentation, optimization of indenter geometry and load-displacement range, an appropriate model for analyzing experimental data, maintaining hydration state of the biological samples, etc. Commercially available instruments are usually designed for time independent materials, but the mechanical response of biological materials such as cells is mostly time-dependent. Due to the low elastic modulii of several biological samploes such as cells the evaluation of force displacement curves on soft samples is challenging. Indentation tip force is directly related to the tip geometry and material properties of the specimen. If a sharp indenter is used for indentation on soft tissues, the contact area and the corresponding force is very small for a shallow indentation. It makes it very complicated to determine when the indenter touches the sample which leads to a zero-point error [55]. Another nanoindentation instrumentation challenge for biological materials like cells or tissue is maintaining hydration state at the physiological condition. For this purpose, the Katti's research group has used cell culture media in a fluid cell on the temperature controlled stage, but it is a still a challenge to maintain physiological pH, as no CO_2 was supplied to the cell culture media [48, 49]. Using fluid to hydrate the sample and temperature-controlled stage might introduce further experimental complexities which have not been sufficiently addressed in the literature. Most popular indenter for nanoindentation experiments is three sided Berkovich tip. The Berkovich indenter has been used for soft tissues and glossy polymers [56-59]. Sharp indenters such as Berkovich can

introduce plastic deformation and stress concentration as well as damage the specimen. In an attempt to minimize this problem, blunt tips such as spherical, conosperical and cylindrical punch have been used [46, 47, 59-62]. The disadvantage of using flat tips is that it has a high-stress concentration at the contact perimeter. In addition to the indenter geometry, the size of the indenter needs to be considered as well. Indenters with small radius can provide nanomechanical properties of a single cell meanwhile indenter with a larger diameter will provide information on nanomechanical characteristics of the whole tissue including extracellular matrix.

Most of the commercially available nanoindentation instruments are designed with software to analyze experimental data using Oliver and Pharr method [42]. This approach works extremely well for the specimen with a time-independent mechanical response. But this method introduces significant errors to calculate elastic modulus for samples with a viscoelastic time-dependent response like soft tissues as the assumption of elastic unloading is invalidated by the continuing time-dependent deformation [63, 64]. Creep or sinking of tip under constant force into the specimen is the most common effect of viscoelasticity. For viscoelastic specimen, a 'nose' is observed on the unloading curve when there is no hold time which results in a negative slope at the beginning of the unloading curve and makes it very difficult to measure the elastic modulus [65]. Some correction has been proposed to minimize the creep effect in calculating elastic modulus of the viscoelastic materials [66-68]. Other than this, some other models have been developed to analyze the nanoindentation experimental data obtained from soft tissue like viscoelastic materials [56, 63, 69, 70].

Another problem associated with indenting soft tissue samples is the adhesion between the indenter and the sample [71, 72]. It has been reported that modulus calculation is significantly affected due to adhesion between the tip and the soft tissues [71, 72]. JKR [73]

model has been reported to be more accurate to minimize the contact effect between the soft samples and the indenters while measuring elastic modulus [71, 72, 74]. More complicated approaches have also been reported combining JKR model and viscoelastic analysis [74-76].

Overall, as instrumentation capabilities improve, including improved and reliable feedback mechanisms, the capability to conduct AFM force curve experiments and nanoindentation is likely to become routine and thus present itself as a new and novel mechanistic approach to understanding disease progression as well as diagnostics. Next generation medical treatments and research will see a large increase in evaluation of mechanics using these techniques. The critical advances will arise from making implicit connections between gene expression and other traditional biochemical assays evaluated for disease diagnostics and mechanisms and mechanics of the cell during the time evolution of the disease state.

6.6. Acknowledgements

The authors would like to acknowledge partial support from the NDSU Grand Challenge program for the Center for Engineered Cancer Test-Beds.

6.7. References

[1] B.J. Alberts, A. Lewis, J. Raff, Molecular biology of the cell, 35(1) (2008) 40-42.

[2] D. Boal, D.H. Boal, Mechanics of the Cell, Cambridge University Press, 2012.

[3] L.H. Miller, D.I. Baruch, K. Marsh, O.K. Doumbo, The pathogenic basis of malaria, Nature 415(6872) (2002) 673-9.

[4] F. Wang, H.Y. Yu, J.S. Li, X.W. Sun, X.C. Wang, H.Y. Zheng, Optical absorption enhancement in nanopore textured-silicon thin film for photovoltaic application, Optics Letters 35(1) (2010) 40-42.

[5] G. Bao, S. Suresh, Cell and molecular mechanics of biological materials, Nature Materials 2(11) (2003) 715-725.

[6] R. Suwanarusk, B.M. Cooke, A.M. Dondorp, K. Silamut, J. Sattabongkot, N.J. White, R. Udomsangpetch, The deformability of red blood cells parasitized by Plasmodium falciparum and P. vivax, J Infect Dis 189(2) (2004) 190-4.

[7] A.J. Engler, H.L. Sweeney, D.E. Discher, J.E. Schwarzbauer, Extracellular matrix elasticity directs stem cell differentiation, J Musculoskelet Neuronal Interact 7(4) (2007) 335.

[8] M.M. Yallapu, K.S. Katti, D.R. Katti, S.R. Mishra, S. Khan, M. Jaggi, S.C. Chauhan, The roles of cellular nanomechanics in cancer, Medicinal research reviews 35(1) (2015) 198-223.

[9] R.R. Chaturvedi, T. Herron, R. Simmons, D. Shore, P. Kumar, B. Sethia, F. Chua, E. Vassiliadis, J.C. Kentish, Passive stiffness of myocardium from congenital heart disease and implications for diastole, Circulation 121(8) (2010) 979-88.

[10] P.C. Georges, J.J. Hui, Z. Gombos, M.E. McCormick, A.Y. Wang, M. Uemura, R. Mick, P.A. Janmey, E.E. Furth, R.G. Wells, Increased stiffness of the rat liver precedes matrix deposition: implications for fibrosis, Am J Physiol Gastrointest Liver Physiol 293(6) (2007) G1147-54.

[11] R.G. Wells, The role of matrix stiffness in regulating cell behavior, Hepatology 47(4) (2008) 1394-400.

[12] H.M. Wyss, J.M. Henderson, F.J. Byfield, L.A. Bruggeman, Y. Ding, C. Huang, J.H. Suh, T. Franke, E. Mele, M.R. Pollak, J.H. Miner, P.A. Janmey, D.A. Weitz, R.T. Miller, Biophysical

properties of normal and diseased renal glomeruli, Am J Physiol Cell Physiol 300(3) (2011) C397-405.

[13] Y.-B. Lu, K. Franze, G. Seifert, C. Steinhäuser, F. Kirchhoff, H. Wolburg, J. Guck, P. Janmey, E.-Q. Wei, J. Käs, Viscoelastic properties of individual glial cells and neurons in the CNS, Proceedings of the National Academy of Sciences 103(47) (2006) 17759-17764.

[14] P.C. Georges, W.J. Miller, D.F. Meaney, E.S. Sawyer, P.A. Janmey, Matrices with compliance comparable to that of brain tissue select neuronal over glial growth in mixed cortical cultures, Biophys J 90(8) (2006) 3012-8.

[15] I. Levental, P.C. Georges, P.A. Janmey, Soft biological materials and their impact on cell function, Soft Matter 3(3) (2007) 299-306.

[16] S. Kumar, V.M. Weaver, Mechanics, malignancy, and metastasis: the force journey of a tumor cell, Cancer Metastasis Rev 28(1-2) (2009) 113-27.

[17] R.K. Assoian, E.A. Klein, Growth control by intracellular tension and extracellular stiffness, Trends in cell biology 18(7) (2008) 347-352.

[18] E.A. Klein, L. Yin, D. Kothapalli, P. Castagnino, F.J. Byfield, T. Xu, I. Levental, E. Hawthorne, P.A. Janmey, R.K. Assoian, Cell-cycle control by physiological matrix elasticity and in vivo tissue stiffening, Current biology 19(18) (2009) 1511-1518.

[19] K.R. Levental, H. Yu, L. Kass, J.N. Lakins, M. Egeblad, J.T. Erler, S.F.T. Fong, K. Csiszar, A. Giaccia, W. Weninger, Matrix crosslinking forces tumor progression by enhancing integrin signaling, Cell 139(5) (2009) 891-906.

[20] N. Bolgen, I. Vargel, P. Korkusuz, Y.Z. Menceloglu, E. Piskin, In vivo performance of antibiotic embedded electrospun PCL membranes for prevention of abdominal adhesions, Journal of Biomedical Materials Research Part B-Applied Biomaterials 81B(2) (2007) 530-543.

[21] E.L. Baker, R.T. Bonnecaze, M.H. Zaman, Extracellular matrix stiffness and architecture govern intracellular rheology in cancer, Biophysical journal 97(4) (2009) 1013-1021.

[22] M.J. Paszek, N. Zahir, K.R. Johnson, J.N. Lakins, G.I. Rozenberg, A. Gefen, C.A. Reinhart-King, S.S. Margulies, M. Dembo, D. Boettiger, Tensional homeostasis and the malignant phenotype, Cancer cell 8(3) (2005) 241-254.

[23] L. De Stefano, I. Rea, E. De Tommasi, I. Rendina, L. Rotiroti, M. Giocondo, S. Longobardi, A. Armenante, P. Giardina, Bioactive modification of silicon surface using self-assembled hydrophobins from Pleurotus ostreatus, European Physical Journal E 30(2) (2009) 181-185.

[24] A.J. Engler, C. Carag-Krieger, C.P. Johnson, M. Raab, H.Y. Tang, D.W. Speicher, J.W. Sanger, J.M. Sanger, D.E. Discher, Embryonic cardiomyocytes beat best on a matrix with heart-like elasticity: scar-like rigidity inhibits beating, J Cell Sci 121(Pt 22) (2008) 3794-802.

[25] M. Cecelja, P. Chowienczyk, Dissociation of aortic pulse wave velocity with risk factors for cardiovascular disease other than hypertension: a systematic review, Hypertension 54(6) (2009) 1328-36.

[26] G.F. Mitchell, S.-J. Hwang, R.S. Vasan, M.G. Larson, M.J. Pencina, N.M. Hamburg, J.A. Vita, D. Levy, E.J. Benjamin, Arterial stiffness and cardiovascular events, Circulation 121(4) (2010) 505-511.

[27] S.S. DeLoach, R.R. Townsend, Vascular stiffness: its measurement and significance for epidemiologic and outcome studies, Clinical Journal of the American Society of Nephrology 3(1) (2008) 184-192.

[28] V.D. Uzunova, C. Cullinane, K. Brix, W.M. Nau, A.I. Day, Txicity of Cucurbit[7]uril and Cucurbit[8]uril: An exploratory in vitro and in vivo study, Org. Biomol. Chem. 8 (2010) 2037-2042.

[29] Z. Li, J.A. Dranoff, E.P. Chan, M. Uemura, J. Sévigny, R.G. Wells, Transforming growth factor-β and substrate stiffness regulate portal fibroblast activation in culture, Hepatology 46(4) (2007) 1246-1256.

[30] R. Tandon, I. Levental, C. Huang, F.J. Byfield, J. Ziembicki, J.R. Schelling, L.A. Bruggeman, J.R. Sedor, P.A. Janmey, R.T. Miller, HIV infection changes glomerular podocyte cytoskeletal composition and results in distinct cellular mechanical properties, American Journal of Physiology-Renal Physiology 292(2) (2007) F701-F710.

[31] A.J. Bailey, L. Knott, Molecular changes in bone collagen in osteoporosis and osteoarthritis in the elderly, Experimental Gerontology 34(3) (1999) 337-351.

[32] J. Chen, T. Gupta, J.A. Barasz, Z. Kalajzic, W.C. Yeh, H. Drissi, A.R. Hand, S. Wadhwa, Analysis of microarchitectural changes in a mouse temporomandibular joint osteoarthritis model, Archives of Oral Biology 54(12) (2009) 1091-1098.

[33] S. Abdulghani, J. Caetano-Lopes, H. Canhão, J.E. Fonseca, Biomechanical effects of inflammatory diseases on bone-rheumatoid arthritis as a paradigm, Autoimmunity Reviews 8(8) (2009) 668-671.

[34] D. Guo, W. Tan, F. Wang, Z. Lv, J. Hu, T. Lv, Q. Chen, X. Gu, B. Wan, Z. Zhang, Proteomic analysis of human articular cartilage: Identification of differentially expressed proteins in knee osteoarthritis, Joint Bone Spine 75(4) (2008) 439-444.

[35] E. Karouzakis, M. Neidhart, R.E. Gay, S. Gay, Molecular and cellular basis of rheumatoid joint destruction, Immunology Letters 106(1) (2006) 8-13.

[36] H. Hertz, Miscellaneous papers, Macmillan1896.

[37] A.E.H. Love, Boussinesq's problem for a rigid cone, The Quarterly Journal of Mathematics 10 (1939) 161-175.

[38] U. Lange, E. Neumann, Bone and inflammation - molecular mechanisms, new pathophysiological relevant metabolic pathways and future innovative therapies, Osteologie 18(1) (2009) 41-44.

[39] S.I. Bulychev, V.P. Alekhin, M.K. Shorshorov, A.P. Ternovskij, G.D. Shnyrev, Determination of Young modulus by the hardness indentation diagram, Zavodskaya Laboratoriya 41(9) (1975) 1137-1140.

[40] G.M. Pharr, W.C. Oliver, F.R. Brotzen, On the generality of the relationship among contact stiffness, contact area, and elastic modulus during indentation, Journal of materials research 7(03) (1992) 613-617.

[41] I.G. Otterness, E. Weiner, A.C. Swindell, R.O. Zimmerer, M. Ionescu, A.R. Poole, An analysis of 14 molecular markers for monitoring osteoarthritis. Relationship of the markers to clinical end-points, Osteoarthritis and Cartilage 9(3) (2001) 224-231.

[42] P. Granitzer, K. Rumpf, A.G. Roca, M.P. Morales, P. Poelt, M. Albu, Investigation of a Mesoporous Silicon Based Ferromagnetic Nanocomposite, Nanoscale Research Letters 5(2) (2010) 374-378.

[43] G.M. Odegard, T.S. Gates, H.M. Herring, Characterization of viscoelastic properties of polymeric materials through nanoindentation, Experimental Mechanics 45(2) (2005) 130-136.

[44] P. Kannu, J.F. Bateman, S. Randle, S. Cowie, D. du Sart, S. McGrath, M. Edwards, R. Savarirayan, Premature Arthritis Is a Distinct Type II Collagen Phenotype, Arthritis and Rheumatism 62(5) (2010) 1421-1430.

[45] J.M. Hootman, C.G. Helmick, Projections of US prevalence of arthritis and associated activity limitations, Arthritis & Rheumatism 54(1) (2006) 226-229.

[46] A.A. Cole, K.E. Kuettner, Molecular basis for differences between human joints, Cellular and Molecular Life Sciences 59(1) (2002) 19-26-26.

[47] J.R. Kirwan, A.J. Silman, Epidemiological, sociological and environmental aspects of rheumatoid arthritis and osteoarthrosis, Baillière's Clinical Rheumatology 1(3) (1987) 467-489.

[48] M.P. Ginebra, M. Espanol, E.B. Montufar, R.A. Perez, G. Mestres, New processing approaches in calcium phosphate cements and their applications in regenerative medicine, Acta Biomaterialia 6(8) (2010) 2863-2873.

[49] A. Kerin, P. Patwari, K. Kuettner, A. Cole, A. Grodzinsky, Molecular basis of osteoarthritis: biomechanical aspects, Cellular and Molecular Life Sciences 59(1) (2002) 27-35-35.

[50] T. Tanaka, L.S. Mangala, P.E. Vivas-Mejia, R. Nieves-Alicea, A.P. Mann, E. Mora, H.D. Han, M.M.K. Shahzad, X.W. Liu, R. Bhavane, J.H. Gu, J.R. Fakhoury, C. Chiappini, C.H. Lu, K. Matsuo, B. Godin, R.L. Stone, A.M. Nick, G. Lopez-Berestein, A.K. Sood, M. Ferrari, Sustained Small Interfering RNA Delivery by Mesoporous Silicon Particles, Cancer Research 70(9) (2010) 3687-3696.

[51] E. Tasciotti, X.W. Liu, R. Bhavane, K. Plant, A.D. Leonard, B.K. Price, M.M.C. Cheng, P. Decuzzi, J.M. Tour, F. Robertson, M. Ferrari, Mesoporous silicon particles as a multistage delivery system for imaging and therapeutic applications, Nature Nanotechnology 3(3) (2008) 151-157.

[52] X.Y. Tao, L.X. Dong, X.N. Wang, W.K. Zhang, B.J. Nelson, X.D. Li, B4C-Nanowires/Carbon-Microfiber Hybrid Structures and Composites from Cotton T-shirts, Advanced Materials 22(18) (2010) 2055-+.

[53] X. Wang, X. Li, R.A. Bank, C.M. Agrawal, Effects of collagen unwinding and cleavage on the mechanical integrity of the collagen network in bone, Calcified Tissue International 71(2) (2002) 186-192.

[54] R.C. Lawrence, D.T. Felson, C.G. Helmick, L.M. Arnold, H. Choi, R.A. Deyo, S. Gabriel, R. Hirsch, M.C. Hochberg, G.G. Hunder, J.M. Jordan, J.N. Katz, H.M. Kremers, F. Wolfe, Estimates of the prevalence of arthritis and other rheumatic conditions in the United States: Part II, Arthritis & Rheumatism 58(1) (2008) 26-35.

[55] E. Hedbom, H.J. Häuselmann, Molecular aspects of pathogenesis in osteoarthritis: the role of inflammation, Cellular and Molecular Life Sciences 59(1) (2002) 45-53-53.

[56] M. Davis, W. Ettinger, J. Neuhaus, S. Cho, W. Hauck, The association of knee injury and obesity with unilateral and bilateral osteoarthritis of the knee., Am J Epidemiol 130(2) (1989) 278-88.

[57] A. Gelber, M. Hochberg, L. Mead, N. Wang, F. Wigley, M. Klag, Joint injury in young adults and risk for subsequent knee and hip osteoarthritis., Ann Intern Med 133(5) (2000) 321-8.

[58] D. Felson, R. Lawrence, P. Dieppe, R. Hirsch, C. Helmick, J. Jordan, R. Kington, N. Lane, M. Nevitt, Y. Zhang, M. Sowers, T. McAlindon, T. Spector, A. Poole, S. Yanovski, G. Ateshian, L. Sharma, J. Buckwalter, K. Brandt, J. Fries, Osteoarthritis: new insights. Part 1: the disease and its risk factors., Ann Intern Med 133(8) (2000) 635-46.

[59] W. Newberry, J. Garcia, C. Mackenzie, C. Decamp, R. Haut, Analysis of acute mechanical insult in an animal model of post-traumatic osteoarthrosis., J Biomech Eng 120(6) (1998) 704-9.

[60] J. Samuels, S. Krasnokutsky, S. Abramson, Osteoarthritis: a tale of three tissues., Bull NYU Hosp Jt Dis 66(3) (2008) 244-50.

[61] W.J. Horton, P. Bennion, L. Yang, Cellular, molecular, and matrix changes in cartilage during aging and osteoarthritis., J Musculoskelet Neuronal Interact 6(4) (2006) 379-81.

[62] C. Petibois, G. Gouspillou, K. Wehbe, J. Delage, G. Déléris, Analysis of type I and IV collagens by FT-IR spectroscopy and imaging for a molecular investigation of skeletal muscle connective tissue., Anal Bioanal Chem 386(7-8) (2006) 1961-6.

[63] L. Zhang, A. Aksan, Fourier transform infrared analysis of the thermal modification of human cornea tissue during conductive keratoplasty., Appl Spectrosc 64(1) (2010) 23-9.

[64] J. Wang, W. Zhou, W. Hu, L. Zhou, S. Wang, S. Zhang, Collagen/silk fibroin bi-template-induced biomimetic bone-like substitutes., J Biomed Mater Res A (2009).

[65] F. Bonnier, S. Rubin, L. Debelle, L. Ventéo, M. Pluot, B. Baehrel, M. Manfait, G. Sockalingum, FTIR protein secondary structure analysis of human ascending aortic tissues., J Biophotonics 1(3) (2008) 204-14.

[66] B. Tang, A.H.W. Ngan, Accurate measurement of tip–sample contact size during nanoindentation of viscoelastic materials, Journal of Materials Research 18(05) (2003) 1141-1148.

[67] W. Hübner, A. Blume, R. Pushnjakova, Y. Dekhtyar, H. Hein, The influence of X-ray radiation on the mineral/organic matrix interaction of bone tissue: an FT-IR microscopic investigation., Int J Artif Organs 28(1) (2005) 66-73.

[68] J. Brauner, C. Flach, R. Mendelsohn, A quantitative reconstruction of the amide I contour in the IR spectra of globular proteins: from structure to spectrum., J Am Chem Soc 127(1) (2005) 100-9.

[69] G. RAMACHANDRAN, G. AMBADY, Oriented crystallization of inorganic salts in collagen., Experientia 11(9) (1955) 343-4.

[70] J. Bella, M. Eaton, B. Brodsky, H. Berman, Crystal and molecular structure of a collagen-like peptide at 1.9 A resolution., Science 266(5182) (1994) 75-81.

[71] G. Ramachandran, G. Kartha, Structure of collagen., Nature 176(4482) (1955) 593-5.

[72] J. Mansell, J. Tarlton, A. Bailey, Biochemical evidence for altered subchondral bone collagen metabolism in osteoarthritis of the hip., Br J Rheumatol 36(1) (1997) 16-9.

[73] M. Seibel, A. Duncan, S. Robins, Urinary hydroxy-pyridinium crosslinks provide indices of cartilage and bone involvement in arthritic diseases., J Rheumatol 16(7) (1989) 964-70.

[74] S. Lee, S. Lin, R. Liang, Secondary conformational structure of type IV collagen in different conditions determined by Fourier-transform infrared microscopic spectroscopy., Artif Cells Blood Substit Immobil Biotechnol 23(2) (1995) 193-205.

[75] M. Attur, M. Dave, K. Tsunoyama, M. Akamatsu, M. Kobori, J. Miki, S. Abramson, M. Katoh, A. Amin, "A system biology" approach to bioinformatics and functional genomics in complex human diseases: arthritis., Curr Issues Mol Biol 4(4) (2002) 129-46.

[76] A. Stewart, A. Black, S. Robins, D. Reid, Bone density and bone turnover in patients with osteoarthritis and osteoporosis., J Rheumatol 26(3) (1999) 622-6.

CHAPTER 7. MECHANOBIOLOGICAL EVALUATION OF PROGRESSION OF PROSTATE CANCER METASTASIS TO BONE IN AN IN VITRO PROSTATE CANCER TEST BED[6]

This chapter presents the evaluation of nanomechanical properties prostate cancer cells using nanoindentation experiment and establishing a correlation between changes in nanomechanical properties and alteration in cytoskeletal orientation. The content of this chapter is submitted for publication and is currently under review. The submitted article is coauthored by MD. S. Molla; D. R. Katti; and K.S. Katti.

7.1. Introduction

Prostate cancer exhibits a propensity to metastasize to bone often leading to morbidity in patients. Bone metastasis is characterized by complex biochemical, morphological, pathophysiological, and genetic changes to cancer cells as they colonize at remote bone sites. These changes can be captured in sum by changes to nanomechanical properties of cancer cells during metastasis. In this study, we report changes to nanomechanical properties of prostate cancer cells during mesenchymal to epithelial transition (MET) and during the progression of the disease at the metastatic site. A nanoindenter has been used to assess the elastic modulus of living cells. Bone-mimetic tissue engineered 3D nanoclay scaffolds have been used to create an in vitro metastatic site for prostate cancer cells. Immunocytochemistry and qRT-PCR experiments illustrate the correlation between cytoskeletal vicissitudes and nanomechanical

[6]This chapter was co-authored by MD. S. Molla, Kalpana Katti, and Dinesh Katti. MD. S. Molla had primary responsibility for preparing samples, conducting all tests, and drafting this chapter. Kalpana Katti and Dinesh Katti directed the research orientation and revised this chapter.

changes of prostate cancer cells. We observed significant softening of prostate cancer cells during MET and then further softening during the disease progression at the metastatic site. We found a significant reduction in elastic modulus of prostate cancer cells during MET arising from actin reorganization and depolymerization. This is the first study that reveals changes to nanomechanical characteristics of prostate cancer cells with correlation to cytoskeletal changes during MET and progression of the disease at the bone metastatic site.

The investigation of the relationship between mechanical properties of cells and tissues and the state of disease condition has been a topic of immense scientific engagement in recent years due to the advances in imaging techniques, and novel experimental capabilities [1-3]. In recent years, considerable interest has grown to investigate the mechanisms relating the nanomechanical properties of cells to a state of the disease since it has been shown that abnormalities in the biophysical characteristics of cells are associated with disease pathogenesis and progression [4-7]. In this aspect cancer is a paradigmatic case [8]. Stiffness of cells measured using AFM has been established as a potential biomarker for the disease progression [9, 10]. Yet studies of nanomechanical behavior of cancer cells at the secondary metastatic site are lacking. Also not well understood is the association of nanomechanical changes during the metastatic cascade with the structural changes inside cells. Many studies have demonstrated that nanomechanical characteristics or deformability of individual cells play a significant role in cell growth, motility, and cancer metastasis [4]. Several studies have shown that cancer cells possess different nanomechanical properties, such as elastic modulus and stiffness, as compared to their normal counterparts [11-15]. Biophysical studies have shown that the metastatic potential is correlated with the stiffness of cancer cells [9, 13, 16, 17]. An AFM based study reported that Young's modulus of cancer cells is reduced during malignant progression [17] while another

reported increase in Young's modulus of cancer cells during invasion into collagen matrices [18]. Considering all these observations, it appears that the nanomechanical properties of cancer cells vary during different stages of the metastatic cascade depending on the biomolecular and biochemical restructure. Unrevealing the changes in biophysical properties of cancer cells during the disease progression could be very crucial in understanding the mechanism of metastasis and ultimately lead to its prevention.

A wide variety of experimental techniques have been used to evaluate the mechanical properties of cells at different scale level [19]. However, the design and development of techniques to characterize the nanomechanical properties of live cells are still under active investigation. Among these techniques, use of nanoindentation instruments involves the application of a controlled load/displacement to penetrate an indenter into the surface of a cell and use the recorded load-displacement curve to measure the stiffness, elastic modulus, and, various other nanomechanical characteristics of the cells. A nanoindenter instrumented with AFM apparatus allows better control of the indentation load and displacement [20]. A cell consists of dynamically deformable rheology that is highly complex due to the heterogeneous local structure. A nanoindenter with an in situ AFM allows to characterize the localized microstructure of a cell and provide a fingerprint of the heterogeneous cellular structure. Different theoretical models have been applied to describe the Young's modulus of load-displacement (L-D) curves obtained from cellular indentation [21]. In the last few years, many advances have been made to raise the accuracy and flexibility in evaluating Young's modulus of living cells [22]. In these studies, various L-D curve fitting models, indenter geometries, displacements, substrate stiffnesses have been used [21, 23]. Despite using different methodologies, significant amount of works revealed consistency in the difference of Young's

modulus between healthy and cancerous cells as healthy cells exhibit larger resistance to deformation which results in a larger force [4, 12, 24, 25]. These studies motivated our current research to investigate the changes to the elastic modulus of cells during cancer progression.

Cancer metastasis is a variegated process requiring dramatic remodeling of the cell cytoskeleton, an interconnected network of filamentous polymers and regulatory proteins [26]. The nanomechanical properties of human cells are predominantly directed by their cytoskeleton [27]. Recent works have shown that during cancer metastasis, physical forces act through the cytoskeleton to affect local mechanical properties of cancer cells [28]. Two very significant events occur during cancer metastasis, one is epithelial to mesenchymal transition (EMT) at the primary tumor site when epithelial cancer cells gain mesenchymal phenotype to invade surrounding tissues and another at the secondary metastatic tumor site when the reverse of EMT process happens which is known as mesenchymal to epithelial transition (MET) [29]. The metastatic cascade of prostate cancer cells is depicted in the schematic diagram of figure 1a. Continuous remodeling and reorganizing of the cytoskeletal structure from thin cortical bundles in epithelial cells to thick, parallel, contractile bundles in mesenchymal cells are accompanied by progressive changes in cellular morphology during these two events [30]. However, how the mechanical properties of cancer cells change and its cause-effect relationship with cytoskeletal changes during these two events, remain unknown.

Prostate cancer is rarely life-threatening when localized and detected at primary site with a 5-year survival rate of about 99%, but the prognosis deteriorates dramatically to about 29% for a 5-year survival rate when detected under metastatic conditions [31, 32]. This alarming statistic is often the result of metastasis of prostate cancer cells to bone. Currently, treatment for preexisting bone metastatic prostate cancer is only palliative. Hence, translational models that

mimic skeletal metastasis of prostate cancer are very critical for investigation of the late stage of the disease [33]. The time and expense of animal models and the fact that metastasis to bone is preceded by death in most animal models as well as limited availability of human prostate cancer samples necessitate the use of humanoid in vitro models. 3D in vitro tumor models recently become enticing to a greater extent for investigating cancer metastasis [34, 35].

A biomimetic 3D in vitro tumor model designed and developed in our previous studies to mimic the bone metastasis of prostate cancer cells [36-38], is used to obtain prostate cancer tumor samples. Bone tissue engineering scaffolds using nanoclays are used to develop remodeling bone structures [39-41] in vitro that are known to be the niche to which prostate cancer cells migrate to. The polymer-clay nanocomposite was designed using a simulation guided methodology called 'altered phase theory'[42] that elucidates how properties of clay nanocomposites can be tailored with use of appropriate clay modifications. Vesicular delivery of calcium minerals to the extracellular matrix, widely regarded as the mechanism of biomineralization in skeletal tissues [43, 44], was observed to occur on the tissue-engineered bone [45] indicating that the in vitro bone mimics the biological mineralization processes. In addition this tissue-engineered bone exhibits the lower Ca\P stoichiometry of mineral characteristic of remodeling bone[45] the niche to which prostate cancer cells are known to migrate to. Further, the sequential culture of prostate cancer cells on the tissue-engineered bone led to the development of large tumoroids of prostate cancer which were observed to be in the MET stage of metastasis on analysis of gene expressions characteristic of MET [36, 38]. In this study, we sought to probe the nanomechanical changes of prostate cancer cells and tumoroids during the progression of the disease at the metastatic site. An in situ displacement-controlled nanoindentation technique (using Hysitron Triboscope) was used to perform nanomechanical

characterization of living cells. A sample stage with culture media and temperature control for indenting live cells was developed earlier [46, 47]. The L-D curves were analyzed to measure elastic modulus, the maximum force required for a specific displacement and the residual indentation depth at different stages of the disease. In addition, we have also investigated the relationship between the cell stiffness and the cytoskeletal changes of prostate cancer cells at the bone metastatic site. We observed a significant reduction in stiffness of prostate cancer cells during MET which is attributed to the reorganization and depolymerization of actin filaments during the progression of the disease. We also have observed a steady decrease of cell stiffness during the progression of the disease at the metastatic site. This is the first study that reveals changes to nanomechanical properties of prostate cancer cells at the metastatic bone site during MET and progression of cancer.

7.2. Materials and methods

7.2.1. Preparation of 3D porous scaffolds

Osteoinductive 3D porous scaffolds for bone tissue engineering was prepared using modified NaMMT clay, hydroxyapatite (HAP), and polycaprolactone (PCL). NaMMT clay was purchased from Clay Minerals Respiratory at the University of Missouri, Columbia and then modified with 5-aminovaleric acid as described in prior studies [48]. In situ HAP was biomineralized on intercalated nanoclay (modified clay) to achieve osteoconductivity following the protocol described in our previous studies [39]. Finally, 3D porous scaffolds were prepared by adding 10 wt% PCL polymer into the in situ HAPClay using the freeze-drying method as illustrated in our previous study [39]. Before using the scaffolds for tissue culture, they were cylindrically shaped into 12 mm diamter and 3 mm thckness.

7.2.2. Cell lines and culture reagents

Human prostate cancer cell line MDA PCa 2b was purchased from American Type Culture Collection (VA, USA) and maintained in the media consisting of 80% BRFF-HPC1 (AthenaES, 0403) and 20% fetal bovine serum (ATCC, 30–2020). Human bone marrow-derived mesenchymal stem cells (MSCs) were purchased from Lonza, Walkersville (PT-2501), and maintained in MSCGM™ Bulletkit™ medium (Lonza, Walkersville, PT-3001). The Bulletkit™ medium was prepared by adding MSCGM™ SingleQuots™ (Lonza, Walkersville, PT-4105) to MSCBM™ (Lonza, Walkersville, PT-3238). All the cells were maintained at 37 °C and 5% CO_2 in a completely humidified incubator. Also, cell culture media was changed in evry alternative days.

7.2.3. 3D sequential culture to mimic MET

Mesenchymal to epithelial transition (MET) of PCa cells (cell line MDA PCa 2b) were recapitulated using bone tissue-engineered PCL/HAPclay 3D scaffolds following the protocol described in our previous studies [38]. Initially, the cylindrical-shaped 3D scaffold with12 mm diameter and 3 mm thickness were sterilized and placed in 24-well plates for cell seeding. MSCs were seeded on each scaffold at a density of 5×10^4 and cultured for 23 days to allow bone tissue formation. MSCs were maintained in MSCGM™ Bulletkit™ medium, and fresh media was added every other day. After 23 days, MDA PCa 2b cells were added into the newly formed bone tissue containing scaffolds at a density of 5×10^4 per scaffolds. For the sequential culture, MSCs and PCa media was used in a ratio of 1:1. The detailed schematic diagram of the sequential culture technique is illustrated in figure 7.1b. Also, cell culture media was changed in evry alternative days.

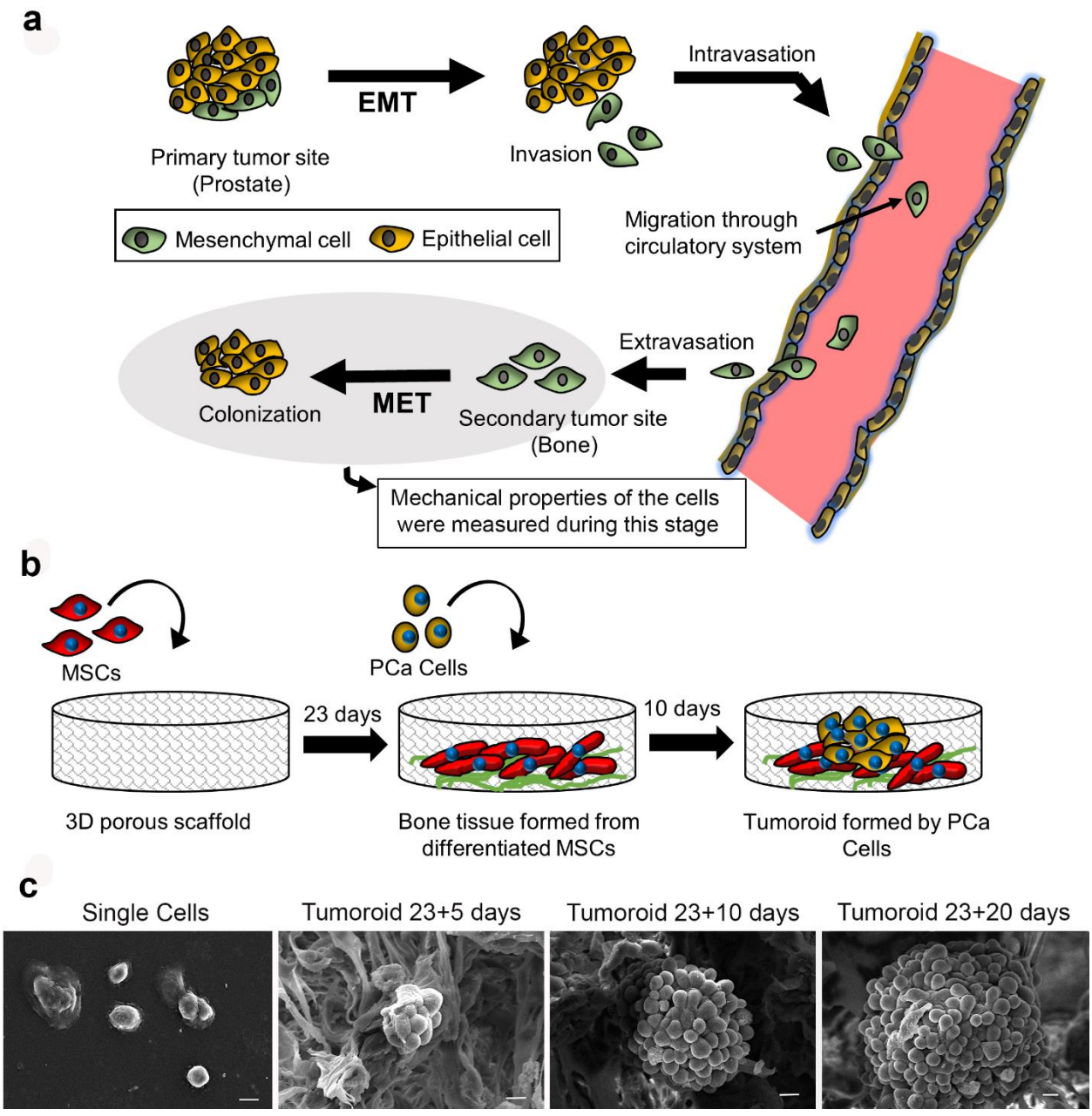

Figure 7.1. Tumoroid formation in the sequential culture. Prostate cancer cells (PCa) cells form multicellular tumoroids when sequentially cultured with mesenchymal stem cells (MSCs) mimicking the last stage of prostate cancer bone metastasis. (a) Schematic diagram showing the multistep process of prostate cancer metastasis to bone. It includes the sequence of phases: local invasion, intravasation, circulation, extravasation, and colonization. (b) Schematic diagram showing the sequential culture of PCa cells with MSCs. MSCs were cultured in osteoinductive 3D scaffolds for 23 days. After 23 days when bone tissue is formed by MSCs, PCa cells were seeded where they formed multicellular tumoroids. (c) SEM micrographs showing PCa single cells and tumoroids formed by PCa cells at day 23+5, 23+10, and day 23+20 (day 23+X means MSCs cultured for 23 days to form bone tissue and then PCa cells cultured on bone tissue for X days). The length of the micron bar is 10 μm.

7.2.4. Nanoindentation experiment

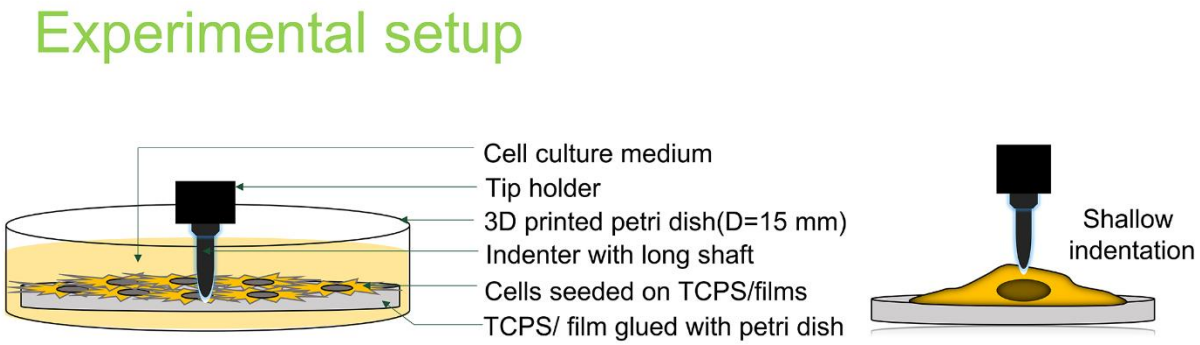

Figure 7.2. Experimental set up of nanoindentation experiment on living cells.

For nanomechanical characterization of PCa cells, a Hysitron Triboscope nanomechanical instrument (Minneapolis, MN) equipped with multimode AFM (Nanoscope IIIa controller and J-type piezo scanner system) (Veeco Metrology, Santa Barbara, CA). For testing in a fluid environment, a special fluid cell was designed, consisting of a steel disk glued onto a steel disc glued on the bottom of a custom-made 3D printed petri dish. A piece of tissue culture polystyrene (TCPS) was fixed with the steel disk. Then the petri dish was filled with culture media (BRFF-hPC1+2%FBS) and PCa cells were seeded onto TCPS for nanoindentation. Tumoroids from the 3D scaffolds were extracted using TrypLE Reagents (Thermofisher Scientific, 12605036) and then seeded into 3D printed Petri dishes for nanoindentation. A Berkovich diamond indenter fluid tip (three-sided pyramidal; 100–200 nm tip radius) with long shaft was used that allowed liquid levels to be maintained well above the sample surface and also ensured the instrument calibration in the liquid. The petri dish containing cell-seeded TCPS samples were placed onto the nanoindentation stage, and the whole assembly is heated and maintained at 37 °C. Schematic description of the indenter-sample assembly is shown in figure 7.2. The stage temperature was maintained using a MultiMode^{TM} low-temperature heater from Veeco Metrology (Santa Barbara, CA) was used. All the indentation experiments were

completed within two hours. Displacement controlled nanoindentation tests on PCa cells were performed at maximum displacements of 500 nm and 1000 nm at a loading and unloading rate of 10 nm/s. Methodologies described in our previous study were followed to identify cellular response and differentiate between cellular and substrate nanomechanical response [46, 47]. In this current study, only cellular indentation response is presented.

7.2.5. Analysis of nanomechanical response

Oliver & Pharr method was used to calculate contact stiffness by applying a power–law fit to the initial unloading portion of the load-displacement (L-D) curve and analytically differentiating the power–law relation [49]. HYSITRON analysis software was used to obtain the reduced modulus from the stiffness and contact area measurements. Elastic moduli of the PCa cells were calculated from the reduced modulus using the following equation:

$$\frac{1}{Er} = \frac{(1 - v_s^2)}{E_s} + \frac{(1 - v_i^2)}{E_i}$$

Where Er =reduced elastic modulus, E_s=elastic modulus of the sample, E_i=elastic modulus of indenter which is =1141 GPa for diamond, v_s= Poisson's ratio of the sample which is considered as 0.5 v_i= Poisson's ratio of the indenter which is = 0.07 for diamond. For all types of cell samples, at least 22 indentation is reported in this study. To ensure repeatability and reproducibility, all the experiments were repeated on at least triplicate samples. To ensure repeatability and reproducibility, all the experiments were repeated on at least triplicate samples. Distribution of elatic modulus is presented as box plots in this study where median value, 25^{th} percentile and 75^{th} percentile are indicated. Statistical analyses were performed on all the elastic modulus data obtained from PCa single cells and tumoroid cells indentation experiments.

7.2.6. Scanning electron microscopy

Scanning electron microscopy was performed to determine the morphology of the PCa tumoroids formed in bone tissue engineered scaffolds. A JEOL JSM 6490LV scanning electron microscope was used. The tissue-cultured scaffold samples were removed from the culture condition and washed with PBS. The tissue-cultured scaffold samples were then fixed with 2.5% glutaraldehyde followed by ethanol series treatment (10%, 30%, 50%, 70%, and100% v/v) for dehydration. The samples were dried using hexamethyldisilazane after alcohol treatment. The samples were then gold-coated and mounted on SEM stubs for observation using the scanning electron microscope. Samples were collected for scanning electron microscopy in predetermined specific days.

7.2.7. Immunocytochemistry, phalloidin staining and analysis

Immunocytochemical analysis was performed for F-Actin Tubulin and Nuclei of the PCA single cells and Tumoroid cells formed in MSCs+PCa SC (Sequential culture of MSCs with prostate cancer cells). Tumoroid cells were analyzed at day 23+5, 23+10 and 23+20. PCa single cells and Tumoroid samples were fixed with 4% paraformaldehyde (PFA) for 30 minutes and then washed three times with fresh 1X PBS (Each wash for five minutes). Samples were treated with 0.5% Triton X-100 in PBS for 5 minutes to permeabilize cells followed by 45 minutes blocking with 1% fish skin gelatin (FSG). For alpha-tubulin staining, samples were incubated overnight with Anti α-Tubulin antibody (Abcam, ab18251) at 4°C (1:150 dilution of anti-alpha-tubulin with 1% FSG in PBS). Further, samples were washed with fresh PBS three times and then incubated with Goat Anti-Rabbit IgG H&L Alexa Fluor® 488 for an hour at room temperature. For staining F-actin, Rhodamine-Phalloidin (ThermoFisher Scientific, R415) was used to stain F-actin following manufacturer's protocol. For staining the nuclei, samples were

treated with 4',6-diamidino-2-phenylindole (DAPI) for 5 minutes. Zeiss Axio Observer Z1 was used for inverted confocal microscopy. Z-stacked images obtained from Zeiss Axio Observer Z1 was deconvoluted using the software Autoquant X3. Deconvoluted Z-stacked images were used for 3D surface reconstruction. Imaris software developed by Bitplane was used for surface reconstruction of F-actin, α-tubulin and nuclei surfaces. Volumes of F-actin, α-tubulin and nuclei were calculated in Imaris using developer's protocol. The size of individual cells were measured using the Z-stack images of single and tumoroid cells.

7.2.8. qRT-PCR experiment and gene expression analysis

For the qRT-PCR experiment, mRNAs were extracted from the PCa single cells and tumoroids using TRI reagent (Sigma) and purified using Direct-zol™ RNA MiniPrep (Zymo Research). For tumoroid samples, RNAs were collected from the sequential culture at day 23+5, 23+10, and 23+20. Then, cDNA was reverse transcribed from the Total RNA collected from the cells using random primers and M-MLV reverse transcriptase (Promega). A 7500 Fast Real-Time PCR system (Applied Biosystems, USA) and SYBR Green Master MIX (ThermoFisher Scientific) were used for template amplification with a primer for each of the transcripts by following manufacturer's protocol. The samples were incubated for 2 minutes at 50 °C, and PCR was performed at 95 °C for 10 minutes followed by 40 cycles of 15 seconds denaturation at 95 °C, 30 seconds annealing at primer specific temperature and elongation at 60 °C for 1 minute. Gene expression of GAPDH, N-WASp, Arp2/3, Thymosin β4, CDC42, and Cortactin was evaluated for PCa single cells and tumoroids and each characterization assessed in triplicate. GAPDH served as the house-keeping gene, and PCa single cell culture served as control. Target gene expressions were calculated as $2^{-\Delta\Delta Ct}$. Primer sequences were obtained from the primer bank. The primer sequences used in this experiment are listed in the table 7.1.

7.2.9. Statistical analysis

Statistical analysis was performed using Student's t-test to compare two conditions. Differences were considered significant at *P<0.05, **P<0.005, and ***P<.001. For the distribution of Elastic modulus, E; maximum force, maxF; and residual indentation depth, h_f; Tukey's box-and-whiskers plots were used indicating median value, 25^{th} percentile, and 75^{th} percentile. All experiments were done with minimum 3 biological replicates. The column bar data is represented as a mean ± standard deviation.

7.3. Results

7.3.1. Sequentially cultured (with MSCs) PCa cells form multicellular tumoroids

A unique tissue engineered bone microenvironment was created as a secondary metastatic site for human prostate cancer (PCa) cells using the sequential culture (SC) technique that has been described in our previous study [36, 38]. Human prostate cancer (PCa) cell line MDA PCa 2b was sequentially cultured with human mesenchymal stem cells (MSCs). A schematic diagram of the sequential culture is shown in the figure 7.1b. Initially, human mesenchymal stem cells (MSCs) were seeded on osteoinductive porous 3D scaffolds and cultured for 23 days to generate mineralized bone tissue. After 23 days, human prostate cancer (PCa) cells were seeded on the mineralized bone tissue. As observed earlier[38], at the bone tissue engineered microenvironment, the PCa cells had undergone mesenchymal to epithelial transition (MET) and formed multicellular tumoroids to mimic the last stage of prostate cancer bone metastasis. The morphology of the tumoroids is probed using scanning electron microscopy (SEM). The SEM micrographs of the tumoroids are sh own in the figure 7.11c. Figure 7.6a also

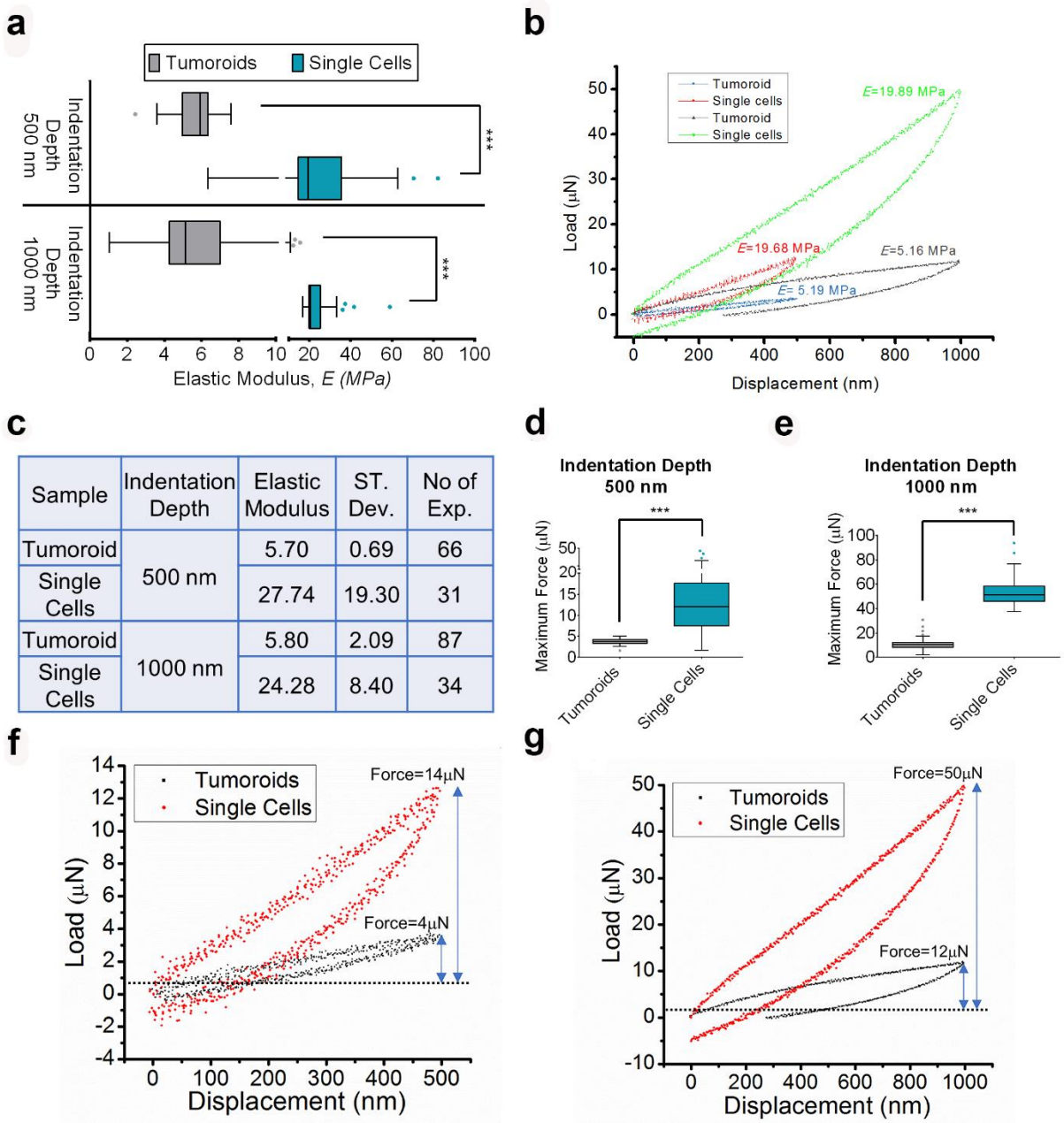

Sample	Indentation Depth	Elastic Modulus	ST. Dev.	No of Exp.
Tumoroid	500 nm	5.70	0.69	66
Single Cells		27.74	19.30	31
Tumoroid	1000 nm	5.80	2.09	87
Single Cells		24.28	8.40	34

Figure 7.3. PCa cells become softer when they undergo MET and form tumoroids at the bone microenvironment. (a) The distribution of elastic modulus, at the maximum indentation depths 500 nm and 1000 nm shown by Tukey's Boxplot. (b) Representative load-displacement (L-D) curves of PCa single cells and tumoroid cells at the maximum indentation depth 500 nm and 1000 nm. (c) The table shows the mean value of the elastic modulus, E of PCa single cells and tumoroid cells at the maximum indentation depths 500 nm and 1000 nm. (d) The distribution of the maximum force required (maxF) to indent 500 nm for PCa single cells and tumoroid cells shown by Tukey's Boxplot. (e) The distribution of the maximum force required (maxF) to indent 1000 nm for PCa single cells and tumoroid cells shown by Tukey's Boxplot. (f) Representative L-D curves indicate maxF for PCa single cells and Tumoroids at maximum indentation depth 500 nm. (g) Representative L-D curves indicate maxF for PCa single cells and Tumoroids at maximum indentation depth 1000 nm.

shows the immunostained confocal micrographs of the tumoroids. These SEM and confocal micrographs show that in the tumoroids, the PCa cells are organized in a grape-like morphology with tight cellular junctions, distinguishable cellular boundaries, and hypoxic core regions. On the other hand, PCa cells before seeding to the bone tissue scaffolds (figure 1B, 5A), are mostly unattached without cellular junctions and hypoxic regions. In this study, we termed these PCa cells (those are not seeded to the tissue engineered scaffolds) as 'single cells.'

7.3.2. PCa cells soften as they undergo MET and form tumoroids

To assess how the nanomechanical properties of prostate cancer cells alter during mesenchymal to epithelial transition (MET), we performed displacement-controlled nanoindentation experiments at maximum indentation depths 500nm and 1000 nm using a nanoindenter instrumented with AFM apparatus (Hysitron Triboindenter). The box plot in Figure 7.3a shows the distribution of elastic modulus, E of prostate cancer (PCa) cells before (single cells) and after (tumoroid cells) undergoing MET at maximum indentation depths of 500 nm and 1000 nm. The box plot indicates the median values, 25^{th} percentile, and 75^{th} percentile of elastic modulus E. The outliers are indicated by whiskers. Figure 7.3a evidently indicates that the elastic modulus, E of tumoroid cells is significantly lower than the elastic modulus of single cells. It also indicates that elastic moduli are independent of indentation depth. At both 500 nm (P-value=1.04E-14) and 1000 nm (P-value=1.32E-36) indentation depths, the tumoroid cells exhibit significantly lower elastic moduli as compared to single cells. In the case of both tumoroid cells and single cells, there are no significant differences observed between elastic modulus values at indentation depth 500nm and 1000 nm. The representative load-displacement (L-D) curves for tumoroid cells and single cells at the indentation depth 500 nm and 1000 nm are shown in figure 7.3b, and the respective elastic moduli, or E values are indicated in the figure. The table in the

figure 7.3c shows the mean elastic modulus for each type of cells at indentation depths of 500 nm and 1000 nm. At 500 nm indentation depth, the elastic modulus of tumoroid cells is 5.7 MPa (Standard Deviation 0.69) which is ~4.8 times lower than the elastic modulus of single cells (E=27.74, Standard Deviation= 19.3). At 1000 nm indentation depth, the elastic modulus of tumoroid cells is 5.8 MPa (Standard Deviation 2.09) which is ~4.1 times lower than the elastic modulus of single cells (E=24.28 MPa, Standard Deviation= 8.4). Though there is statistical difference between the mean E values for the single cells at 500 nm and 1000 nm indentation depths due to large standard deviation I both cases, the median E values are fairly close. The median E values for the single cells at 500 nm and 1000 nm indentation depth are 19.43 MPa and 20.52 MPa respectively. We further analyzed the maximum force required in each indent for each type of cells at the indentation depths 500nm and 1000 nm. We were motivated by the fact that stiffer cells exhibit larger resistance to deformation which results in a larger force. The distribution of the maximum force required for indenting tumoroid and single cells at the indentation depth 500 nm is shown in the figure 7.3d and at the indentation depth 1000 nm in the figure 7.3e. At the indentation depth 500 nm (figure 7.3d), the median maximum forces required for tumoroid cells and single cells are 3.78 μN and 12.06 μN respectively. At the indentation depth 1000 nm (figure 7.3e), the median maximum forces required for tumoroid cells and single cells are 10.48 μN and 51.26 μN respectively. For both indentation depths 500 nm (P-Value=8.13E-13) and 1000 nm (P-Value=7E-42), the maximum force required to indent tumoroid cells is significantly lower than for the single cells. In the figure 7.3f and figure 7.3g, the representative L-D curves indicating maximum force needed are shown for tumoroid cells and single cells at the indentation depths 500 nm and 1000 nm respectively. It is also evident that the L-D curves for single cells are much steeper than the tumoroid cells. All the data in figure 7.3

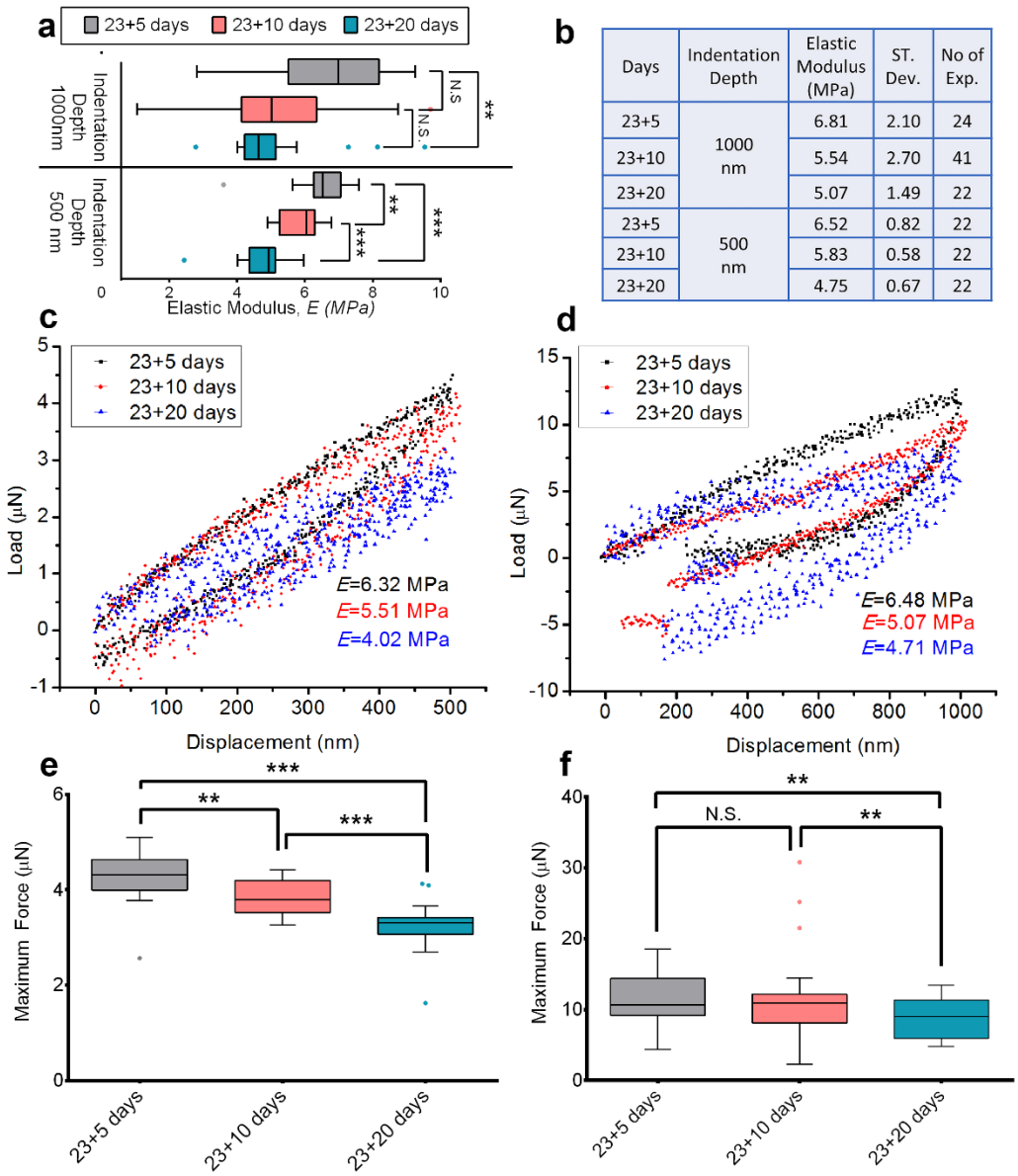

b

Days	Indentation Depth	Elastic Modulus (MPa)	ST. Dev.	No of Exp.
23+5	1000 nm	6.81	2.10	24
23+10		5.54	2.70	41
23+20		5.07	1.49	22
23+5	500 nm	6.52	0.82	22
23+10		5.83	0.58	22
23+20		4.75	0.67	22

Figure 7.4. Tumoroid cells become softer with the cancer progression at the metastatic bone site. (a) The distribution of elastic modulus, E of PCa cells in the tumoroids. (b) The table shows the mean value of the elastic modulus, E of PCa cells in the tumoroids at the maximum indentation depths 500 nm and 1000 nm on day 23+5, day 23+10 and day 23+20. (c) Representative L-D curves obtained from indenting PCa cells in the tumoroids at maximum indentation depth 500 nm. (d) Representative L-D curves obtained from indenting PCa cells in the Tumoroids at maximum indentation depth 1000 nm. (e) The distribution of the maximum force required (maxF) to indent 500 nm for PCa cells in the tumoroids on day 23+5, day 23+10 and day 23+20 shown by Tukey's Boxplot. The median, 25th percentile and 75th percentile are indicated. Error bars indicate 5th and 95th percentiles. Whiskers indicate outliers. ***$p < 0.001$, **$p < 0.005$. (f) The distribution of the maximum force required (maxF) to indent 1000 nm for PCa cells in the tumoroids on day 23+5, day 23+10 and day 23+20 shown by Tukey's Boxplot. The median, 25th percentile and 75th percentile are indicated. Error bars indicate 5th and 95th percentiles. Whiskers indicate outliers. **$p < 0.005$.

indicates that the stiffness of prostate cancer cells downturns significantly after mesenchymal to epithelial transition (MET) and tumoroid formation.

7.3.3. Tumoroids soften with the cancer progression

To probe how the nanomechanical characteristics of prostate cancer (PCa) tumoroid cells alter during the progression of the disease, we performed nanoindentation experiments at day 5, 10 and 20 after seeding the cancer cells on bone tissue-engineered scaffolds. PCa cells were seeded on the scaffolds after 23 days of initial MSCs seeding, and the progression of the disease is indicated as day 23+5, 23+10 and 23+20 throughout this article. The distribution of elastic modulus, E for tumoroid cells at day 23+5, 23+10, and 23+20 for two different indentation depths 500 nm and 1000 nm is shown in figure 7.4a by the box plot. At the indentation depth 1000 nm, the differences between E_{23+5} and E_{23+10}, as well as E_{23+10} and E_{23+20} are not statistically significant (E_{23+X}= Elastic modulus of tumoroid cells at day 23+X). But E_{23+20} is significantly lower than the E_{23+5} (P-value=0.00342). At the indentation depth 500 nm, E_{23+10} is significantly lower than E_{23+5} (P-value=0.0031), and E_{23+20} is significantly lower than E_{23+10} (P-value=1.39E-06). The table in figure 7.4b indicates that at the indentation depth of 1000 nm, the elastic modulus of tumoroid cells decreased by ~25.55% from day 23+5 to day 23+20. At the indentation depth 500 nm, the elastic modulus of tumoroid cells decreased by ~10.58% from day 23+5 to day 23+10, by ~18.52% from day 23+10 to day 23+20, and by ~27.15% from day 23+5 to day 23+20. In the figure 7.4c and figure 7.4d, the representative L-D curves indicating respective elastic modulus, E for tumoroid cells during the progression of the disease are shown at the indentation depths 500 nm and 1000 nm respectively. It appears that the slopes of the L-D curves reduce during the disease progression from day 23+5 to day 23+20. Additionally, we analyzed the maximum force required in each indent for the tumoroid cells during the

progression of the disease at the indentation depths 500nm and 1000 nm. The distribution of the maximum force (maxF) needed for each indent at the indentation depth 500 nm and 1000 nm are shown in the figure 7.4e and figure 7.4f respectively. At the indentation depth 1000 nm, the differences between $maxF_{23+5}$ and $maxF_{23+10}$, as well as $maxF_{23+10}$ and $maxF_{23+20}$ are not statistically significant ($maxF_{23+X}$= maximum force required to indent tumoroid cells at day 23+X). But $maxF_{23+20}$ is significantly lower than the $maxF_{23+5}$ (P-value=0.007). At the indentation depth 500 nm, $maxF_{23+10}$ is significantly lower than $maxF_{23+5}$ (P-value=0.0024), and $maxF_{23+20}$ is significantly lower than E_{23+10} (P-value=5.69E-05). Here is apparent from the figure 7.4 that there is a progressive reduction in the stiffness of prostate cancer cells at the bone-metastatic site with progression of the disease.

7.3.4. Mechanical plasticity of tumoroid cells increases with the disease progression

The load-displacement curves obtained from indentation experiments suggest that there is incomplete shape recovery by cancer cells after each indentation. This incomplete shape recovery of cancer cell structure during indentation experiment can occur due to plastic deformation of cellular components [50]. To assess how the plastic deformation of cancer cells alters during the disease progression at the metastatic site, we analyzed the residual indentation depth (unrecovered displacement) from the L-D curves for the single cells and tumoroid cells at day 23+5, day 23+10, and day 23+20. The distributions of residual indentation depth, h_f for the single cells and tumoroid cells at day 23+5, day 23+10, and day 23+20 are shown in the figure 7.5a for the indentation depth 1000 nm and in the figure 7.5b for the indentation depth 500 nm by the box plots. At the indentation depth 1000 nm (figure 7.5a), $h_{f(23+5)}$ is significantly higher than $h_{f(single)}$ (P-Value=0.00037; $h_{f(23+X)}$ is the residual indentation depth for tumoroid cells at

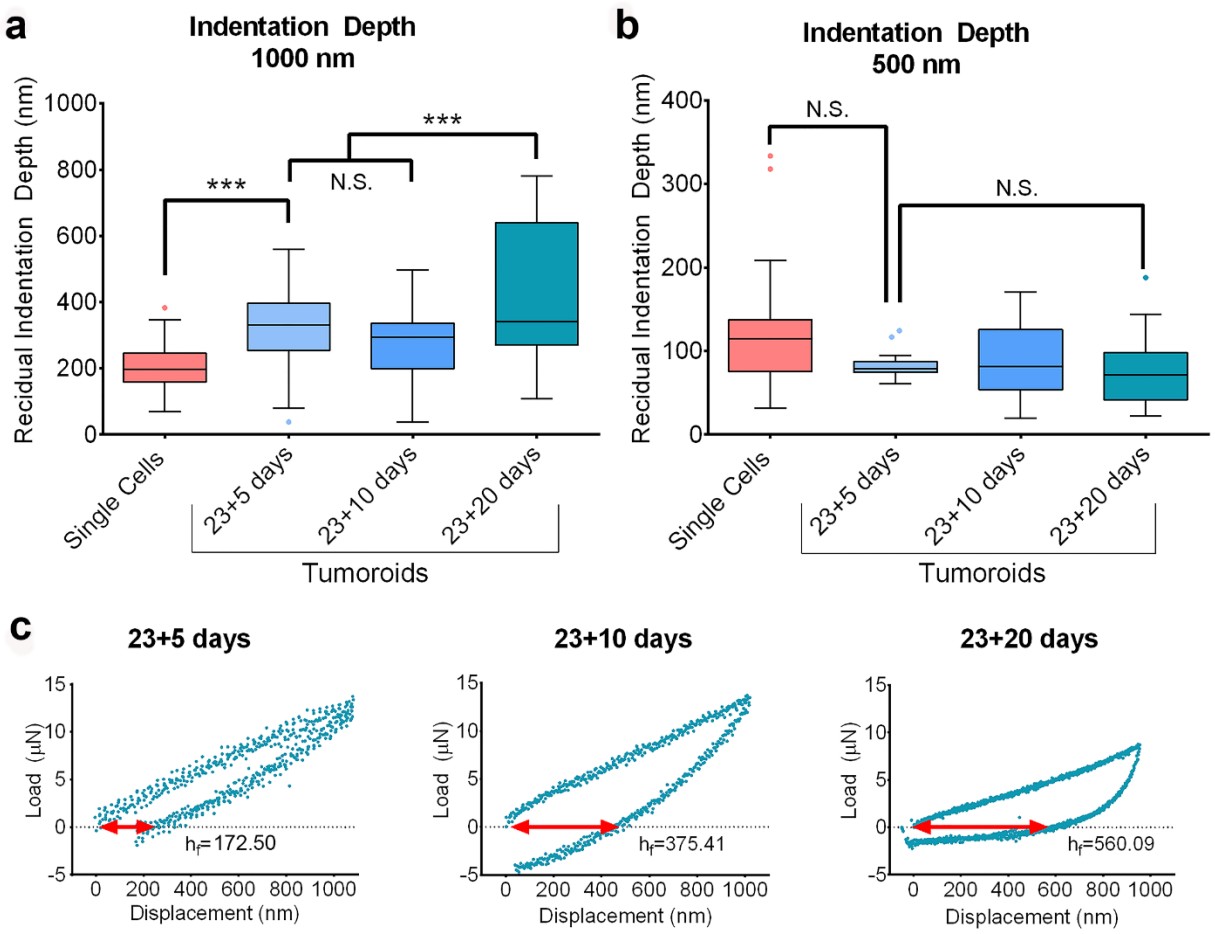

Figure 7.5. Mechanical plasticity of the PCa cells increases with disease progression at the metastatic site. (a) The distribution of the residual indentation depth (unrecovered deformation) for the maximum indentation depth 1000 nm obtained from indenting PCa single cells and PCa cells in the tumoroids on day 23+5, day 23+10 and day 23+20 shown by Tukey's Boxplot. The median, 25th percentile and 75th percentile are indicated. Error bars indicate 5th and 95th percentiles. Whiskers indicate outliers. ***$p < 0.001$. (b) The distribution of the residual indentation depth (unrecovered deformation) for the maximum indentation depth 500 nm obtained from indenting PCa single cells and PCa cells in the tumoroids on day 23+5, day 23+10 and day 23+20 shown by Tukey's Boxplot. The median, 25th percentile and 75th percentile are indicated. Error bars indicate 5th and 95th percentiles. (c) Representative L-D curves obtained from indenting PCa cells in the tumoroids at maximum indentation depth 1000 nm on day 23+5, day 23+10 and day 23+20 indicating respective residual indentation depth, hf.

day 23+X, and $h_{f(single)}$ is the residual indentation depth for single cells). The difference between $hf_{(23+5)}$ and $hf_{(23+10)}$ is not statistically significant. But $h_{f(23+20)}$ is significantly higher than the $h_{f(23+5)}$ and $h_{f(23+10)}$ (P-value=0.029 and 0.00087 respectively). At the indentation depth of 500 nm (figure 7.5b), the difference between h_f values are not significant possibly due to the shallow

indentation. In figure 7.5c the representative L-D curves (indicated by red arrows) show gradual increase of residual indentation depth for tumoroid cells from day 23+5 to day 23+20. All the data from figure 7.5 patently suggest that the mechanical plasticity of tumoroid cells increases with the disease progression at the bone-metastatic site.

7.3.5. Softening of PCa cells is mediated by actin

The cytoskeleton of a cell, an interconnected network of filamentous polymers and regulatory proteins such as actin and tubulin, is the structural framework that principally shapes a cell and provides mechanical integrity. The alteration in the cytoskeletal organization of prostate cancer (PCa) cells during MET and then during the disease progression at the bone-metastatic site was detected by immunofluorescence confocal microscopy to determine its relationship with alteration in nanomechanical properties. The PCa single cells and tumoroid cells were immunostained for F-actin (red stained) and α-tubulin (green stained), and the representative micrographs are shown in the figure 7.6a (additional micrographs are provided in figure 7.7). From the immunocytochemical analysis, we observed that the density of F-actin is significantly lower in tumoroid cells as compared to single cells, but regardless of cell type, there is no significant difference in the density of α -tubulin. To further confirm the observation that the amount of F-actin is reduced but there were no significant changes of α-tubulin in the tumoroid cells after undergoing MET, we calculated the total volume of F-actin and α -tubulin per cell in the single cell and tumoroid samples (The calculation method is described in the materials and method section). Figure 7.6b indicates that the volume of F-actin per cell is significantly reduced in the tumoroid cells as compared to single cells (P-value=0.00054). As figure 7.6c suggests,

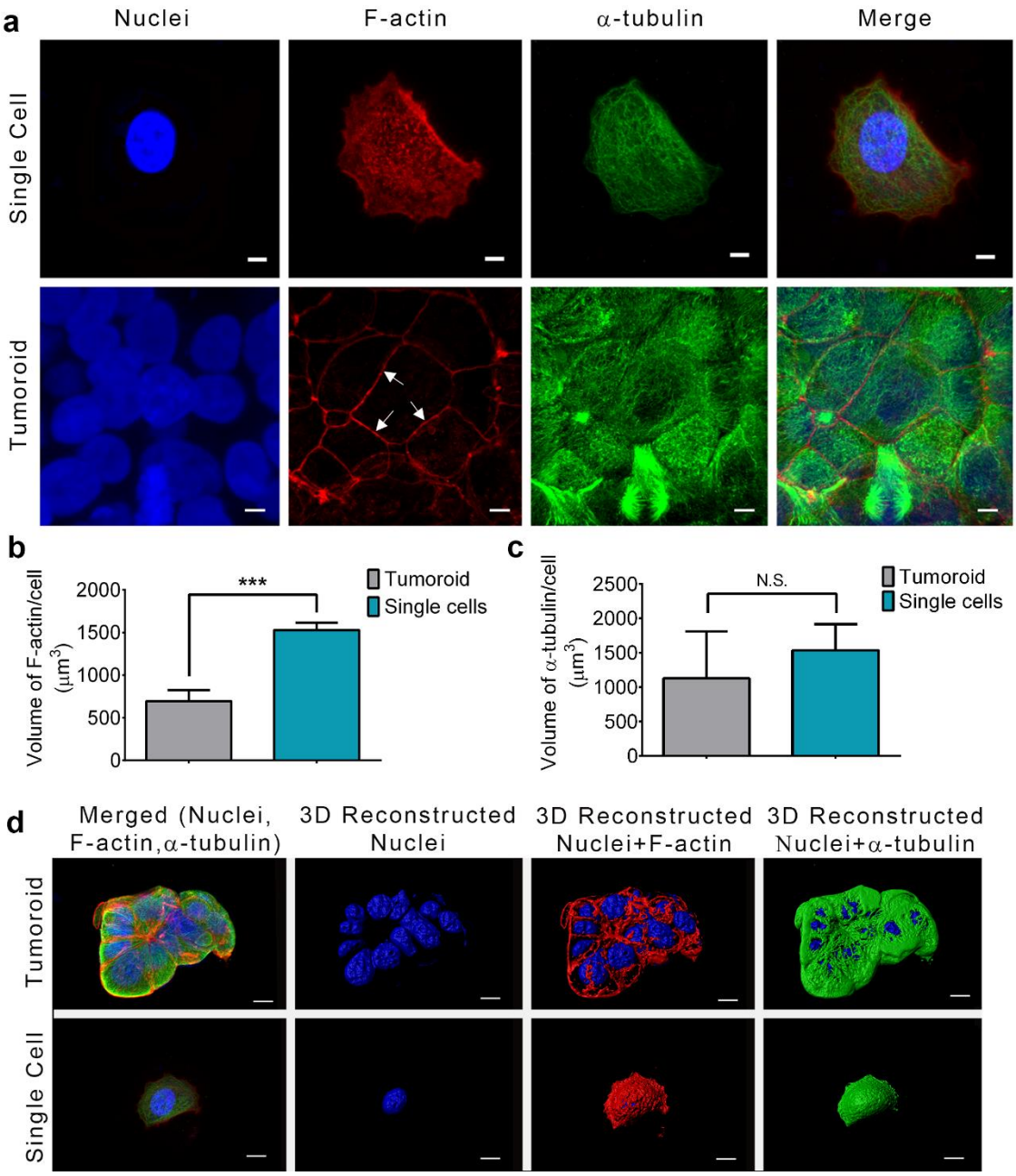

Figure 7.6. Softening of PCa cells with disease progression is mediated by F-actin. (a) Immunostained confocal micrographs of PCa single cell and PCa cell in the tumoroid stained with Phalloidin (F-actin, red), Anti-α-tubulin (α-tubulin, green), and DAPI (Nucleus, blue). Arrows indicate localization of F-actin at the cellular junctions in the tumoroid. The length of the micron bar is 5 μm. (b) The volume of F-actin/cell in the PCa single cells and tumoroids. Data presented as mean±standard deviation. ***$p < 0.001$. (c) The volume of α-tubulin/cell in the PCa single cells and tumoroids. Data presented as mean±standard deviation. (d) 3D reconstructed immunostained confocal micrographs of PCa single cell and PCa cell in the tumoroid stained with Phalloidin (F-actin, red), Anti-α-tubulin (α-tubulin, green), and DAPI (Nucleus, blue). Arrows indicate localization of F-actin at the cellular junctions in the tumoroid. The length of the micron bar is 5 μm.

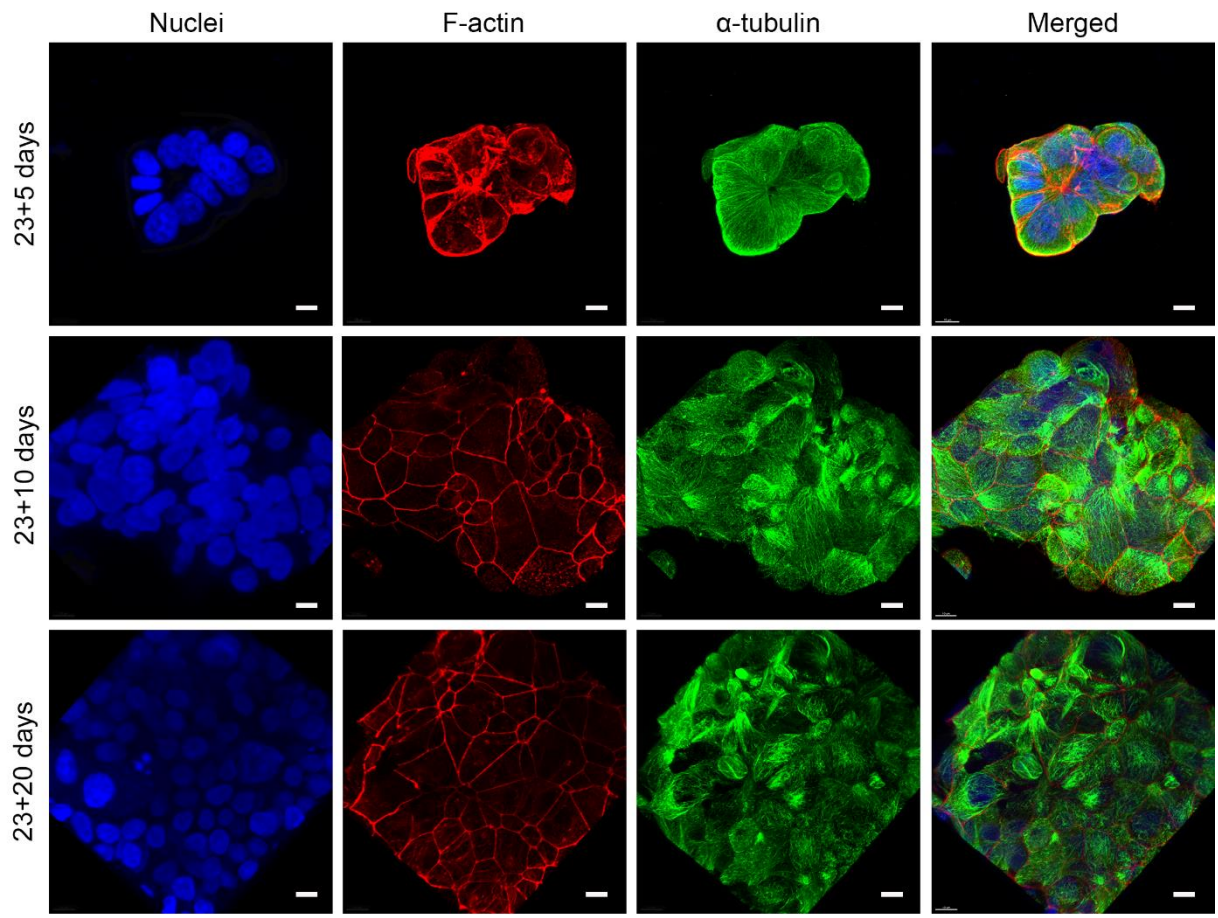

Figure 7.7. Immunostained confocal micrographs of PCa cell in the tumoroids stained with Phalloidin (F-actin, red), Anti-α-tubulin (α-tubulin, green), and DAPI (Nucleus, blue). The length of the micron bar is 10 μm.

there were no significant changes in the amount of α -tubulin after MET in the tumoroid cells (statistically nonsignificant). From the micrographs (figure 7.6a) we can there were no significant changes in the amount of α -tubulin after MET in the tumoroid cells (statistically nonsignificant). From the micrographs (figure 7.6a) we can observe that green stained α -tubulin exhibit well defined fibrous structure arising from the perinuclear region. α -tubulins are randomly spread to the cytoplasm, and there are no significant differences in their distribution between the single cells and the tumoroid cells. In both single and tumoroid cells, F-actin fibers are not well defined and exhibit a diffuse distribution in the cytoplasm. F-actin molecules are

distributed throughout the cell body of the single cells. But in tumoroid cells, F-actin is predominantly concentrated at the cell-junctions. In order to obtain better insight of the cytoskeletal structure in the cancer cells, we reconstructed the 3D structure of F-actin, α -tubulin and nucleus of the cells from the immunostained confocal micrographs using the software IMARIS (Detail of the reconstruction method is described in the materials and method section). Representative 3D reconstructed images are shown in figure 7.6d (additional photos are shown in figure 7.8) These images clearly reveal the significant presence of F-actin on the apical region of the single cells but localization of F-actin mostly at the cellular junctions in the tumoroid cells.

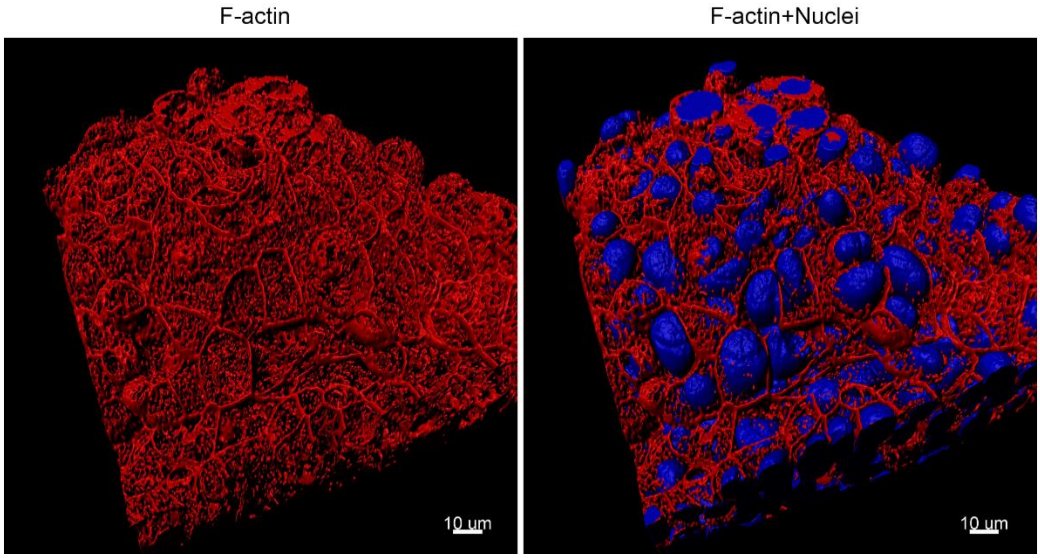

Figure 7.8. Surface reconstructed images of F-actin and Nuclei in a tumoroid showing localization of F-actin in the cell-cell junction region.

7.3.6. Actin-associated genes downregulate with the cancer progression

From the immunocytochemical analysis, we found that actin is predominantly associated with regulating nanomechanical properties of cancer cells. So to further investigate the role of actin, we evaluated the expression of genes related to actin dynamics using qRT-PCR experiment. The schematic diagram in the figure 7.9a describes the role of different molecules associated with actin.

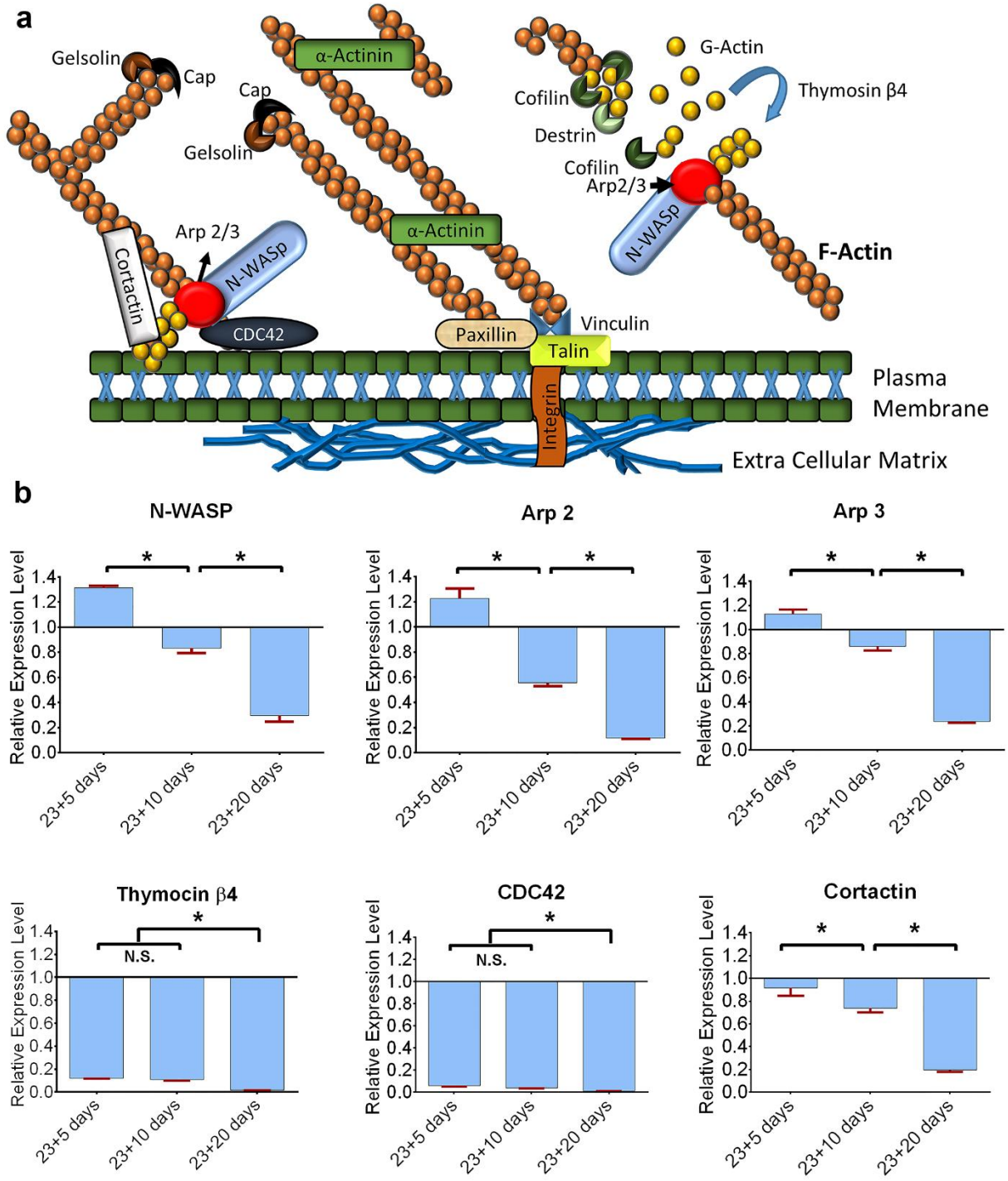

Figure 7.9. Actin regulatory genes downregulate with the cancer progression at the metastatic site. (a) The schematic diagram shows the role of different proteins in actin dynamics. (b) Relative gene expression levels of N-WASp, Arp2/3, thymosin β4, CDC42, and cortactin for PCa tumoroid cells on day 23+5, day 23+10 and day 23+20. Expression levels are normalized to GAPDH, and PCa single cells served as a control. Results are shown as a mean ± standard deviation. *$p < 0.05$.

We evaluated the expression of N-WASp, Arp2, Arp 3, thymosin β4, CDC42 and cortactin in mRNA level. Figure 7.9b shows the expression of these genes in the tumoroid cells at day 23+5, day 23+10, and day 23+20 where PCa single cells (PCa cells before undergoing MET) served as control and GAPDH was used as a housekeeping gene. There were no significant changes of N-WASp in the tumoroid cells at day 23+5 and day 23+10, but N-WASp downregulated ~3 fold at day 23+20 as compared to PCa single cells. Arp 2 downregulated ~2 fold at day 23+10 and ~8.5 fold at day 23+20 in the tumoroid cells as compared to PCa single cells. There were no significant changes of Arp 3 expression in the tumoroid cells at day 23+5 and day 23+10, but Arp 3 downregulated ~4 fold at day 23+20 as compared to PCa single cells. Thymosin β4 significantly downregulated in the tumoroid cells and fold change was ~8, ~9 and ~58 at day 23+5, 23+10, and 23+20 respectively as compared to PCa single cells. CDC42 downregulated ~17 fold, ~28 fold, and ~108 fold at day 23+5, 23+10, and 23+20 respectively in the tumoroid cells as compared to PCa single cells. There were no significant changes of cortactin in the tumoroid cells at day 23+5 and day 23+10, but cortactin downregulated ~5 fold at day 23+20 as compared to PCa single cells.

7.3.7. Size of nucleus and cells decreases with the disease progression

Alteration in the size of the nucleus has been reported as one of the morphological changes that have been observed in cancer cells with the disease progression [51]. The nucleus and cellular size measurement were performed using ImageJ software developed by NIH (figure 7.10). Size of the nucleus in the single cells is significantly higher as compared to tumoroid cells (P-value=1.81E-26). The difference of median nucleus size of the cells in the tumoroid between day 23+5 and day 23+10 is not statistically significant. However, the median size of the nucleus in the tumoroids at day 23+20 is significantly lower as compared to day 23+5 and day 23+10

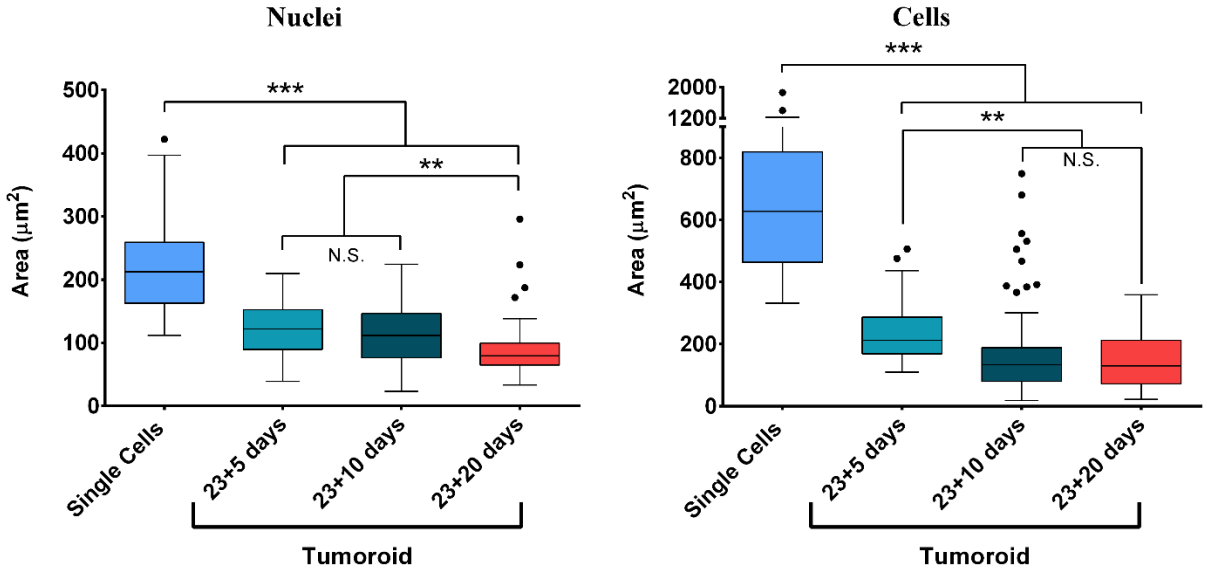

Figure 7.10. Alteration in nucleus and cell size. Nucleus and cell size distribution of the single cells and the tumoroid cells at day 23+5, day 23+10, and day 23+20 shown by Tukey's Boxplot. The median, 25th percentile and 75th percentile are indicated. Error bars indicate 5th and 95th percentiles. Whiskers indicate outliers. ***p < 0.001, **p < 0.005, *p < 0.05. Size of the nucleus in the single cells is significantly higher as compared to tumoroid cells (P-value=1.81E-26). The difference of the median cell size in the tumoroids between day 23+10 and day 23+20 are is not statistically significant. F-actin stained confocal micrographs were used for measuring the cellular size, and DAPI stained micrographs were used to measure the nucleus size.

(P-value is 2.59E-05 and .0015 respectively). Size of the cells in the single cell samples is significantly higher as compared to tumoroid cells (P-value=3.50E-43). The difference of the median cell size in the tumoroids between day 23+10 and day 23+20 are is not statistically significant. However, the median size of the cells in the tumoroids at day 23+5 is significantly higher as compared to day 23+10 and day 23+20 (P-value is 0.0045 and 1.16E-06 respectively). F-actin stained confocal micrographs were used for measuring the cellular size, and DAPI stained micrographs were used to measure the nucleus size. As the micrographs in the figure 7.6, 7.7, and 7.8 show, F-actin is mostly concentrated at the cell-junctions, the cellular boundaries were distinctly visible to calculate the area of the cells. Cell size analysis was performed using the area of the cells from top view. Orthogonal view (figure 7.11) of the cells indicates height of

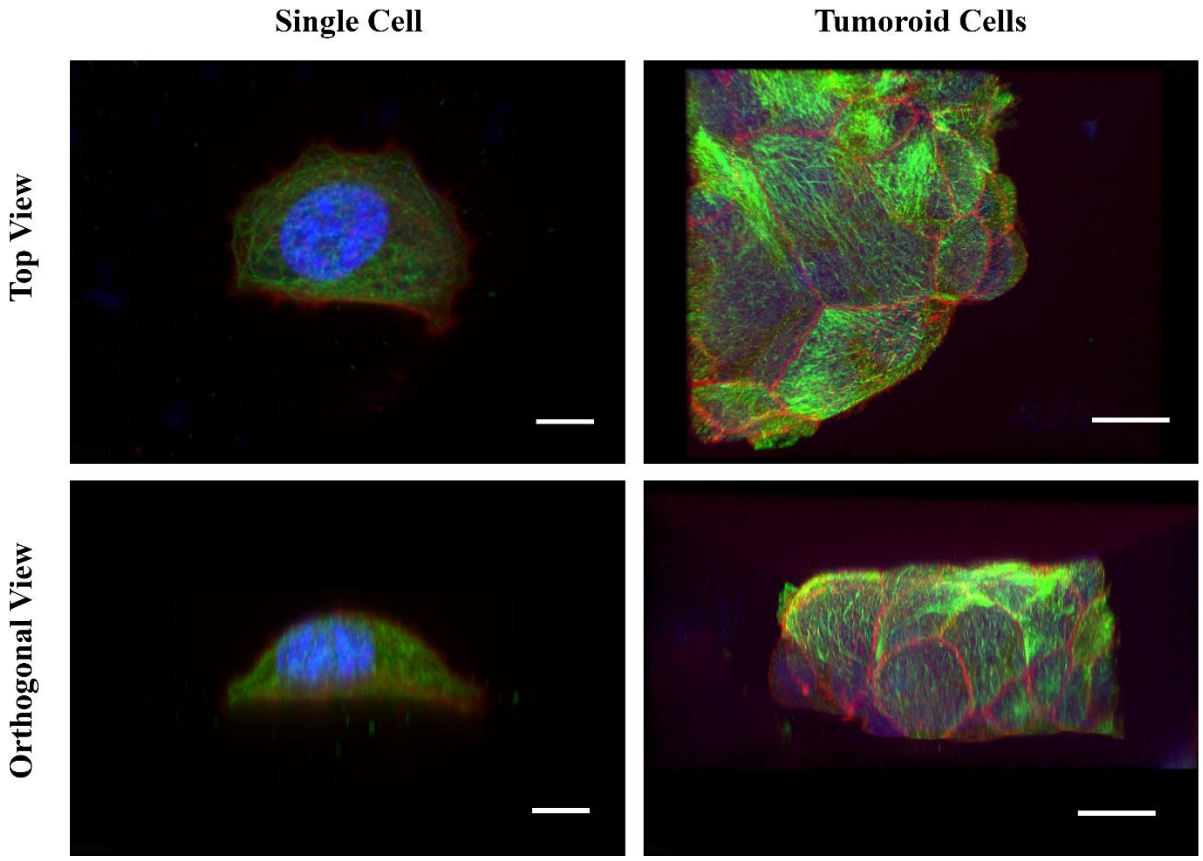

Figure 7.11. Top view and orthogonal view of the single cells and the tumoroid cells stained with F-actin (red), α-tubulin and nuclei (blue). Bar is 10 μm. Orthogonal view of the cells indicates height of the tumoroid and single cells are almost same (~10 μm).

the tumoroid and single cells are almost same (~10 μm) which justifies the use of area from top view to be used to calculate cell size. We observed a gradual reduction of the nucleus size in the tumoroid cells with the cancer progression. We observed a gradual reduction of the nucleus size in the tumoroid cells with the cancer progression. Mechanically stiffer PCa single cells possess significantly larger nucleus size. So, it is possible that a larger nucleus size is responsible for a stiffer mechanical response and smaller nucleus size is responsible for a softer mechanical response of the PCa cells. A similar observation was made by Zhou et al. who reported cells with smaller nucleus size possess lower elastic modulus values [15].

7.3.8. A 3D finite element model for cancer cell mechanics and cytoskeletal behavior

The computational model of a single cancer cell developed in a previous study described cellular mechanics and role of cytoskeleton degradation on overall elastic properties of the cancer cell [52]. This modeling study was a necessary first step to develop robust predictive methodologies for cancer progression. This study indicates that the cytoskeleton of cancer cells significantly influences the mechanical properties. The finite element modeling study evidently shows that the mechanical response of the cell is dramatically affected by the mechanical degradation of the cytoskeleton. From the nanoindentation experiment and immunocytochemical analysis we concluded that the dramatic reduction in mechanical properties of prostate cancer cells is mostly regulated by F-actin degradation and reorganization. Similar results were obtained from the 3D finite element model that was reported by our research group [52]. From the modeling study it was observed that the load-displacement response of the cell with nondegraded cytoskeleton has a larger inelastic response than the cell with the degraded cytoskeleton. It has been reported in the modeling study that the force-displacement response of the cancer cells is attributed to movement and rearrangement of cytoskeleton elements during loading. The load-displacement response of the cancer cell obtained from FEM simulations under increasing load mimicking nanoindentation tests indicates that the stiffness of cells decreases with the increased degradation of cytoskeletal components. Nondegraded cells exhibit stiffer response as compared to the cells with degraded cytoskeleton. Similar observation was made in this current study. We have observed that tumoroid cells exhibit softer response in nanoindentation experiment as compared to single cells and total amount of F-actin in the tumoroid cells is significantly lower as compared to single cells. Lower amount of total F-actin per cell in the tumoroids is possibly because of degradation of F-actin during the mesenchymal to epithelial transition (MET).

7.4. Discussion

In this study, we report changes to nanomechanical properties of prostate cancer cells and tumoroids during mesenchymal to epithelial transition (MET) and with the progress of the disease in a tissue-engineered in vitro bone microenvironment. We evaluated mechanical properties of living PCa cells under physiological conditions using a nanoindenter instrumented with AFM. A pyramidal shaped Berkovich tip, with 100–200 nm tip diameter, was used for obtaining localized nanomechanical responses from PCa single cells and tumoroid cells. In previous studies, for indenting human biological tissue samples, a blunt tip was recommended by investigators [53] while a several studies have also
shown that stiffness of cells measured by using sharp indenters is similar to stiffness measured by blunt tips [54, 55]. Moreover, sharp indenters allow probing localized cellular mechanics from deeper penetration into the probed sample with no detrimental effect, given a certain amount of applied force [47, 55, 56]. These facts justify the use of Berkovich indenter in this study. Nanomechanical properties of human cells assessed by indentation experiment are routinely described by the elastic modulus [15, 17, 18, 57]. But it remains debatable to date if the cell mechanics can be described by elastic modulus due to the unreliability of the theoretical models to derive elastic modulus [21, 58]. Analysis based on the Hertz model has been traditionally applied for the studies of soft biological samples [59]. However, for deeper indentation, human cells exhibit heterogeneous nonlinear elastic behavior which does not satisfy the assumptions of the Hertz model [21]. In this study, we applied Oliver and Pharr analysis method[49] to derive the elastic modulus of the PCa cells. The disadvantage of Oliver and Pharr method is that it does not consider the adhesion between tip indenter and the sample which leads to overestimation of elastic modulus [60]. Some other challenging procedures associated with

measuring accurate elastic modulus include precise calibration of the indenter spring constant [61], the accurate depiction of the indenter geometry [62], and precise identification of the contact point [63]. To overcome the theoretical and practical limitations of Oliver & Pharr method for calculating elastic modulus from L-D curves, several alternatives equations have been proposed [21, 58, 60, 62, 64]. To analyze the appositeness of these models to estimate the elastic modulus from the L-D curves, we obtained by indenting PCa cells is beyond the scope of the current study. In this study, the magnitude of changes in nanomechanical properties of PCa cells has been described quantitatively by using the relative value of the elastic's modulus. A more precise calculation of elastic modulus is still required, but this does not compromise the significance of our current nanoindentation experiment results describing the changes of nanomechanical properties with cancer progression and hence the use of mechanics as a potential new biomarker for cancer metastasis.

Indentation depth has been reported to influence the measurement of elastic modulus of cells. Most of the indentation studies on human cells are performed within an indentation depth range of ~300-500nm [55]. Structurally, human cells consist of a complex-multilayered-structures with distinct mechanical properties for distinct components. The mechanical properties observed at shallow indentation arises mostly from actin filaments, whereas, at deeper indentation (~500-1400 nm), the overall mechanics of whole cells can be observed [65]. At shallow indentation, no difference was found in elastic moduli between cancerous and benign cells, but significant lower elastic modulus of cancer cells was reported as compared to their normal counterparts at deeper indentation [65]. Considering these facts, we used two different indentation depths, 500 nm and 1000 nm for displacement controlled nanoindentation experiments. Since the sizes of most of the PCa cells observed were ≥10 μm, an indentation

depth >1000 nm was not used to avoid substrate effect on the measured elastic moduli [66]. We found no significant difference between the calculated elastic moduli for the same type of samples at two different indentation depths.

EMT and MET are two very critical stages in cancer progression and metastasis and unfolding the underlying mechanisms of these processes is the first step to forestall the dissemination of cancer cells to a distant organ. In this study, we found that the stiffness of PCa cells is decreased (figure 7.3/7.4) but mechanical plasticity is increased (figure 7.5) suggesting PCa cells become significantly softer when they undergo MET and further with the disease progression. It has been reported that cell softening is associated with the induction of EMT (the reverse process of MET at the primary tumor site) in human lung and tongue squamous cancer cells [15, 17]. But it has also been reported that metastatic cancer cells stiffen after EMT during the invasion into surrounding tissues [18]. Since we found that PCa cells soften after undergoing MET which is a reverse process of EMT, so our observation is in agreement with the noted mechanical behavior of cancer cells during the induction of EMT and after undergoing EMT during the invasion into surrounding tissues.

The changes to the mechanical properties of cancer cells has been linked to the deformability of the cytoskeleton, which has long been known to play a major role in metastasis [17, 67]. Among different components of cytoskeleton, F-actin, which mostly localized at the periphery of the cells under the membrane, provides maximum resistance to deformation and is the predominant factor that determines mechanical cell elasticity [68, 69]. From the immunocytochemical analysis in this study, we observed that PCa single cells possess a more pronounced network of F-actin filaments as compared to PCa tumoroid cells. The amount of F-actin is decreased with the decreased elastic modulus of PCa cells, but there were no significant

changes in the amount of α-tubulin suggesting a lower level of F-actin is mostly responsible for cell softening. It has been reported that a decrease in the elastic modulus of cancer cells is accompanied by a reduction in the amount of F-actin [14]. Several studies have reported sharp cutback of cell stiffness with the depolymerization of F-actin but not with the depolymerization of microtubules [70, 71]. Also, we observed a significant reduction of F-actin on the apical regions of PCa cells in the tumoroids and organization of the F-actin at the cellular junctions (figure 7.6a, indicated by white arrows). We have reported tight cell-cell junction in the tumoroid cells is associated with the overexpression of E-cadherin in our previous study [38]. It is well known that trans-membrane adhesion molecule E-cadherin binds to F-actins via β-catenin to stabilize tight junctions [72, 73], and that could be the possible reason of F-actin to assemble into the cell junctions. Since phalloidin only stains filamentous F-actin but not monomeric G-actin, we could not observe the depolymerized actins on the apical regions of tumoroid cells suggesting radical depolymerization of F-actin is associated with the gradual decrease of stiffness in the tumoroid cells with the disease progression. Dramatic depolymerization of F-actin is further confirmed by the gene expression analysis study of actin regulatory molecules. N-WASp activates Arp 2/3 and activated Arp 2/3 nucleates new F-actin [74]. Cortactin recruits Arp2/3 in the cortical region of a cell [74]. CDC42 help initiates actin reorganization and localize the N-WASp-Arp2/3 complex to the plasma membrane [74]. Thymosin β4 also plays a role in actin polymerization [74]. Dramatic downregulation of these genes suggests a reduction of F-actin polymerization with the disease progression.

In summary, here we report for the first time how nanomechanical properties of prostate cancer cells change during mesenchymal to epithelial transition (MET) and with the disease progression at the metastatic site. This demonstrates the use of mechanics as a biomarker for

disease progression at metastasis. Our immunocytochemical and gene expression analysis results suggest that softening of PCa cells in the tumoroids is induced by depolymerization and reorganization of F-actin to the cellular junctions. Our data indicates the mechanical properties of prostate cancer cells could be used as possible biomarker of prostate cancer cell progression. This study could be pivotal in understanding the biophysical mechanism associated with skeletal metastasis of prostate cancer cells.

Table 7.1. Primer sequences used in qRT-PCR experiments.

Gene	Forward Primer	Reverse Primer
N-WASp	5’ -ACTGTTAGACCAGATACG ACAGGGT-3’	5’-TGCAGGTGTTGGTGGTGT AGA-3’
Arp2	5’-GGAGTTGGTGTTGCTGAAT-3’	5’-TAGTAGACCCTCCAGAAAGC-3’
Arp 3	5’-CAATCCTTGGAAACTGCTA-3’	5’-CCATTTTGACCCATCTGTA-3’
CDC42	5’-ATGCAGACAATTAAGTGTG TTGTTGTGGGCGA-3’	5’- TCATAGCAGCACACACC TGCGGCTCTTCTT-3’
Thymosin β4	5'-GGCCACTGCGCAGACCAG ACT-3'	5'-CTTGATCCAACCTCTTTGCAT CTTACAA-3’
Cortactin	5’-AAAGCTTCAGCAGGCCAC-3’	5’-TTTGGTCCTGTTTCAAGT TCC-3’

7.5. Acknowledgments

This work was supported by NDSU grand challenges grant for “Center for Engineered Cancer Test-Beds.” The SEM experiments conducted in this work are made possible through instrumentation obtained using MRI grant from the National Science Foundation. Dr. Tao Wang, manager of core biology facility at NDSU, is acknowledged for help in use of the qRT PCR experiments. Dr. Pawel Borowicz, Director of NDSU Advanced Imaging and Microscopy (AIM) Core Lab, is acknowledged for help in use of the confocal microscope. Support from ND EPSCoR for tissue engineering laboratory is also acknowledged. ND EPSCoR is also acknowledged for “Doctoral Dissertation Award.”

7.6. References

[1] G. Bao, S. Suresh, Cell and molecular mechanics of biological materials, Nature Materials 2(11) (2003) 715-725.

[2] M. Radmacher, M. Fritz, C.M. Kacher, J.P. Cleveland, P.K. Hansma, Measuring the viscoelastic properties of human platelets with the atomic force microscope, Biophys J 70(1) (1996) 556-67.

[3] J.A. Hessler, A. Budor, K. Putchakayala, A. Mecke, D. Rieger, M.M.B. Holl, B.G. Orr, A. Bielinska, J. Beals, J. Baker, Atomic force microscopy study of early morphological changes during apoptosis, Langmuir 21(20) (2005) 9280-9286.

[4] S. Suresh, Biomechanics and biophysics of cancer cells, Acta Materialia 55(12) (2007) 3989-4014.

[5] S. Suresh, J. Spatz, J.P. Mills, A. Micoulet, M. Dao, C.T. Lim, M. Beil, T. Seufferlein, Reprint of: connections between single-cell biomechanics and human disease states: gastrointestinal cancer and malaria, Acta biomaterialia 23 (2015) S3-S15.

[6] D. Ingber, Mechanobiology and diseases of mechanotransduction, Annals of medicine 35(8) (2003) 564-577.

[7] R.W. Van Zwieten, S. Puttini, M. Lekka, G. Witz, E. Gicquel-Zouida, I. Richard, J.A. Lobrinus, F. Chevalley, H. Brune, G. Dietler, Assessing dystrophies and other muscle diseases at the nanometer scale by atomic force microscopy, Nanomedicine 9(4) (2014) 393-406.

[8] M.M. Yallapu, K.S. Katti, D.R. Katti, S.R. Mishra, S. Khan, M. Jaggi, S.C. Chauhan, The roles of cellular nanomechanics in cancer, Medicinal research reviews 35(1) (2015) 198-223.

[9] W.W. Xu, R. Mezencev, B. Kim, L.J. Wang, J. McDonald, T. Sulchek, Cell Stiffness Is a Biomarker of the Metastatic Potential of Ovarian Cancer Cells, Plos One 7(10) (2012).

[10] K. Hoyt, B. Castaneda, M. Zhang, P. Nigwekar, P.A. di Sant'Agnese, J.V. Joseph, J. Strang, D.J. Rubens, K.J. Parker, Tissue elasticity properties as biomarkers for prostate cancer, Cancer Biomarkers 4(4-5) (2008) 213-225.

[11] M. Lekka, P. Laidler, D. Gil, J. Lekki, Z. Stachura, A.Z. Hrynkiewicz, Elasticity of normal and cancerous human bladder cells studied by scanning force microscopy, European Biophysics Journal 28(4) (1999) 312-316.

[12] M. Lekka, Discrimination Between Normal and Cancerous Cells Using AFM, Bionanoscience 6(1) (2016) 65-80.

[13] V. Swaminathan, K. Mythreye, E.T. O'Brien, A. Berchuck, G.C. Blobe, R. Superfine, Mechanical Stiffness Grades Metastatic Potential in Patient Tumor Cells and in Cancer Cell Lines, Cancer Research 71(15) (2011) 5075-5080.

[14] J. Guck, S. Schinkinger, B. Lincoln, F. Wottawah, S. Ebert, M. Romeyke, D. Lenz, H.M. Erickson, R. Ananthakrishnan, D. Mitchell, Optical deformability as an inherent cell marker for testing malignant transformation and metastatic competence, Biophysical journal 88(5) (2005) 3689-3698.

[15] Z. Zhou, C. Zheng, S. Li, X. Zhou, Z. Liu, Q. He, N. Zhang, A. Ngan, B. Tang, A. Wang, AFM nanoindentation detection of the elastic modulus of tongue squamous carcinoma cells with different metastatic potentials, Nanomedicine: Nanotechnology, Biology and Medicine 9(7) (2013) 864-874.

[16] J. Guck, S. Schinkinger, B. Lincoln, F. Wottawah, S. Ebert, M. Romeyke, D. Lenz, H.M. Erickson, R. Ananthakrishnan, D. Mitchell, J. Kas, S. Ulvick, C. Bilby, Optical deformability as an inherent cell marker for testing malignant transformation and metastatic competence, Biophysical Journal 88(5) (2005) 3689-3698.

[17] K. Iida, R. Sakai, S. Yokoyama, N. Kobayashi, S. Togo, H.Y. Yoshikawa, A. Rawangkan, K. Namiki, M. Suganuma, Cell softening in malignant progression of human lung cancer cells by activation of receptor tyrosine kinase AXL, Scientific reports 7(1) (2017) 17770.

[18] J.R. Staunton, B.L. Doss, S. Lindsay, R. Ros, Correlating confocal microscopy and atomic force indentation reveals metastatic cancer cells stiffen during invasion into collagen I matrices, Scientific reports 6 (2016) 19686.

[19] P.-H. Wu, D.R.-B. Aroush, A. Asnacios, W.-C. Chen, M.E. Dokukin, B.L. Doss, P. Durand-Smet, A. Ekpenyong, J. Guck, N.V. Guz, A comparison of methods to assess cell mechanical properties, Nature methods (2018) 1.

[20] J. Chen, Nanobiomechanics of living cells: a review, Interface focus 4(2) (2014) 20130055.

[21] N. Guz, M. Dokukin, V. Kalaparthi, I. Sokolov, If cell mechanics can be described by elastic modulus: study of different models and probes used in indentation experiments, Biophysical journal 107(3) (2014) 564-575.

[22] D.R. Katti, K.S. Katti, S. Molla, S. Kar, Biomechanics of Cells as Potential Biomarkers for Diseases: A New Tool in Mechanobiology, in: R. Narayan (Ed.), Encyclopedia of Biomedical Engineering, Elsevier, Oxford, 2019, pp. 1-21.

[23] A. Vinckier, G. Semenza, Measuring elasticity of biological materials by atomic force microscopy, FEBS letters 430(1-2) (1998) 12-16.

[24] M. Lekka, P. Laidler, D. Gil, J. Lekki, Z. Stachura, A.Z. Hrynkiewicz, Elasticity of normal and cancerous human bladder cells studied by scanning force microscopy, European Biophysics Journal with Biophysics Letters 28(4) (1999) 312-316.

[25] C.L. Sawyers, The cancer biomarker problem, Nature 452(7187) (2008) 548.

[26] M. Yilmaz, G. Christofori, EMT, the cytoskeleton, and cancer cell invasion, Cancer and Metastasis Reviews 28(1-2) (2009) 15-33.

[27] D.A. Fletcher, R.D. Mullins, Cell mechanics and the cytoskeleton, Nature 463(7280) (2010) 485.

[28] D. Wirtz, K. Konstantopoulos, P.C. Searson, The physics of cancer: the role of physical interactions and mechanical forces in metastasis, Nature Reviews Cancer 11(7) (2011) 512.

[29] C.L. Chaffer, R.A. Weinberg, A Perspective on Cancer Cell Metastasis, Science 331(6024) (2011) 1559-1564.

[30] C.M. Fife, J.A. McCarroll, M. Kavallaris, Movers and shakers: cell cytoskeleton in cancer metastasis, British journal of pharmacology 171(24) (2014) 5507-5523.

[31] N. Howlader, A.M. Noone, M. Krapcho, D. Miller, K. Bishop, C.L. Kosary, M. Yu, J. Ruhl, Z. Tatalovich, A. Mariotto, SEER cancer statistics review, 1975–2014. Bethesda, MD: National Cancer Institute; 2017, 2017.

[32] A. Jemal, L.A. Torre, The Global Burden of Cancer, The American Cancer Society's Principles of Oncology: Prevention to Survivorship (2018) 33-44.

[33] R.B. Berish, A.N. Ali, P.G. Telmer, J.A. Ronald, H.S. Leong, Translational models of prostate cancer bone metastasis, Nature Reviews Urology (2018) 1.

[34] L.G. Griffith, M.A. Swartz, Capturing complex 3D tissue physiology in vitro, Nature reviews Molecular cell biology 7(3) (2006) 211.

[35] D.W. Hutmacher, Biomaterials offer cancer research the third dimension, Nature materials 9(2) (2010) 90.

[36] K.S. Katti, M.D.S. Molla, F. Karandish, M.K. Haldar, S. Mallik, D.R. Katti, Sequential culture on biomimetic nanoclay scaffolds forms three-dimensional tumoroids, Journal of Biomedical Materials Research Part A 104(7) (2016) 1591-1602.

[37] K.S. Katti, D.R. Katti, M.S. Molla, S. Kar, Evaluation of Cancer Tumors in 3D Porous Bone Mimetic Scaffolds, Poromechanics VI, pp. 881-888.

[38] S. Molla, D.R. Katti, K.S. Katti, In vitro design of mesenchymal to epithelial transition of prostate cancer metastasis using 3D nanoclay bone-mimetic scaffolds, Journal of Tissue Engineering and Regenerative Medicine 12(3) (2018) 727-737.

[39] A.H. Ambre, D.R. Katti, K.S. Katti, Biomineralized hydroxyapatite nanoclay composite scaffolds with polycaprolactone for stem cell-based bone tissue engineering, Journal of Biomedical Materials Research Part A 103(6) (2015) 2077-2101.

[40] A.H. Ambre, D.R. Katti, K.S. Katti, Nanoclays mediate stem cell differentiation and mineralized ECM formation on biopolymer scaffolds, Journal of Biomedical Materials Research Part A 101(9) (2013) 2644-2660.

[41] A.H. Ambre, K.S. Katti, D.R. Katti, Nanoclay Based Composite Scaffolds for Bone Tissue Engineering Applications, Journal of Nanotechnology in Engineering and Medicine 1(3) (2010) 031013-9.

[42] D. Sikdar, S.M. Pradhan, D.R. Katti, K.S. Katti, B. Mohanty, Altered phase model for polymer clay nanocomposites, Langmuir 24(10) (2008) 5599-5607.

[43] J. Mahamid, A. Sharir, D. Gur, E. Zelzer, L. Addadi, S. Weiner, Bone mineralization proceeds through intracellular calcium phosphate loaded vesicles: A cryo-electron microscopy study, Journal of Structural Biology 174(3) (2011) 527-535.

[44] S. Boonrungsiman, E. Gentleman, R. Carzaniga, N.D. Evans, D.W. McComb, A.E. Porter, M.M. Stevens, The role of intracellular calcium phosphate in osteoblast-mediated bone apatite formation, Proceedings of the National Academy of Sciences 109(35) (2012) 14170-14175.

[45] K.S. Katti, A.H. Ambre, S. Payne, D.R. Katti, Vesicular delivery of crystalline calcium minerals to ECM in biomineralized nanoclay composites, Materials Research Express 2(4) (2015).

[46] R. Khanna, D.R. Katti, K.S. Katti, AFM and Nanoindentation Studies of Bone Nodules on Chitosan-Polygalacturonic Acid-Hydroxyapatite Nanocomposites, Cmes-Computer Modeling in Engineering & Sciences 87(6) (2012) 530-555.

[47] R. Khanna, K.S. Katti, D.R. Katti, Experiments in Nanomechanical Properties of Live Osteoblast Cells and Cell–Biomaterial Interface, J Nanotechnol Eng Med 2(4) (2012) 041005 (Pages 13).

[48] K.S. Katti, A.H. Ambre, N. Peterka, D.R. Katti, Use of unnatural amino acids for design of novel organomodified clays as components of nanocomposite biomaterials, Philosophical Transactions of the Royal Society a-Mathematical Physical and Engineering Sciences 368(1917) (2010) 1963-1980.

[49] W.C. Oliver, G.M. Pharr, An improved technique for determining hardness and elastic modulus using load and displacement sensing indentation experiments, Journal of materials research 7(06) (1992) 1564-1583.

[50] N. Bonakdar, R. Gerum, M. Kuhn, M. Spörrer, A. Lippert, W. Schneider, K.E. Aifantis, B. Fabry, Mechanical plasticity of cells, Nature materials 15(10) (2016) 1090.

[51] D. Zink, A.H. Fischer, J.A. Nickerson, Nuclear structure in cancer cells, Nature reviews cancer 4(9) (2004) 677.

[52] D.R. Katti, K.S. Katti, Cancer cell mechanics with altered cytoskeletal behavior and substrate effects: A 3D finite element modeling study, Journal of the mechanical behavior of biomedical materials 76 (2017) 125-134.

[53] D.M. Ebenstein, L.A. Pruitt, Nanoindentation of biological materials, Nano Today 1(3) (2006) 26-33.

[54] Y.-W. Chiou, H.-K. Lin, M.-J. Tang, H.-H. Lin, M.-L. Yeh, The influence of physical and physiological cues on atomic force microscopy-based cell stiffness assessment, PLoS One 8(10) (2013) e77384.

[55] N. Gavara, A Beginner's guide to atomic force microscopy probing for cell mechanics, Microscopy research and technique 80(1) (2017) 75-84.

[56] N. Gavara, R.S. Chadwick, Relationship between cell stiffness and stress fiber amount, assessed by simultaneous atomic force microscopy and live-cell fluorescence imaging, Biomechanics and modeling in mechanobiology 15(3) (2016) 511-523.

[57] Q.S. Li, G.Y.H. Lee, C.N. Ong, C.T. Lim, AFM indentation study of breast cancer cells, Biochemical and biophysical research communications 374(4) (2008) 609-613.

[58] Y.M. Efremov, W.-H. Wang, S.D. Hardy, R.L. Geahlen, A. Raman, Measuring nanoscale viscoelastic parameters of cells directly from AFM force-displacement curves, Scientific reports 7(1) (2017) 1541.

[59] H. Hertz, On the contact of elastic solids, J. reine angew. Math 92(156-171) (1881) 110.

[60] D.M. Ebenstein, Nano-JKR force curve method overcomes challenges of surface detection and adhesion for nanoindentation of a compliant polymer in air and water, Journal of Materials Research 26(8) (2011) 1026-1035.

[61] T. Senden, W. Ducker, Experimental determination of spring constants in atomic force microscopy, Langmuir 10(4) (1994) 1003-1004.

[62] A.B. Mathur, A.M. Collinsworth, W.M. Reichert, W.E. Kraus, G.A. Truskey, Endothelial, cardiac muscle and skeletal muscle exhibit different viscous and elastic properties as determined by atomic force microscopy, Journal of biomechanics 34(12) (2001) 1545-1553.

[63] E.K. Dimitriadis, F. Horkay, J. Maresca, B. Kachar, R.S. Chadwick, Determination of elastic moduli of thin layers of soft material using the atomic force microscope, Biophysical journal 82(5) (2002) 2798-2810.

[64] C. Jin, D.M. Ebenstein, Nanoindentation of compliant materials using Berkovich tips and flat tips, Journal of Materials Research 32(2) (2017) 435-450.

[65] K. Pogoda, J. Jaczewska, J. Wiltowska-Zuber, O. Klymenko, K. Zuber, M. Fornal, M. Lekka, Depth-sensing analysis of cytoskeleton organization based on AFM data, European Biophysics Journal 41(1) (2012) 79-87.

[66] R. Saha, W.D. Nix, Effects of the substrate on the determination of thin film mechanical properties by nanoindentation, Acta materialia 50(1) (2002) 23-38.

[67] B. Xuan, D. Ghosh, E.M. Cheney, E.M. Clifton, M.R. Dawson, Dysregulation in Actin Cytoskeletal Organization Drives Increased Stiffness and Migratory Persistence in Polyploidal Giant Cancer Cells, Scientific reports 8 (2018).

[68] P.A. Janmey, U. Euteneuer, P. Traub, M. Schliwa, Viscoelastic properties of vimentin compared with other filamentous biopolymer networks, The Journal of cell biology 113(1) (1991) 155-160.

[69] S. Tojkander, G. Gateva, P. Lappalainen, Actin stress fibers–assembly, dynamics and biological roles, J Cell Sci (2012) jcs-098087.

[70] G.T. Charras, M.A. Horton, Single cell mechanotransduction and its modulation analyzed by atomic force microscope indentation, Biophysical journal 82(6) (2002) 2970-2981.

[71] C. Rotsch, M. Radmacher, Drug-induced changes of cytoskeletal structure and mechanics in fibroblasts: an atomic force microscopy study, Biophysical journal 78(1) (2000) 520-535.

[72] S. Hong, R.B. Troyanovsky, S.M. Troyanovsky, Binding to F-actin guides cadherin cluster assembly, stability, and movement, J Cell Biol 201(1) (2013) 131-143.

[73] W.I. Weis, W.J. Nelson, Re-solving the cadherin-catenin-actin conundrum, Journal of biological chemistry 281(47) (2006) 35593-35597.

[74] C.G. Dos Remedios, D. Chhabra, M. Kekic, I.V. Dedova, M. Tsubakihara, D.A. Berry, N.J. Nosworthy, Actin binding proteins: regulation of cytoskeletal microfilaments, Physiological reviews 83(2) (2003) 433-473.

CHAPTER 8. SUMMARY AND CONCLUSION

Design and development of a new scaffold system using nanoclays seeded with a sequential culture of human mesenchymal stem cells followed by human prostate cancer cells are evaluated as a model to study cancer cell interaction with bone microenvironment as well as the efficacy of anticancer drugs. In this dissertation, we present a novel sequential cell culture system in 3D in vitro bone model which can provide a unique environment, mimicking the physiological cell-cell and cell-matrix interactions and leading more relevant osteotropic cancer cell behavior. The scaffolds with newly formed bone tissue are seeded with two different prostate cancer cell lines, MDA PCa 2b and PC-3. In this dissertation, we investigate the effects of sequential culture of MDA PCa 2b prostate cancer cells with MSCs in the PCL/HAPClay scaffolds on the regulation of key genes involved in bone metastasis of prostate cancer cells. The sequential culture of MDA PCa 2b with MSCs (PCa SC) on the scaffolds has shown organized tight cellular junctions, or tumoroids. The hMSCs or differentiated hMSCs are quite distinguishable from the prostate cancer cells due to their flattened morphology and arrangement on the surface of the scaffolds. We analyzed key genes expression related to skeletal metastasis of prostate cancer cells by qRT-PCR experiment in the sequential culture of MDA PCa 2b with MSCs (PCa SC) and other culture methods. The results indicate that PCa SC in PCL/HAPClay scaffolds closely mimics early stage of osteoblastic PCa colonization by developing tight junction tumoroids and inducing MET. To further confirm MET and angiogenesis, we performed immunocytochemical analysis of the proteins involved in these to processes in the PCa SC. We demonstrated that tight junction tumoroids were formed and MSCs differentiated to matured osteoblasts in PCa SC. The gene expression and immunocytochemical analysis data are

indicative of inhibited EMT, enhanced MET, and increased angiogenesis by hypoxia when MDA PCa 2b cells were sequentially cultured with MSCs in PCL/HAPClay scaffolds.

We have repeated the same set of experiments for the sequential culture of highly metastatic PC-3 cells with MSCs (PC-3 SC). Unlike MDA PCa 2b cells, PC-3 cells formed multicellular tumoroid like clusters with both tight junctions and gap junctions. Like PCa SC, we have also observed inhibited EMT, enhanced MET, and increased angiogenesis by hypoxia when PC-3 cells were sequentially cultured with MSCs in PCL/HAPClay scaffolds.

In this dissertation we have investigated the effect of metastasized prostate cancer cells on bone regeneration, degradation, mineralization, and collagen synthesis using two different prostate cancer cell lines, PC-3 and MDA PCa 2b. By performing tranwell migration assay we found that PC-3 is highly metastatic cell line while MDA PCa 2b is less metastatic in nature. Experiments such as ELISA, qRT-PCR immunocytochemical analysis, SEM imaging, FESEM imaging, and cell-based assays were performed to investigate the effect of metastasized prostate cancer cells on bone microenvironment. From all these experiments we concluded that MDA PCa 2b cells created an osteolytic lesion whereas, PC-3 cells caused an osteoblastic lesion in the tissue-engineered bone microenvironment.

The in vitro 3D tumor model has been developed using a unique sequential culture technique and mesenchymal stem cells to study the interaction between prostate cancer cells and bone microenvironment. Our in vitro model does not entirely recapitulate the bone tumor microenvironment found in a patient with metastatic disease, but with the inclusion of human MSCs and sequential culture technique, it certainly provides an improved reproducible and controllable system which is a useful tool to elucidate the osteotropism of prostate cancer cells. The model may be extended by including more human components, such as human

hematopoietic stem cells, to provide osteoclast and immune cells in the bone microenvironment. This model provides an intriguing opportunity to dissect the role of genes, proteins, and other factors in the bone microenvironment subsequent to the arrival of prostate cancer cells with a significant contribution to the understanding of the molecular, cellular and mechanical mechanism. The model can be used to investigate the various aspect of prostate cancer-bone interaction at a cellular, molecular and genetic level as well as to test various cancer therapeutics.

In this dissertation we report for the first time how nanomechanical properties of prostate cancer cells change during mesenchymal to epithelial transition (MET) and with the disease progression at the metastatic site. This demonstrates the use of mechanics as a biomarker for dieses progression at metastasis. Our results suggest that softening of prostate cancer cells in the tumoroids is induced by depolymerization of F-actin. This study could be pivotal in understanding the biophysical mechanism associated with skeletal metastasis of prostate cancer cells.

The 3D prostate cancer test-bed platform, which strikes a balance between experimental efficiency and retention of biological complexity, could be used for studying osteotropic cancer cell biology in the early stage cell colonization and in vitro testing of anticancer drugs.

CHAPTER 9. FUTURE DIRECTIONS

In this study, we reported the first MET based prostate cancer bone metastatic model using tissue-engineered PCL/nanoclay scaffolds that closely resemble in vivo bone. This study serves as a successful proof-of-concept that this in vitro 3D cancer test-bed has the potential of providing new insight into the crosstalk between bone and metastatic prostate cancer cells. Based on the understanding gained about the interactions between prostate cancer cells and bone microenvironment during this work following suggestions can be made for future research.

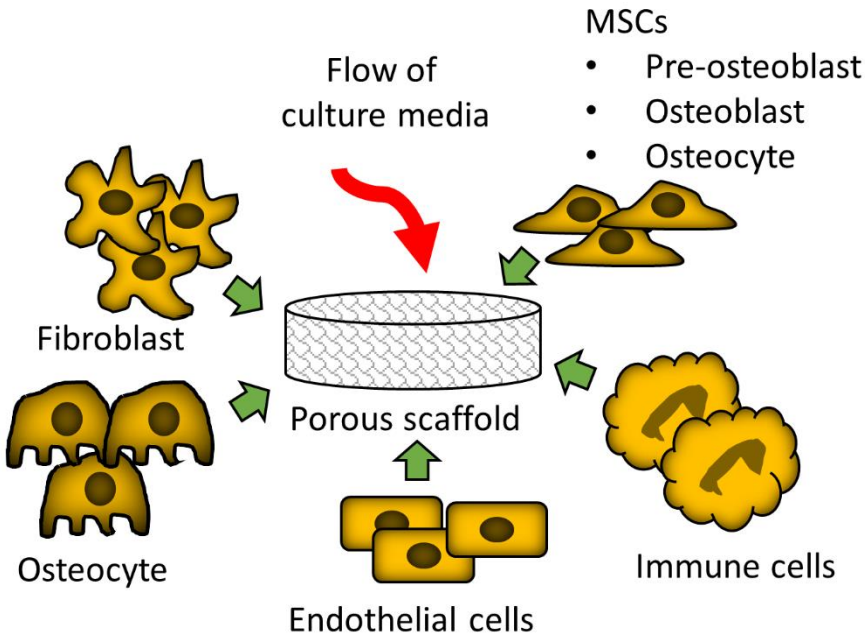

Figure 9.1. The incorporation of more cellular features and dynamic fluid flow in 3D tumor model might help to increase our understanding of the dynamic interactions between metastasized prostate cancer and bone microenvironment.

- 3D models have dramatically improved over the last decade. However, animal models have some advantages over 3D in vitro models since they can be used to study cancer dissemination, blood flow, angiogenesis, the role of immune cells, fibroblast, endothelial cells and metabolic-systemic influences on cancer all within the same animal. In vitro 3D tumor models are becoming ever more refined as bioreactors are being incorporated to

better model in vivo fluid dynamics and mechanical stress. The incorporation of more cellular features and dynamic fluid flow in 3D tumor model might help to increase our understanding of the dynamic interactions between metastasized prostate cancer and bone microenvironment (figure 9.1).

- In this dissertation, we have reported the mimicking the last stage of prostate cancer skeletal metastasis. Mimicking the first stage if prostate cancer metastasis by incorporating normal prostate cells and prostate cancer cells in a prostate mimicking 3D scaffold and joining the two different stages through a bioreactor could be helpful to understand the overall mechanism of prostate cancer metastasis.
- Katti's research group has already begun modeling dynamic cellular components and mechanical behavior of cells using computational models [1]. Computational models of prostate cancer cells and the interactions of prostate cancer and bone microenvironment might help us to develop a complete understanding of the prostate cancer metastasis and to predict outcomes.
- Usage of patient-derived bone cells in the 3D scaffolds to create a metastatic bone site with the use of patient derive prostate cancer cells might help us to predict possible patient outcomes to specific therapeutics.
- In this dissertation, we have investigated the nanomechanical properties of prostate cancer cells during the disease progression at the secondary metastatic site using the 3D tumor model that we have developed. We have shown that tumor cells become softer with the disease progression at the bone microenvironment. We have established that nanomechanical properties of prostate cancer cells can be used as a potential biomarker for the disease progression. Currently, there are no biomarkers available to study the

progression of prostate cancer when prostate cancer cells metastasize to the bone. This is because when prostate cancer metastasizes to bone, at that time patients are already in the hospice. So, using mechanical properties of prostate cancer cells as a biomarker to study the disease progression would be a considerable advantage in the endeavor of finding a cure for the disease. Bone scanning can be performed on patients with bone metastasized prostate cancer to locate the bone with metastasized prostate cancer. A bone scanning is a nuclear imaging procedure when tiny amounts of radioactive materials (known as tracers) are injected into a vein. Areas of the body where tissues and cells are remodeling take up these tracers most actively. As metastasized prostate cancer initiates osteoblastic/osteolytic bone remodeling, bone-metastatic site of prostate cancer takes a higher amount of tracers which could be detected using Micro-Computed Tomography. Once the bone metastatic site is detected, the biopsy samples could be collected by fine needle aspiration. To study the progression of the disease, the mechanical properties of the biopsy samples could be investigated. Though biopsy technique allows more detailed investigation of mechanical properties of tumor cells, it is limited to very small samples as large biopsy samples lead to significant discomfort to the patients. Elastography could be an alternative for mechanical testing on biopsy samples. This technique creates a distortion in the tissue, observes and processes the tissue response to translate the mechanical properties of the cells, and then displays the results as an image. Mechanical properties of cells are obtained in specialized imaging modes that can detect cell stiffness in response to an applied shear or compression wave. Ultrasound elastography and magnetic resonance elastography (MRE) techniques are the two most commonly used elastography method to study the mechanical properties of tissues of a patient.

Ultrasound elastography uses ultrasound-generated traveling shear wave stimuli to create tissue distortion and has shown promising results for non-invasive assessment of mechanical properties of tissue. In the 1990s, it was first described that ultrasound elastography could be used to measure the mechanical properties of tissues [2]. In recent years, this technique has been further refined for the quantitative analysis of cell stiffness [3]. Magnetic resonance elastography (MRE) is another non-destructive imaging method that quantitatively measures the stiffness of soft tissues by introducing shear waves and imaging their propagation using MRI. The effective spatial resolution of the elastography technique increases as the frequency of the applied waves is increased. Unfortunately, high-frequency shear waves are attenuated more rapidly than low-frequency waves, so there can be a compensation between the distance from the vibration source and the spatial resolution in some applications.

9.1. References

[1] D.R. Katti, K.S. Katti, Cancer cell mechanics with altered cytoskeletal behavior and substrate effects: A 3D finite element modeling study, Journal of the mechanical behavior of biomedical materials 76 (2017) 125-134.

[2] J.L. Gennisson, T. Deffieux, M. Fink, M. Tanter, Ultrasound elastography: principles and techniques, Diagnostic and interventional imaging 94(5) (2013) 487-495.

[3] I.Z. Nenadic, M.W. Urban, J.F. Greenleaf, J.-L. Gennisson, M. Bernal, M. Tanter, Ultrasound Elastography for Biomedical Applications and Medicine, Wiley2019.

APPENDIX

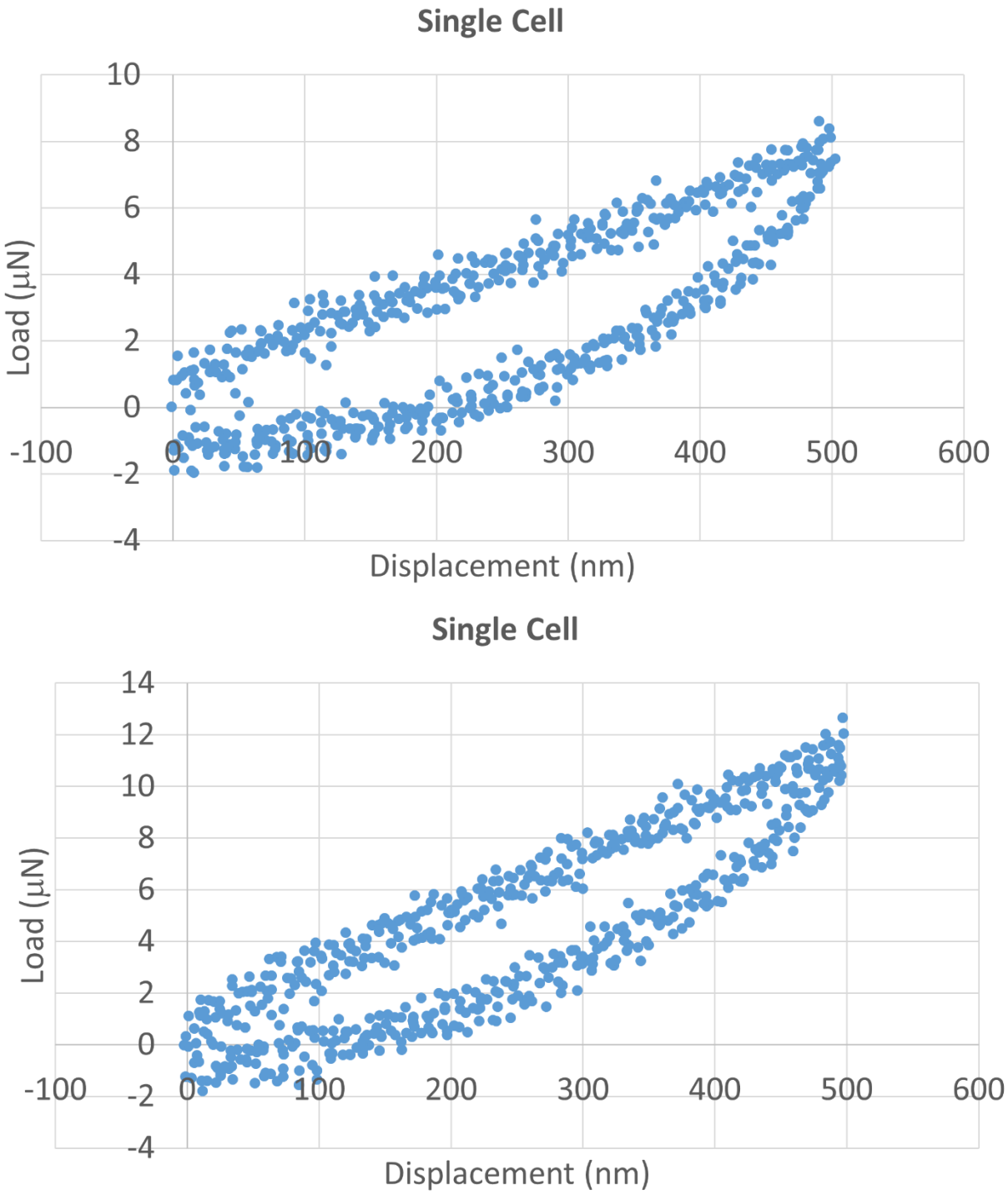

Figure A1. L-D curve on PCa single cell at maximum displacement 500 nm.

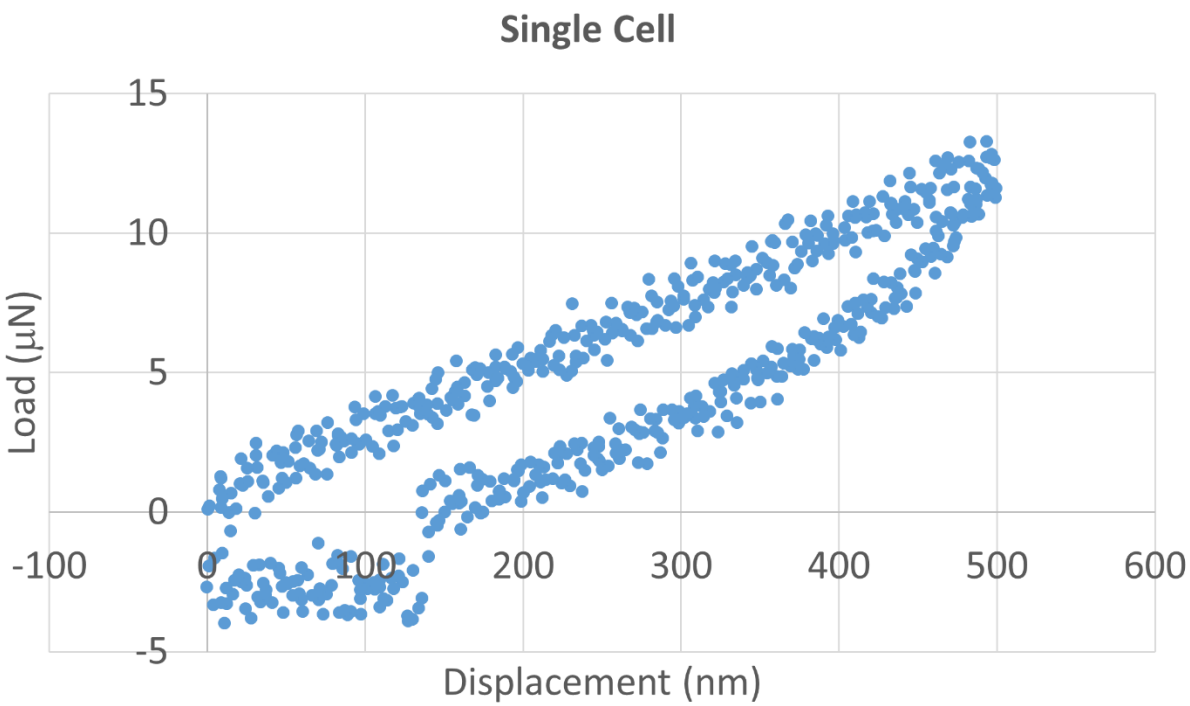

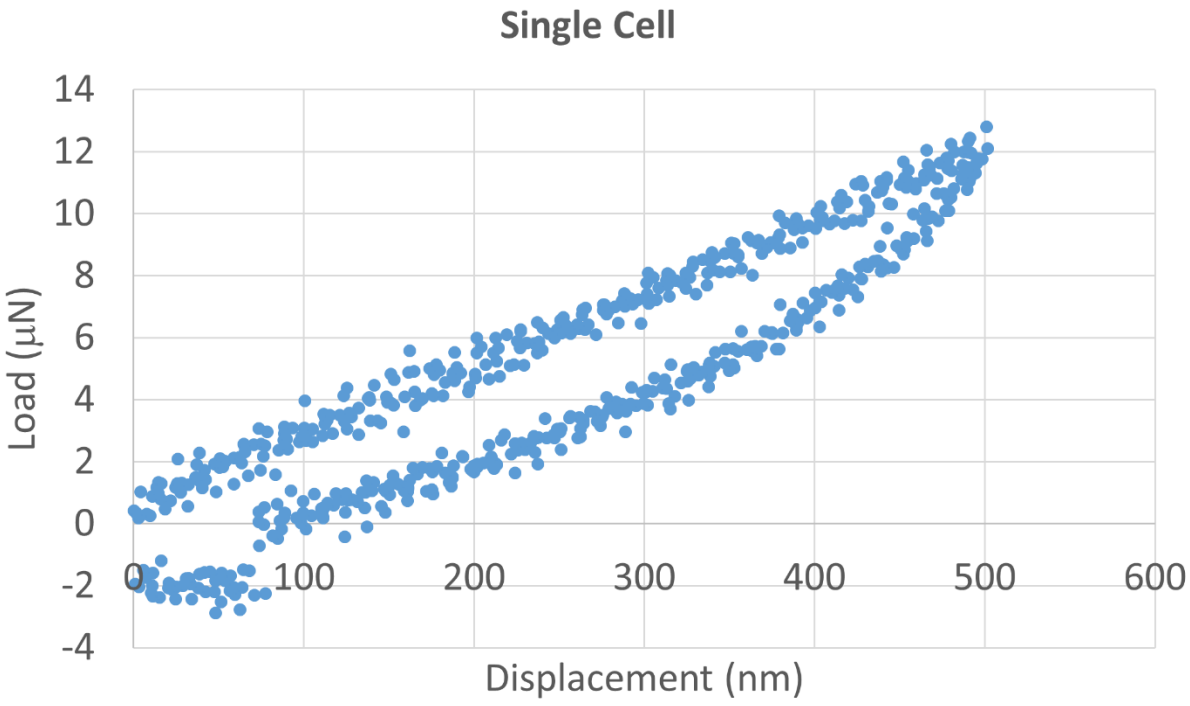

Figure A1. L-D curve on PCa single cell at maximum displacement 500 nm (Continued).

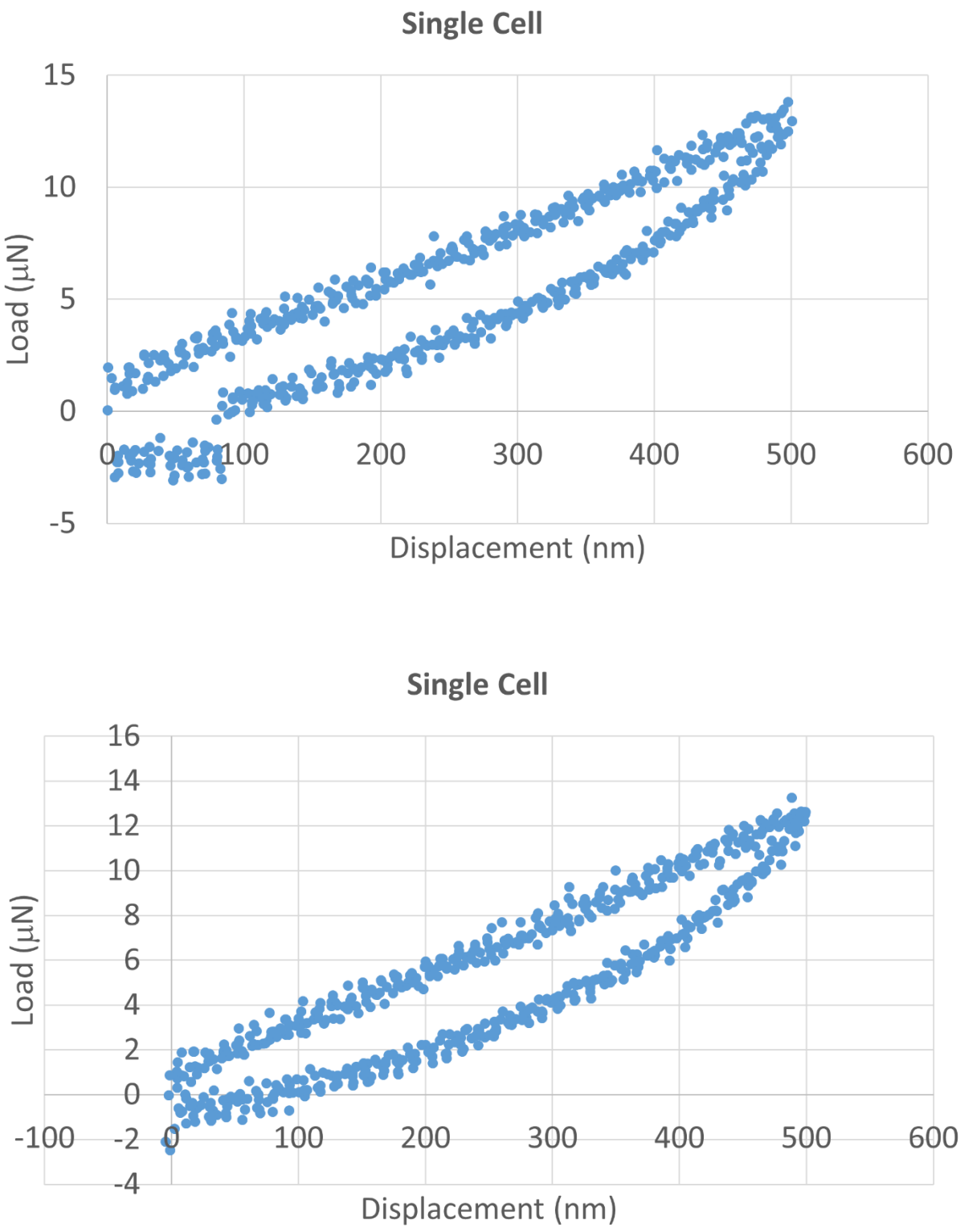

Figure A1. L-D curve on PCa single cell at maximum displacement 500 nm (Continued).

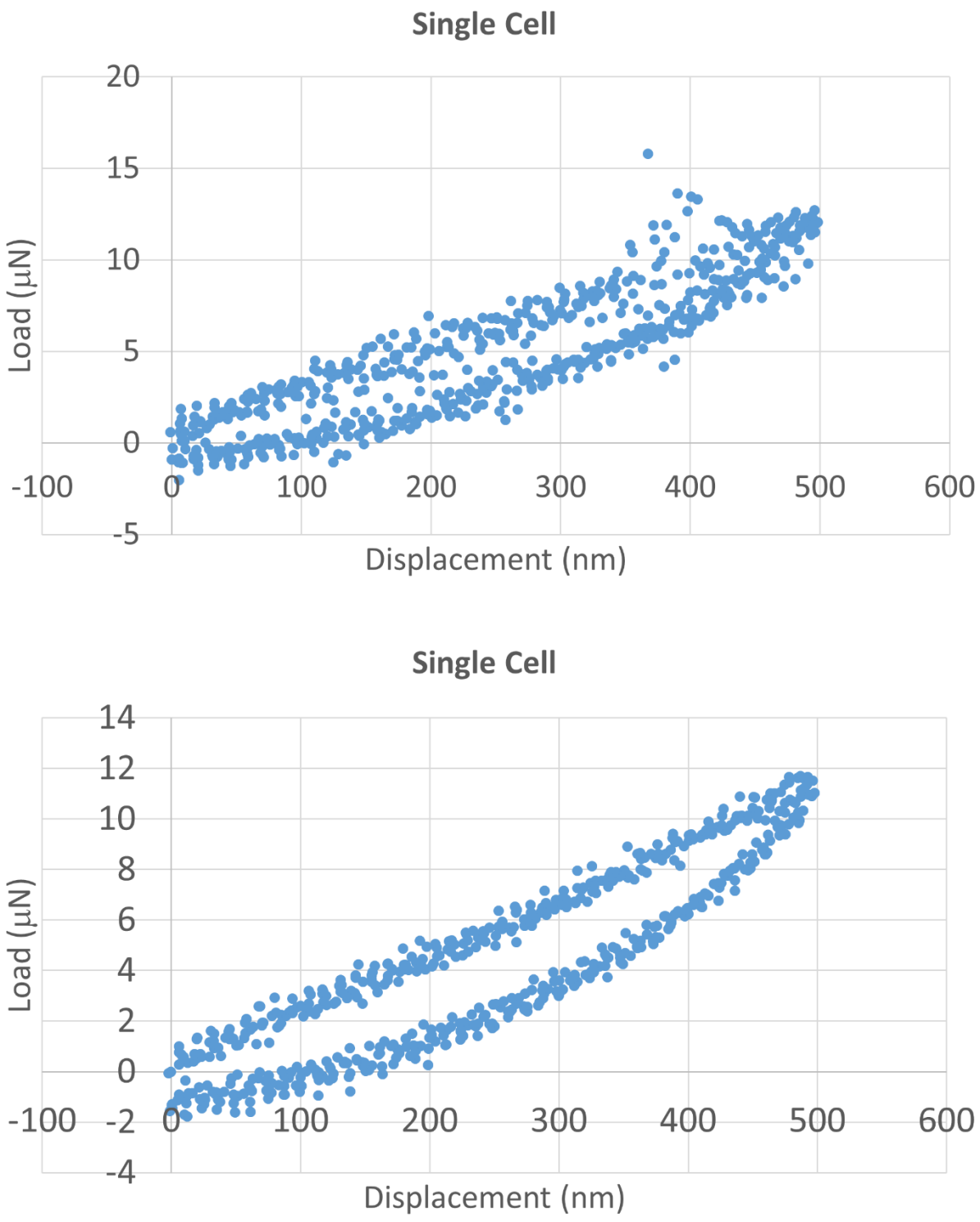

Figure A1. L-D curve on PCa single cell at maximum displacement 500 nm (Continued).

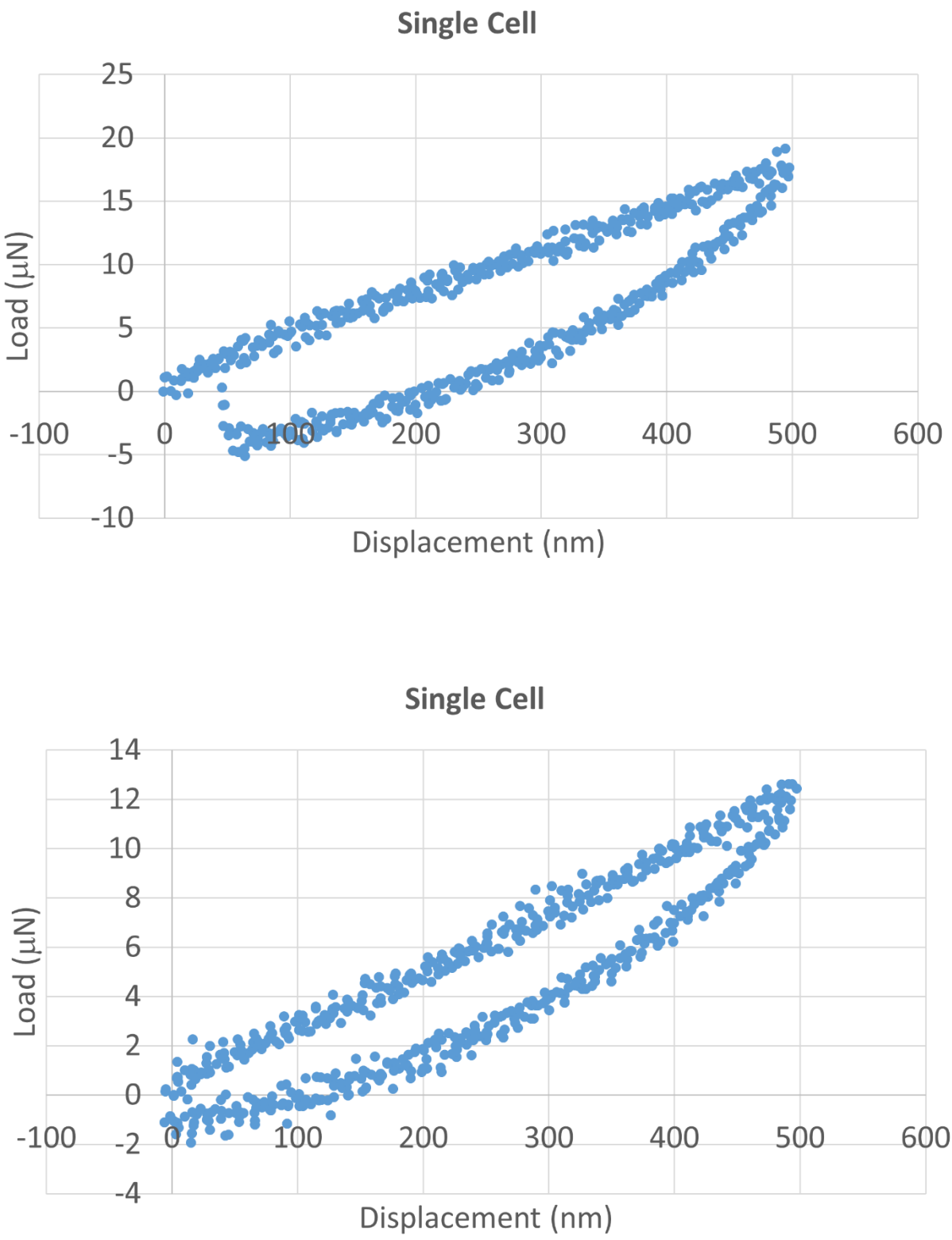

Figure A1. L-D curve on PCa single cell at maximum displacement 500 nm (Continued).

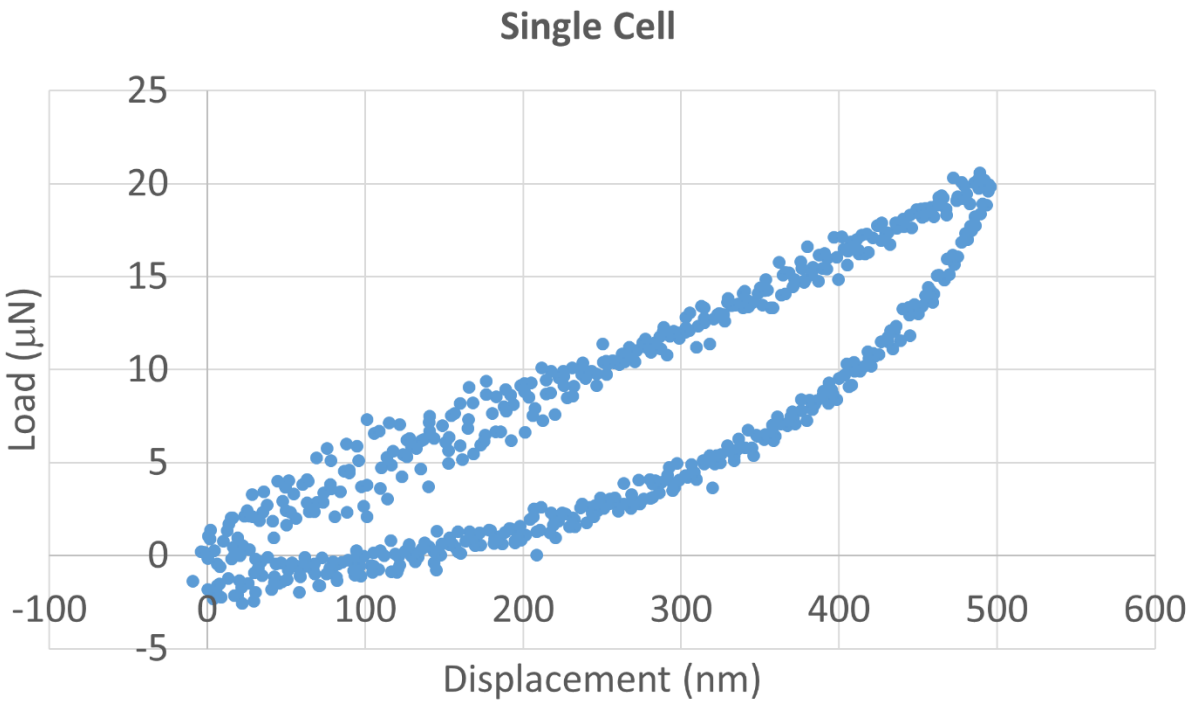

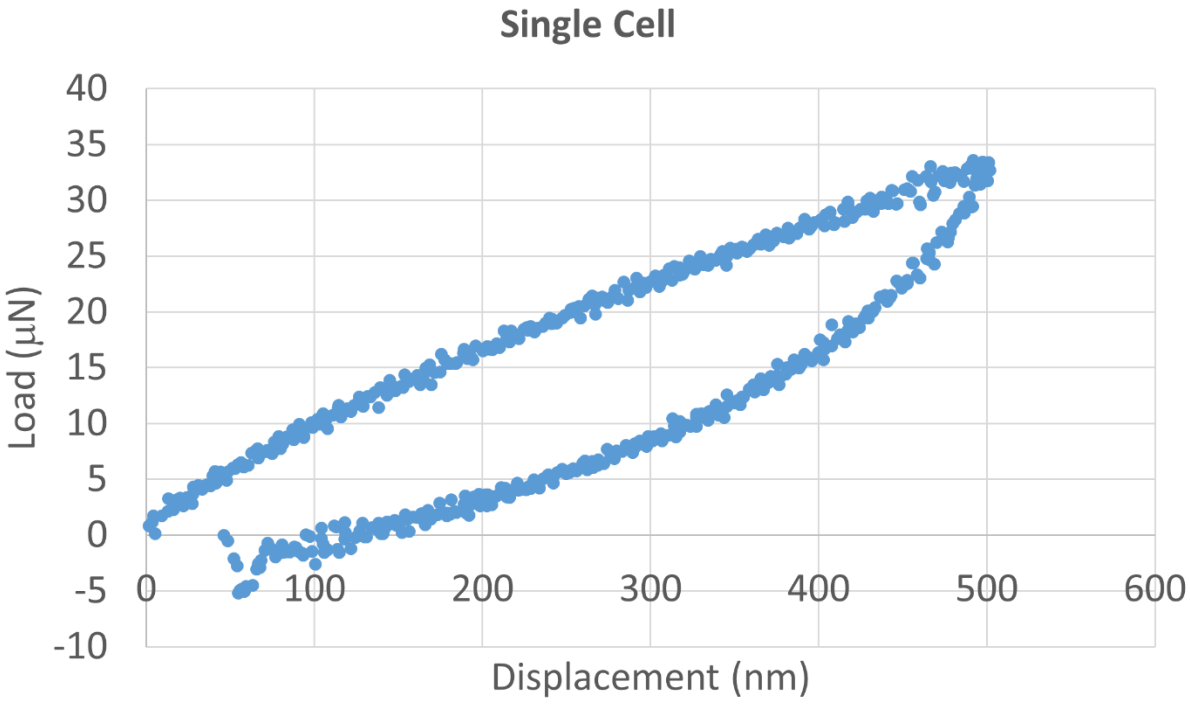

Figure A1. L-D curve on PCa single cell at maximum displacement 500 nm (Continued).

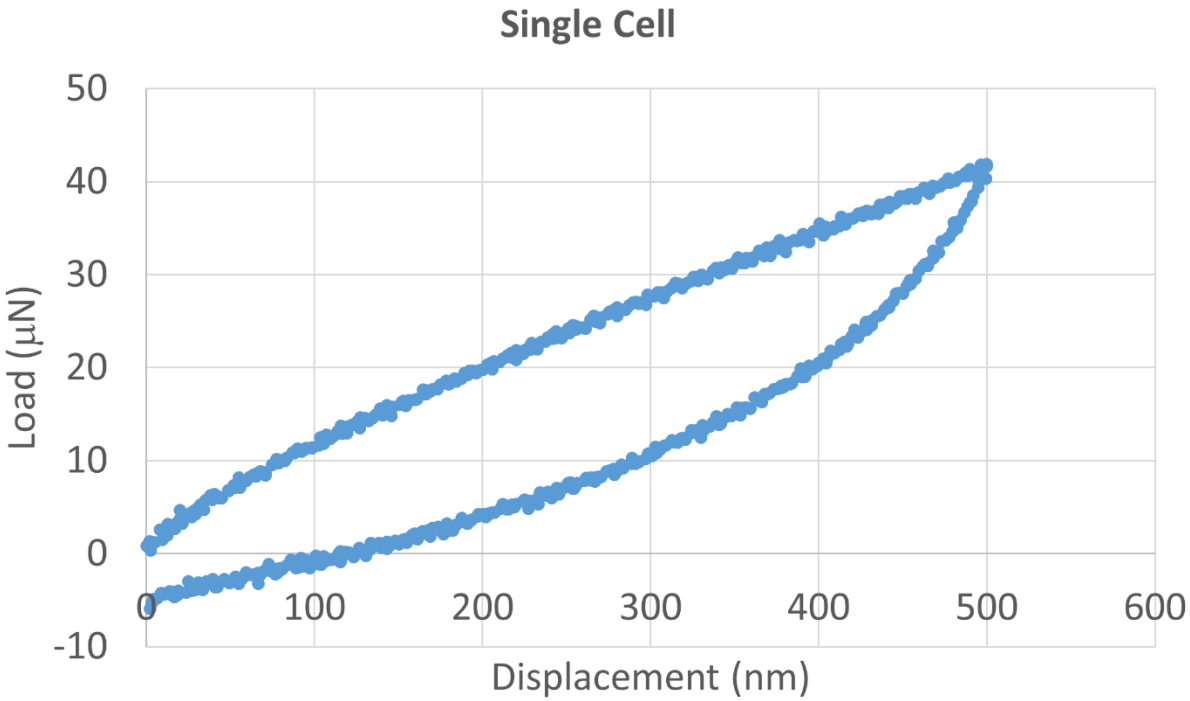

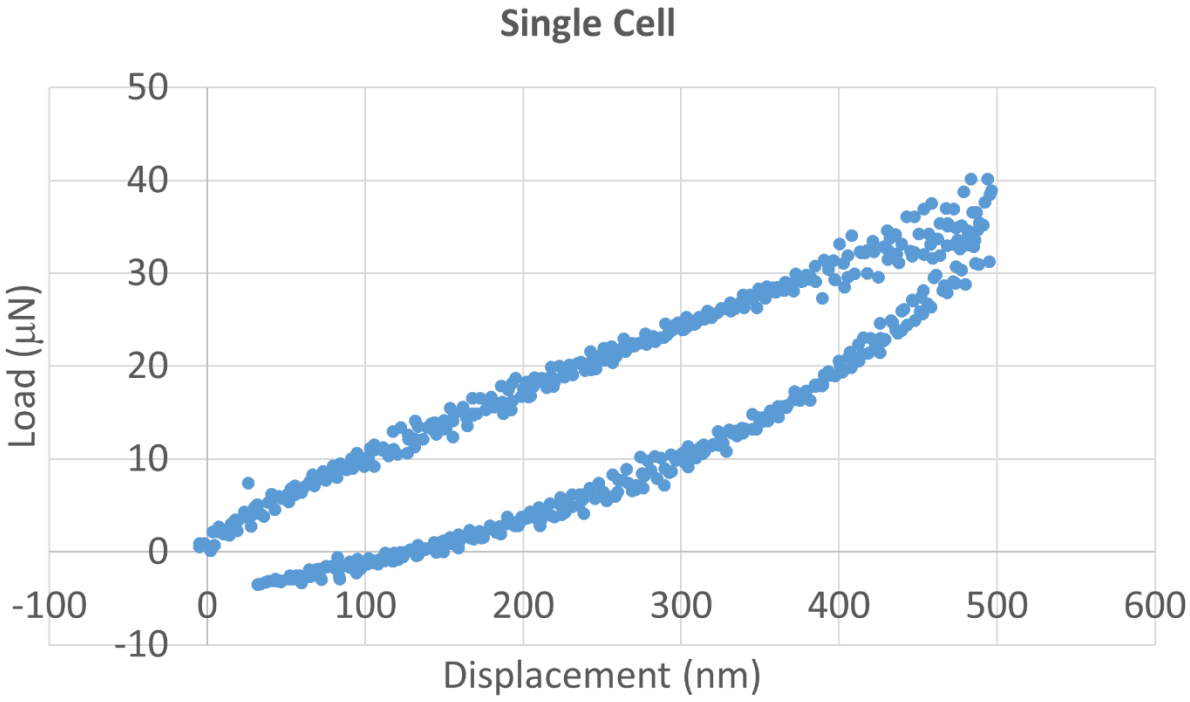

Figure A1. L-D curve on PCa single cell at maximum displacement 500 nm (Continued).

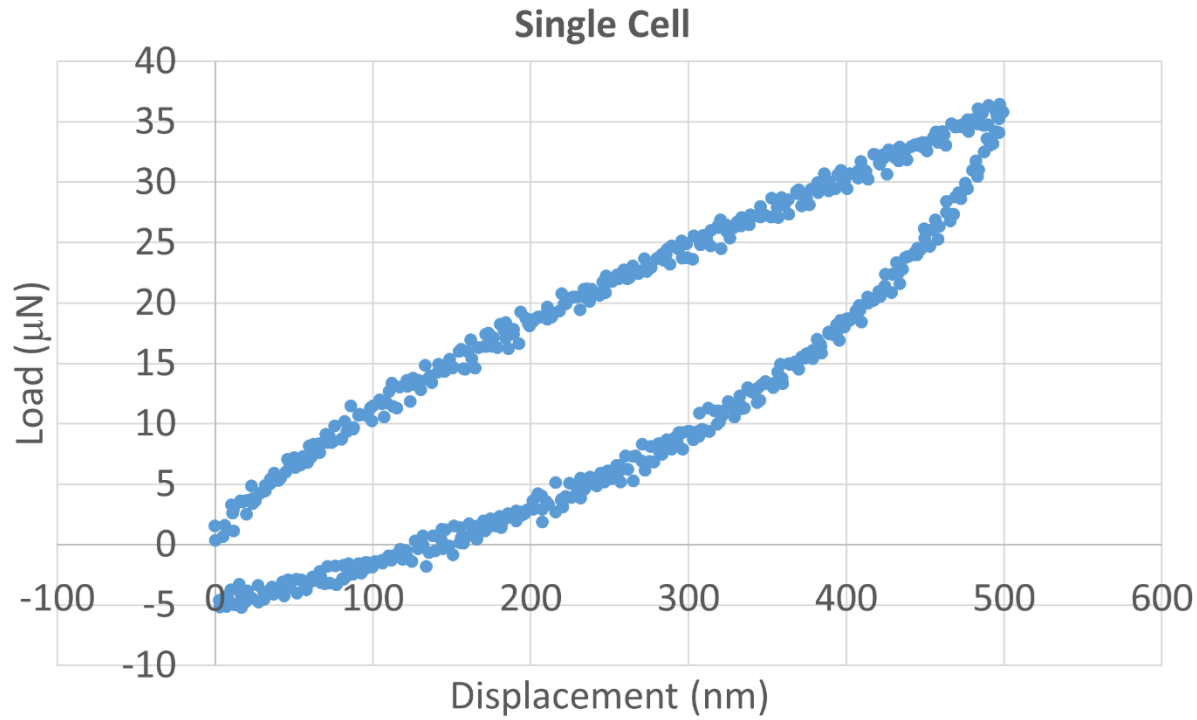

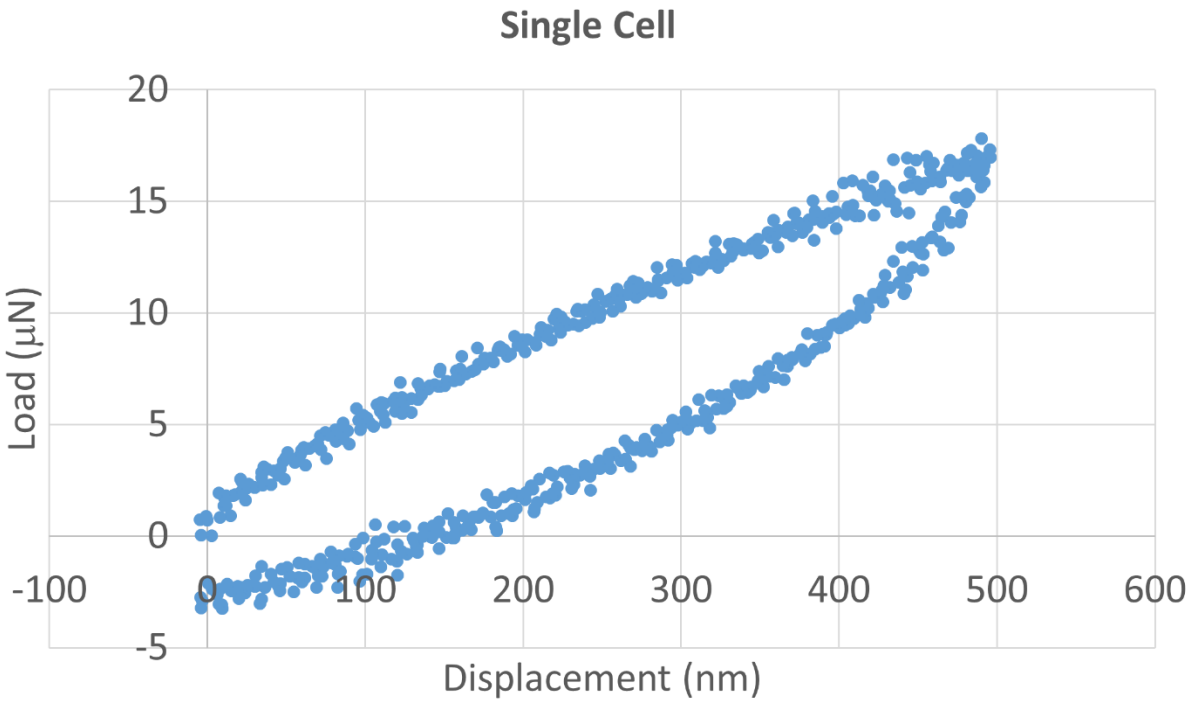

Figure A1. L-D curve on PCa single cell at maximum displacement 500 nm (Continued).

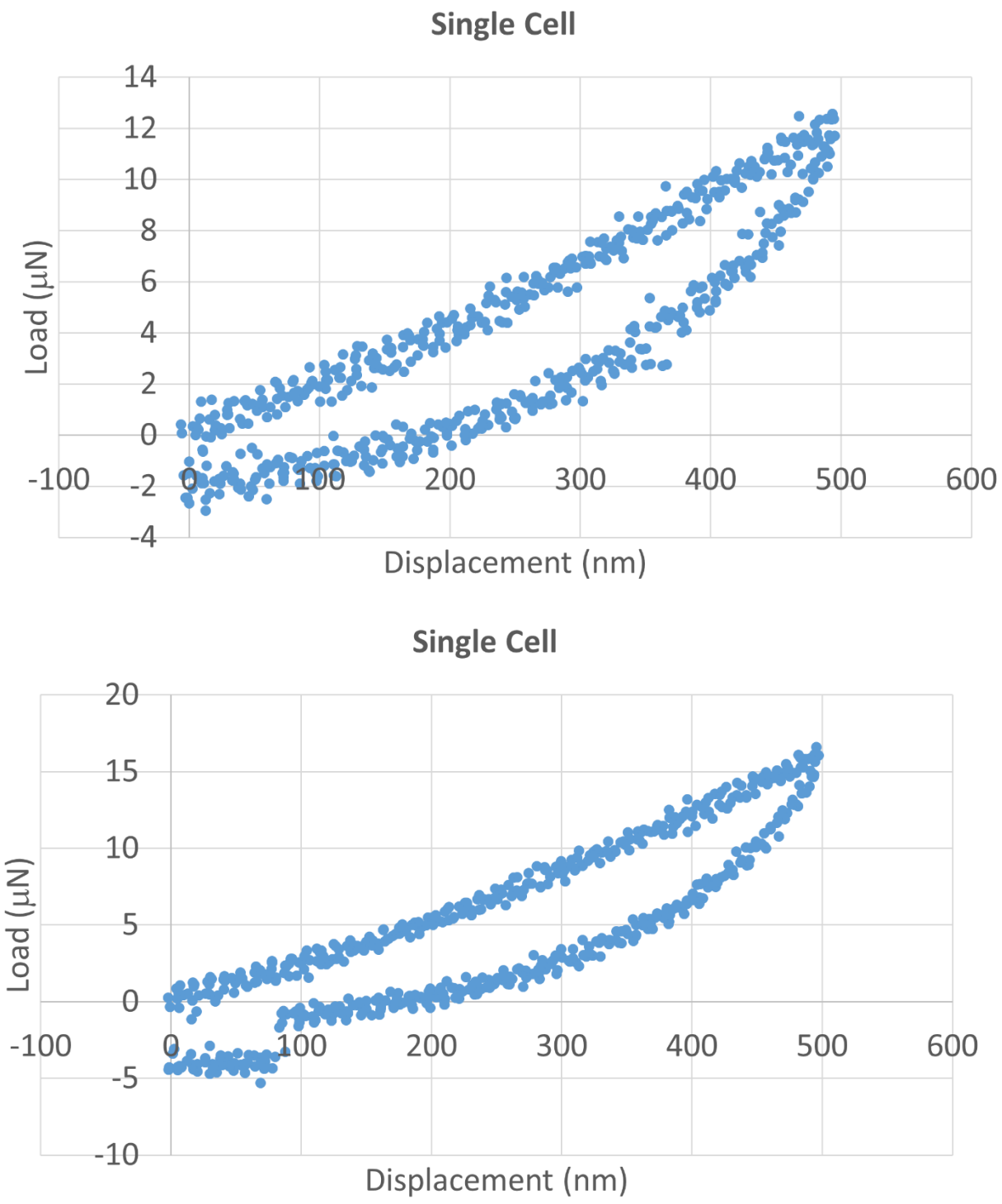

Figure A1. L-D curve on PCa single cell at maximum displacement 500 nm (Continued).

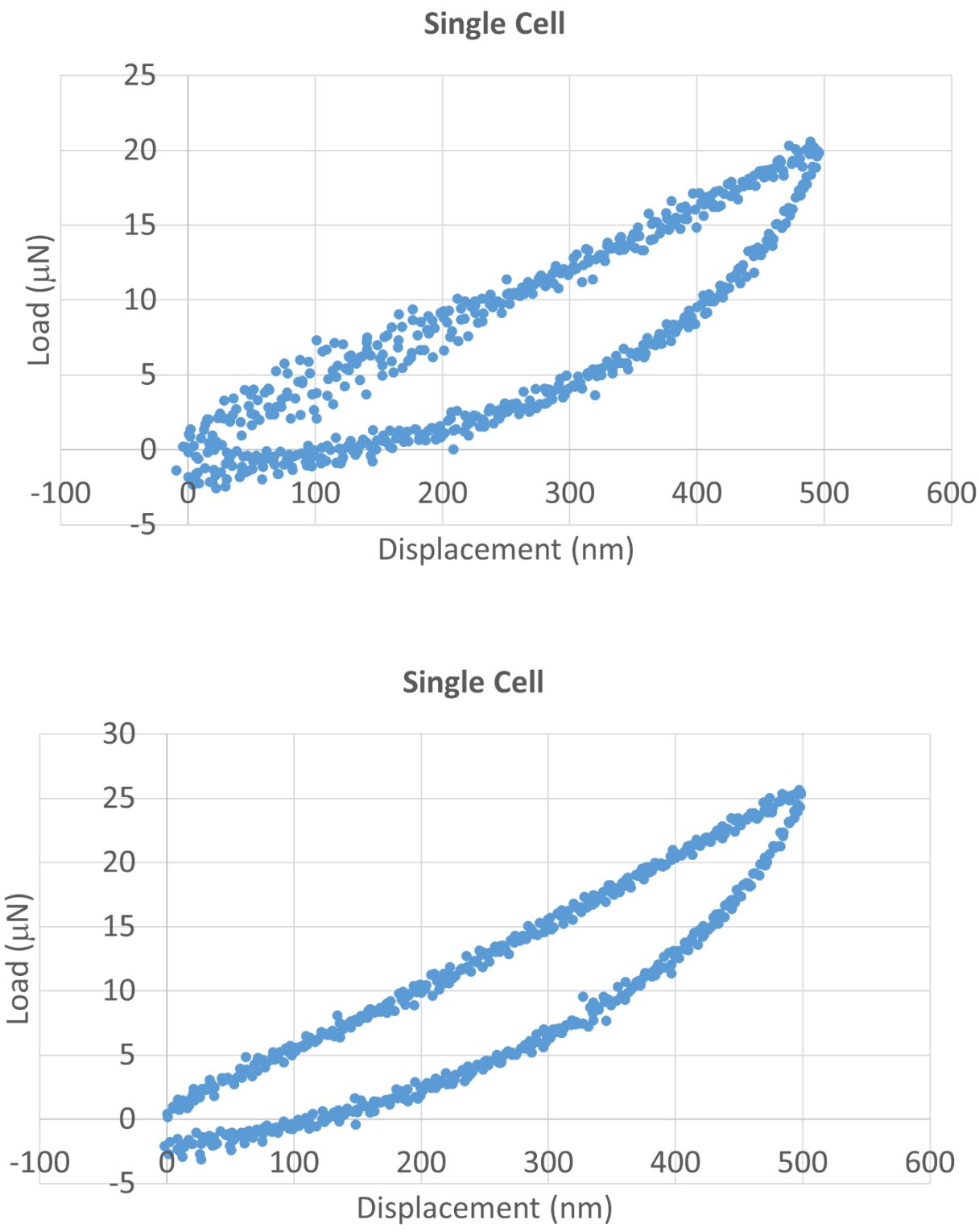

Figure A1. L-D curve on PCa single cell at maximum displacement 500 nm (Continued).

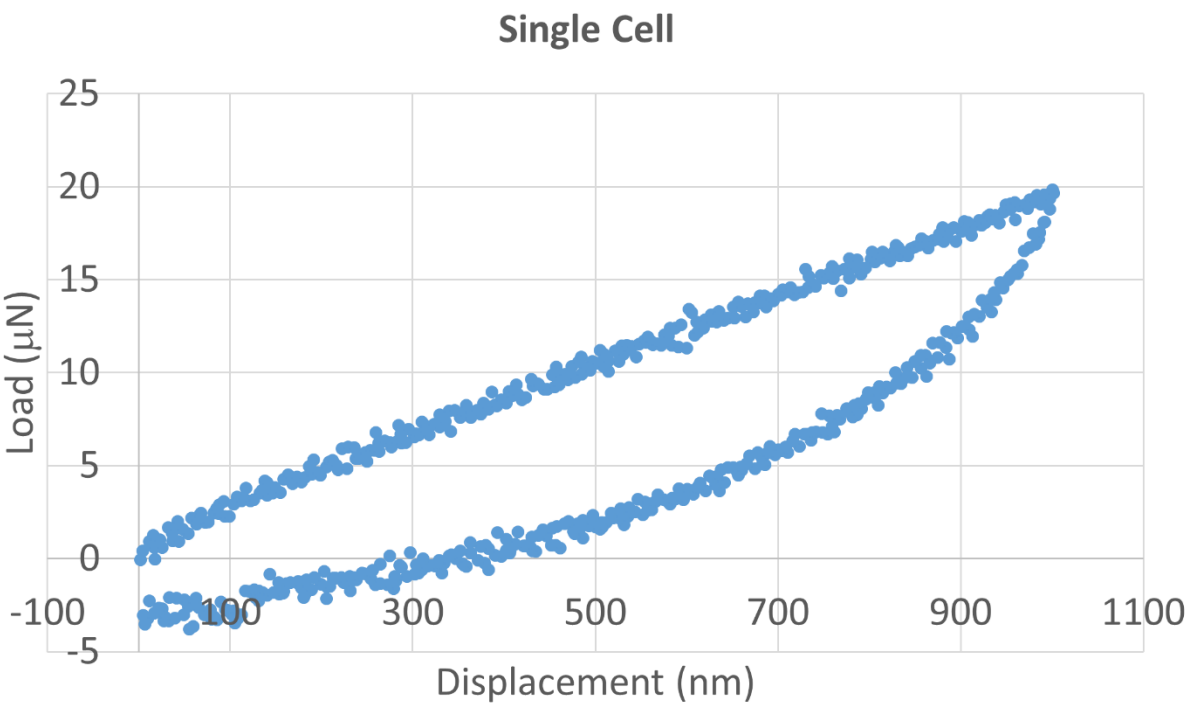

Figure A1. L-D curve on PCa single cell at maximum displacement 500 nm (Continued).

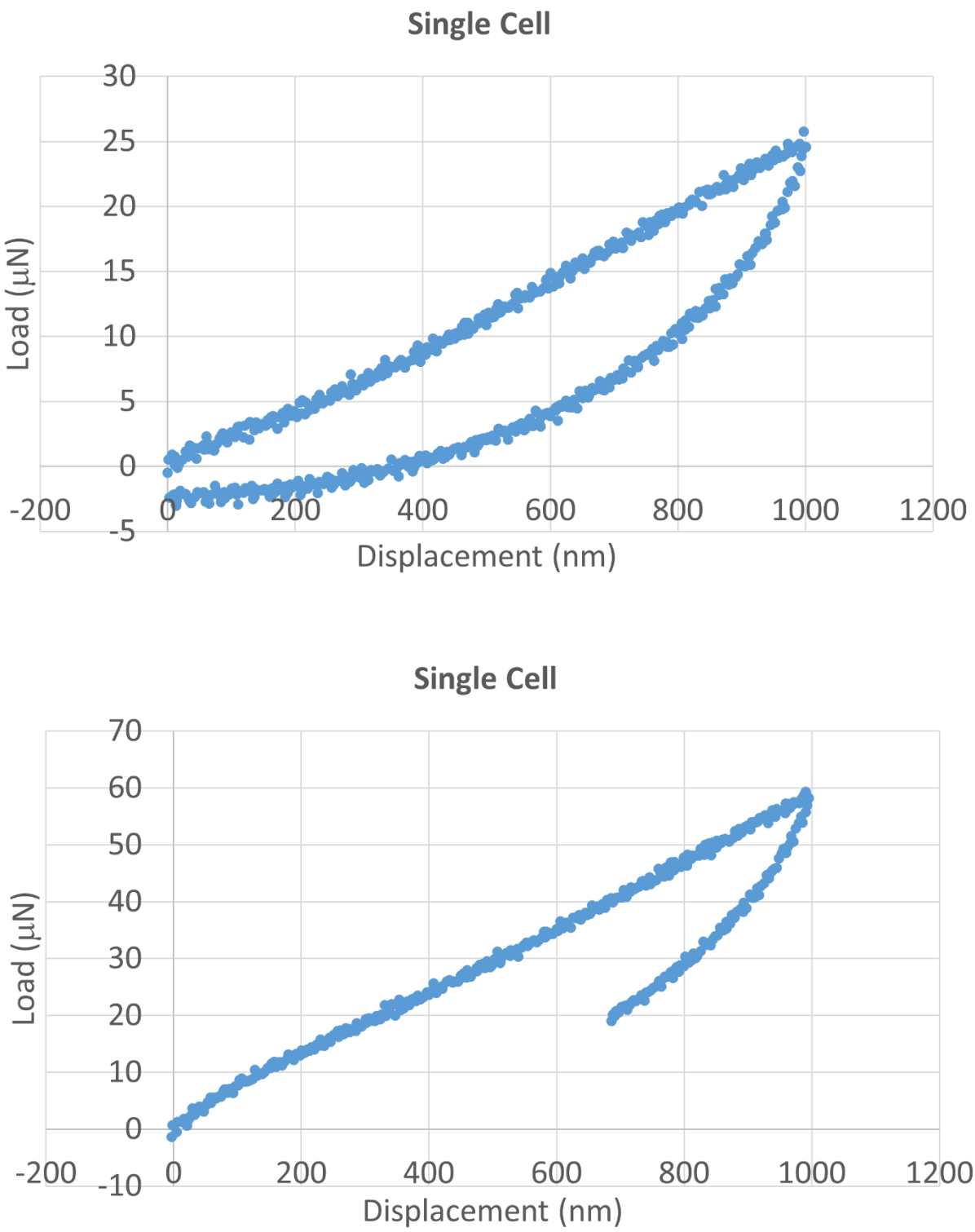

Figure A2. L-D curve on PCa single cell at maximum displacement 1000 nm.

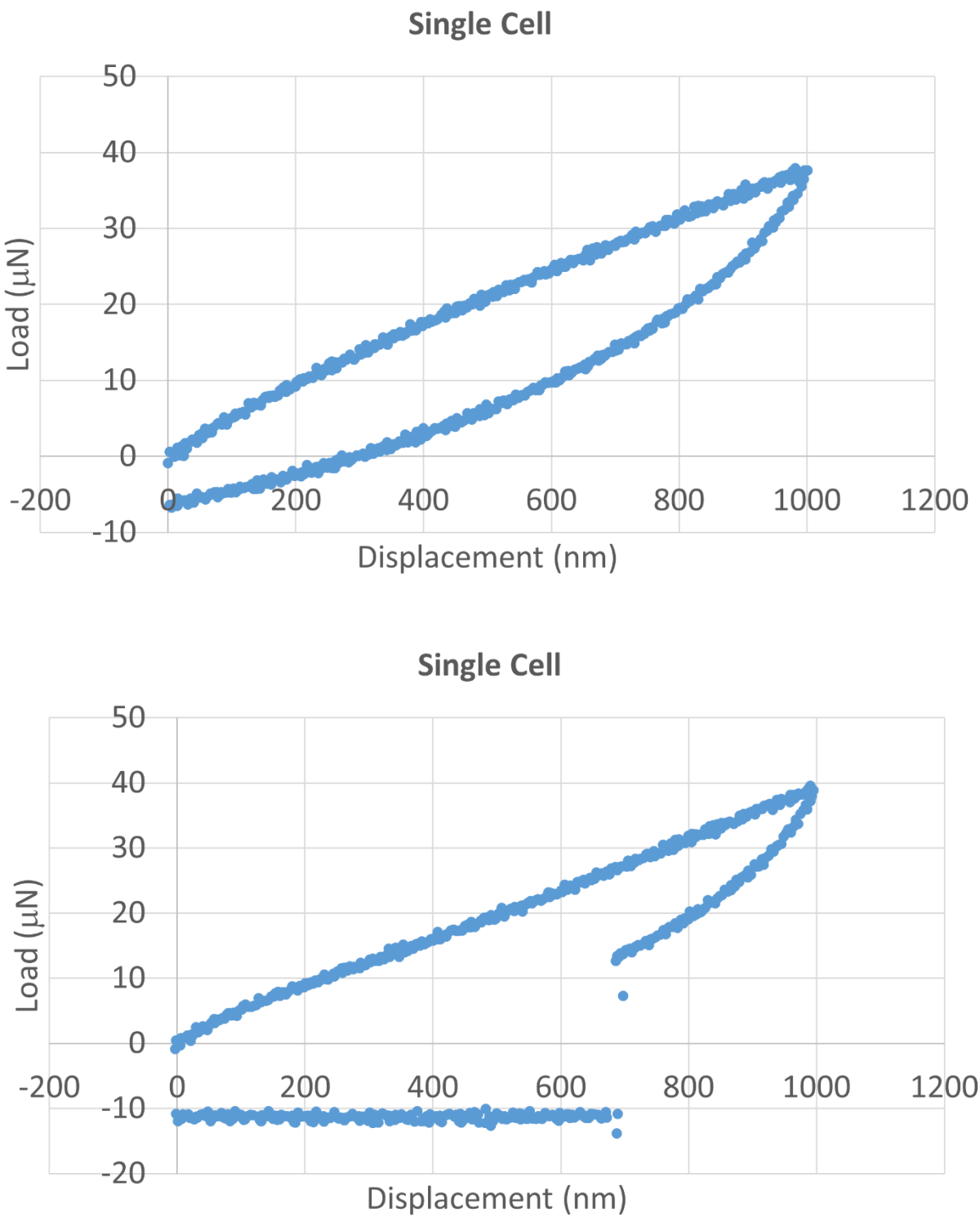

Figure A2. L-D curve on PCa single cell at maximum displacement 1000 nm (Continued).

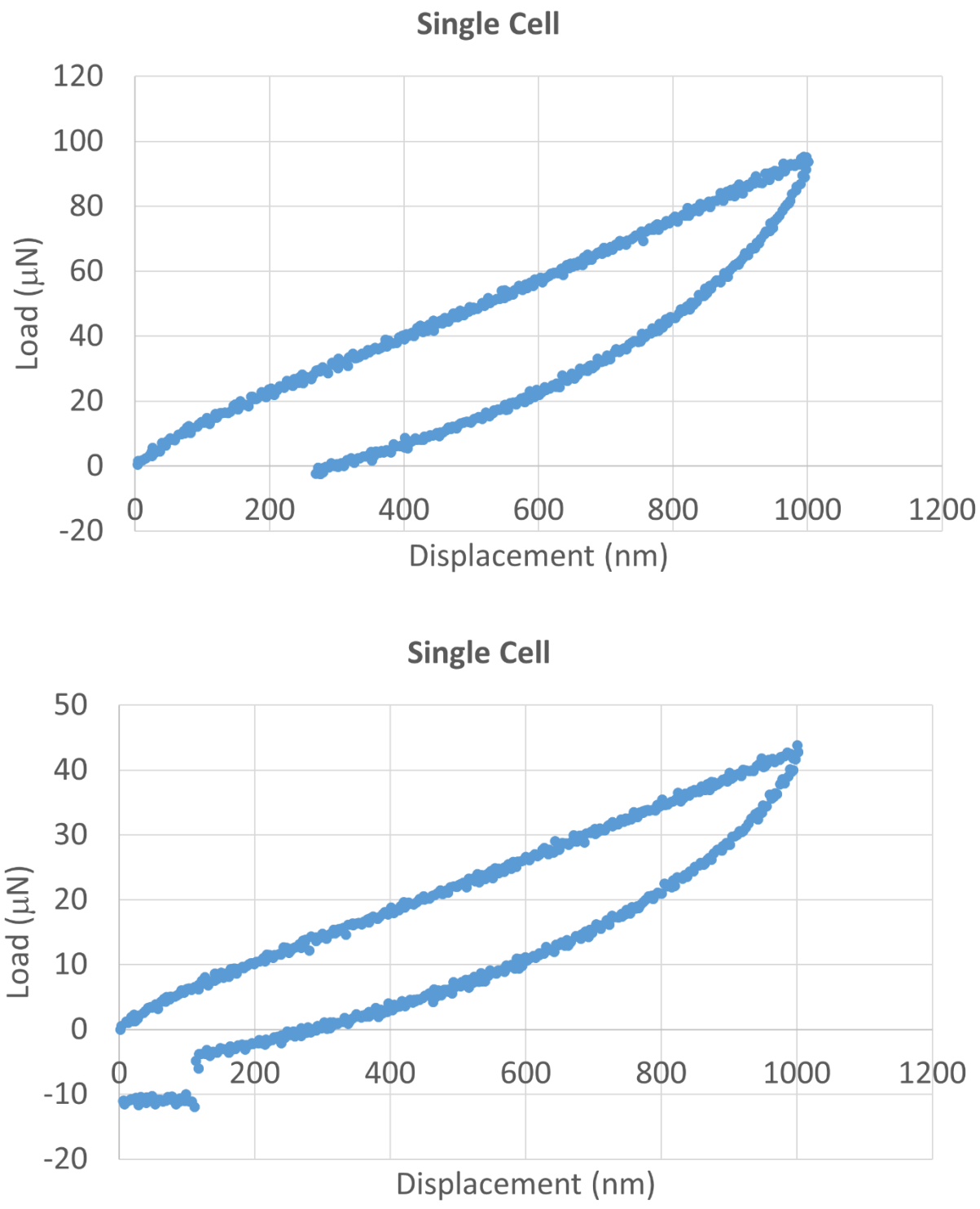

Figure A2. L-D curve on PCa single cell at maximum displacement 1000 nm (Continued).

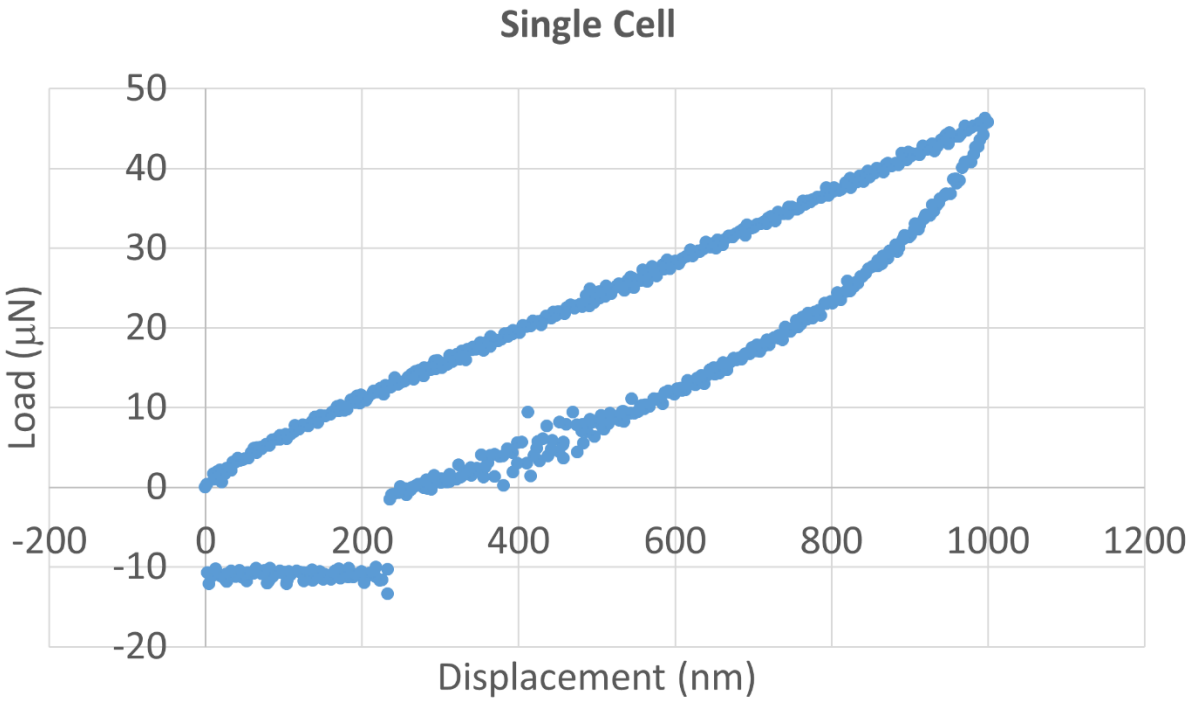

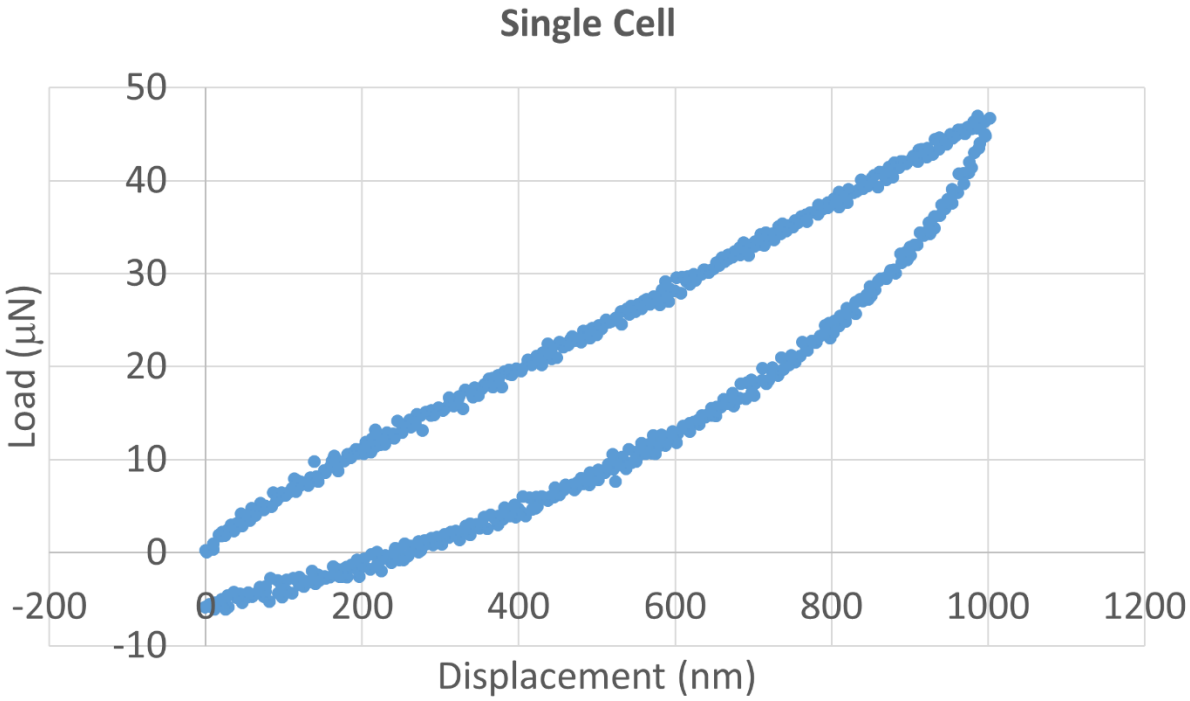

Figure A2. L-D curve on PCa single cell at maximum displacement 1000 nm (Continued).

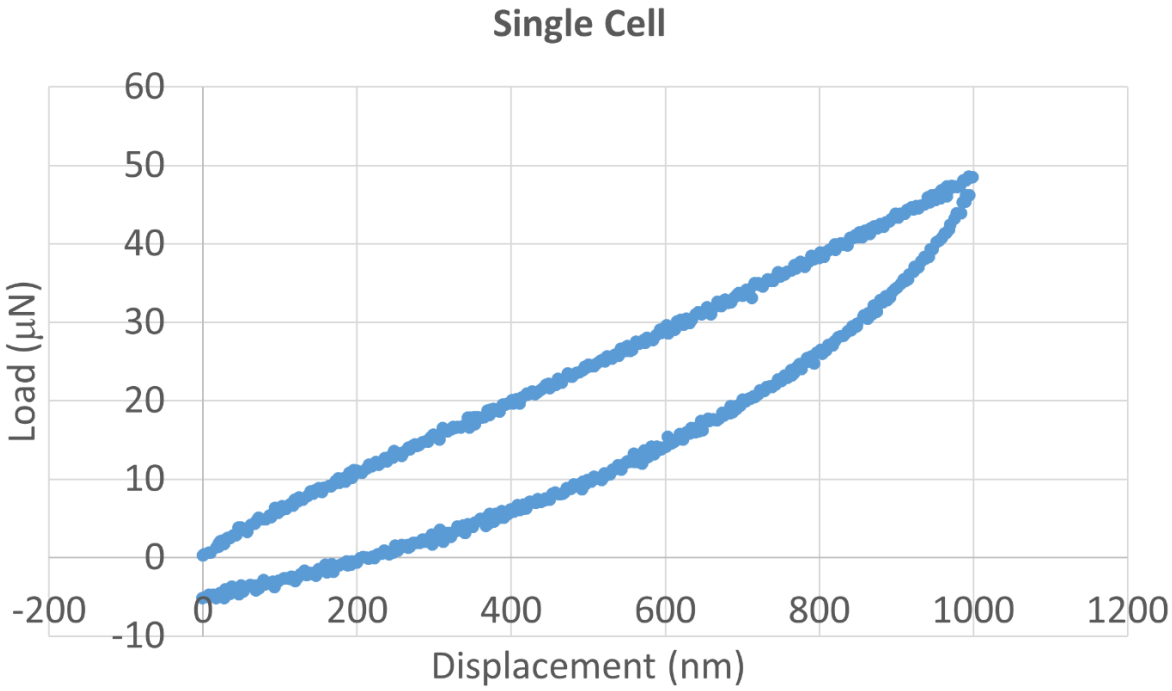

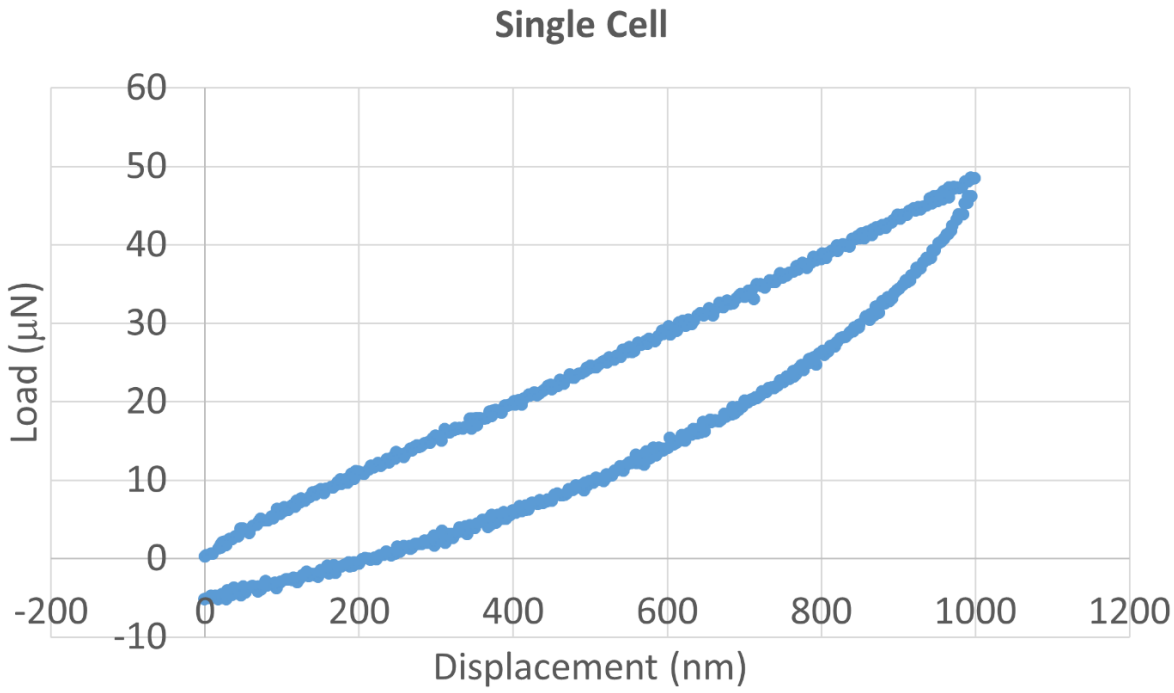

Figure A2. L-D curve on PCa single cell at maximum displacement 1000 nm (Continued).

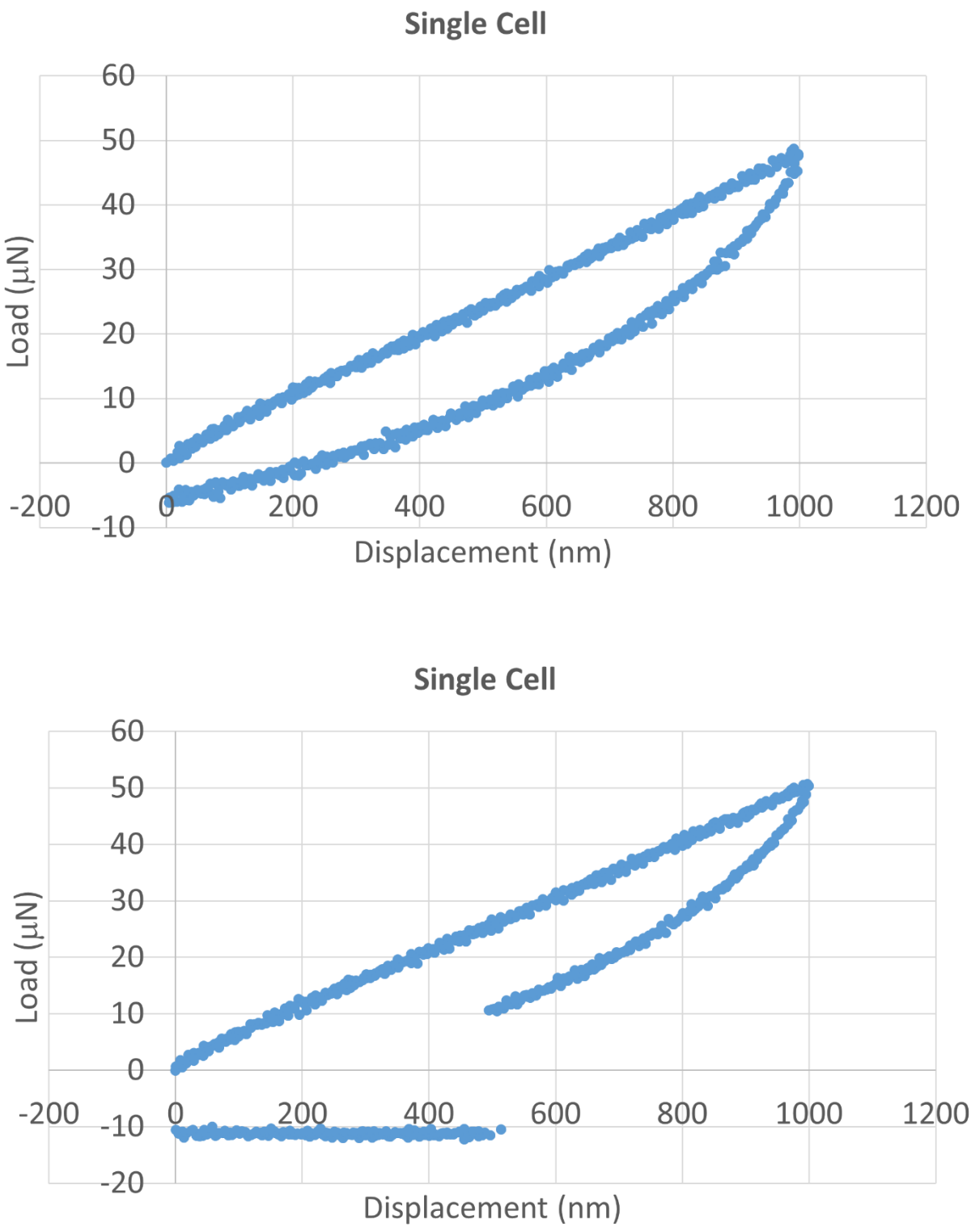

Figure A2. L-D curve on PCa single cell at maximum displacement 1000 nm (Continued).

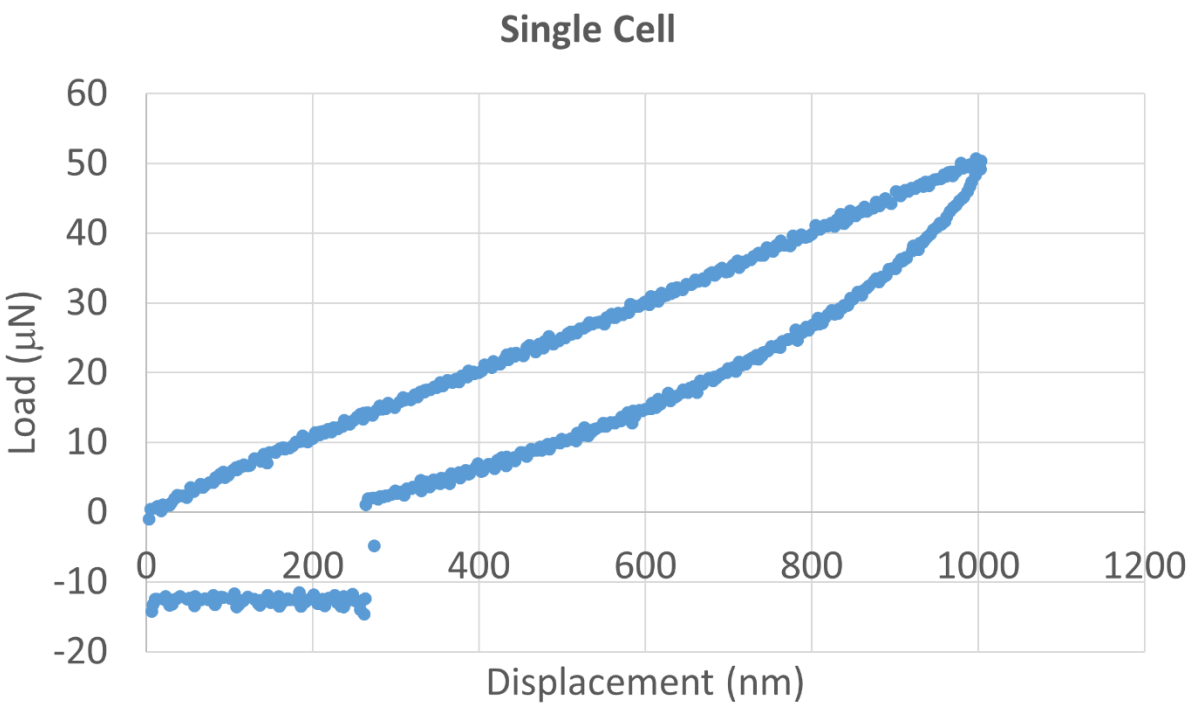

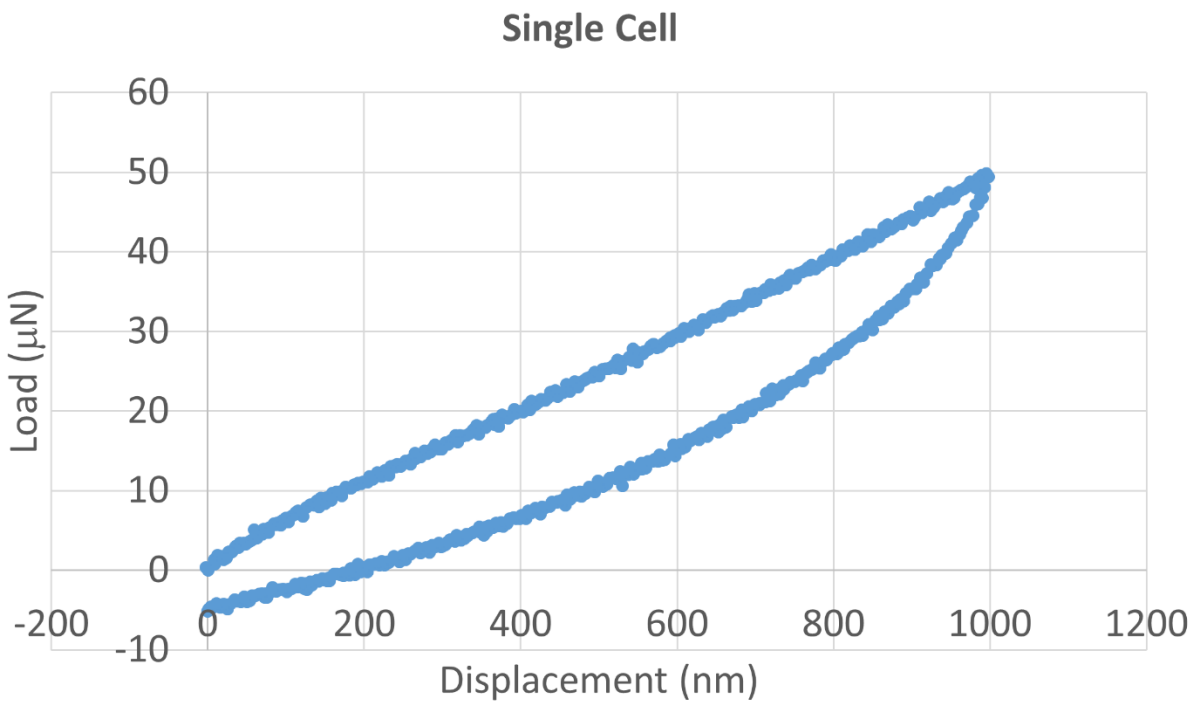

Figure A2. L-D curve on PCa single cell at maximum displacement 1000 nm (Continued).

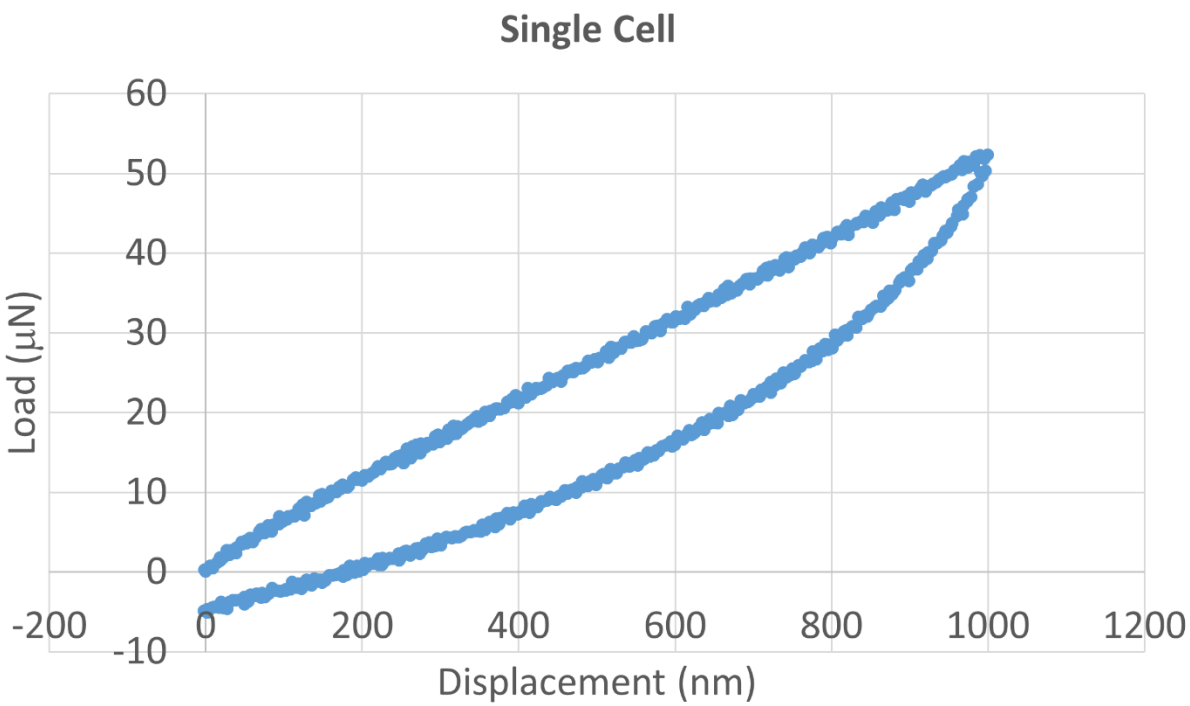

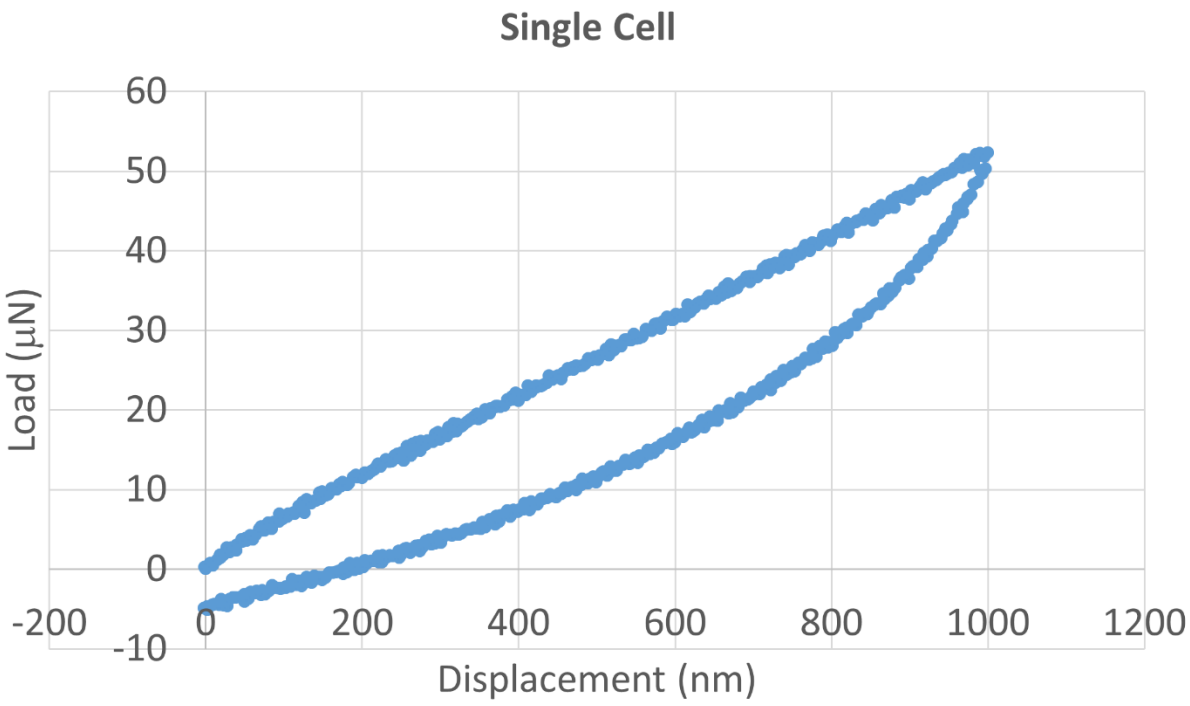

Figure A2. L-D curve on PCa single cell at maximum displacement 1000 nm (Continued).

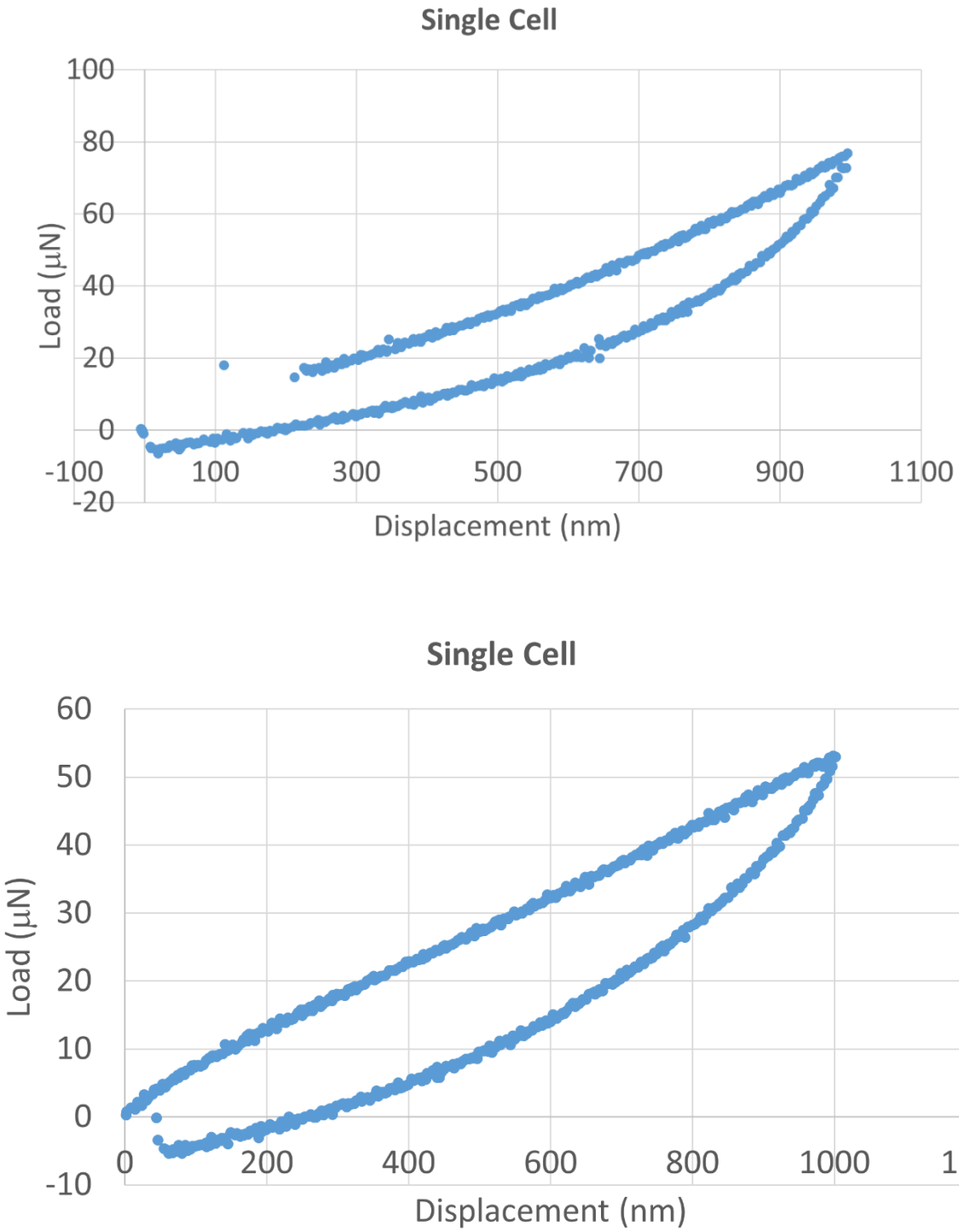

Figure A2. L-D curve on PCa single cell at maximum displacement 1000 nm (Continued).

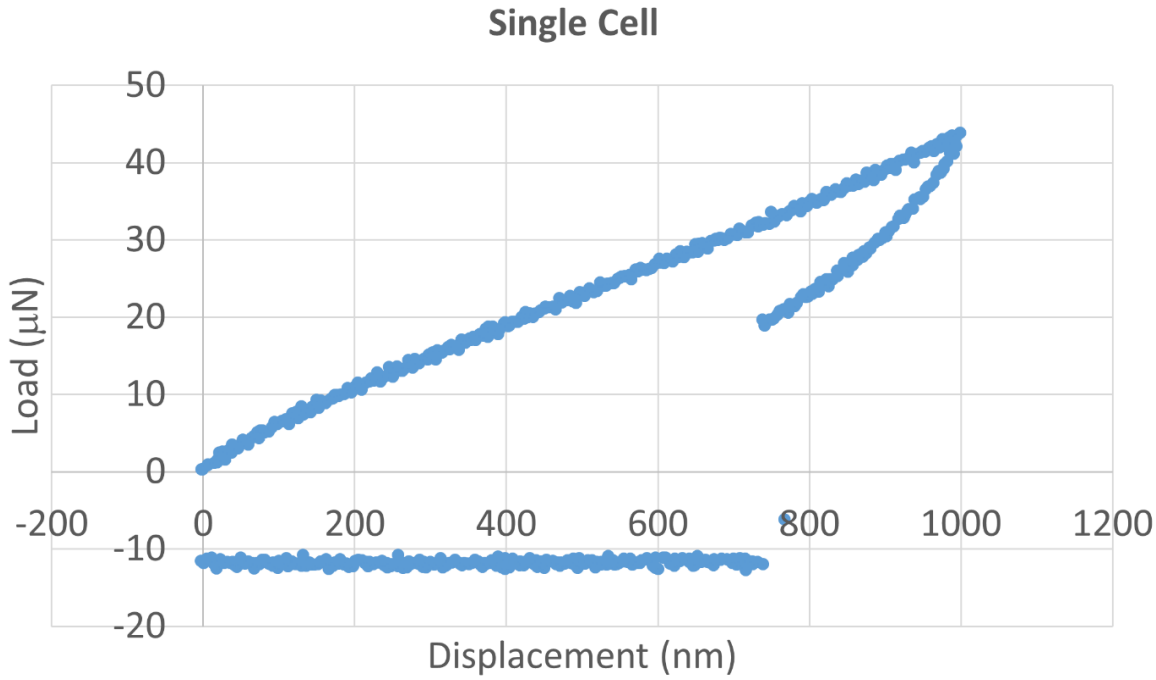

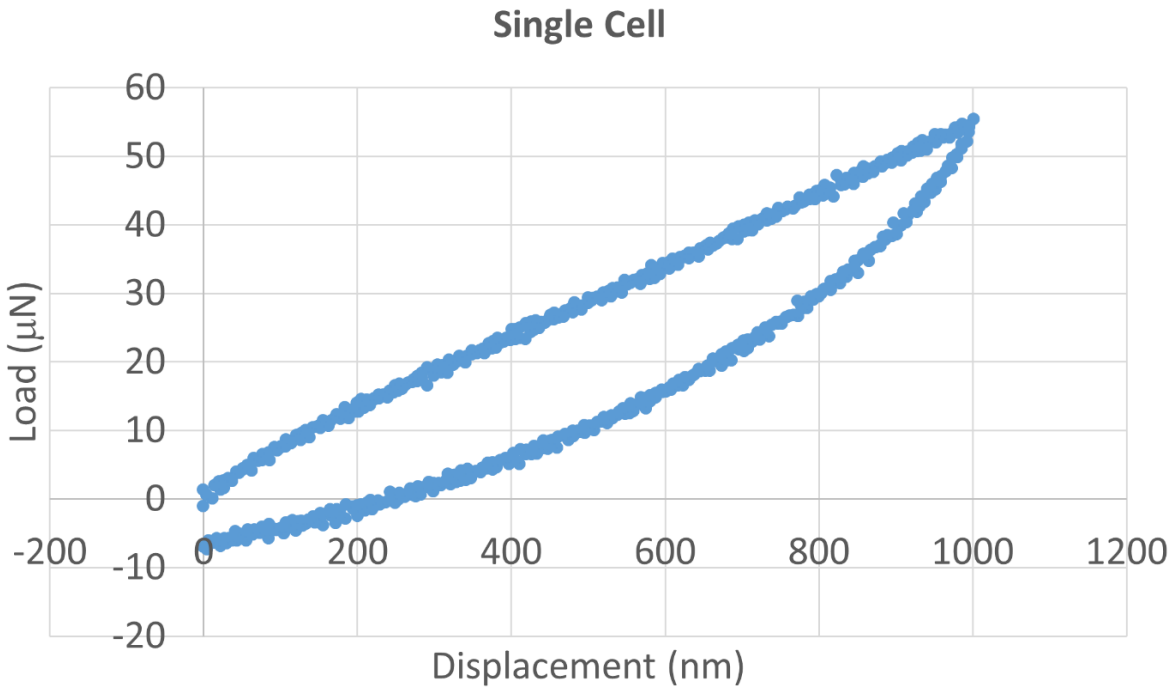

Figure A2. L-D curve on PCa single cell at maximum displacement 1000 nm (Continued).

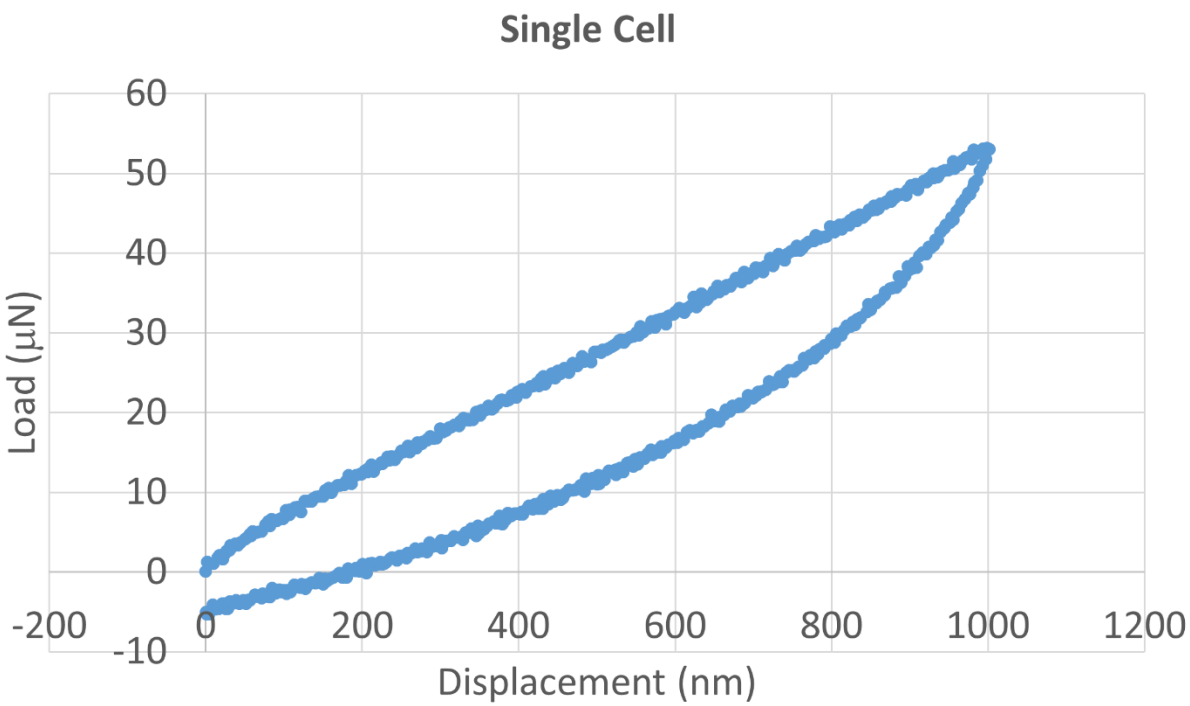

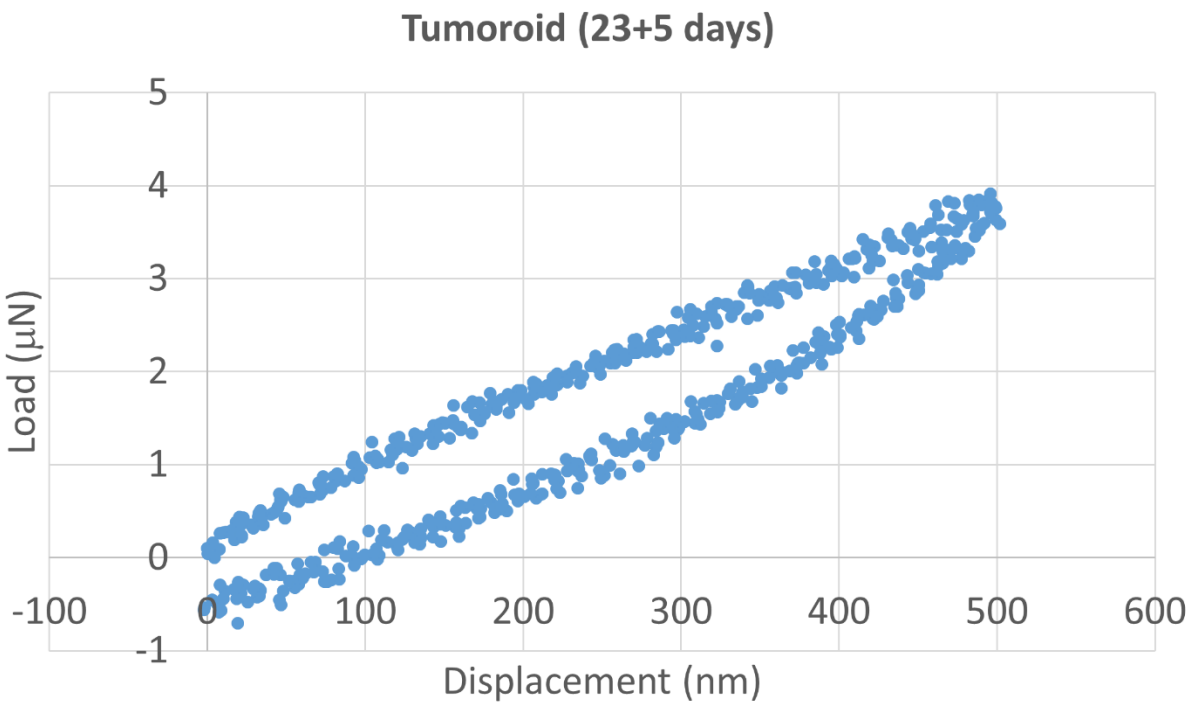

Figure A2. L-D curve on PCa single cell at maximum displacement 1000 nm (Continued).

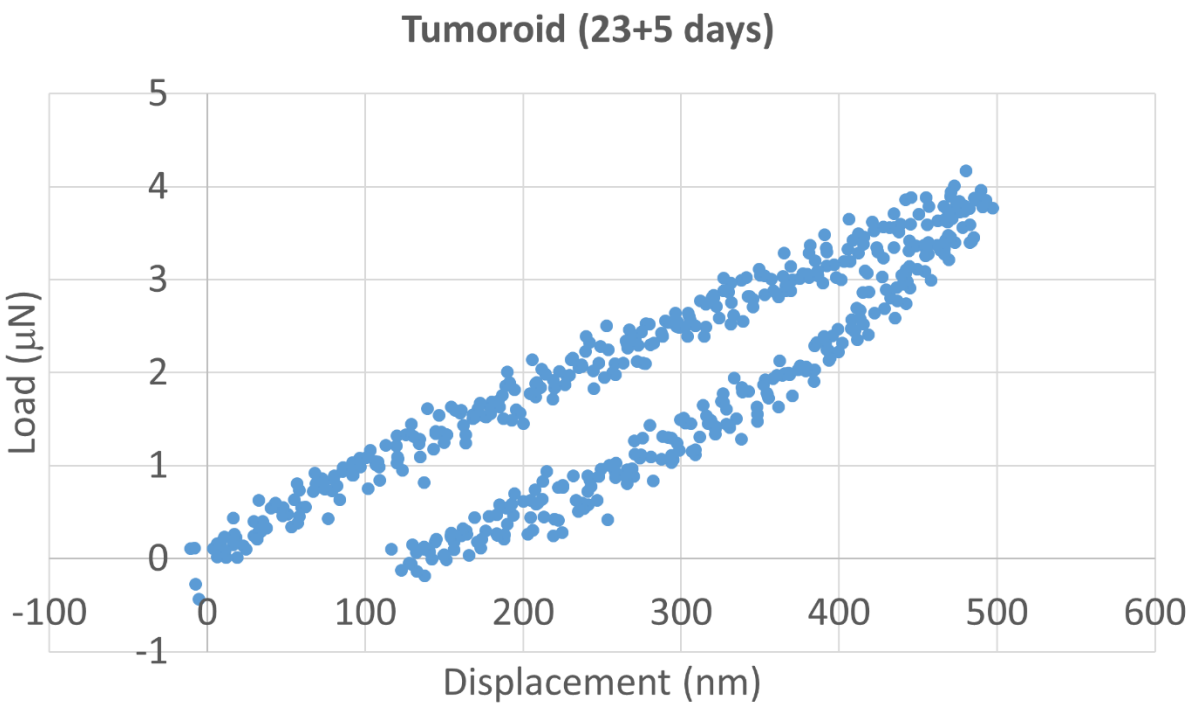

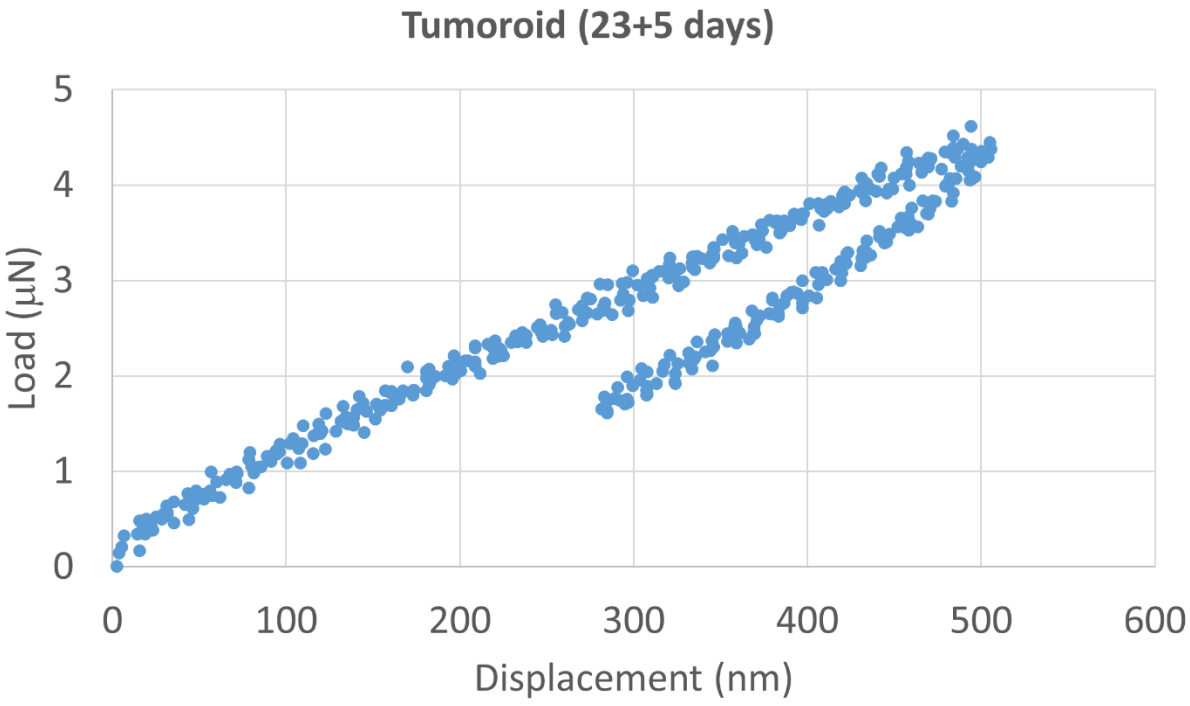

Figure A3. L-D curve on tumoroid at maximum displacement 500 nm (day 23+5).

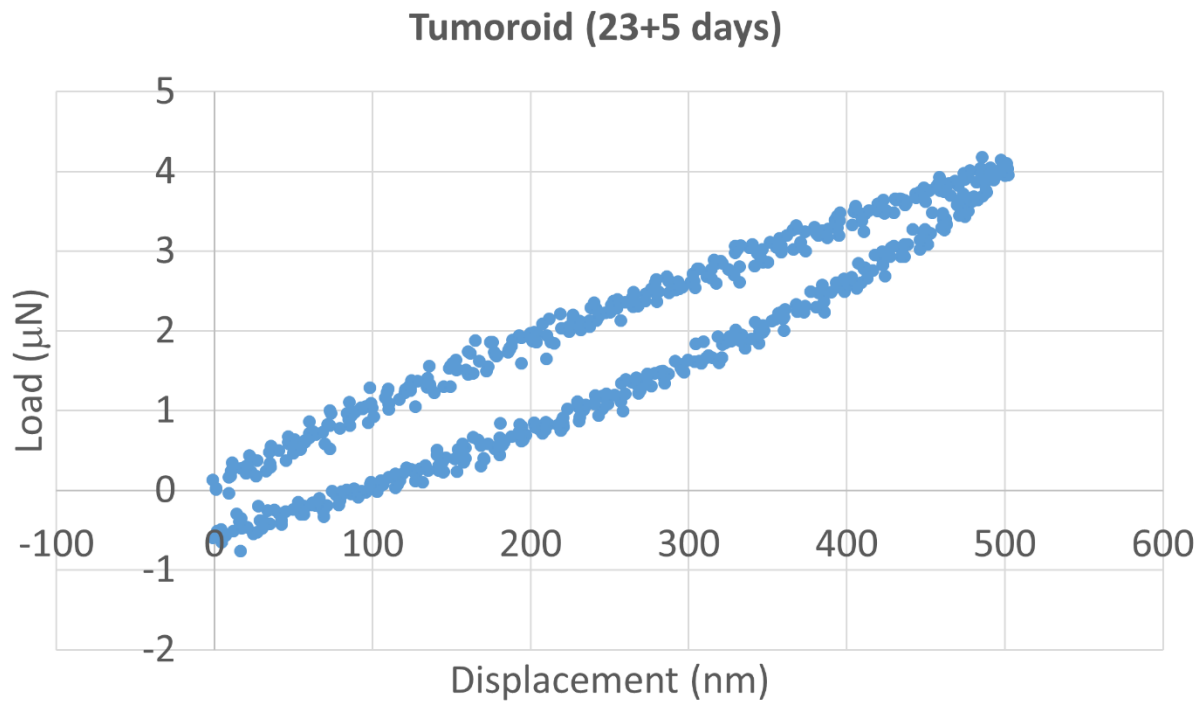

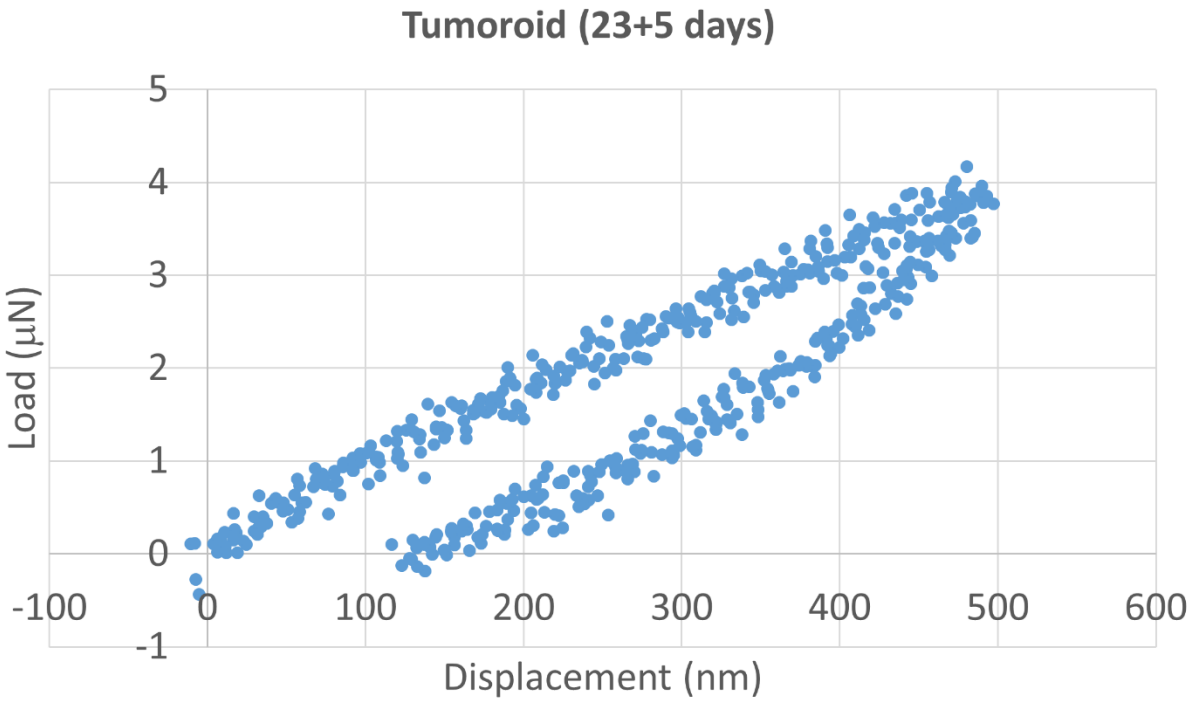

Figure A3. L-D curve on tumoroid at maximum displacement 500 nm (day 23+5) (Continued).

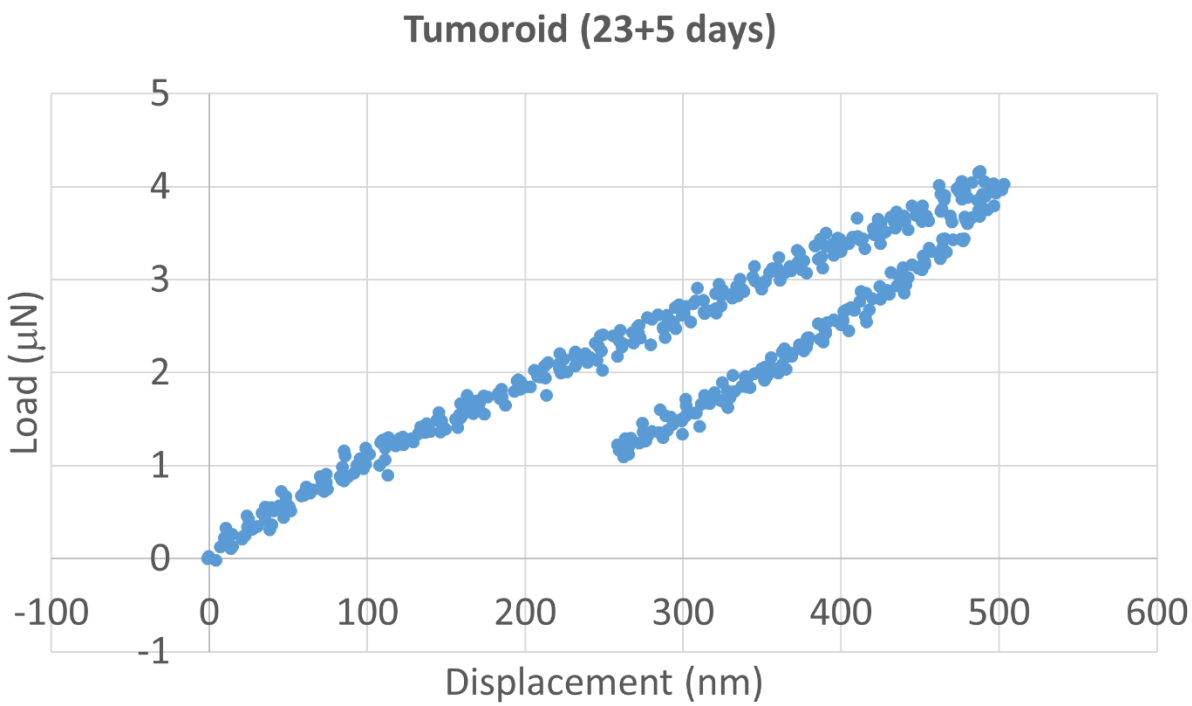

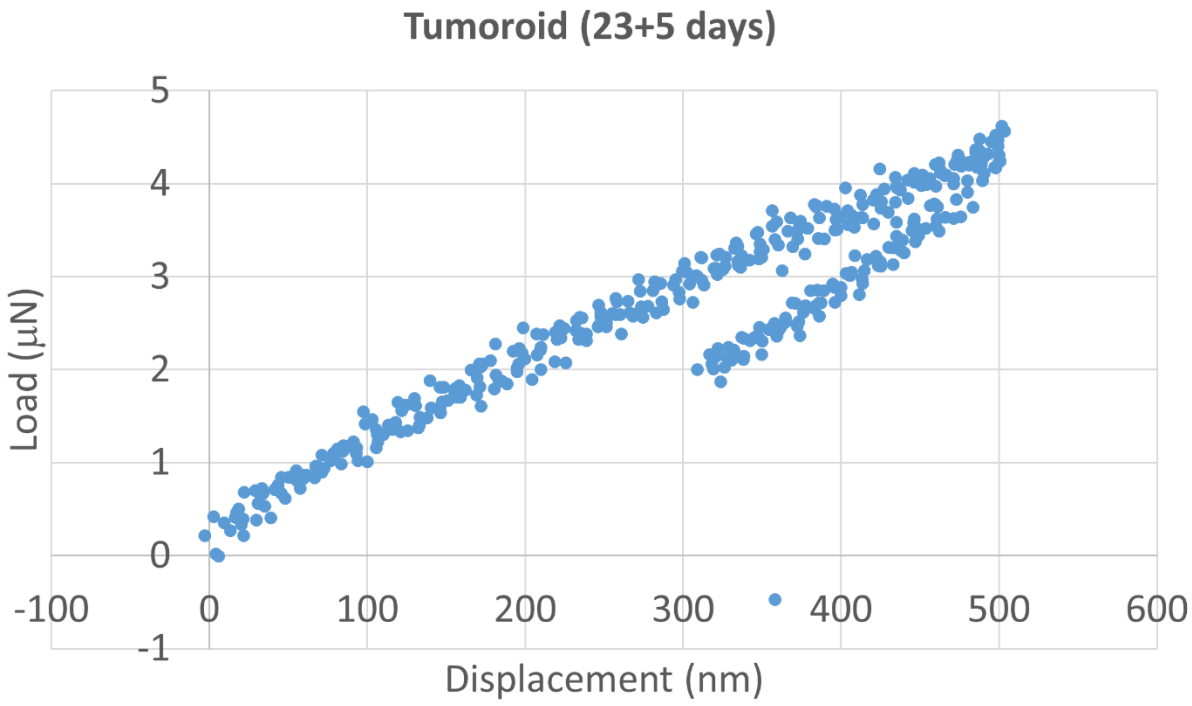

Figure A3. L-D curve on tumoroid at maximum displacement 500 nm (day 23+5) (Continued).

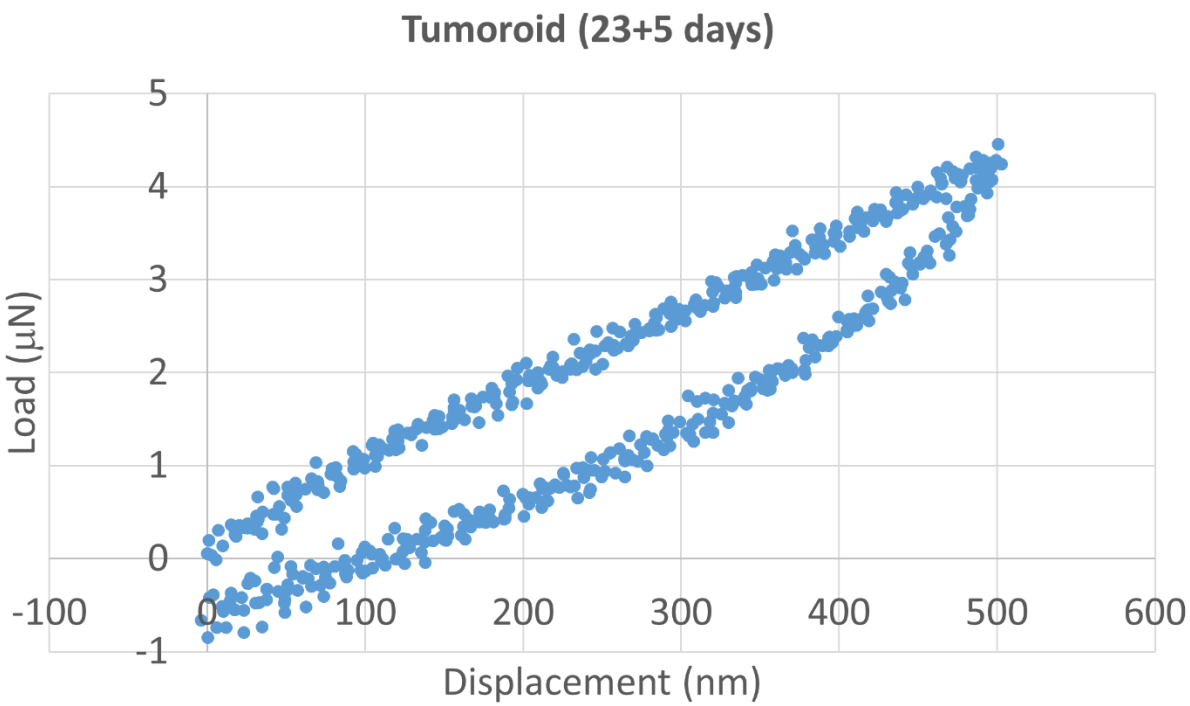

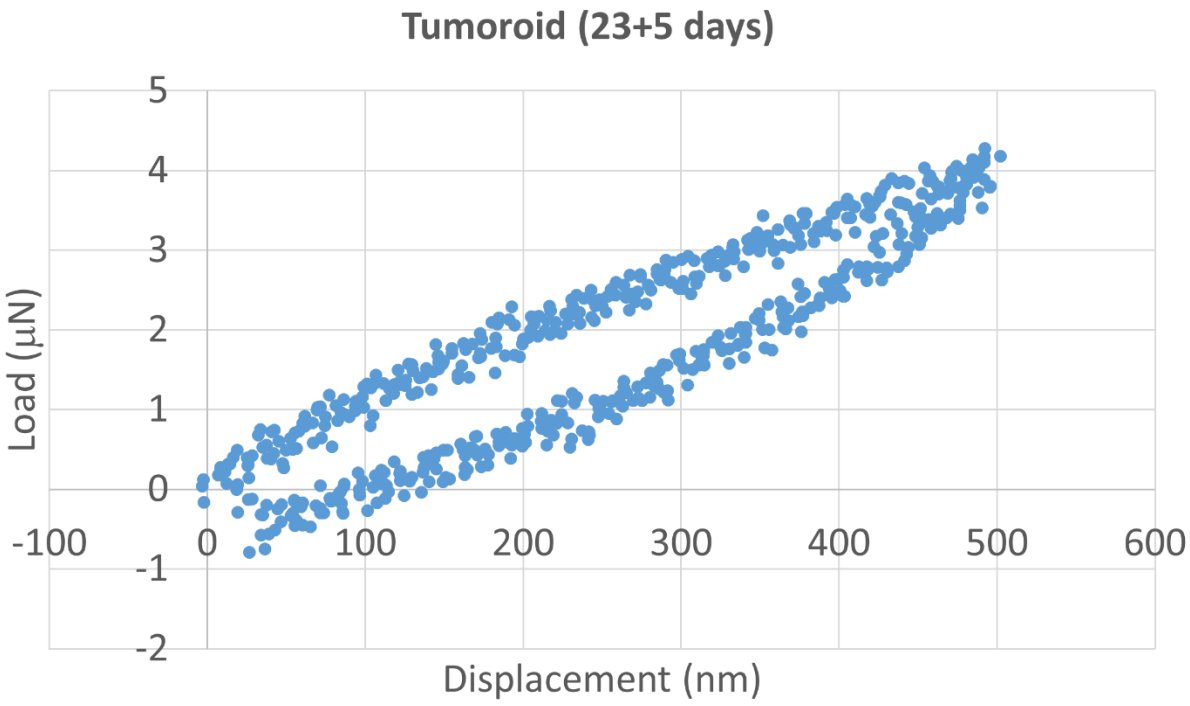

Figure A3. L-D curve on tumoroid at maximum displacement 500 nm (day 23+5) (Continued).

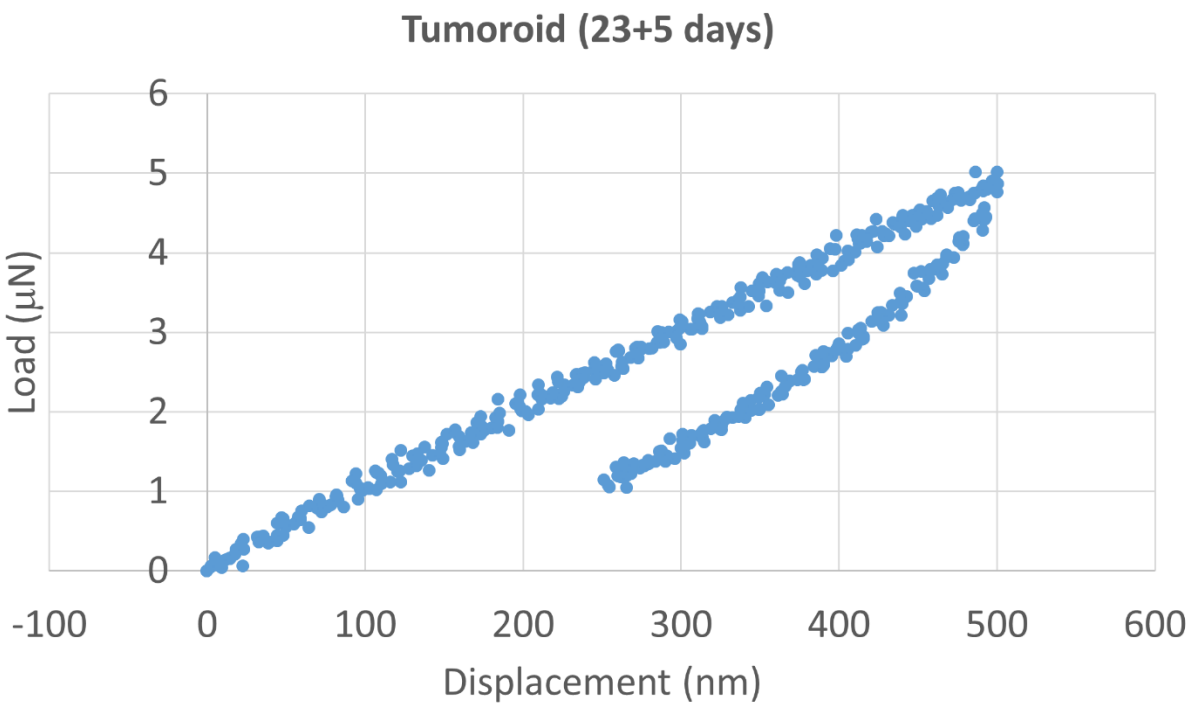

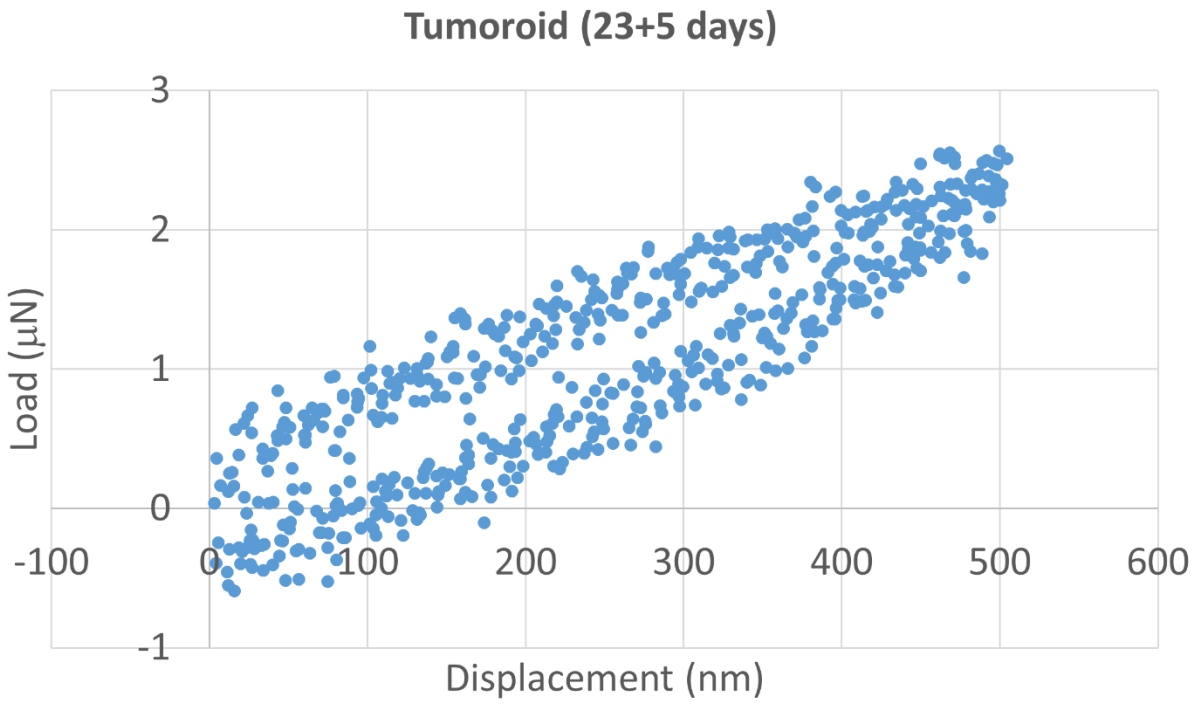

Figure A3. L-D curve on tumoroid at maximum displacement 500 nm (day 23+5) (Continued).

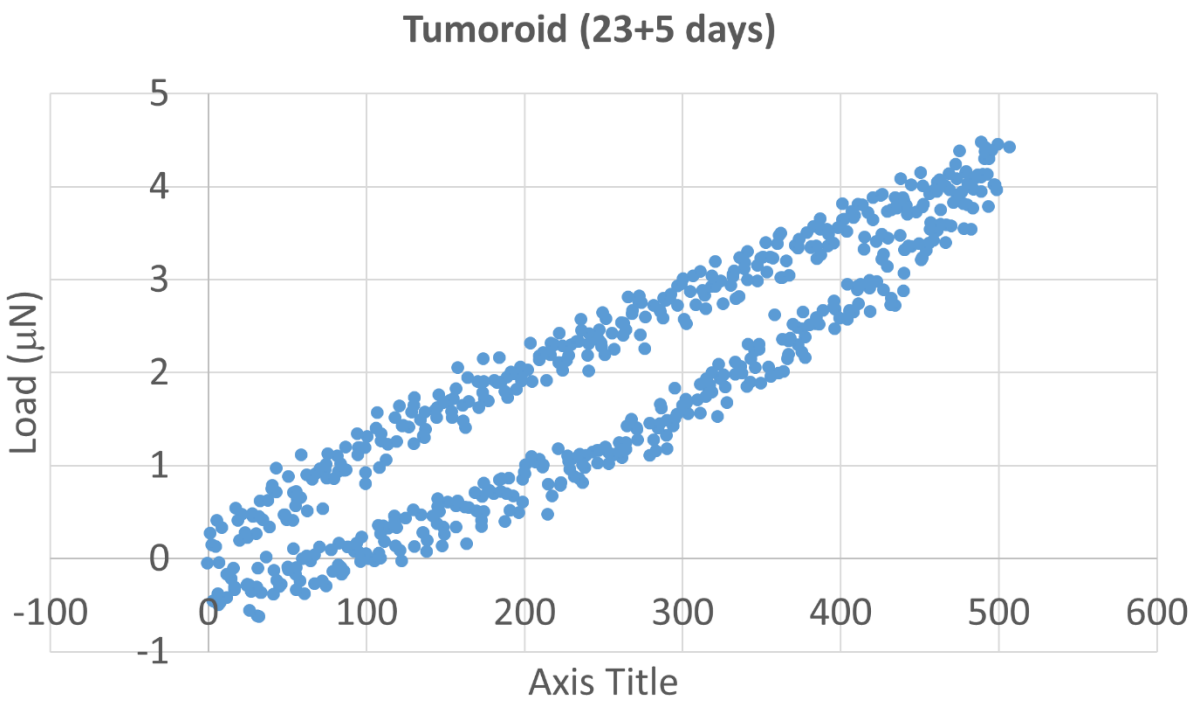

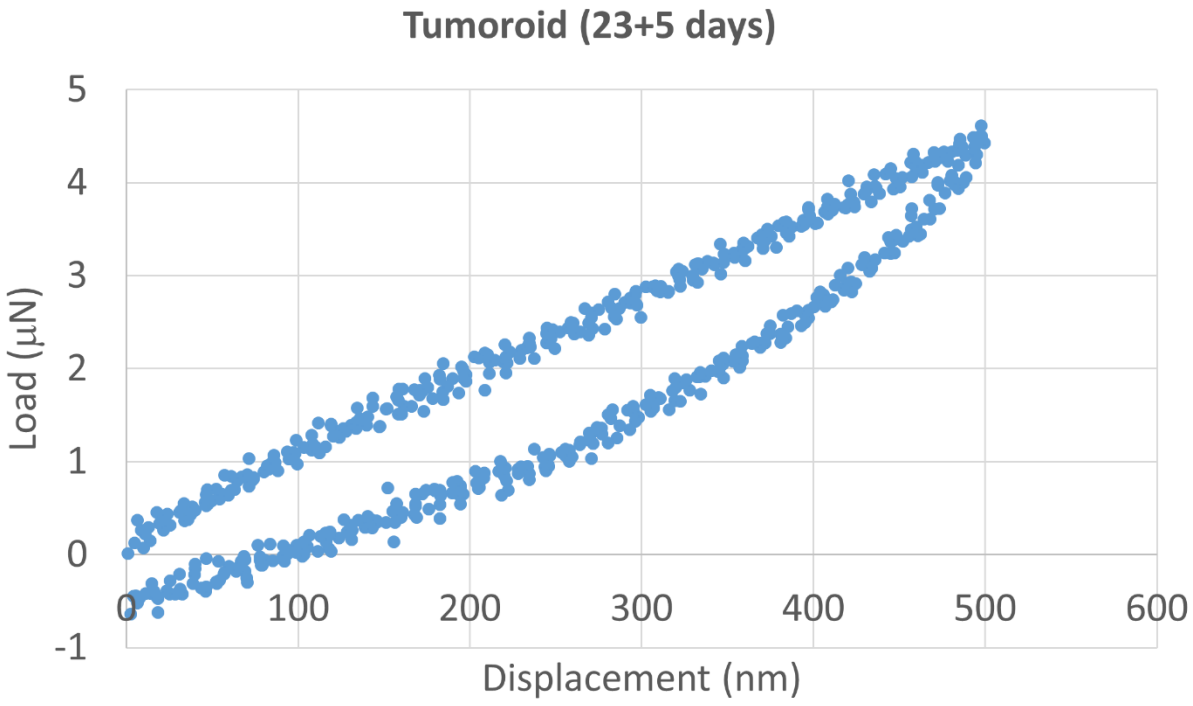

Figure A3. L-D curve on tumoroid at maximum displacement 500 nm (day 23+5) (Continued).

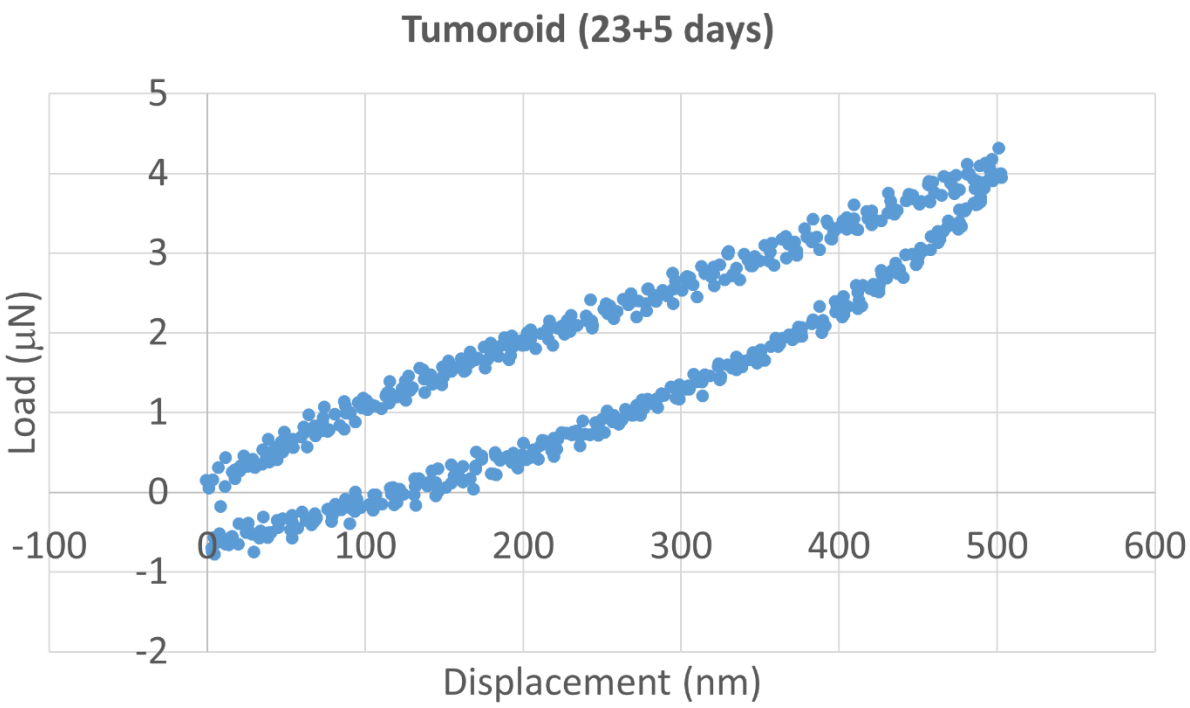

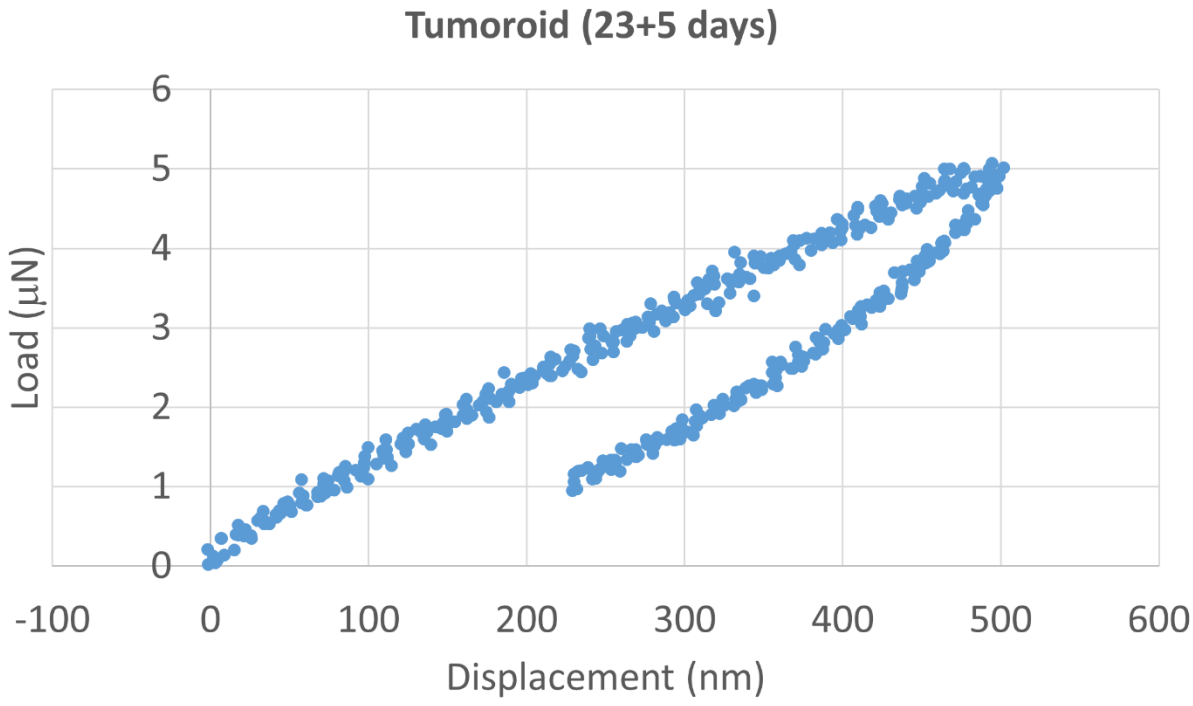

Figure A3. L-D curve on tumoroid at maximum displacement 500 nm (day 23+5) (Continued).

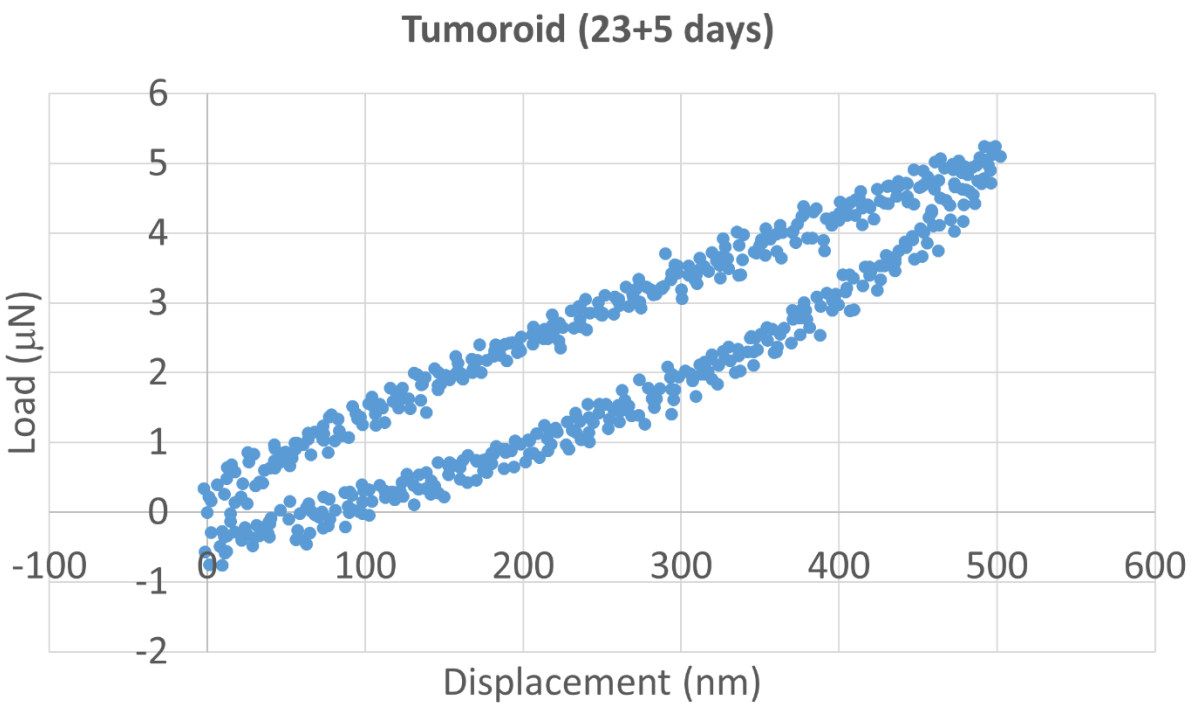

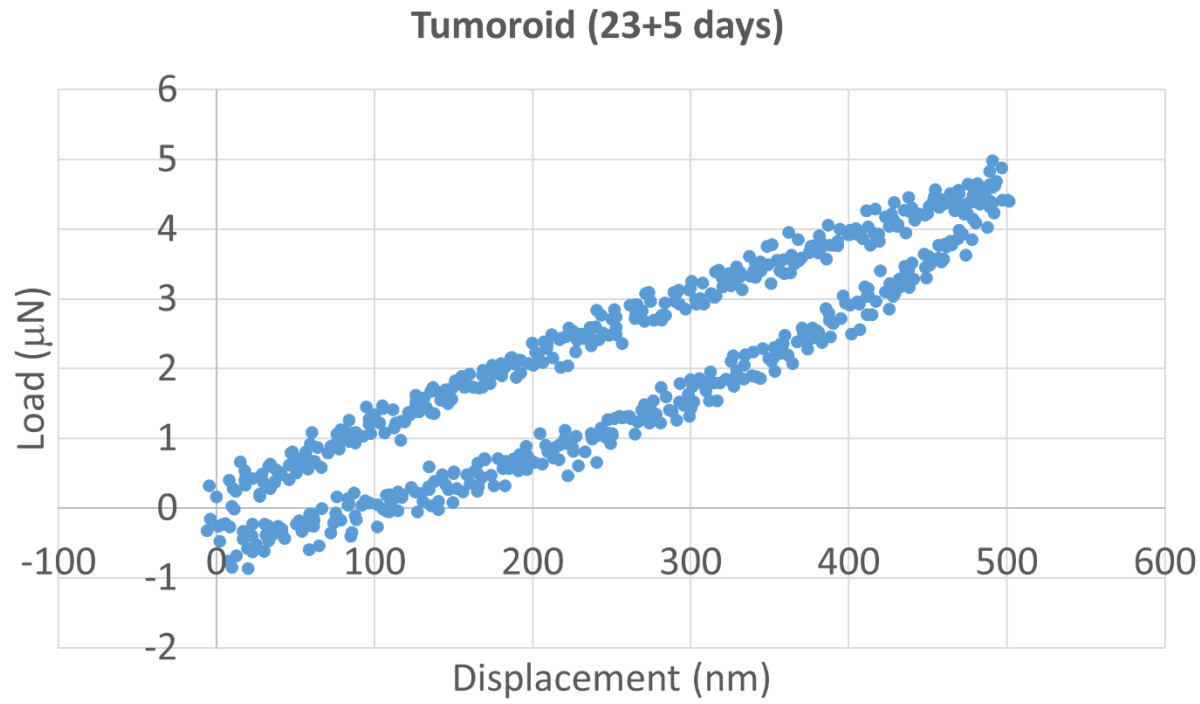

Figure A3. L-D curve on tumoroid at maximum displacement 500 nm (day 23+5) (Continued).

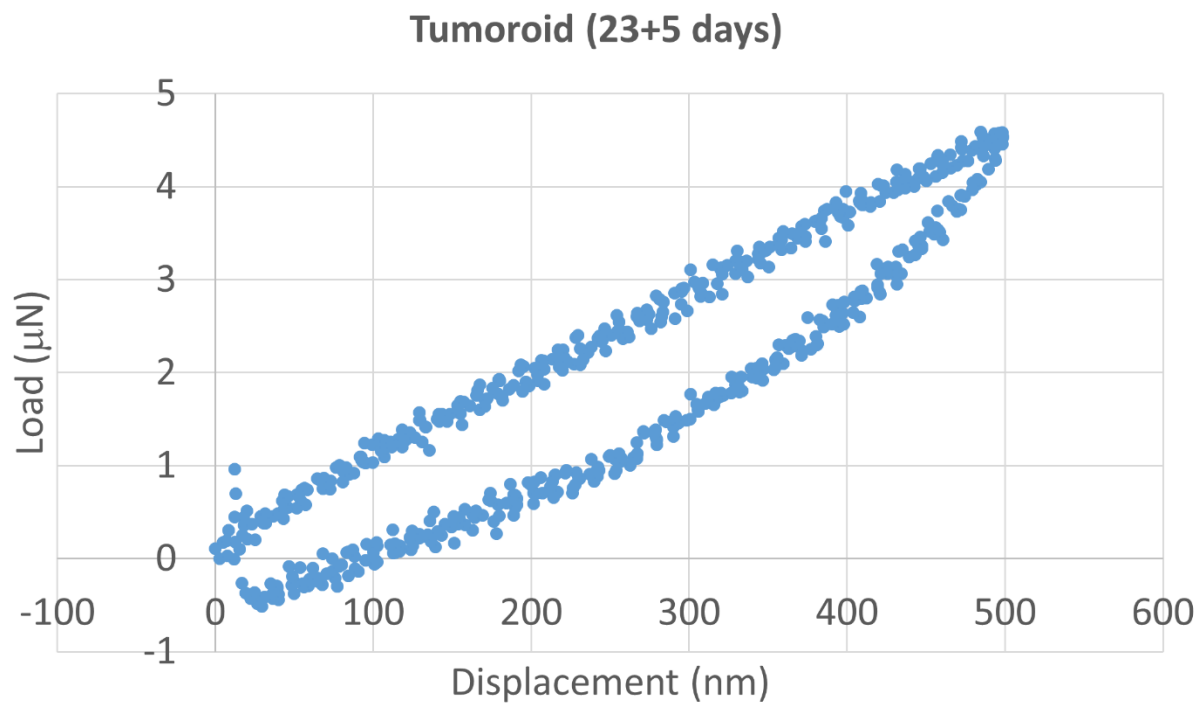

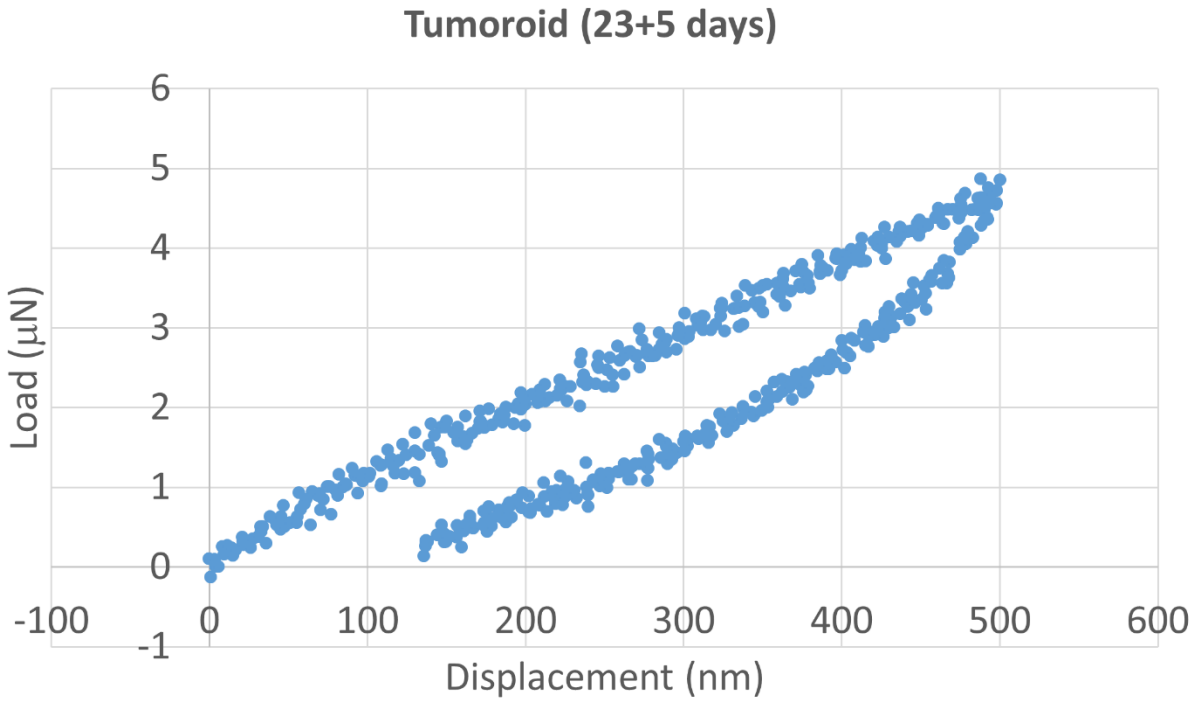

Figure A3. L-D curve on tumoroid at maximum displacement 500 nm (day 23+5) (Continued).

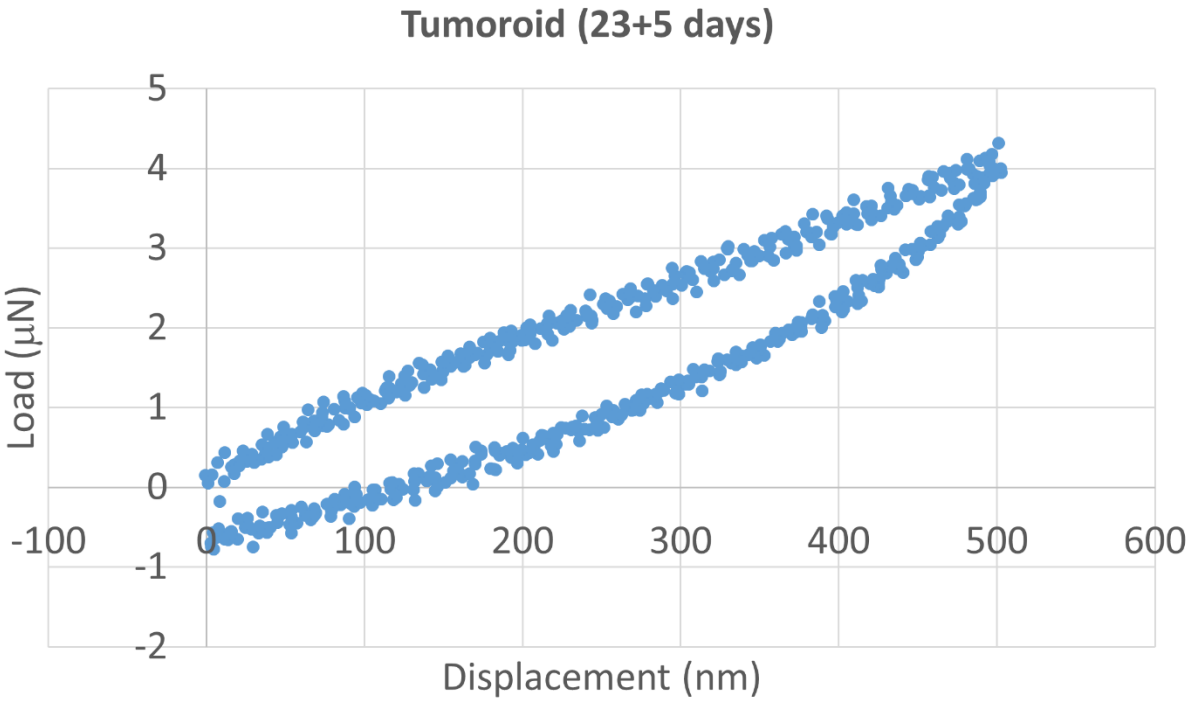

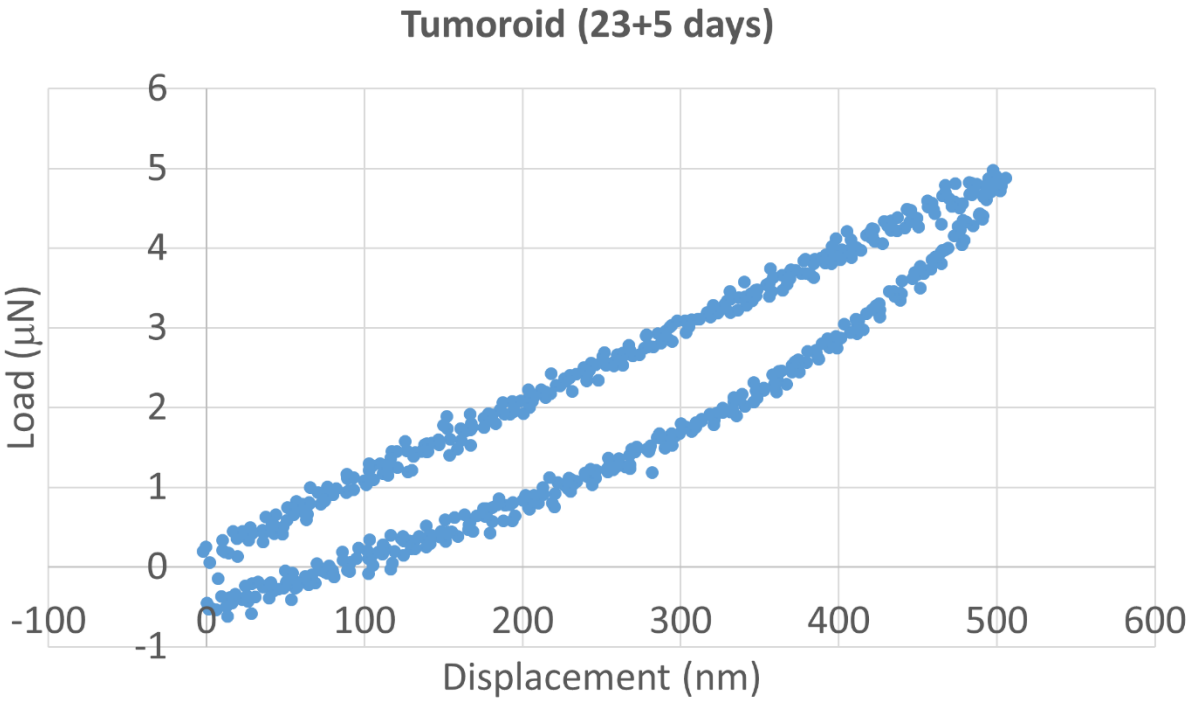

Figure A3. L-D curve on tumoroid at maximum displacement 500 nm (day 23+5) (Continued).

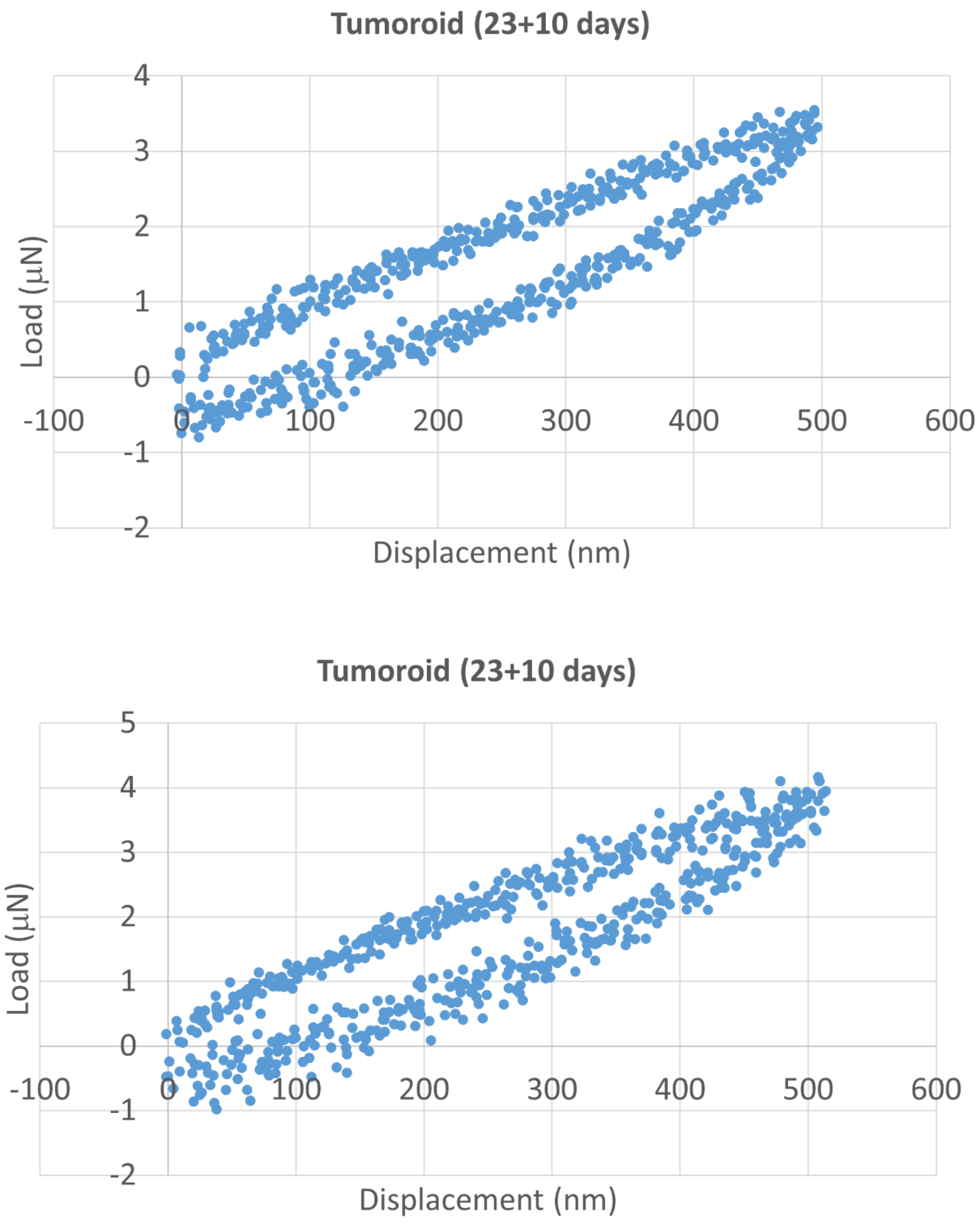

Figure A4. L-D curve on tumoroid at maximum displacement 500 nm (day 23+10).

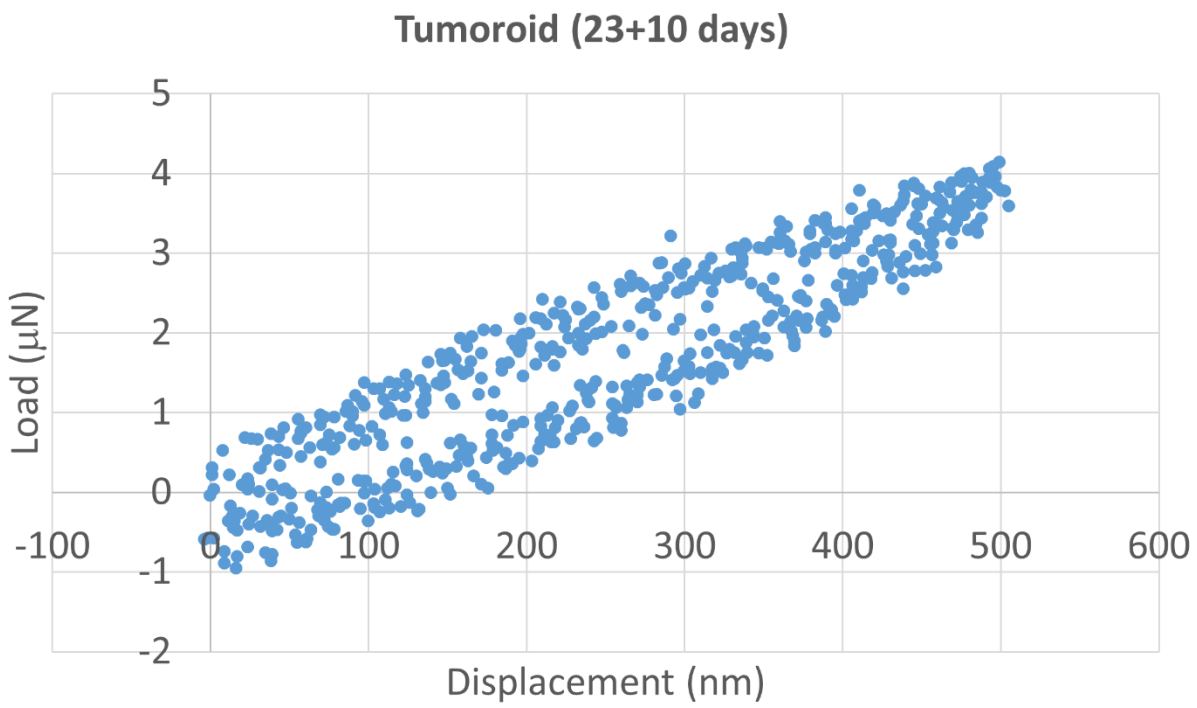

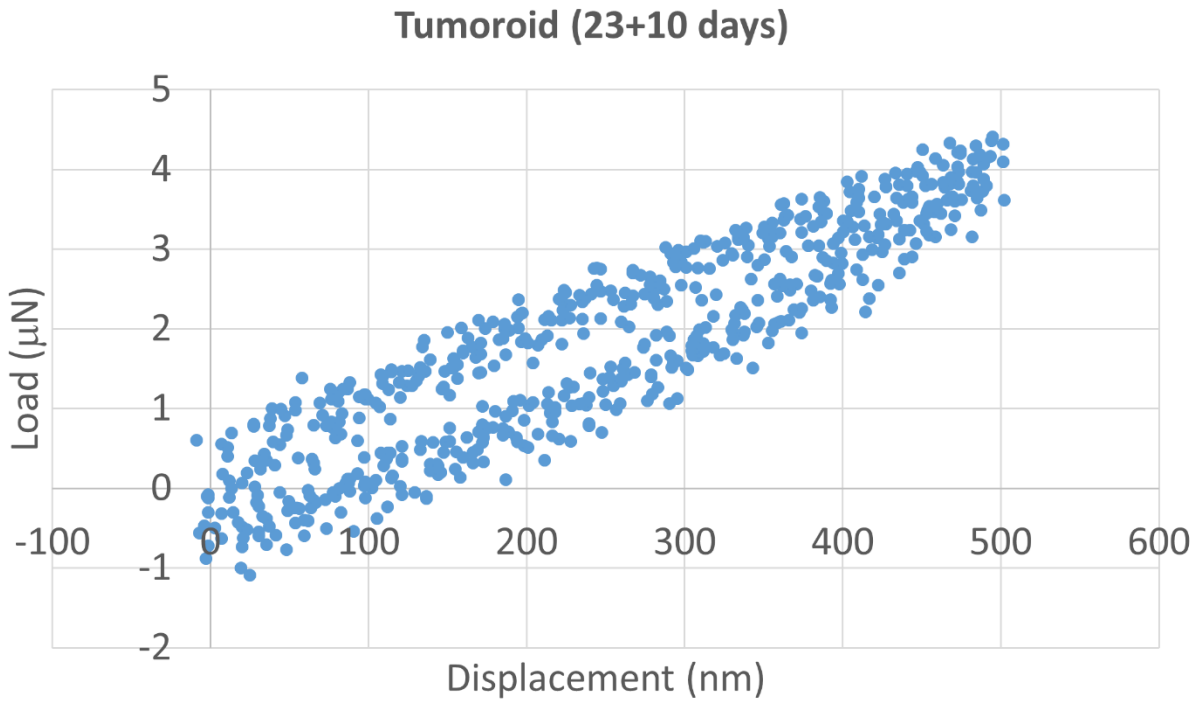

Figure A4. L-D curve on tumoroid at maximum displacement 500 nm (day 23+10) (Continued).

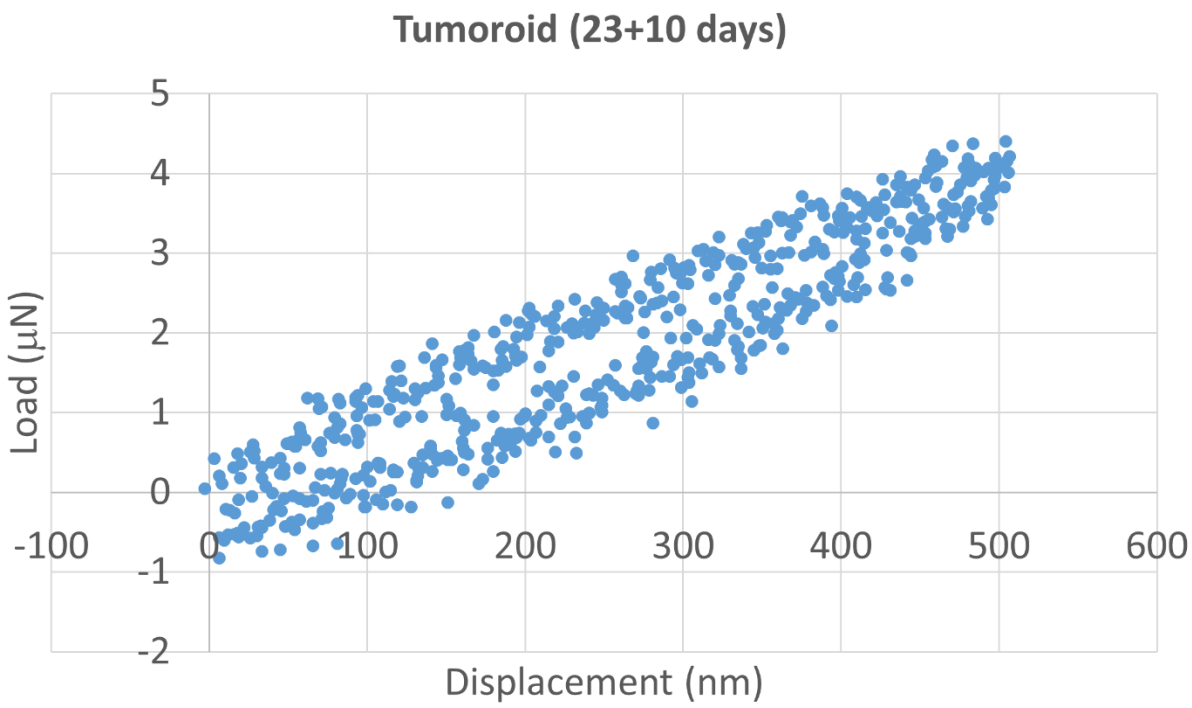

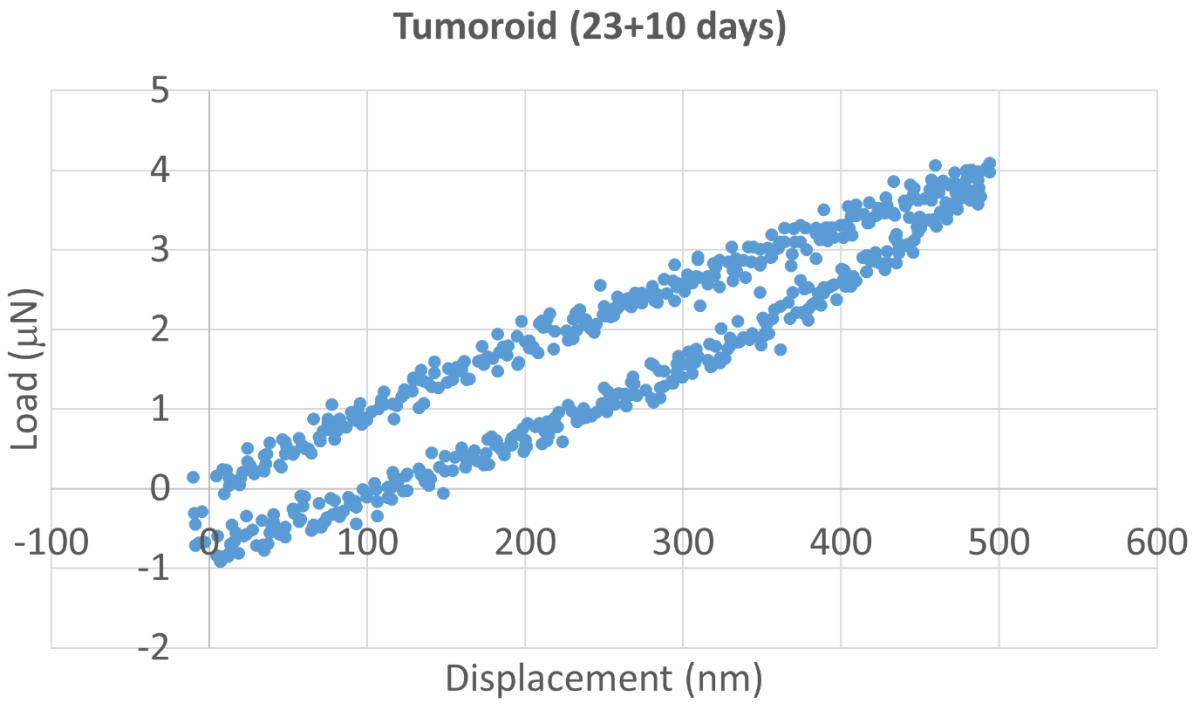

Figure A4. L-D curve on tumoroid at maximum displacement 500 nm (day 23+10) (Continued).

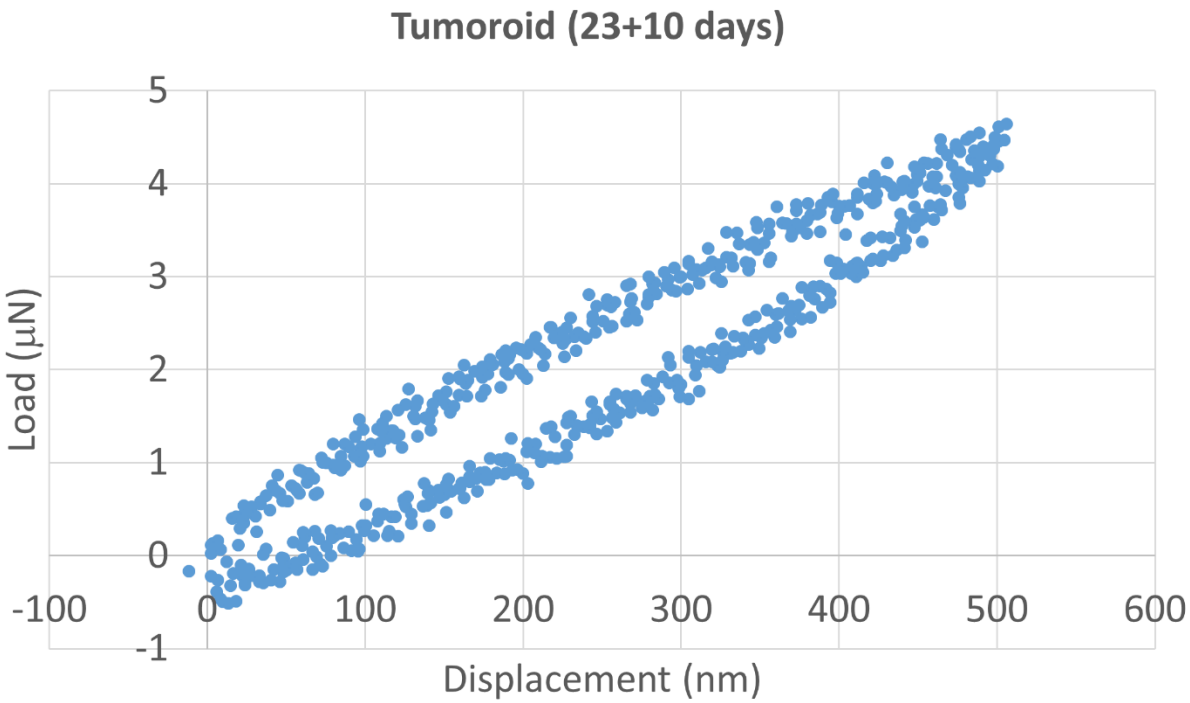

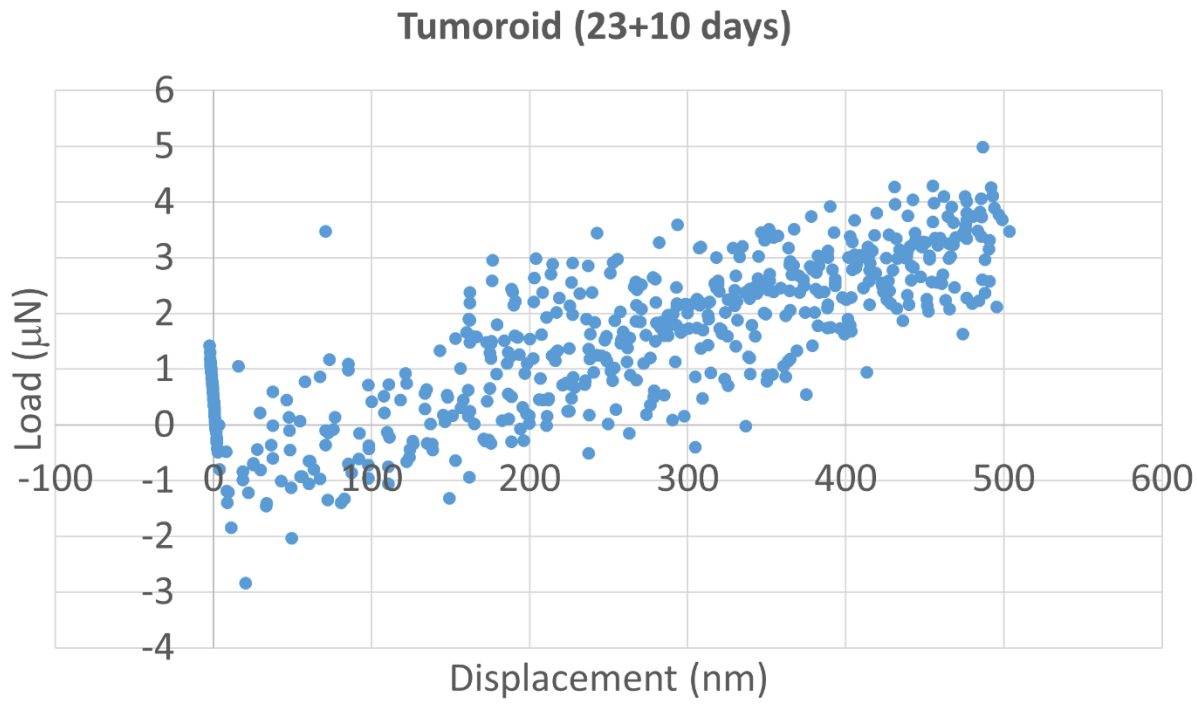

Figure A4. L-D curve on tumoroid at maximum displacement 500 nm (day 23+10) (Continued).

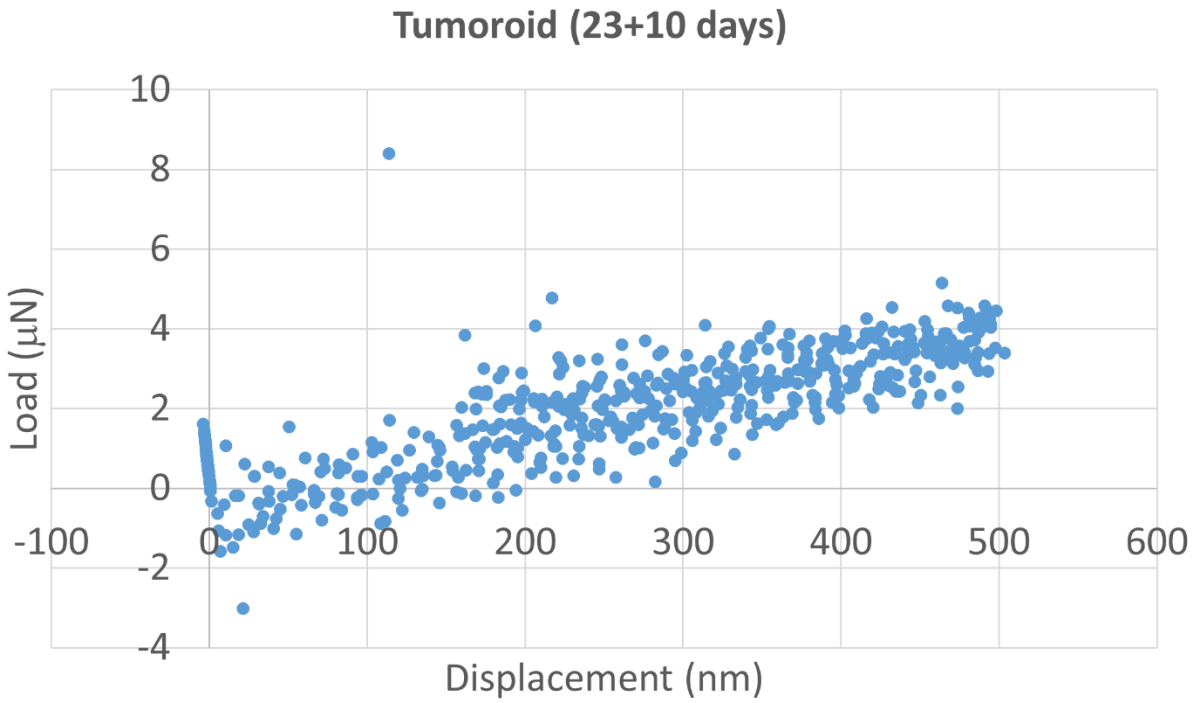

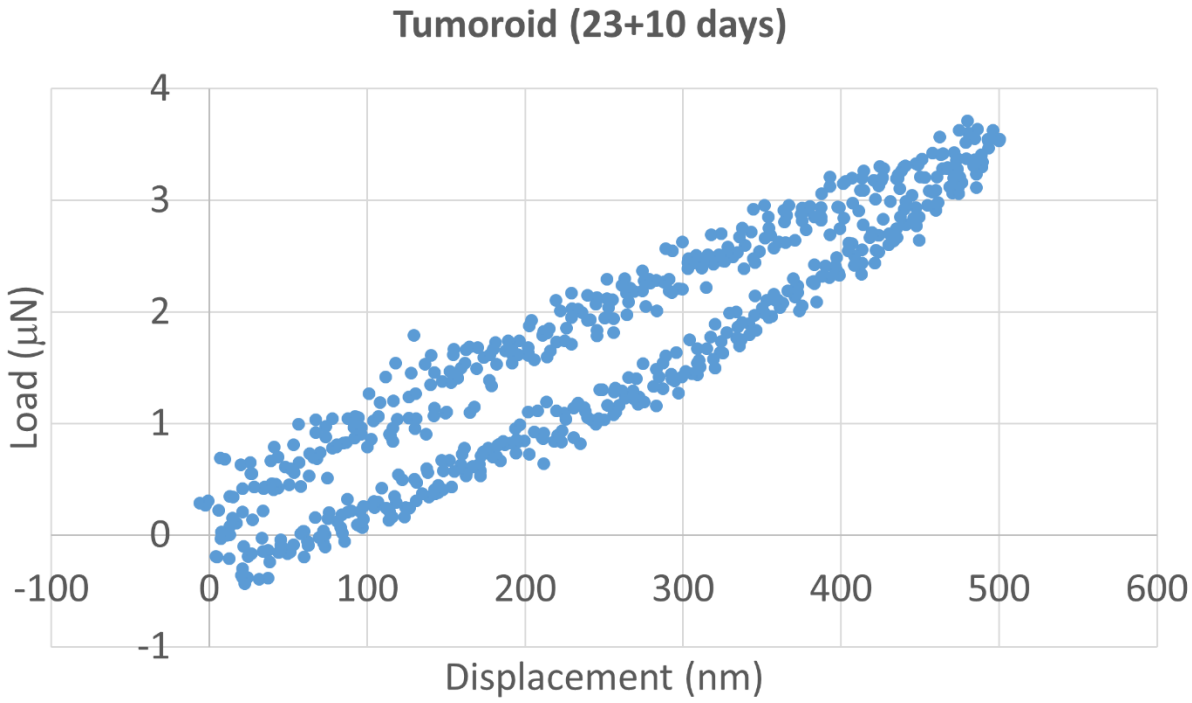

Figure A4. L-D curve on tumoroid at maximum displacement 500 nm (day 23+10) (Continued).

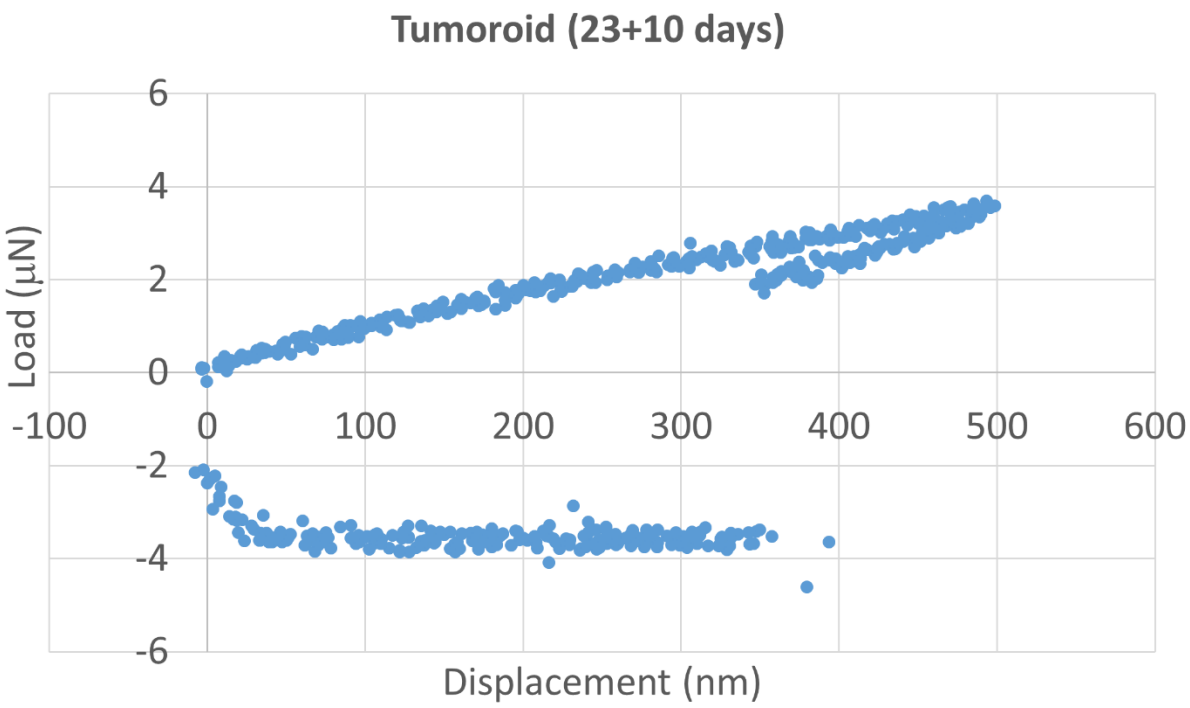

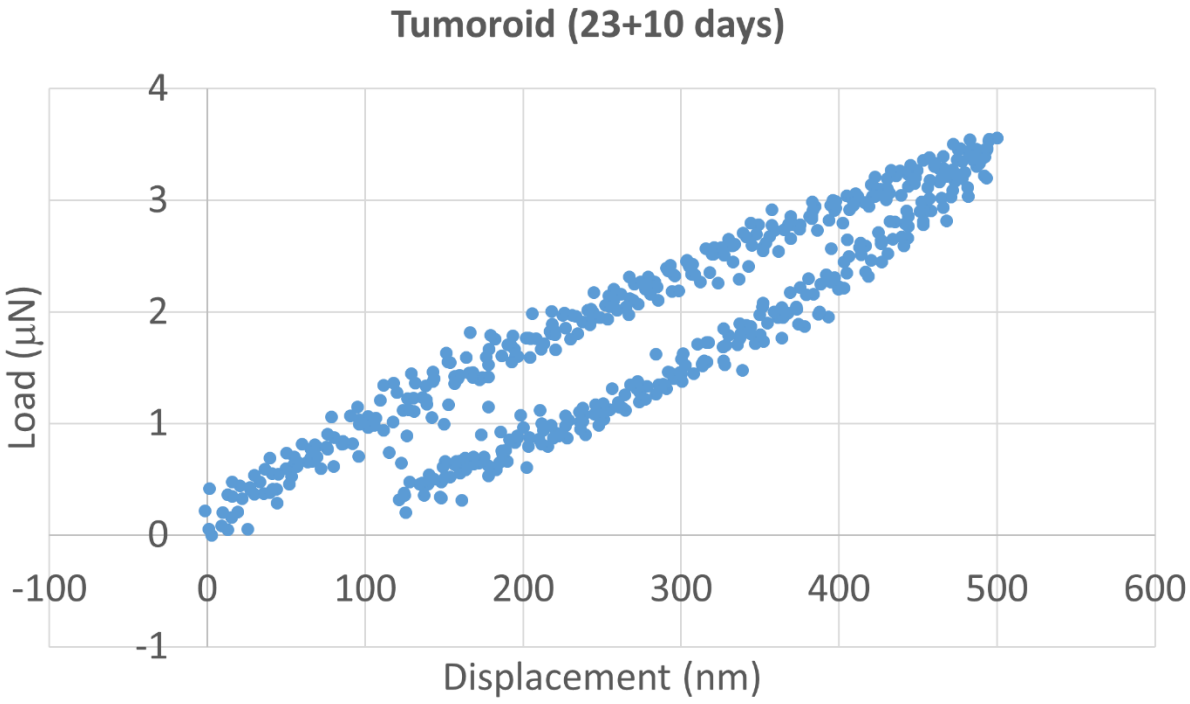

Figure A4. L-D curve on tumoroid at maximum displacement 500 nm (day 23+10) (Continued).

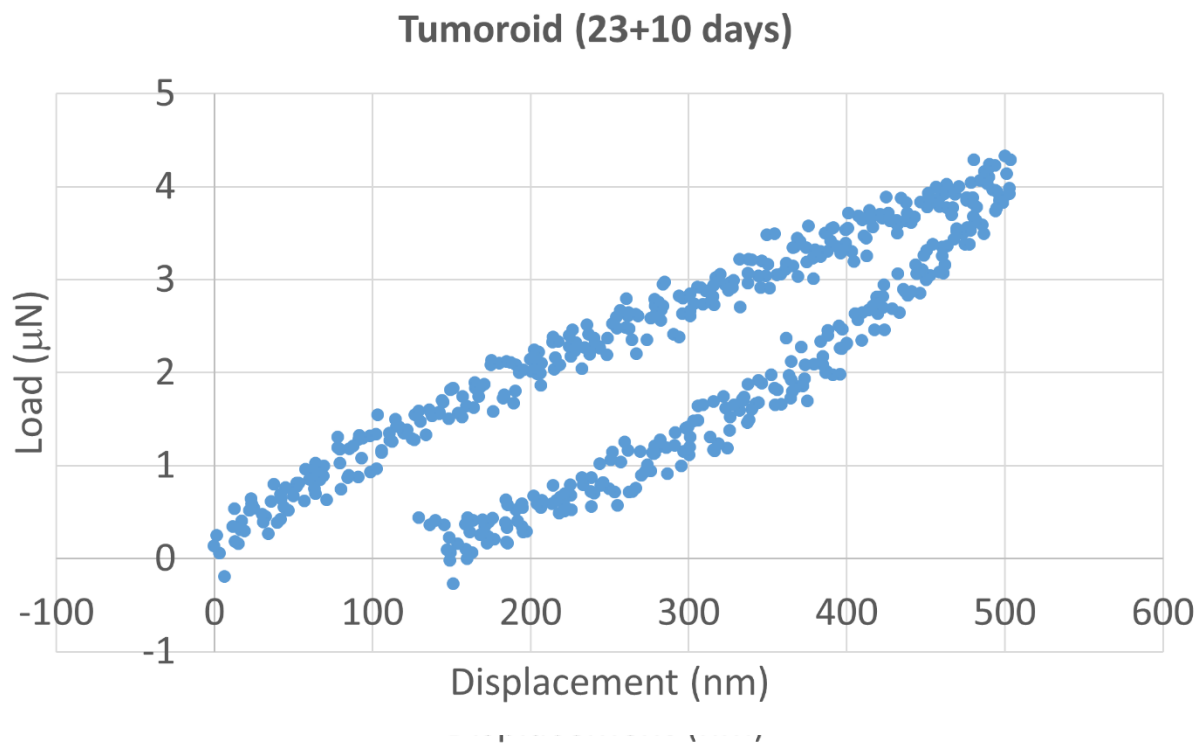

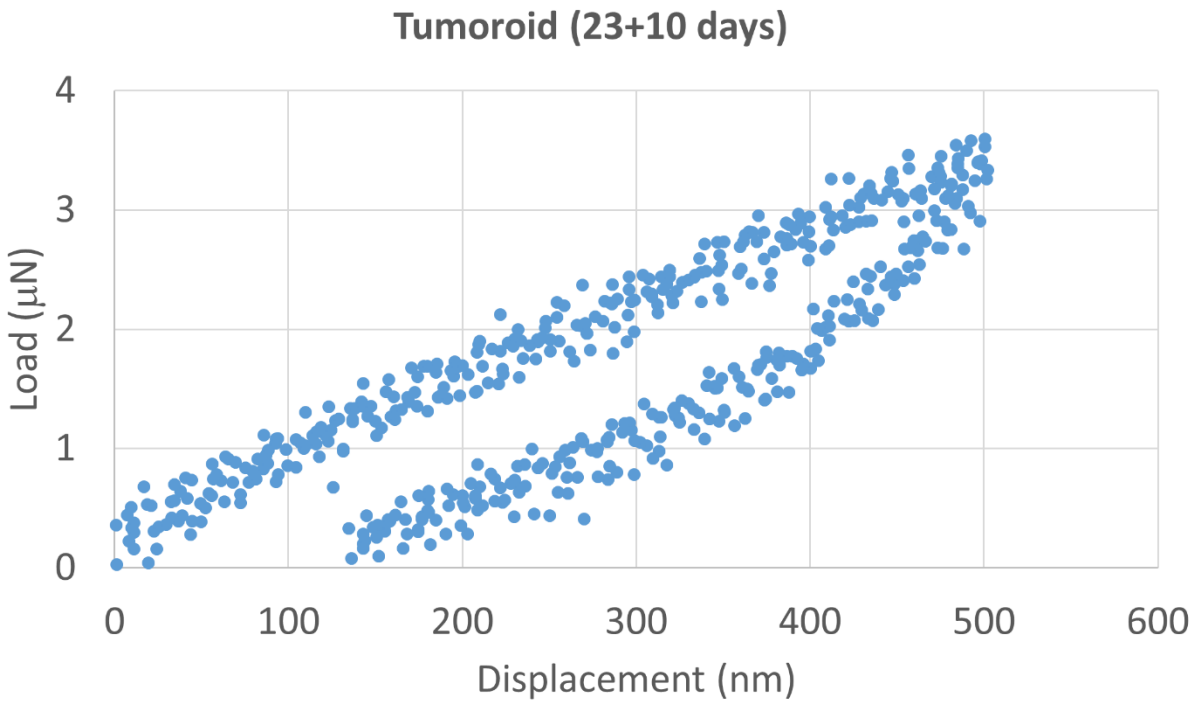

Figure A4. L-D curve on tumoroid at maximum displacement 500 nm (day 23+10) (Continued).

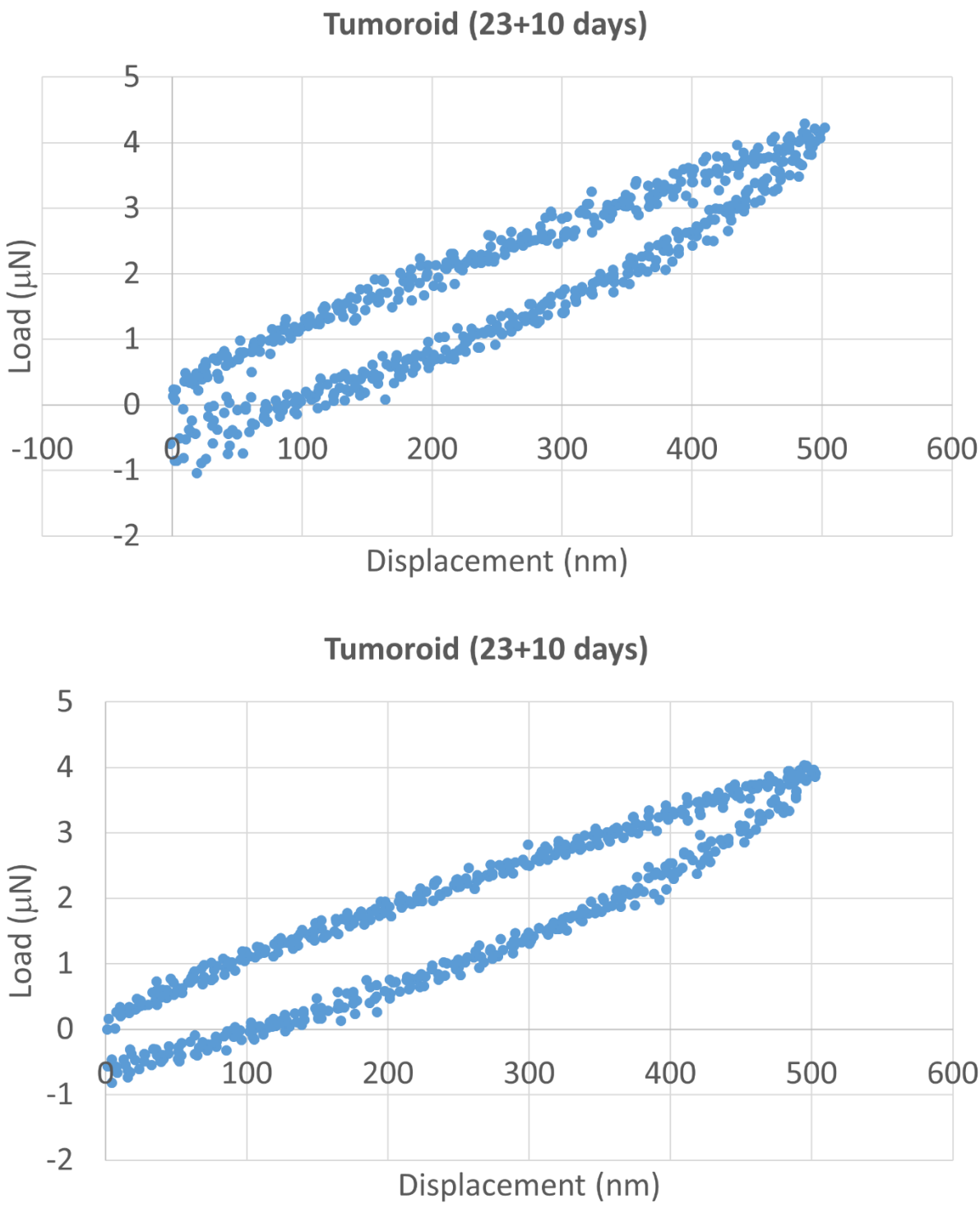

Figure A4. L-D curve on tumoroid at maximum displacement 500 nm (day 23+10) (Continued).

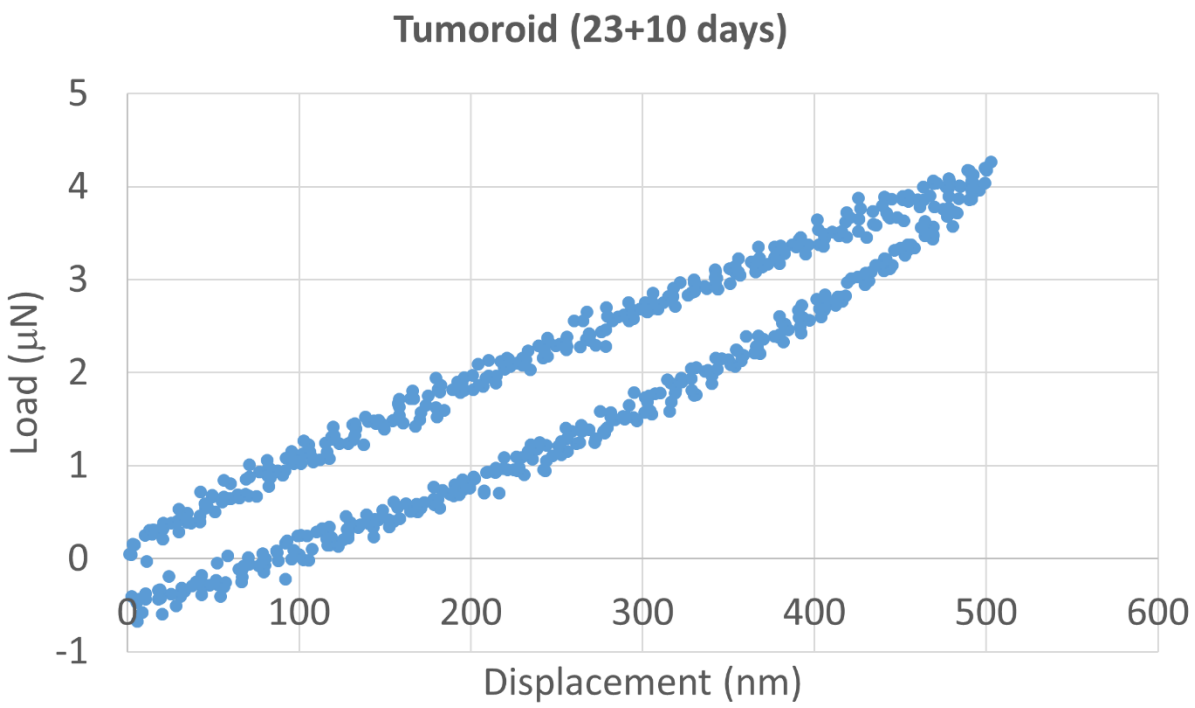

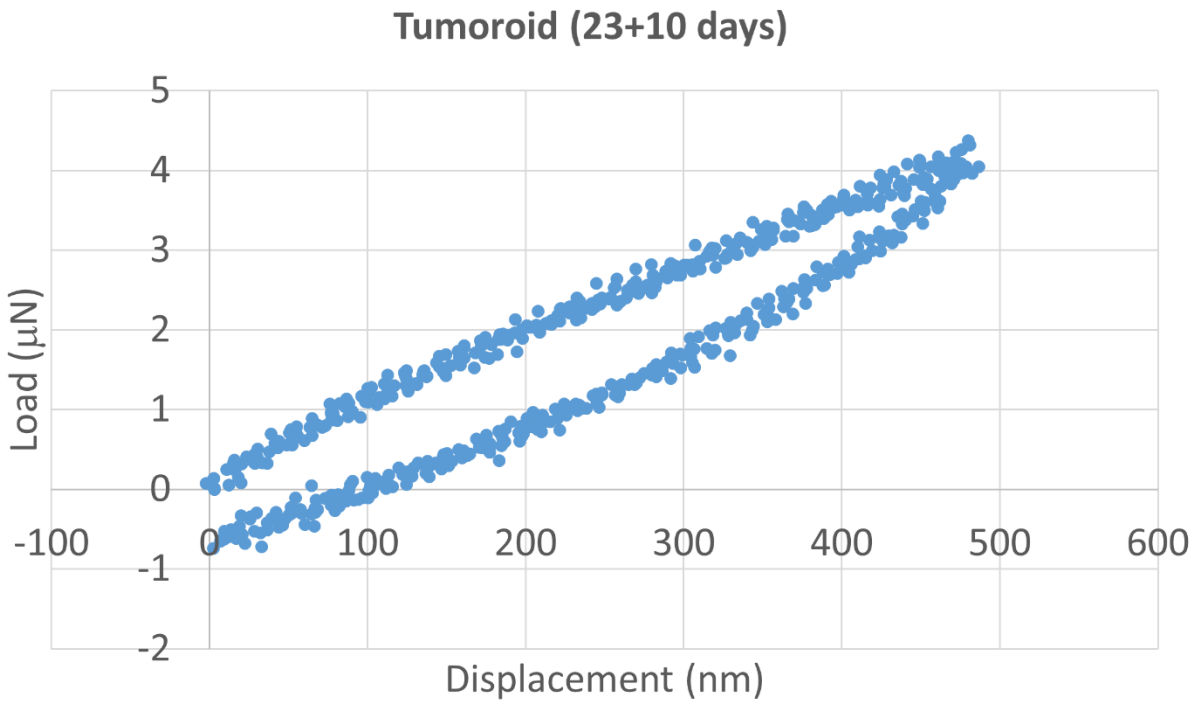

Figure A4. L-D curve on tumoroid at maximum displacement 500 nm (day 23+10) (Continued).

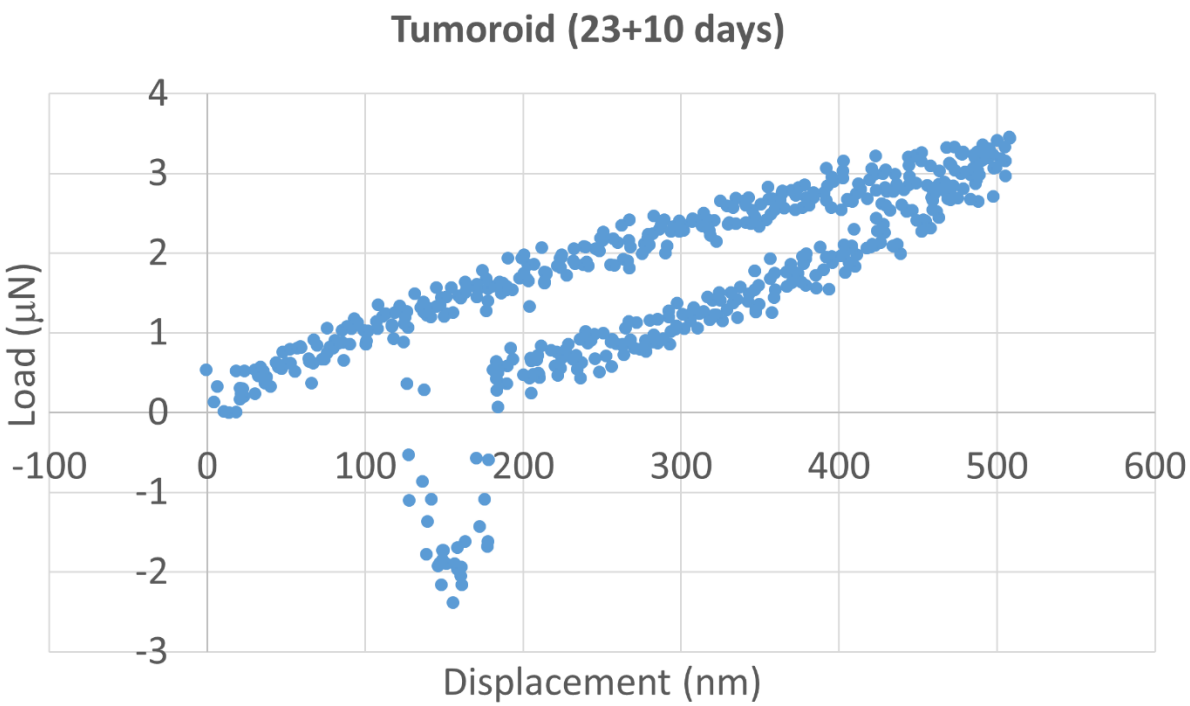

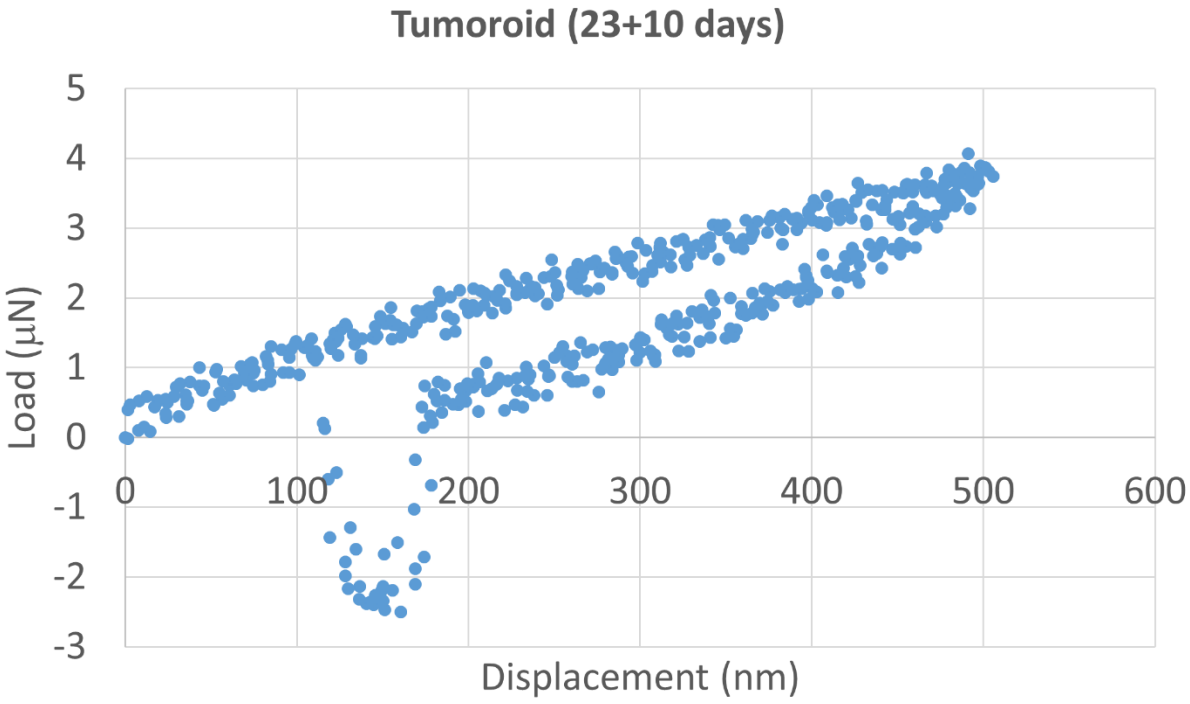

Figure A4. L-D curve on tumoroid at maximum displacement 500 nm (day 23+10) (Continued).

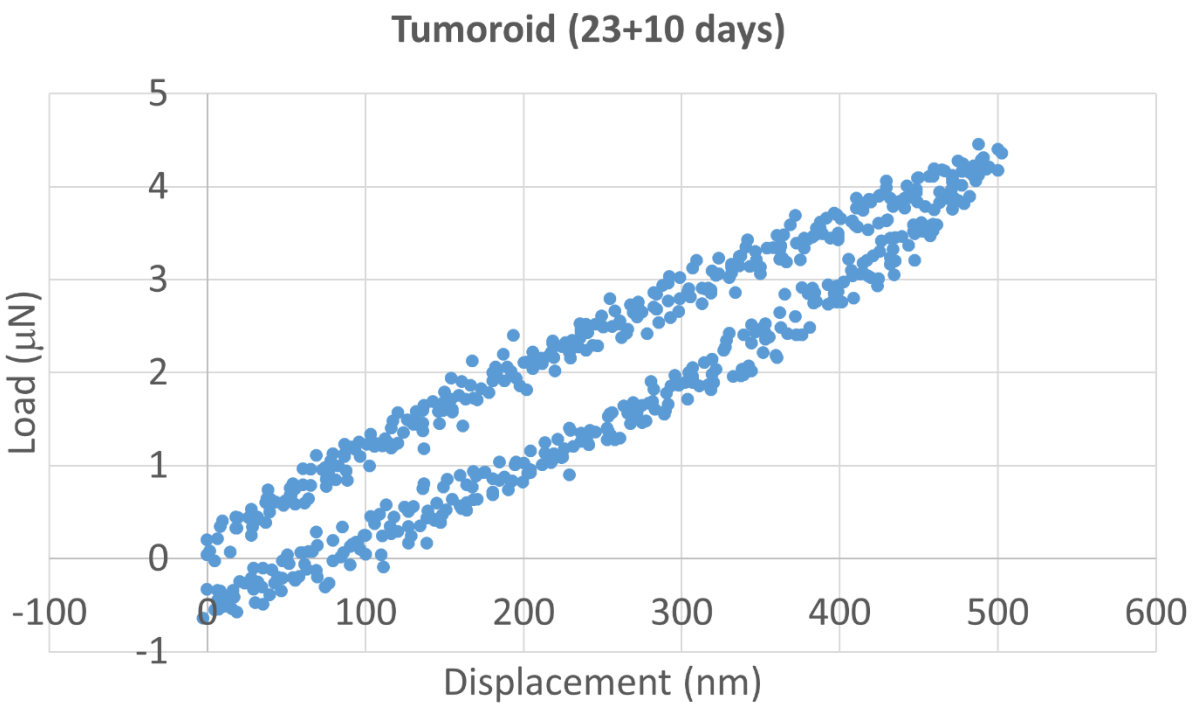

Figure A4. L-D curve on tumoroid at maximum displacement 500 nm (day 23+10) (Continued).

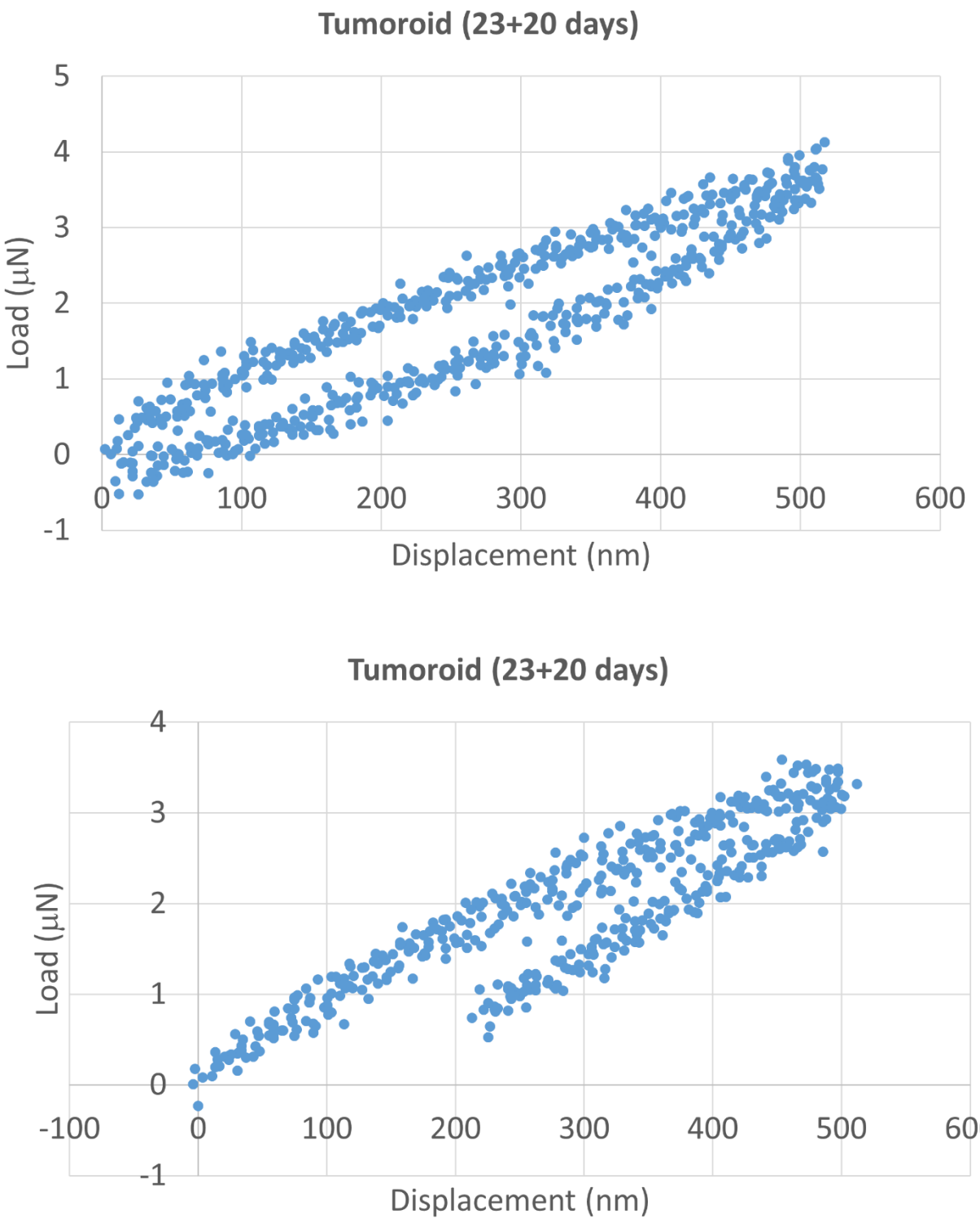

Figure A5. L-D curve on tumoroid at maximum displacement 500 nm (day 23+20).

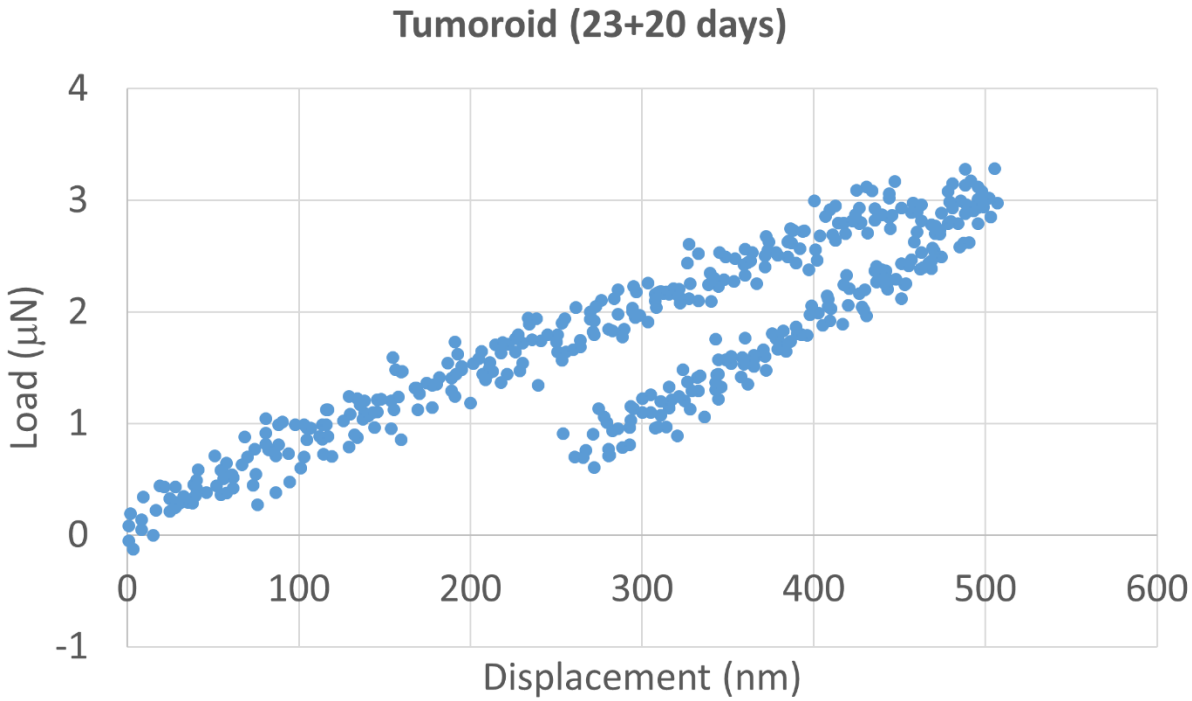

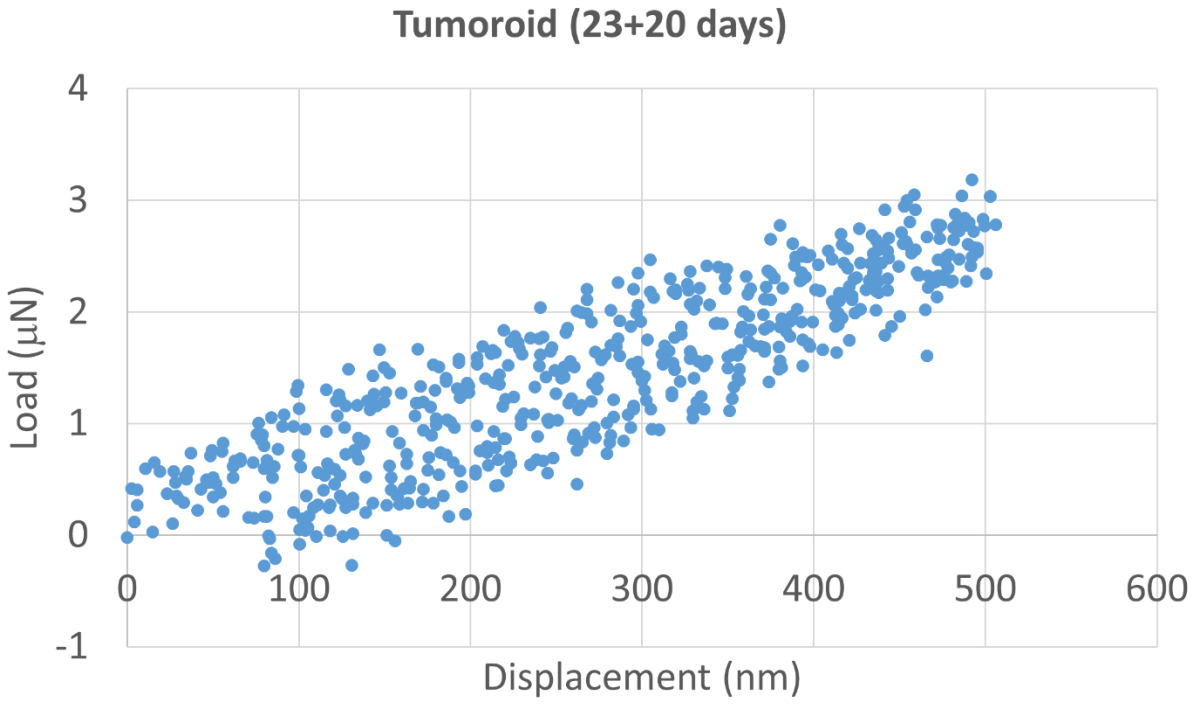

Figure A5. L-D curve on tumoroid at maximum displacement 500 nm (day 23+20) (Continued).

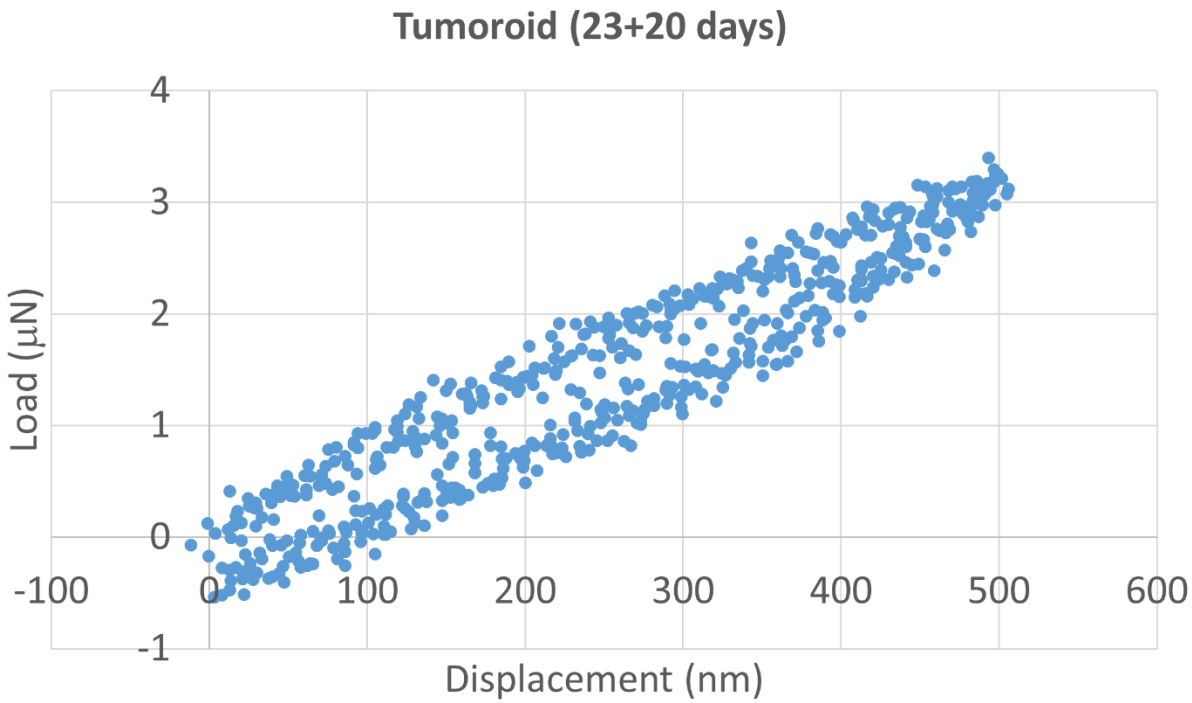

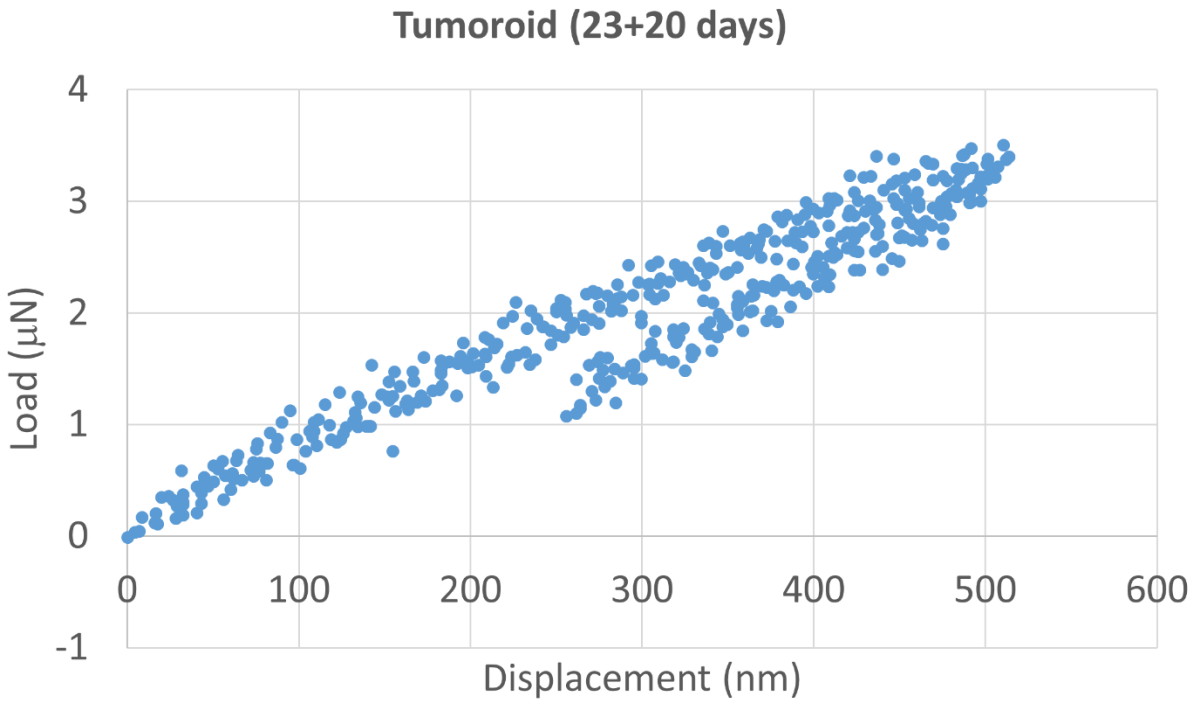

Figure A5. L-D curve on tumoroid at maximum displacement 500 nm (day 23+20) (Continued).

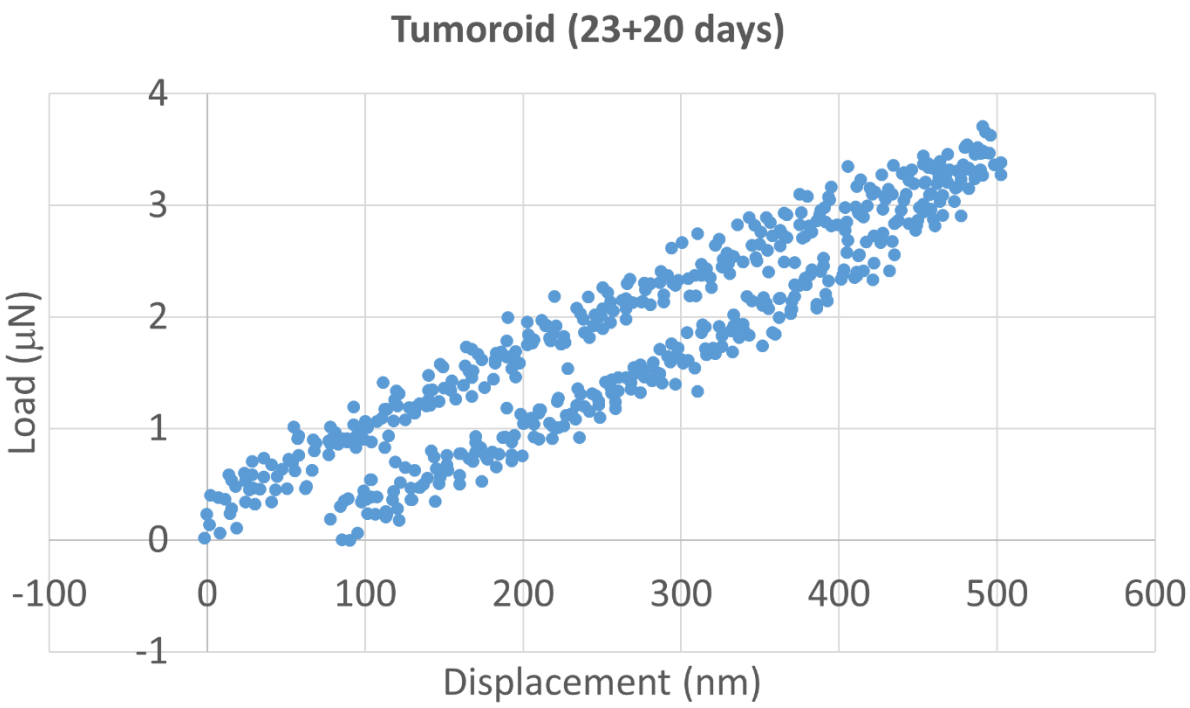

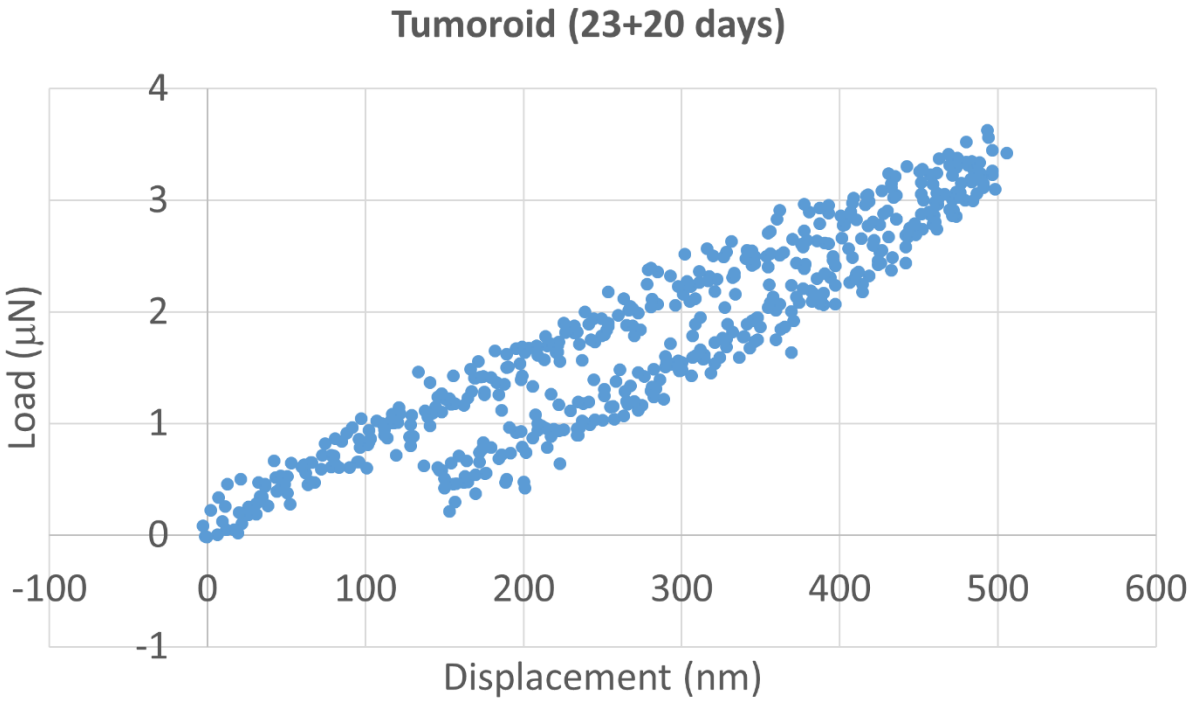

Figure A5. L-D curve on tumoroid at maximum displacement 500 nm (day 23+20) (Continued).

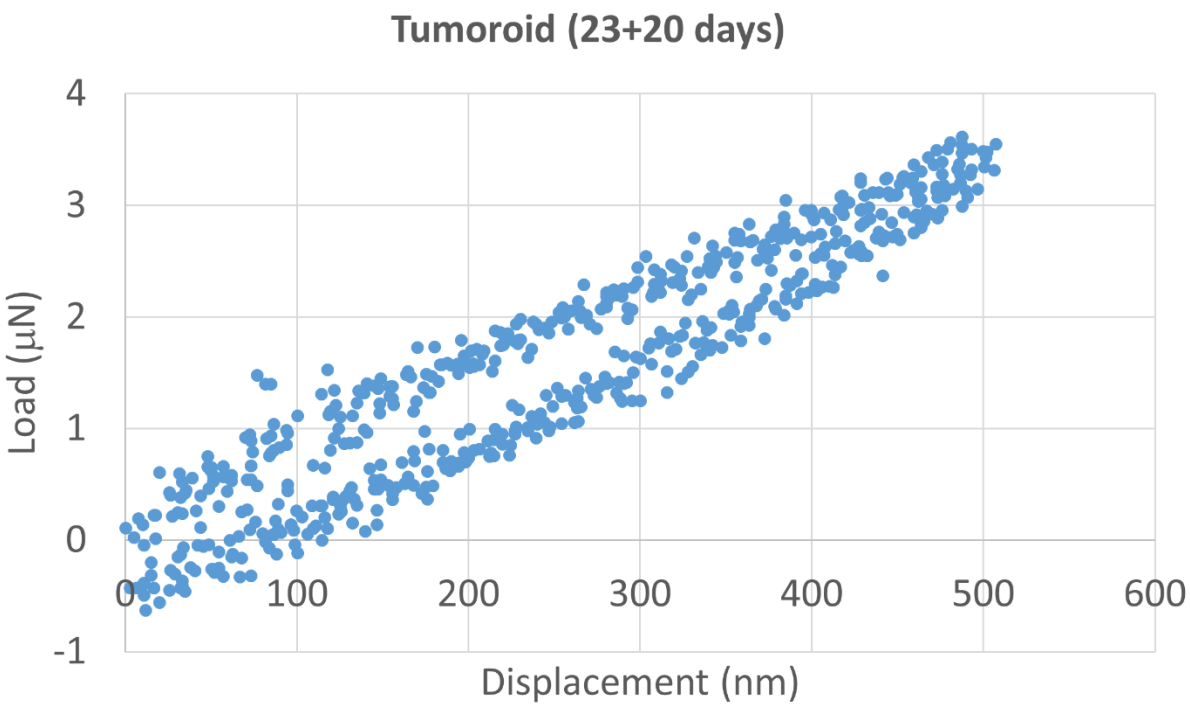

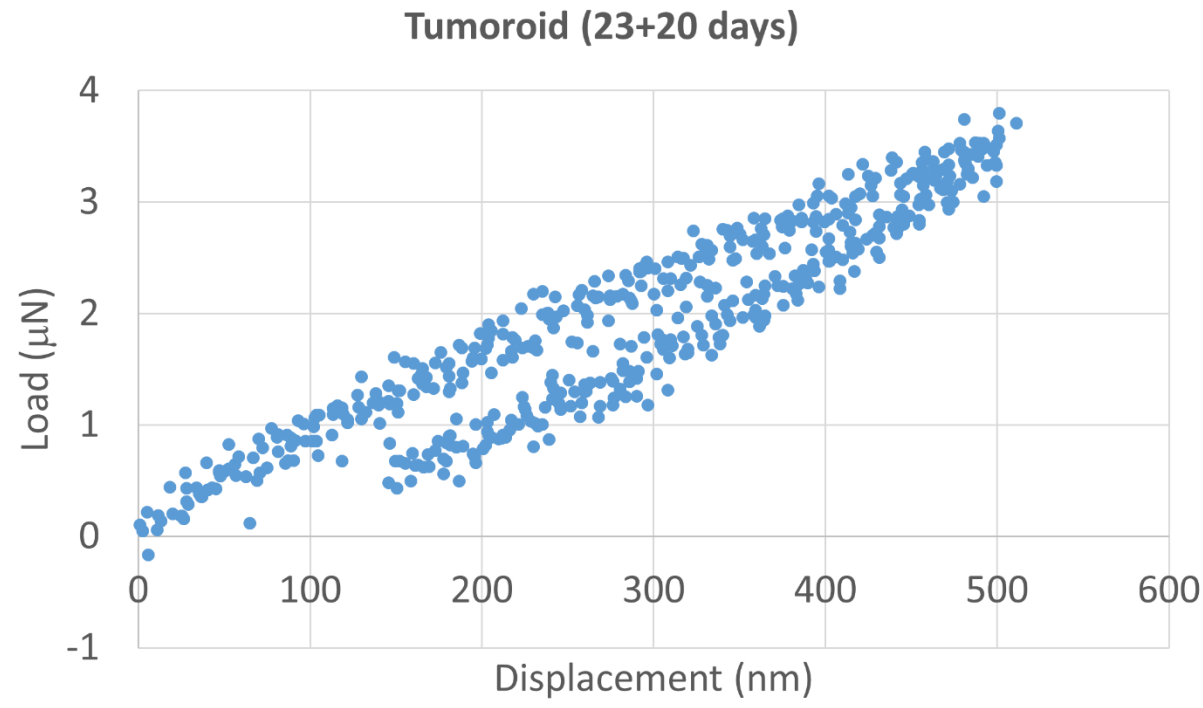

Figure A5. L-D curve on tumoroid at maximum displacement 500 nm (day 23+20) (Continued).

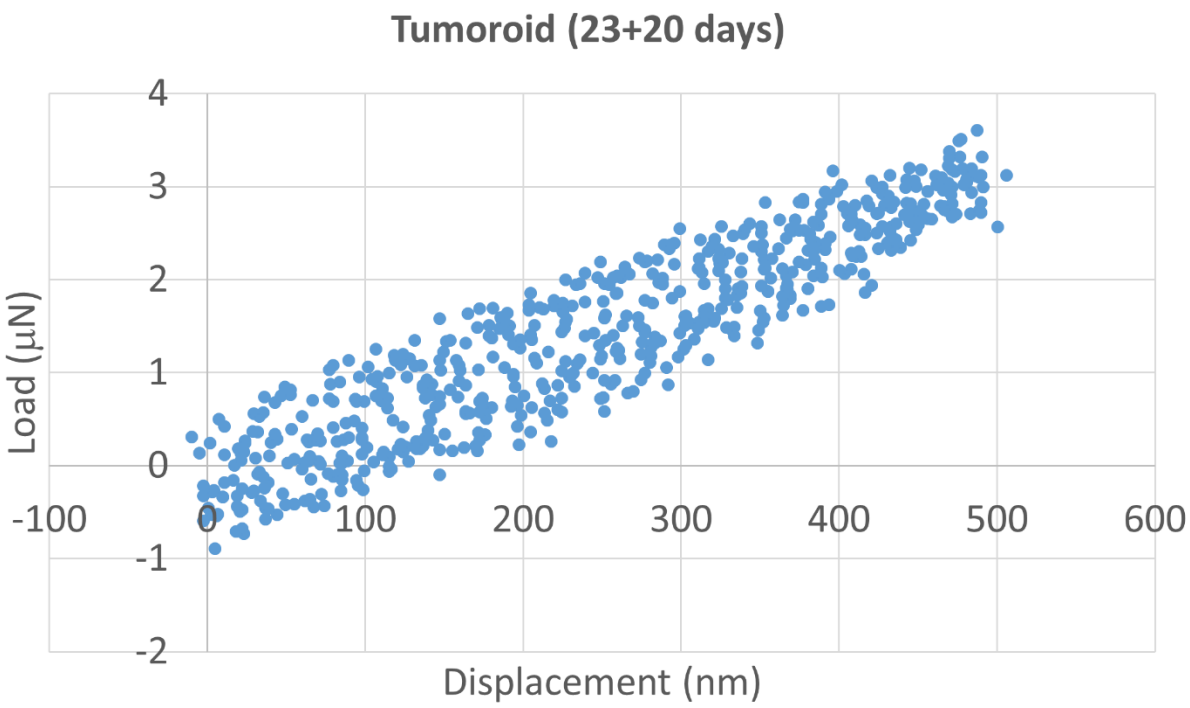

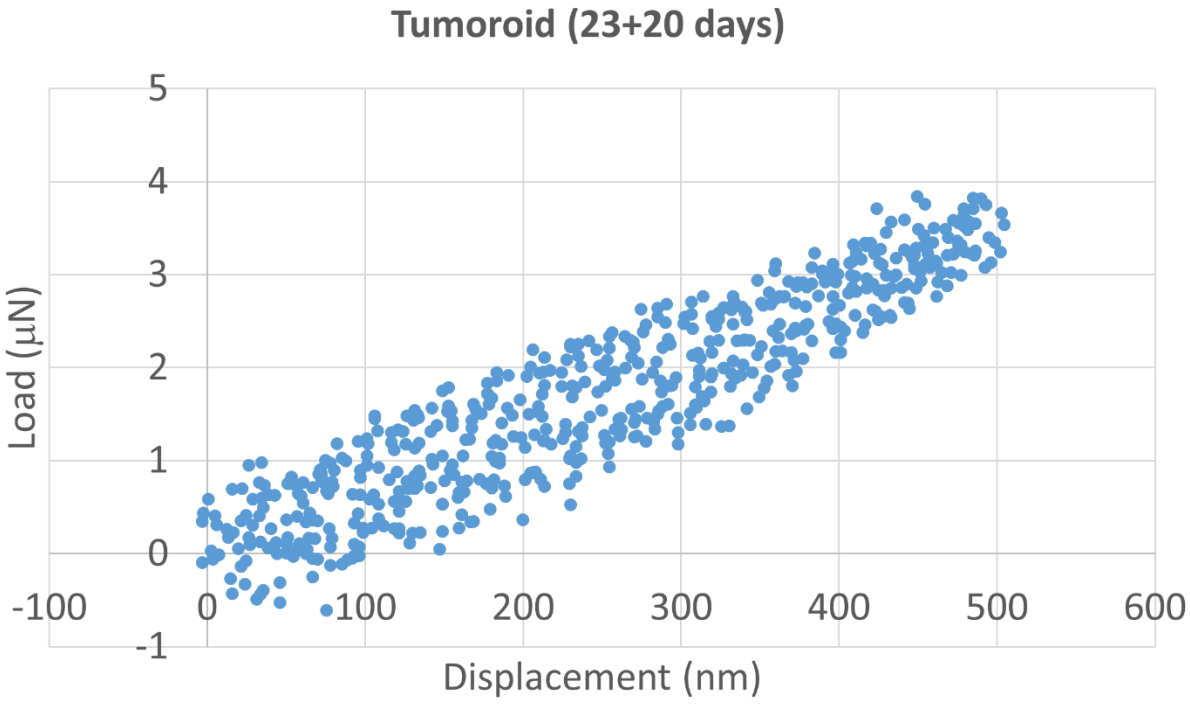

Figure A5. L-D curve on tumoroid at maximum displacement 500 nm (day 23+20) (Continued).

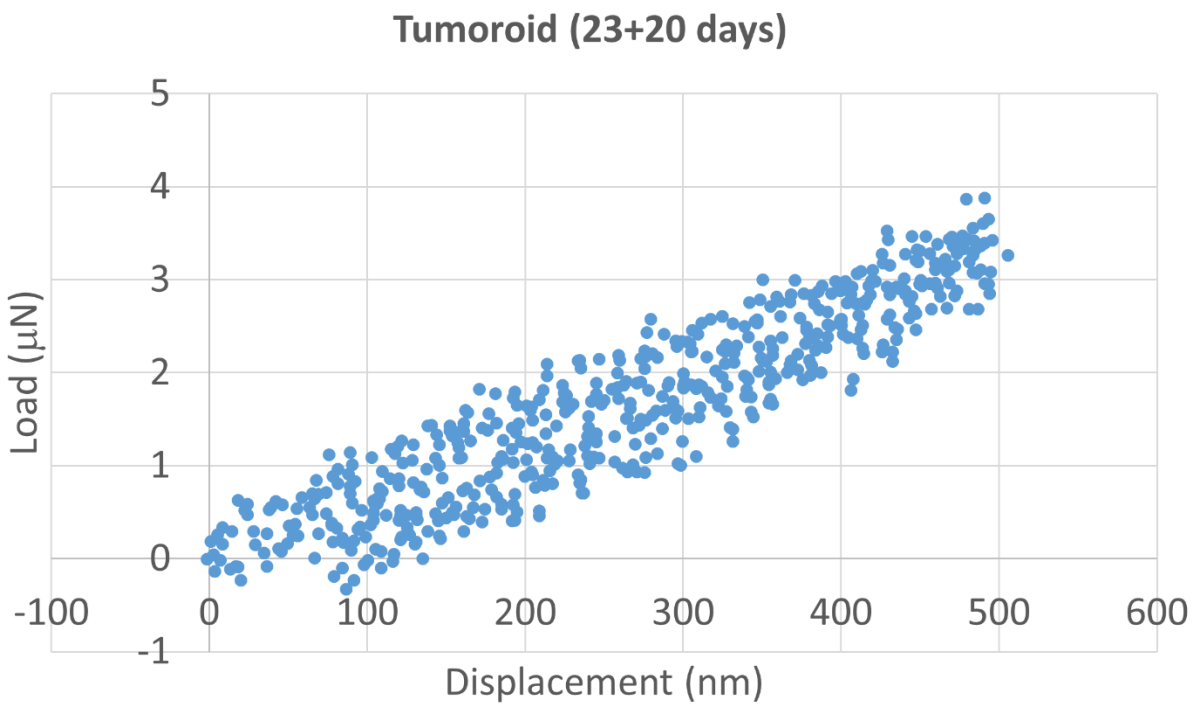

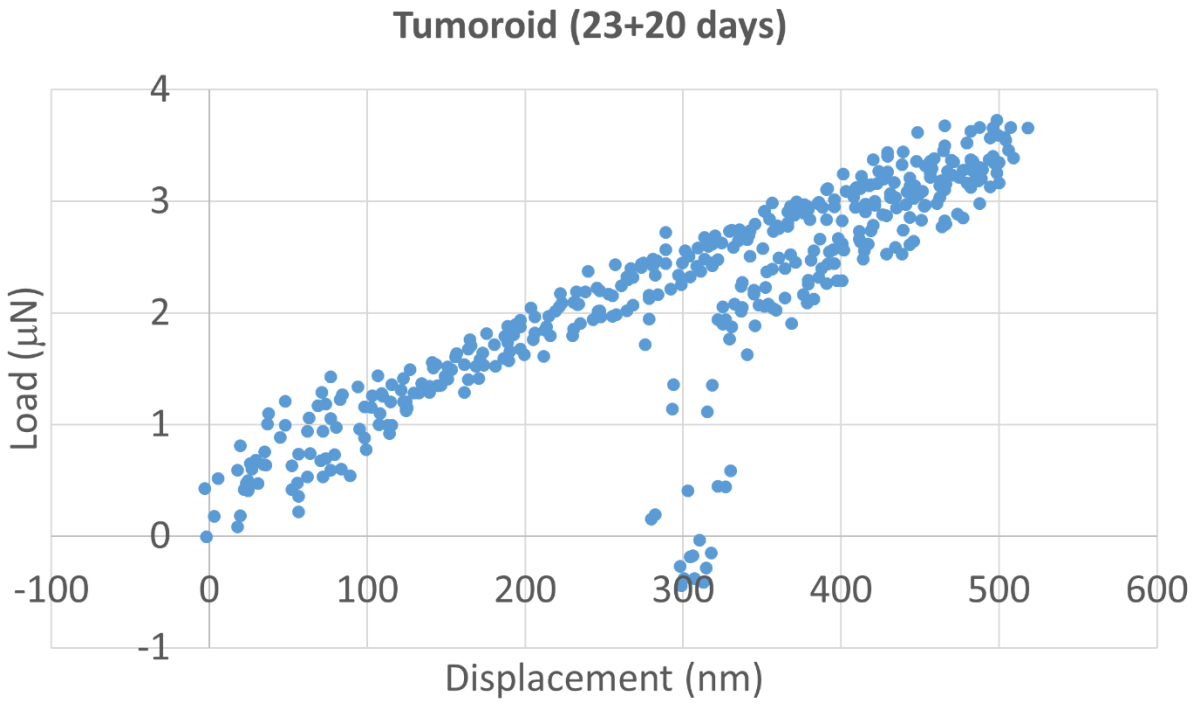

Figure A5. L-D curve on tumoroid at maximum displacement 500 nm (day 23+20) (Continued).

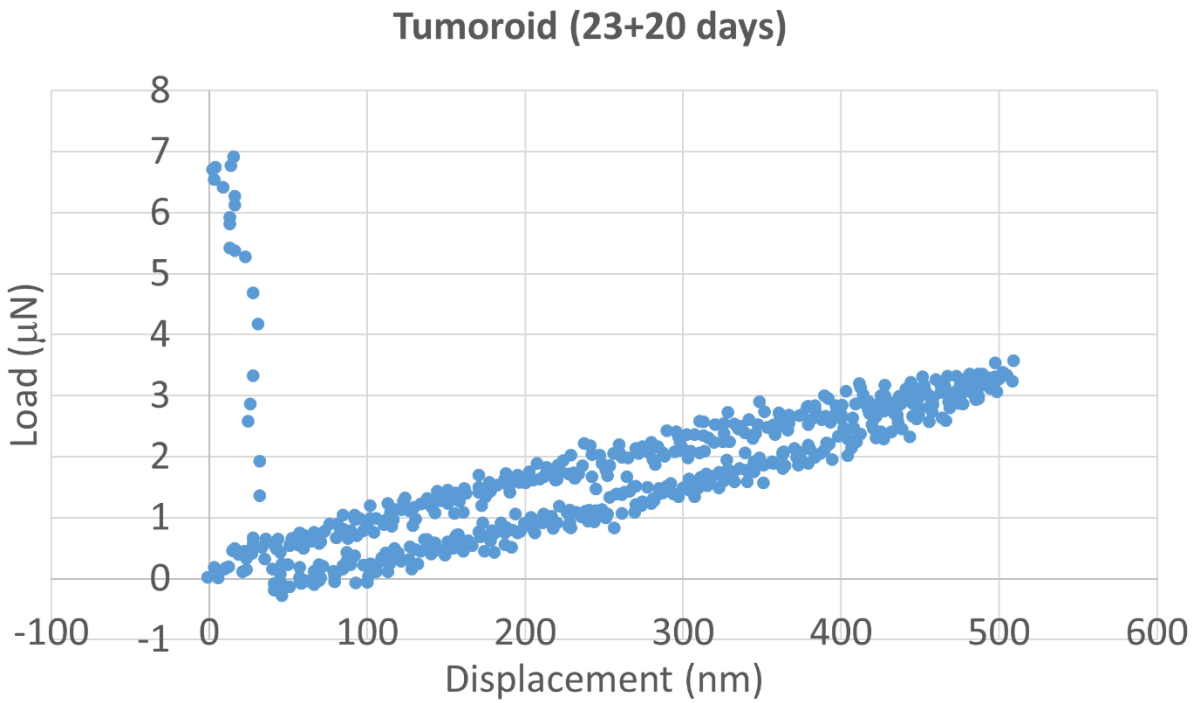

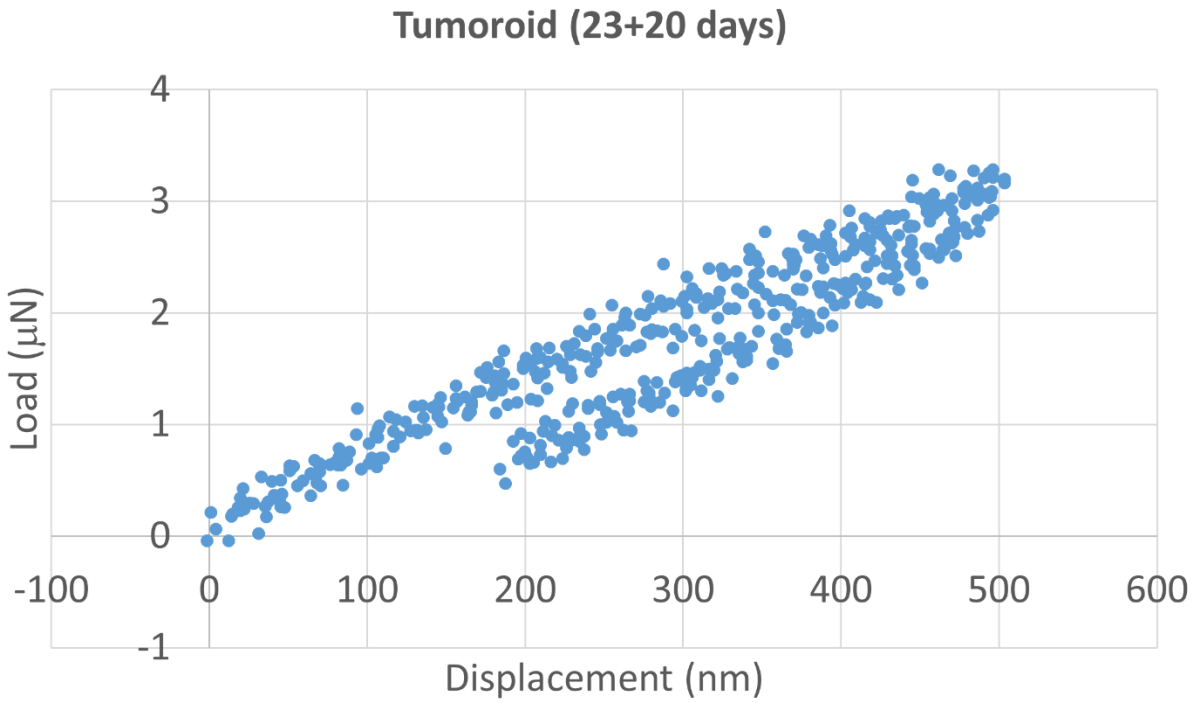

Figure A5. L-D curve on tumoroid at maximum displacement 500 nm (day 23+20) (Continued).

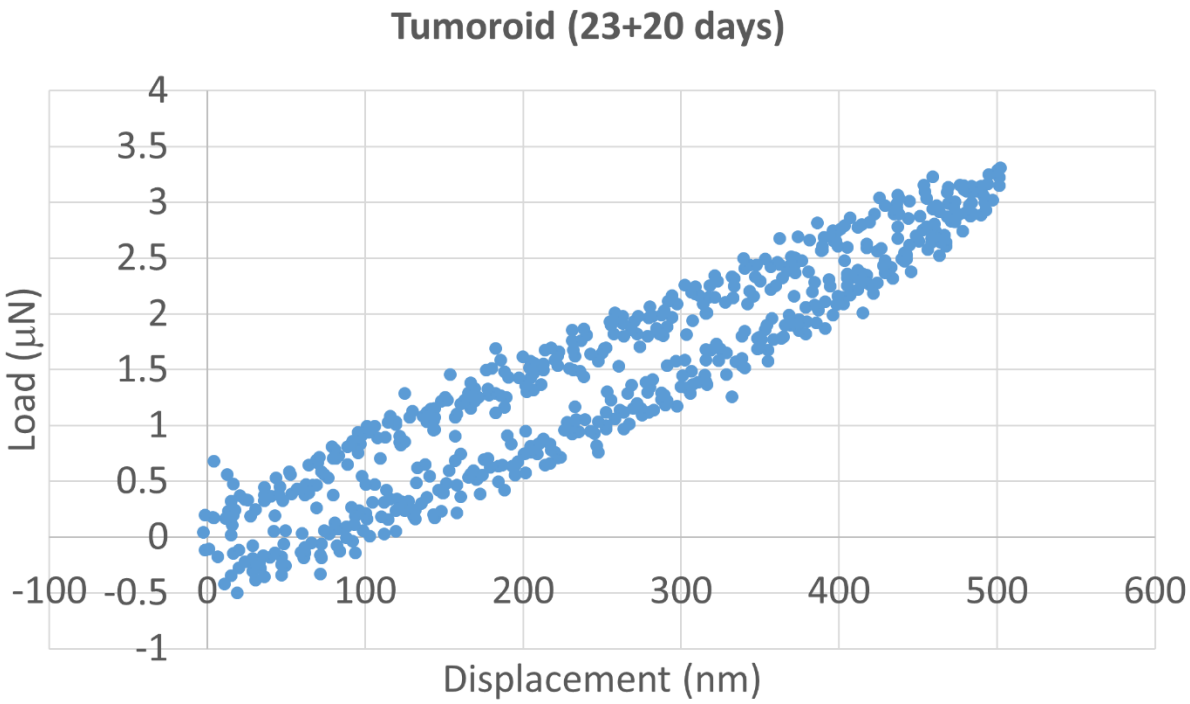

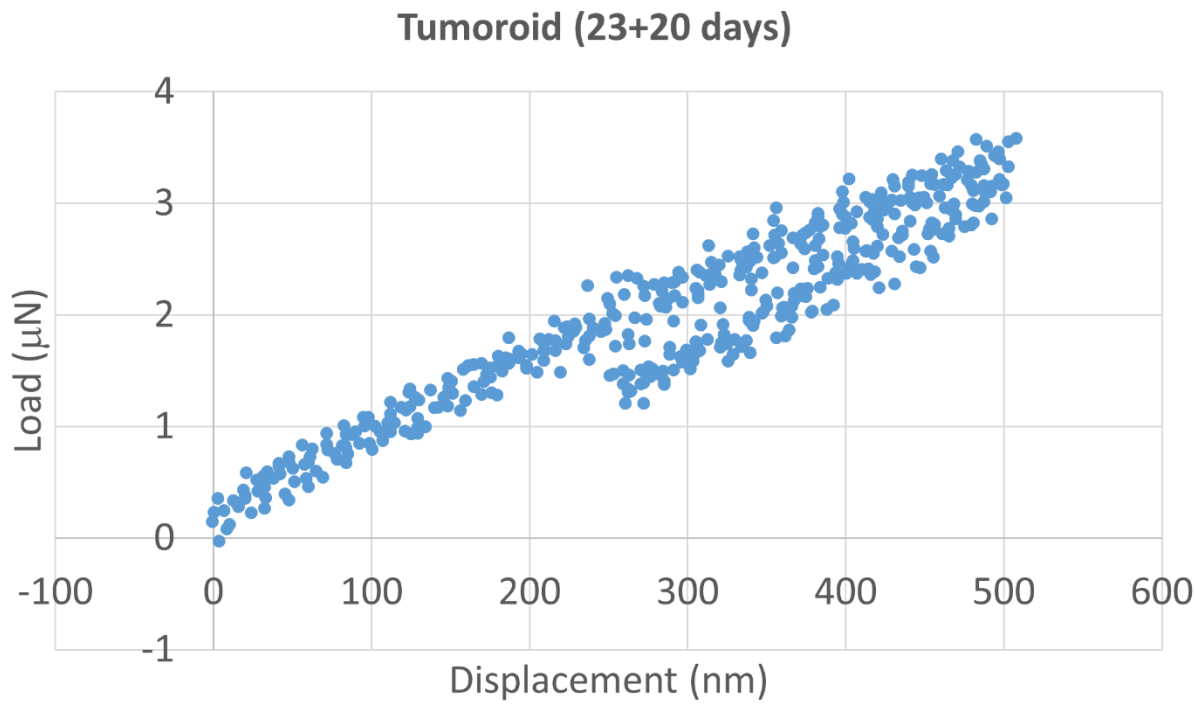

Figure A5. L-D curve on tumoroid at maximum displacement 500 nm (day 23+20) (Continued).

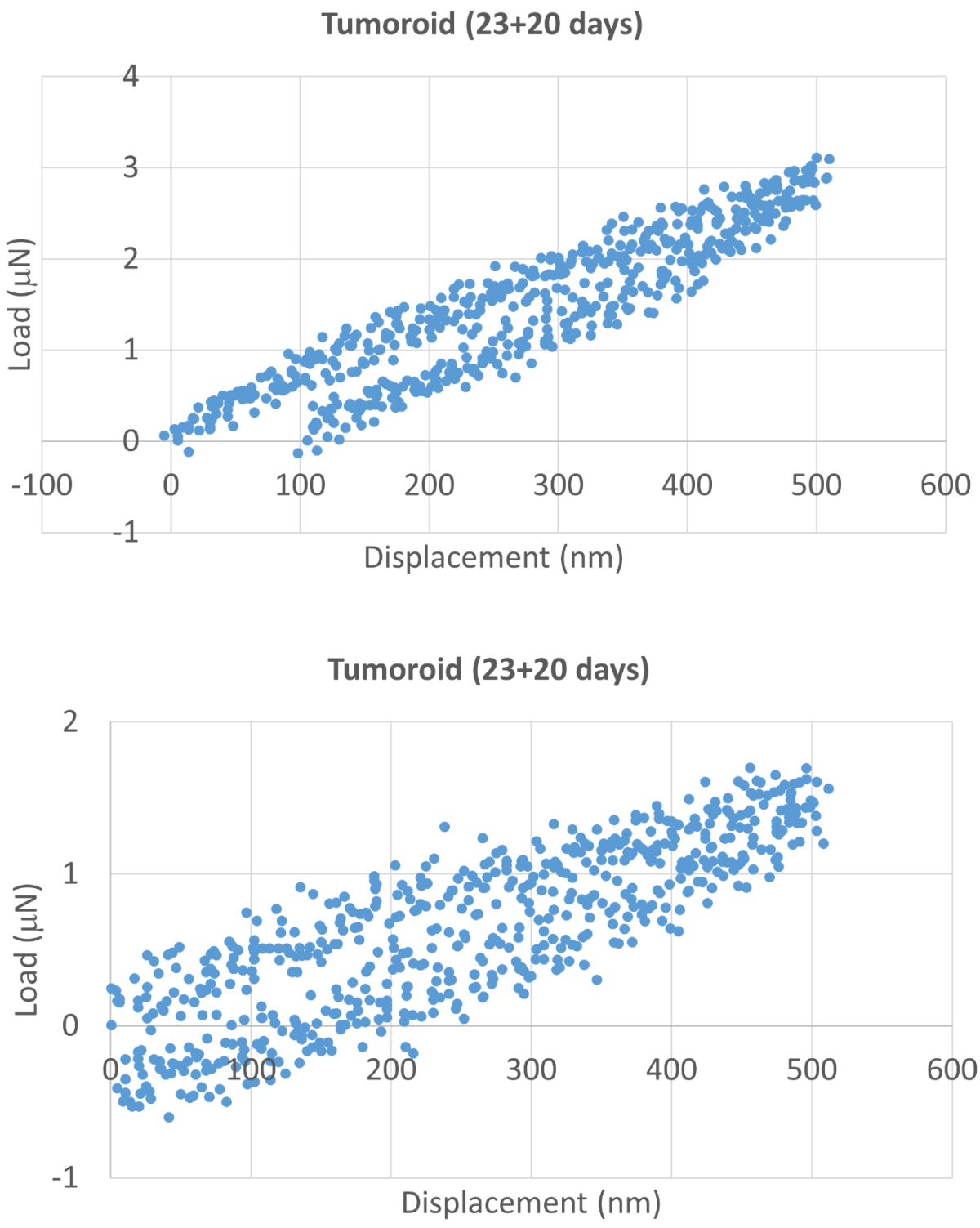

Figure A5. L-D curve on tumoroid at maximum displacement 500 nm (day 23+20) (Continued).

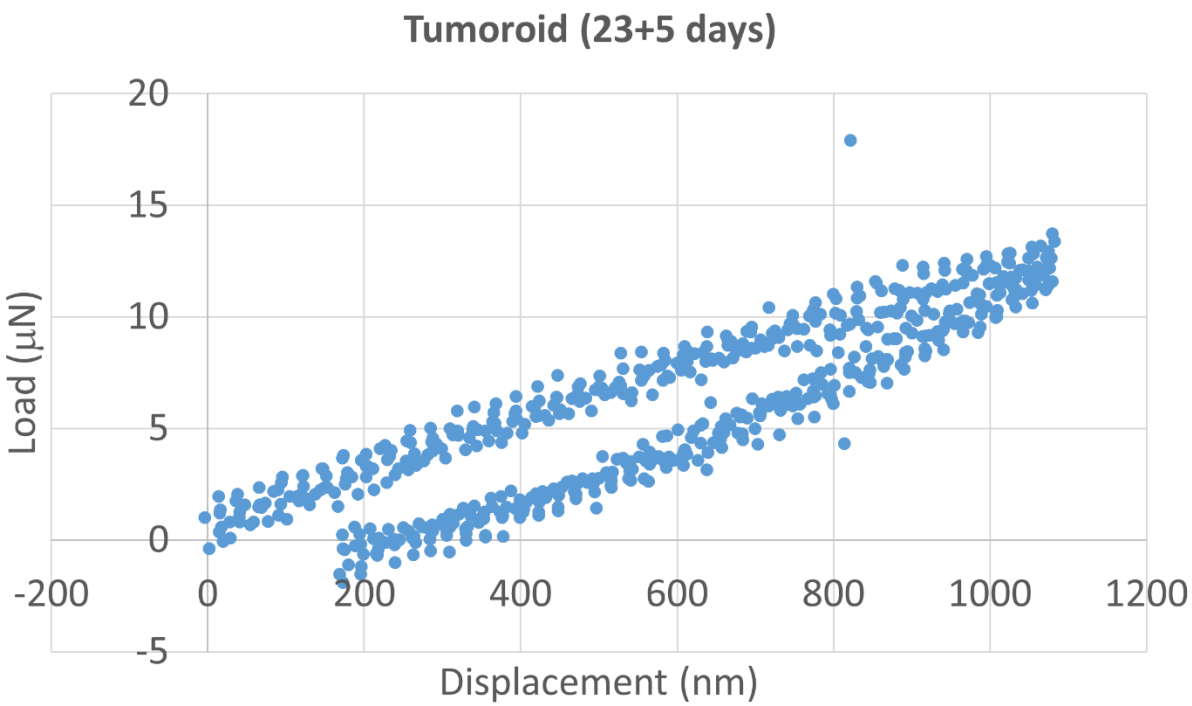

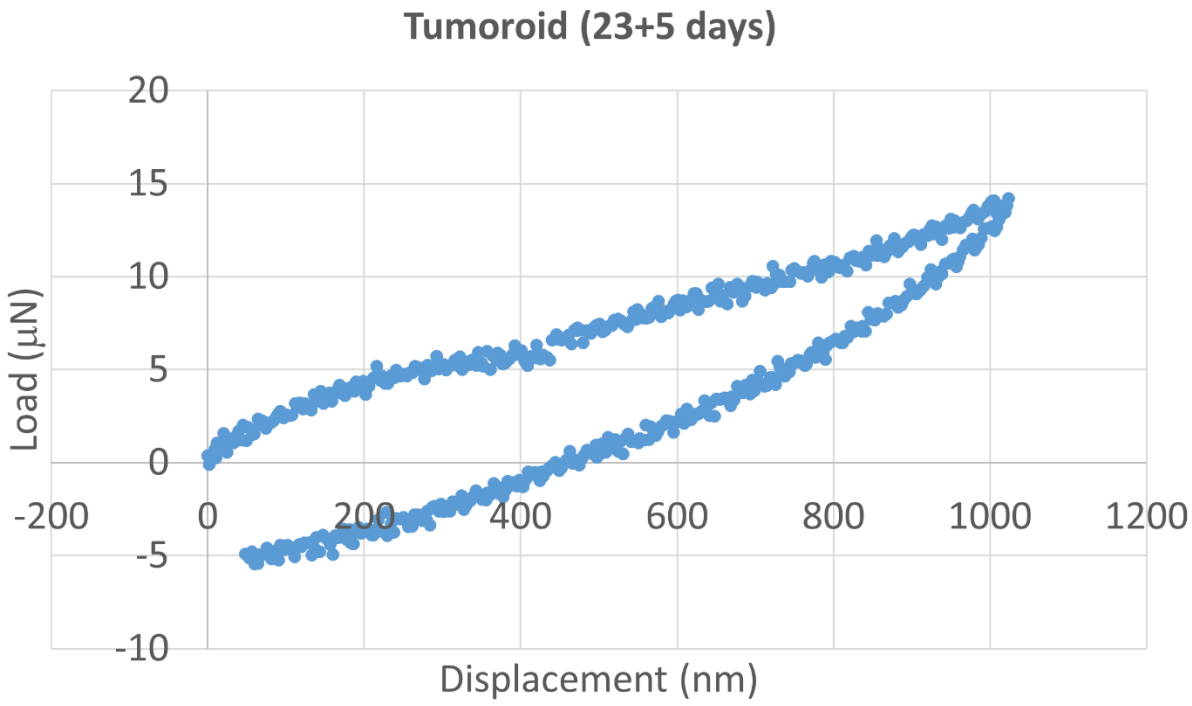

Figure A6. L-D curve on tumoroid at maximum displacement 1000 nm (day 23+5).

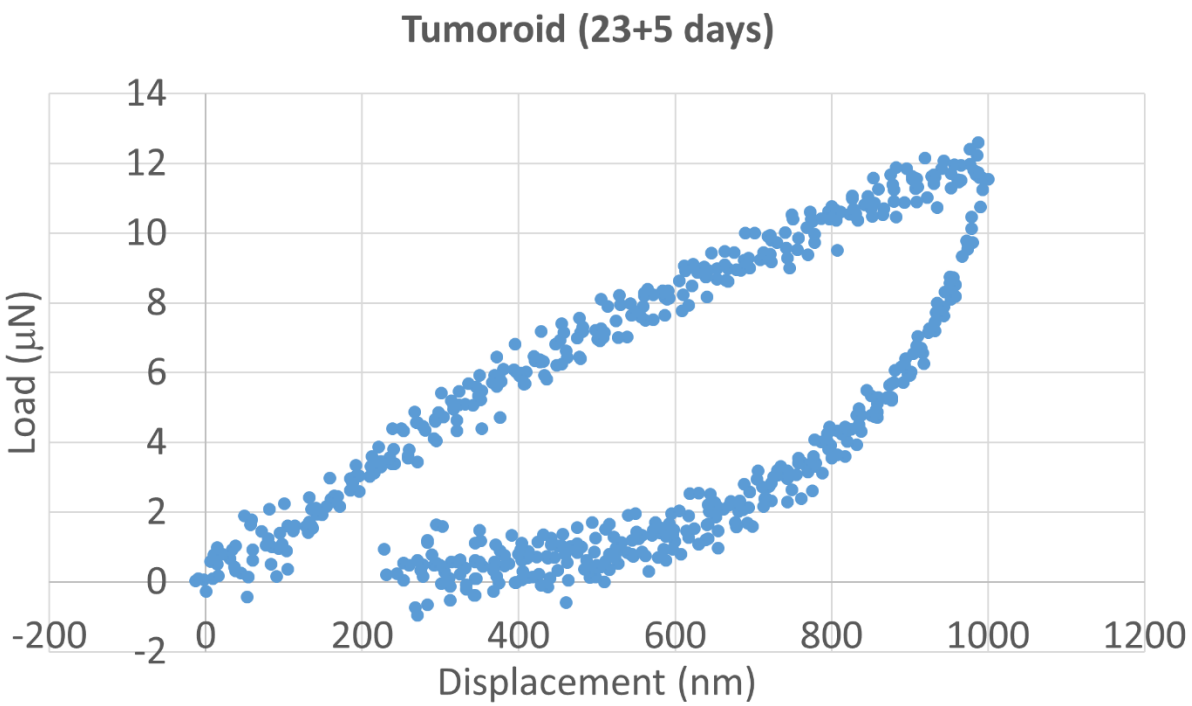

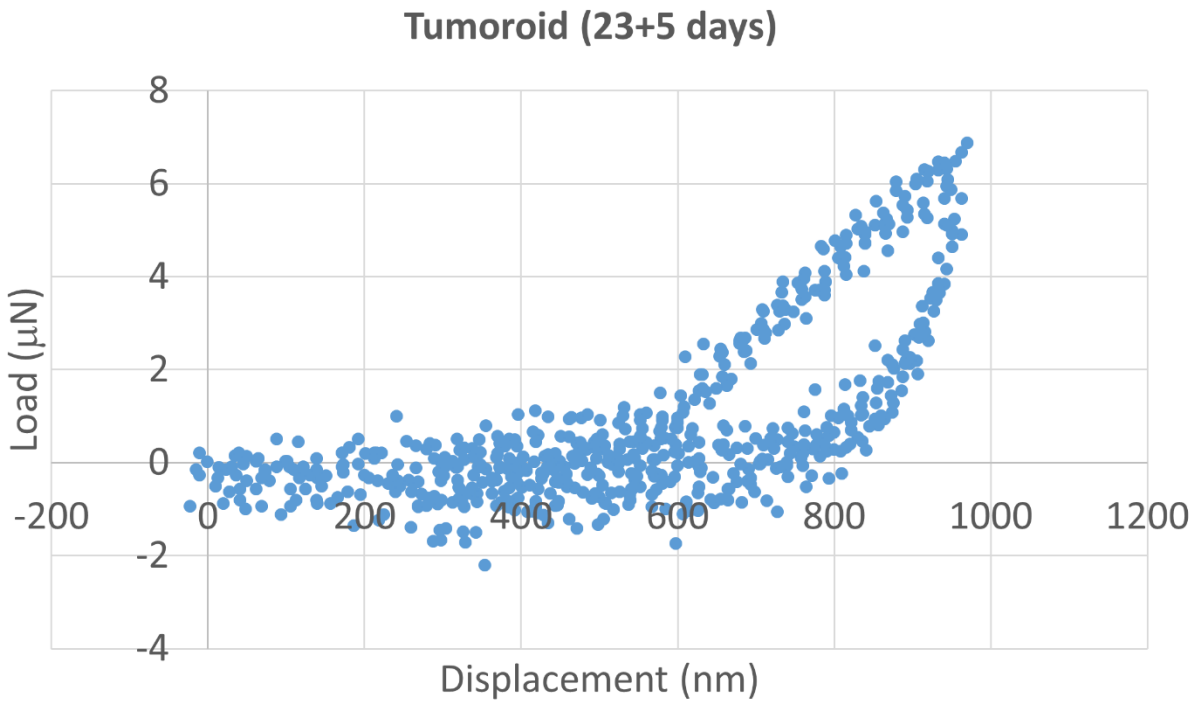

Figure A6. L-D curve on tumoroid at maximum displacement 1000 nm (day 23+5) (Continued).

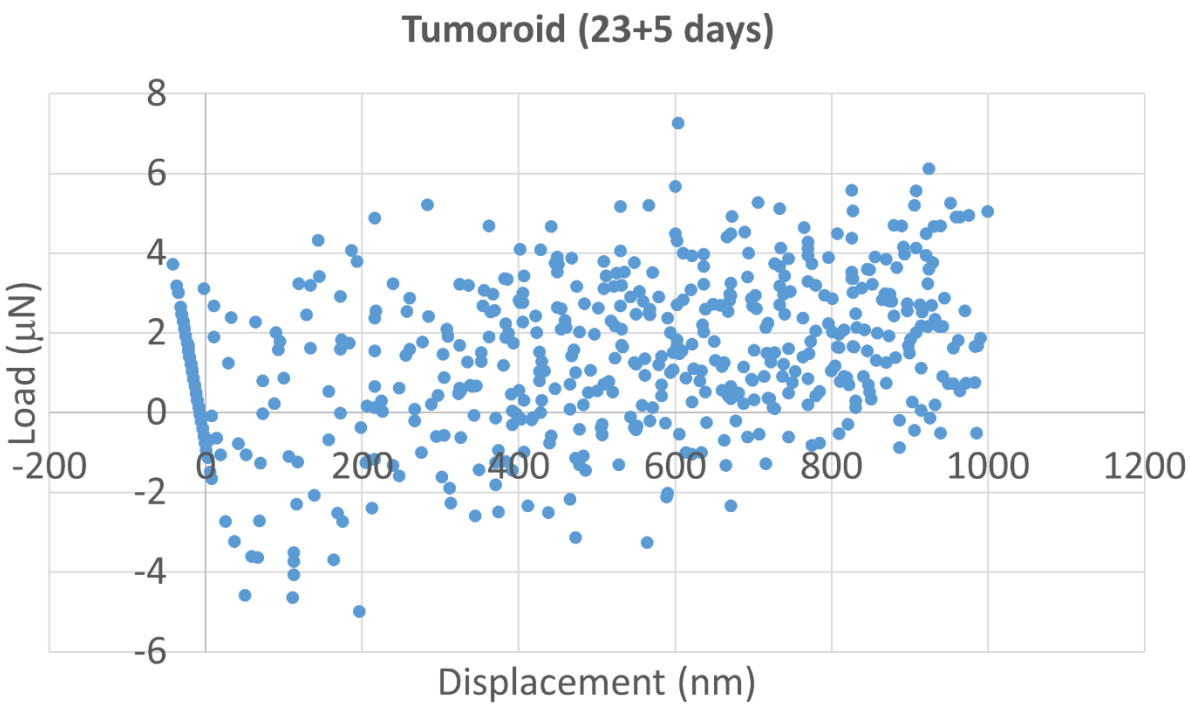

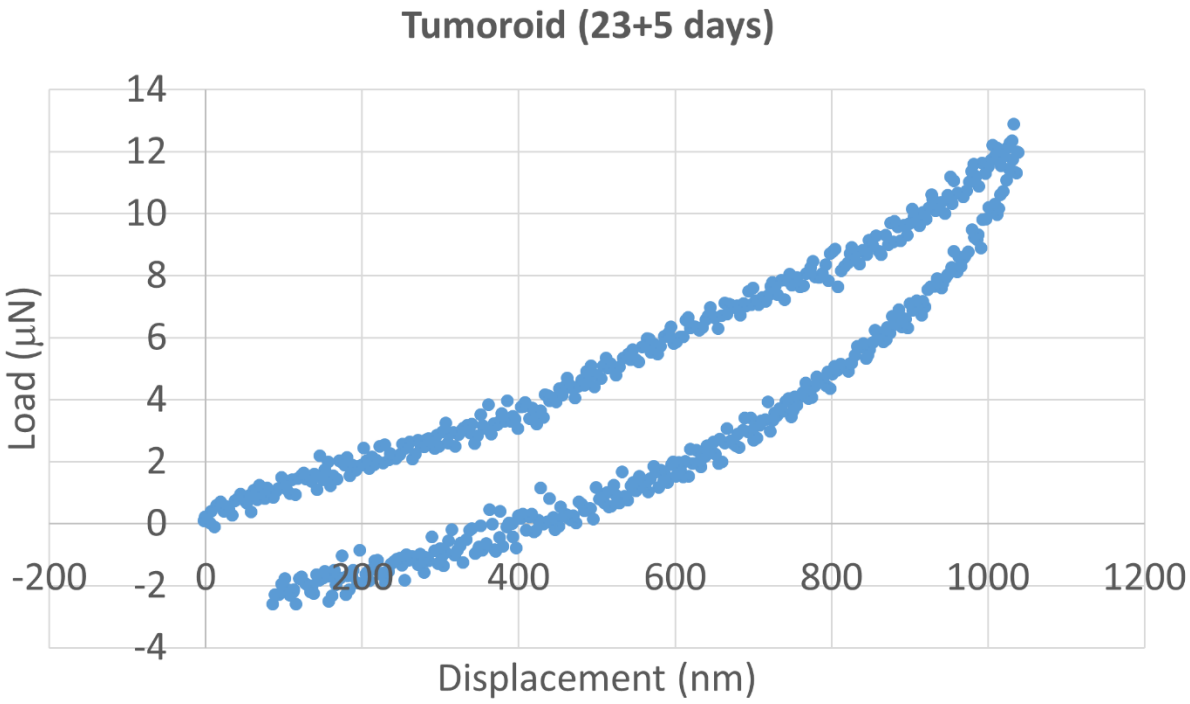

Figure A6. L-D curve on tumoroid at maximum displacement 1000 nm (day 23+5) (Continued).

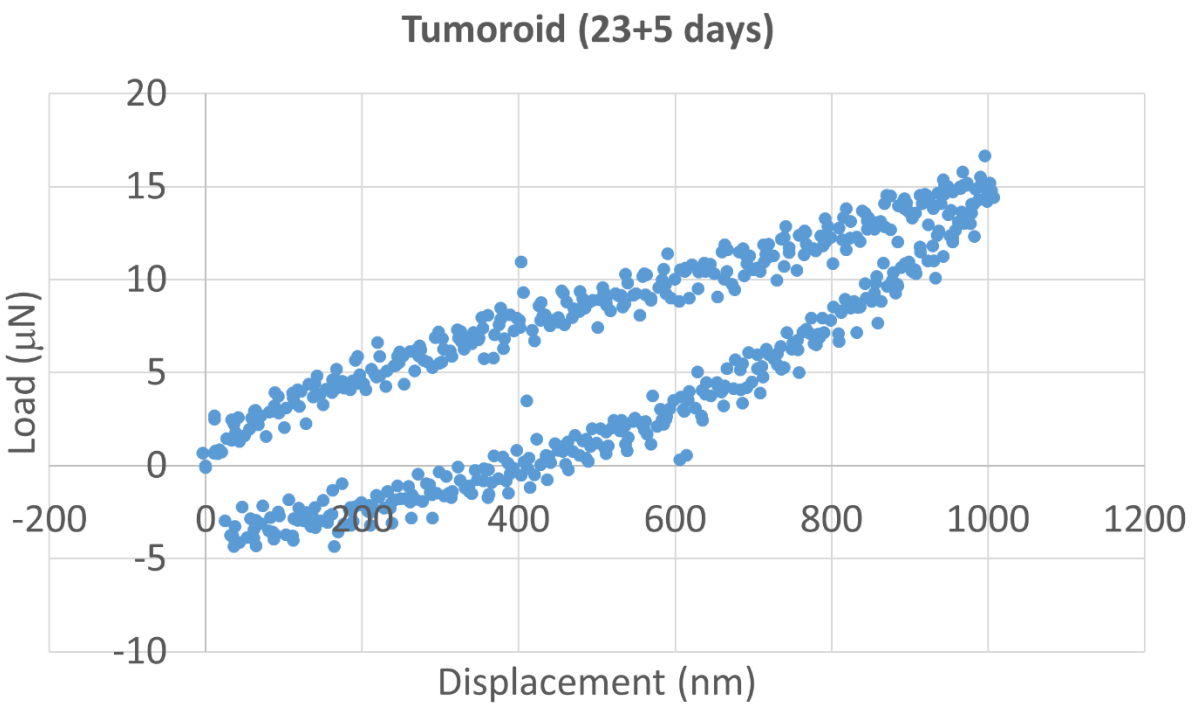

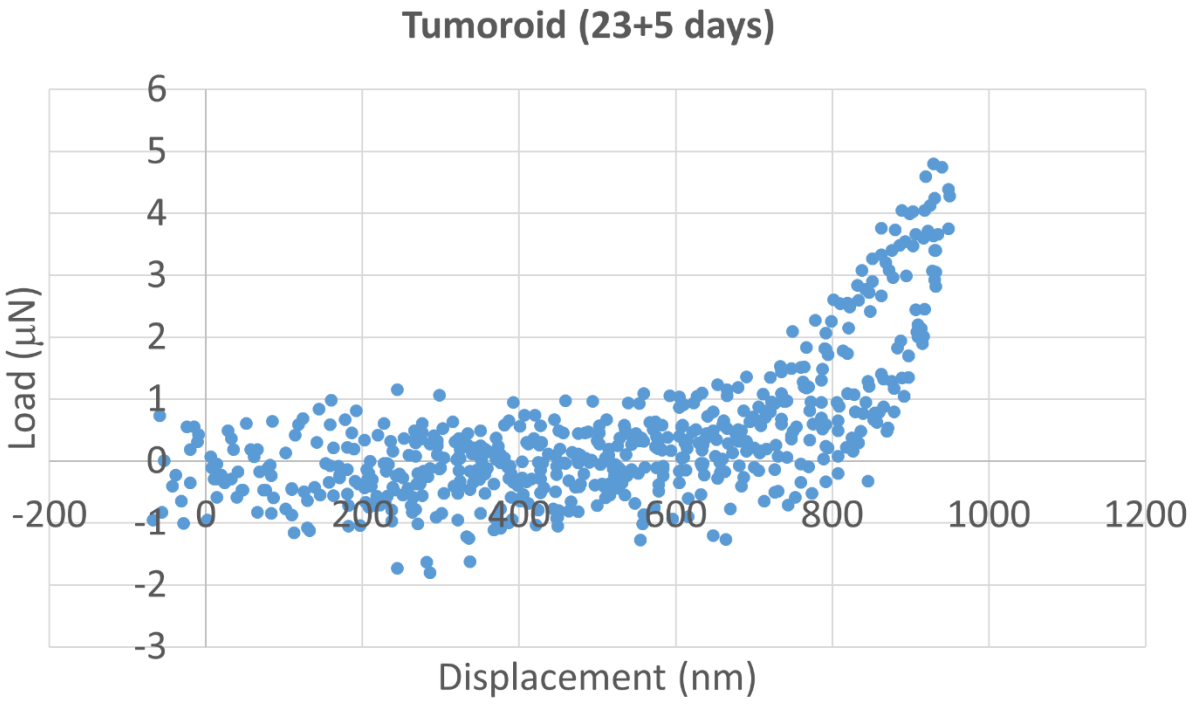

Figure A6. L-D curve on tumoroid at maximum displacement 1000 nm (day 23+5) (Continued).

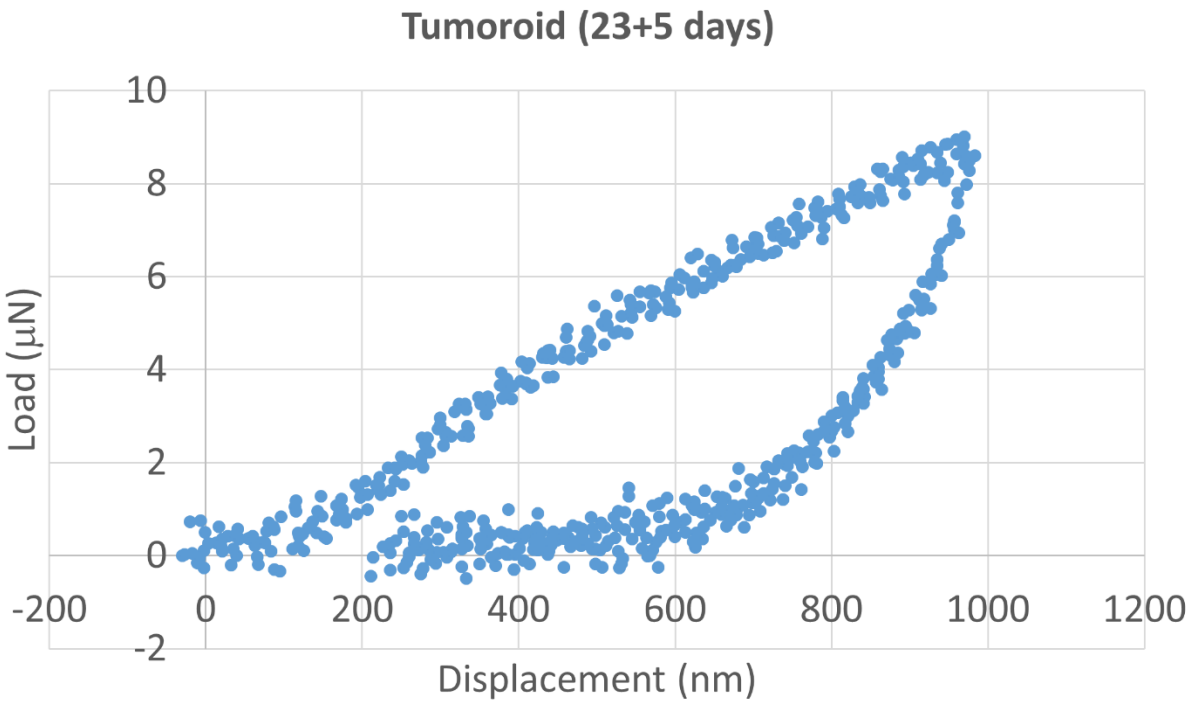

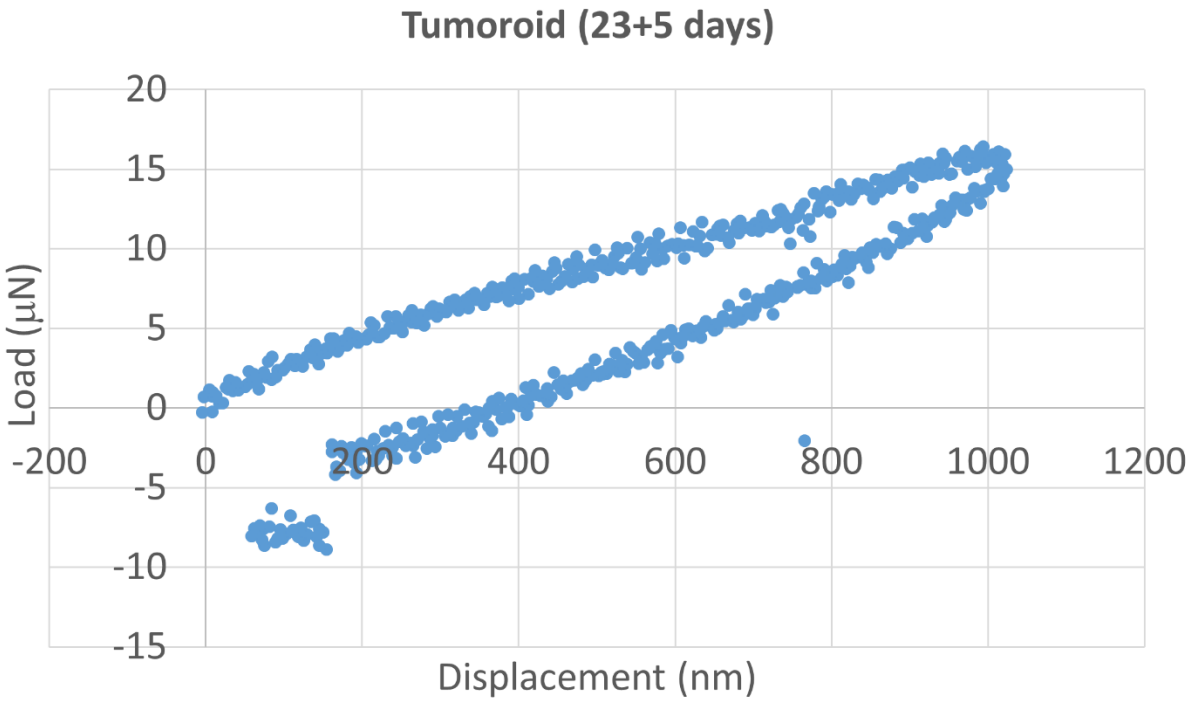

Figure A6. L-D curve on tumoroid at maximum displacement 1000 nm (day 23+5) (Continued).

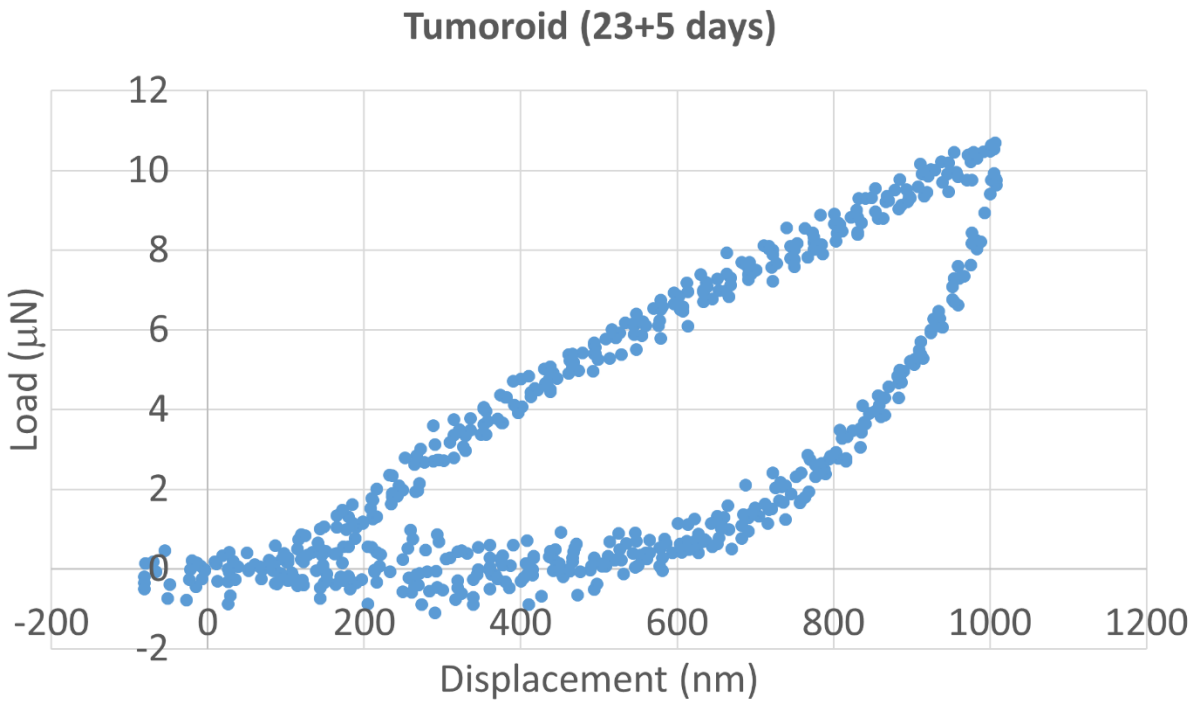

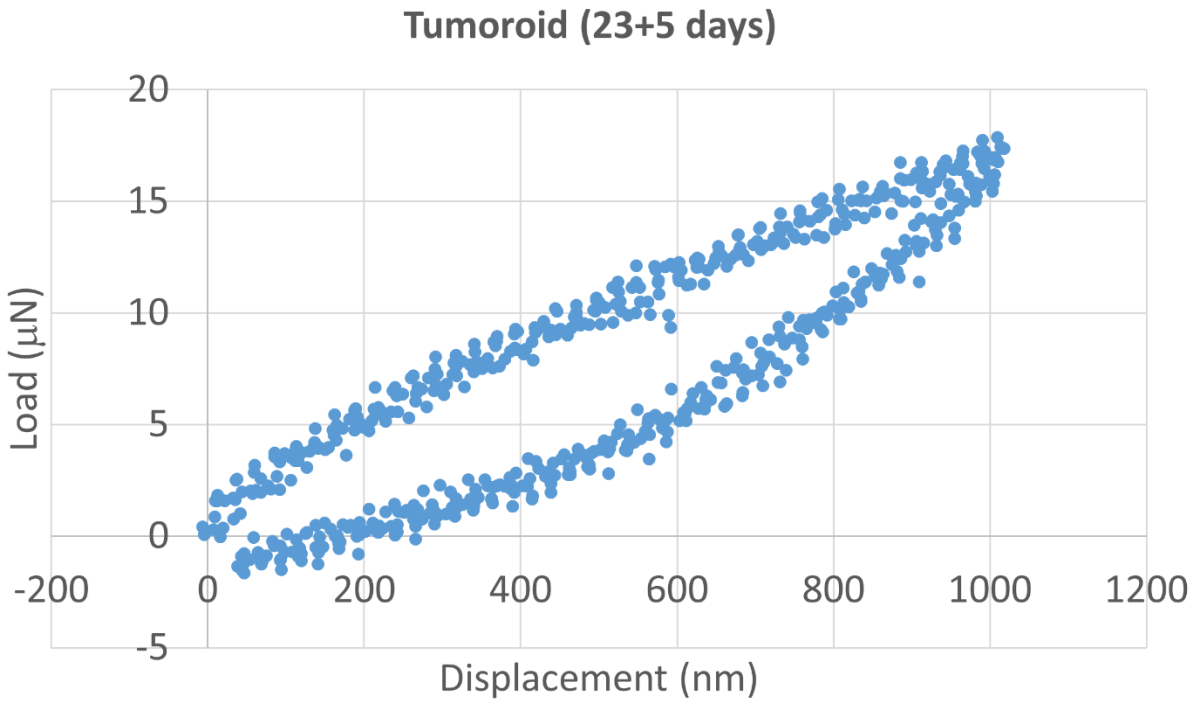

Figure A6. L-D curve on tumoroid at maximum displacement 1000 nm (day 23+5) (Continued).

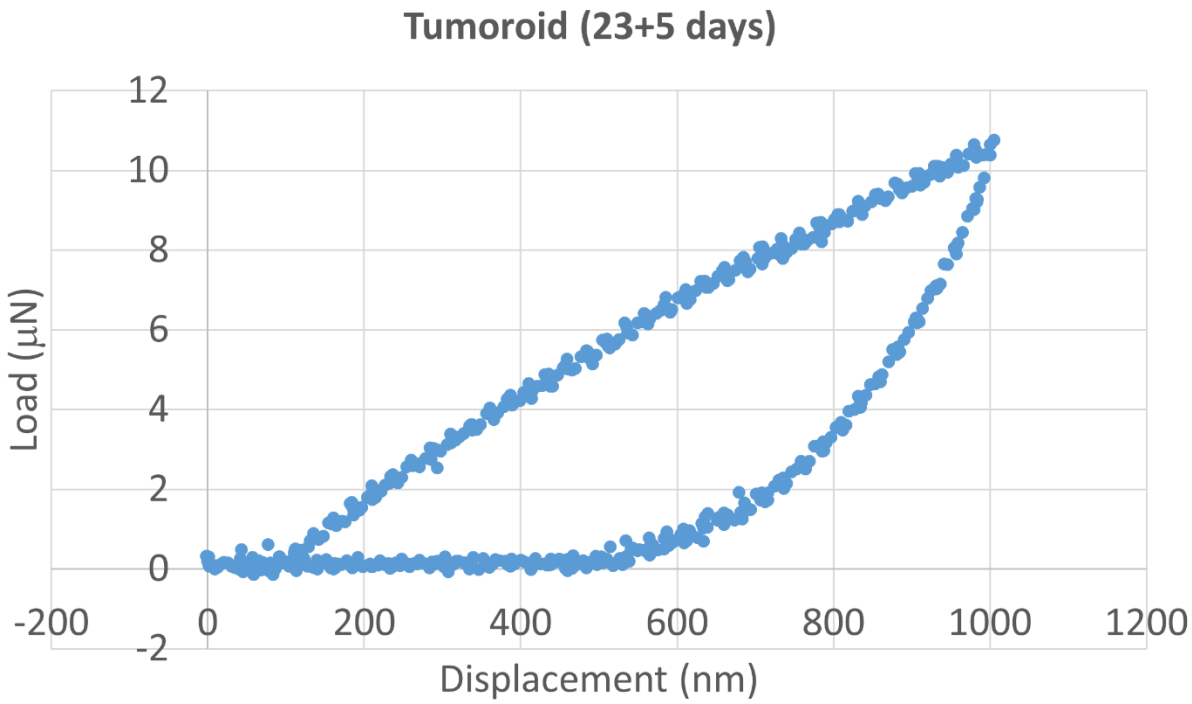

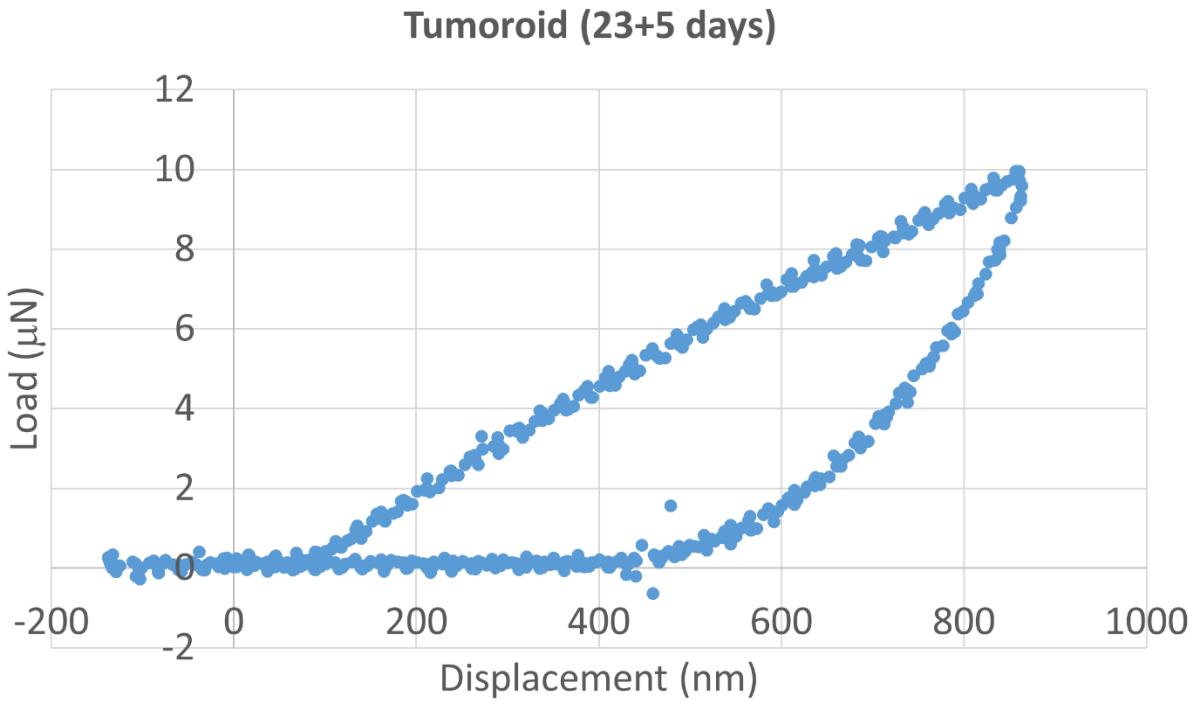

Figure A6. L-D curve on tumoroid at maximum displacement 1000 nm (day 23+5) (Continued).

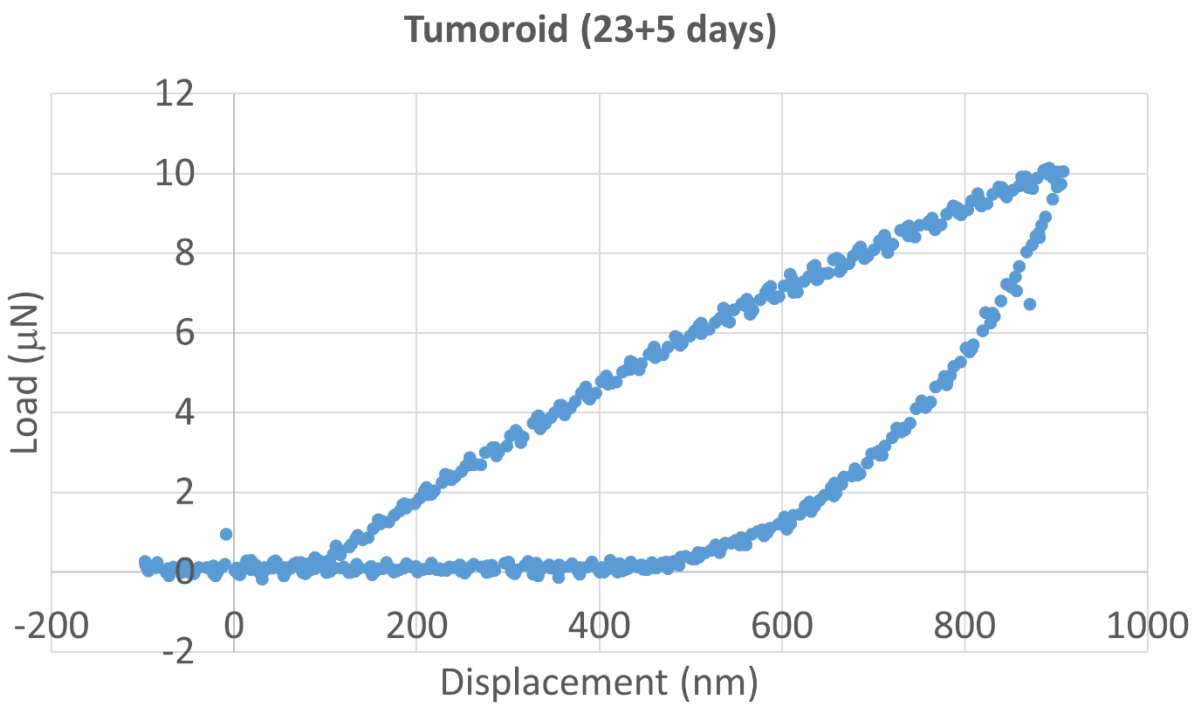

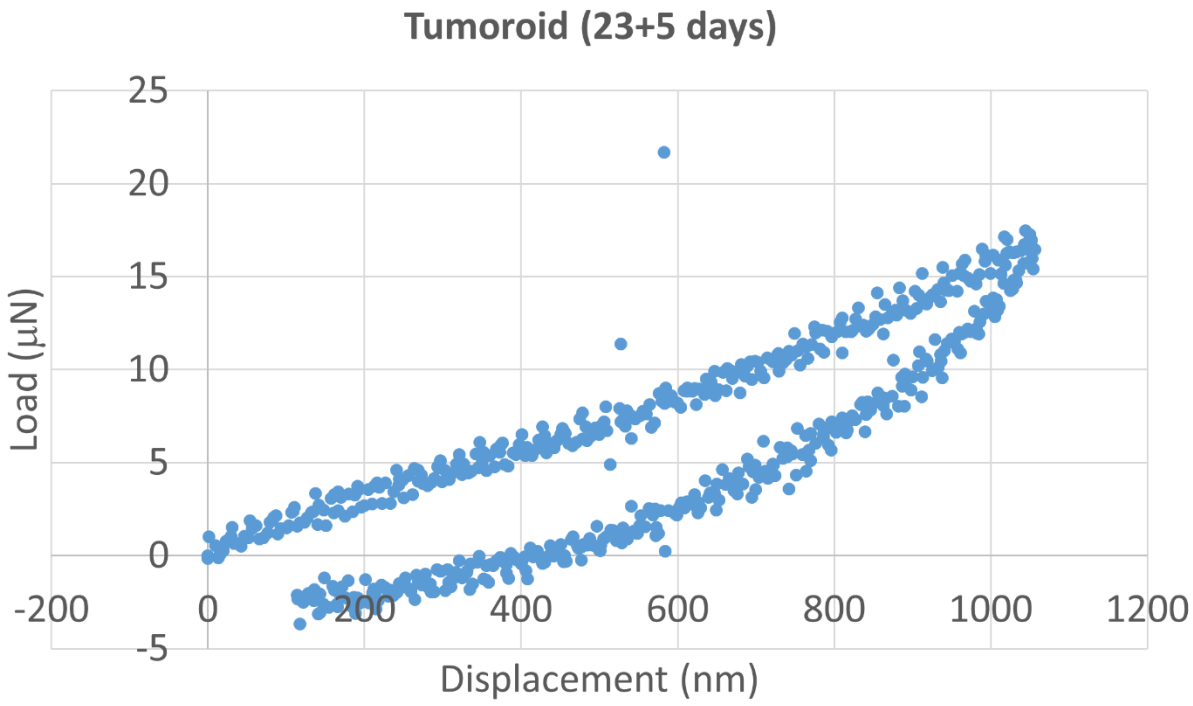

Figure A6. L-D curve on tumoroid at maximum displacement 1000 nm (day 23+5) (Continued).

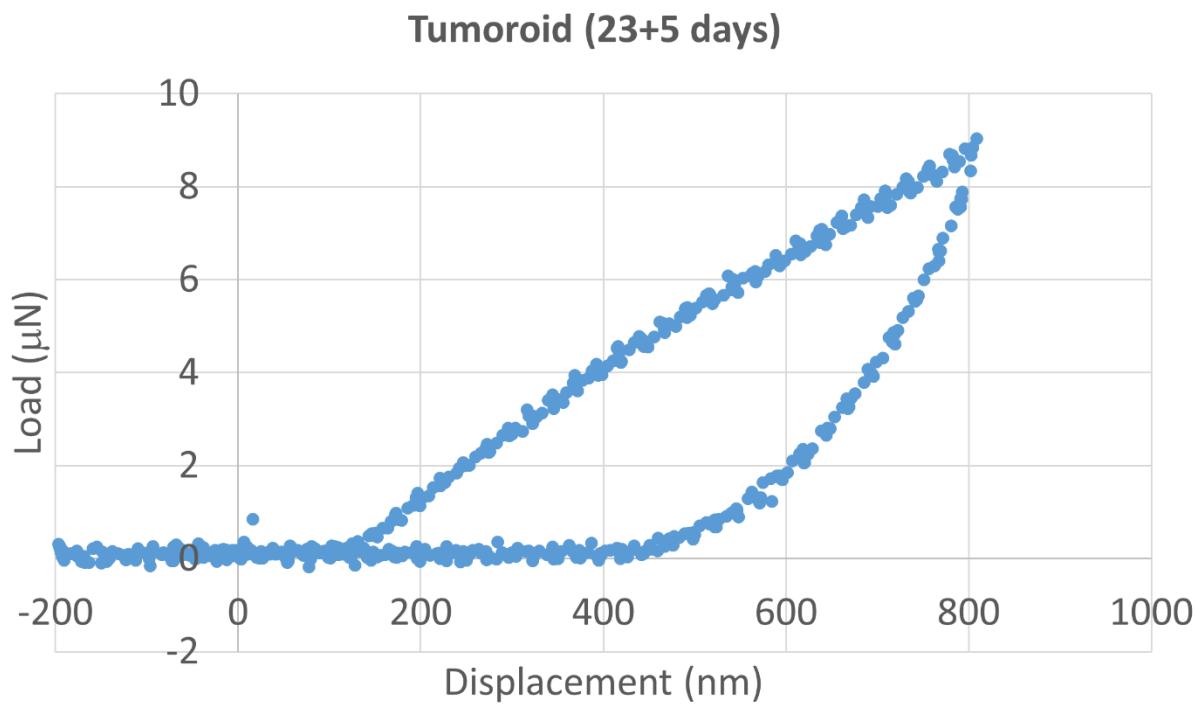

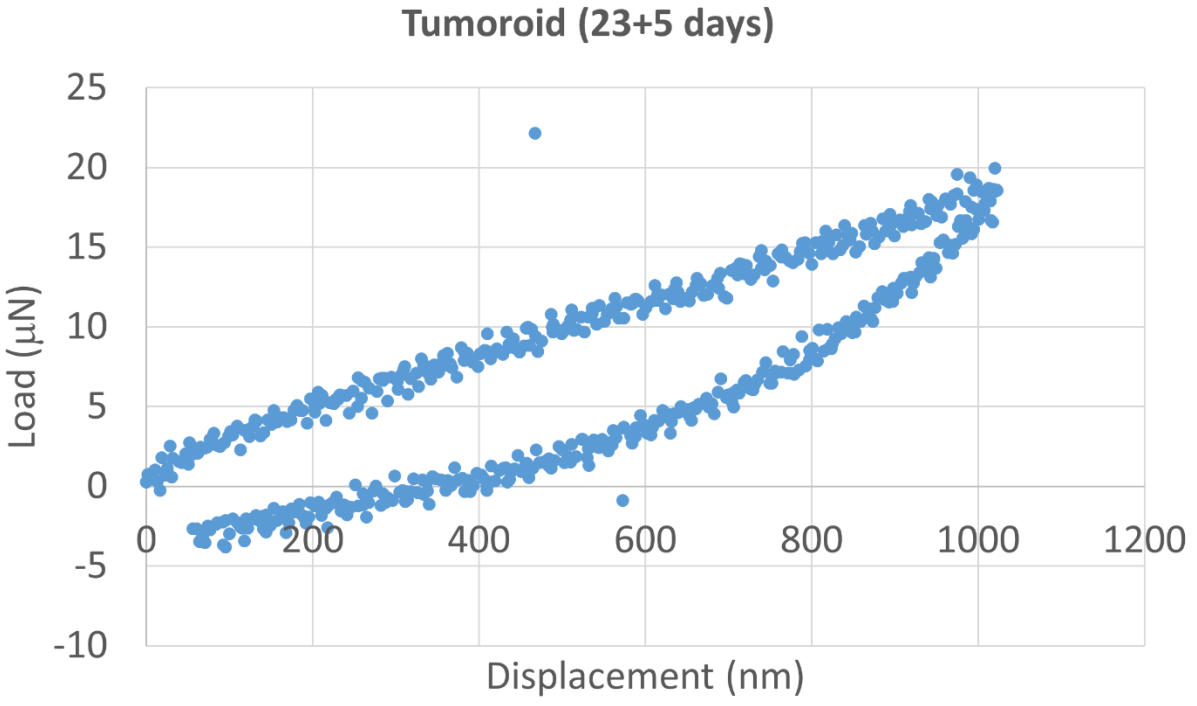

Figure A6. L-D curve on tumoroid at maximum displacement 1000 nm (day 23+5) (Continued).

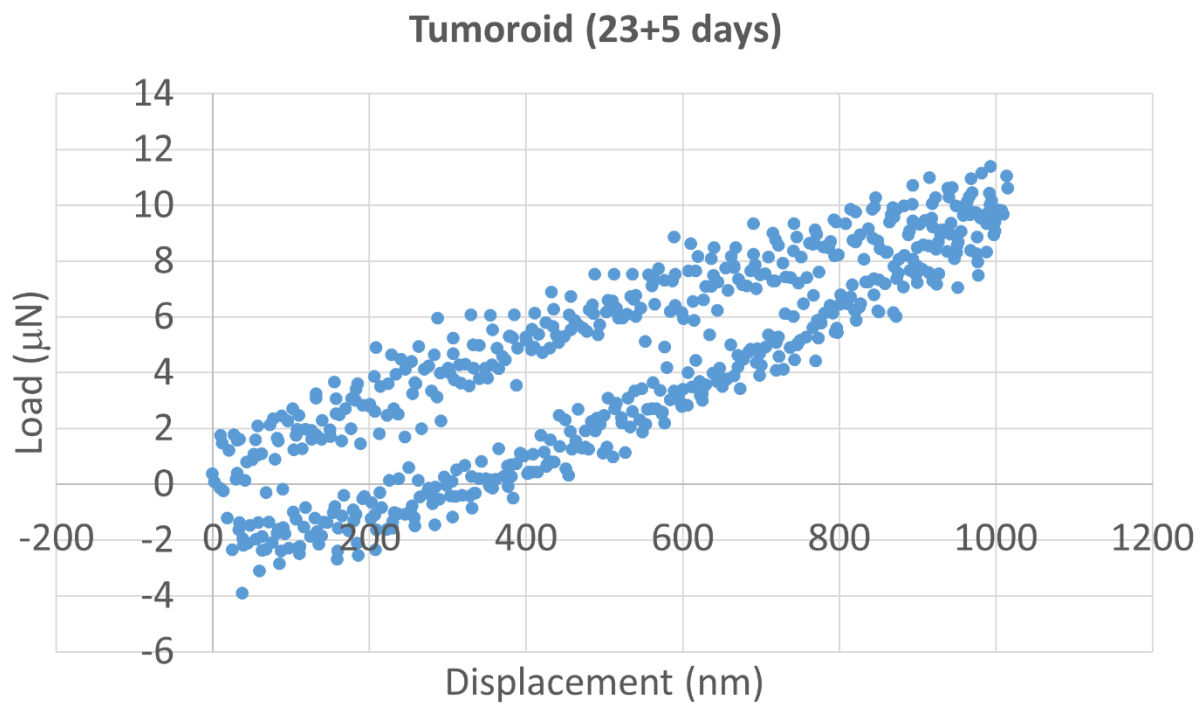

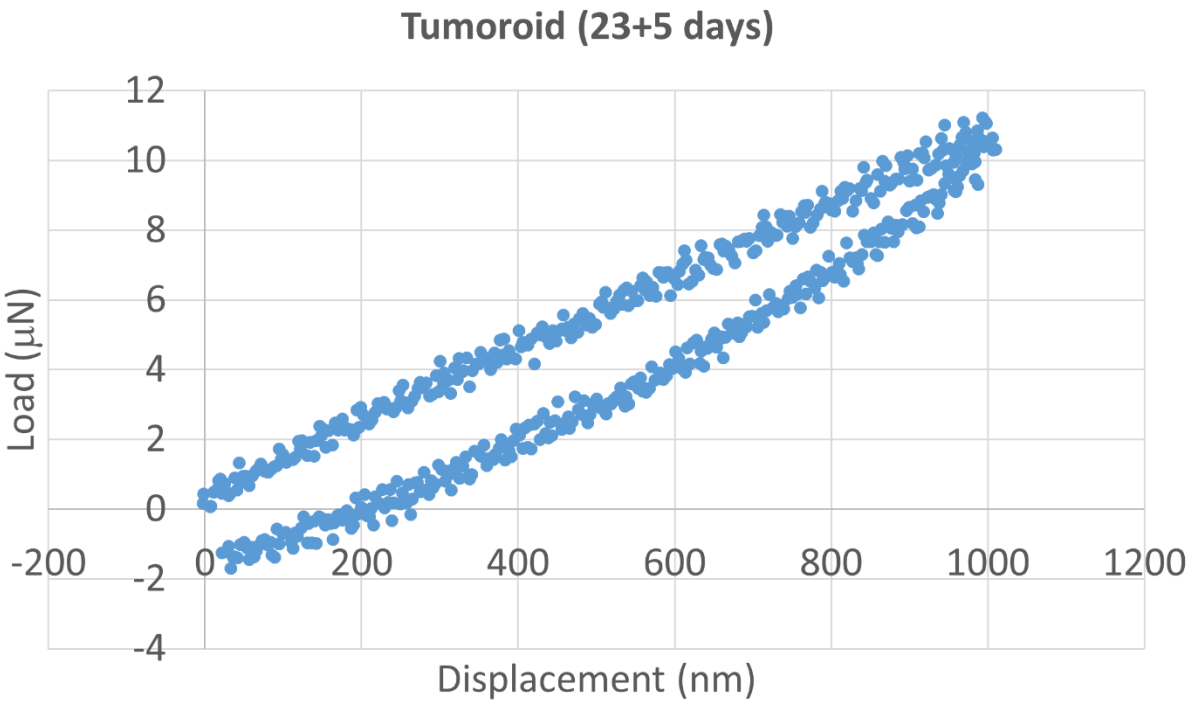

Figure A6. L-D curve on tumoroid at maximum displacement 1000 nm (day 23+5) (Continued).

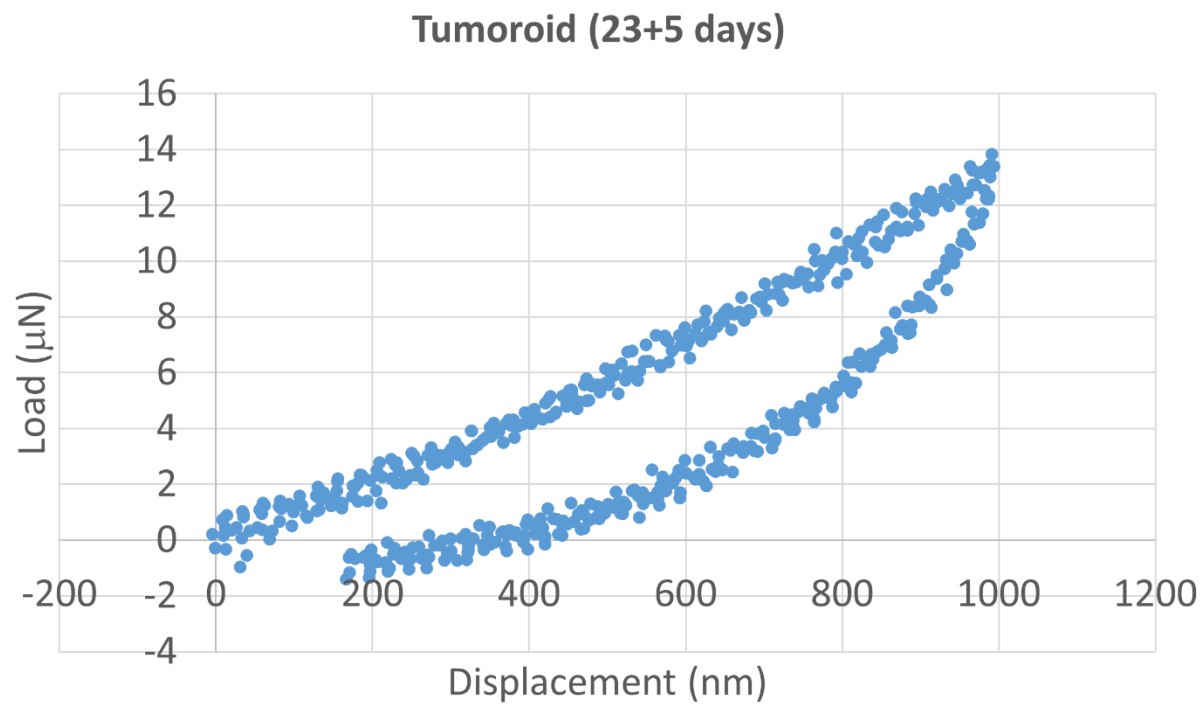

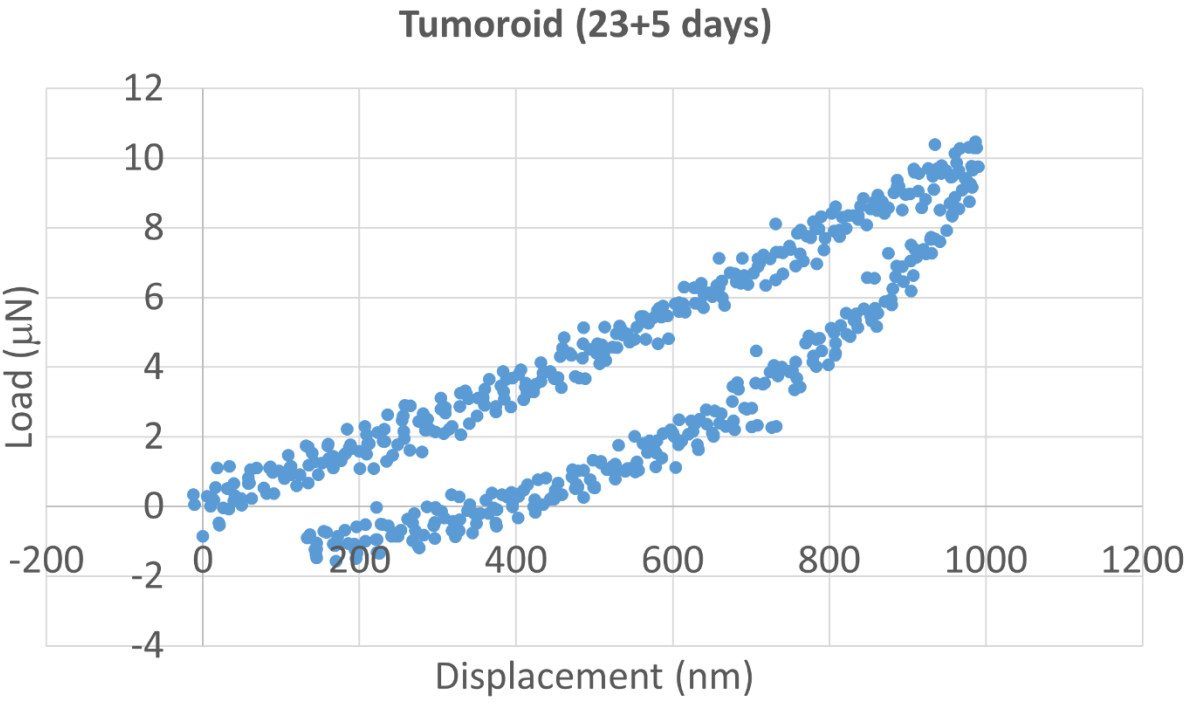

Figure A6. L-D curve on tumoroid at maximum displacement 1000 nm (day 23+5) (Continued).

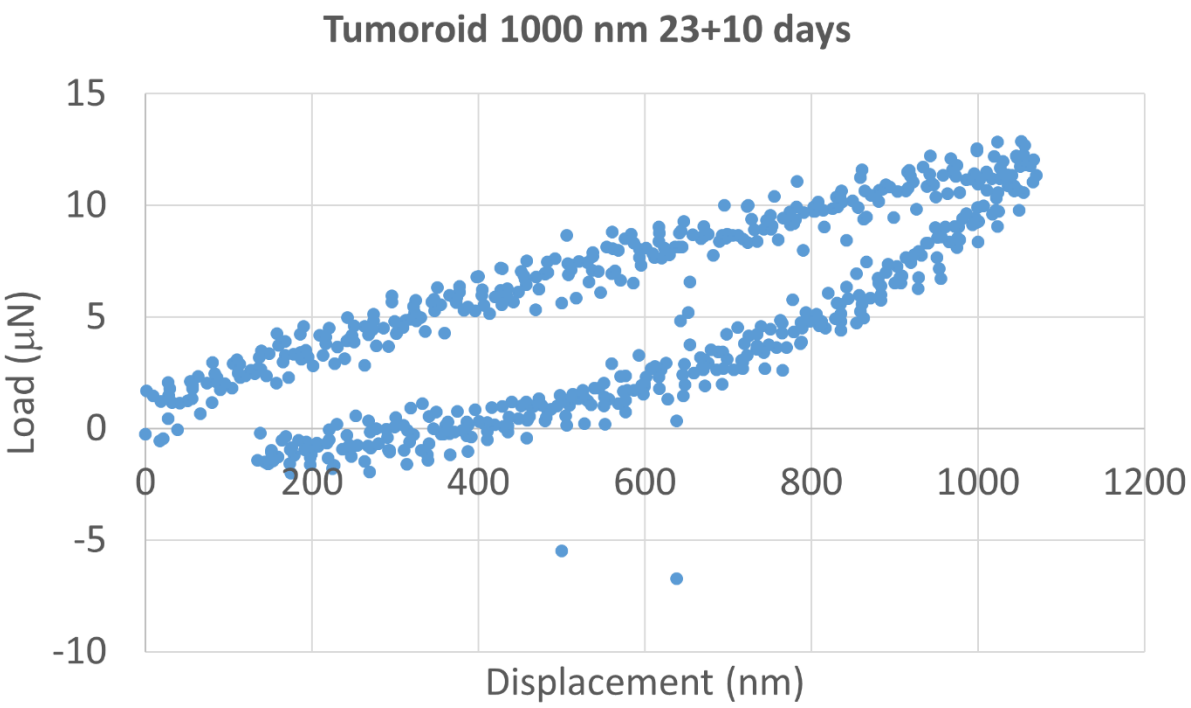

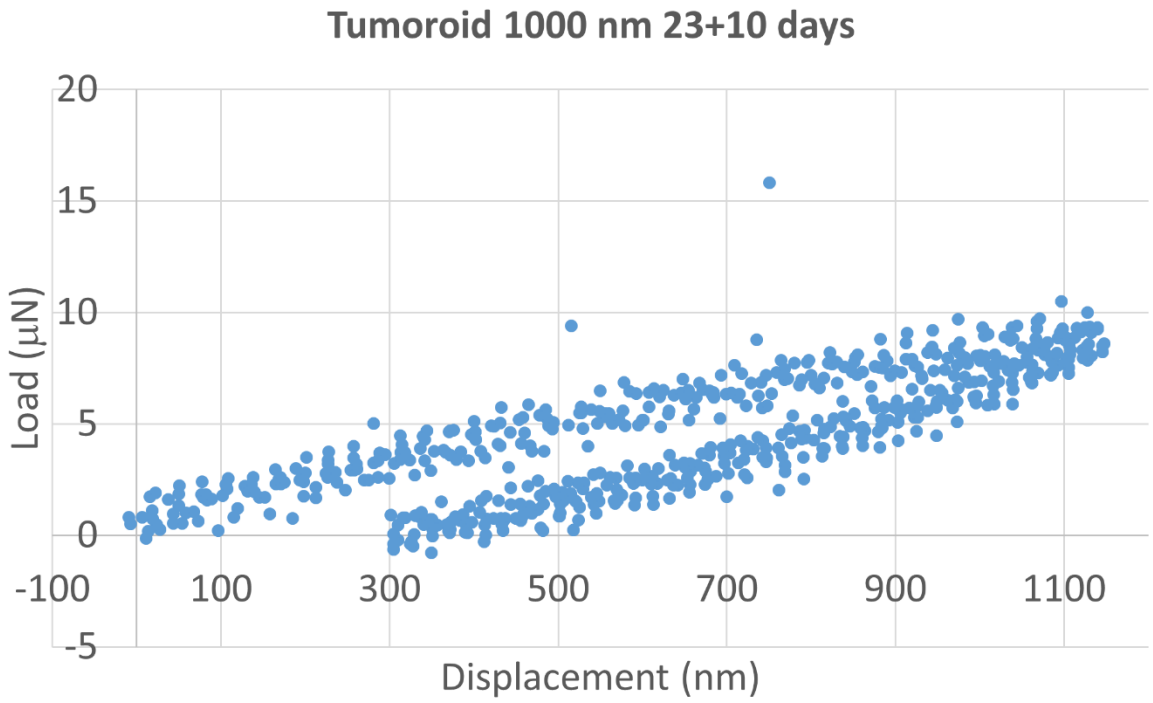

Figure A7. L-D curve on tumoroid at maximum displacement 1000 nm (day 23+10).

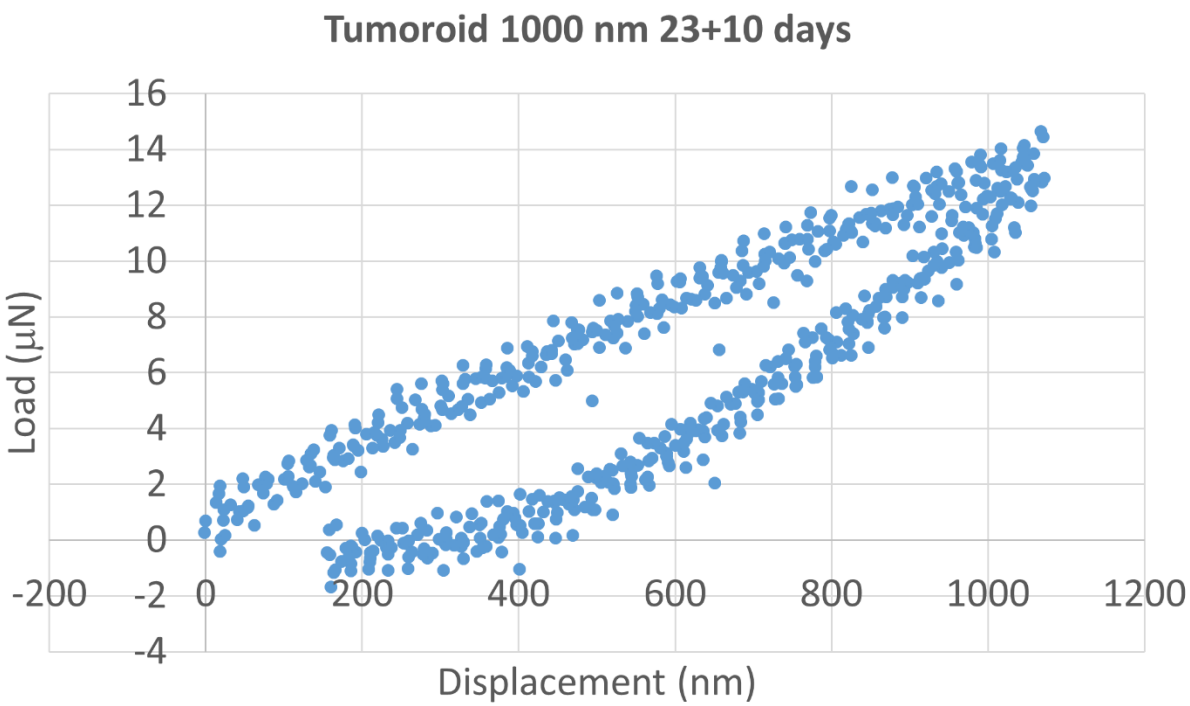

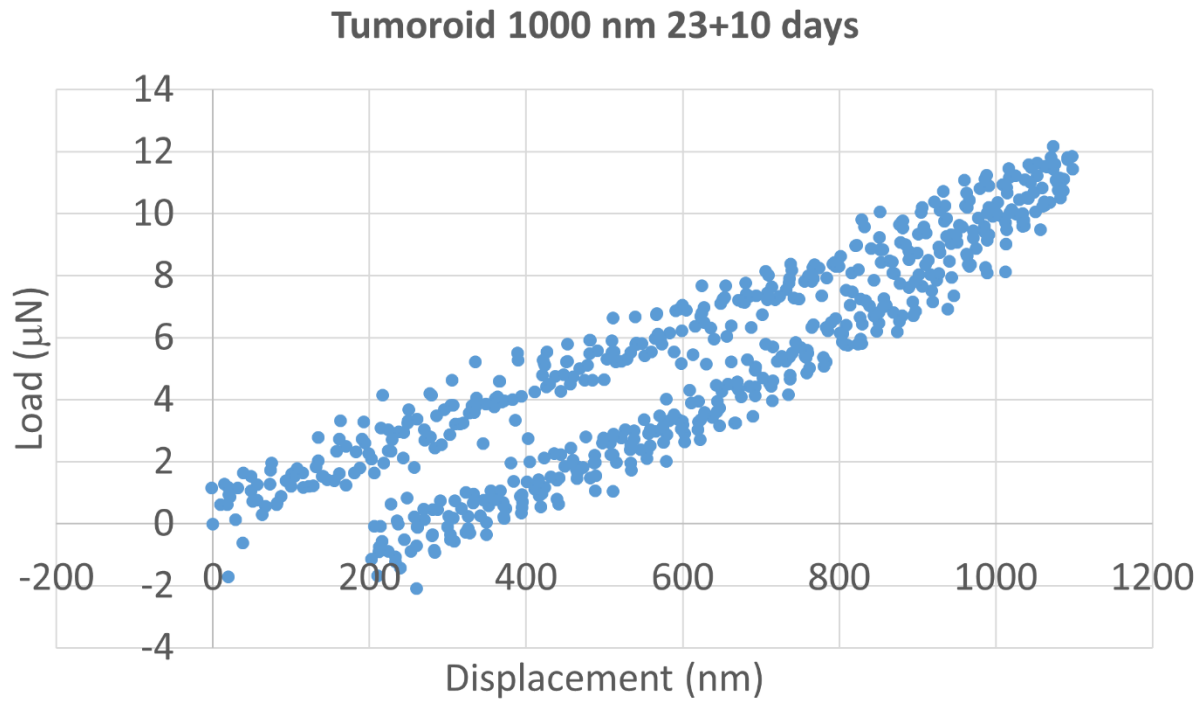

Figure A7. L-D curve on tumoroid at maximum displacement 1000 nm (day 23+10) (Continued).

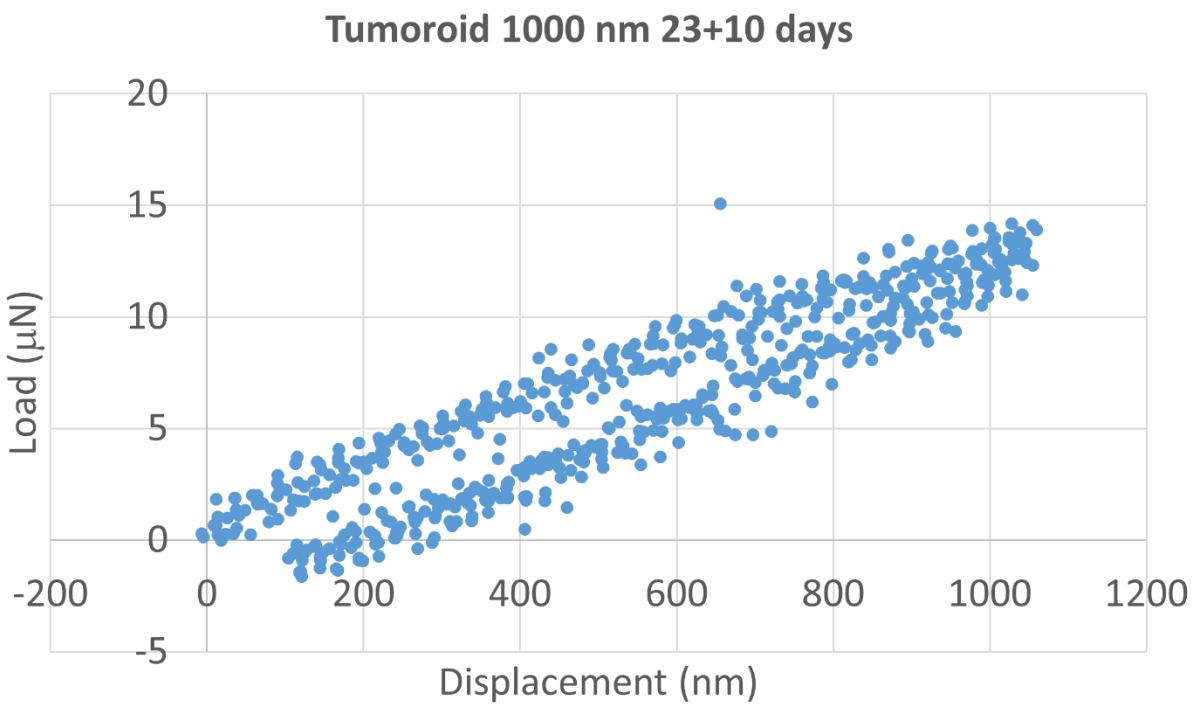

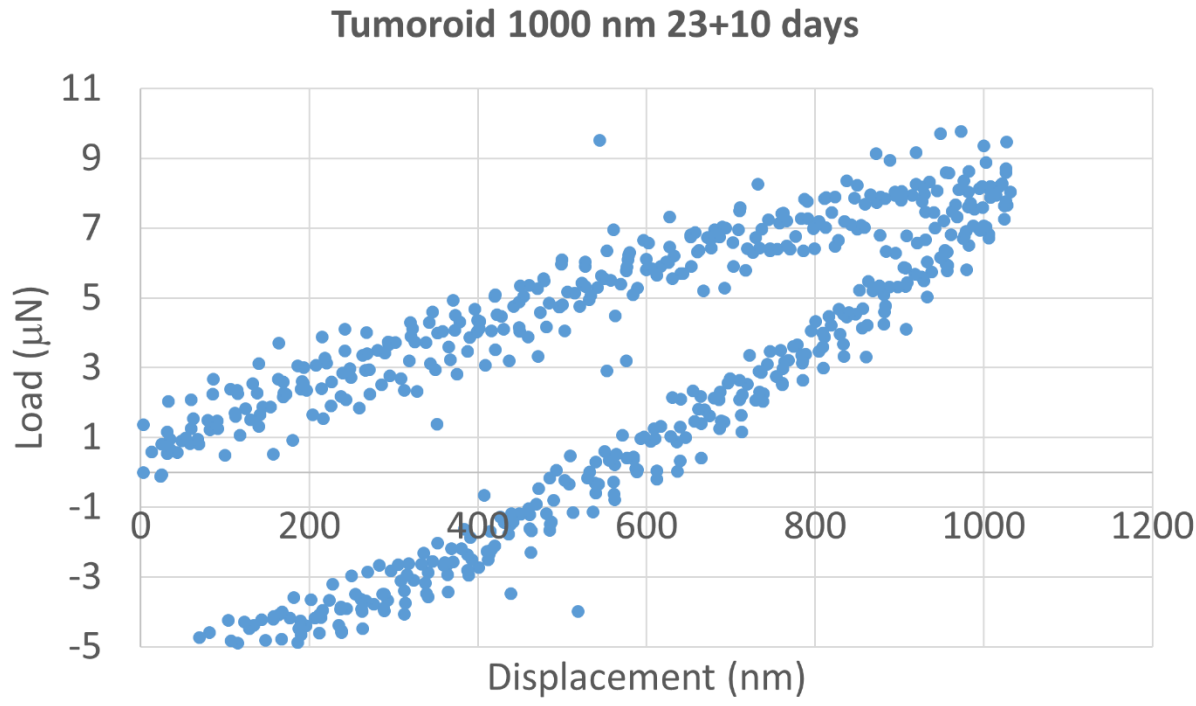

Figure A7. L-D curve on tumoroid at maximum displacement 1000 nm (day 23+10) (Continued).

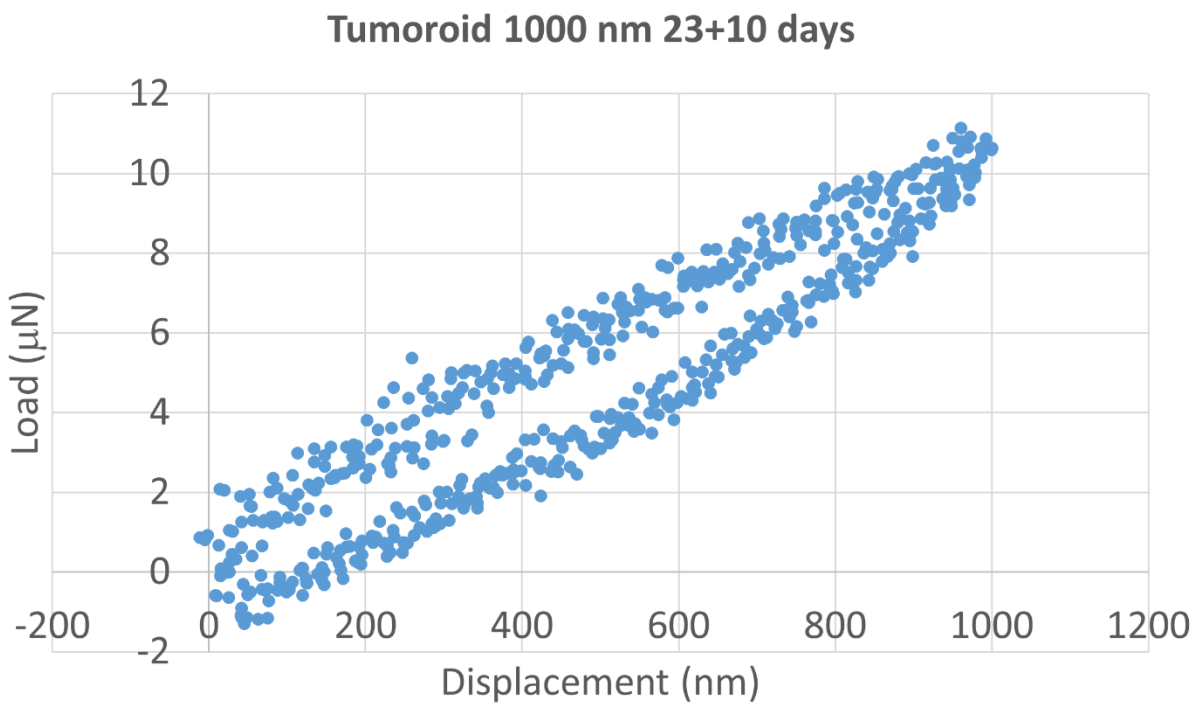

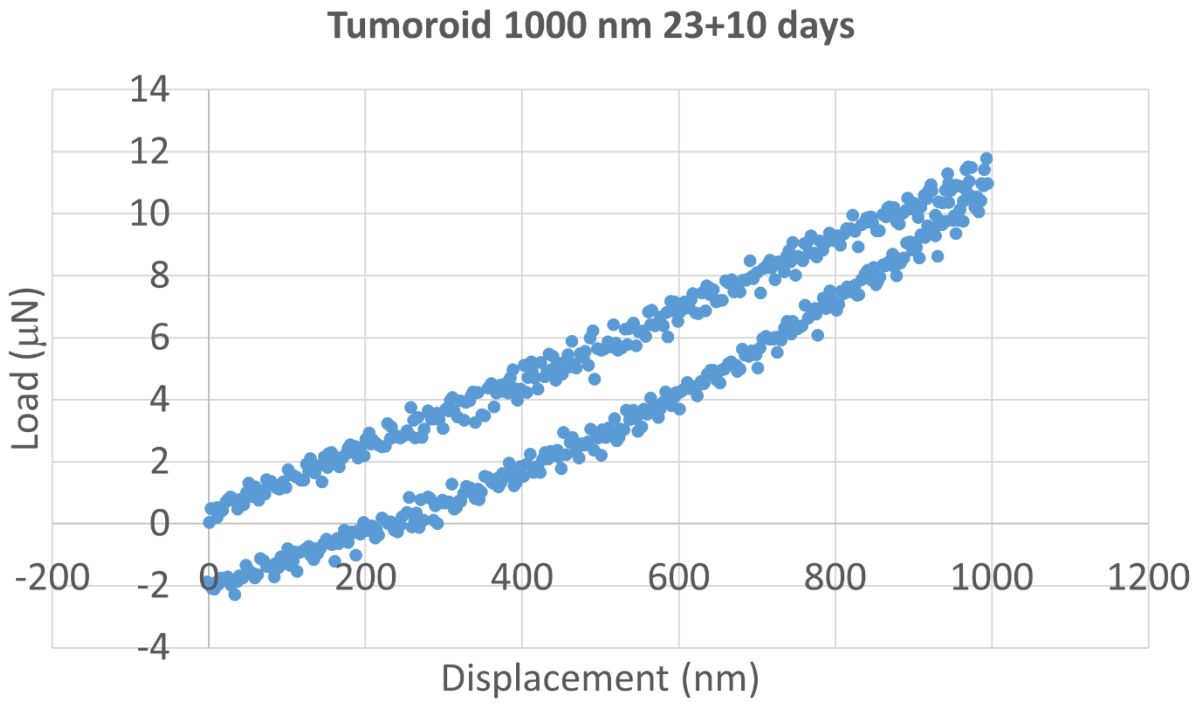

Figure A7. L-D curve on tumoroid at maximum displacement 1000 nm (day 23+10) (Continued).

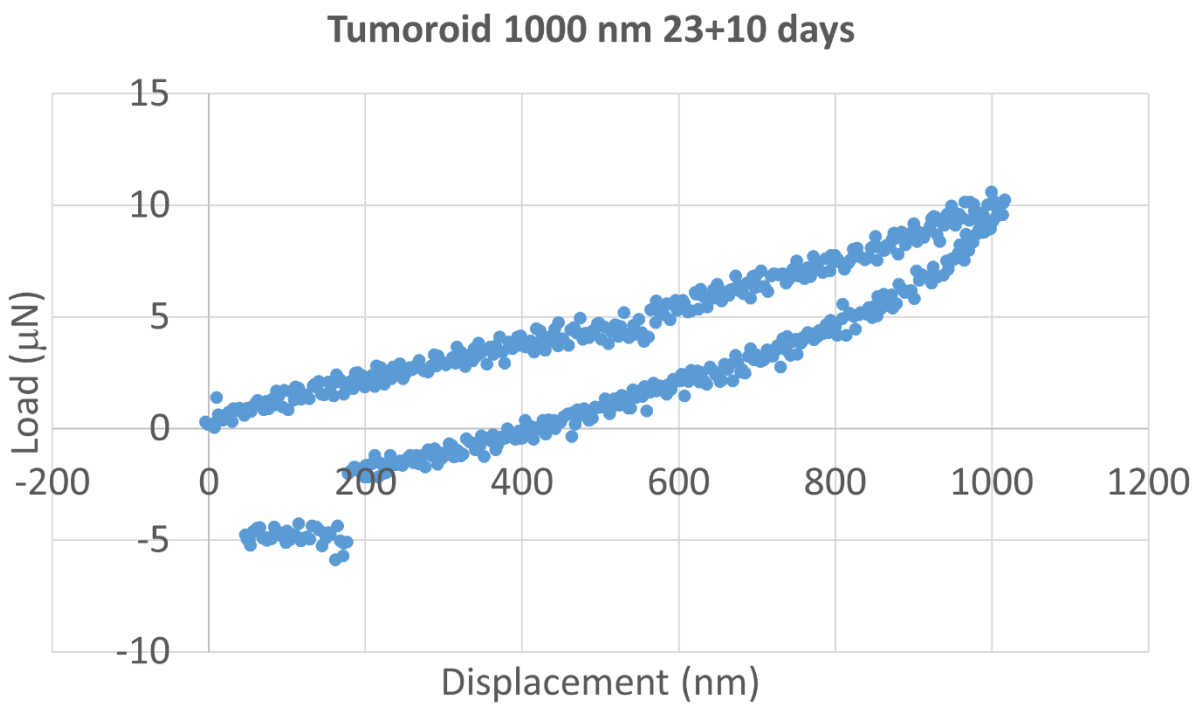

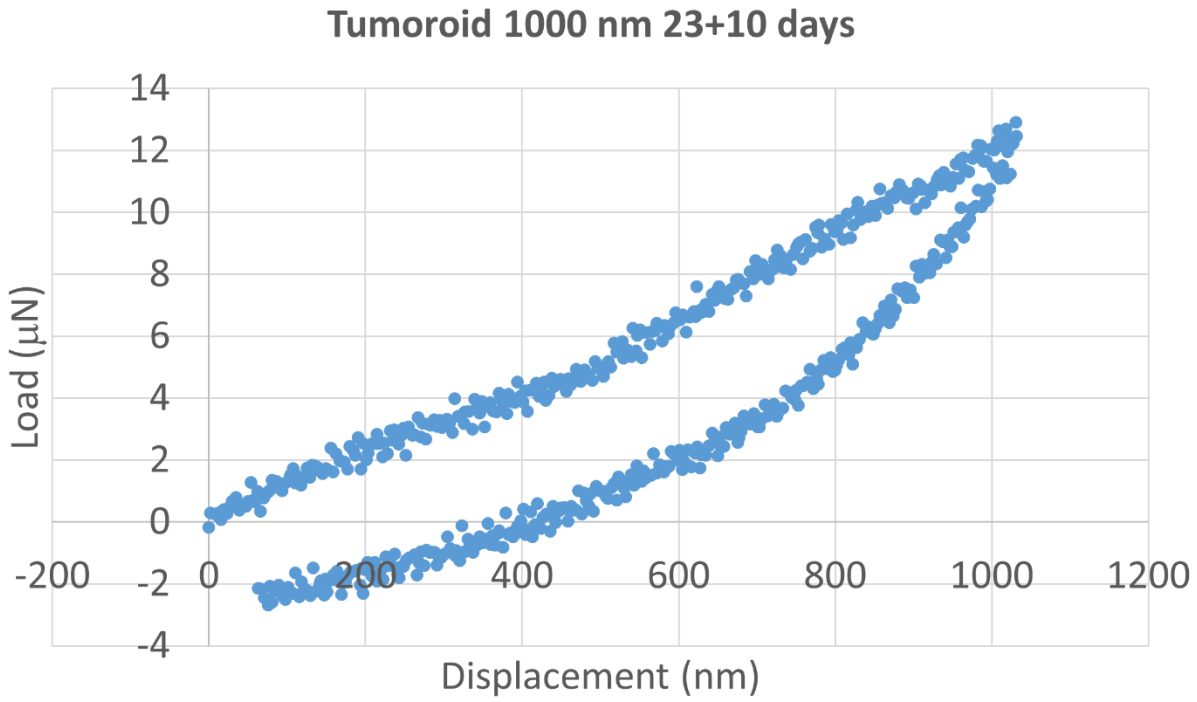

Figure A7. L-D curve on tumoroid at maximum displacement 1000 nm (day 23+10) (Continued).

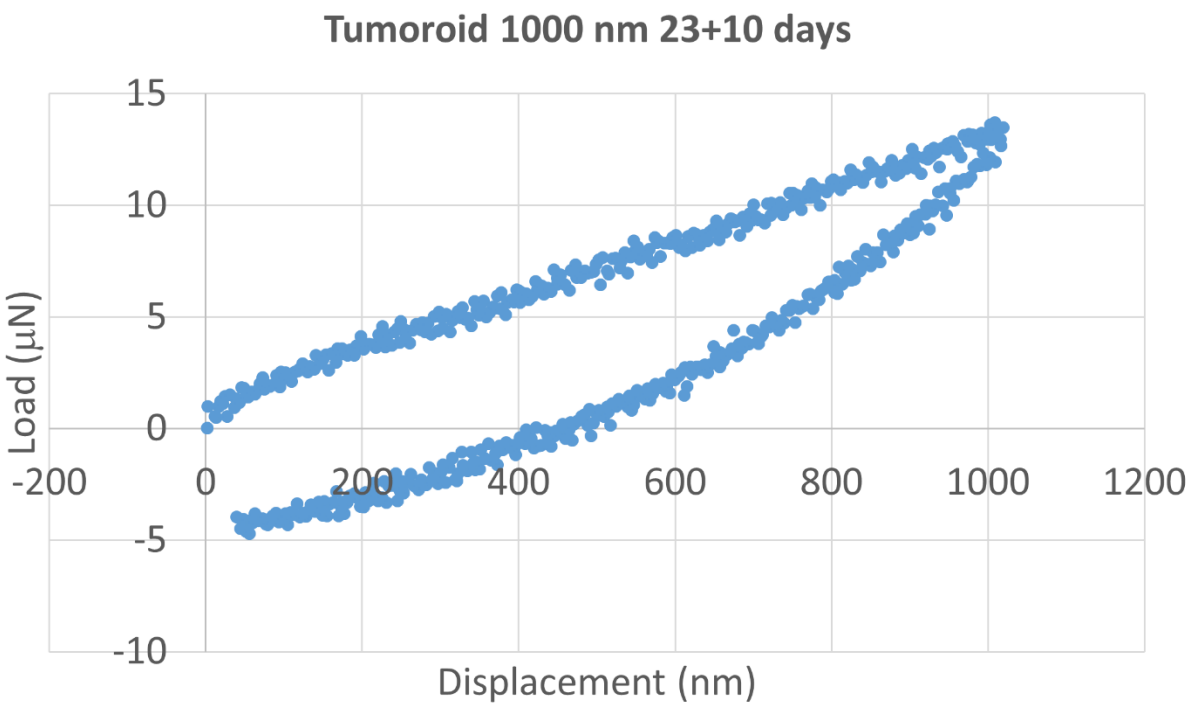

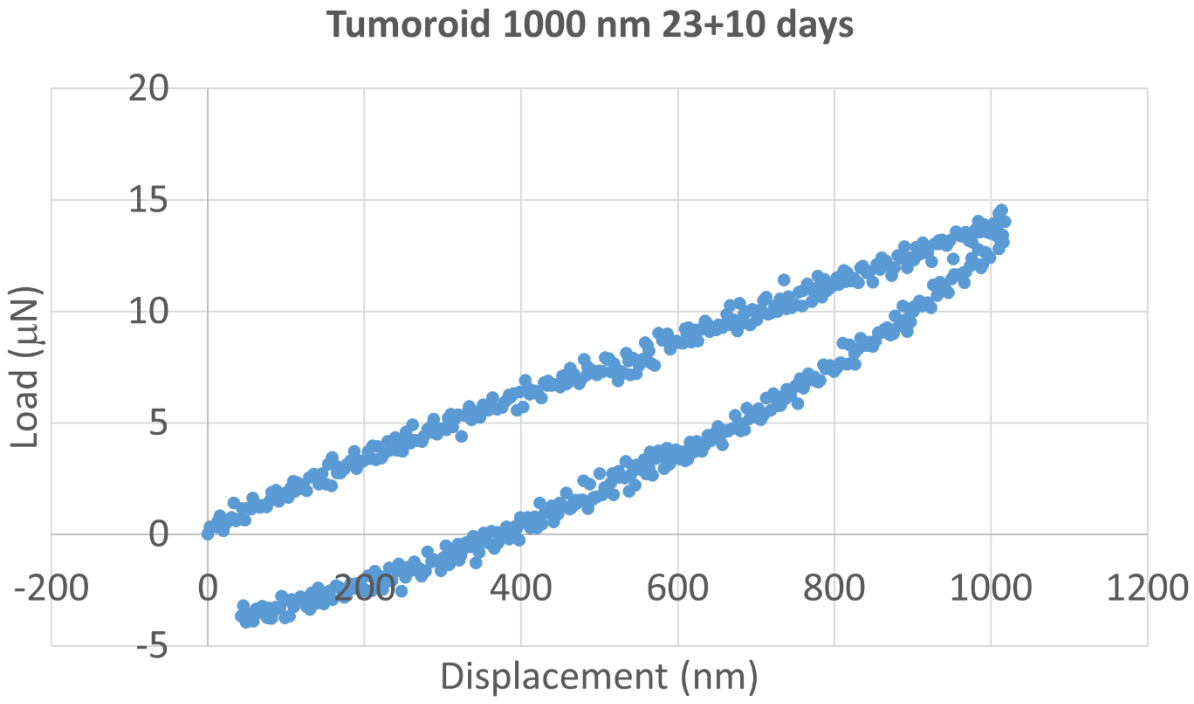

Figure A7. L-D curve on tumoroid at maximum displacement 1000 nm (day 23+10) (Continued).

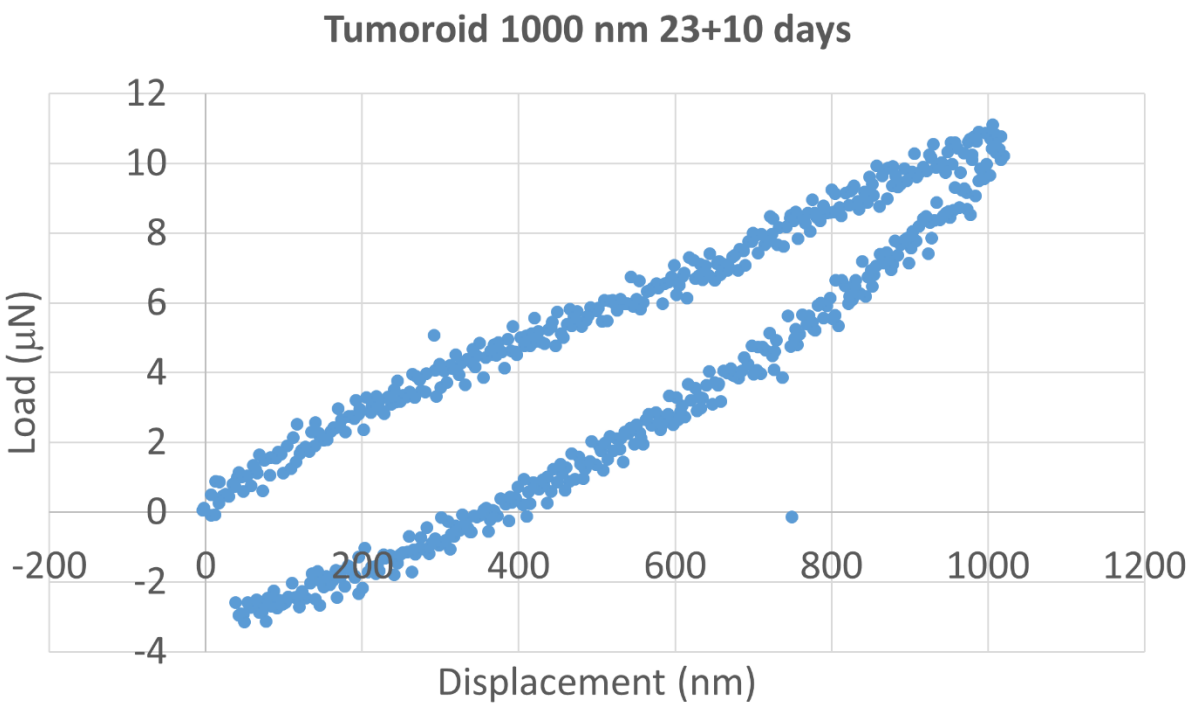

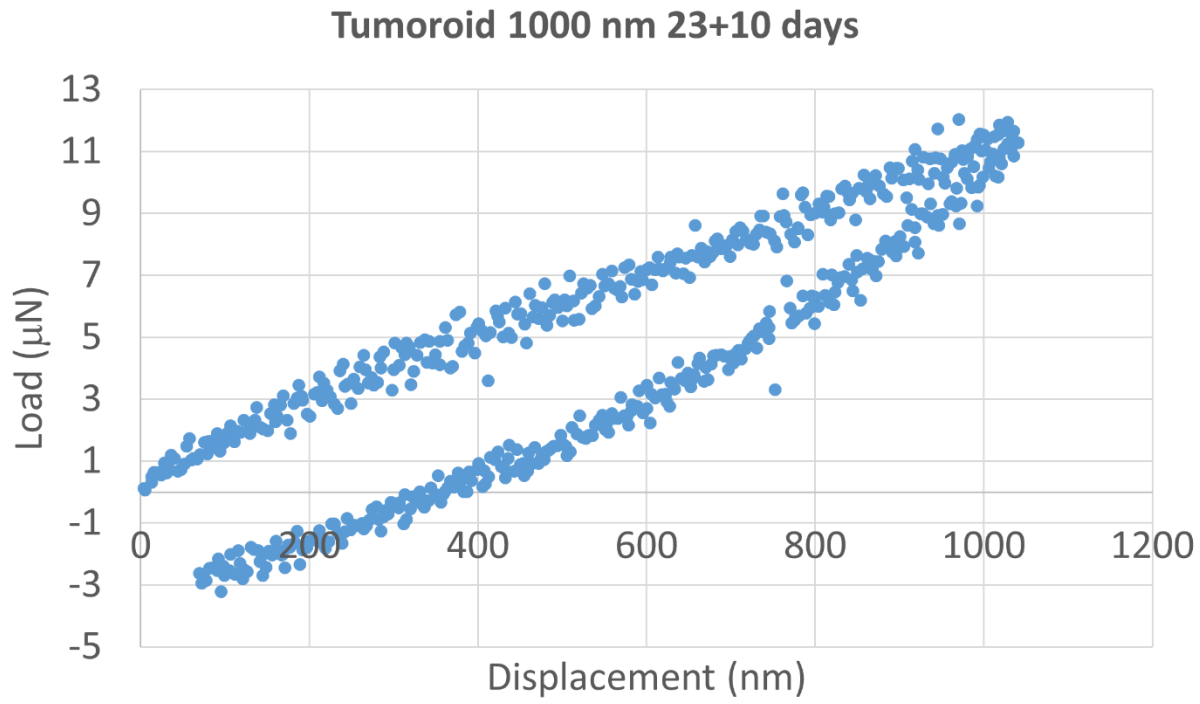

Figure A7. L-D curve on tumoroid at maximum displacement 1000 nm (day 23+10) (Continued).

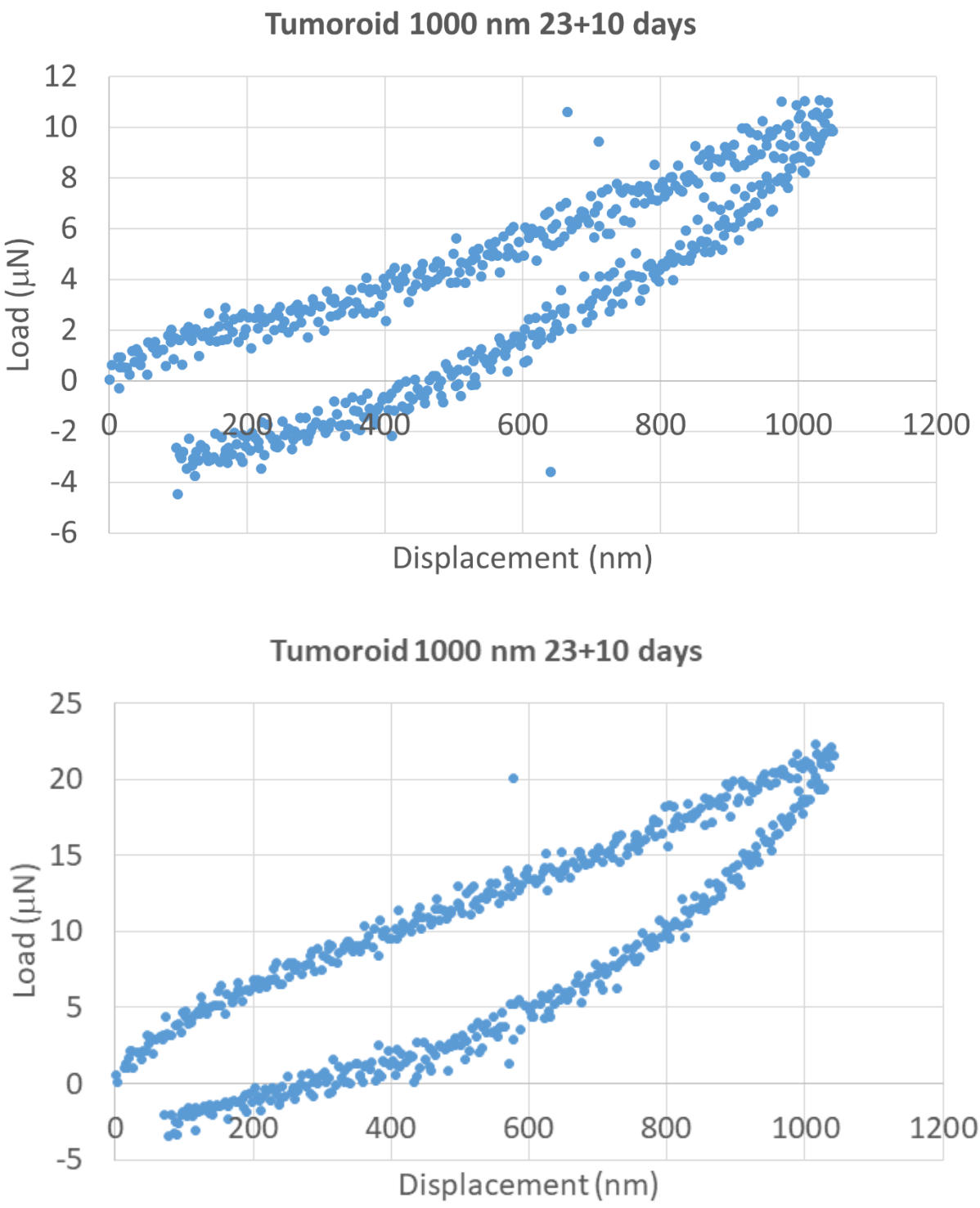

Figure A7. L-D curve on tumoroid at maximum displacement 1000 nm (day 23+10) (Continued).

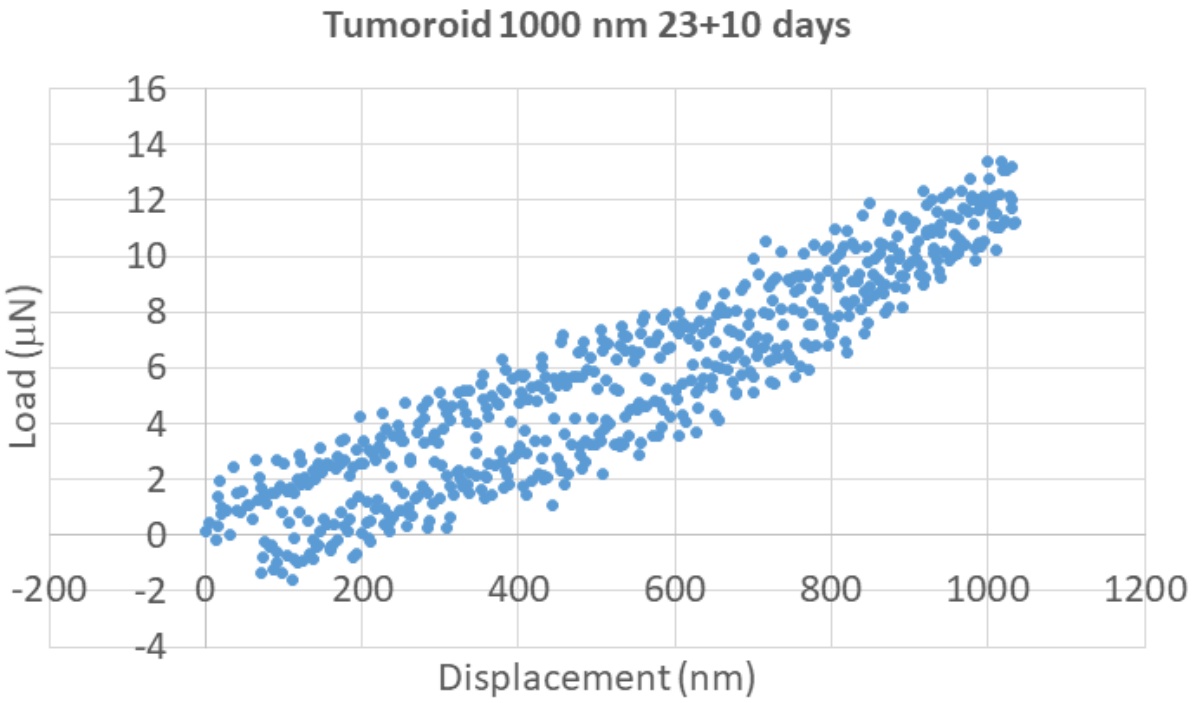

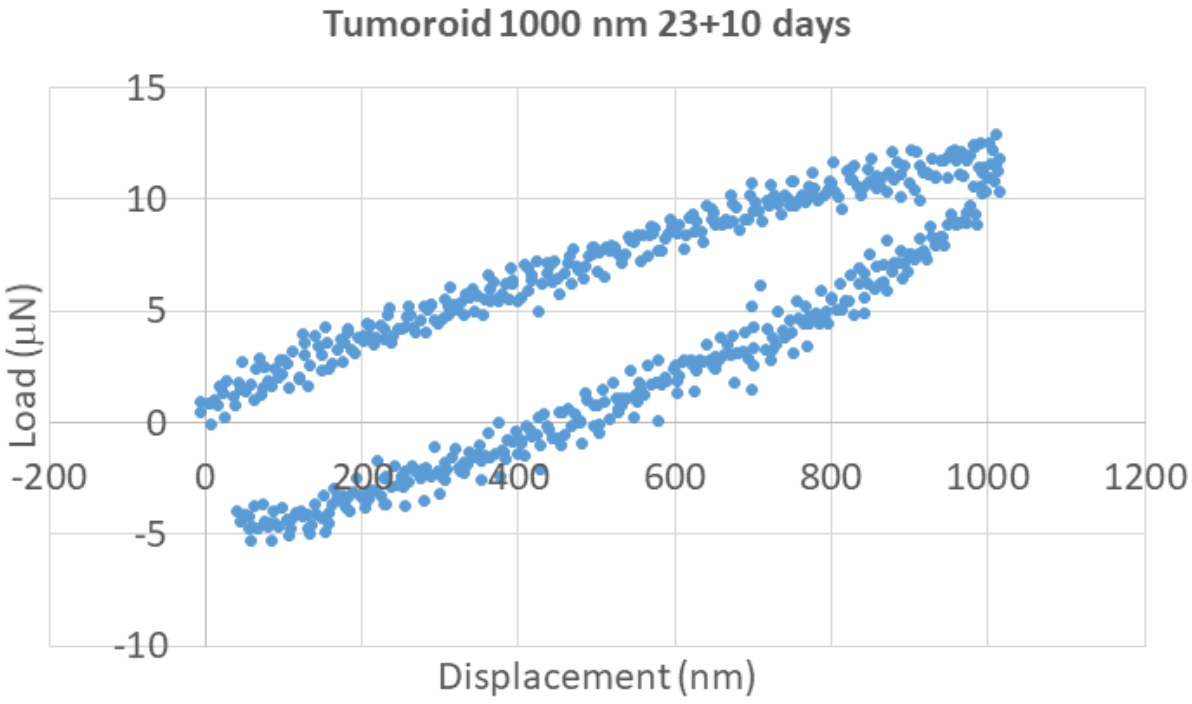

Figure A7. L-D curve on tumoroid at maximum displacement 1000 nm (day 23+10) (Continued).

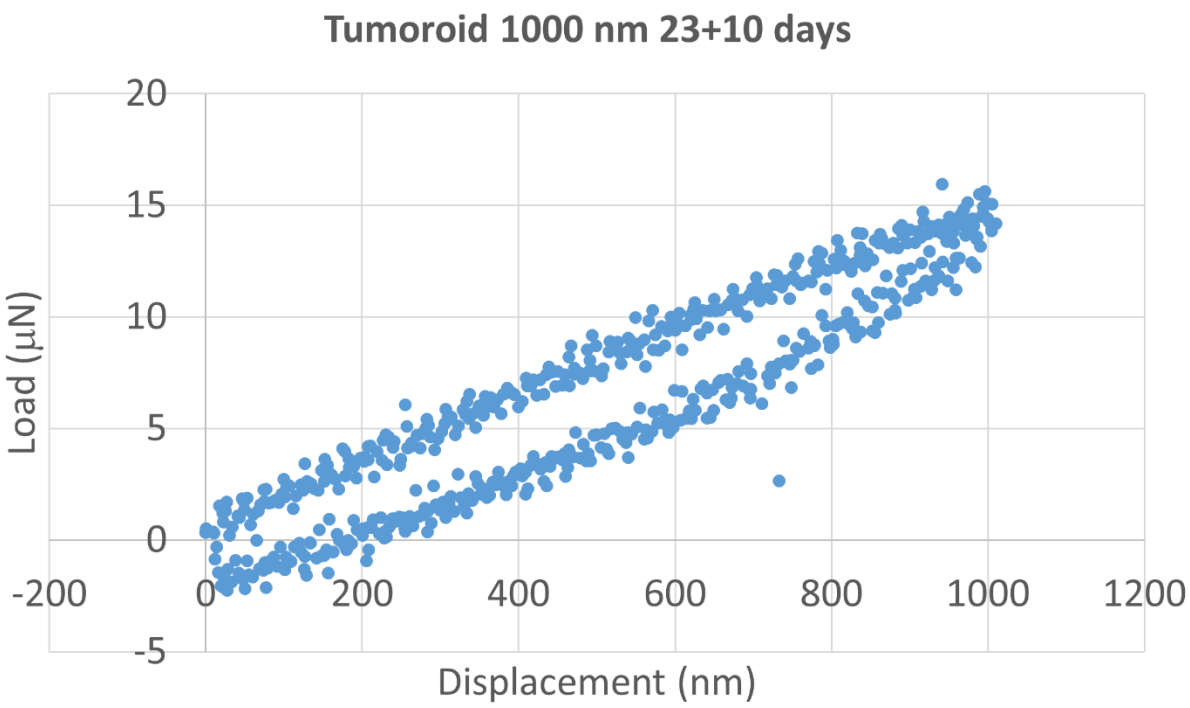

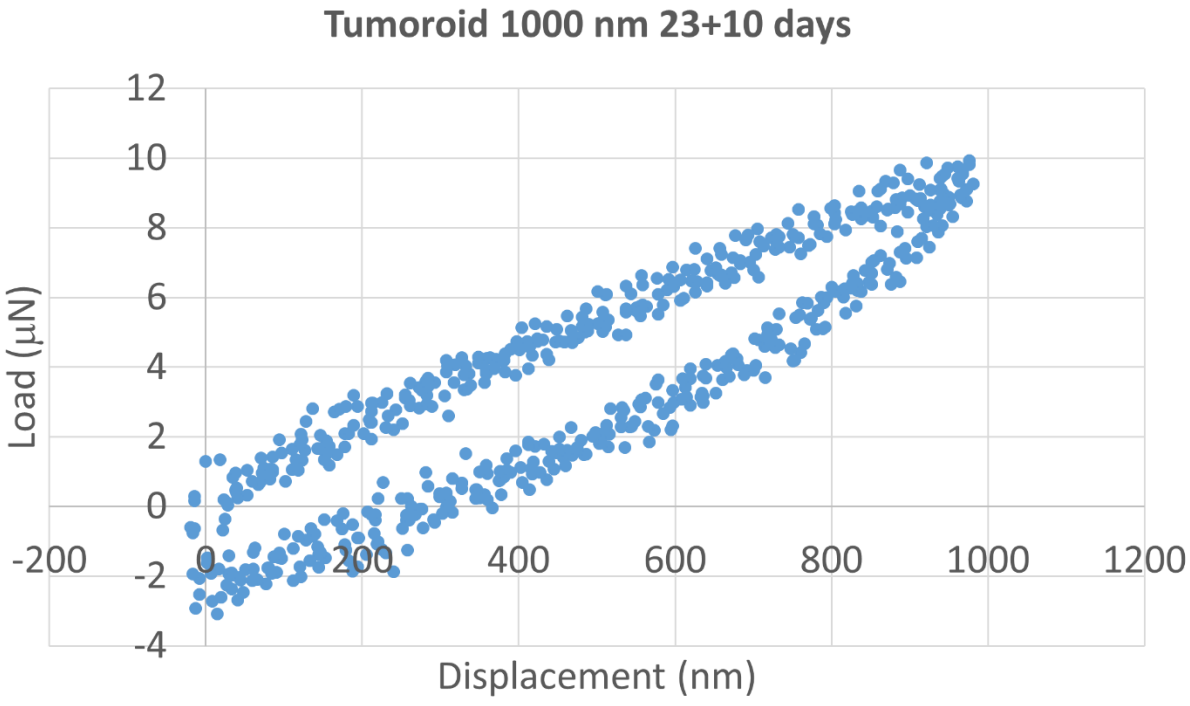

Figure A7. L-D curve on tumoroid at maximum displacement 1000 nm (day 23+10) (Continued).

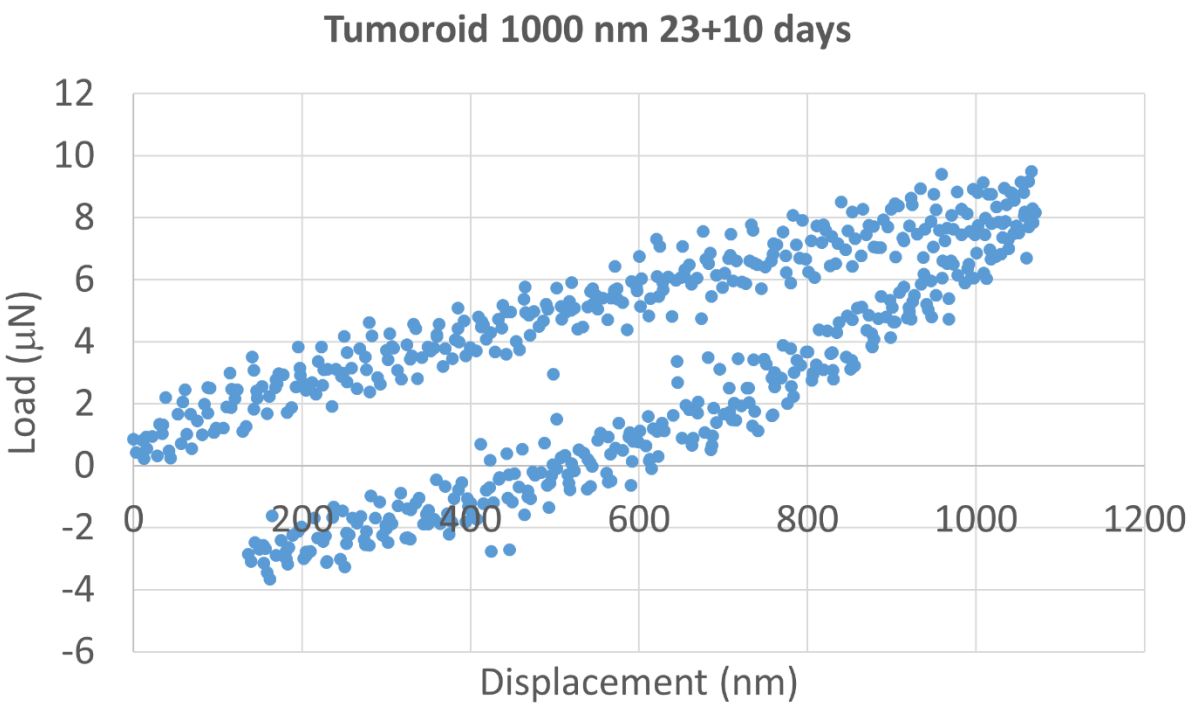

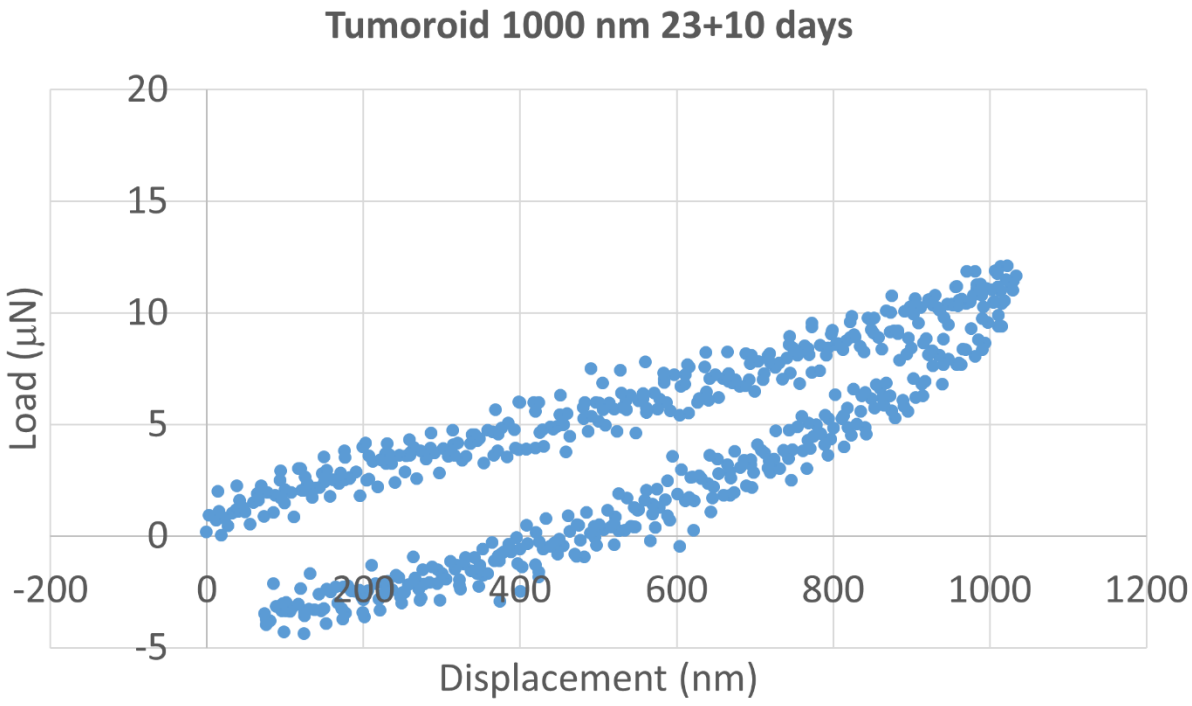

Figure A7. L-D curve on tumoroid at maximum displacement 1000 nm (day 23+10) (Continued).

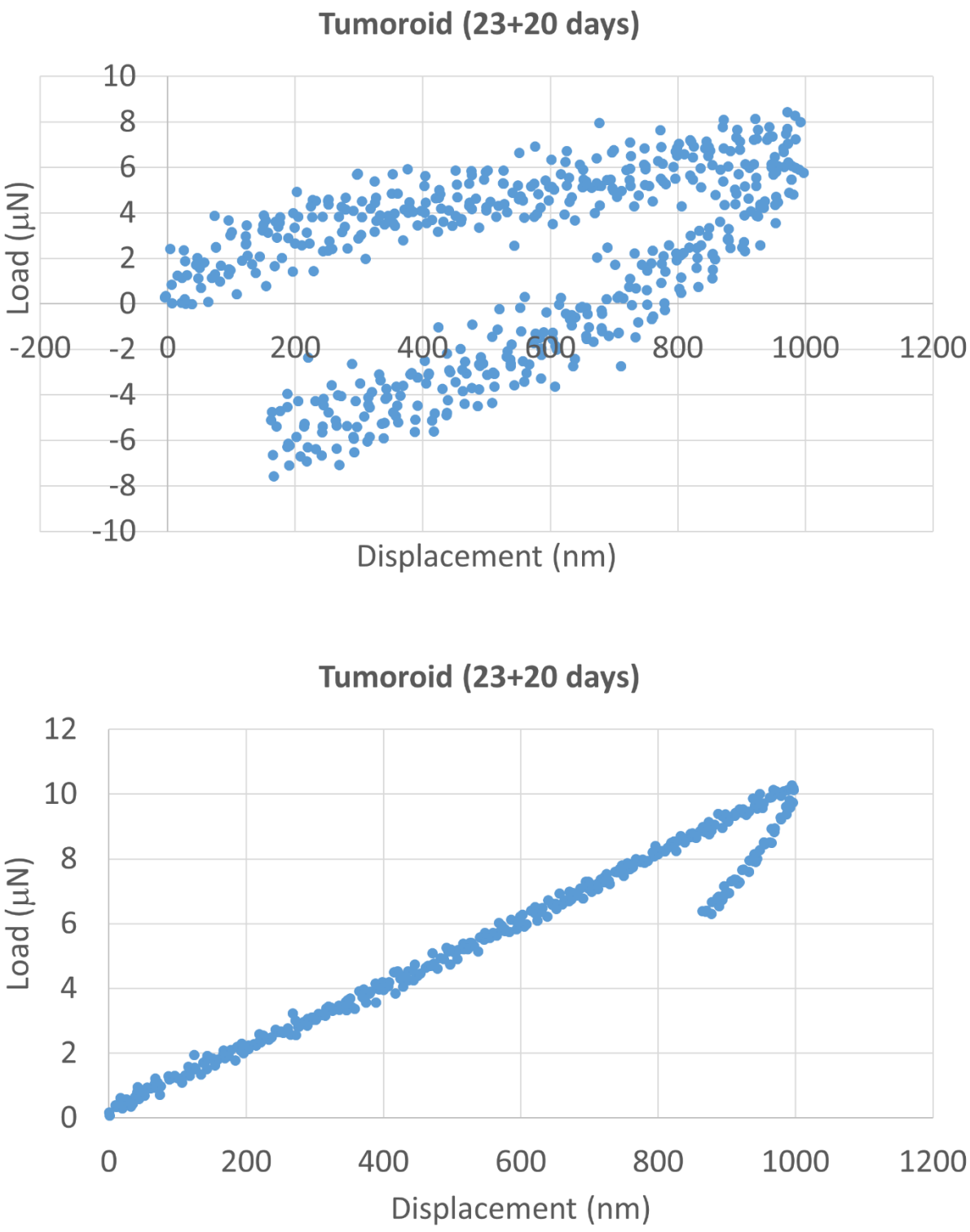

Figure A8. L-D curve on tumoroid at maximum displacement 1000 nm (day 23+20).

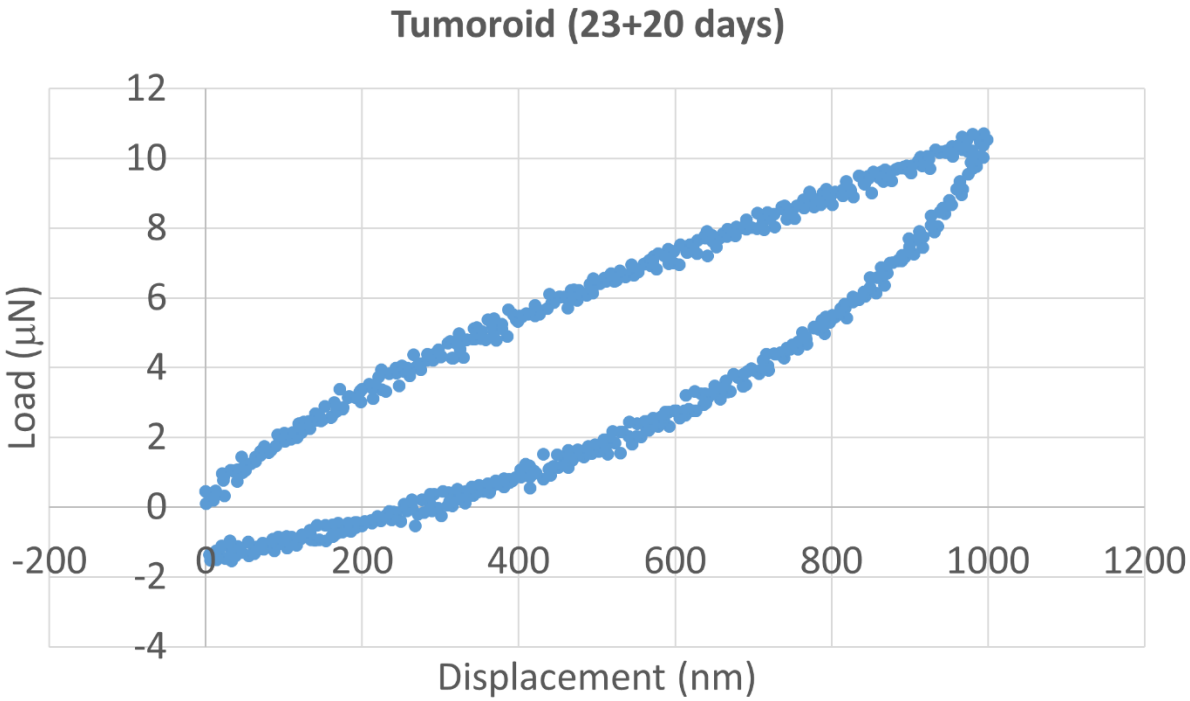

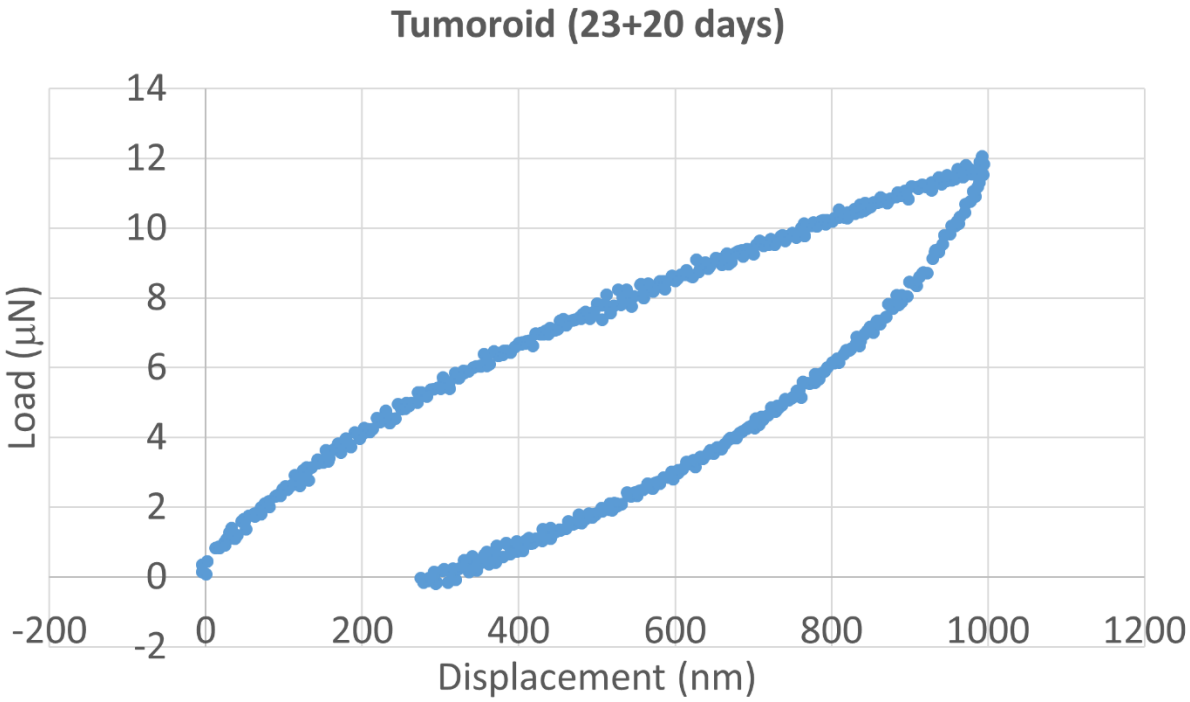

Figure A8. L-D curve on tumoroid at maximum displacement 1000 nm (day 23+20) (Continued).

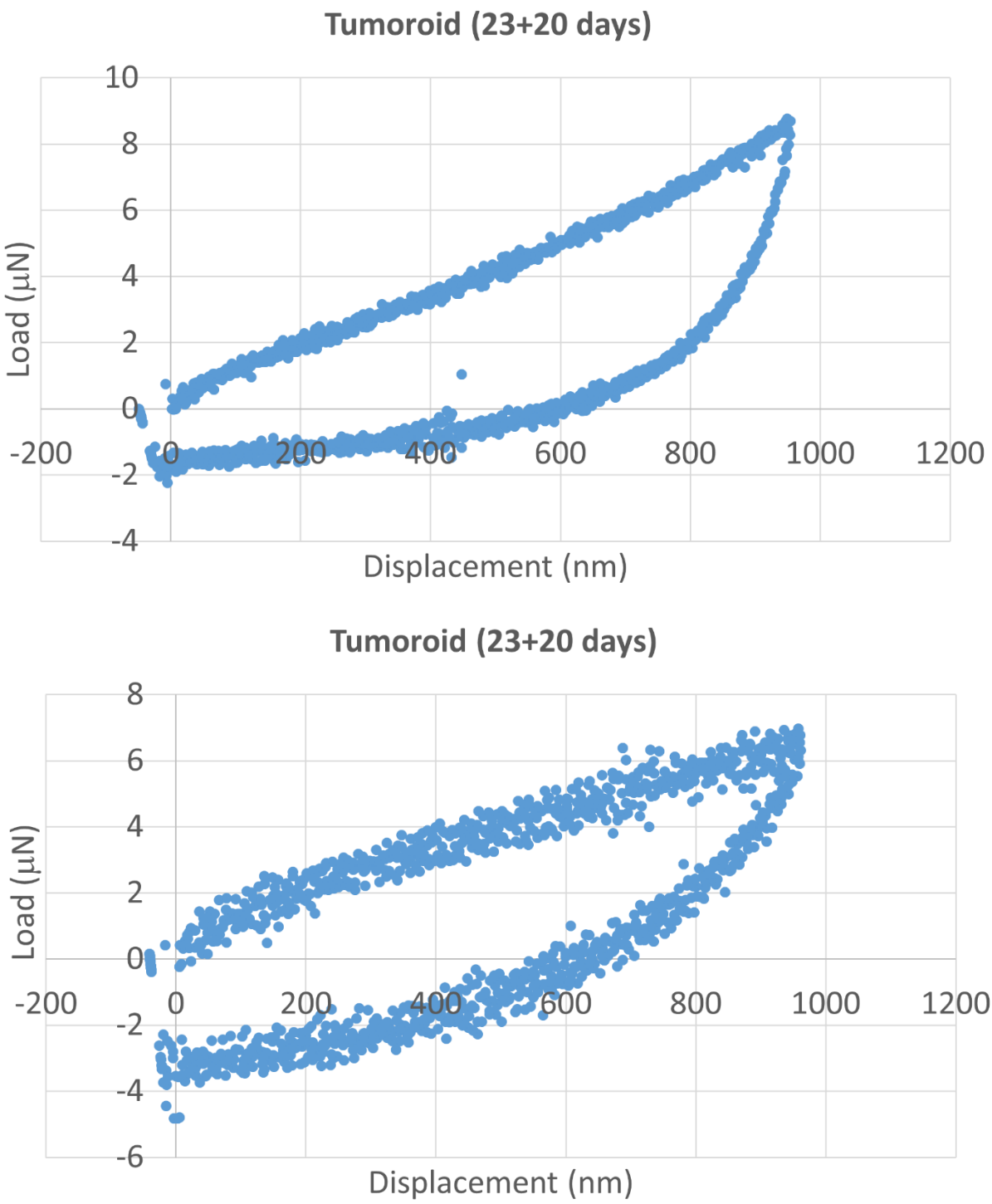

Figure A8. L-D curve on tumoroid at maximum displacement 1000 nm (day 23+20) (Continued).

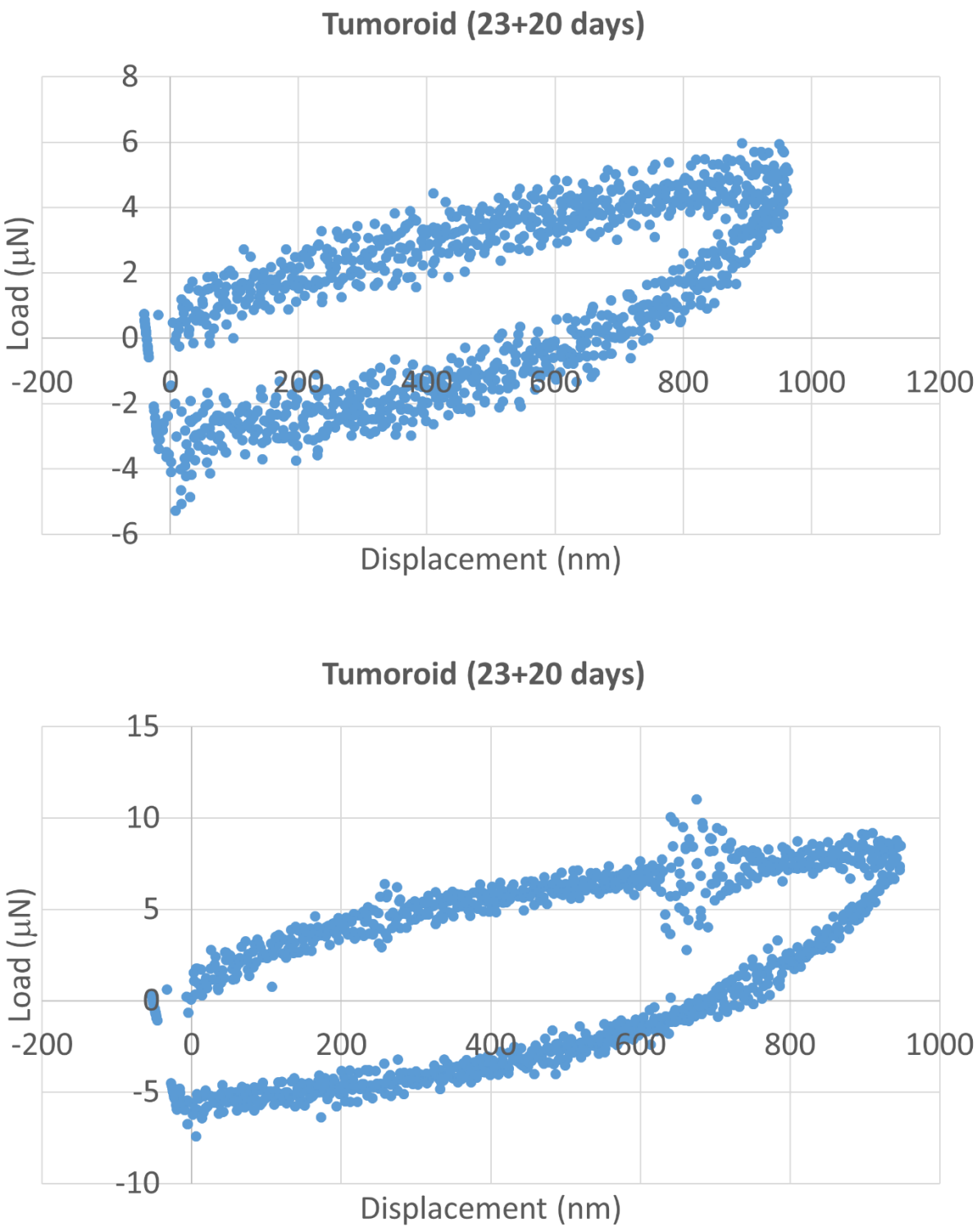

Figure A8. L-D curve on tumoroid at maximum displacement 1000 nm (day 23+20) (Continued).

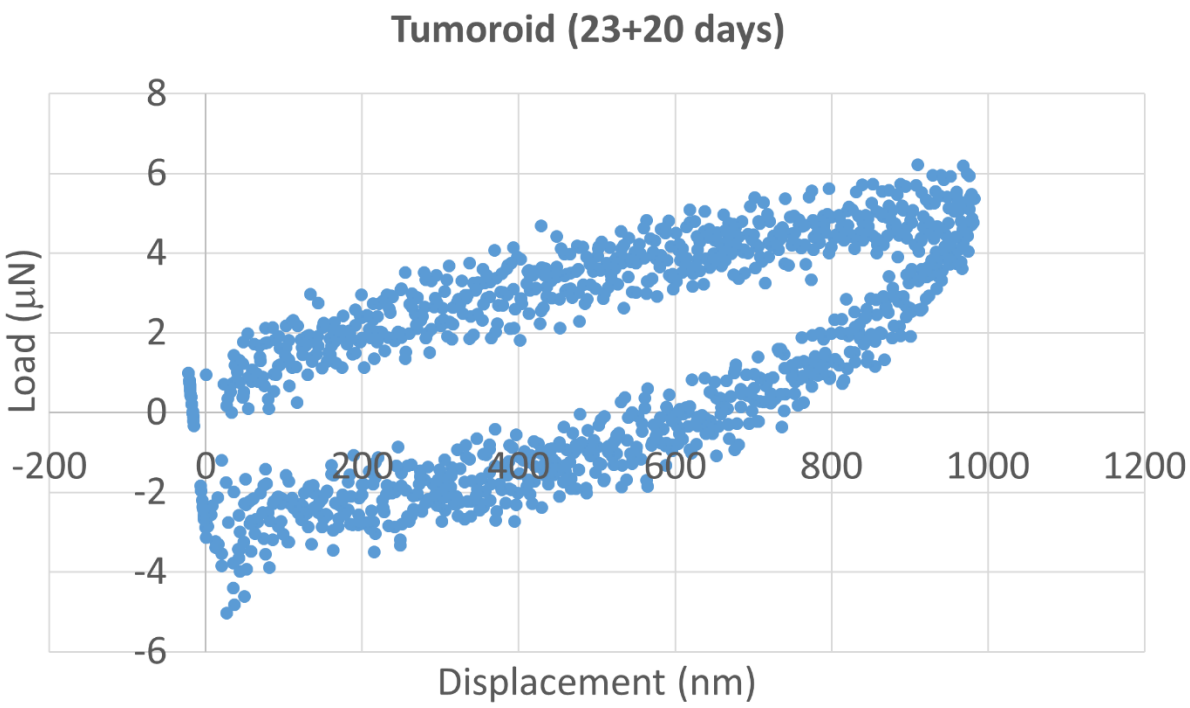

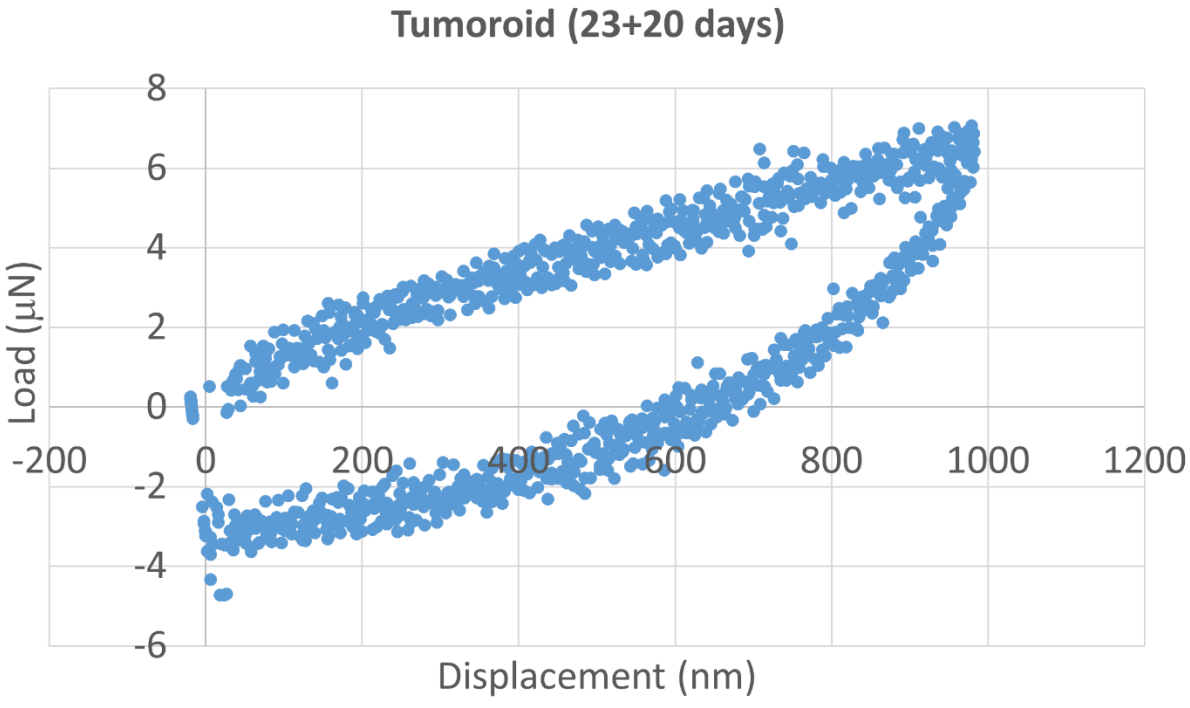

Figure A8. L-D curve on tumoroid at maximum displacement 1000 nm (day 23+20) (Continued).

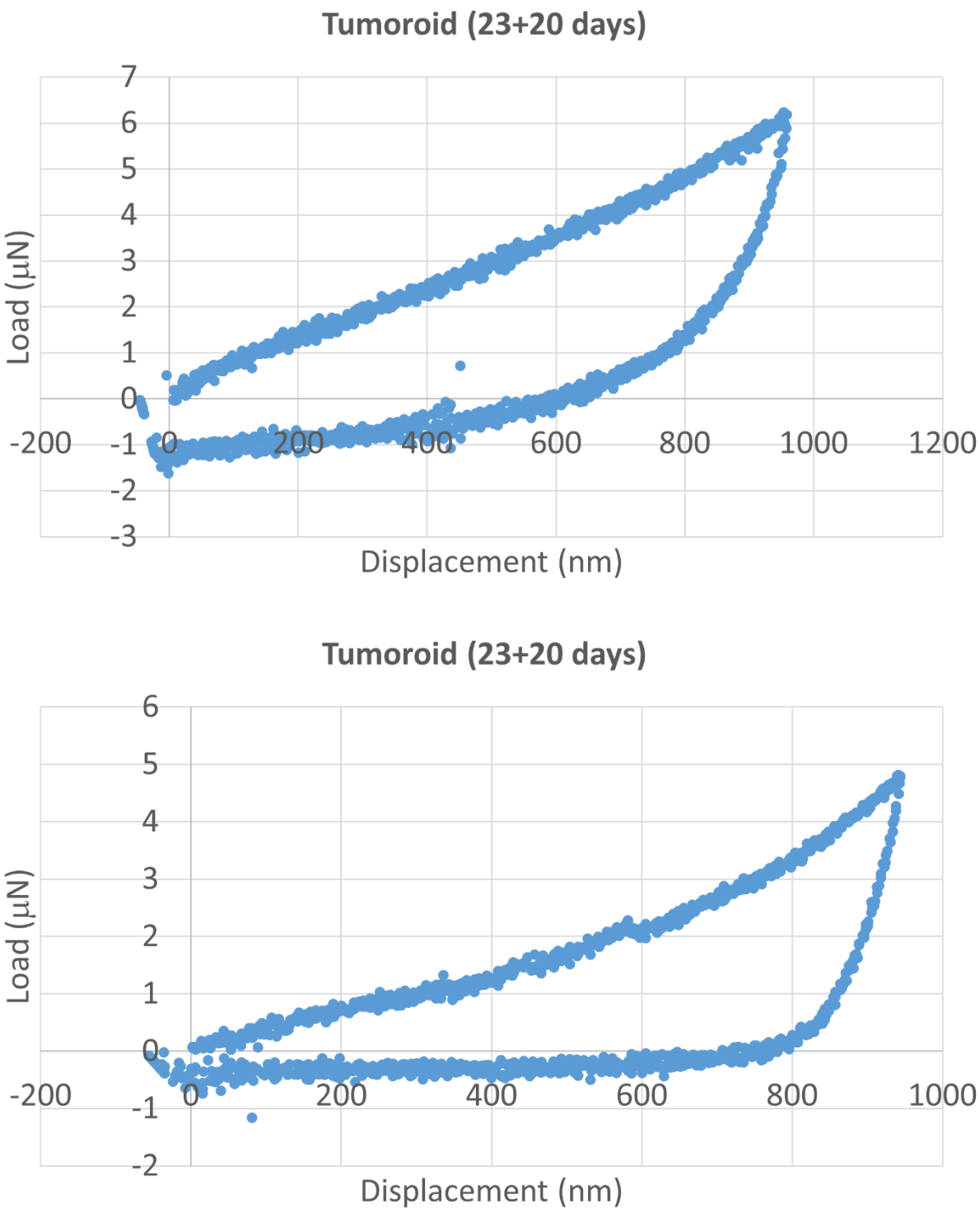

Figure A8. L-D curve on tumoroid at maximum displacement 1000 nm (day 23+20) (Continued).

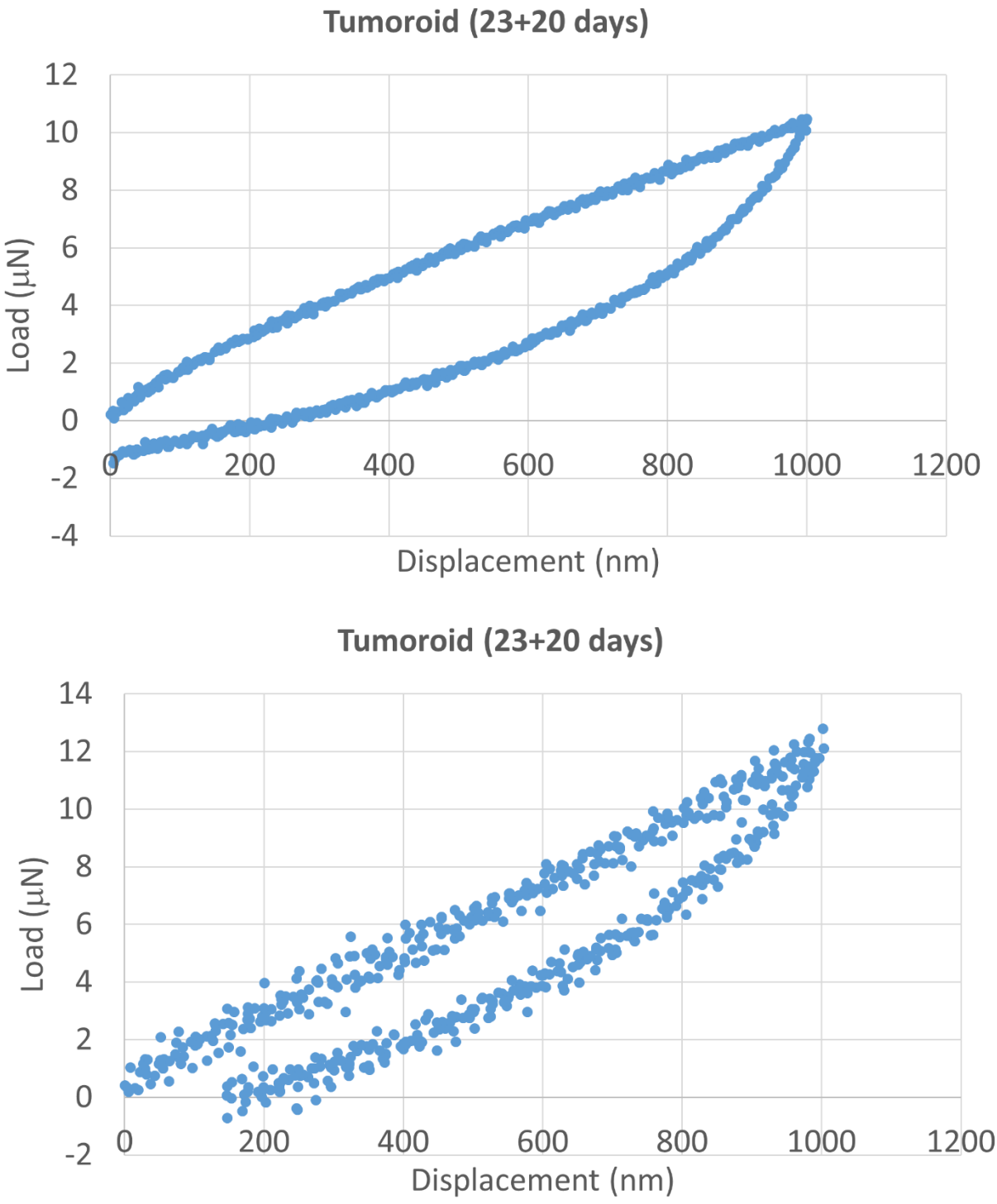

Figure A8. L-D curve on tumoroid at maximum displacement 1000 nm (day 23+20) (Continued).

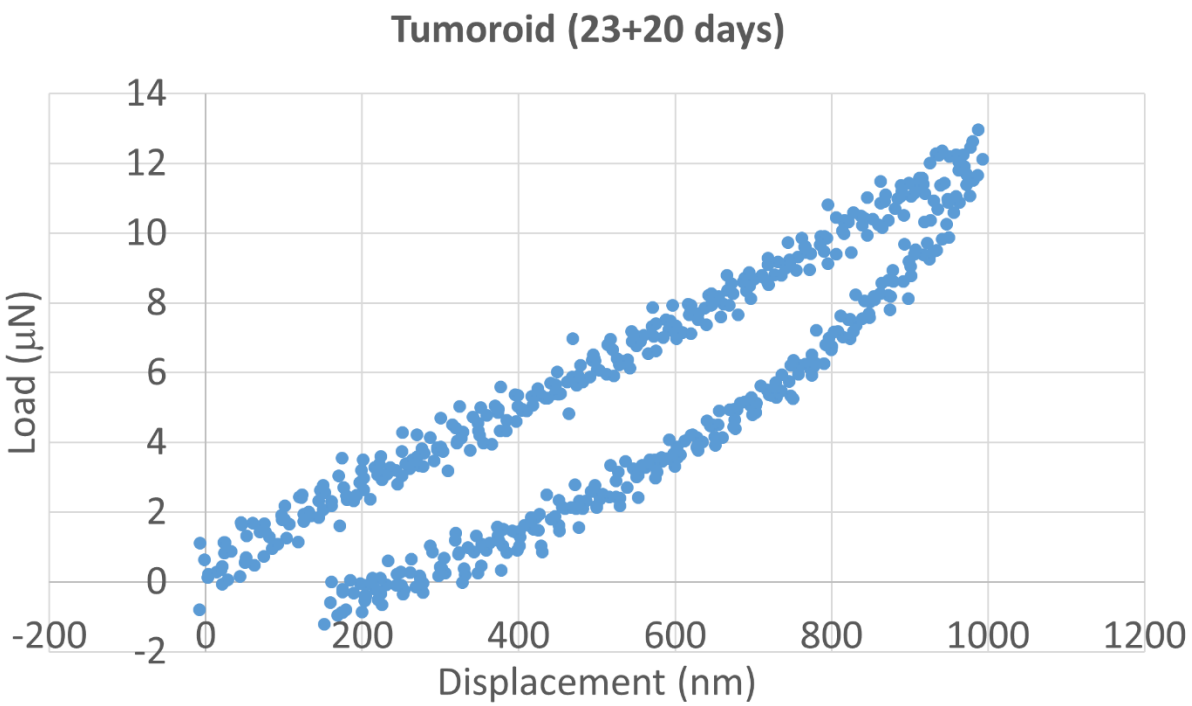

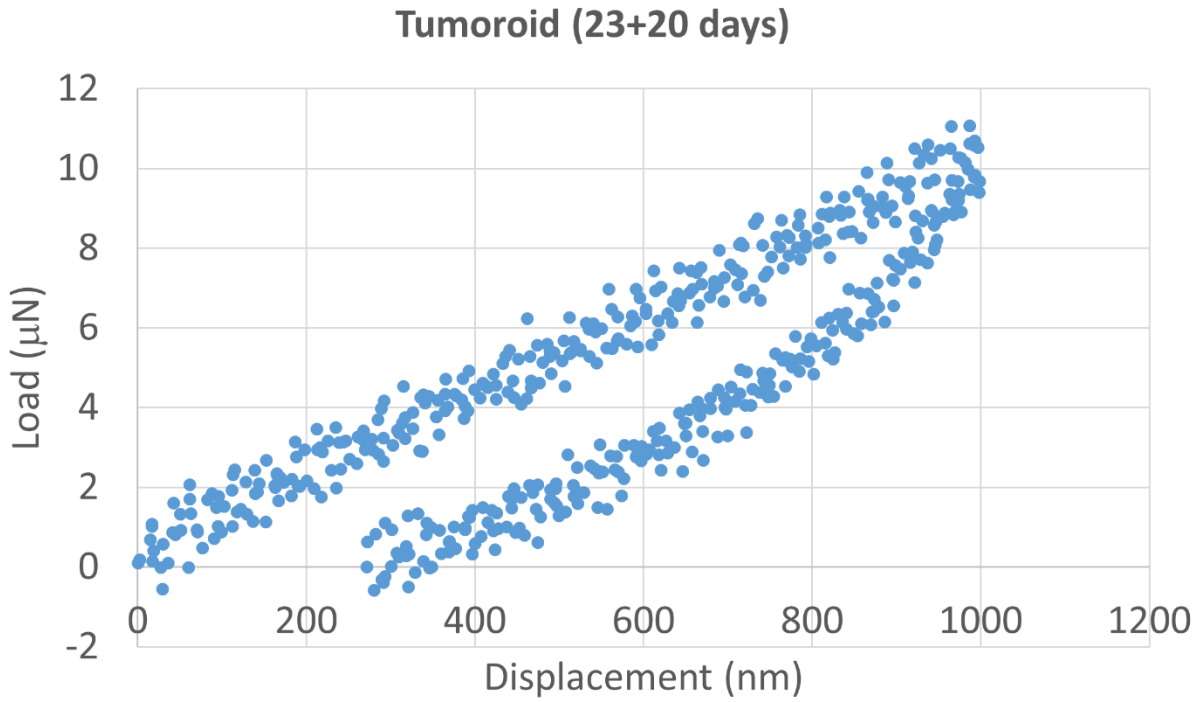

Figure A8. L-D curve on tumoroid at maximum displacement 1000 nm (day 23+20) (Continued).

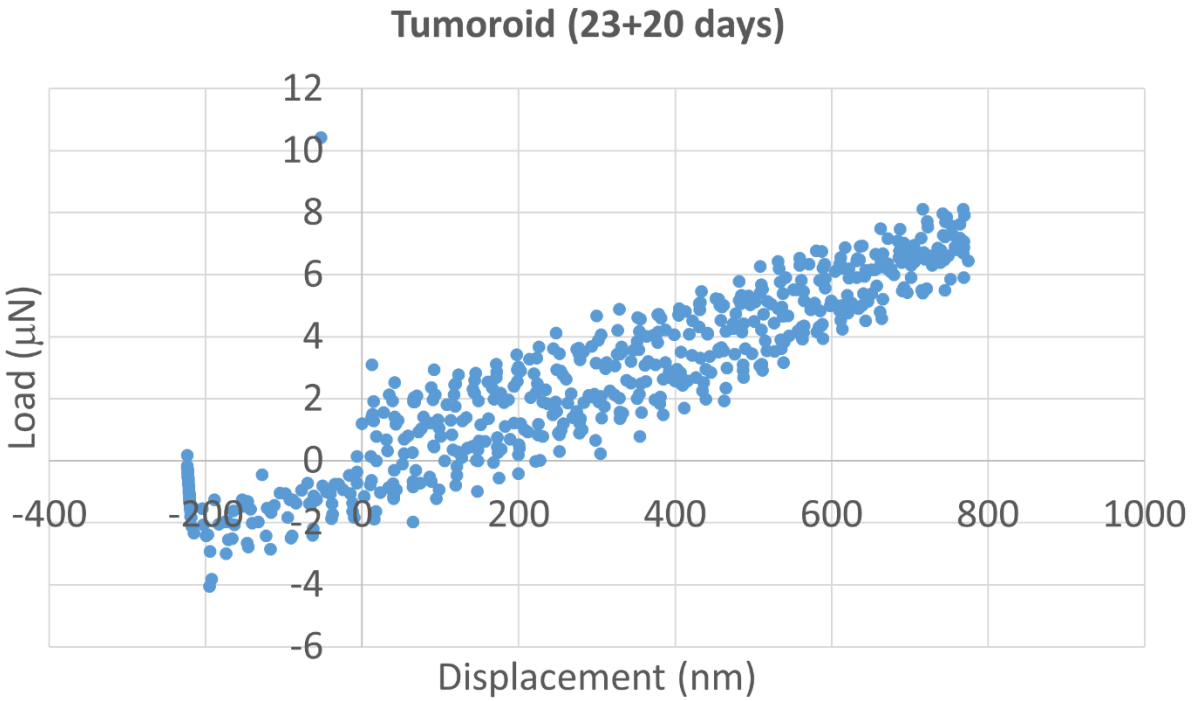

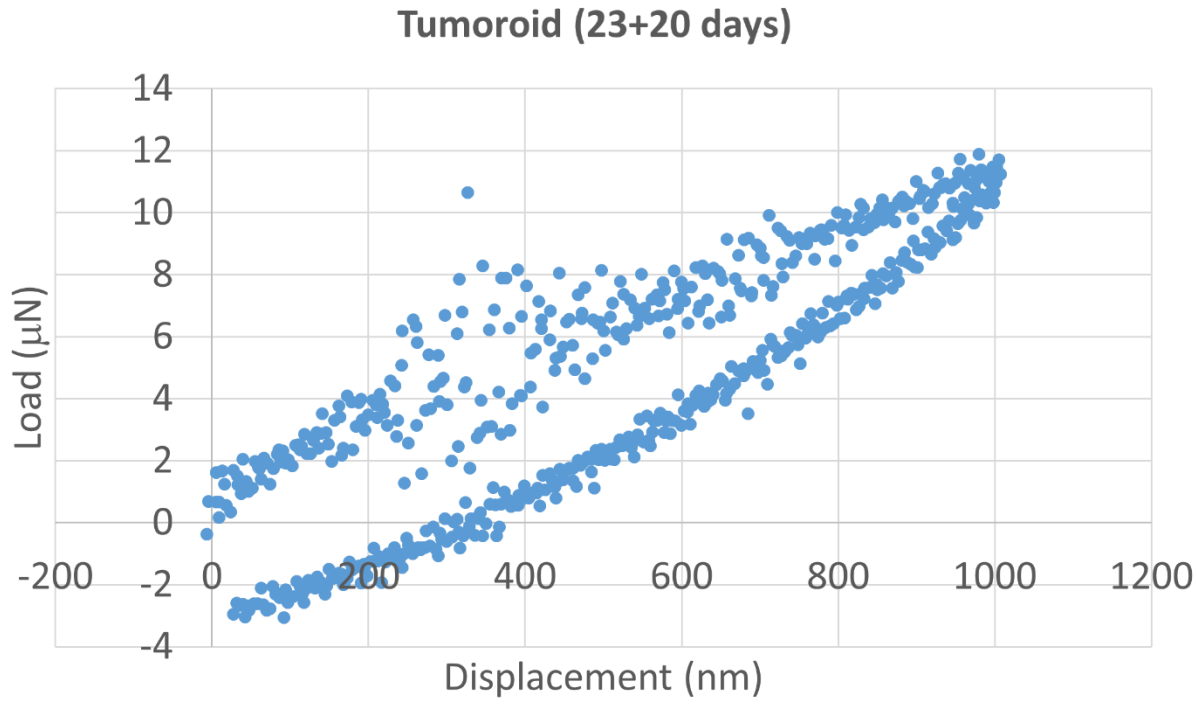

Figure A8. L-D curve on tumoroid at maximum displacement 1000 nm (day 23+20) (Continued).

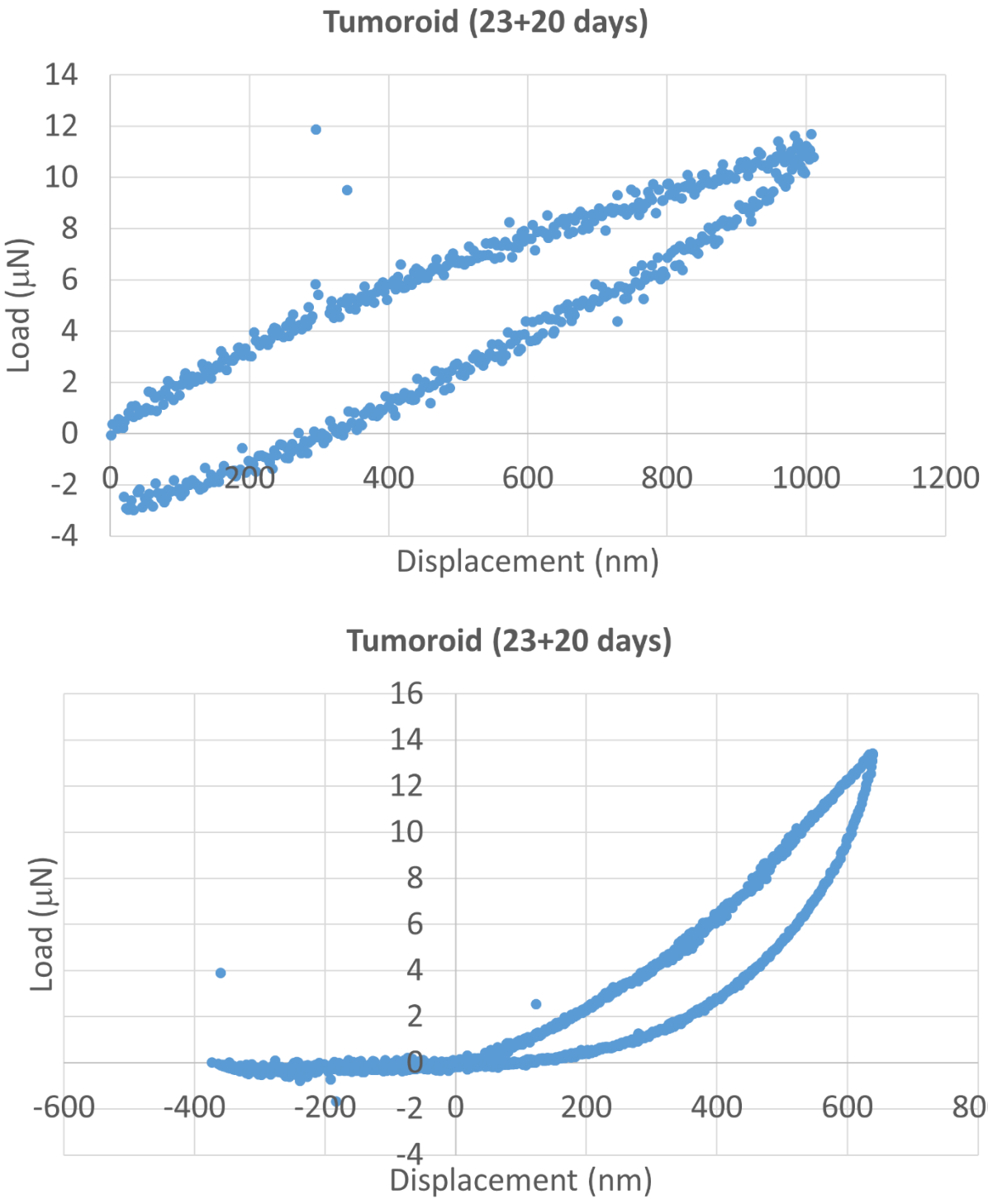

Figure A8. L-D curve on tumoroid at maximum displacement 1000 nm (day 23+20) (Continued).

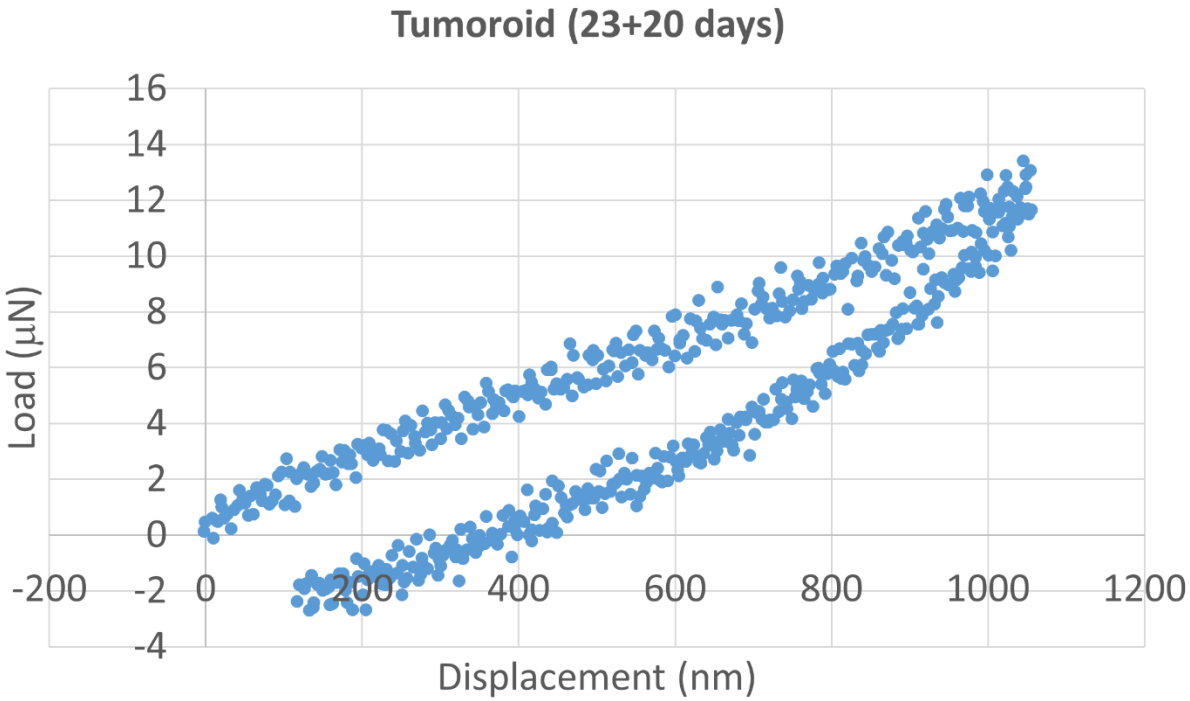

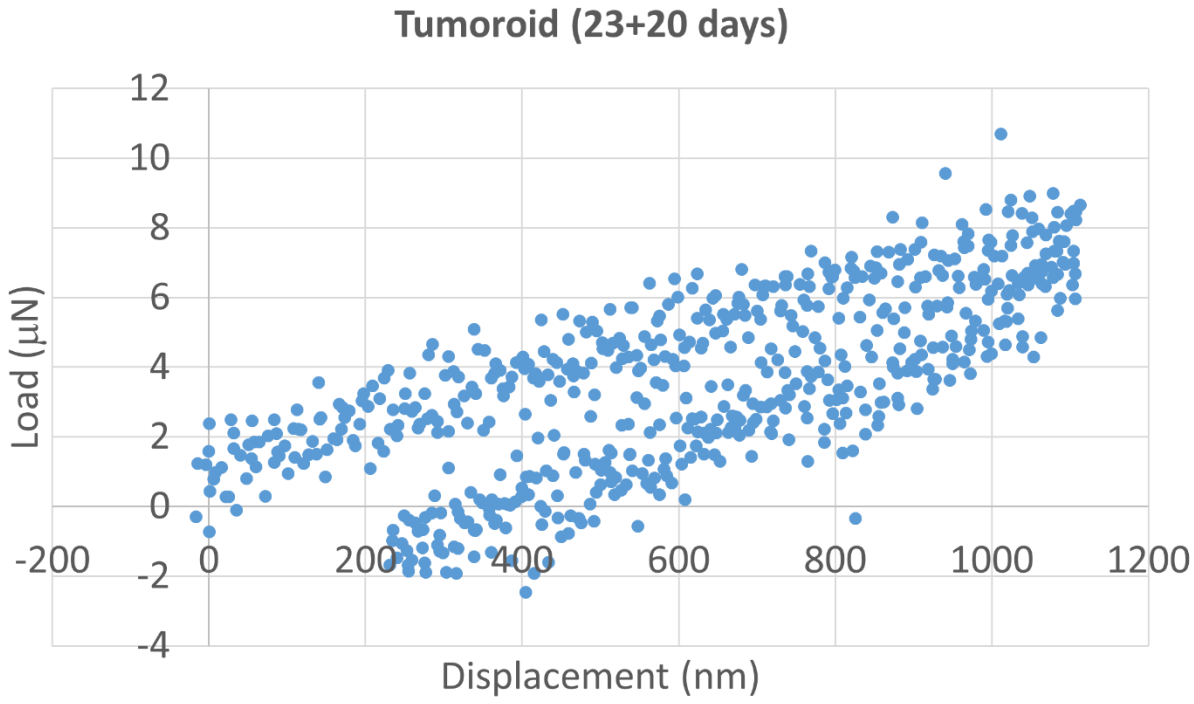

Figure A8. L-D curve on tumoroid at maximum displacement 1000 nm (day 23+20) (Continued).